Development of Nanogel Templated and Sustainable Nanomaterials for Environmental Applications

by

Jiaxin Xu

A thesis
presented to the University of Waterloo
in fulfillment of the
thesis requirement for the degree of
Doctor of Philosophy
in
Chemical Engineering (Water)

Waterloo, Ontario, Canada, 2022
© Jiaxin Xu 2022

Examining Committee Membership

The following served on the Examining Committee for this thesis. The decision of the Examining Committee is by majority vote.

External Examiner	Dr. Lee Wilson Professor Department of Chemistry, University of Saskatchewan
Supervisor	Dr. Michael K.C. Tam Professor Department of Chemical Engineering, University of Waterloo
Internal Member	Dr. Xianshe Feng Professor Department of Chemical Engineering, University of Waterloo
Internal Member	Dr. Michael Pope Associate Professor Department of Chemical Engineering, University of Waterloo
Internal-external Member	Dr. Wayne Parker Full Professor Department of Civil and Environmental Engineering, University of Waterloo

Author's Declaration

This thesis consists of material all of which I authored or co-authored: see Statement of Contributions included in the thesis. This is a true copy of the thesis, including any required final revisions, as accepted by my examiners.

I understand that my thesis may be made electronically available to the public.

Statement of Contributions

Chapter 3 of this thesis consists of a manuscript that was co-authored by myself, my supervisor, Dr. Michael Tam, and three PhD students, Yi Wang, Weinan Zhao, and Lian Han. I wrote the entire manuscript, and planned and executed the experiments, Yi Wang executed some of the experiments related to the DLS measurements, Weinan assisted in the execution of some experiments related to titration, and Lian conducted some TEM imaging experiments.

Chapter 4 of this thesis consists of a paper published in the "Journal of Industrial and Engineering Chemistry" that was co-authored by myself, my supervisor, Dr. Michael Tam, undergraduate student, Yuan Tian and three collaborators (Zibiao Li, Beng Hoon Tan and Yuanting Tang) from the Institute of Materials Research and Engineering, A*STAR (Agency of Science, Technology and Research) in Singapore, who helped with additional characterization of the system. I wrote the entire manuscript, and planned and executed experiments, Yuan Tian assisted in the execution of some experiments related to FMNP development.

Chapter 5 of this thesis consists of a manuscript that was co-authored by myself, my supervisor, Dr. Michael Tam, and three PhD students, Yi Wang, Weinan Zhao, and Lian Han. I wrote the entire manuscript, and planned and executed the experiments, Yi Wang executed some of the experiments related to particle size measurements, Weinan assisted in the execution of some experiments related to adsorption isotherm, and Lian conducted some TEM imaging experiments.

Chapter 6 of this thesis consists of a paper published in "Journal of Colloidal and Interface Science" that was co-authored by myself, my supervisor, Dr. Michael Tam, a former postdoc, Mohankandhasamy Ramasamy and two PhD students, Yi Wang, Weinan Zhao, and one undergraduate student, Teresa Tang. I wrote the entire manuscript, and planned and executed the experiments, Dr. Ram performed the antimicrobial tests, Yi Wang and Weinan assisted in the

execution of some experiments related to fluorescence microscope, and Teresa assisted with yeast test experiments.

Chapter 7 of this thesis consists of a manuscript that was co-authored by myself, my supervisor, Dr. Michael Tam and three PhD students, Yi Wang, Weinan Zhao, and Lian Han. I wrote the entire manuscript, and planned and executed the experiments, Yi Wang assisted with the synthesis of the material, Weinan assisted in the execution of some experiments related to catalytic reduction, and Lian conducted some TEM imaging.

Chapter 8 of this thesis consists of a manuscript that was co-authored by myself, my supervisor, Dr. Michael Tam and one research associate, Fatemah Haji, Dr. Chong Meng, Master student Hanyoung Choi, Dr. Chunxia Tang, Xiaoming Zhou, Gaili Cao. I wrote the entire manuscript, and planned and executed the experiments, Fatemah assisted with some experiments, Dr. Meng assisted with the SEM, Hanyoung conducted membrane preparation and gravity filtration, Dr. Tang provided her experience related to the membrane fabrication, Xiaoming Zhou and Gaili Cao assisted with dynamic filtration experiments.

Abstract

Water treatment is continuously attracting attentions due to its important role in providing secure water supplies for human activities. In this thesis, various advanced nanomaterials were developed and demonstrated in several environmental applications, including adsorption, catalytic and membrane filtration processes. Nanogel templating strategy and sustainable nanomaterial enhanced all the processes from the perspectives of size and morphology control, improved catalytic performance, and enhanced porosity of the membrane. Nanogel, as a colloidal based soft material formed by physical or chemical crosslinking to form a 3-D network to yield polymeric particle. It has many advantages, such as, stability, biocompatibility, stimuli-responsive property and ease of modification through the functional groups. Thus, the nanogel possessed promising potential as a templating scaffold to prepare metallic clusters. Wood, as one of the most abundant natural materials existed in earth can be processed to produce different types of wood derivatives like cellulose nanocrystals (CNC) and soft wood fiber used in this doctoral study. Cellulose based nanomaterials possess excellent mechanical property, high colloidal stability, large surface area and can be readily modified via the abundant hydroxyl groups on their surface. Thus, CNC was used as a supporting matrix to prepare noble metallic particles without sacrificing their catalytic performance. CNCs possessed high aspect ratio that enabled them to be ideal candidates for preparing stable Pickering emulsion. Both the nanogel scaffold and CNC matrix were used to impart different properties to the final system in enhancing the water treatment processes. Nanogel scaffold method was also used as a nano-reactor to prepare silver clusters for antimicrobial and bio-labelling applications.

pH-responsive nanogel was fabricated by crosslinking methacrylate acid (MAA) and ethyl acrylate (EA) with diallyl phthalates (DAP) via a conventional semi-continuous emulsion

polymerization technique. Highly reproducible nanogels with different monomer ratios and crosslinking degree were prepared, and various characterizations were used to investigate the physicochemical properties, including morphology, shape factor, particle size, surface charge, pKa, quantification of carboxyl groups and swelling ratio. A “S” and “U” shaped profiles for particle size and zeta potential versus pH were observed for the 50:50 MAA-EA nanogel crosslinked with various DAPs respectively. Monodispersed nanogel was observed from TEM images and the pH responsive property was observed for the particle size variation with pHs. More carboxyl groups were recorded as more MAA was added during the nanogel synthesis, and a similar amount of carboxyl groups was found for the 50:50 MAA crosslinked with various amounts of DAP. This robust nanogel was successfully synthesized and studies using various characterization methodologies, which allowed the nanogel being used as a nano-reactor to synthesis metal particles or clusters.

The MAA-EA nanogels were used as templates for synthesizing magnetic nanoparticles (MNPs) inside the nanogel and used as templates for the in-situ co-precipitation of Fe^{2+} to produce stable functional magnetic nanoparticles (MNPs) (<500 nm) decorated with beta-cyclodextrin (β-CD) (FMNP). Emulsion polymerization with the controlled addition of monomer mixtures allowed for good size control, and silica coating was introduced to prevent the oxidation of FMNP. The superparamagnetic FMNP with high saturation magnetization (33 emu/g) could be readily separated from water using a high gradient magnetic separator (HGMS). Procaine hydrochloride (PrHy) was used as a model pharmaceutical compound to evaluate the performance of the FMNP, and 53.65 mg PrHy/g FMNP was removed using 600 ppm FMNP. A fast (30 min) adsorption kinetic followed by a pseudo-first-order kinetic model could describe the physical adsorption through a 1 to 1 host–guest inclusion mechanism, which obeyed the Freundlich model. The

proposed system is scalable and adaptable to existing water treatment processes, and it can be used for the detection of low concentration pharmaceuticals via a pre-concentrating strategy.

Various quantities of β-CD were grafted onto the FMNPs, and their adsorption performance depended on (i) alignment of CD cavities on the surface of FMNPs, (ii) amounts of accessible CD cavities available for binding, and (iii) pH. The adsorption isotherms of FMNPs were fitted to the Langmuir and Freundlich models, and the data for PrHy below 30 ppm fitted to the Langmuir model confirming a monolayer surface adsorption. However, the adsorption isotherms obeyed the Freundlich model for PrHy between 5 to 100 ppm suggesting the occurrence of multiple-stage adsorption on the CD cavities associated with different accessibility due to overlapping or steric hindrance of CM-β-CD. The correlation of CD cavity alignment and adsorption behavior was demonstrated, where the adsorption capacity of the FMNP was depended on to the amount of β-CD on the adsorbents, and steric hindrance of the CD cavities.

The development of noble metal catalysts with high catalytic performance and low metal loading has attracted increasing interests. However, the separation of spent nano-catalyst from the process is challenging, most of the proposed systems led to a sacrifice of the high surface area as well as catalytic efficiency. In this study, two series of recyclable catalysts were synthesized by loading palladium (Pd) particles onto melamine formaldehyde (MF) modified CNC and dopamine (DA) coated CNC. *In situ* co-precipitation of magnetic nanoparticle (MNP) clusters were used to impart magnetic characteristic to the catalyst systems. The amount of palladium precursor added to the catalytic systems was optimized, where 10-Pd-PDC yielded 10.83 ± 2.43 nm discrete Pd hybrid systems. The catalytic performance of the catalysts was assessed by the reduction of 4-nitrophenol (4-NP) in the presence of sodium borohydrides ($NaBH_4$). The 4-NP reduction mechanisms using MNP2-Pd-MC were analyzed using the Langmuir-Hinshelwood model and the

apparent rate constant k (s^{-1}), turnover frequency (TOF, h^{-1}) and activity factor ($s^{-1}g^{-1}$) were 2.142×10^{-3}, 305.82 and 535.5 respectively. An induction time was observed for MNP-4 or 5-Pd-PDC, where was attributed to the diffusion time for reagents to cross the thick PDA and MNP layers. The separation efficiency of the magnetic catalysts was evaluated by monitoring the absorbance at 400 nm as a function of separation time, and the MNP2-Pd-MC could be recycled 7 times without severe loss of activity. Pd-MF-CNC displayed excellent catalytic performance for the reduction of 4-NP, while Pd-PDA-CNC possessed a lower catalytic activity due to the inferior catalytic surface area. The developed templated MNP could be extended to other systems allowing for the recycling and reuse of the catalysts or adsorbents.

Besides magnetic particles, silver nanoclusters (AgNCs) were also produced inside the nanogel scaffold via UV-photoreduction. The impact of UV irradiation time on the formation of AgNCs and their application in biolabeling and antimicrobial properties were examined. The AgNCs formation is described by two stages; (1) Ag_n (n=2-8) nanoclusters formation between 0-25 min, and (2) larger silver nanoparticles (AgNPs) formed via aggregation inside the nanogel. The antimicrobial performance depended on the size and concentration of silver ions (Ag^+). The minimum inhibitory concentration (MIC) of 1.1 ppm was reported for the antimicrobial test with yeast, and a MIC of 11 and 22 ppm was recorded for *Escherichia. coli* and *Staphylococcus aureus* respectively. Combining with the green illumination property of AgNCs (emitted at 525 nm) with dead yeast, it could be used for biolabeling. By tuning the size through photoirradiation, the nanogel templated AgNC is a promising candidate for antimicrobial and biolabeling applications.

Persistence contaminants, such as perfluoroalkyl and polyfluoroalkyl substance (PFAS) are widely reported in our water systems posing a threat to human beings due to their negative impact on the reproductive system. Also, heavy metal and organic dyes have continued to contribute to a

the wastewater contamination due to the human activities and industrialization. We developed a sustainable membrane from soft wood fiber (WF) crosslinked with (3-glycidyloxypropyl)trimethoxy silane (GPTMS) and poly(ethyleneimine) (PEI), a Pickering emulsion consisting of Tanfloc (TF) (a natural tannin based commercial flocculant) coated CNC and hexane. With the Pickering emulsion, the porosity of the membrane WGP-111-EM45 increased to 41.60 % compared to the membrane without emulsion (23.65 %). Gravity filtration with methyl orange (MO) was used to evaluate the performance of the membrane with various amounts of PEI, and emulsion loading, and WGP-111-EM45 was selected for further evaluation in dynamic filtration. A simple pressure controlled dynamic filtration system was designed and inlet flowrate, inlet concentration and number of membranes loaded to the filtration system were evaluated. The highest filtration capacity was obtained for 22679.06 mg/g MO, with an inlet concentration of 50 ppm and flowrate of 11.22 ml/min. The increase in the number of membranes (bed height) led to an increase removal efficiency with a lower slope in the breakthrough curve, due to the enhanced mass transfer diffusion. Furthermore, the membrane filtration efficiency of the membrane towards copper ions (Cu^{2+}) and methylene blue (MB) was evaluated by gravity filtration and a 98% removal efficiency for 10 ml 1000 ppm Cu^{2+} was achieved with WGP-111-EM45 and an 89 % removal efficiency was achieved for 10 ml, 20 ppm MB. This sustainable porous membrane provided adsorption sites towards cationic/anionic dye and heavy metal ions based on ion exchange, electrostatic interactions, chelation and π-π interactions. Also, a 99.4 % and 99.2 % removal efficiency were achieved by passing 10 ml of 500 μg/L and 1000 μg/L PFOA through the WGP-111-EM45 membrane (gravity filtration), where the concentration was reduced to 2.19 μg/L and 7.82 μg/L, respectively. This membrane displayed promising potential to remove pollutants via gravity filtration and pressure driven dynamic filtration.

In summary, this study advanced the development of a highly stable pH-responsive nanogel, which could be replicated. The robust nanogel scaffold was used as a nano-reactor to prepare MNPs and AgNCs, which were further demonstrated in water treatment and antimicrobial applications. Additionally, soft wood fiber crosslinked membrane was also developed for multi-pollutant removal, which showed promising potential for the removal of emerging contaminants with a low carbon footprint.

Acknowledgments

Together with my two-year master's program, I had spent seven years of my graduate life at the University of Waterloo. I started by PhD study for 8 months and due to some circumstances beyond my control, I could not continue due to the funding situation. At that moment, two key people changed my life. Professor Xianshe Feng provided me a lot of valuable suggestions and encouraged me to continue pursuing my doctoral study. At the same time, Professor Tam provided me the opportunity to join his group to work on functional nanomaterials, a topic that was new to me. Without them, I would have given up my research career several years ago and pursue a routine job.

I would like to express my sincere appreciation to my supervisor Prof. Michael Tam for his guidance, support, and patience during my PhD study. He gave me a lot of help both in my research project, and also advice on other aspects of my life, such as my personality, be gentle and positive, which helped me overcome many challenging situations in my research career. I would also like to thank my committee members, Prof. Xianshe Feng, Prof. Michael pope, Prof. Wayne Parker and Prof. Lee Wilson for their feedback and suggestion regarding my thesis research.

I would like to thank Dr. Farmer for sharing with me his experience on emulsion polymerization technique, and without his help, I would have encountered difficulties in preparing the nanogels. I would like to thank Profs. Juewen Liu, Leonardo Simon and Boxin Zhao for allowing me to use their laboratory equipment. Dr. Ram, Yuan (Molly) Tian, Dr. Nathan, Dr. Yingzhan Li, Dr. Chong Meng, Lian Han, Yebin Lee, Yi Wang, Weinan Zhao, Fatemah Haji, Iflah Shahid, Dr. Chunxia Tang, Dr. Parinaz Ataeian, Gaili Cao, Xiaoming Zhou, Dr. Elnaz Halakoo, Michael Celarek, Dr. Muhammad Waqas Lqbal, Dr. Dihua Wu, Dr. Silu Chen, Yiran Wang, Dr.

Qiang Zhou and many other colleagues and coop students had offered help and support to me during my PhD study.

Last but not least, I would like to thank my dear parents Yubing Xu, Bin Zhou and my grandmother Xiuying Hu for their selfless love, support and encouragement in my life. Without them, I would not have the opportunity to study abroad and see the big world. Finally, I am deeply grateful that I could meet Ben Kinh Tan during my PhD study and who later became my dear husband. I could not achieve my dream without his support, trust and encouragement, and he is one of my greatest gifts to me.

Table of Contents

List of Figures ..... *xxii*

List of Schemes ..... *xxxi*

List of Tables ..... *xxxii*

Chapter 1: Introduction *1*

1.1 Overview **1**

1.2 Research Objectives **3**

1.3 Thesis Outline **4**

Chapter 2: Literature Review *6*

2.1 Introduction **6**

2.2.1 Definition, history and background 7

2.2.2 Classification of nanogels 8

2.2.3 Synthesis of nanogels 10

2.2.3 Nanogels applications 17

2.2 Sustainable material selected for water treatment process **27**

2.2.1 Cellulose nanocrystals (CNC) 28

2.2.2 Tanfloc (TF) 29

2.2.3 Cellulose nanofiber (CNF) 30

2.2.4 Beta-cyclodextrin (***β***-CD) 30

2.2.5 Wood fiber (WF) 31

2.3 Synthesis of magnetic particles (MNP) **32**

2.3.1 Co-precipitation 32

2.3.2 High temperature thermal decomposition 36

2.3.3 Hydrothermal and solvothermal synthesis 38

2.3.4 Sol-gel reactions and polyol method 39

2.3.5 Microemulsion 42

2.3.6 Sonolysis or sonochemical method 43

2.3.7 Microwave assisted synthesis 45

2.4 Water treatment technologies 48

2.4.1 Wastewater treatment ad drinking water purification 48

2.4.2 Categories of water treatment processes 49

2.4.3 $\boldsymbol{\beta}$-CD absorbents applied to various pollutants removal 61

2.4.4 Beta-cyclodextrin based adsorbents 76

Chapter 3: Synthesis and Characterization of pH-responsive Methacrylic acid/ Ethyl Acrylate Crosslinked Nanogel by Semi-continuous Emulsion Polymerization 106

3.1 Introduction 106

3.2 Experimental 111

3.2.1 Materials 111

3.2.2 Synthesis of Poly (MAA-EA-DAP) nanogels 111

3.3 Characterization method 114

3.3.1 Fourier transform infrared spectroscopy (FTIR) 114

3.3.2 Potentiometric and conductometric titration 114

3.3.3 Multi-angle dynamic light scattering and static light scattering (MADLS and SLS) 114

3.3.4 Zeta potential and average particle size measurement 115

3.3.5 Transmission electron microscopy (TEM) 115

3.3.6 Swelling factor 116

3.4 Results and discussion 116

3.4.1 Fourier transform infrared spectroscopy (FTIR) 116

3.4.2 Potentiometric and conductometric titration 117

3.4.3 Multi-angle dynamic light scattering and static light scattering (MADLS and SLS) 122

3.4.4 Zeta average diameter and zeta potential 126

3.4.5 Morphology investigation (TEM) 130

3.4.6 Shape factor and pH dependent conformation transition 132

3.4.7 MAA-EA nanogel ionization process 135

3.4.8 Swelling factor 136

3.5 Conclusions 138

*Chapter 4: β-cyclodextrin functionalized magnetic nanoparticles for the removal of pharmaceutical residues in drinking water * 140*

4.1 Introduction 141

4.2 Experimental 145

4.2.1 Materials 145

4.3 Methods 146

4.3.1 Synthesis of MAA-EA nanogel scaffold 146

4.3.2 Synthesis of nanogel based magnetic nanoparticles (MNPs) 146

4.3.3 Synthesis of silica coated MNPs (Si-MNP) 147

4.3.4 Synthesis of CM-β-CD 148

4.3.5 Grafting of CM-β-CD onto Si-40-MNP 149

4.4 Characterization methods 149

4.4.1 Transmission electron microscopy (TEM) 149

4.4.2 Fourier transform infrared spectroscopy (FTIR) 150

4.4.3 Dynamic light scattering (DLS) 150

4.4.4 Zeta potential measurement 150

4.4.5 Adsorption kinetic study 150

4.4.6 FMNP concentration screening 151

4.4.7 Adsorption isotherm study 152

4.4.8 X-Ray Diffraction (XRD) 152

4.4.9 Vibrating sample magnetometer (VSM) 152

4.4.10 Thermogravimetric analysis (TGA) 153

4.5 Results and discussion 153

4.5.1 Morphology of Nanogel, MNP and Si-MNP 153

4.5.2 XRD analysis of the chemical structure of silica shell 157

4.5.3 Size control and stability of nanogel template, MNP, Si-MNP and FMNP 158

4.5.4 Magnetization of Magnetic nanoparticles (VSM) 162

4.5.5 Thermogravimetric analysis (TGA) 164

4.5.6 Adsorption kinetic study 165

4.5.7 FMNP concentration screening 168

4.5.8 Equilibrium Adsorption study 169
4.5.9 Enrichment process of trace pharmaceuticals from drinking water system 171

4.6 Conclusions 173

Chapter 5: Adsorption Mechanism of β-cyclodextrin Functionalized Magnetic Nanoparticles for the Removal of Procaine Hydrochloride 174

5.1 Introduction 174

5.2 Experimental section 178

5.2.1 Materials 178

5.3 Methods 179

5.3.1 Nanogel preparation 179
5.3.2 Magnetic nanoparticles (MNPs) preparation 179
5.3.3 Silica coating of MNPs 180
5.3.4 Grafting of CM-β-CD onto Si-40-MNP 181

5.4 Characterization Methods 181

5.5 Adsorption experiments 182

5.5.1 Concentration screening of FMNP-L, FMNP-M and FMNP-H 182
5.5.2 pH effect on isotherm adsorption of PrHy with FMNP-L, FMNP-M and FMNP-H 183

5.3 Results and discussion 184

5.3.1 Fourier-transform infrared spectroscopy (FTIR) 184
5.3.2 Morphology investigation 185
5.3.3 Particle size and stability 187
5.3.4 Chemical composition 188
5.3.5 Magnetization of magnetic nanoparticles 190
5.3.6 Concentration screening of FMNP-L, FMNP-M and FMNP-H 192
5.3.7 Equilibrium Adsorption study 193
5.3.8 Removal percentage (R %) 199
5.3.9 Quantification of active β-CD cavities 201

5.4 Conclusions 202

*Chapter 6: Synthesis of Silver Nanoclusters in Colloidal Scaffold for Biolabeling and Antimicrobial Applications**.....*204*

6.1 Introduction **205**

6.2 Experimental.....**208**

6.2.1 Materials 208

6.3 Methods **208**

6.3.1 Synthesis of MAA-EA nanogel template 208

6.3.2 Synthesis of nanogel templated Ag^{+}-nanogel system 209

6.3.3 In-situ photoreduction of Ag^{+} to AgNCs inside the nanogel template 210

6.4 Characterization methods.....**211**

6.4.1 Fourier transform infrared spectroscopy (FTIR) 211

6.4.2 Transmission electron microscopy (TEM) 211

6.4.3 Dynamic light scattering (DLS) 211

6.4.4 Zeta potential measurement 212

6.4.5 UV-Vis Spectroscopy 212

6.4.6 Fluorescence Spectroscopy 212

6.4.7 Silver ions concentration determination using a silver electrode 212

6.4.8 Highest Maximum Inhibitory Concentration (HMIC) of antifungal test (yeast test) 213

6.4.9 Antimicrobial Tests 213

6.4.10 Microscope and fluorescent microscope 214

6.5 Results and discussion.....**214**

6.5.1 Fourier-transform infrared spectroscopy (FTIR) 214

6.5.2 Transmission electron microscopy (TEM) 215

6.5.3 Particle size and zeta potential 217

6.5.4 UV-Vis analysis of formation of Ag^{0} 217

6.5.5 Fluorescence characteristics of AgNCs 220

6.5.6 Electrochemical monitoring Ag^{+} concentration under UV irradiation 222

6.5.7 Yeast test and CO_2 release studies 229

6.5.8 Microscopic and biolabeling applications 232

6.5.9 Antibacterial test 234

6.6 Conclusions 238

Chapter 7: A Novel Magnetic Cluster modified Palladium-Cellulose Nanocrystal Hybrids as Recyclable Catalyst for 4-Nitrophenol Reduction 240

7.1 Introduction 241

7.2 Experimental 244

7.2.1 Materials 244

7.3 Methods 244

7.3.1 Preparation of MAA-EA nanogel template 244

7.3.2 Synthesis of nanogel templated magnetic particles (MNP) 245

7.3.3 Synthesis of PVP-PDA coated CNC (PDC) 246

7.3.4 Synthesis of melamine formaldehyde modified CNC (MF-CNC or MC) 246

7.3.5 Deposition of Pd particles onto MF-CNC and PVP-PDA-CNC 246

7.3.6 Optimization of Pd loading for Pd-PDC synthesis 247

7.3.7 Assembly of MNP and Fe_3O_4 particles onto Pd-MC and Pd-PDC 248

7.4 Characterization methods 250

7.4.1 Fourier transform infrared spectroscopy (FTIR) 250

7.4.2 Transmission electron microscopy (TEM) 250

7.4.3 Dynamic light scattering (DLS) 250

7.4.4 Zeta potential measurement 251

7.4.5 UV-Vis measurements 251

7.4.6 Evaluation of catalytic performance 251

7.4.7 Magnetic separation efficiency 252

7.4.8 Reusability 252

7.5 Results and discussion 253

7.5.1 Fourier-transform infrared spectroscopy (FTIR) 253

7.5.2 Particle morphology 254

7.5.3 Particle size and stability 258

7.5.4 Optimization of Pd loading for Pd-PDC 259

7.5.5 Evaluation of catalytic performance 261

7.5.6 Separation efficiency 270
7.5.7 Reusability 271
7.6 Conclusions 273
Chapter 8: Sustainable high porosity adsorptive membrane for cationic/anionic dye, heavy metal ions, and PFAS removal 275
8.1 Introduction 276
8.2 Experimental 280
8.2.1 Materials 280
8.3 Methods 281
8.3.1 Preparation of Tanfloc coated CNC (TF-CNC) 281
8.3.2 Preparation of TF-CNC stabilized hexane emulsion 281
8.3.3 Fabrication of TF-CNC EM contained wood fiber membrane 281
8.4 Characterization 283
8.4.1 FTIR 283
8.4.2 Microscopic imaging 283
8.4.3 Particle size and zeta potential 283
8.4.4 Emulsion particle size 285
8.4.5 Porosity measurement 285
8.4.6 Gravity filtration 285
8.4.7 pH effect on gravity filtration 286
8.4.8 Multi-layer gravity filtration 286
8.4.9 Mechanical test for membranes 286
8.4.10 Scanning Electron Microscope (SEM) 287
8.4.11 Dynamic adsorption experiments 287
8.5 Results and discussion 289
8.5.1 FTIR 289
8.5.2 Stability of the Pickering emulsions 290
8.5.3 Emulsion particle size 293
8.5.4 Porosity and permeation flux 294

8.5.5 Gravity Filtration Performance 295
8.5.6 pH effect on MO gravity filtration 299
8.5.7 Gravity filtration of MO with different layers of membrane 301
8.5.8 Mechanical Strength (Tensile Index) 303
8.5.9 Morphology and macrostructure (SEM) 305
8.5.10 Dynamic filtration (Concentration effect) 307
8.5.11 Dynamic filtration (Effect of flow rate) 310
8.5.12 Dynamic filtration (Effect of number of membranes) 312
8.5.13 Gravity filtration of PFOA and PFOS 313

Conclusions ***314***

Chapter 9: Original Contributions and Recommendations ***316***

9.1 Original Contribution to Research **316**

9.1.1 Facile synthesis and characterization of pH-responsive methacrylic acid/ethyl acrylate crosslinked nanogel by semi-continuous emulsion polymerization 317

9.1.2 $\boldsymbol{\beta}$ -cyclodextrin functionalized magnetic nanoparticles for the removal of pharmaceutical residues in drinking water 318

9.1.3 Adsorption mechanism of $\boldsymbol{\beta}$ -cyclodextrin functionalized magnetic nanoparticles for the removal of procaine hydrochloride 319

9.1.4 Synthesis of silver nanoclusters in colloidal scaffold for biolabeling and antimicrobial applications 319

9.1.5 A novel magnetic cluster modified palladium-cellulose nanocrystal hybrids as recyclable catalyst for 4-nitrophenol reduction 320

9.1.6 Sustainable high porosity adsorptive membrane applied for cationic/anionic dye, heavy metal and PFAS removal 321

9.2 Recommendations for Future Studies **322**

References ***325***

List of Appendices ***369***

Appendix ***372***

List of Figures

Figure 2-1 Types of nanogel formulations. Adapted with permission from ref [24]. Copyright © 2019 F. Sabir et al. 9

Figure 2-2 Schematic illustration of micellar nucleation, where blue color represents surfactant molecules, red color stands for monomer molecules, green color indicates growing polymer chains, and black color represents the nanogel particles. Adapted with permission from ref [45]. Copyright © 2010 Published by Elsevier. H. Wang et al. 13

Figure 2-3 HLB value and corresponding application. Adapted with permission from ref [54]. Copyright © 2018 R. Setiati et al. 16

Figure 2-4 Schematics of the preparation and antifouling mechanism of the nanogel coating. Adapted with permission from ref [2]. Copyright © 2020 American Chemical Society D. Keskin et al. 20

Figure 2-5 The schematic of the production mechanism of a bioactive nanogel by gamma reduction strategy. Adapted with permission from ref [56]. Copyright © 2018 The Authors. Published by WILEY-VCH Verlag GmbH & C0. KGaA, Weinheim. 20

Figure 2-6 The schematic illustration of thiol abundant nanogel synthesis procedure. Adapted with permission from ref [3]. Copyright © 2021. American Chemical Society Y. Zhang et al. 22

Figure 2-7 The synthesis pathway of PAATC nanogel and the mechanism of ionizing radiation doses detection. Adapted with permission from ref [59]. Copyright © The Royal Society of Chemistry 2019. 25

Figure 2-8 Surface modification pathways of CNC depending on the pollutant type. Adapted with permission from ref [67]. Copyright © 2017, Springer Science Business Media Dordrecht. 29

Figure 2-9 The formation of cellulose fibres obtained from wood pulp, and the following production process of CNC and CNF. Adapted with permission from ref [71]. Copyright © The Royal Society of Chemistry 2018. 31

Figure 2-10 Schematic representation of the effect of different types of base on the thickness of the ‘dead’ layer (shadowed region) and spin rearrangement at the surface of the MNPs(a) for NaOH (b) for MIPA and DIPA. Adapted with permission from “A. G. et al. Pereira, Clara, André M. Pereira, Carlos Fernandes, Mariana Rocha, Ricardo Mendes, María Paz Fernández-

García, “Superparamagnetic MFe_2O_4 (M = Fe, Co, Mn) Nanoparticles: Tuning the Particle Size and Magnetic Properties through a Novel One-Step Coprecipitation Route Clara,” *Chem. Mater.*, vol. 24, pp. 1496–1504, 2012” [78]. Copyright 2012 American Chemical Society.34

Figure 2-11 Schematic of the MNPs synthesis process. Adapted with the permission from “K. W. Bong, P. S. Doyle, D. K. Hwang, T. A. Hatton, S. K. Suh, and K. Yuet, “ Synthesis of Nonspherical Superparamagnetic Particles: In Situ Coprecipitation of Magnetic Nanoparticles in Microgels Prepared by Stop-Flow Lithography ,” *J. Am. Chem. Soc.*, vol. 134, no. 17, pp. 7337–7343, 2012” [80]. Copyright © 2012 American Chemical Society. 35

Figure 2-12 Scheme for the ultra-large scale synthesis of monodisperse nanocrystals. Adapted with permission from “A. P. et al Patsula, Vitalii, Lucie Kosinová, Marija Lovrić, Lejla Ferhatovic Hamzić, Mariia Rabyk, Rafal Konefal, “Superparamagnetic Fe_3O_4 Nanoparticles: Synthesis by Thermal Decomposition of Iron(III) Glucuronate and Application in Magnetic Resonance Imaging,” Appl. Mater. surfaces, vol. 8, pp. 7238–7247, 2016” [84]. Copyright © 2016 American Chemical Society. 38

Figure 2-13 The schematic illustration of the sol-gel process of Fe_3O_4@SiO_2-NH_2 and the effect of APTMS loading on the formation of core/shell structure. Adapted with permission from ref [88]. Copyright © 2012 Elsevier B.V. 40

Figure 2-14 The schematic diagram of the procedure for the encapsulation of magnetic nanoparticles and monomer droplet to latex particle conversion. Adapted with permission from “ M. A. Teo, Boon M., Fei Chen, T. Alan Hatton, Franz Grieser, “Novel one-pot synthesis of magnetite latex nanoparticles by ultrasound irradiation,” Langmuir, vol. 25, no. 5, pp. 2593–2595, 2009 [95]. Copyright © 2009 American Chemical Society. 45

Figure 2-15 A typical flow schematic of a wastewater treatment plant (Source: https://www.lacsd.org/home/showpublisheddocument/3578/637644521003970000) 49

Figure 2-16 Schematics of the adsorption and desorption process of adsorbate molecules with adsorbent 51

Figure 2-17 Characteristic of Langmuir adsorption isothermal. Adapted from ref [107]. Copyright © 2014 Wiley Periodicals, R. A. Latour. 54

Figure 2-18 The mechanism of semiconductor photocatalysis, adapted from ref [111] 56

Figure 2-19 The reaction mechanisms of ROS generation and the degradation of organic molecules by using photocatalyst. Adapted with permission from ref [113]. Copyright © 2016 The Royal Society of Chemistry, K. Mondal et al. 57

Figure 2-20 The separation of different components via pressure driven membrane filtration process. Adapted from ref [51]. Copyright © 2018 The Royal Society of Chemistry, MK. Selatile et al. 59

Figure 2-21 The configuration of cross-flow membrane filtration (left) and the dead-end membrane filtration (right). 61

Figure 2-22 The schematics representation of PCD-VI and the inclusion mechanism. Adapted with permission from ref [144]. Copyright © 2019 Elsevier B.V. X. Qin et al. 66

Figure 2-23 Perfluorooctanoic acid (PFOA) and perfluorooctanesulfonic acid (PFOS) referred to as per- and polyfluorinated alkyl substances (PFAS). Adapted with permission from ref [161]. Copyright © 2019 American Chemical Society, Nicholas A. Lundquist et al. 72

Figure 2-24 Scheme of adsorption mechanism of PFAS onto DFP-CDP, EPI-CDP, and IEM-CDP. Adapted from "L. Xiao *et al.*, "Cross-linker Chemistry Determines the Uptake Potential of Perfluorinated Alkyl Substances by β-Cyclodextrin Polymers," Macromolecules, 2019."[163]. Copyright © 2019 American Chemical Society, L. Xiao et al. 75

Figure 2-25 Preparation of DM-β-CD/urethane polymers by crosslinking DM-β-CD with different diisocyanate linkers. Adapted with permission from ref [170]. Copyright © 2015, The society of Polymer Science, Japan, Shintaro Kawano et al. 79

Figure 2-26 Synthesis, adsorption and recovery schematic of Fe_3O_4 @ ***β***-CD-CDI composites. Adapted with permission from ref [180]. Copyright © 2019 Elsevier Ltd. D. Liu et al. 80

Figure 2-27 Schematic of CDNS synthesis procedure. Adapted with permission from ref [181]. Copyright © 2019, Springer Nature B.V. L. Li et al. 81

Figure 2-28 Synthesis of ***β***-PMDA(a) and ***β***-CITR (b). Adapted from ref [143].Copyright © 2019, A. R. Pedrazzo. 83

Figure 2-29 EPI crosslinked with ***β***-cyclodextrins forming insoluble poly(CD-EPI) gel under basic environment. Adapted with permission from ref [189]. Copyright © 2017 Elsevier B.V. N. M. Crini et al. 84

Figure 2-30 Structure of the 3-D polymeric network of CD crosslinked with EPI. Adapted with permission from ref [189]. Copyright © 2017 Elsevier B.V. Nadia Morin-Crini et al. 85

Figure 2-31 The schematic of material preparation of MNPs/ $\boldsymbol{\beta}$-CDP and its application for adsorption and degradation of APAP in a combination with $KMNO_4$ oxidation process. Adapted with permission from ref [207]. Copyright © 2019 Elsevier Ltd. Y. Shi et al. 92

Figure 2-32 Schematic representation of $\boldsymbol{\beta}$-CD composite porous membrane preparation. Adapted with permission from ref [213]. Copyright © 2019 Elsevier B.V. Z. Wang et al. 95

Figure 2-33 The synthesis procedure of Ce-CS-$\boldsymbol{\beta}$-CD hybrid microsphere. Adapted with permission from ref [216]. Copyright © 2019 Elsevier B.V. P. Karthikeyan. 98

Figure 2-34 The preparation process of $\boldsymbol{\beta}$-CD grafted cellulose beads. Adapted with permission from ref [222]. Copyright © 2019 Elsevier B.V, Q. Lin et al. 100

Figure 2-35 (a)Preparation procedure of Fe_3O_4-CTs@MIP (b)Preparation schematic of Fe_3O_4-MAH-$\boldsymbol{\beta}$-CD @MIP and application of 2-aminoyridine removal. Adapted from ref [236]. Copyright © W. Zhang et al. 105

Figure 3-1 Nanogel classified based on different structures 109

Figure 3-2 FTIR spectrum of different weight percentage of crosslinker (DAP) incorporated with 50:50 MAA-EA nanogels (a), and the FTIR spectrum of different combination of MAA:EA crosslinked with 8% DAP 117

Figure 3-3 The potentiometric-conductometric curves of 0.5 wt% 50:50 MAA-EA crosslinked with 8 wt% DAP with 0.5M NaOH and 0.5M HCl as the titrant under forward (a) and reverse (b) titration 118

Figure 3-4 The conductivity and pH of different amounts of DAP wt% crosslinked nanogels versus volume of titrant (0.5M NaOH) under forward titration (a), (b), and the conductivity and pH of different amounts of DAP % crosslinked nanogels versus volume of titrant (0.5M HCl) under reverse titration (c), (d) 119

Figure 3-5 The conductivity and pH of different monomer ratios MAA-EA nanogels crosslinked with 8 wt% DAP as the addition of titrant (0.5 M NaOH) under forward titration (a), (b), and the conductivity and pH of different monomer ratios MAA-EA nanogels crosslinked with 8 wt% DAP nanogels as the addition of titrant (0.5M HCl) under reverse titration (c), (d) 123

Figure 3-6 Rh and Rg value of 50:50 MAA-EA nanogels crosslinked with 0.5 to 8 wt% DAP under pH 3-11 (a,b); Rh and Rg value of MAA-EA nanogels consisted with different monomer ratios under pH 3-11(c,d). (All of the measurements were conducted with MADLS and SLS) 127

Figure 3-7 Zeta avergae diameter (nm) and zeta potential (mV) of 50:50 MAA-EA nanogels crosslinked with 0.5 to 8 wt% DAP under pH 3-11 (a, b); Zeta avergae diameter (nm) and zeta potential (mV) of MAA-EA nanogels consisted with different monomer ratios under pH 3-11(c, d) 129
Figure 3-8 TEM images of 50:50 MAA-EA crosslinked with 0.5% DAP (a, b), 1% DAP (c, d), 2%DAP (e, f), 4% DAP (g, h), 8% DAP (i, j) 132
Figure 3-9 The shape factor, ionization degree and internal structure of 50:50 MAA-EA nanogels crosslinked with 0.5 to 8 wt% DAP upon pH variation (a); The shape factor and ionization degree of MAA-EA nanogels consisted with different monomer ratios as a function of pH 134
Figure 3-10 pKa (a) and conductivity (b) versus ionization degree of 50:50 MAA-EA nanogels crosslinked with 0.5 to 8 DAP%; pKa (c) and conductivity (d) versus ionization degree of MAA-EA nanogels consisted with different monomer ratios 136
Figure 3-11 The pH dependent swelling ratio of 50:50 MAA-EA nanogels crosslinked with 0.5 to 8 wt% DAP (a); The pH dependent swelling ratio of MAA-EA nanogels consisted with different monomer ratios (b) 137
Figure 4-1 TEM images of MAA-EA nanogel (A); MNP (B); MNP-wash-out from the HGMS (C); Si-40-MNP (D); Si-50-MNP (E) ;Si-100-MNP (F); Si-150-MNP (G) and Si-200-MNP (H) 155
Figure 4-2 FTIR of CM-CD-MNP, CM-β-CD and β-CD (a), MAA-EA nanogel and 10 to 50 μL coated MNP 157
Figure 4-3 XRD pattern of the Si-MNP and MNP 158
Figure 4-4 Particle size (a) and zeta potential of nanogel synthesized with 5 to 25 wt% of the monomer mixture used for seed formation 160
Figure 4-5 Average particle size (a) and zeta potential (b) of MAA-EA nanogel template, MNP, Si-40-MNP and FMNP 162
Figure 4-6 The magnetic hysteresis loops of MNP, Si-40-MNP and FMNP measured by SQUID at 300K between -1T and 1T 163
Figure 4-7 TGA curves of MNP, Si-40-MNP and FMNP 165
Figure 4-8 Final concentration of PrHy after adsorption test with 500 ppm Si-40-MNP (Black squares) and 500 ppm FMNP (Red circles) 167

Figure 4-9 The adsorption kinetic of 500 ppm FMNP with 15 ppm PrHy in a 3ml batch solution fitted to the Pseudo-first order kinetic (A) and Pseudo-second order kinetic (B) 167
Figure 4-10 The UV-vis spectrum of 15 ppm PrHy after 30 mins adsorption test with 100 to 1000 ppm of FMNP (A), the final concentration of PrHy (ppm) and removal efficiency of 100 to 1000 ppm FMNP (B) 168
Figure 4-11 Adsorption isothermal of FMNP with 5 to 30 ppm PrHy fitted with Langmuir isothermal (A) and adsorption isothermal of FMNP with 5 to 100 ppm PrHy fitted with Freundlich model are presented in (B) 169
Figure 5-1 FTIR of β-CD, CM-β-CD, nanogel, Si-40-MNP and FMNP-H 185
Figure 5-2 TEM images of (A) MAA-EA nanogel; (B) MNP; (C) Si-40-MNP; (D) FMNP-H 186
Figure 5-3 The particle size and zeta potential of nanogel, MNP, Si-40-MNP and FMNPs at neutral pH 188
Figure 5-4 TGA curves of MNP, Si-40-MNP, FMNP-L, FMP-M and FMNP-H 189
Figure 5-5 The magnetic hysteresis loops of MNP, Si-40-MNP, FMNP-L, FMNP-M and FMNP-H obtained by SQUID at 300K between -1T and 1T 191
Figure 5-6 The final concentration of PrHy (ppm) (A), and the removal (%) of PrHy (B) after 30 mins adsorption with 100-100 ppm of FMNP-L, FMNP-M and FMNP-H 193
Figure 5-7 The adsorption isotherm of FMNP-L at pH 6.5 (A), 8.0 (B) and 9.5 (C) fitted with Langmuir and Freundlich isotherm model 196
Figure 5-8 The adsorption isotherm of FMNP-M at pH 6.5, 8.0 and 9.5 fitted with Langmuir and Freundlich isotherm model is shown in A, B and C, respectively 197
Figure 5-9 The adsorption isotherm of FMNP-H at pH 6.5, 8.0 and 9.5 fitted with Langmuir and Freundlich isotherm model is shown in A, B and C, respectively 198
Figure 5-10 The removal percentage of 5 to 100 ppm PrHy by using 3ml of FMNP-L (A), FMNP-M (B) and FMNP-H (C) at pH 6.5, 8.0 and 9.5 201
Figure 5-11 Estimation of active β-CD cavities at different PrHy initial concentration and pH by using FMNP-L (A), FMNP-M (B) and FMNP-H (C) 202

Figure 6-1 Schematic illustrating the preparation of AgNCs under UV irradiation 210
Figure 6-2 FTIR of MAA-EA nanogel, $AgNO_3$ and AgNCs with different time of UV irradiation 215

Figure 6-3 TEM images of normal and magnified views of stained MAA-EA nanogel (a, b), formation of AgNCs @ (c, d) 0, (e, f) 6, (g, h) 25, (i, j) 60, and (k, l) 360 min of UV irradiation 216

Figure 6-4 The UV curve of AgNCs under 0, 3, 6, 25, 120, 200, 280 and 360 min of UV irradiation (A), and the peak wavelength of different AgNCs (B). The picture of AgNCs under 0, 3, 6, 15, 40, 80, 120, 160, 200, 240, 280, 320, 360 and 400 min under visible light (from 12 o'clock point) is shown in (A) intersection image. The picture of AgNCs under 0, 3, 6, 15, 40, 80, 120, 160, 200, 240, 280, 320, 360 and 400 min under UV light (from 12 o'clock point) is shown in (B) intersection image 218

Figure 6-5 Ag^+ concentration as a function of UV irradiation time (A), and concentration in log scale (B), Ag^+ concentration of silver ion chelated nanogel (after dialysis) with or without UV irradiation during the silver titration process (C), Ag^+ concentration of $AgNO_3$ mixed with nanogel with or without UV irradiation during the silver titration process (D) 225

Figure 6-6 (A) Highest minimal inhibitory concentration (HMIC) of AgNCs under different UV irradiation time, (B) Proposed antimicrobial mechanism of AgNCs@ different UV irradiation times against yeast 231

Figure 6-7 The CO_2 production rate versus concentrations of AgNCs 232

Figure 6-8 Microscopic image and fluorescence image (FITC filter) of nanogel treated yeast test sample dyed with MB (washed 2 times) a, b; Microscopic image and fluorescence image (FITC filter) of AgNCs@6min-1.1 ppm yeast test sample dyed with MB c, d; Microscopic image of AgNCs@6min-11 ppm yeast test sample dyed with MB e; Fluorescence microscopic image of AgNCs@6min-11 ppm yeast test sample dyed with MB under FITC, f and FITC merged with TRITC filter, g; Fluorescence microscopic image of AgNCs@6min-2.2 ppm under FITC filter, h 233

Figure 6-9 Antibacterial activity of AgNCs under 0, 6, 25, 80, 120 and 200 min UV irradiation time against E. coli (top) and S. aureus (bottom) 235

Figure 7-1 FTIR of (A) CNC, Melamine formaldehyde modified CNC, Pd loaded MF-CNC and Fe3O4 or MNP functionalized Pd-MC, (B) CNC, PVP-CNC, PDA-PVP-CNC, Pd loaded PDA-PVP-CNC and Fe3O4 or MNP functionalized Pd-PDC 254

Figure 7-2 TEM images of pristine CNC (a), MF-CNC (b), Pd loaded MF-CNC (Pd-MC) (c), MNP2-Pd-MC (d), Fe-Pd-MC (e), PVP-CNC (f), PDA-PVP-CNC (g), 5-Pd-PDC (h), 10-Pd-PDC (i), 15-Pd-PDC (j) 256
Figure 7-3 Average particle diameter (nm) and zeta potential (mV) of CNC, MF-CNC, Pd-MC, 2ml-MNP-Pd-MC and Fe-Pd-MC are shown in (A), average particle diameter (nm) and zeta potential (mV) of CNC, CNC-PVP, CNC-PVP-PDA, MNP2-PDC and Fe-PDC 259
Figure 7-4 UV spectra of catalytic reduction of 4-NP using (A) 5-Pd-PDC, (B) 10-Pd-PDC, (C) 15-Pd-PDC and (D) 10-Pd-PDC+PDA for a 30 min reaction time 261
Figure 7-5 The UV spectra of 4-NP, 4-AP and 4-NP in the presence of NaBH4 are presented in (A), the summary of logarithm of absorbance at 400 nm versus time of 30 ppm Pd-MC, 30 ppm MF-CNC and 4-NP solutions (B) 262
Figure 7-6 The logarithm of absorbance at 400 nm versus time of (A) MNP1 to 5-Pd-MC, and the logarithm of absorbance at 400 nm versus time of (B) MNP1 to 5-Pd-PDC 269
Figure 7-7 Separation performance of MNP1 to 5-Pd-MC (A), and MNP1 to 5-Pd-PDC samples evaluated by magnet separation (B) 271
Figure 7-8 Recyclability test of Fe-Pd-MC and MNP-Pd-MC (A), recyclability test of MNP-Pd-PDC and MNP-Pd-MC 272
Figure 8-1 FTIR spectra of CNC, Tanfloc, TF-CNC, softwood fiber and WGP-111-EM45 membrane 290
Figure 8-2 Microscopic images of 0.1, 0.2, 0.3, 0.4, 0.5, 1.0 wt% of CNC stabilized hexane Pickering emulsion (water: oil= 2:1) (A); the microscopic images of 0.3, 0.6, 1.0, 1.3, 1.5, 2.0 wt% of TF-CNC stabilized hexane Pickering emulsion (water: oil= 2:1) (B); the digital image of 0.1 to 1.0 wt% of CNC stabilized hexane Pickering emulsion (C); and the digital image of 0.1 to 1.0 wt% of TF-CNC stabilized hexane Pickering emulsion (D) 292
Figure 8-3 Emulsion particle size versus TF-CNC concentration (Volume ratio of TF-CNC suspension to hexane = 2: 1) 293
Figure 8-4 The effect of emulsion volume on the removal efficiency (%) of 10 ml 200 ppm MO and porosity (A); the effect of PEI mass ratio on the removal efficiency (%) of 10 ml 200 ppm MO and porosity (B) 295
Figure 8-5 Removal efficiency and permeation flux for the gravity filtration of 10 ml MO (20, 30, 40, 50, 70, 100 and 200 ppm) by using WGP-11 (0.2/0.5/1.0/1.5) -EM45 membrane (a, b, c,

d); Removal efficiency and permeation flux for the gravity filtration of 10 ml MO (20, 30, 40, 50, 70, 100 and 200 ppm) by using WGP-111.5-EM0 (e) membrane; Summary of removal efficiency of MO with WGP-11 (0.2/0.5/1.0/1.5) -EM45 membrane and WGP-111.5-EM0 (f) 296

Figure 8-6 The permeation flux and removal efficiency of 20, 30, 40, 50, 70, 100 and 200 ppm of MB via gravity filtration by WGP-111-EM0 (A) and WGP-111-EM45 (B); the permeation flux and removal efficiency of 20, 30, 40, 50, 70, 100, 200 and 1000 ppm of Cu^{2+} via gravity filtration by WGP-111-EM0 (C) and WGP-111-EM45 (D) 298

Figure 8-7 Summary graph of the removal efficiency (%) of MO, MB and Cu^{2+} by using WGP-111-EM45 and WGP-111-EM0 299

Figure 8-8 Removal efficiency and permeation flux of 10 ml, 50 ppm MO with different pH conditioned WGP-111.5-EM45 301

Figure 8-9 Removal efficiency (%) and permeation flux of WGP-111-EM45 when used for gravity filtration of 30 ml, 100 ppm MO by using1, 3, 5 and 10 membranes 302

Figure 8-10 Wet and Dry tensile index of membranes with various mass ratios of PEI to WF, from 0.2 to 1.5 305

Figure 8-11 Cross-sectional SEM images of WGP-11 (0/0.2/0.5/1.0/1.5) -EM45 and WGP-111-EM45 (PEI→EM) (A); Cross-sectional SEM images of WGP-111-EM(0/20/45/85/120) (B) 307

Figure 8-12 Dynamic filtration of various concentrations of MO solution with one layer of WGP-111-EM45 membrane (d = 23.9 mm), under 0.075 MPa 310

Figure 8-13 Dynamic filtration of 15 ppm MO solution with one layer of WGP-111-EM45 membrane (d = 23.9 mm), under various pressures (0.050, 0.075 and 0.100 MPa) 311

Figure 8-14 Dynamic filtration of 15 ppm MO solution with 1, 3, 6, 10 layers of WGP-111-EM45 membrane (d = 23.9 mm), under 0.075 MPa 313

Figure 8-15 Filtrate concentration and removal efficiency of WGP-111-EM45 by removing 10 ml of 0.5 and 1 ppm PFOA and PFOS 314

List of Schemes

Scheme 3-1 Schematic illustration of the emulsion polymerization synthesis procedure of MAA-EA nanogel 113

Scheme 4-1 Schematic describing the in-situ synthesis magnetic nanoparticles inside MAA-EA nanogel template 147

Scheme 4-2 Schematic of silica coating on MNP (silica coating shown in blue) 148

Scheme 4-3 Schematic of FMNP preparation via grating carboxyl-β-CD (CM-β-CD) onto silica coated MNP (top), chemical structure (bottom) 149

Scheme 4-4 Flow chart on the enrichment and purify of trace amounts of pharmaceuticals from drinking water system by employing recyclable FMNP 172

Scheme 5-1 Schematic illustration of in-situ synthesis magnetic nanoparticles inside MAA-EA nanogel scaffold and the synthesize of FMNP-L, FMNP-M and FMNP-H 180

Scheme 5-2 Schematic illustration of the adsorption mechanism between FMNPs and PrHy molecules 198

Scheme 7-1 The schematics of synthesis pathway of MNP-Pd-PDC (A), and MNP-Pd-MC (B) 249

Scheme 7-2 Scheme illustration and high magnification TEM images of (a) 5-Pd-PDC, (b) 10-Pd-PDC, (c) 15-Pd-PDC, (d) 10-Pd-PDC+PDA, (e) stained MAA-EA nanogel, (f) MNP clusters, (g) MNP1-Pd-PDC and (h) MNP5-Pd-PDC 257

Scheme 7-3 The schematic illustration of the possible mechanism of 4-NP degraded to 4-AP in the presence of Pd-MC and Pd-PDC (A), and the possible mechanism in the presence of extra PDA and MNP in the system (B) 268

Scheme 8-1 Fabrication process for sustainable softwood fiber, GPTMS, crosslinked membrane with or without emulsion (A); Chemical reaction of the crosslinking process (B); Chemical structure of the crosslinked membrane (C) 284

Scheme 8-2 Dynamic filtration setup with one membrane build into the system (A); Dynamic filtration setup with 10 membranes build into the system (B); Cross section of the designed membrane holder and the way membrane stacked in the membrane holder (C); Flow diagram of the designed dynamic filtration system (D) 288

List of Tables

Table 2-1 Comparison of different synthesis methods for MNPs [99] 47
Table 2-2 Various crosslinking agents applied for CD polymer synthesizing, adapted from [168] 78
Table 3-1 Reagents for nanogel synthesis. Mass of components required for the synthesis a series of nanogels with different combinations of monomer ratios and quantity of crosslinking agents 113
Table 3-2 Summary of quantities of COOH groups, MAA wt% and pKa value at half ionization degree(0.5 $\boldsymbol{\alpha}$) of 50:50 MAA-EA nanogel crosslinked with 0.5 to 8 wt% DAP calculated from both forward and reverse titrations 120
Table 3-3 Summary table of the amount of COOH groups and MAA wt%, pKa value at half ionization degree ($\boldsymbol{\alpha}$= 0.5) of 20:80, 30:70, 40:60 and 50:50 MAA-EA nanogel crosslinked with 8 wt% DAP calculated from both forward and reverse titration 123
Table 3-4 Comparison of 20:80 and 50:50 MAA-EA nanogel (8 wt% DAP) particle size measured by MADLS, Zeta sizer and TEM 132
Table 4-1 Summary of MNPs coated with varying amounts of TEOS 148
Table 4-2 The PDI value (number based) of nanogel , MNP, Si-40-MNP and FMNP at pH6 162
Table 4-3 Summary of the thickness of silica shell (obtained from Images J) 162
Table 4-4 Parameters of Pseudo-first order and Pseudo-second order model for FMNP adsorption kinetics 168
Table 4-5 Parameters of Langmuir and Freundlich isotherm fitting and the experimental Qe of 600 ppm FMNP with 5 to 100 ppm PrHy 170
Table 4-6 Adsorption capacity of β-CD based materials 171
Table 5-1 Chemical composition (in wt%) in MNP, Si-40-MNP, FMNP-L, FMNP-M and FMNP-H 190
Table 5-2 The summary table of experimental data and the parameters of the fitted Langmuir and Freundlich isotherm models 198
Table 6-1 The summary of QY results of quinine sulphate and AgNCs 222
Table 6-2 The concentration of remaining silver ions in the nanogel solution and the fitted 0 order and 1st order reaction rates 229
Table 7-1 Comparison of catalytic performance of Pd-MC and Pd-PDC based catalyst 264

Table 7-2 Summary of average particle size measure by Image J 269
Table 7-3 Comparison of different palladium-based catalysts applied for 4-NP reduction 270
Table 8-1 Summary of zeta size and zetapotential 293
Table 8-2 Summary of the titration results and calculated amine quantity (mmol/g) 300
Table 8-3 Parameters of the dynamic filtration test with various initial concentrations of MO 309
Table 8-4 Parameters of the dynamic filtration test with various inlet flow rates of MO solution 312
Table 8-5 Parameters of the dynamic filtration test with various bed heights 313

Chapter 1: Introduction

1.1 Overview

Even though 72% of the earth is covered by water, however only 2.5% of the water is fresh water that is suitable for consumption to sustain life. Moreover, the population growth and industrialization of modern cities have exacerbated the water crisis. Thus, the treatment of wastewater from different sources, such as human household activity, agriculture activities, textile and mining are now a challenge to society. Many strategies have been developed for the purification of wastewater generated from various resources. Some of the commonly used method includes, adsorption, flocculation, catalytic and biological processes, ion exchange and membrane filtration. Among all these strategies, adsorption is the most frequently used technique to remove contaminants, and the adsorption capacities of activated carbon (AC) are commonly used as the benchmark to evaluate the effectiveness of adsorbents. However, the high cost for regenerating AC using high temperature combustion leads to a large carbon footprint that balances the fast adsorption kinetics and high adsorption capacity. Also, AC does not have high selectivity and need a secondary separation after use. As a result, there is an increasing research interest to develop advanced adsorbent for specific pollutant that can be readily recovered after use. Hence, magnetic based adsorbent was selected as a good candidate for use as a promising adsorbent that can be readily separated and recovered. In addition to the adsorption process, catalytic processes have also been widely used since they can degrade toxic chemicals into less toxic by-products that can then be discharged to the environment. Membrane filtration is another popular alternative for wastewater treatment by rejecting contaminants while allowing clean water to pass through. The participation of nanomaterials in various advanced water treatment processes can effectively enhance the purification performance from different perspectives, namely; (1) provided large

surface area for the loading of noble metal catalytic particles, (2) nanogel templating method as a nano-reactor for synthesising nanometal clusters with no aggregation , and (3) nanomaterial stabilized Pickering emulsion to enhance the porosity of the membrane with improved the water purification efficiency.

By considering the global warming issue, green and sustainable material has attracted increasing attention. Cellulose based material originated from trees, is one of the most abundant resources in the world, provided many research possibilities with a low carbon footprint. Cellulose nanocrystals (CNC), cellulose nanofibril (CNF) and wood fiber (WF) are widely used to prepare sustainable material for environmental remediation. CNC possesses a high aspect ratio, and is considered as a good candidate for use as a matrix to load other functional material with enhanced colloidal stability in aqueous solution. The high aspect ratio of CNC also allows it to be used as an emulsifier for preparing stable Pickering emulsion, which can be further used as a template to introduce porosity to the system after the removal of the volatile organic phase. From this strategy, more surface area could be achieved to further improve the performance of separation media to remove pollutants. Another major topic of this thesis is nanogel, a colloidal based soft material formed by physical or chemical crosslinking of polymeric chains. The physicochemical property of the nanogel can be tuned by varying the monomer, crosslinker content and reaction conditions. Therefore, nanogel is attracting increasing attention in many fields, especially biomedical [1] and antimicrobial applications [2] due to their flexibility and biocompatibility. However, only a few studies used nanogel for water treatment, such as in the removal of mercury [3]. Nanogel scaffold provides an ideal template to control the size of nano-clusters and reduce aggregation during the synthesis, thereby maintaining a high surface area for further modification. Thus, both cellulose

based nanomaterial and nanogel show promise in developing advanced nanomaterial for environmental applications.

In addition to the size and shape control of the nanogel, the abundance of functional groups makes them a good candidate for use as a nanoreactor to prepare organic or inorganic particles. Nano metallic clusters can be slowly generated and grew into the desired size and shape with desirable physicochemical properties, since the abundant functional can acted as a growth modifier or capping agent. Metallic nanoclusters prepared using these strategies possess unique properties, such as antimicrobial and photo illumination that can be used for antimicrobial and biolabeling applications.

1.2 Research Objectives

The motivation of this research is to develop advanced material and systems to address the environmental challenge, such as drinking water purification, wastewater treatment and antimicrobial applications. To obtain a well-controlled magnetic nanoparticle for the development of beta-cyclodextrin (β-CD) functionalized nano adsorbent, nanogel scaffold was employed to achieve this synthesis. However, the preparation of nanogel reported in the literature was complex with specific monomers or initiator additions that were difficult to be reproduced. Thus, the first objective of this study is to develop a reproducible nanogel with carboxy groups via a facile synthetic process, and the physiochemical properties of the nanogel will be fully studied. Then, β-CD functionalized magnetic adsorbents will be developed by grafting β-CD onto the magnetic nanoparticles (MNPs) prepared with the nanogel scaffold and future applied in drinking water purification. The adsorption efficiency and mechanisms will be studied and evaluated using a model drug, procaine hydrochloride (PrHy). Besides the adsorption process, the catalytic process is also considered as a good system for the conversion of toxic chemicals into non-toxic

compounds. Harmful microorganisms and fungi are also considered as significant threat to human beings and animals. Fungal species was found to be resistant to many wastewater treatment processes. Therefore, a nanogel assisted fabrication of silver nanoclusters (AgNCs) will be developed for antimicrobial and biolabeling applications. The last objective of this thesis to development of sustainable membrane for the removal of common pollutants like dyes and heavy metals, and also for the removal of emerging contaminates, such as perfluoroalkyl and polyfluoroalkyl substances (PFAS). The filtration process will be evaluated in both the batch system and dynamic filtration system. The major research studies conducted in this thesis is summarized below:

1) Facile synthesis of a pH-responsive nanogel and their characterizations.
2) Synthesis of a β-CD functionalized magnetic nano adsorbents and applied for drinking water purification
3) Adsorption mechanism of β-CD functionalized magnetic nanoparticles for the removal of procaine hydrochloride
4) The development of a silver nanoclusters (AgNCs) using a colloidal scaffold for biolabeling and antimicrobial applications
5) Synthesis of magnetic clusters modified palladium-cellulose nanocrystals hybrids as a recyclable catalyst for 4-nitophennol (4-NP) reduction
6) The development of a high porosity and sustainable adsorption membrane for cationic/anionic dye, heavy metal and PFAS removal

1.3 Thesis Outline

This thesis comprises 9 chapters, where Chapter 3 to 8 summarize the research results presented in the format of manuscript to be submitted for publication consideration. Chapter 1

describes the current water crisis and common methods used for wastewater treatment, and how nanogel and cellulose-based nanomaterial can be used as templating materials to address environmental issues. This chapter also summarizes the major objectives and contents covered in this thesis. Chapter 2 outlines and summarizes the background knowledge of nanogel, such as history, definition, synthesis method and applications. Various methods used to prepare magnetic nanoparticles are also summarized and compared. The various water treatment technologies, such as adsorption, photocatalysis and filtration was discussed and analyzed, and the β-CD based adsorbents were introduced, and related research work was comprehensively reviewed. Chapter 3 reports on the synthesis and characterization of a pH-responsive MAA-EA nanogel, and the physicochemical properties were fully elucidated. Chapter 4 explores the synthetic method of a β-CD functionalized magnetic nanoparticles (FMNP), and the adsorption kinetics and isotherm were investigated. Chapter 5 extends the study from Chapter 4 describing the synthesis of FMNP with different amounts of β-CD, and the effect of pH on the adsorption performance with procaine hydrochloride was reported. Chapter 6 discusses silver nanoclusters (AgNCs) fabricated via a photo-induced method within a nanogel scaffold that were applied to antimicrobial and biolabeling applications. Chapter 7 reports on a magnetic catalyst synthesized by attaching MNP onto melamine formaldehyde modified CNC and polydopamine coated CNC, and the catalytic performance was evaluated in the reduction of 4-nitrophenol (4-NP) to 4-aminophenol (4-AP). Chapter 8 examines a wood fiber (WF) membrane crosslinked with GPTMA and PEI and Pickering emulsion with enhanced porosity, and the filtration performance with MO, MB, Cu^{2+} and PFAS was evaluated by both gravity filtration and column dynamic filtration system. Chapter 9 provides an overview of the major conclusions, and also recommendation for future study in this thesis research.

Chapter 2: Literature Review

2.1 Introduction

This chapter presents a comprehensive review of the literature, including basic knowledge and progress of current research on the topics discussed in this thesis. First, an introduction on the history, definition, synthesis, classification and application of nanogels will be provided. Following the introductory section on cellulose-based material, the basic properties and benefits of the systems using for water treatment will be discussed. Some common techniques used for the synthesis of magnetic particles (MNP) will be described and compared, and which offers the motivation for using nanogel templated method to prepare MNP. In the last section, different water treatment processes will be introduced, such as adsorption, catalytic processes and membrane filtration. In addition, various water treatment processes enhanced by β-CD, are presented and discussed, followed by a review and summary on the modification and development of β-CD based adsorbent. The literature review provides necessary background information, comparison and summary of nanogels, cellulose-based materials (CNC, CNF, WF and β-CD) used for water treatment. Such information will help the reader to understand all the topics being covered in this dissertation.

2.2.1 Definition, history and background

Nanogels are aqueous dispersions of hydrophilic or amphiphilic polymeric particles crosslinked at the nanoscale (10-1000 nm) [4], [5]. They possess attractive features, such as high loading capacity, tunable chemical structure, biocompatibility, and stimuli-responsiveness which make them suitable for applications in tissue engineering [6], environmental remediation [3], and biomaterial science [7]. Nanogels have recently been highlighted as a simpler, versatile and more effective alternatives to hydrogel as the latter has several shortcomings, namely low diffusion rates and load capacities [8]. The term nanogel was first use in 1999 to describe a system of chemically crosslinked polyethyleneimine (PEI) and imidazole-modified poly(ethylene glycol) (PEG) designed for the delivery of antisense oligonucleotides to cells [9], [10]. However, earlier reports describe the phenomenon of physical crosslinking of cholesterol-modified polysaccharides (including pullulan, mannan, amylopectin and dextran) that resulted in the formation of swollen hydrogels in nano dimension, which were be classified as nanogels [8]. The most attractive property of nanogels is their distinct ability to swell and shrink in water or compatible solvents due to external stimuli such as temperature, ionic strength, magnetic field, light, or pH. During this process, the nanogels are able to maintain structural integrity while absorbing a large amounts of solvents. This is because of the involvement of hydrophilic functional groups, i.e. ($-OH$, $-COOH$, $-CONH$, $-CONH_2$, and $-SO_3H$) within the nanogel network [5], [11]–[14]. Stimuli-responsive nanogel can rapidly swell and shrink according to environmental changes making the nanogels suitable in applications, such as controlled drug delivery, wastewater treatment, biomedical sensors, and actuators [12], [14]–[16]. On top of that, the small dimension of the nanogel introduces the swelling behaviour, characteristic of macroscopic hydrogel systems, to the nanoscale [17]–[20]. This allows the nanogels to achieve many targeted intracellular sites or generate intramolecular interactions, which are not easily accessible by macromolecular

materials [21], [22]. The large specific surface area and high charge of nanogel improve the stability and accessibility of the loaded agents, which has also increased the sensitivity to respond to changes in the physiological environment [23]. Before reviewing the application of different nanogel systems, the classification of nanogel and synthetic method of nanogel fabrication will be introduced in the following section.

2.2.2 Classification of nanogels

- **Structure based classification**

  Researchers prepare nanogels with different structures or conformations to achieve the desired functions, which can be used to classify them. As seen in **Figure 2-1**, these conformations include artificial chaperones, multilayer, hairy, core-shell, hollow, and functionalized nanogels [24], [25]. Artificial chaperones can capture proteins and hydrophobic drugs via hydrophobic interactions. This makes them excellent carriers for active agents that can be used in vaccines, medical imaging and disease therapies. They are also able to act as molecular chaperones by preventing the aggregation of denatured proteins [26], [27]. The layer-by-layer conformation involves multiple polymer layers stack on top of each other through hydrogen bonding, ionic pairing, or hydrophobic interactions. Their outermost layer is responsive to external stimuli and the nanogel's physicochemical properties vary depending on the surrounding environment [28]–[30]. The core-shell conformation has two distinct areas, which allows different functionalities to be present in one particle [31]. Hairy nanogels consist of a core of inorganic or polymeric material and shell with grafted polymer chains. Thermosensitive hairy nanogels differ from other nanogels because of their unique sensitivity to the changes in the external temperature [24], [32]. Hollow structure nanogels have a cavity inside them, resulting in a larger surface area, which dramatically improve the drug loading capacity [33]. Functionalised nanogels have functional groups attached

to the nanogel, either before or after synthesis to impart selectivity toward an external stimulus, encapsulation of active agents, or stability [34].

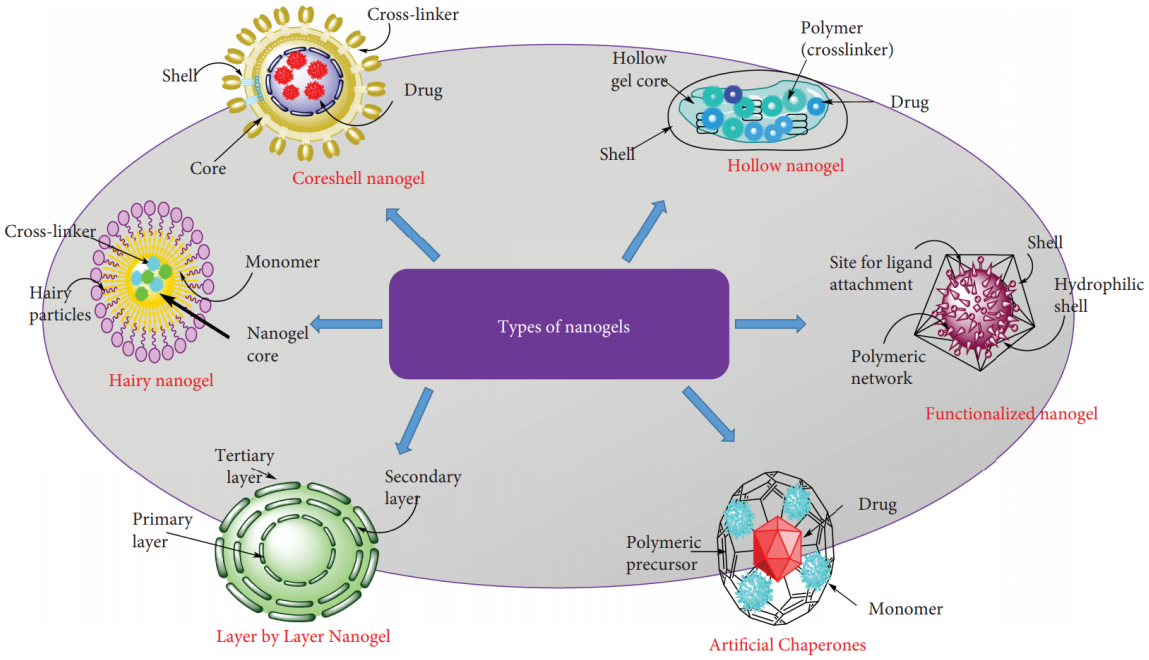


Figure 2-1 Types of nanogel formulations. Adapted with permission from ref [24]. Copyright © 2019 F. Sabir et al.

- **Stimuli-responsive based classification**

As mentioned before, one leading feature of nanogels is their ability to respond to external stimuli and they can be classified by it. The physicochemical properties (volume, refractive index, permeability, hydrophilicity, matrix integrity) of responsive nanogels are dependent on external stimuli [33]. Nanogel's can swell or shrink according to the change in environmental conditions, whether it be a physical stimulus (light, magnetic field, temperature) or chemical stimuli (pH, redox agents, enzyme condition concentration). The selectivity and responding of the nanogel are controlled by the fabrication technique and the structure of the nanogel [23]. In contrast, non-responsive nanogels act independently of external conditions and swell by absorbing the applicable solvent [10].

- **Classification of crosslinking method**

Another way to classify nanogels are based on the way they are crosslinked. Nanogels can be synthesized with natural or synthetic polymers that are either covalently crosslinked or physically crosslinked [5]. The loading of active compounds is achieved by interactions between the charged agent and the polymer matrix. Chemical crosslinking provides a much more stable matrix compared to physically crosslinks. That is due to the nature of covalent crosslinking (amine-based, disulfide-based, photo-induced) being stronger than non-covalent crosslinking (hydrophobic, van der Waals, electrostatic, hydrogen bonding) [34], [35]. Chemical crosslinking introduces permanent stability to the nanogel, while the physical crosslinking nanogel does not need any toxic crosslinkers or catalysts and can dissociate after completing its mission [36].

In this section, common methods and mechanisms on nanogel synthesis will be discussed and popular applications of nanogels will be reviewed and some perspectives into future applications will be discussed.

2.2.3 Synthesis of nanogels

Nanogels are promising templates and nano-reactors for preparing organic/inorganic nanoclusters, therefore, great efforts have been devoted to the synthetic technology of preparing the nanogels with different characteristics. Nanogels have been widely studied and prepared by a variety of methods, including emulsion polymerization, precipitation polymerization, reverse polymerization, micro-emulsion polymerization, mini-emulsion polymerization etc [37]. In the following section, some common methods used to synthesis nanogel will be introduced and their mechanisms will be elucidated.

- **Emulsion polymerization (EP)**

The most popular technique used to prepare nanogel is emulsion polymerization, which has been widely used for synthetic latex production [38]. Emulsion polymerization is a special type of

free radical polymerization, where the sub-micron size polymer particles formed in the presence of water insoluble monomers, surfactant, water-soluble initiator and solvent (mostly water) mixtures. The versatile applications of natural rubbers led to the interest on synthetic latex production in 1912 [39] and was scaled up to industrial level in mid-1930s [38]. The lack of natural rubber supplies during the Second World War motivated extensive research on the production of synthetic rubber, which was considered the key turning point of synthetic polymer development [40].

Before understanding the mechanism of emulsion polymerization, most of the synthetic polymer formulations were obtained through large amounts of trial and error experiments. One of the most precise description of emulsion polymerization was described by Gilbert, where the initial stage of emulsion polymerizations was like "put together with some physical feeling and a lot of black magic, and are made after trying many different formulations" [41]. However, the reproducibility and quality of synthetic polymer production cannot be well-controlled without understanding the fundamentals and mechanisms of the emulsion polymerization process. After a large quantity of research focusing on emulsion polymerization theories in different conditions and assumptions, the first emulsion polymerization mechanisms were proposed. Currently, there are three prevalent processes that describe the particle formation during the emulsion polymerization process, including micellar nucleation, homogeneous nucleation and droplet nucleation [38].

1. Micellar nucleation

For conventional emulsion polymerization, the concentration of surfactant used should be greater than the critical micelle concentration (CMC). Once all the air-water surface are covered by surfactant molecules, additional surfactant molecules would diffuse in the continuous phase (water) and self-assemble into micelles. Another large amounts of surfactant molecules functioned

to stabilize the monomer droplets. The hydrophobic monomers diffuse from the monomer droplets to the water and further diffuse from the water to the hydrophobic center of the micelles. The initiators form reactive radicals in the aqueous phase and enter the monomer swollen micelles to initiate the polymerization process. Monomers in the micelles quickly polymerize and a dispersion of polymer particles are formed after the termination of the growing chains (**Figure 2-2**). Usually, one of 100-1000 micelles will grow into a polymer particle. The number of polymer particle is decided once the nucleation process was terminated as indicated by the disappearance of the micelles. The size of monomer droplet is much larger than the micelles and serves as a monomer reservoir until 30 to 40% of monomer conversion is reached in the emulsion polymerization process [41], [42].

2. Homogeneous nucleation

In the case of homogeneous nucleation mechanism, the initiator radicals form in the aqueous phase and propagate into water-soluble oligomers with the monomers diffusing continuously to the reactive polymer chains. The oligomers will precipitate from the solution once they grow longer and reach the limit of solubility in the aqueous phase. Precipitated oligomers will form primary particles after absorbing sufficient surfactant that stabilize the polymer particle in the aqueous phase. The final polymer particles will form by the coagulation or propagation of primary particles. The major difference between micellar nucleation and homogenous nucleation is that the number of particles and the size of particles in homogenous nucleation are highly depending on the concentration, types and efficiency of stabilizer used [39], [43].

3. Homogenous-coagulative nucleation

The homogeneous-coagulative nucleation mechanism is a combination of coagulation of the primary particles formed from the micelles and homogeneous nucleation. Primary particles are

usually colloidally unstable, they become stable after slow coagulation with each other and absorbing enough surfactant molecules to the polymer particles [42], [44].

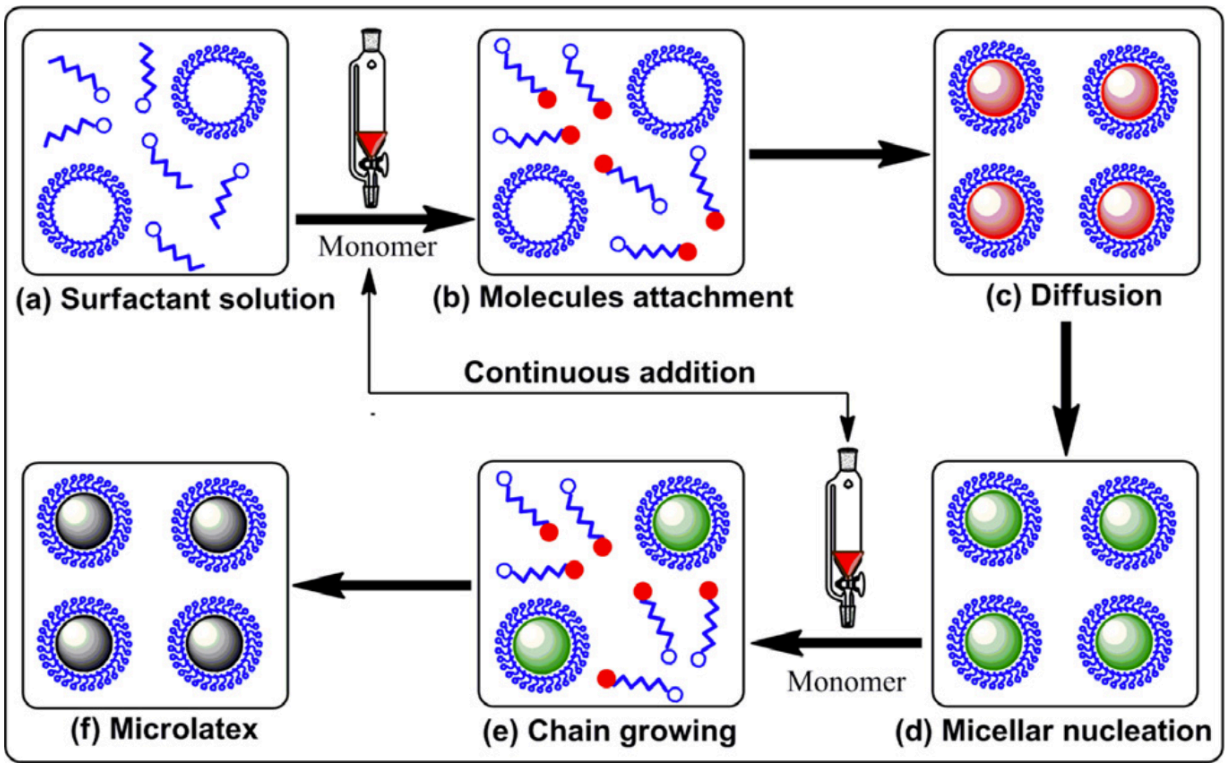


Figure 2-2 Schematic illustration of micellar nucleation, where blue color represents surfactant molecules, red color stands for monomer molecules, green color indicates growing polymer chains, and black color represents the nanogel particles. Adapted with permission from ref [45]. Copyright © 2010 Published by Elsevier. H. Wang et al.

4. Coagulative or droplet nucleation

For coagulative nucleation or droplet nucleation, the reactive radicals formed in the aqueous phase, and propagate with monomers in the continuous phase. Or the initiator radicals formed in the aqueous phase would enter the monomer swollen micelles and start to form the primary particles. The final polymer particles stabilized by surfactant will be generated by the coagulations of primary particles [42], [44]. One thing to note is that the functionality of surfactants are different for micelle nucleation/homogeneous nucleation compared with homogeneous-coagulative

nucleation/ coagulative nucleation. The surfactant works only as a stabilizer for homogeneous-coagulative nucleation/coagulative nucleation, while they also function as nucleation centers for micellar nucleation/ homogeneous nucleation [42]. After understanding the basic rules and mechanisms, it will be more effective when design and operate the experiments. More information on the kinetic based studies and related historical experiments can be found in these references [46], [47].

- **Precipitation polymerization (PP)**

Precipitation polymerization is another type of heterogenous polymerization techniques used to prepare high quality polymer particles, which does not require surfactant during the synthesis step. It is very efficient in term of clean particle preparation compared with other polymerization techniques, since the removal of surfactant after the polymerization process is always a time-consuming process. Also, the precipitation polymerization is a simple system that only consist of monomers, crosslinkers, initiators and solvent. The polymerization starts from the self-crosslinking of monomers and crosslinking agents, the polymer particle will precipitate from the system after it reaches the solubility limit in the solvent following the homogeneous nucleation mechanism [48]. The stability of the nanogel particles is derived from the electrostatic repulsion between the particles resulting from the participation of initiator segment in the polymer chains, such as sulfate groups [49]. Even though precipitation polymerization can produce clean nanogel particles, the difficulty in obtaining regular and uniformly-shaped particles limited their applications. Recently, more complex precipitation polymerization techniques were introduced in order to meet different requirements of particle size, including distillation precipitation polymerization (DPP) [50], photo initiated precipitation polymerization (PIPP) [51] , and living radical precipitation polymerization (LRPP) [52].

- **Mini-emulsion polymerization**

The oil-in-water emulsion can be classified by the size of the emulsion droplets, including macroemulsion (1-100 μm), miniemulsion (50-500 nm) and microemulsion (1-100 nm) systems. The stability of these three emulsion systems is another important factor to note when designing nanogel for specific applications. The stability of the emulsion system depends on many factors, such as the characteristic of monomers, types of surfactant, oil to water ratio, etc. Usually, the nanogel particles possess a size ranging from 50 to 500 nm that are suitable for many applications. Also the size range is specifically ideal for the human body's blood circulation making the nanogel compatible for biomedical applications [53]. In this section, only mini-emulsion polymerization will be discussed.

The kinetics, particle size distribution and other physiochemical properties of latex produced from emulsion polymerization are determined by the mode of nucleation of the polymer particles. Mini-emulsion polymerization is usually designed to allow the whole nucleation process to occur in the emulsion droplets, instead of micelles or aqueous phase. This needs to be accomplished by varying the concentration of the surfactant added to the system and reduce the lifetime of oligomeric radicals in the aqueous phase. The biggest advantages of mini-emulsion polymerization compared to other traditional polymerization technique is their ability to control the final amount of particles produced. This can solve the biggest concern, irreproducibility, of the latex particle production. However, the accurate control of the nucleation stage is not easy to implement, and large amount of experiments need to be conducted to control the concentration of surfactant to below the CMC, the accurate control of the types and concentration of initiators etc. [38].

- **Inverse polymerization**

In short, inverse polymerization describes a water-in-oil system consisting of hydrophilic monomers and oil-based continuous phase. The inverse polymerization process is commonly used

to prepare high molar mass latex, since the initial monomer content is as high as 30-35% of the total mass. Also, limiting the growth of free radicals in each particle can effectively prevent the possibility of coagulative termination. In essence, inverse polymerization belongs to a heterophase polymerization, where the emulsifier plays an important role in term of the colloidal stability both before and after the polymerization. The key parameter of the emulsifier used is the hydrophile-lipophile balance (HLB) value, oil-in-water emulsion forms when HLB exceeds 7, while the water-in-oil emulsion forms when the HLB is less than 7. **Figure 2-3** illustrates the HBL value and corresponding applications.

HLB Range	General application
2 – 6	W/O emulsification
7 - 9	Wetting and Speading
8 - 18	O/W emulsification
3 - 15	Detergency
15 - 18	Solubilization

Figure 2-3 HLB value and corresponding application. Adapted with permission from ref [54]. Copyright © 2018 R. Setiati et al.

The kinetics of inverse emulsion polymerization is determined by the solubility of the initiator. The presence of monomer (amides, a commonly used monomer for inverse polymerization) can greatly increase the solubility of the initiator in the aqueous phase. However, the homogeneous nucleation can occur due to the low solubility of hydrophilic monomer in the oil phase. Another key factor that affects the inverse polymerization kinetic is the emulsifier concentration; higher polymerization rate can be achieved when the emulsifier concentration is increased. Many other experimental factors can affect the reaction kinetics, such as the reaction temperature and types of hydrophobic solvent used that can alter the interfacial tension on the oil/water phase. After the initial development of inverse polymerization, the inverse

microemulsion polymerization was developed around 1980s. It effectively addresses the issues of broad size distribution and the formation of unstable latex particles by using excess amounts of surfactant. It was popularly used to produce individual Mannich polyacrylamide emulsions without severe interparticle entanglement, which typically occurs in conventional inverse polymerization [38].

2.2.3 Nanogels applications

The versatility of nanogel and microgel systems has attracted a lot of interest in fundamental research and industrial applications. Their crosslinked-swellable structure and stimuli-responsive property gives them promising potential for biomedical applications, environmental remediations, and tissue engineering. In the following section, some of the recent advances in nanogel applications research will be presented.

- **Biological applications**

The flexible nanogel structure allows them to integrate bioactive components and release them under appropriate conditions. The nano or microscale impart the nanogel with a high specific area, low non-target adsorption and long-lasting colloidal stability. All these advantages allow them to address many difficulties in the biological domain, which cannot be solved using other materials. In the following section, some advanced nanogel applied in biological field will be introduced, including their preparation method, unique properties and superior profit over other materials for the same applications.

The implant related infections due to autoimmune rejection are still a big concern in the current medical field, which is mainly caused by the biofilm formed on the implant surface. The conventional antibiotic can cause non-target delivery and bacterial resistance, which cannot prevent infection and inflammation. Nanogel, as a type of hydrated flexible polymeric particles capable of encapsulating antibacterial compounds can be effectively used to control the infections

in a non-invasive way. Damla and coworkers recently developed a Triclosan loaded nanogels to prepare an antifouling surface that offer an alternative way to combat biofilm growth, with the performance of 99.99% kill for *S. aureus*. The nanogel was fabricated by co-polymerizing poly (N-isopropylacrylamide) with 3(dimethylamino)propyl]methacrylamide (P (NIPAM-co-DMAPMA)) through precipitation polymerization. After the quaternization of the tertiary amine of DMAEMA, further modification with Triclosan was achieved by hydrophobic interaction with the nanogel network (**Figure 2-4**). This drug-loaded nanogel system with a target release function can be used as a multifunctional surface coating with anti-fouling and antimicrobial properties [2]. Another advanced implanted device, contact lens, were fabricated by drug-loaded nanogels used for glaucoma treatment. The drawbacks of burst release and low capability for sustainable release with eye drops and drug-soaked contact lenses was solved by this drug-loaded nanogel systems. A nanodiamond (ND)-containing contact lens were fabricated from enzyme-cleavable nanogels that entrapped timolol maleate (TM). The release of TM can be triggered by lysozyme and release in a continuous manner. The drug-loaded nanogel was prepared by crosslinking PEI coated ND with 50% N-acetylated chitosan in the presence of TM. Compared with the release of drug from imprinted contact lenses and drug soaking contact lenses within 1 hour, this drug-loaded nanogel system could retain TM for 24 hours with minor elution. While, it could cumulatively release less than 9.41 μg over 24 hours when lysozyme was present, since chitosan could be degraded by lysozyme. This drug-loaded nanogel system addressed the problem during storage and also achieved control release [1].

Except for control-release, nanogels are also used as a nano-carrier for encapsulating metallic alloys, such as gold, silver, titanium and copper nanoparticles. Among them silver nanoparticles are popularly applied in antimicrobial application. However, pure silver

nanoparticles tend to aggregate, have low stability and separation after use. It can only weakly bind to other materials, resulting in leaching and direct contact of silver nanoparticles with the surrounding medium, such as organs presents some toxicity concerns. Nanogel with different functional groups can incorporate with metal particles and provide a non-invasive binding between the metal nanoparticles and the surface. Also, the barriers of the nanogel help to eliminate the toxicity issues caused by direct contact. A popular strategy for preparing silver nanocomposite with nanogel is a one-pot mini-emulsion method. The polymerization was conducted with metal precursor, and a subsequent reduction will be applied to obtain the final product.

However, a more intelligent method using the state of the art such as irradiation to produce metallic nanoparticles in a three-in-one simultaneous process. It uses the energy of irradiation to initiate the polymerization, crosslinking and nanoparticle reduction at the same time. **Figure 2-5** presents the mechanism of silver nanoparticles and nanogel composite synthesized by gamma irradiation. Recently, a biofunctionalized fabric consisted of essential oil encapsulated nanogel was developed for skin contact applications. The bioactive nanogel was synthesized via mini-emulsion polymerization of polyacrylamide in the presence of silver nitrate, the polymerization proceeded under γ-irradiation for 2 hours. Then, the bioactive nanogels mixed with polyethylene glycol (PEG) consisting of the water phase and three different kinds of essential oils stabilized with AOT were used as the oil phase. The bioactive emulsion was formed by dropwise addition of the oil phase into the water phase under continuous stirring for two hours. Finally, the bio functionalized skin contact pad was obtained by immersing the O_2 plasma exposed polypropylene (PP) fabric into the mini-emulsion system for 2 hours. The emulsion was confirmed with no irritation effect or any adverse inflammation in Swiss albino mice. Also the nanogel barrier

eliminated the burst release and the indirect bonding of silver nanoparticles to the mice skin, which effectively reduced the toxicity level of free silver ions [55].

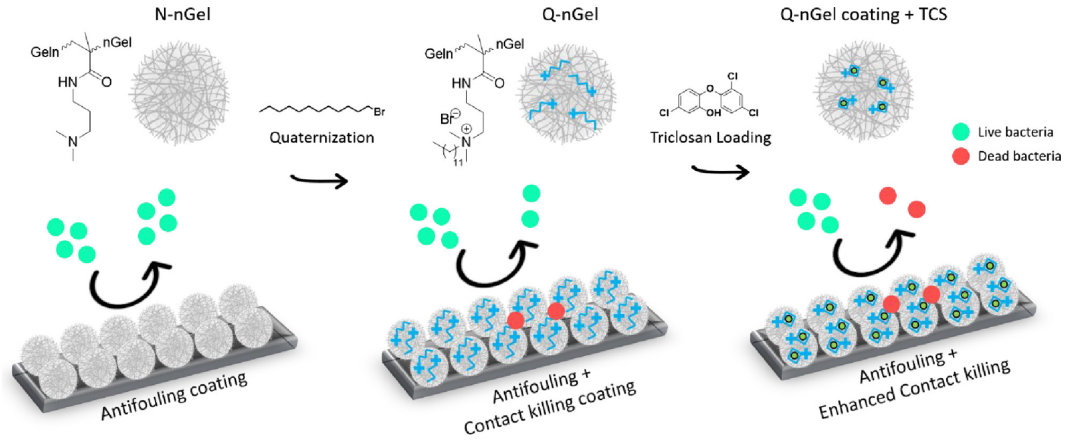


Figure 2-4 Schematics of the preparation and antifouling mechanism of the nanogel coating. Adapted with permission from ref [2]. Copyright © 2020 American Chemical Society D. Keskin et al.

Multifunctional nanogel combining with bioactive compounds is an important branch of bioengineering, more research effort should be devoted to developing nanogel with innovative structures and functions to address more bio-related challenges [56]. In addition, further consideration should be given to the current limitation on the application of nanogel to real applications, including long-term stability, purification of synthesized nanogel, use of organic solvents and reproducibility of large-scale production.

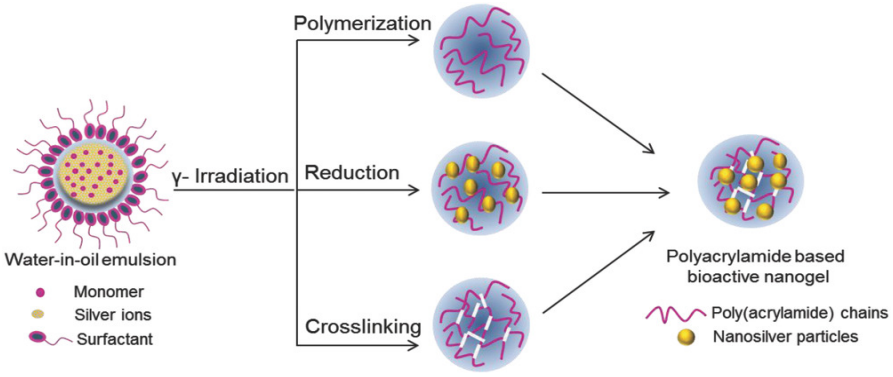


Figure 2-5 The schematic of the production mechanism of a bioactive nanogel by gamma reduction strategy. Adapted with permission from ref [56]. Copyright © 2018 The Authors. Published by WILEY-VCH Verlag GmbH & C0. KGaA, Weinheim.

- **Environmental remediation**

Nanogel has a high surface area, which can be modified with various functional groups compared with bulk material. Nanogel can be easily dispersed in both hydrophilic or hydrophobic systems enabling them to be a good candidate for adsorbent development. Nanogel based adsorbents are applied for removing various pollutants, such as heavy metals, dyes and pharmaceuticals. Recently, Zhang et al. developed a thiolated amphiphilic nanogel to remove environmentally relevant concentration of mercury from both water and hydrocarbon systems. Firstly, the disulfide containing crosslinker (BMOD) was prepared by a single step reaction of 2-hydroxyethyl disulfate and methacryloyl chloride. The disulfide nanogel was synthesized via mini-emulsion polymerization, then tributylphosphine (Bu_3P) was used to break the disulfide networks to generate a nanogel with abundant thiol groups (**Figure 2-6**). This strategy effectively avoided the inhibition of polymerization, which was caused by the chain transfer nature of the thiol groups. The maximum adsorption capacity (Q_m) of Hg(II) in water was 470 mg/g when the initial concentration was 200 mg/L, which is two times more than a commercial silica based sorbent. The Q_m of Hg-dissolved organic matters (Hg-DOM) in water and the Q_m of di(hexanethio) mercury (Hg-alkyl thiol) in n-dodecane were 26 mg/g and 40 mg/g respectively. Even though the sorption capacities are much lower compared with Hg(II), they can be removed more than 70% at an environmental relative concentration [3].

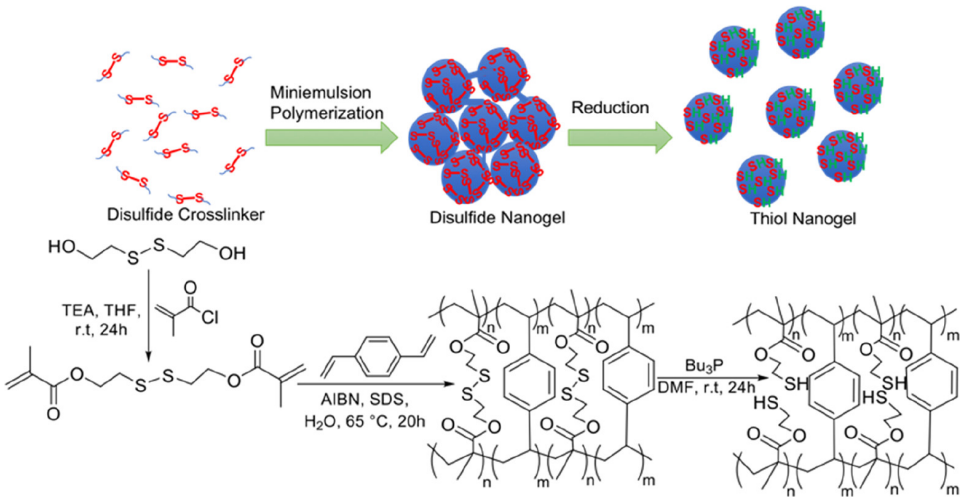


Figure 2-6 The schematic illustration of thiol abundant nanogel synthesis procedure. Adapted with permission from ref [3]. Copyright © 2021. American Chemical Society Y. Zhang et al.

The ability to incorporate different organic or inorganic particles into the nanogel is another active research topic. Lately, a bio-mimic magnetic nanogel was developed to purify bleaching effluents. Amino-acidified lignin (Gly-lignin) was first prepared to simulate the ingredient of reed root. The reed root is a natural material that can remove heavy metals from the soil by reducing heavy metal ions through the functional groups found in the reed root. Then, the Gly-lignin, cellulose and nanoscale Fe_3O_4 were mixed to prepare the nanogel (LDMNGs) through sol-gel method. It was found that the adsorption capacities of Ni^{2+}, Pb^{2+} and Hg^{2+} were highly dependent on pH, their adsorption capacity could reach 0.596, 0.174 and 0.339 mmol/g respectively at pH 5. The differences in the adsorption capacities are mainly determined by the steric hindrance caused by the ionic radius. The adsorption performance of three different dyes (malachite green (MG), methyl orange (MO) and methylene blue (MB)) were also investigated. The adsorption capacities were mainly decided by the chemical structure of different dyes, and also the surface charge at different pHs. In terms of reusability, all of the adsorbents could achieve 90% removal efficiency even after three times regeneration with hydrochloride acid. This work provides an insight into the

natural material's functionality to build sustainable nanogel based adsorbent by replenishing the natural waste with useful functional groups [57].

Nanogels also possess excellent film formation character, which can be used for membrane fabrication by the assembling process. Zang et al. developed a zwitterionic nanogel modified membrane for oil/water separation. The zwitterionic nanogel was prepared from dimethyl-(3-sulfopropyl) ammonium hydroxide (DMAPS), N, N-methylenebis (acrylamide) (MBA) and acrylamide (AA) monomers through reverse emulsion polymerization. The zwitterionic nanogels modified polyacrylonitrile (ZPAN) nanofibrous membrane was obtained by immersing the hydrolyzed PAN membrane into the MES solution with N-(3-dimethyla- minopropyl) -N-ethylcarbodiimide hydrochloride (EDC) and N- hydroxysuccinimide (NHS) for 1h and followed by 24 hours immersing into the nanogel solution. This ZPAN membrane possess superwetting and antifouling properties, which effectively separated oil and water by low pressure driving process. As high as 99.6% of oil rejection was achieved due to the enhanced surface roughness of PAN membrane after nanogel modification, and also the zwitterionic nanogel imparted to the membrane a high tolerance of the harsh environment in some applications. This work is promising for large scale oil removal, such as crude oil leakage from the drilling process, the low working pressure and antifouling property can significantly reduce the energy and capital costs [58]. In conclusion, both pure nanogel and nanogel composite can be applied in versatile applications for environmental remediation, which can achieve multiple functions with one material. For instance, the incorporation of magnetic particles into the nanogel based adsorbent can avoid the secondary separation after adsorption. More focus should be devoted to the development of the advanced nanogel system to address environmental related issues.

- **Sensing or detecting applications**

Sensing or detection technology is an important domain in biomedical science, such as the cancer screening, bacterial detection, disease detection, and bio-markers in diagnostic devices. Nanogel is a 3D structure with lots of water, which is very similar to the radiological properties of tissues. Lately, a nanogel sensor was developed to measure the ionizing radiation (IR) doses via colorimetric fluorescence method. The nanogel was prepared by reverse emulsion polymerization with three monomers, including acrylamide (AAm), N-(3-aminopropyl) methacrylamide (APMA) and APMA modified-5(6)-carboxytetramethylrhodamine (TAMRA) and crosslinker N, N'-methylenebisacrylamide (BIS). After the fabrication of the supporting nanogel (PAAT), an IR sensitive fluorescent responsive component, coumarin-3-carboxylic acid (CCA) was incorporated into the nanogel via the coupling of the amino groups. When the PAAT nanogel was exposed to UV excitation, it emitted a strong blue fluorescence light, while TAMRA as an IR inert probe emitted stable red fluorescence (**Figure 2-7**). The colorimetric fluorescence signals of this nanogel based sensor presented good linear relationship with IR doses within 20 Gy (LOD=0.1 Gy). This sensor exhibited great potential in terms of colorimetric fluorescence measurement of IR dosing, and it possessed high reproducibility and low error compared to other nanogel or metal nanoparticle based IR sensor. The high accuracy and straightforward of this sensor enable it to be applied in radiotherapy [59].

Nanogels are also commonly used as a sensing probe to investigate the conformation or transition of composition in a polymeric network, such as hydrogel, due to their adjustable chemical properties and small scales. For example, a nanogel based sensing probe was first synthesized by crosslinking methyl methacrylate (MMA), methacrylic acid (MAA) and ethyleneglycol dimethacrylate (EGDMA) via emulsion polymerization. This precursor nanogel

was vinylated by a ring opening reaction with glycigyl methacrylate (GMA) to form vinyl-functionalized nanogel (NG).

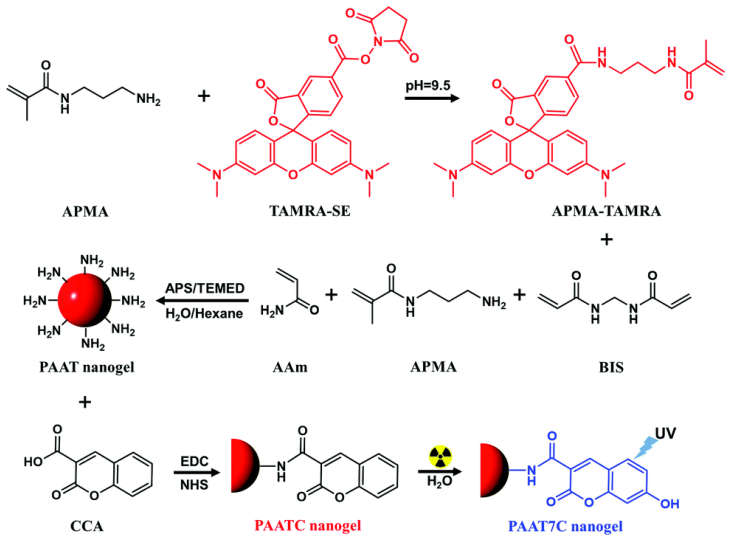


Figure 2-7 The synthesis pathway of PAATC nanogel and the mechanism of ionizing radiation doses detection. Adapted with permission from ref [59]. Copyright © The Royal Society of Chemistry 2019.

The nanogel probe containing the photoexcited fluorophore (donor): (9-phenanthryl)methyl methacrylate (Ph), and a ground-state fluorophore (acceptor): (9-anthryl)methacrylate (An) was prepared by a free radical precipitation polymerization [60]. Finally the double crosslinking nanogel DX NG(NGPh/An)x were formed by polymerizing the NG precursors with fluorescence labelled nanoparticles (NGPh/An). The NGPh/An dispersions were highly sensitive to pH and the photoliminescene (PL) intensity was changed correspondingly. With the increase of the pH from 4.5 to 9.0, the intensity of the pH donor band (ID) at 366 nm increased, while the intensity of the acceptor band (IA) at 414 nm decreased. The ratio of ID/IA increased with increasing pH, since the resonance energy required to transfer from Ph to An reduced due to their separation caused by the swelling of the nanogel. The strain sensing possibility of this nanogel was investigated by incorporating it into a robust PAAm-Laponite RD (LAP) nanocomposite gel. This composite gel

changed from purple to blue when it was compressed, and the ID/IA decreased from 1.25 to 0.85 when the applied strain increased from 0 to 72%. The nanogel probes have a great potential for exploring the conformation transition and strain sensing of a gel indicated by a pH triggered ratiometric fluorescence intensity [61]. Besides single functional nanogels, the simultaneous application of nanogels for diagnosis and treatment is a new trend in biomedical science. Wu reported a series of core-shell multifunctional hybrid nanogels with adjustable magnetic properties and fluorescent response induced by changes in the pH. The model nanogel was prepared by coating the Ni-Ag metallic core with a pH responsive nanogel shell. Most of the work mention above were only focused on translating the fluorescence signal to other detectable signal through a linear relationship upon the changing of surrounding conditions. However, this work not only made use of the fluorescence property of metal particles, but also incorporated the inclusion property of nanogels. The hybrid nanogel also encapsulated chemotherapeutic drugs into the nanogel shell, which enabled a new prototype that could simultaneously detect and treat the disease [62]. Similar nanogel systems were also applied in cancer diagnosis and therapy [63], [64].

After a comprehensive review of the nanogel including background, history, classification, synthetic methods and applications, there exists many benefits and unique features of nanogel motivated the Chapter 3 of my PhD study. It described a facile synthesis of a pH responsive nanogel, and various characters of the nanogel system was fully investigated. Chapter 4, 5, 6, 7 described and discussed the use of nanogel as a template together with other organic or inorganic particles to address different environmental based problems, such as wastewater treatment and antimicrobial application.

2.2 Sustainable material selected for water treatment process

The green and sustainable materials used as building blocks to prepare novel adsorbents in my study will be introduced in this section. Currently, there are many traditional materials used for wastewater treatment, including activated carbons (ACs) and petroleum-based materials, which have large carbon footprint during the production and utilization [65]. Therefore, in order to reduce negative impacts during the preparation of adsorbents and the disposal of the used adsorbents, it is necessary to select low cost, environmentally friendly and lower carbon footprint materials to prepare the adsorbents. The cellulose-based material is regarded as one of the most promising materials for constructing different systems suitable for various applications, since they are one of the most abundant biopolymers that originate from trees. Cellulose materials are used in micro or nanoscales, since many limitations (low diffusion rate, low loading capacity, pore mechanical properties) of bulk materials can be addressed by their high surface area. There are several different types of cellulosic sourced material were considered in my PhD study, including cellulose nanocrystals (CNC), (cellulose nanofibrils) CNF, beta-Cyclodextrins (β-CD) and wood fibers (WFs). In the following sections, the history, properties and production of each material will be introduced. Different strategies used to modify these cellulose-based nanomaterial will be introduced as well. Also, the incorporation with other materials to fabricate effective adsorbents applied for water treatment process will be discussed.

2.2.1 Cellulose nanocrystals (CNC)

Cellulose fibers derived from plants consist of amorphous regions and crystalline regions, and CNCs are obtained from the acid hydrolysis of cellulosic fibers. After acidic hydrolysis, the amorphous domains will disintegrate, and the remaining intact crystalline segments comprise of CNCs. The plant based CNCs obtained after acid hydrolysis possess a length of 100-250 nm and diameters of 5-70 nm, with a high aspect ratio nano-rods (**Figure 2-9**) [65]. The surface chemistry and colloidal stability of CNCs are mainly determined by the types of mineral acids used in the acid hydrolysis process. For example, sulfuric acid hydrolysis imparts abundant negative sulfate half-ester groups on the CNC surface that impart high colloidal stability due to the electrostatic repulsive forces, while hydrochloride acid hydrolysis yields CNCs with hydroxyl and carboxyl groups rendering the particle will low stability [66]. Except the functional groups generated during the acid hydrolysis process, their abundant hydroxyl groups driven from sugar units provide the possibilities for various surface modifications (**Figure 2-8** imparting specific functional groups to the CNCs for various environmental remediation). CNCs were selected as the basic building block for constructing adsorbents, and their non-toxicity, biodegradability and sustainability impart them low carbon footprint. Their large area, high aspect ratio provides numerous active adsorption sites for the removal of pollutants. Lastly, their abundant sources, low cost, producing them for real water treatment applications.

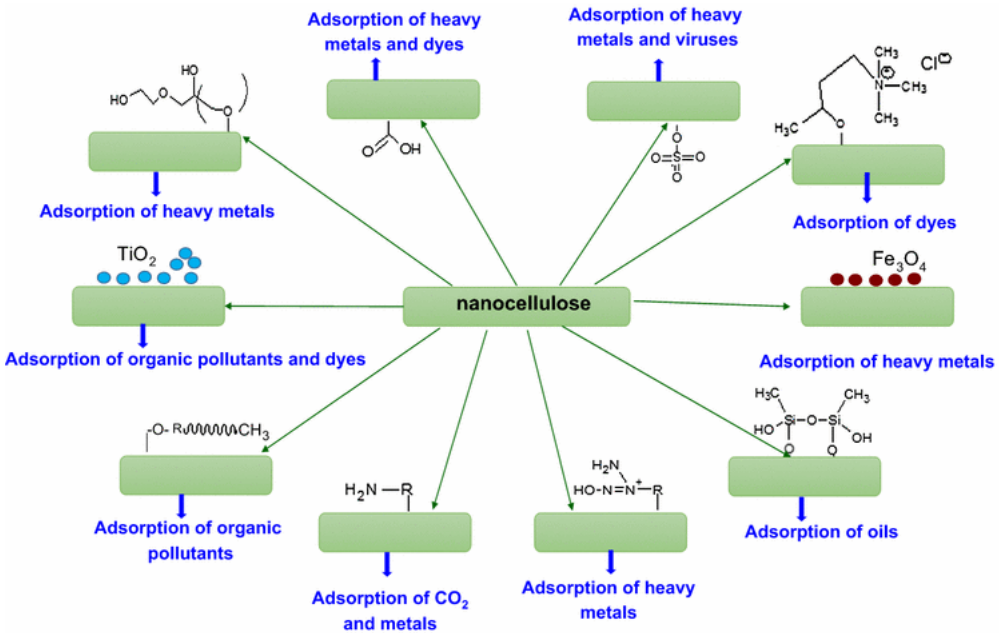


Figure 2-8 Surface modification pathways of CNC depending on the pollutant type. Adapted with permission from ref [67]. Copyright © 2017, Springer Science Business Media Dordrecht.

2.2.2 Tanfloc (TF)

Tanfloc (TF) is a tannin-based cationic polymer driven from the black wattle tree (*Acacia Decurrens*), which is a commercial flocculant used in water treatment. Tannins belong to a class of natural materials known as plant phenols, which is the fourth plentiful by-product of the forest. The tannins are initially negatively charged, the tanfloc is obtained after the introduction of an amino group in the structure of the tannin [68]. TF possess repeated unit of substituted amine group with a pKa value lower than 6.0, results in a positive charge density when pH below 6 [69]. In contrast to the chemical flocculant, tannin-based material are extracted from plants, they are biodegradable, non-toxic with abundant sources, which is considered as a promising alternative to iron salt, aluminum and other conventional inorganic flocculants. The high positive surface charge and the ability to interact with negatively charged material allow TF a good coating material with no complex reaction.

2.2.3 Cellulose nanofiber (CNF)

CNF with nanometric lateral dimensions was obtained from softwood pulp suspensions by passing it through a high pressure homogenizer several times to break the cellular walls. The CNF obtained from the mechanical treatment, such as homogenization, extrusion and grinding contains both crystalline and amorphous regions [70]. Sometimes, chemical treatment was also utilized to reduce the mechanical energy required to produce CNF. Commonly the chemical pretreatments using 2,2,6,6-tetramethyl-1-piperidinyloxy (TEMPO), periodate-chloride, glycidyltrimrthylammonium chloride (GTMAC) and (2,3-eppoxypropyl)trimethylammonium chloride are being reported [71]. The main differences between CNC and CNF are their dimensions and crystallinity, the CNF was 5 to 100 nm laterally and 0.5 to 5 μm in length, which is much larger than CNC. CNF contains both crystalline and amorphous domains with a crystallinity of 60 to 80%, while CNC contains mainly crystalline domains. The high aspect ratio of CNF makes them suitable for the production of larger-scale adsorbent, such as microbeads, hydrogel or thin film membrane (TFM), which can be easily separated after the water treatment process. **Figure 2-9** shows the production process of CNC and CNF from different processes.

2.2.4 Beta-cyclodextrin (β-CD)

Cyclodextrins (CDs) are nature polymers generated from enzymatic degradation of starch, and there are three major types of cyclodextrins classified based on the number of sugar units it contains. They are designed as α, β and γ cyclodextrins with 6,7 and 8 sugar unit respectively [72]. Among them, β-CD is widely studied because of their inner cavity size (7.8 Å), which is suitable for many aromatic pollutants. Combining with the hydrophobicity of the internal cavity, that can form inclusion complexes with many organic molecules. And the hydrophilic property of the outer shell imparts high stability to the functionalized system, which allows them to be a promising building block for adsorbent construction. The low solubility of β-CD makes it easier to purify via

a non-solvent process. Because of the unique properties of β-CD, they are used to eliminate various types of pollutants, including dyes, heavy metals, pharmaceutical residues and even PFAS. β-CD based adsorbent can effectively remove PFAS under real environmental conditions, since size exclusion can avoid the competitive adsorption of natural organic matters (NOM), which commonly existed as a disrupting compound for PFAS removal. Due to the small size of β-CD cavities, many works have been devoted to improving the stability and accessibility of the β-CD cavities by loading onto the high surface area matrix. Therefore, a stable high surface area nanogel templated magnetic particles functionalized with β-CD was developed in my PhD study. It was applied for the removal of a model pharmaceutical, procaine hydrochloride, and the adsorption mechanisms under different pH was investigated.

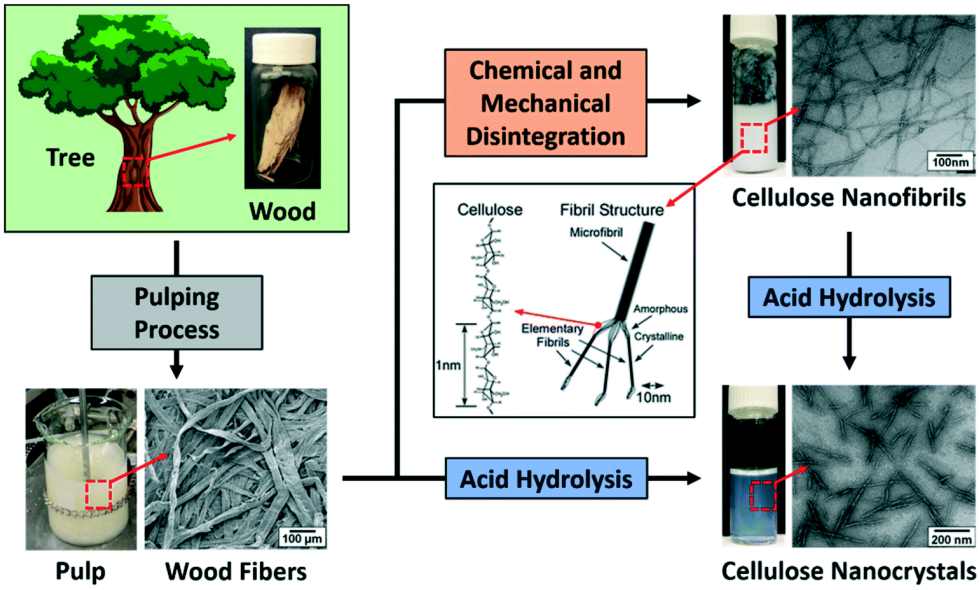


Figure 2-9 The formation of cellulose fibres obtained from wood pulp, and the following production process of CNC and CNF. Adapted with permission from ref [71]. Copyright © The Royal Society of Chemistry 2018.

2.2.5 Wood fiber (WF)

Wood fibers (WF) can be classified into two categories: softwood fiber and hardwood fiber, which were extracted from soft conifers and hard deciduous trees, respectively [73]. Hardwood

fiber with heterogeneous structure possess a more complex vessel elements for transport functions, while softwood fiber has a simpler structure with only long and slender cells and ray parenchyma [74]. The major difference between softwood fiber and hardwood fiber is the fiber length, which closely related to the mechanical property of the fibers. Softwood fiber possess a length of 3 to 7 mm, while hardwood fiber has only 1 to 2 mm length lead to a lower tensile strength [75].

2.3 Synthesis of magnetic particles (MNP)

Among the development of nanomaterials, magnetic nanoparticles (MNPs) are attracting a great deal of research interest. They have been used in a wide range of applications, such as controlled drug release, magnetic resonance imaging, data storage, and environmental remediation such as water treatment. These applications were achieved by manipulating the particles using an external magnetic field. Currently, many synthetic pathways have been developed to prepare shape-controlled, highly stable and monodispersed magnetic nanoparticles. The most common synthetic methods include co-precipitation, thermal decomposition, metal salt reduction, micelle synthesis, hydrothermal synthesis, and laser pyrolysis technology. The methodologies and mechanisms of these synthesis methods will be introduced in the following section.

2.3.1 Co-precipitation

Co-precipitation is the easiest way to synthesize magnetic nanoparticles from aqueous Fe^{2+}/Fe^{3+} salt solutions by adding a base solution under inert atmosphere at ambient or higher temperatures. The reaction mechanism can be described as:

$$Fe^{2+} + 2Fe^{3+} + 8OH^- \rightleftharpoons Fe(OH)_2 + 2Fe(OH)_3 \rightarrow Fe_3O_4 \downarrow + 4H_2O$$

Based on the chemical thermodynamic theory of this reaction, the precipitation of Fe_3O_4 should be conducted at a pH of between 8 and 14, with a stoichiometric ratio of 2:1 (Fe^{3+}/Fe^{2+}) in an inert

environment. Many factors can affect the size, shape, morphology, and composition of the MNPs, such as the type of salts used (chloride, sulfate or nitrite), the ratio of Fe^{2+} to Fe^{3+}, the reaction temperature, pH value, and the ionic strength of the solvent. The magnetic saturation values of MNPs synthesized by this method are usually between 30 and 50 emu/g, which is lower than the value of their bulk counterpart, 90 emu/g. Magnetite (Fe_3O_4) particles are not stable under ambient atmosphere and can easily convert to maghemite (Fe_2O_3, γ-Fe_2O_3), which is chemically stable under ambient conditions; or dissolved in acidic media [76].

One big challenge in synthesizing MNPs by co-precipitation method is the broad size distribution. It is difficult to manipulate the size and distribution of particles by co-precipitation, since the nucleation rate of the particle is rapid at the beginning of the synthetic process. The particle size distribution is important, since it can affect various properties of the MNPs that can further affect their performance in some applications. For example, the temperature at which the thermal energy can overcome the anisotropic energy is defined as blocking temperature (T_B), and this T_B depends on particle size. Also, T_B is the critical point of MNPs, in terms of transformation from ferromagnetic to superparamagnetic status. When the particle size is close to the size of a single magnetic domain and the temperature is higher than T_B, it will become superparamagnetic. A range of particle sizes will yield a range of T_B values, offering superparamagnetic properties for different applications at varying temperatures. Although MNP prepared by coprecipitation is generally polydispersed, this can be resolved by separating nucleation and particle growth during the synthesis [76], which can be achieved by adjusting pH, since the nucleation of MNPs is promoted at a pH below 11, while particle growth is favored when the pH exceeds 11 [77].

Thus far, many revised co-precipitation methods have been developed to achieve a narrow particle size distribution and higher saturation magnetisation. Pereira and coworkers developed a

novel one-step co-precipitation route to prepare superparamagnetic MFe_2O_4 (M= Fe, Co, Mn) nanoparticles. They used alkanolamines isopropanolamine (MIPA) and diisopropanolamine (DIPA) instead of sodium hydroxide. The size of these stable superparamagnetic MFe_2O_4 nanoparticles was between 4 and 12 nm. Compared with MNPs prepared via the traditional precipitation method, the particle size decreased by 6 times and the saturation magnetization increased by 1.3 times. The alkanolamines can both be used as an alkaline reagent and complexing agent to have a better control of the particle size during synthesis. They also reduced the nonmagnetic portion ('dead layer') of the particle by the rearrangement of the spins. They proposed that the sub-coordinated metal atoms interacted with the nitrogen and oxygen atoms of MIPA and DIPA, which reduced the volume ratio of spin disorder to spin order domains of the MNPs. **Figure 2-10** shows the schematic of the 'dead' layer reducing mechanism by using MIPA and DIPA for MNPs synthesis [78].

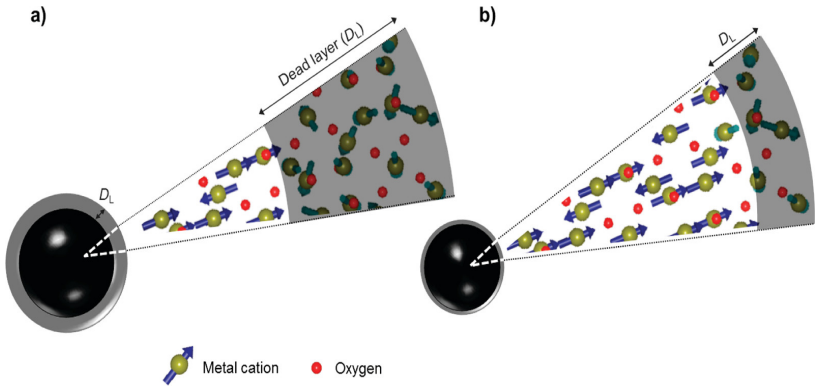


Figure 2-10 Schematic representation of the effect of different types of base on the thickness of the 'dead' layer (shadowed region) and spin rearrangement at the surface of the MNPs(a) for NaOH (b) for MIPA and DIPA. Adapted with permission from "A. G. et al. Pereira, Clara, André M. Pereira, Carlos Fernandes, Mariana Rocha, Ricardo Mendes, María Paz Fernández-García, "Superparamagnetic MFe_2O_4 (M = Fe, Co, Mn) Nanoparticles: Tuning the Particle Size and Magnetic Properties through a Novel One-Step Coprecipitation Route Clara," *Chem. Mater.*, vol. 24, pp. 1496–1504, 2012" [78]. Copyright 2012 American Chemical Society.

Except for the challenge of narrow particle distribution, other obstacles that can stop MNPs from being applied in biomedical field are aggregation and biocompatibility. Several studies have attempted to add surfactant and biomolecules during the co-precipitation process to address these problems. Hoang used plyvinylpyrrolidone (PVP) and cetyltrimethylammonium bromide (CTAB) as a co-surfactant system to synthesize spherical Fe_3O_4 MNPs. Compared with the MNPs prepared without surfactant, there was a slight increase of the particle size and less aggregation [79]. Suh reported another novel approach to co-precipitate Fe_3O_4 inside a polymer matrix, which was realized by placing iron ions into the deprotonated carboxyl-rich polymer matrix and forming magnetic particles by nucleation. **Figure 2-11** shows the polymer matrix MNPs synthesis process, showing that the polymer matrix still has unoccupied carboxyl groups after the first cycle of co-precipitation process. This feature imparts such magnetic polymer matrix a pH responsive property, even after loading Fe_3O_4, which can be useful for biomedical applications. [80]

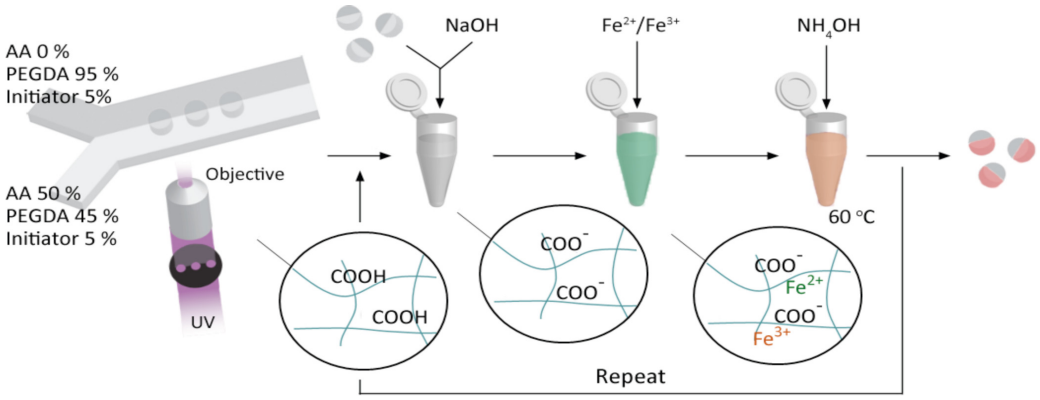


Figure 2-11 Schematic of the MNPs synthesis process. Adapted with the permission from "K. W. Bong, P. S. Doyle, D. K. Hwang, T. A. Hatton, S. K. Suh, and K. Yuet, " Synthesis of Nonspherical Superparamagnetic Particles: In Situ Coprecipitation of Magnetic Nanoparticles in Microgels Prepared by Stop-Flow Lithography ," *J. Am. Chem. Soc.*, vol. 134, no. 17, pp. 7337–7343, 2012" [80]. Copyright © 2012 American Chemical Society.

Even though the co-precipitation method is one of the simplest approaches to prepare MNPs with high saturation magnetization particles, more research should focus on addressing the disadvantages like the wide range of particle size distribution and agglomeration. Only when these issues are addressed, can the applications of MNPs prepared by the co-precipitation be expanded.

2.3.2 High temperature thermal decomposition

The high temperature thermal decomposition method was developed to address the disadvantage of high levels of particle nucleation in the co-precipitation process. The thermal decomposition method consists of two stages: hot-injection step and conventional reaction step. During the hot-injection step, precursors are injected into the reaction vessel containing the hot reaction mixtures. During the conventional reaction step, the reaction mixtures are heated to 300℃ to form the final magnetic nanoparticles. Compared to low crystallinity MNP synthesized by co-precipitation methods, MNP prepared by thermal decomposition of organometallic complexes possess high crystallinity, mono-dispersity and narrow size distributions. These desirable properties were obtained by separating nucleation from particle growth and the complex hydrolysis process. In order to produce monodisperse MNPs, oleic acid, 1-octadecene, oleyamine and 1-tetradecene are commonly used as stabilizer during the reaction, and they can effectively reduce the nucleation rate. The adsorption of the additives on the nuclei can affect the growth rate of the crystals, so smaller MNPs can be obtained by the thermal decomposition process [81]. The MNPs prepared by thermal decomposition are usually smaller than 30 nm with a narrow size distribution.

Alivisatos and coworkers synthesized monodispersed γ-Fe_2O_3 by thermal decomposition of iron cupferron in octylamine [82]. William reported high quality Fe_3O_4 nanocrystals less than 30 nm were successfully prepared by thermal decomposition of iron carboxylate salts [83]. Vitalii and coworkers synthesized monodispersed superparamagnetic Fe_3O_4 nanoparticles by thermal

hydrolysis of iron (III) glucoronate. The morphology and particle size distribution of MNP can be controlled by reaction temperature, stabilizer concentration, and types of solvents used. When the temperature exceeded 300 ℃, the size distribution was found to be narrow. Also, the particle size of MNPs could be controlled by the concentration of oleic acid (OA), where higher concentration yielded smaller particle sizes [84]. Park reported on an ultra-large-scale synthesis of monodisperse magnetic nanocrystals by reacting inexpensive and non-toxic metal salts with yields greater than 95%. **Figure 2-12** shows the overall scheme for the ultra-large-scale synthesis of monodispersed nanocrystals. Firstly, the metal-oleate precursors were prepared from metal chlorides and sodium oleate. Then, the monodisperse nanocrystals were synthesized by thermal decomposition of metal-oleate precursors in high boiling point solvent. The size of the MNPs was controlled by varying the aging temperature and other experimental parameters. Based on TEM, DSC/TGA and infrared results, they proposed a mechanism for the nanocrystal formation. The nucleation phase occurred at 200 to 240℃ and was initiated by the dissociation of one oleate ligand from the $Fe(oleate)_3$ precursor by CO_2 elimination. The main nanocrystal growth occurred at around 300℃, which was triggered by the dissociation of two oleate ligands, even though slow particle growth still occurred when the temperature was below 250℃. The most impressive part of their work was that high quality monodispersed nanocrystals were successfully synthesized by separated particle nucleation and growth stages. This was achieved by the discovery of the different temperature dependencies of nucleation and growth kinetics. They also confirmed that this synthesis strategy can be applied in preparing other transition metal oxides, such as MnO, CoO, and ZnO [85].

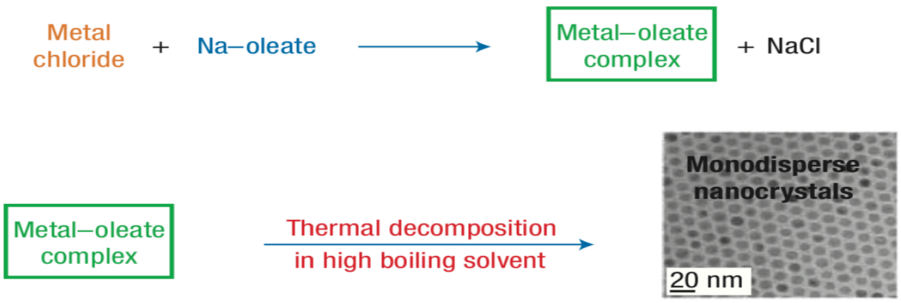


Figure 2-12 Scheme for the ultra-large scale synthesis of monodisperse nanocrystals. Adapted with permission from "A. P. et al Patsula, Vitalii, Lucie Kosinová, Marija Lovrić, Lejla Ferhatovic Hamzić, Mariia Rabyk, Rafal Konefal, "Superparamagnetic Fe_3O_4 Nanoparticles: Synthesis by Thermal Decomposition of Iron(III) Glucuronate and Application in Magnetic Resonance Imaging," Appl. Mater. surfaces, vol. 8, pp. 7238–7247, 2016" [84]. Copyright © 2016 American Chemical Society.

Another benefit of thermal decomposition method is that it can be used to prepare MNPs with different morphologies, such as nano-cubes and nanospheres. Amara synthesized Fe_3O_4 nanotubes and nanospheres using a modified method of thermo decomposition, which is a one-step solvent-free reaction. The size of the nanocubes was controlled by adjusting the weight ratio of ferrocene to PVP. Nanosphere MNPs were obtained when the ferrocene/PVP ratio was 1:5, and annealed at 350℃ for 4 hours. This method can also be used to prepare other transition metal oxides like ZnO and Bi_2O_3 with different morphologies [86]. Even though the thermal decomposition method was successfully applied to produce specific sized nanocrystals, the solvent boiling results in poor shape control. It has been revealed that the gas bubbles generated by solvent boiling has a stronger effect on the nucleation step than the growth step, which lead to the inaccurate control of the particle size [77].

2.3.3 Hydrothermal and solvothermal synthesis

Hydrothermal or solvothermal synthesis of MNPs is a wet-chemical technique to crystallize the compounds in a sealed reaction vessel with solvent at 130-250℃ under 0.3-4 MPa. This method

has been widely used for producing dislocation-free single crystal particles, and the particles prepared by this method possess better size and morphology control compared to other techniques. As a result, it is desirable to synthesis highly crystalline MNPs by hydrothermal or solvothermal strategy because of the good control of the composition of nanocrystals. When the aqueous reaction media is replaced with organic solvent, it becomes known as the solvothermal process [77].

Wang reported on a solvothermal method to prepare well-dispersed $LiFePO_4$ nanorods with diameters of 70 nm and a length of 90-150 nm. The XRD and TEM results showed that the $LiFeO_4$ nanorod was a single crystal with the b-axis along the axial direction. This nanoparticle orientation improved the electrochemical performance of the nanocomposite by accelerating the electrode reaction [87]. Clearly, the MNPs prepared by the hydrothermal and solvothermal method are superior to those prepared by other techniques, since they could generate high quality iron oxides with accurate control of the composition.

2.3.4 Sol-gel reactions and polyol method

The sol-gel method is commonly used in the fields of material science and ceramic engineering for synthesizing nanostructured metal oxides. This process consists of the hydroxylation and condensation of molecular precursors in a solution, which initiates a “sol” of nanoscale particles. The metal oxide gel is formed by condensation and inorganic polymerization of the precursors. Traditional precursors for synthesizing magnetic nanoparticles are iron alkoxides and iron salts like chlorides, nitrates, sulfates, and acetates. Generally, the MNPs will be generated via a two stage form transitions:

$$Fe(OH)_3 \rightarrow \beta\text{-}FeOOH \rightarrow \gamma\text{-}Fe_2O_3$$

For example, Zhang reported on a green sol-gel process to synthesis core-shell structured

Fe_3O_4@SiO_2-NH_2 nanoparticles for Pb(II) removal. The Fe_3O_4 MNPs were first prepared by a solvothermal method, followed by the co-condensation of Fe_3O_4@SiO_2-NH_2. It was achieved by adding 3-aminopropyl trimethoxysilane (APTMS) after the hydrolysis of tetraethyl orthosilicate (TEOS). The Fe_3O_4@SiO_2-NH_2 nanoparticles could be easily recovered using an external magnet, and the Q_m of Pb(II) was as high as 243.9 mg/g at 25℃. **Figure 2-13** shows the schematic that describes the co-condensation process and the effect of different loading amounts of APTMS. It was demonstrated that the concentration of APTMS has a significant effect on the morphology of the silica shells. As the increase of APTMS loading, the uniformity and dispersibility of the Fe_3O_4@SiO_2-NH_2 MNPs decreased. If the amount of APTMS was further increased, aggregated MNPs and some isolated small silica particles appeared, which could be attributed to the self-condensation of silica. It was demonstrated that the basic amino-groups on APTMS promoted the hydrolysis of TEOS and APTMS. Also, when the amount of APTMS increased, the growth rate of silicate surpassed the nucleation rate, resulting in the formation of larger particles. Another important factor in the formation of uniform spherical core-shell structure was the alkalinity of the system [88].

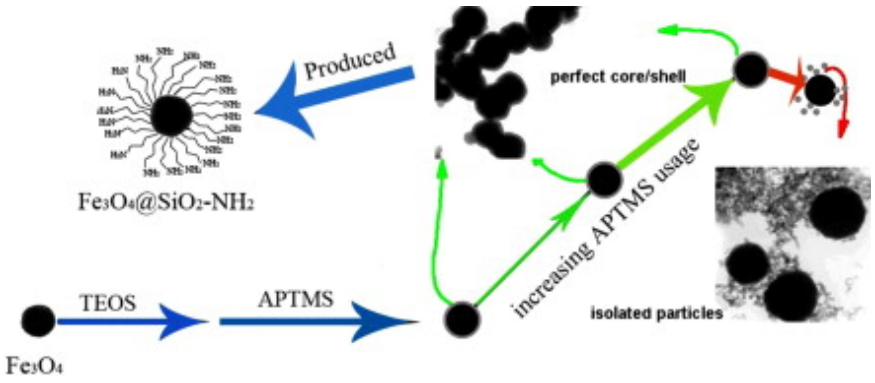


Figure 2-13 The schematic illustration of the sol-gel process of Fe_3O_4@SiO_2-NH_2 and the effect of APTMS loading on the formation of core/shell structure. Adapted with permission from ref [88]. Copyright © 2012 Elsevier B.V.

Lemine successfully synthesized monodispersed magnetite (Fe_3O_4) nanoparticles with an average size of 8 nm via a sol-gel process. The saturation magnetization (M_s) of these particles was 47 emu/g, which is promising for biomedical applications [89]. Xu prepared MNPs using a sol-gel process and investigated how the synthesized Fe_3O_4 nanoparticles could be transformed into α-Fe_2O_3, γ-Fe_3O_4 and α-Fe via different annealing processes. The synthesized Fe_3O_4 nanoparticles transformed to γ-Fe_3O_4 when it was annealed in air at 300℃. However, the Fe_3O_4 nanoparticles transformed into α-Fe_2O_3 when it was oxidized at 500℃. This method was found to be environmentally friendly and could be extended to fabricate other metal oxides [90].

The polyol method is also considered an inverse sol-gel method, which can be used to obtain MNPs with specific morphology. During the polyol process, the polyol acts as solvent, reducing agent, and stabilizers to control the particle growth and avoid particle aggregation. Typically, the iron precursor is suspended in a liquid polyol, where is stirred and heated up to a specific temperature. Compared with hydrothermal processes, the polyol process does not require high pressures, so there is no need to use a Teflon-lined stainless steel autoclave [91]. Cheng synthesized the MNPs using different polyol processes and investigated the resulting morphological evolutions. Two kinds of polyols, ethylene glycol (EG) and 1,2-propylene glycol (PG) were investigated, and the morphological evolution of the MNPs was very different in these two polyols. This can be attributed to the different reductive capabilities of the polyols that leads to different growing rates of the nanoparticles. The faster growing rate of MNPs in PG led to a quicker aggregation of the particles and generated misalignments in the clusters. Every cluster composed of several ordered mesocrystals, and the neighboring nanoparticles combined to become a single crystal with porous structure during the Ostwald ripening process. On the other hand, when EG was the reducing agent, the nanoparticles could self-assemble in the same direction in

the clusters due to the low formation rate of nanoparticles. The mesocrystal could maintain its flower like cluster, due to the low surface energy [92].

Compared with the co-precipitation method, the sol-gel process and polyol method have many benefits. The MNPs prepared by the sol-gel process can be easily dispersed in water or other polar media, since there are many hydrophilic groups on the surface of MNPs. The MNPs prepared by the sol-gel process possess high crystallinity and saturation magnetization, which can be attributed to the high reaction temperature. However, there are still some limitations of the sol-gel process, such as the high cost of precursors and safety concerns related to the production of alcohol during the process. [77].

2.3.5 Microemulsion

Microemulsion is a thermodynamically stable isotropic dispersion of a liquid mixture. It consists of oil, water, surfactant, and may also contain a co-surfactant. Generally, the surfactant forms a monolayer at the interface between oil and water. The hydrophobic tails of the surfactant will dissolve in the oil phase and the hydrophilic head will dissolve in the water phase, and vice versa. In the case of preparing MNPs, the liquid phase contains metal salts or other precursors, and the oil phase is a mixture of hydrocarbons and olefins. Traditional microemulsions are either oil dispersed in water (O/W) or water dispersed in oil (W/O), and both have been used to prepare MNPs. There are many surfactants commonly applied for the synthesis of MNPs, such as bis (2-ethylhexyl) sulfosuccinate (AOT), sodium dodecyl sulfate (SDS), CTAB, and PVP. A number of factors impact the size and mechanism of MNP synthesis, including droplet size, monomer concentration and surfactant properties [77].

For example, Okoli prepared MNPs via two different W/O microemulsion systems for biological applications. The MNPs obtained from microemulsion system I, ME 1-MION, was

prepared by mixing two W/O microemulsion solutions together. One of the W/O emulsions contained metal precursors with surfactants dispersed in an oil phase. Then, it was added dropwise to the other emulsion under vigorous stirring, which is a mixture of precipitating agent and surfactants dispersed in an oil phase. Several washing steps were applied to the ME 1-MION before any further usage. The second microemulsion process was a one-step synthesis procedure. The formation of the ME 2-MION was achieved by adding the precipitating agent to the microemulsion which included metal precursor and surfactants. A dark brown color emulsion system indicated the formation of ME 2-MION. The prepared ME-MIONs was 7 to 10 nm with well-defined spherical shape. The MNPs prepared by microemulsion process possessed desirable magnetic properties allowing easy separation from the solution. Along with the good control of particle size, the process is promising for producing MNPs for protein purification [93]. However, the drawbacks included several cleaning and stabilization steps required due to MNP aggregation, even though surfactants were used during the synthesis procedure.

2.3.6 Sonolysis or sonochemical method

The sonochemical method is also called ultrasound irradiation, which uses the chemical effects of ultrasound generated from acoustic cavitation to initiate the reaction. The sonochemical method provides an alternative approach to produce novel structured materials without requiring high temperatures, high pressures, or long reaction times. The ultrasound irradiation produces alternating expansive and compressive acoustic waves, and the acoustic waves will create oscillating bubbles or cavities. Ultrasonic energies will accumulate in the oscillating bubbles until the bubbles grow to tens of millimeters. Sometimes under appropriate conditions, a bubble will overgrow and collapse, releasing the accumulated energy stored in the bubble in a short time (together with a heating or cooling rate over 10^{10} K/s). This bubble implosion results in high

temperatures and pressures in a small area, around 500 K and 1000 bars respectively. As a result, the sonochemical method is a good alternative to produce MNPs by sonicating ferric or ferrous salt solution in mild reaction conditions [94].

For instance, Teo reported a novel one-pot synthesis of latex MNPs with particle sizes of around 100 nm by ultrasound irradiation. The mechanism of mini-emulsion process is summarized in **Figure 2-14**. The particle formation process was controlled by a droplet nucleation mechanism. The mini-emulsion droplet was considered as a nanoreactor that contains the preformed Fe_3O_4 nanoparticles. The Fe_3O_4 nanoparticles were prepared by a hydrothermal method, and the purified Fe_3O_4 nanoparticles were dispersed in n-butyl methacrylate (BMA) monomers. An O/W mini-emulsion was prepared by mixing water with SDS as the dispersant for the nanoparticles or monomer dispersion. Before further sonication, the liquid mixture was purged with argon to remove oxygen and increase the amount of the radicals in the solution. Then, the liquid mixture was subjected to 20 s of sonication at 8 W/cm^2 to obtain a uniform mini-emulsion. The polymerization reaction was completed with an additional 50 min sonication process. They explained that the polymerization reaction was initiated by primary radicals formed during the acoustic cavitation. The particles were superparamagnetic with a saturated magnetization of 24 emu/g, and the magnetic fluid remained stable over 12 months. This work has provided a new ultrasound procedure, which can be used as an effective method for producing a range of nanocomposites, including various polymer matrices and encapsulated materials [95].

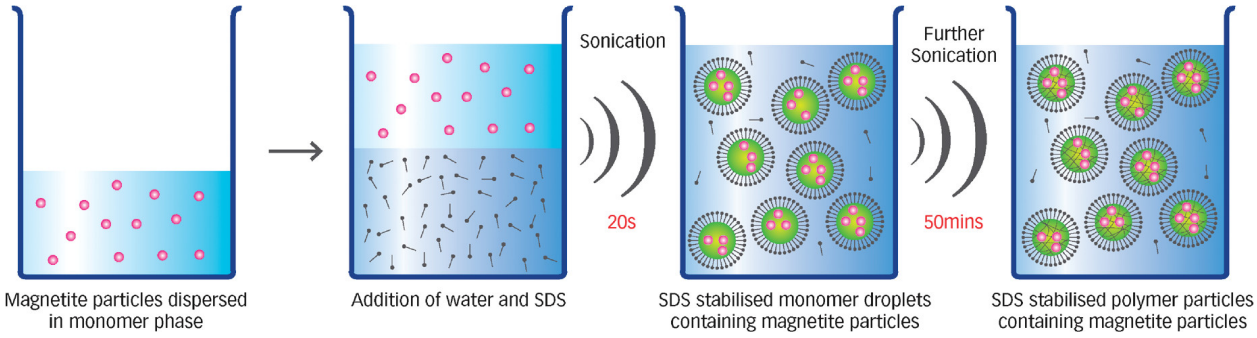


Figure 2-14 The schematic diagram of the procedure for the encapsulation of magnetic nanoparticles and monomer droplet to latex particle conversion. Adapted with permission from " M. A. Teo, Boon M., Fei Chen, T. Alan Hatton, Franz Grieser, "Novel one-pot synthesis of magnetite latex nanoparticles by ultrasound irradiation," Langmuir, vol. 25, no. 5, pp. 2593–2595, 2009 [95]. Copyright © 2009 American Chemical Society.

The sonochemical method is superior compared to other techniques in terms of uniform mixing, reduction of crystal growth rate, and accelerated polymerization rates. However, the inability to synthesis MNPs with specific particle shape and the low dispersity stop them from many applications that requires high stability and accurate control of the particles [77].

2.3.7 Microwave assisted synthesis

The microwave assisted synthesis method has been used to prepare organic particles, organometallics, and peptides since the 1980s. Recently, the microwave assisted methodology was applied for inorganic material synthesis. It has been demonstrated that the molecules will experience excitation when exposed to electromagnetic radiation. The molecules will align their dipoles with the external field when excited by the microwave radiation. Microwave synthesis is a promising method because it significantly reduces the reaction time, side reactions, energy cost, and usually have a high yield [77].

Waseem reported a microwave-hydrothermal method for synthesising γ -Fe_2O_3 nanoparticles, the superparamagnetic particles had an average particle size of 10 nm. Their work confirmed that lower temperatures and reaction times were required in comparison with other

preparation methods [96]. Hu reported on the synthesis of magnetite, maghemite and hematite nanoparticles by microwave assisted hydrothermal process, and it can be achieved by varying the reaction parameters. The production of pure hematite was fulfilled using a single precursor $FeCl_3$. Magnetite and maghemite nanoparticles were prepared by using $FeCl_2$ as the single precursor with different drying processes. The maghemite particles were prepared by a one-step microwave assisted process within 6 min from a mixture of $FeCl_2$ and $FeCl_3$ [97]. The microwave assisted synthesis method is used to prepare biocompatible magnetic nanoparticles. For example, Liu reported on a synthesis of biocompatible polyacid-conjugated Fe_3O_4 superparamagnetic hybrid nanoparticles through microwave assisted synthesis. The particle size of this hybrid MNPs was depended on the $FeCl_3$ loading during the reaction. The hybrid MNPs were not only well dispersed in aqueous systems, but the uncoordinated carboxylate groups on the particle surface also provided the possibilities for grafting with antibodies, drugs and proteins [98]. Compared with the thermal decomposition method, the preparation of MNPs by the microwave assisted process could be easily dispersed in water without complicated stabilization such as using surfactant or homogenizer [77].

A summary and comparison of MNP synthetic strategies discussed in this section are listed in **Table 2-1**. In terms of ease of the reaction process, co-precipitation method should be the first choice for MNPs preparation. In terms of good shape control, thermal decomposition appeared to be the best process for preparing MNPs smaller than 20 nm, while hydrothermal or solvothermal method was best suited for synthesis of MNPs larger than 20 nm [77]. Other processes such as sol-gel, microemulsion, and sono-synthesis can also be alternatives for synthesizing MNPs with narrow size distributions and controllable morphologies. Nevertheless, the major challenges for synthesizing MNPs are to obtain specific sizes, shapes, compositions, and narrow nanoscale size

distribution particles. These difficulties exist because MNPs tend to aggregate to minimize the system surface energy. At present, all methods of magnetic nanoparticle synthesis require several steps with different microstructure problems that may have side effects on the magnetic properties. Therefore, the development of a simple and flexible synthesis method for preparing MNPs with desired size and morphologies without aggregation is essential to applying these materials in different applications.

Table 2-1 Comparison of different synthesis methods for MNPs. Adapted from ref [99]. Copyright © 2015 W. Wu et al.

Method	Reaction conditions	Reaction temperature℃	Reaction time	Size distribution	Shape control	Yield
Co-precipitation	Very simple, ambient	20-150	Minutes	Relatively narrow	Not good	High, scalable
Thermal decomposition	Complicated, inert atmosphere	100-350	Hours-days	Very narrow	Very good	High, scalable
Hydro- or solvolthermal synthesis	Simple, high pressure	150-220	Hours-days	Very narrow	Very good	High, scalable
Sol-gel and polyol method	Complicated, ambient Complicated, ambient	25-200	Hours	Narrow	Good	Medium
Microemusion	Complicated, ambient Complicated, ambient	20-80	Hours	Narrow	Good	Low
Sonosynthesis or sonochemical method	Very simple, ambient	20-50	Minutes	Narrow	Bad	Medium
Microwave-assisted synthesis	Very simple, ambient	100-200	Minutes	Medium	Good	Medium

Based on the above review and discussion, traditional MNP preparation methods can be used to synthesize MNPs with defined shape and size. However, monodispersed MNPs can only be generated under high temperature and high pressure, which is energy intensive. In my PhD study, the colloidal scaffold approach was used to achieve size control under mild synthetic conditions. The MNPs was prepared by in-situ co-precipitation of Fe^{2+} inside the MAA-EA colloidal scaffold followed by oxidation process. This nanogel scaffold worked as a nanoreactor to prepare magnetic

nanoparticles with a narrow-scale distribution. The nanogel scaffold was also used as a nano reactor for synthesizing other types of metal clusters like silver and applied to biomedical related applications.

2.4 Water treatment technologies

2.4.1 Wastewater treatment ad drinking water purification

Water is essential for humans, so it is important to make sure the water supply is still adequate. Also, the water quality is closely associated with human health and plays an important role in the balance of the ecosystem. However, water resources are increasingly threatened by pollution caused by overcrowding, industrial and agricultural activities and climate change. These lead to the generation of wastewater, which can be divided into three parts: 1) human household activities, 2) agriculture related water pollution (such as fertilizer, pesticides, herbicides, animal waste and salts from irrigation water evaporation), and 3) industrial related water pollution (heavy metals from mining industries, and toxic chemicals and dyes come from textile industries). For these reasons, water quality assessment is necessary to evaluate the drinkability of water coming from different water resources. Generally, water quality can be assessed using performance indexes, such as biochemical oxygen demand (BOD) and chemical oxygen demand (COD). COD corresponds to the oxygen consumption for all chemical processes in water. BOD describes the amount of bio-degradable organic matter in water and is primarily used to assess domestic wastewater, while COD is most used to assess industrial wastewater. The values of BOD and COD are also affected by other indicators such as pH, total suspended solids (TSS), total suspended solids (TS), and water temperature (T) [100].

Typically, the wastewater treatment process consists of three stages: primary, secondary and tertiary treatments (**Figure 2-15**). In the primary treatment phase, heavy solids settle at the bottom

of the quiescent basin, while oils and other light impurities float to the surface. After removal of sediment and suspended impurities, the water will be discharged to the secondary treatment system based on specific discharge requirements. Secondary and tertiary treatments will be bypassed during heavy rainfall to prevent hydraulic overload. The main objective of secondary treatments is to break down the biological content mainly from household waste, such as food waste, detergents and personal care products. This process is usually accomplished through aerobic biological processes, and sometimes another classifier is used to deposit and separate biological flocculants. Finally, if wastewater is discharged into highly sensitive or fragile systems, physical or chemical disinfection such as microfiltration will be applied at the tertiary level [101].

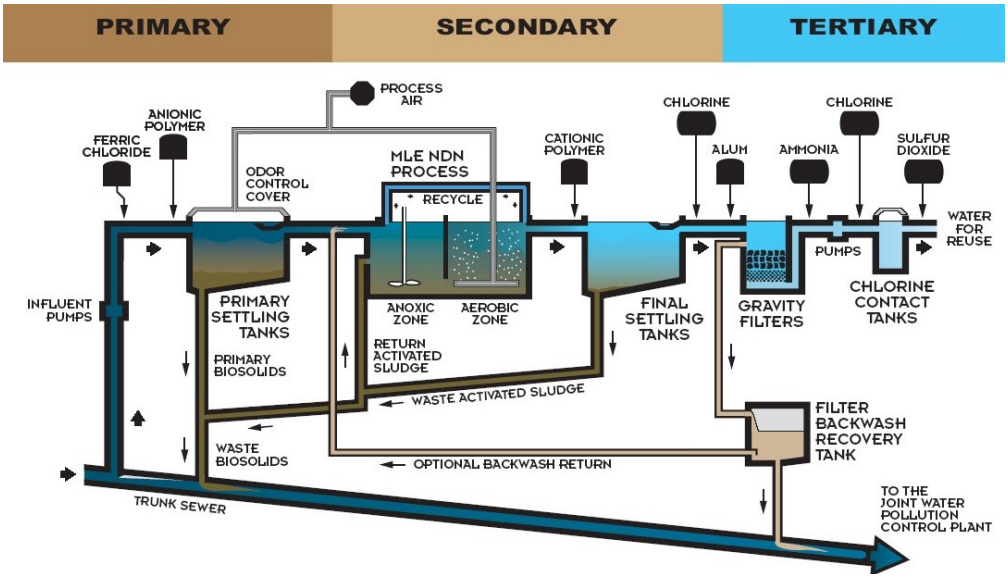


Figure 2-15 A typical flow schematic of a wastewater treatment plant (Source: https://www.lacsd.org/home/showpublisheddocument/3578/637644521003970000)

2.4.2 Categories of water treatment processes

Common techniques applied to water purification can be divided into six types: adsorption, biotechnology, catalytic processes, membrane processes, ionizing radiation processes and magnetic assist processes. In addition, nanomaterial-based water treatment processes are also

emerging as promising alternatives to water treatment. Some important water treatment technique will be introduced in the following section.

a) Adsorption

Adsorption is widely used to remove low concentrations of non-degradable organic compounds from different water sources. It is a surface phenomenon that describes the accumulation of a specific compound on the surface or at the interface of two phases such as solid/liquid or solid/gas (**Figure 2-16**). "Adsorbate" is the removed pollutant, and the phase that collects the adsorbate is called "adsorbent". At the interface of the two phases, there are unbalanced attracting forces that are responsible for adsorption. When adsorption is caused by weak forces such as van der Waals forces or dipole-dipole interaction, it is defined as physical adsorption. When adsorption is induced by valence forces equal to the strength of chemical bond formation, it is called chemosorption [102]. The physisorption is a reversible exothermic process with an energy release from 10 to 40 kJ/mol , while the chemisorption is usually irreversible together with a much higher heat release of 20 to 400 kJ/mol [103]. Adsorption will stop where there is no concentration difference of the adsorbate in the two phases. The adsorption capacity can be affected by various factors, such as the type of adsorbents and pollutants, other competing species in the waste stream and the surrounding conditions like temperature, pH, pressure, and contact time.

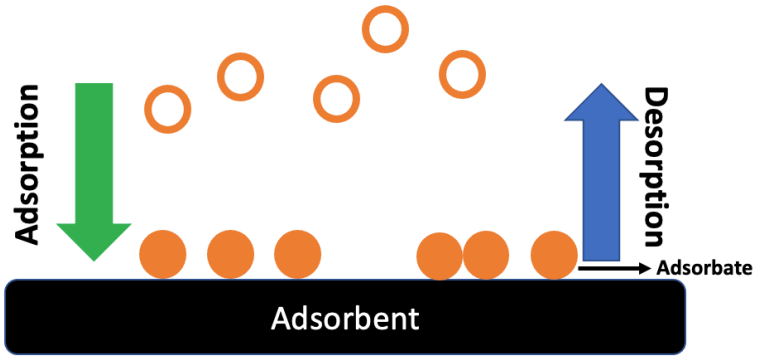


Figure 2-16 Schematics of the adsorption and desorption process of adsorbate molecules with adsorbent

Adsorption is one of the most common methods used for wastewater treatment, many researchers are focusing on developing novel adsorbent with high capacity and low cost. In order to better understand the adsorption system and to evaluate the performance among various adsorbents, adsorption isothermal was widely used. The adsorption isotherm is an important curve describing the mechanism of retention or release of the adsorbed molecules from the bulk system with an adsorbent surface at certain temperature and pH [104]. The adsorption system reaches equilibrium when the absorbate is in sufficient contact with the adsorbent and the rate of adsorption and desorption reaches a dynamic equilibrium. Several types of adsorption isothermal have been well established, including Langmuir, Freundlich, Brunauer–Emmett–Teller, Sips, Redlich–Peterson, Koble–Corrigan, and Flory–Huggins Radke–Prausnitz isotherm. They can provide detail information on how adsorbate molecules interact with the adsorbent surface. Also, the physiochemical parameters can be revealed by adsorption isotherm, it can also give the theoretical maximum adsorption capacity, the character of the adsorption site and its affinity to adsorbent. Only the most commonly used adsorption isotherms Langmuir and Freundlich will be discussed in the next section.

In general, the concentration of adsorbate deposited onto the adsorbent can be obtained from batch adsorption experiments, the adsorption capacity and removal efficiency can be calculated from Eq. (2.1) and Eq. (2.2).

$$Q_t = \frac{(C_0 - C_t) * V}{m} \tag{2.1}$$

$$R\% = \frac{C_0 - C_t}{C_0} * 100 \tag{2.2}$$

where Q_t (mg/g) is the mass of adsorbate adsorbed on to the adsorbent at time t, C_0 (mg/L) is the initial concentration of adsorbate and C_t (mg/L) is the concentration of the adsorbate in the bulk solution at time t, V (L) is the volume of adsorption system, and m (g) is the mass of adsorbent used in the batch adsorption system. Q_t is obtained after the system reaching equilibrium, it is defined as Q_e (mg/g), and R% is the removal percentage of the adsorbent relative to its initial concentration. After knowing the basic terms related to the adsorption process, more detailed information can be obtained by looking at the adsorption isotherms.

I. Langmuir isotherm model

The Langmuir adsorption isotherm model was first proposed by Irving Langmuir in 1916 to explain the adsorption of species on different surfaces. It is the most common adsorption isotherm to obtain the amount of adsorbate adsorbed onto the adsorbent surface at a certain temperature. Many experiments have been conducted to confirm the phenomenon of single-layer adsorption [105]. This model relies on several hypotheses:

- All the specific adsorption sites are located at the surface of the adsorbent
- There is no difference between any adsorption sites
- The surface of adsorbent can only be covered with a single layer of adsorbed molecules
- Adsorbed molecules are unable to interact with each other

The Langmuir adsorption isotherm can be presented by Eq. (2.3), where C_e (mg/L) is the concentration of adsorbate at equilibrium, Q_{max} (mg/g) is the maximum adsorption capacity, and K_L (L/mg) is the Langmuir constant [106].

$$\frac{C_e}{Q_m} = \frac{1}{K_L Q_{max}} + \frac{C_e}{Q_{max}} \tag{2.3}$$

Figure 2-17 is a standard Langmuir isotherm graph, and different adsorption stages are presented in the insets. The adsorption of solute on the surface is a dynamic interchange between the bulk solution and the surface. The adsorption of solute will not be affected by the adjacent adsorbed solute molecules, since all the adsorption sites are equivalent and the adsorbed molecules will not interact with each other. Each point of the isotherm curve represents a steady state, where the absorption rate is equal to the desorption rate. In the initial stage, the amount of solute adsorbed on the surface per unit area (q) increases as the concentration of solute (C) increases. However, once all adsorption sites are occupied by the solute molecules, q will not increase with further increase in the bulk solute concentration. At this point, the status of a specific amount of adsorbent is defined as saturated [107].

Furthermore, the Langmuir isotherm has associated the rapid decrease of the intermolecular forces with the increasing space. Webber and Chakkravorti defined a dimensionless constant called separation factor (R_L), it can be presented by Eq. (2.4):

$$R_L = \frac{1}{1+K_L C_0} \tag{2.4}$$

As explained above, the lower R_L value indicates a more favorable adsorption process, and the nature of the adsorption process can be evaluated by R_L. The R_L value can be classified into 4 classes: $R_L>1$, $R_L=1$, $0<R_L<1$, or $R_L=0$ representing an unfavourable, linear, favourable or irreversible adsorption process respectively [104].

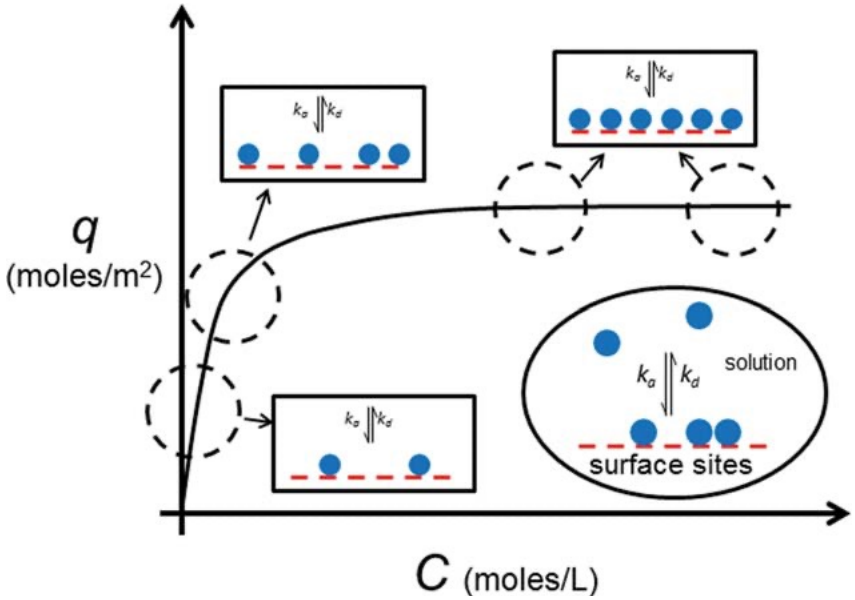


Figure 2-17 Characteristic of Langmuir adsorption isothermal. Adapted from ref [107]. Copyright © 2014 Wiley Periodicals, R. A. Latour.

II. Freundlich isotherm model

The Freundlich adsorption isotherm was initially proposed by Herbert Freundlich in 1909. It was used to describe the variation in the quantity of gas molecules adsorbed by a unit mass of solid adsorbent in terms of pressure changes at a constant temperature [108]. The Langmuir isotherm is an ideal theoretical model, limited by numerous assumptions that cannot normally be satisfied with the actual adsorption system. The Freundlich isotherm first describes a non-ideal reversible adsorption isotherm, which is an empirical model that can be implemented to heterogeneous adsorption sites and to multiple-layer adsorption. The non-linear Freundlich isotherm model is presented in Eq. (2.5), where K_F and n are the parameters of Freundlich model, which illustrated the relationship of adsorption capacity and adsorption intensity [109].

$$Q_e = K_F C_e^{1/n} \tag{2.5}$$

The linear form of Freundlich model is shown in Eq. (2.6), and the Freundlich adsorption isotherm constants can be obtained by plotting $Ln(Q_e)$ versus $Ln(C_e)$, the slope of this line is equal to 1/n and the intercept value is equal to $Ln(K_f)$. The value of n indicates the adsorption affinity between

adsorbate and adsorption sites, linear adsorption to all the active sites happens when n equals to 1[110].

$$LnQ_e = LnK_f + \frac{1}{n}LnC_e \quad (2.6)$$

b) Catalytic process

Adsorption using activated carbon (AC) is always considered the first choice for wastewater treatment, as it is cost-effective, easy to operate and scale-up. However, the low selectivity and heavy carbon footprint when regenerating the spent AC limits their applications. In most cases, further treatment is required for concentrated pollutants resulting from the regeneration of the adsorbents used or the rejection stream from membrane filtration. Therefore, it is necessary to have a water treatment technology that not only remove pollutants from the water system, but also degrade or transfer the toxic pollutants into non-toxic compounds. Consequently, it can be directly discharged into the environment after treatment. To that end, catalytic processes may provide a competitive alternative to traditional water treatment technologies. On the other hand, catalytic process can completely degrade the toxic compounds within a short time, and the used catalyst can be easily reactivated and reused, since the catalyst will not change or being consumed during the catalytic process. The mechanism of a semiconductor photocatalysis is shown in **Figure 2-18**.

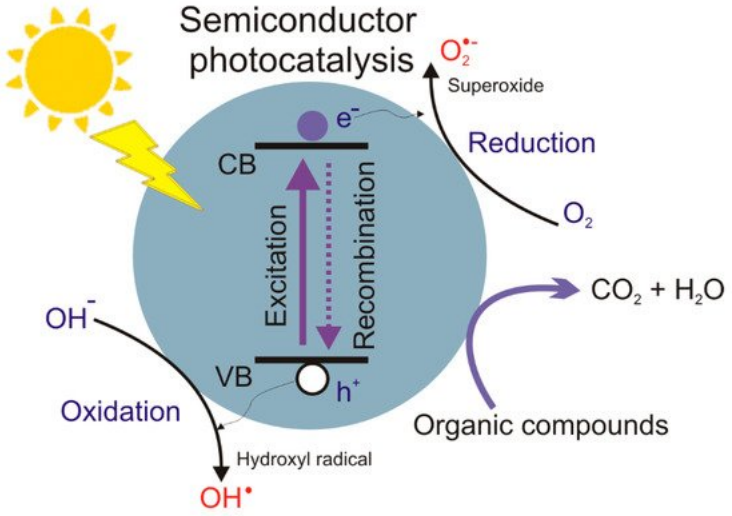


Figure 2-18 The mechanism of semiconductor photocatalysis, adapted from ref [111]

Organic molecules can be degraded through both reduction and oxidation processes depending on the types of organic molecules and the types of catalyst used. There are two major oxidation processes classified by operation conditions: near ambient conditions or at elevated temperature and high pressure. The advanced oxidation processes (AOPs) belong to the first category, which is achieved by producing reactive oxygen species (ROS) like hydroxyl radicals (·OH) [112]. AOPs are commonly used in wastewater treatment plant for degrading toxic organic compounds into less harmful compounds that can be directly discharged. The photocatalyst has to be a semi-conductor, which can release an electron (e^-) from the valence band (VB) to the conduction band (CB) and leave a positively charges hole (h^+) staying in the VB when it is getting excited by a light. This only happens when the light has a same or greater energy than the band gap (E_g), which is defined as the energy difference between the conducting band and the valence band (**Figure 2-19**). The generated unstable electron/hole pair is responsible for the following reduction and oxidation reactions. Different ROS species can be generated depending on either water or oxygen that reacted with the electron/hole pair. Figure 2-19 illustrates the reactions that occur after the excitation of the photocatalyst and explained how ROS degrades the organic pollutants. The electron-hole pair will be produced after light excitation (i); The positively charged hole in the valence band can react with water or hydroxyls and generate highly reactive hydroxyl

$$\text{Semiconductor photocatalyst} + h\nu \rightarrow e_{CB}^{-} + h_{VB}^{+} \quad \text{(i)}$$

$$h^{+} + H_2O \rightarrow H^{+} + OH^{\bullet} \quad \text{(ii)}$$

$$h^{+} + OH^{-} \rightarrow OH^{\bullet} \quad \text{(iii)}$$

$$e^{-} + O_2 \rightarrow O_2^{-} \quad \text{(iv)}$$

$$2e^{-} + O_2 + 2H^{+} \rightarrow H_2O_2 \quad \text{(v)}$$

$$e^{-} + H_2O_2 \rightarrow OH^{\bullet} + OH^{-} \quad \text{(vi)}$$

$$\text{Organic pollutant} + OH^{\bullet} \rightarrow \text{degradation products} \quad \text{(vii)}$$

$$\text{Organic pollutant} + \text{semiconductor photocatalyst } (h_{VB}^{+}) \rightarrow \text{oxidation products} \quad \text{(viii)}$$

$$\text{Organic pollutant} + \text{semiconductor photocatalyst } (e_{CB}^{-}) \rightarrow \text{reduction products} \quad \text{(ix)}$$

Figure 2-19 The reaction mechanisms of ROS generation and the degradation of organic molecules by using photocatalyst. Adapted with permission from ref [113]. Copyright © 2016 The Royal Society of Chemistry, K. Mondal et al.

free radicals (ii); The electron is able to react with oxygen and generate superoxide anion (iv); The electron can also react with oxygen and protons to produce hydrogen peroxide (v); And the electron can still react with hydrogen peroxide to produce more reactive hydroxy radials (vi); The degradation of the organic pollutants can occur both in aqueous media (vii) or on the semi-conductor surface (vii) & (ix) [113].

Except semi-conductors (metal oxides), noble metal-based catalysts are another type of catalyst commonly used to degrade organic compounds. Even though, the high cost and rareness of the noble metal enable more research on the development of non-noble metal catalyst. However, the high efficiency of noble metal catalyst still attracts a lot of attention. Thus, many research are focusing on the fabrication of high performance catalyst via constructing high surface area material. The catalytic experiment is usually conducted by mixing catalyst with a waste stream in a quartz cell, and the catalytic process can be monitored by a UV-Vis instrument. The electron-hole pair

generated by the catalyst can further react with water and produce reactive radicals, such as ·OH and ·OOH, and the reactive radicals can continuously degrade the organic pollutants. The apparent rate constant is used to evaluate the performance of a series of catalyst for the same catalytic reaction, the equation is shown in Eq. (2.7), where C_0 is the initial concentration of the compounds that need to be degraded (t=0), C is the concentration of the compounds at time t, and k_{app} is the rate constant.

$$\ln\left(\frac{C_0}{C}\right) = k_{app}t \tag{2.7}$$

Catalytic performance is closely influenced by the surface area of the catalyst, so there has been considerable interest in the nanoscale catalyst. The easy separation of the applied system is also a concern, as the catalyst can be reused several times if there is no deposition of degraded compounds. Thus, fixing nano catalyst on a high surface area matrix and aided with magnetic particles is promising in catalytic processes. Thus, one of my thesis chapters focuses on the development of a nanosized palladium catalyst onto melamine formaldehyde resin modified CNC and anchored with nanogel templated magnetic particles for 4-NP degradation.

c) Membrane filtration

Membrane filtration is another common technique used for wastewater treatment, it can reject the pollutant molecules from the main stream by size exclusion mechanism. The membrane separation can effectively enrich low concentration waste from a dilute system, while the concentrated waste stream (retentate) or the fouling membrane still needs to go through a secondary treatment. The pressure driven membrane separation process can be divided into 4 types according to the membrane pore size: microfiltration (MF: 50-500 nm), ultrafiltration (UF: 2-50 nm), nano filtration (NF: <2 nm) and reverse osmosis (RO: 0.3-0.6 nm). The schematic representation of pressure driven membrane filtration is shown in **Figure 2-20**. Accordingly,

microfiltration can remove suspended solids, bacteria and macromolecules; ultrafiltration can remove virus, colloidal organic matter and oil; nano filtration can remove small compounds and salt ions can be removed by reverse osmosis [51]. The membrane separation is achieved by passing the feed stream through a semipermeable membrane through a driving force (concentration difference or pressure drop), where the feed stream is divided into two streams: permeate and retentate. The permeate is defined as the stream that passes through the membrane during the filtration process, while the fluid rejected from the membrane is defined as retentate [114].

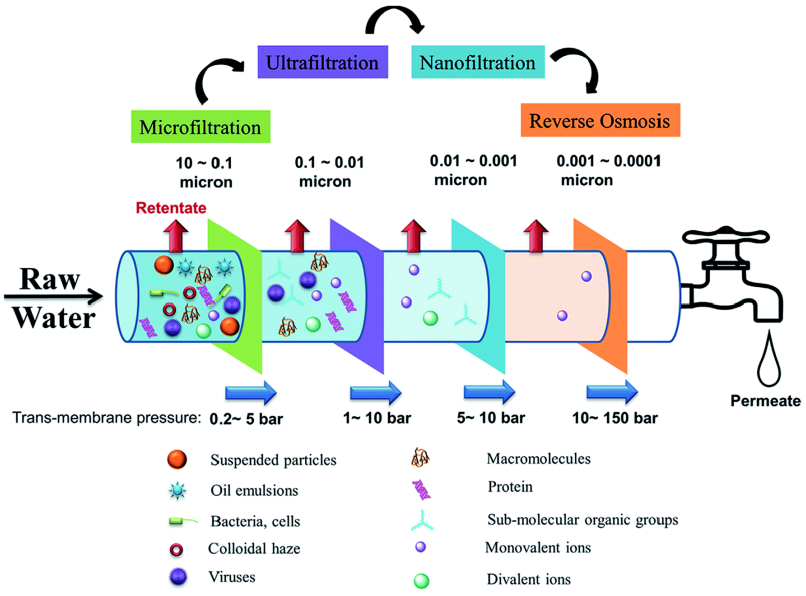


Figure 2-20 The separation of different components via pressure driven membrane filtration process. Adapted from ref [51]. Copyright © 2018 The Royal Society of Chemistry, MK. Selatile et al.

One of the most important aspects in evaluating the performance of a membrane process is the rejection ratio towards specific compound. The equation is shown in Eq. (2.8) [115]:

$$R(\%) = \left(1 - \frac{C_{pm}}{C_0}\right) * 100\% \qquad (2.8)$$

where C_0 is the concentration of the pollutant in the feed stream (mg/L); C_{pm} is the concentration of the pollutant in the permeate (mg/L); Furthermore, the permeate flux (J) is another important value to note during the filtration process, which is also an indicator for membrane fouling. The equation is shown in Eq. (2.9), where Q represents the flowrate across the membrane (L/h) and A is the cross-sectional area of the membrane (m^2).

$$J = \frac{Q}{A} \tag{2.9}$$

The filtration process can be further divided into dead-end filtration and cross-flow filtration depending on the flowing direction of the feed stream and the permeate stream. In the cross-flow filtration system, the feed stream flows tangentially to the membrane, while the feed stream is vertical to the membrane surface in dead-end filtration system (**Figure 2-21**). The membrane assembled as the dead-end configuration easily becomes fouled, while the shear forces in the cross-flow filtration significantly slows the accumulation of the waste compounds on the membrane surface [116]. The membrane separation can be highly efficient when the compounds exist in the waste molecules are very different. Typically, membrane separation is superior to other water treatment process in terms of low carbon footprint, however when used to separate multiple similar structured compounds, further modification should be performed on the membrane for better selectivity.

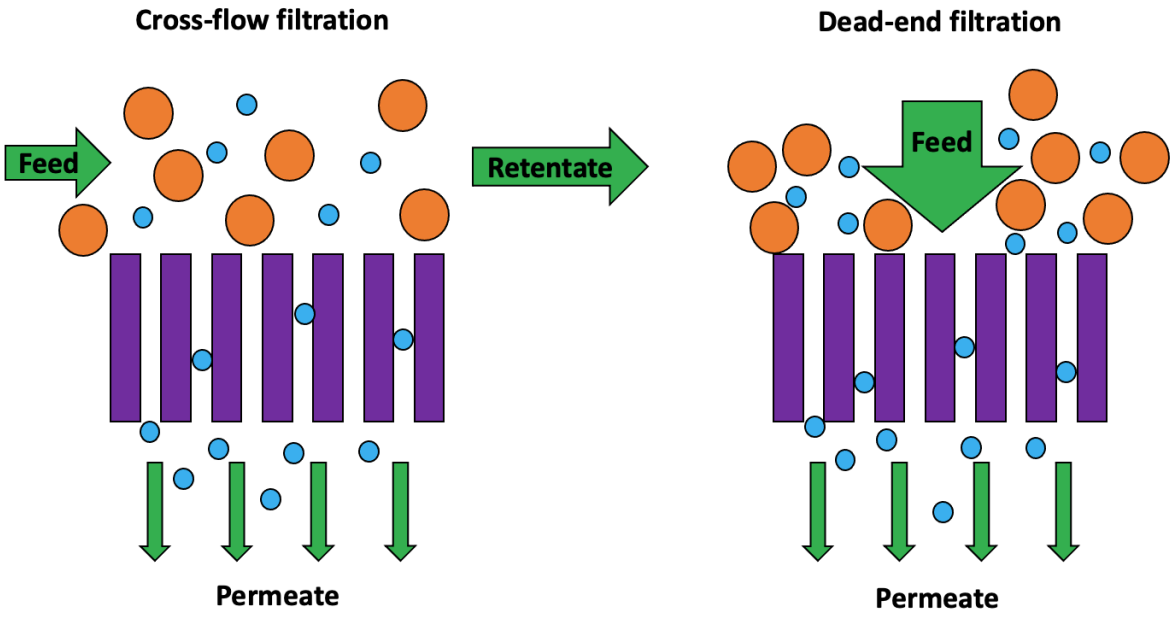


Figure 2-21 The configuration of cross-flow membrane filtration (left) and the dead-end membrane filtration (right).

2.4.3 *β*-CD absorbents applied to various pollutants removal

The composition of sewage is an important factor that need to be considered when developing high performance adsorbents. Emerging contaminants in the water system can be very different depending on their chemical, physical and biological properties, such as reactivity, hydrophobicity and biodegradability. Typically, a multiple barrier process is commonly used in a concurrent or sequential approach to meet a certain level of discharge standard, as the one step treatment cannot eliminate all contaminants. β-CD based adsorbents applied for removing various types of contaminants will be reviewed and discussed in the following section.

- **Pharmaceuticals**
  In the past decade, pharmaceuticals have become emerging contaminants in the water cycle. Traces of pharmaceutical residues were detected in surface water, wastewater, ground water, and drinking water. It was only brought to our attention in the past few decades due to the

improvements in analytical technology, since the concentrations of pharmaceutical residues in water are typically low. In 2012, a report by the World Health Organization (WHO) indicated that the traces of pharmaceuticals in drinking water are unlikely to evoke a pharmacological effect, and that the risks to human health are very low. However, very limited studies on this topic have been conducted to date. Furthermore, even though the concentration of pharmaceutical residues is not high enough to trigger immediate response, the effects of long-term exposure remain unclear [117]. Pharmaceutical residues in water come in many different types, such as endocrine-disrupting chemicals (EDCs), antibiotics, and anesthetic compounds. Long term exposure to bisphenol A (BPA), a class of EDCs, was proven to be detrimental to the reproduction of wildlife. It was also suspected that BPA would be carcinogenic to human and affect fetal development [118]. Currently, most countries do not have guidelines for pharmaceuticals level in drinking water. As a result, most wastewater treatment plants were not designed for the remediation of pharmaceuticals [119]. Recently, β-CD-based materials have been identified as having the potential to remove many types of pharmaceutical compounds from water [120], [121], [122], [123].

Wood-based cellulose material has been a popular choice for the immobilization of β-CD because of their cost-effectiveness, biodegradability, and the large amount of hydroxyl groups on cellulose that are available for modification [121], [124]. A filtration composite with cross-flowing channels (β-CD/WS) was prepared by the reaction between wood dust cellulose, β-CD, and tetrafluoroterephthalonitrile (TFP). The sawn-off microchannels formed by sawdust and the micropores on the surface of the sawdust allowed maximum availability of β-CD cavity to pharmaceutical molecules. For propranolol, a beta blocker for hypertension, the removal efficiency by β-CD/WS reached 97% after 90s of contact time. In comparison, natural wood sawdust only removed about 26% of propranolol under the same condition. The adsorption performance of β-

CD/WS was also stable over a wider pH range of 5 to 12, showing potential for practical application. The β-CD/WS composite also demonstrated an excellent ability to treat more complex wastewater containing multiple pharmaceuticals. In the simultaneous adsorption test of amitriptyline, chlortetracycline, diclofenac, and levofloxacin, β-CD/WS were able to remove over 95% for all of the above tests [124]. Other than cellulose materials, graphene oxide (GO) is also an excellent nanomaterial for the matrix of adsorbents due to its large planar surface area and rich functional groups for easy grafting. A nanocomposite synthesized by surface modification of GO with β-CD showed promising results for BPA adsorption, reaching a calculated Langmuir adsorption capacity of 373.4 mg/g [125]. A study on a matrix containing β-CD and poly-L-glutamic acid supported by magnetic GO demonstrated that the material was capable of removing 17 β-estradiol (E2), which also belongs to the EDCs family. The adsorption was reported to be highly dependent on pH, but unaffected by ionic strength. One of the advantages of this material is that it allows for rapid separation after adsorption, which is attributed to the magnetism from the modification of GO [126].

Another citric acid-crosslinked β-cyclodextrin polymer (CA-β-CD) was designed for the simultaneous removal of BPA, copper, and methylene blue (MB). The experimental data suggested that the adsorption followed the pseudo-second-order kinetic model and Langmuir isotherm model, indicating monolayer adsorption on a homogeneous adsorption site. It was proposed that BPA binds with β-CD via host-guest inclusion with a stoichiometry ratio of 1:1. Also, the adsorption of BPA was independent of the adsorption of MB and copper ion, since β-CD is the only active adsorption site for BPA. The Q_m of BPA onto CA-β-CD was estimated to be 83.01 mg/g based on the Langmuir model. The removal efficiency of BPA was between 84.2% and 87.2% over a wide pH range of 1 to 11. Finally, it is worth mentioning that the adsorption performance of CA-β-CD

was mostly unaffected by the presence of humic acid. Humic acid could inhibit the performance of many adsorbents including activated carbon. It was observed that the pollutants uptakes remained mostly unchanged even when the humic acid concentration reached 1000 mg/L, demonstrated the high selectivity for CA-β-CD polymer [127]. Similarly, another study also used citric acid as the crosslinking agent for β-CD monomers, but with the addition of 2-dimethylamino ethyl methacrylate monomer (DMAEMA) grafted onto β-CD. While preserving its ability to adsorb BPA over a wide pH range of 2-10, this material could also selectively remove anionic and cationic dyes, depending on the pH [128]. In conclusion, the β-CD adsorbent showed a great affinity with pharmaceutical molecules, as most pharmaceuticals are hydrophobic and the aromatic portion matched to the size of the CD cavities.

- **Heavy metals**

Heavy metals have been used by human beings for thousands of years. For example, lead was used to produce water pipes and sweeten old wine. It was not until later that people discovered that the long-term exposure to heavy metals have significant health effects on the human bodies [129]. Chronic exposure to lead could cause effects such as mental retardation, birth defects psychosis and autism. Cadmium is particularly toxic to the kidneys and long-term exposure could lead to kidney disease, bone and lung damage. Exposure to high level of chromium could even induce DNA damage in many ways [130]. Despite their toxicity, heavy metals are inevitably used in industrial process or to manufacture specific products. Therefore, it is vital to find an affordable and effective method to process heavy metals containing waste before releasing them to the environment. Some β-CD based materials were found to have the ability to capture metal ions. Normally, pristine β-CD molecules do not have the affinity for metal ions. However, with some modifications such cross-linking and incorporation into other substrates, β-CD based materials were able to adsorb metal ions.

β-CD based polymers prepared by cross-linking β-CD molecules and/or other molecules as substrates have shown good results in heavy metals removal. There are a few well-studied choices of cross-linkers when it comes to synthesizing β-CD polymers, such as epichlorohydrin (EPI) [131][132][133][134], citric acid [135],[136][137], and ethylenediaminetetraacetic acid (EDTA)[138][139][140]. A study on single-component CD polymer used EDTA as a cross-linker for β-CD monomers. Comparing to other cross-linkers, such as EPI and EDC, EDTA is relatively more affordable, less toxic and more eco-friendly. More importantly, EDTA also acts as a chelating agent as it can form stable chelation complexes with metals. When applying EDTA-β-CD polymers for multi-pollutants adsorption tests, β-CD molecules formed inclusion complexes with dye molecules, while the amine groups of EDTA provided chelating sites for metal ions. Therefore, the polymer was able to simultaneously adsorb metals and cationic dyes [141]. Subsequently, chitosan was incorporated with an EDTA cross-linked binary-component (CS-ED-CD) polymer in a form of hydrogel. Chitosan is considered as the backbone of the polymer, and CD molecules were grafted onto the chitosan network by EDTA. The SEM image of the freeze-dried hydrogel confirmed the porous morphology of CS-ED-CD polymer. The adsorbent demonstrated a monolayer adsorption mechanism with the capacity of 0.803 and 1.258 mmol/g towards Pb(II) and Cd(II), respectively. The absorbent also allowed the simultaneous adsorption of other organic micropollutants by forming inclusion complexes with CD cavities [142]. Pedrazzo et al. synthesized two β-CD polymers (β-CTIR and β-PDMA) by cross-linking β-CD with citric acid and pyromellitic dianhydride (PMDA), respectively. It was proposed that a large number of carboxyl groups present on the polymer would enhance its ability to form complex with metal ions. Therefore, a theoretical molar ratio of 8:1 for cross-linker to β-CD was used to synthesize the polymers. At a high initial concentration of metal ions (500 ppm), β-PDMA demonstrated better

adsorption capacity than β-CTIR, especially for Pb(II) and Cu(II). The authors concluded that this was due to the larger amounts of carboxyl groups present on β-PDMA. Interestingly, at lower metal ion concentration (<50 ppm), both β-PDMA and β-CTIR showed very similar metal uptake, in some cases, the performance of β-CTIR was even better than β-PDMA [143]. Qin et al. prepared a β-CD based polymeric adsorbent (PCD-VI) by the copolymerization of methacrylic-modified β-CD (MCD) and 1-vinylimidazole (VI). It was achieved by grafting heterocyclic molecules VI onto the secondary face of β-CD, which in a way expanded the capacity of β-CD. A schematic representation of its structure is shown in **Figure 2-22**. Meanwhile, the heteroatoms on the heterocyclic molecules are capable of binding to metal ions by sharing electrons, also known as coordination. In this way, PCD-VI can adsorb both cationic and anionic dyes, as well as metal ions. More importantly, this material allows the stepwise desorption and recycle of cationic dye molecules and metal ions due to their different adsorption mechanisms. Both XPS and FT-IR spectra confirmed the chelation of Cd (II) with PCD-VI. More specifically, the chelation site was determined to be the C=N group in VI. In an adsorption test with an initial Cadmium concentration of 1000 mg/L, PCD-VI showed a Q_m of 117 mg/g [144].

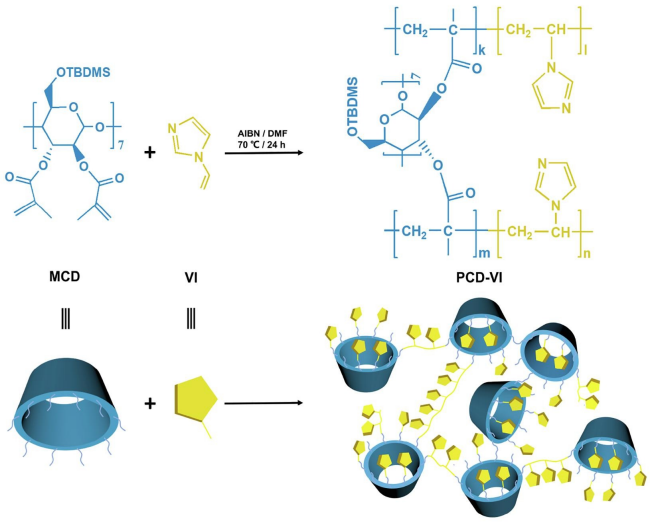


Figure 2-22 The schematics representation of PCD-VI and the inclusion mechanism. Adapted with permission from ref [144]. Copyright © 2019 Elsevier B.V. X. Qin et al.

Other than direct polymerization, β-CD can also be incorporated into the matrix by immobilization or functionalization [145]. Combined with β-CD, GO based β-CD materials have great potential in being excellent adsorbents with both the β-CD cavities and possible interactions with GO contributing to the adsorption. A magnetic β-CD/GO nanocomposite (MCGN) was prepared by coating Fe_3O_4 particles with NH_2-β-CD, where the amine group on NH_2-β-CD interacted with the carboxyl groups on GO. For the adsorption of chromium ions, it was discovered that MCGN performed better in acidic environment. The proposed MCGN adsorption mechanism is electrostatic attraction, and Cr(VI) is mostly in the form of $HCrO_4^-$ when acidic, therefore it interacts well with the positively charged MCGN [146]. Another GO based β-CD material was synthesized by surface-initiated reversible addition–fragmentation chain transfer (RAFT) polymerization. The RAFT agent was immobilized on the surface of magnetic graphene oxide, following by the surface-initiated RAFT polymerization of methacrylated β-CD onto the RAFT agent. The results from the adsorption tests and XPS spectrum at varying pH suggested that this material was capable of removing Cd(II) ions due to electrostatic interactions and complexation between the Cd(II) ion and the adsorbent [147]. In another study, β-CD molecules were mixed with GO in solution form, then freeze-dried to form a three-dimensional (3D) graphene foam (CDGN). The volume, mass, and porosity of CDGN all increased as more β-CD molecules were incorporated into CDGN. The removal rate of Cr(VI) reached 99.8% from a mixture of different metal ions [145]. Aside from GO, there are many other material surfaces that β-CD can be loaded onto. A β-CD based magnetic sorbent was developed by functionalizing the surface of Fe_3O_4 nanoparticles with monochlorotriazinyl-β-CD (MCT-β-CD). The hydroxyl and azinyl nitrogen groups on the MCT-β-CD contributed to its adsorption towards many metal ions, especially Pb^{2+} [148]. Badruddoza et al. developed a magnetic sorbent in a similar way, but the magnetic

nanoparticles were functionalized with β-CD-ionic liquid (β-CD-IL) polyurethanes instead. The results showed that modifying CD molecules with IL enhanced its sorption capacity towards Cr(VI) [149]. Chen et al. modified the surface of Fe_3O_4 nanoparticles first with polyethylenimine (PEI), then react maleoyl-β-CD with pre-synthesized Fe_3O_4-PEI. It was proposed that there were two kinds of active sites for Pb^{2+}, which were both the oxygen-containing groups in the CD and the exposed amino groups on PEI [150].

Although all of the β-CD based materials discussed above showed some degree of metal ion removal efficiency, the adsorption capcity is not the only factor when it comes to the applicability in real life. Some materials require the use of organic solvent in the synthetic process [141][147], which is not very environmental friendly for large scale production. In order to be used in real life, the material also needs to be easily recovered after use. In this case, both solid adsorbents and magnetic adsorbents are advantageous due to the ease in separation. Generally, various β-CD based materials have been developed for the adsorption of metal ions with promising results. However, very few was tested in environmentally relevant concentrations or conducted with a simulated real-sample (i.e. interfering ions and other substances). While trying to enhance the adsorption capacity, new research should aim at the possibility in realistic application.

- **Dyes**

Among all pollutants, the ones that stand out in textile industry wastewater are organic dyes. Releasing untreated dyes into the water cause a series of problems, since it poses significant health risks for human and some of the dyes are carcinogenic or toxic. Moreover, it creates significant adverse effects on the environment, such as decreasing the water oxygen level by blocking sunlight and interrupting photosynthesis, therefore bringing harm to the aquatic organisms [151]. Dye degradation takes years under the natural light condition and bacteria. It also creates a byproduct, carcinogenic aromatic amines, which precipitate in river sediment for an even longer time period

[152]. Therefore, it is vital that proper treatments are applied to the textile industry wastewater before it is discharged.

β-CD is found to be an excellent candidate for dye adsorption due to its chemical structure. The hydrophobic cavity of β-CD allows hydrophobic guest molecules to enter and form a host-guest inclusion complex. It is also shown that β-CD can be easily regenerated and maintained a high adsorption efficiency. Many β-CD contained adsorbents consisted of magnetic materials during the synthesis, which makes the separation process much easier and provides an efficient way to recycle the adsorbents. A polymer composite adsorbent was prepared by cross-linking β-CD with tetrafluoroterephthalonitrile (TNF), and then depositing Fe_3O_4 nanoparticles onto its surface (CDP-Fes). CDP-Fes is highly effective for the removal of cationic dyes, including MB, Natural Red (NR), Crystal Violet (CV) and Malachite Green (MG). The Q_m of MB approached 565 mg/g, which was high compared to other reported β-CD based adsorbents. It was proposed that the excellent adsorption performance could be attributed to multiple adsorption mechanisms, including the dye molecules forming inclusion complexes with β-CD, trapping dyes in a three-dimensional hydrophilic network structure, and electrostatic interactions with the COO^- groups on the polymer. It is also worth mentioning that CDP-Fes has adsorption selectivity and could be used to separate dyes of opposite charges. The anionic dye Methyl Orange (MO) was repelled by the negatively charged adsorbent, while the cationic dye MB was adsorbed and successfully extracted from the mixed MO/MB solution. It was observed that a removal rate of over 90% was retained after four cycles [153]. In another study, a β-CD functionalized magnetic graphene hybrid (mGO-β-CD) was prepared for the removal of organic dyes. In the original mGO complex, the π-π interactions between the dye molecules and the hydrophobic plane of GO had the ability to trap a small amount of dye. After immobilizing β-CD onto the mGO surface, a significant enhancement

in adsorption capacity was observed. It was postulated that β-CD could form inclusion complexes and providing more binding sites for dye molecules. Also, the pH value and the ionic strength of the system was proven to be important factors during adsorption process. For the adsorption of Rhodamine 6G (R6G) onto mGO-β-CD, the uptake of R6G decreased when the ionic strength increased from 0 to 0.01M. When the ionic strength increased from 0.01M to 1M, an increase of R6G adsorption was clearly observed. For the adsorption of a weak basic dye Acid Fuchsin (AF), the pH showed a significant effect. The adsorption of AF reduced progressively as the pH increased from 2 to 10. Very little AF molecules were adsorbed onto mGO-β-CD at pH 10. This provided a convenient method for separation by adjusting the pH value after the adsorption process, where the adsorbent could be reused. This material also showed excellent recyclability as about 90% of removal efficiency could still be maintained after six adsorption-desorption cycle [154].

As mentioned previously, the β-CD polymer cross-linked by EDTA (EDTA-β-CD) were fabricated to be a bifunctional adsorbent for removing not only metals, but also cationic dyes simultaneously. The Q_m of three typical cationic dyes, MB, Safranin O (SO), and Crystal Violet (CV) onto EDTA-β-CD were reported to be 0.262, 0.169, and 0.280 mmol/g, respectively. It was proposed that CD cavities provided most of the active sites for dye binding and the EDTA groups played a minor role in the adsorption. The adsorption of MB onto EDTA-β-CD was spontaneous and exothermic. The negative ΔH value also suggested that the adsorption mainly followed physisorption mechanism. The exothermic reaction nature caused the inclusion complex between β-CD and the dye molecule to disassociate at high temperatures. Above 90% of regeneration efficiency was obtained by washing with ethanol and hydrochloride acid after the fifth cycle, indicating the good stability and reusability of the material [141]. Another β-CD based material for dye removal that is being investigated recently is nanofiber membranes. The manufacturing

process of electrospinning nanofiber membranes is relatively easy and cost-effective. A water insoluble β-cyclodextrin-based electrospun fibers (CDBEF) were prepared for the separation of MB. The electrospinning solution contains β-CD and poly (acrylic acid) (PAA) dissolved in N,N-dimethylformamide (DMF), with citric acid as the cross-linking reagent. The adsorption capacity of MB onto CDBEF increased from pH 2 to 9 and decreased from pH 9 to 11. The optimum adsorption capacity at pH 9 was explained by the strongest electrostatic interactions between MB and CDBEF occurring at this pH value. This result indicated that electrostatic interactions with carboxyl groups on CDBEF also contributed to MB adsorption in addition to forming guest-host complex. The adsorption isotherm followed the Langmuir model and the reaction kinetics was better fitted with the pseudo-second-order model. It was discovered that the adsorption toward the anionic dye methyl orange (MO) was very low due to electrostatic repulsion. Having the self-standing and good film-forming properties, CDBEF could be used in the separation of MB/MO dye mixture via dynamic filtration. When the mixed dye solution was filtered through the CDBEF membrane, MB would be caught on the membrane while MO remained in the filtrate. The process had a separation efficiency of 99.55% while the filtration was performed at a high flow rate of 150 mL/min. The MB-loaded membrane could also be regenerated by rinsing with methanol solution mixed with HCl. The separation efficiency was maintained at over 90% after five filtration-regeneration cycles [155]. In conclusion, the β-CD adsorbent is promising for dye removal, as hydrophobic cavities could easily form inclusion complexes with dye molecules. Moreover, the variation of the pH in the environmental system may allow the selective separation of different dyes from a mixed solution.

- **PFAS removal**

Per- and polyfluorinated alkyl substances (PFAS) are a group of synthetic chemicals that have been used in various industries since the 1940s. They were widely used for food packing [156], commercial household products [157], and fire-supressing aqueous film forming foam (AFFF) [158]. In early 2000s, it was reported that perfluorinated compounds that were widely used, for example in firefighting foams and water-proof textiles were detected in human blood samples worldwide. Two of the PFAS chemicals, perfluorooctanesulfonic acid (PFOS) and perfluorooctanoic acid (PFOA) (**Figure 2-23**) were found and reported to have adverse health effects to humans, including higher probability of cancer, cardiovascular disease, thyroid disease, and low infant birth weight and size [159]. In the United States, there is currently no enforceable Maximum Contaminant Levels (MCLs) regulation on PFASs, however, the health advisory provided by the United States Environmental Protection Agency (EPA) is that the lifetime exposure to FPOS and PFOA from drinking water should be below 70 ng/L [160].

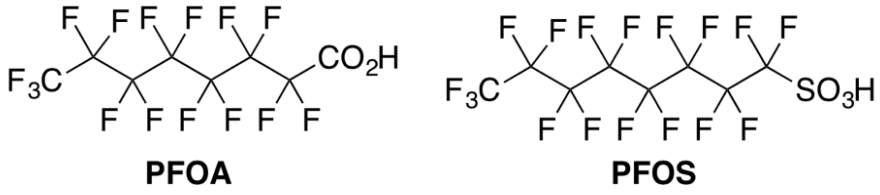


Figure 2-23 Perfluorooctanoic acid (PFOA) and perfluorooctanesulfonic acid (PFOS) referred to as per- and polyfluorinated alkyl substances (PFAS). Adapted with permission from ref [161]. Copyright © 2019 American Chemical Society, Nicholas A. Lundquist et al.

Using CD-based polymers as adsorbent for PFASs removal is becoming a popular research topic because CD polymers have great tunable properties, including forming inclusion complex, surface area, pore structure, solubility, the ability to regenerate, and surface functionality [162]. A novel multifunctional magnetic sorbent (Fe_3O_4-CDI-IL MNPs) was developed to remove PFOS, PFOA and Cr(VI) from aqueous system. Polymers β-CD−ionic liquid (β-CD-IL) polyurethanes

were synthesized first, following by the cross-linking of the β-CD-IL onto the magnetic nanoparticle surface. It was reported that the removal rate of PFOS and PFOA increased as the sorbent concentration increased from 0.025 to 0.8 g/L. The sorption equilibrium was reached after 4 h and 6 h, respectively for PFOS and PFOA. In comparison, research had shown that the sorption of PFOA onto GAC took at least 168 h to complete. The adsorption data was better fitted by the Sips model, which indicated heterogeneous active sites. The proposed adsorption mechanism was that the β-CD cavities might be the major active sites for capturing PFOS and PFOA, while the electrostatic interactions between anionic PFAS chemicals and positively charged sorbent played a minor role in the adsorption. The adsorption performance was also tested under pH 4-11. It was shown that the adsorption of PFOS onto Fe_3O_4-CDI-IL MNPs was only slightly affected at pH greater than 10.6, while the PFOA adsorption was significantly affected by pH. The magnetic sorbent could easily be collected with a magnetic field, and then it was regenerated for 10 times without significant loss of removal efficiency [149].

It was concluded that the performance of β-CD polymers as adsorbents is greatly affected by their composition, such as the cross-linkers [163]. A β-CD based polymer network cross-linked with decafluorobiphenyl (DFB-CDP) was reported to be able to reduce PFOA concentration from 1 μg L^{-1} to less than 10 ng L^{-1}, which is much lower than the EPA advisory level (70 ng L^{-1}). Various DFB: β-CD molar feed ratios ranging from 3 to 7 were tested to explore the significance of cross-link density **Figure 2-24**. It was found that the DFB-CDP polymer synthesized from DFB: β-CD feed ratio of 3 displayed the best performance, whereas those with higher feed ratios (≥5) demonstrated inferior removal efficiency. The kinetics of the adsorption followed the pseudo-second-order model, reaching an observed k_{obs} value of 2.88 g mg^{-1} h^{-1} at $[PFOA]_0$ =1 μg L^{-1} and [DFB-CDP] = 10 mg L^{-1}. The results showed that the kinetics of PFOA adsorption onto DFB-

CDP was comparable to the leading powdered activated carbon (PAC) and better than GAC. It should also be noted that the performance of PFOA adsorption by DFB-CDP was not affected by the presence of humic acid. [164]. Humic acid is a major component of natural organic matter (NOM), which usually inhibits the removal of PFCs by PAC [165]. This unique property of DFB-CDP gives it a major advantage in practical applications over other adsorbents like activated carbon. More in-depth research was conducted on the cross-linker chemistry of β-CD polymers and how it affects PFAS uptake. Three different DFB-CD polymers were synthesized with increasing level of phenolated DFB incorporated into the polymer network. Two other polymers, epichlorohydrin-CD polymer (EPI-CDP) and 2-isocyanatoethyl methacrylate CD polymer (IEM-CDP), were synthesized using different cross-linkers. With the three DFB-CDPs (**Figure 2-24**), the results showed that the level of phenolated DFB in the polymer was inversely proportional to its PFAS uptake. It was suggested that the negative charges due to the phenolation around β-CD inhibited the binding of anionic PFAS onto β-CD. All five polymers were used to investigate the adsorption performance of a mixture of 10 PFAS chemicals. At pH 7.5, EPI-CDP and IEM-CDP demonstrated much lower removal efficiency comparing to DFB-CDPs. The zeta potential values at pH 7.5 of EPI-CDP and IEM-CDP were also less negative than DFB-CDPs. After adjusting the pH to 5.5, all five polymers showed higher removal rates on the majority of the PFAS chemicals, indicating that surface charge might be an important factor affecting the binding efficiency between PFAS and CD cavities. Overall, the EPI-CDP and IEM-CDP still showed lower removal efficiency for 8 out of 10 PFAS chemicals comparing to DFB-CDPs, implying that other factors other than surface charge would impact the uptake potential of PFAS, such as different crosslinking agents and crosslinking density [163].

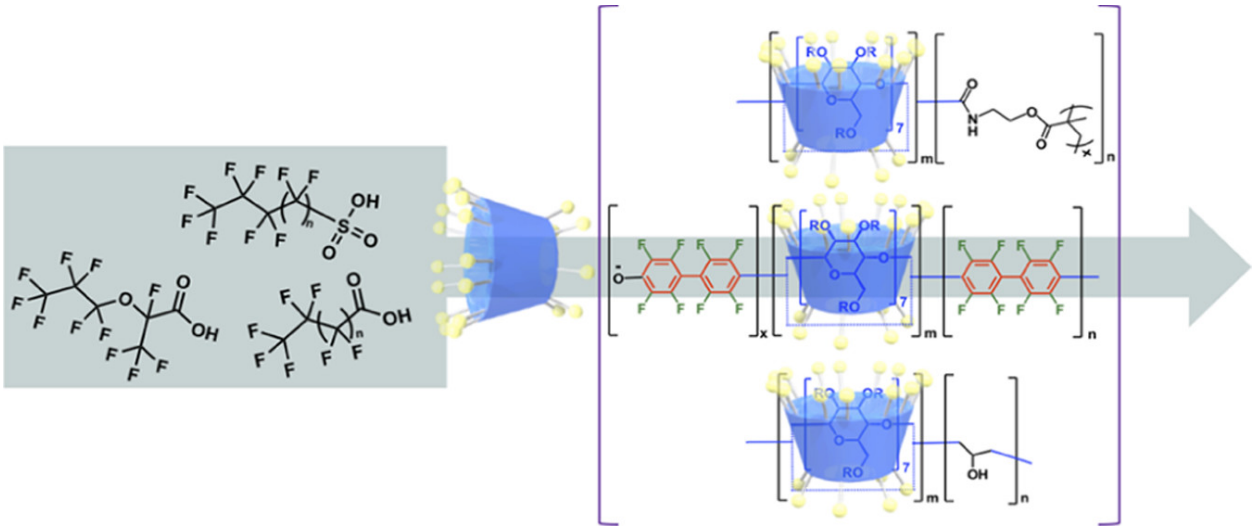


Figure 2-24 Scheme of adsorption mechanism of PFAS onto DFP-CDP, EPI-CDP, and IEM-CDP. Adapted from "L. Xiao *et al.*, "Cross-linker Chemistry Determines the Uptake Potential of Perfluorinated Alkyl Substances by β-Cyclodextrin Polymers," Macromolecules, 2019."[163]. Copyright © 2019 American Chemical Society, L. Xiao et al.

Till now, most of the work on PFASs removal by CDPs were conducted in Milli-Q water, yet their performance in ground water was not widely tested. Recently, two β-CD-based polymers, commercial CDP+ (DEXSORB + ™, CycloPure, Encinitas, CA) and a CDP crosslinked with a reduced terephthalonitrile (amine-CDP, aCDP), were tested in ground water to check if other trace contaminants existed in the ground water would affect PFAS remediation. They were first implemented in MilliQ water for the removal of 20 PFASs, including perfluorocarboxylic acids (PFCAs), perfluorosulfonic acids (PFSAs), fluorotelomer sulfonic acids (FTSs), and perfluoro-2-methyl-3-oxahexanoic acid (GenX). After a 4h contact time, the two CDPs both removed almost 100% of the PFASs, demonstrating their potential in PFASs removal. In ground water, the PFASs removal performance for both CDPs were suppressed to different degrees compared to their performance in Milli-Q water. Although, the adsorption inhibition for PFSAs was significantly less than PFCAs. In two out of four ground water samples, the PFSAs uptake was not affected at all, indicating CDPs have higher affinity towards PFSAs compared to other PFASs. Further study

showed that both pH and inorganic cations contributed to the inhibition of PFASs adsorption by CDPs in ground water. CDP+ has a permanently positive surface charge at all pH levels, while aCDP would be deprotonated at higher pH level, which weakens the electrostatic interaction between the anionic PFASs and aCDP. This also explained why CDP+ outperformed aCDP in FPASs adsorption test conducted in ground water, suggesting that the pH of different ground water samples might be different. The ground water sample that had the highest cations concentration inhibited the PFASs adsorption the most [166]. These new insights should be taken into consideration when developing new CDPs targeting PFASs in practical application.

After reviewing many studies on various pollutants removed by β-CD-based adsorbents, β-CD based adsorbents displayed promising affinity towards various pollutants such as pharmaceuticals, EDCs, dyes, heavy metal and PFASs. High adsorption capacity can be achieved by combining β-CD with other functional materials that possessed the potential to bind with the pollutant molecules other than hydrophobicity. The β-CD-based adsorbents presented unique size exclusion characteristic that would not be impacted by NOM present in the real water system, which show promising potential compared with common commercial adsorbents.

2.4.4 Beta-cyclodextrin based adsorbents

As mentioned in the previous section, adsorption is still being considered as the most common water treatment process. Among all the conventional adsorbents, activated carbon is used as a benchmark for evaluating the performance of most newly developed adsorbents. Even though AC has high adsorption capacity toward most pollutants, while its non-selective adsorption, high energy cost of regeneration and loss of surface area after reuse limit its application. Moreover, AC is venerable to NOM, which restricts its implementation in most real water systems. β-CD has a unique hydrophobic cavity of 0.65Å that can resist the interaction with NOM. This size exclusion

mechanism makes β-CD based adsorbents a hot topic for the removal of organic pollutants and PFAS removal. However, the solubility of β-CD is relatively high in water, suitable modification and functionalization was necessary to develop β-CD based adsorbents that can be easily recovered after use. Depending on the way β-CD is prepared, β-CD based adsorbents can be generally classified into β-CD polymers, β-CD immobilized material and β-CD incorporated composite material. They will be introduced detailed in the following sections.

- **β-CD polymers or β-CD nano sponges (β-CD-NS)**

According to the solubility, β-CD polymers can be divided into soluble and non-soluble polymers, which mainly decide their future applications. In this review, only non-soluble β-CD polymers will be discussed, since they are more stable and compatible with current water treatment technologies. In addition, cyclodextrin-based nanosponges (CD-NS) have been proposed in recent years, which describe CD polymers synthesized through cross-linking reactions [72]. They were named as cyclodextrin nano sponge (CD-NS), since multiple CD molecules connected to each other formed a 3-D network via different crosslinking agents and the CD cavities functionalized as pores in traditional sponge. Even though non-soluble CD polymers crosslinked with dialdehydes, epoxides and epichlorohydrin (EPI) are well documented, the term (CD-NS) was first applied in 1998 [167]. Hydrophobic cavities and hydrophilic tunnels distributed in networks are functionalized as adsorption sites allowing CD polymers to be a promising adsorbent for multiple contaminants. The characters of CD polymers can be tuned by the types of crosslinking agents, the crosslinking degree, particle size, porosity and post modifications towards specific target pollutants. Crosslinking agents are highly reactive chemicals that include at least two electrophilic sites that may interact with 7 nucleophilic hydroxy groups on β-CDs to form a porous network. In terms of CD polymer, both linear and crosslinked structure can be synthesized. Commonly used crosslinking agents are summarized in

Table 2-2 [168]. The CD polymers can be divided into four types depending on the chemical reactions between the CD and crosslinkers, including urethane CD polymers, carbonate CD polymers, ester CD polymers and ether CD polymers.

Table 2-2 Various crosslinking agents applied for CD polymer synthesizing, adapted with permission from ref [168]. Copyright © 2017 Elsevier Ltd, Atul P. Sherje et al.

Types of crosslinker	Commonly used crosslinkers
Dicarboxylic acid chlorides	Glutaryl chloride, adipoyl chloride, sebacoyl chloride, terephthaloyl chloride
Acid anhydrides	Glutaric anhydride, maleic anhydride, phthalic anhydride, pyromellitic anhydride
Diisocyanates	Hexamethylene diisocyanate, isophorone diisocyanate, polydiisocyanate
Dicarboxylic acids	Succinic acid, 2,3-naphthalene dicarboxylic acid, 2,2-bis(acrylamido) acetic acid
Alkyl dihalides	Dichlorodimethyl siloxane, dichloromethane
Chlorohydrin	Epichlorohydrin

a. Diisocyanate crosslinked β-CD polymers (Urethane based)

Urethane β-CD polymers crosslinked by diisocyanate consisted of insoluble network with high stability in both organic and inorganic solvent [169]. Representative crosslinking agents includes: hexamethylene diisocyanate [170][171][172], polydiisocyanate and isophorone diisocyanate. Urethane-β-CD polymers are usually prepared by polymerizing CDs with diisocyanate in pyridine and N,N-dimethylformamide for selective binding with organic molecules. It was explored that the CD-polyurethane presented a strong binding affinity towards organic molecules with heteroatoms, which was confirmed by gas-solid chromatography [173]. After then, more researchers started to explore the insoluble CD-polyurethanes applied for water treatment, which mainly focus on organic compounds removal [171] [172] [174][175]. Kawano et al. used a heptakis(2,6-di-O-methyl)-β-cyclodextrin (DM-β-CD) crosslinked with three different types of diisocyanate crosslinking agents (4,4′-methylenebis(phenyl isocyanate) (MDI), 1,4-phenylene diisocyanate (PDI) and hexamethylene diisocyanate (HMDI)) to produce an adsorbent to remove polychlorobiphenyls (PCB)s from nonpolar organic media. The synthesis pathway of DM-β-

CD/urethane polymer is shown in **Figure 2-25**. The synthesized MDI and PDI crosslinked DM-β-CD possessed a high adsorption capacity of PCBs in both isooctane and insulating oils, and can be easily recovered by acetone at room temperature [170]. Sabelo and coworkers applied nanoporous CD-polyurethane to remove odor producing chemicals (2-meththylisoborneol (2-MIB)), and disinfection by-products (DBPs). The concentrations of most remaining pollutants in water samples were less than 10ng/L after being treated with CD (HMDI) and CD (TDI), while the commercial GAC can only remove most pollutants up to 100ng/L level. Except for the excellent adsorption capacity, these CD-polyurethane polymers were superior than commercial GAC in recyclability, it could maintain its original adsorption capacity even after 20 cycles [171]. These urethane β-CD polymers were also used to remove dyes [176] [177], amino acid [172], aromatic pollutants [178] and NOM [179] from the aqueous system.

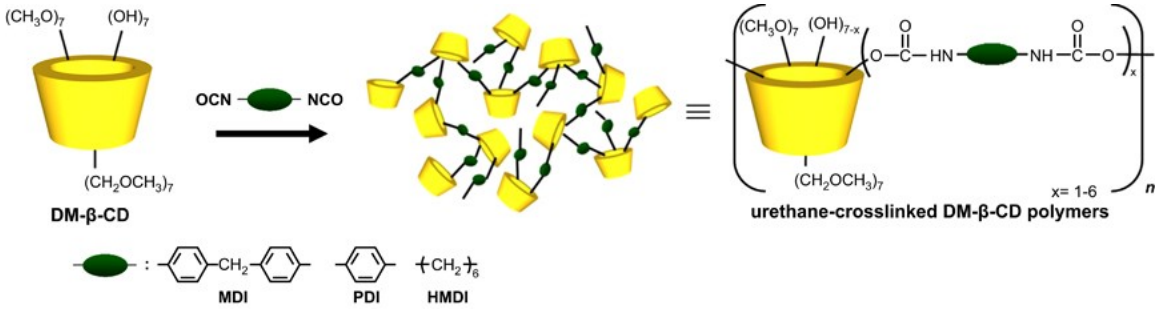


Figure 2-25 Preparation of DM-β-CD/urethane polymers by crosslinking DM-β-CD with different diisocyanate linkers. Adapted with permission from ref [170]. Copyright © 2015, The society of Polymer Science, Japan, Shintaro Kawano et al.

b. Carbonyl compounds crosslinked β-CD polymers (Carbonate based)

Carbonate CD polymers are normally prepared by crosslinking a carbonyl group with crosslinkers such as carbonyl diimidazole, diphenyl carbonate and triphosgene and β-CD. The synthesis could be implemented in either ambient temperature or high temperature, depending on

the required character of the final product, such as crosslinking degree, solubility, swelling ratio, porosity and coupling agents used in the synthesis. This type of CD polymer with low solubility are widely studied in the medical field, rarely these studies are reported for water treatment. Liu et al. proposed a magnetic β-CD nanocomposite fabricated by self-assembling N,N'-carbonate diimidazole (CDI) crosslinked β-CD onto the surface of a Fe_3O_4 modified ZIF-8. The synthesis, adsorption and recovery schematic of Fe_3O_4 @ β-CD-CDI composites is presented in **Figure 2-26**. Fe_3O_4 @ β-CD-CDI composites displayed a rapid adsorption rate and high adsorption capacity towards bisphenol A (BPA) compared with the magnetic adsorbent (Fe_3O_4) and Fe_3O_4@ZIF-8, the one without β-CD-CDI layer. Also, Fe_3O_4@ β-CD-CDI provided a ternary microenvironment as a heterogeneous catalyst, which could attract BPA into the cavity of β-CD and degrade BPA by the OH groups generated around the cavity. This bi-functional magnetic CD composite achieved the removal and degradation of the pollutants in a single process step [180].

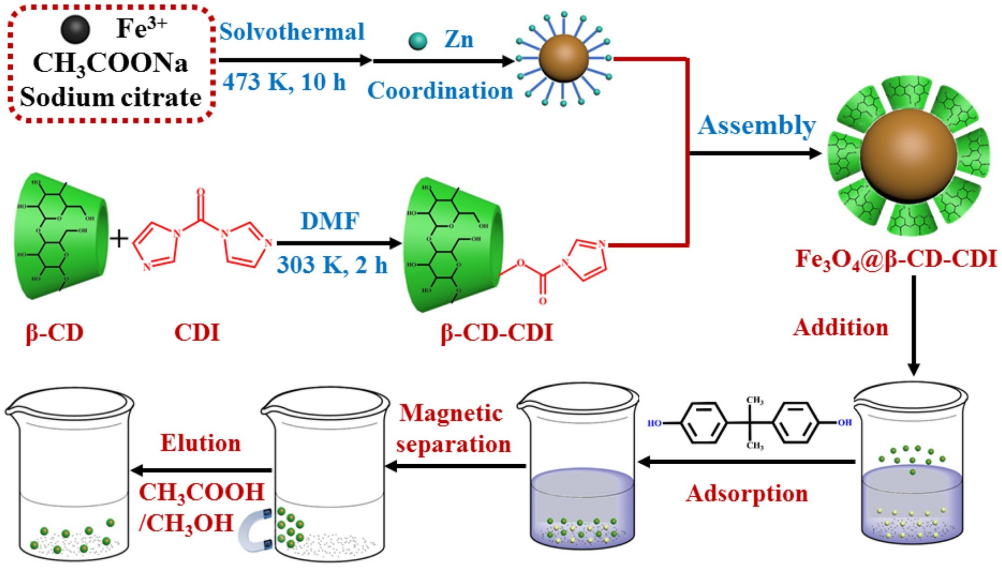


Figure 2-26 Synthesis, adsorption and recovery schematic of Fe_3O_4 @ β-CD-CDI composites. Adapted with permission from ref [180]. Copyright © 2019 Elsevier Ltd. D. Liu et al.

With increasing concern on the environmental destruction, green material is a better choice when fabricating new adsorbents. Hemine et al. synthesized biodegradable α, β-CD-nanosponge

(α,β-NS) for the removal of bio-toxic pimavanerin (PMV) from post reaction raffinates. The adsorption equilibrium was achieved within one minute with over 93% and 81% removal efficiency of PMV by using α-CD-NS and β-CD-NS respectively. The obtained removal efficiency was much higher than biological water treatment plant (37%) without severe foam generation issue [180]. Another environmentally friendly CD nanosponage (CDNS) was prepared by crosslinking β-CD with diphenyl carbonate (DCP) via a solvothermal method (**Figure 2-27**). The adsorption capacity of basic red 46 and Rhodamine B using this CDNS was 101.43 mg/g and 52.33 mg/g respectively. It indicated a promising potential of dye removal from wastewater stream [181]. Based on this review, there is no triphosgene (BTC) crosslinked CD polymer applied for water treatment applications. Most of the BTC crosslinked CD were designed for medical applications, such as drug delivery [182], cancer therapy [183] or control of drug release [184].

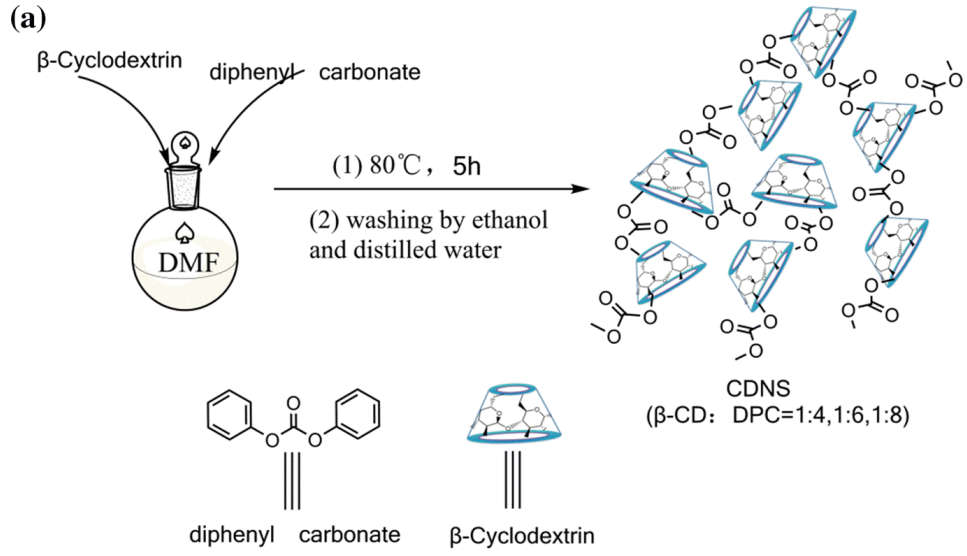


Figure 2-27 Schematic of CDNS synthesis procedure. Adapted with permission from ref [181]. Copyright © 2019, Springer Nature B.V. L. Li et al.

c. Dianhydride or di/polycarboxylic acid crosslinked β-CD polymers (Ester based)

Ester based β-CD polymers are obtained from the esterification of dianhydrides or polycarboxylic acids (like maleic anhydride, pyromellitic anhydride, glutaric anhydrate, phthalic anhydride and ethylenediamine-tetraacetic dianhydride (EDTA)) with β-CDs [168]. The solubility of ester based β-CD polymer is highly depending on the functional groups of crosslinking agent, and also the crosslinking degree. For instance, the ester based β-CD polymers synthesized by crosslinking with citric acid usually can adsorb huge amount of water, which is due to the hydrophilic nature of the carboxyl groups. Currently in water treatment field, one of the most challenging topics is simultaneously decontaminating multiple pollutants, since they usually possess different physical and chemical properties. Zhao et al. fabricated the EDTA-β-CD polymers that could simultaneously remove dyes and heavy metals. Attractively, the adsorption capacities of dyes were almost same as in single component adsorption test, and the adsorption performance of Cu (II) was improved in the binary pollutants system. This was attributed to the different adsorption mechanism of heavy metals and organic molecules [141]. Their team also applied this material for pre-concentrating rare earth elements (REEs) from tap water and seawater. The Q_m of La(III), Ce(III) and Eu (III) are 0.343, 0.353 and 0.365 respectively in mono-component system, while their much lower adsorption capacity obtained with multi-component system indicated similar electrostatic interaction adsorption mechanism for all three REEs. This biodegradable green adsorbent displayed excellent adsorption performance for metal ions and dyes, especially in multi-pollutants mixture. The rapid adsorption rate of REEs when pre-concentrating them from dilute water system made this EDTA-β-CD polymer a promising water treatment adsorbent [185].

Citric acid (CA), a common crosslinker used for synthesizing β-CD polymer, the carboxyl group performs not only as a crosslinker but also could bind and remove cationic dyes. Zhou et al.

designed a CA crosslinked β-CD polymer by esterification followed by 2-dimethylamino methacrylate monomer (PDMAEMA) grafting. This CD/CA-g-PDMAEMA possessed adsorption sites for both anionic and cationic dyes at varying pH and also the adsorption affinity for EDCs, which was superior than Zhao's anionic dye adsorbent. The carboxyl groups in CA were deprotonated and adsorbed cationic MB in basic environment. And the ternary amino groups were protonated and attract MO in the acidic environment. At the same time, the DC cavities were bound to BPA from pH 2 to pH 10, where the adsorption capacity was independent of other dyes present [128]. Another popular crosslinker for β-CD polymer is pyromellitic dianhydride, which is crosslinked with β-CD via the polyaddition reaction. An eco-friendly pyromellitic β-CD polymers (β-PMDA) was applied for heavy metal removal, and this nanosponge possessed a low water absorption capacity (254 wt%) with 8 times molar ratio of crosslinker to β-CD. It exhibited a high retention capacity (up to 94%) of Cu^{2+} and Zn^{2+} in both 500 and 50 ppm ultrapure water. However, in the presence of sea salt, the adsorption of Cu^{2+} was reduced to 36-45%, which was attributed to the salt shielding effect [143]. The schematic of β-PMDA synthesis is presented in **Figure 2-28**.

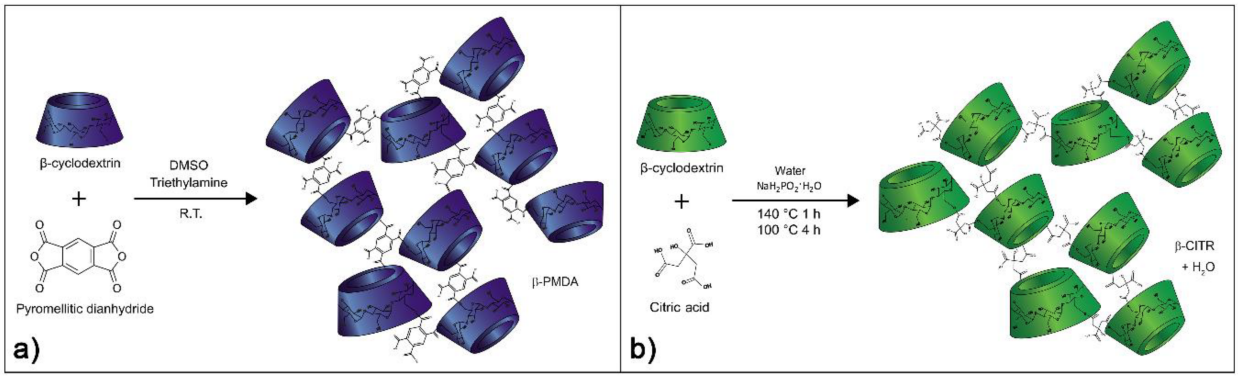


Figure 2-28 Synthesis of β-PMDA(a) and β-CITR (b). Adapted from ref [143].Copyright © 2019, A. R. Pedrazzo.

d. Chlorohydrin and alkyl halides crosslinked β-CD polymers

The earliest crosslinked CD polymer was reported by Solms and Egli in 1965, $\alpha, \beta$and γ cyclodextrin resins were first activated in water by sodium borohydride. Then it was crosslinked with epichlorohydrin (EPI) in an extreme basic environment and applied for binding aromatic compounds [186]. The unique inclusion property of CD-EPI polymer could be used as a separation technique based on size exclusion, shape difference and hydrophobicity. This is the reason why CD-EPI is still being developed in different forms and mostly applied in the separation field [187]. β-CD cross-linked with EPI formed an oxygenated alkylated polymer network known as ECP. EPI or ECH (or 1-chloro-2,3-epoxypropane) is a popular crosslinkers adopted in polysaccharide reaction with two reactive functional groups, alkyl chloride and epoxy groups. EPI can either crosslink with β-CD or crosslink by itself during the polymerization process to form the water soluble or insoluble CD polymer [188]. **Figure 2-29** is a schematic representation of the crosslinking reaction of β-CD and EPI, and the reaction was conducted under extreme basic environment. Different mechanisms could occur during the reaction, the primary reaction was to form a 3-D network during the polymerization of β-CD and EPI. The possible structure of this 3-D structure is represented in **Figure 2-30**, and the two possible mechanisms were the self-crosslinking of EPI or the formation of glycerol by hydrolysis [188].

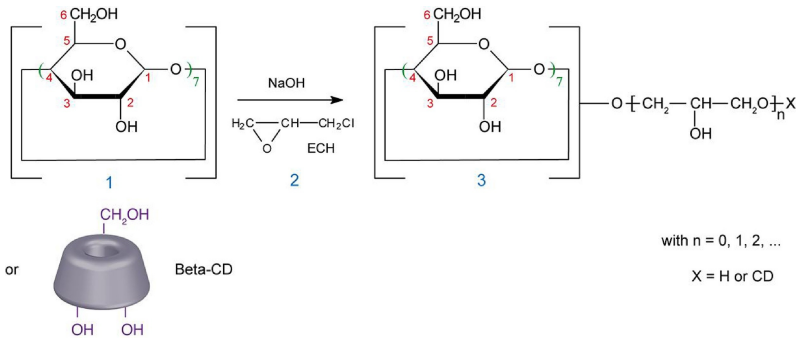


Figure 2-29 EPI crosslinked with β-cyclodextrins forming insoluble poly(CD-EPI) gel under basic environment. Adapted with permission from ref [189]. Copyright © 2017 Elsevier B.V. N. M. Crini et al.

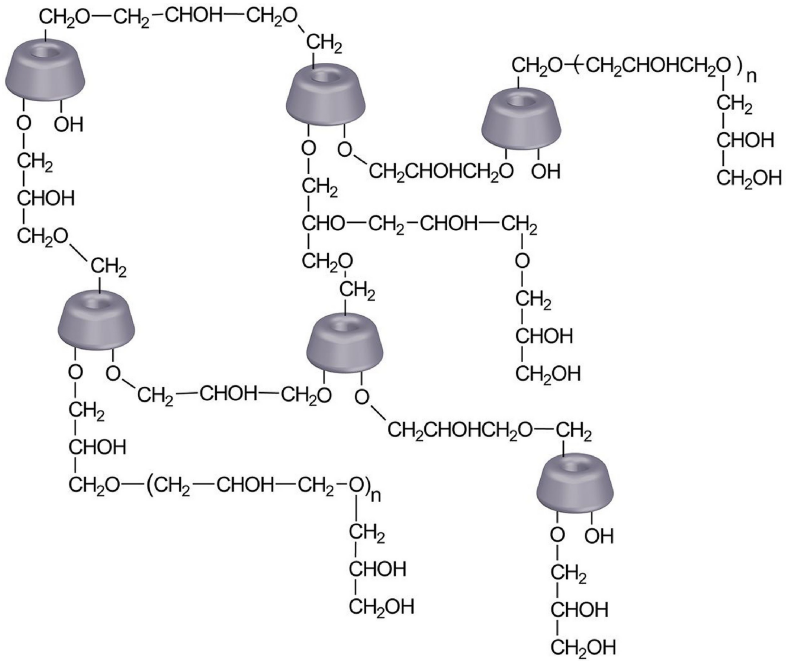


Figure 2-30 Structure of the 3-D polymeric network of CD crosslinked with EPI. Adapted with permission from ref [189]. Copyright © 2017 Elsevier B.V. Nadia Morin-Crini et al.

Celebioglu et al. fabricated a water-insoluble hydrophilic poly(CD-EPI) fibers via the electrospinning of aqueous hydroxypropyl-β-CD crosslinked with EPI by thermal treatment. The synthesized poly (CD-EPI) mat could maintain its fibrous structure in water and various organic solvents. In comparison to granulated poly (CD-EPI), poly (CD-EPI) fiber displayed a faster adsorption mechanism to phenanthrene and phenolphthalein due to their smaller dimensions and highly porous structure. This poly (CD-EPI) membrane had high specific area and high CD loading, which was a promising material for removing dyes from both water and organic solvents [190]. The participation of the organic solvent during the synthesis and the non-biodegradable nature of the spent resin was the main concerned when developing this CD polymers. Xu et al. developed an ultra-microporous β-CD (T-E-CDP) polymer based on flexible EPI and rigid tetrafluoro-terephthalamine (TFTPN), which was synthesized for the first time in aqueous phase. T-E-CDP presented a fast adsorption rate for BPA, 3-phenyphenol (3-PH) and ethinyl estradiol (EE2). The

equilibrium was reached within 2 mins, which was 45 and 581 times faster compared with commercial adsorbents (AC) and XAD-4 resin, respectively. Furthermore, T-E-CDP could remove micropollutants at environmental relevant concentrations without being affected by pH, ionic strength of the aqueous system and the coexistence of NOM. T-E-CDP could be recycled numerous times through simple desorption with methanol at room temperature, and it could be degraded in a natural environment. This promising green synthesis method and the superior rapid adsorption rate facilitated its application in real water purification [191].

- **β-CD immobilized absorbents**

To separate and recover β-CD based adsorbents from aqueous system, different materials have been used as a matrix to support β-CD. The immobilization of β-CD onto a supporting matrix can make use of the inclusion property of β-CD cavity, and also improve the availability of β-CD cavity due to the high surface area of the matrix material. Currently, there are three major types of materials commonly used to immobilize β-CD, including inorganic, organic and natural polymer.

a) Inorganic matrix

The most common inorganic matrices used to support β-CD includes single wall/multi-wall carbon nanotubes (S/MWCNT)s, graphene oxide (GO), silica based material (SiO_2), magnetic particles (MNPs) and titanium oxide (TiO_2), which possess nano-size, high aspect ratio and abundant functional groups on the surface. They address the recovery issues of pristine β-CD, and also improve the dispersity of the matrix material due to the surfactant-like characteristic of β-CD.

Carbon based material, carbon nanotubes (CNTs), graphene (GR) and graphene oxide (GO), is becoming attractive supporting matrix in various fields because of their distinctive physio-chemical properties. CNTs, discovered by Iijima in 1991 [192] have been proven to be a promising adsorbent for removing toxic pollutants from the water system [193], as the large specific surface area imparted from their hollow or multiple layer structure. CNT based adsorbents can be classified

into 3 types: single-walled CNTs (SWCNTs), multi-walled CNTs (MWCNTs) and functionalized CNTs (f-CNTs). SWCNTs ($0.7 < d < 2$ nm) are made from one atom thick allotrope of hexagonal structure carbon nanosheet rolled up into a cylindrical shape during the chemical vapor deposition (CVD) process. SWCNTs have a diameter of about 1 nm with a super high aspect ratio of about 1000 therefore considered a one-dimensional structure [194]. MWCNTs ($1.4 < d < 150$ nm), indicated by its name, consists of multiple layers of SWCNTs coaxially wrapped into a cylindrical tube shape. Double-walled carbon nanotubes (DWCNTs) is a special type of MWCTs that contain two layers of SWCNTs. In CNT, the carbon layers are aligned as hexagonal structure. Two structures of CNT can be represented by its chiral vector (n, m) using the tube axis as a reference point: armchair (n=m) and zigzag (m=0) [195]. Compared to MWCNTs, SWCNTs possess a higher specific surface area resulting in better adsorption performance towards organic pollutants, especially for toluene (9.96mg/g) and benzene (9.98mg/g) [196]. However, due to the high production cost of SWCNTs, MWCNTs are more affordable and applicable in scalable applications. Although, the pristine CNTs has superior properties, the low solubility and dispersity limited their applications. Among various matrix materials, CNTs are widely employed as a supporting material for β-CD in water treatment field, due to their high aspect ratio, high mechanical strength due to the C-C bonds and versatility for chemical modifications. β-CD grafted MWNTs showed promising adsorption capacity for flowing contaminants in aqueous systems with improved dispersity and adsorption performance. A MWCNT/iron oxides modified with β-CD was applied to p-nitrophenol (PNP) removal under different conditions and the adsorption capacity increased from 21.68 to 33.34 mg/g after β-CD grafting [197]. Similar magnetic-based β-CD functionalized MWCNTs had a much higher adsorption capacity towards MB (196.5mg/g), resulting from the high β-CD grafting ratio (17 wt%) [198]. A glycine/β-CD

modified MWCNTs adsorbents exhibited super high adsorption affinity towards organic dyes, including MB, AB113, MO, DR1 with adsorption capacities of 90.90, 172.41, 96.15 and 500 mg/g respectively [199]. A novel Ag/TiO_2 decorated β-CD nanosponge functionalized phosphorylated MWCNTs (pMWCNT/ β-CD/ TiO_2-Ag) possess high surface area (325.5 m^2/g) showed high adsorption capacity for trichloroethylene (TCE) and Congo red (CR) are 27507 and 146.96 mg/g respectively [193]. In conclusion, CNTs based nanomaterial applied in water treatment is promising in many respects, such as high adsorption capacity and high surface areas. However, more effort should be devoted to the development of large-scale, cost-effective synthetic strategies.

Graphene (GR) is a two-dimensional material with a hexagonal honeycomb lattice composed of a single layer of carbon atoms hybrized in sp^2. This unique structure gives GR a high specific area, large pore volume, high transparency, high heat conductivity coefficient, multiple surface chemistry and excellent mechanical strength, that make GR based material to be a promising materials for water treatment [151]. Due to all the advantages described above, GO, as one of the most common derivatives, has also drawn attention in large-scale cleanup techniques. Nie et al. developed a highly porous graphene oxide aerogel microsphere modified with CD (CD-GAM) that shows high adsorption capacities for a wide range of pollutants, including dyes (MB: 439mg/g), pesticides (2,4-D: 17mg/g), pharmaceuticals (propranolol hydrochloride: 49mg/g), plastic compound (BPA: 38 mg/g). The CD-GAM possessed rapid adsorption kinetics (reaching equilibrium within 10 minutes) for most pollutants and still retained 80% of the adsorption capacity after 5 cycles [200]. A nanocomposite synthesized with GO modified β-CD (GO-CD) showed a very high adsorption capacity for BPA (373.4 mg/g), which was superior to most of the existing adsorbents [125]. Another β-CD modified magnetic loaded GO (β-CD/MGO) was fabricated by a simple reverse phase co-precipitation method, which possessed a high adsorption

affinity for both heavy metals (Pb (II), Cu (II)) and dye (MB). As a conclusion, the high aspect ratio of GR/GO and unique molecular structure of β-CD secured higher adsorption capacity for different pollutants. The rich surface chemistry allowed additional modification with specific adsorption sites and the high mechanical strength enabled the recyclability of the adsorbents.

In addition to carbon-based material, mesoporous silica is another common supporting matrix that possess high surface area and porosity. The mesoporous silica applied for gaseous purification is completed by calcination, while the high density of hydroxy groups on the surface of silanol limit its adsorption performance in aqueous systems. Due to the unique hydrophobic adsorption site of β-CD, it is usually incorporated with mesoporous silica for improved hydrophobicity [201]. Bhattarai et al. developed 14 different β-CD modified silica based adsorbents, they were prepared with silica coated with glycidoxypropyl trimethoxysilane (GPTS) or aminopropyl triethoxysilane (APTES). Compared with the silica adsorbents of different β-CD loading, the adsorption capacity of all three model pollutants (17 β-estradiol, PFOA and BPA) increased with increasing CD loading, and the adsorption was partially due to the hydrophobic cavity of β-CD. The highest adsorption capacity was achieved by the combination of HMDI as a crosslinking agent synthesized with β-CD and silica in DMSO, which removed more than 90% of 17 β-estradiol, PFOA and BPA from MQ water. The adsorption capacity of 17 β-estradiol using the synthesized adsorbent approached $38.8 \pm 5.6 \mu$g/g, which was superior to the commercial activated carbon F400 ($23.6 \pm 6.3 \mu$g/g) and could be reused more than 4 times without obvious loss of adsorption capacity [202]. Another fast adsorption process of p-nitrophenol was achieved by a surface immobilized β-CD silica hybrid adsorbent (CD@Si), and the adsorption capacity could reach 69.6 mg/g within 15s at pH 7 and could be reused more than 5 times with a reasonable capacity [203]. These mesoporous silicas provided high surface area offering large amounts of

accessible sites for β-CD modification. β-CD also improved the stability and adsorption capacity of silica-based adsorbents, and the rapid adsorption allowed the CD modified silica-based material to be used as promising adsorbents.

A major concern of β-CD is its solubility in water, so one of the modifications focused on β-CD based adsorbents and its recyclability. Magnetic particles, as a controllable separating material, are frequently used as carriers for β-CD. Lin et al. investigated a novel magnetic β-CD inclusion complex with phosphonobutanetricarboxylic acid (MNP-CD-PBTCA) applied to Hg^{2+} removal. The Q_m was 77.59 mg/g obtained by contacting it absorbent with Hg^{2+} at 55℃ for 150 min at pH 4, and the binding was due to the electrostatic interaction between Hg^{2+} and β-CD complex. The reusability of MNP-CD-PBTCA was confirmed by five adsorption-desorption cycles with acceptable capacity loss [204]. Except for the single pollutant treatment, a β-CD and polyethyleneimine bi-functionalized magnetic particles (Fe_3O_4-PEI/ β-CD) were developed for simultaneous removal of MO and Pb^{2+}. It is challenging to treat complex wastewater via a single step treatment, since the physicochemical properties of different pollutants could be very different. The adsorption capacity of MO and Pb (II) is highly depending on the pH value, the Q_m of MO can reach 192.2 mg/g at pH 1, indicating that electrostatic interaction played an important role in the adsorption process. In addition, the adsorption capacity of Pb (II) was 73.1 mg/g at pH 6, and the adsorption performance was unaffected by adsorption-desorption cycles. Interestingly, the desorption efficiency was closely related to the elute types, and NaOH was preferable for MO saturated adsorbents, while EDTA showed better performance for Pb (II) saturated adsorbents [205]. Excluding nanomaterial-based adsorbents, the magnetic material had also been used in other forms, such as beads, aerosols or membranes. A zerovalent iron incorporated carboxymethyl β-CD beads were developed for arsenic (III) and arsenic (V) removal. The imprinted iron not only

promoted the separation efficiency, but also provided extra adsorption sites (hydroxyl groups) for arsenic species, where the adsorption capacity reached 18.5 mg/g and 13.51 mg/g for As(III) and As(V) respectively [206]. Porous magnetic β-CD polymeric composite (MNPs/β-CDP) was synthesized by grafting β-CD modified tetrafluoroterephthalonitrile (TFT) onto citric acid modified MNP. This MNPs/ β-CDP were firstly applied for both adsorption and the degradation of acetaminophen (APAP) by coupling $KMnO_4$ oxidation into the treatment process. It simultaneously completed discoloration of secondary polluted wastewater and adsorbent regeneration. The synthesis pathway of MNPs/β-CDP and its adsorption, coupling oxidation and regeneration process are shown in **Figure 2-31**. The high magnetization (28 emu/g) MNPs/ β-CDP could be separated from the aqueous system within 60s and possessed a high adsorption capacity towards APAP (126.2 mg/g) at pH 7. The ultra-fast adsorption kinetics were indicated by over 70% of the equilibrium adsorption capability achieved within 60 seconds and the adsorbents became saturated within 5 minutes. MNPs/β-CDP could be reused more than 5 times without additional activation, and this long lifetime was suitable for large-scale water treatment [207]. Unlike most magnetic supported adsorbents using Fe_3O_4 particles, Lee and Kwak developed a new β-CD functionalized mesoporous magnetic clusters (CD-MG) applied for BPA removal. The superior adsorption capacity (52.7 mg/g) of BPA at pH 6.5-7 could be achieved via CD-MG without significant loss over 4 adsorption-desorption cycles [208]. In conclusion, the fast adsorption kinetics, the excellent magnetic separation property, the high recovery efficiency and the commercially comparable adsorption capacity enabled them to be used as promising adsorbent in the large-scale process.

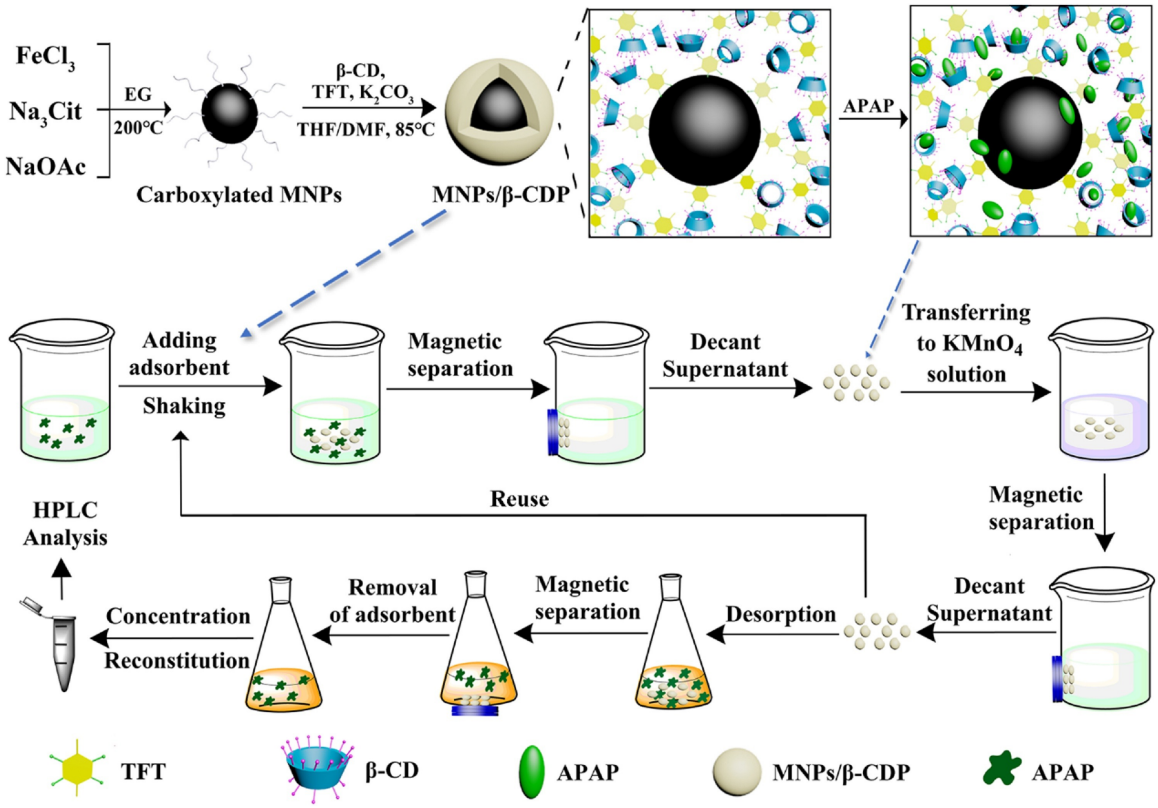


Figure 2-31 The schematic of material preparation of MNPs/ β-CDP and its application for adsorption and degradation of APAP in a combination with $KMNO_4$ oxidation process. Adapted with permission from ref [207]. Copyright © 2019 Elsevier Ltd. Y. Shi et al.

b) Organic matrix

Except for using inorganic material as supporting matrix, various organic materials have been used to prepare β-CD based adsorbents. Synthetic polymers have abundant functional groups, which can effectively bond with β-CD and provide more adsorption sites. In addition, polymers act as spacers when preparing the β-CD-based polymer, making more CD cavities accessible to the target molecules. For example, a branched polyethyleneimine (b-PEI)-polyethylene glycol (PEG)-β-CD polymer (X-CD/b-PEI-PEG-β-CD polymer) was developed for simultaneous removal of BPA and Cu^{2+}. Epoxy functionalized glycol, PEG as a nontoxic crosslinker combined with a metal ion favorable crosslinker PEI was used for β-CD grafting. X-CDs were simply synthesized by mixing PEGDE and b-PEI with alkaline dissolved β-CD at 60℃ for 5h and dried

after washing steps. From the elemental analysis, the crosslinking degree of X-CD was significantly reduced after the addition of b-PEI as a secondary crosslinker, and the adsorption performance of BPA was improved. The Q_m of BPA and Cu(II) were 65.3 and 52.4 mg/g at pH 6, respectively. Surprisingly, higher adsorption capacity was obtained from this nonporous X-CD, which is unusual compared with other types of β-CD based adsorbents. Furthermore, the adsorption capacity of both BPA and Cu(II) in binary pollutants removal test have almost no difference compared to single pollutant system. This remarkable adsorption performance was attributed to the expansion of a crosslinked structure of X-CD [209]. Another study that investigated the anti-fouling property of a hollow fiber composite membrane prepared by interfacial polymerization and layer by layer assembling method. The membrane was prepared on a polyvinylidene fluoride (PVDF) hollow fiber ultrafiltration (UF) membrane. Firstly, the membrane was soaked in different weight% of PEI solution, isophthaloyl dichloride (IPC) and β-CD in sequence. The prepared membrane presented no obvious effect of rejection flux, and presented excellent anti-fouling property with over 97.6% flux recovery ratio. This positively charged membrane can potentially be applied to capture organic and anionic contaminants from salt water (such as seawater) [210].

Considering biodegradability, aliphatic-aromatic co-polyesters were used as a supporting matrix for the β-CD grafting. Liu et al. synthesized a novel biodegradable poly ((butylene succinate-co-terephthalate) -co-serinol terephthalate) (PBSST) co-polyesters with NH_2 end groups, and the CM-β-CD was further grafted via the amination reaction to obtain PBSST-g- β-CD. The PBSST-g- β-CD were fabricated into nanofibrous membrane via electrospinning for MB removal. The Q_m of MB was 543.48 mg/g and still possessed a 98% removal efficiency after 5 cycles of use [211]. To solve the recovery issues of β-CD, most of current studies focus on the development of

insoluble β-CD polymers in powder form, which requires a secondary filtration process after adsorption test. The β-CD based adsorbents were evaluated under bath system, which is not realistic for large scale water treatment. By considering these issues, fixing β-CD onto insoluble matrix and applied in a dynamic adsorption test is critical. A novel palladium loaded β-CD monolith (Pd-NP-loaded β-CD) was developed and loaded into a flow reaction system for 4-NP removal, conversion and 4-AP enrichment. The 3-D network Pd-NP-loaded β-CD monolith was synthesized by a crosslinking reaction between monoclorotriazine modified β-CD (MCT-β-CD) crosslinked with PEI. The monolith was prepared by adding MCT-β-CD and PEI solution into a polytetrafluoroethylene (PTFE) tube and reacted at 10℃ for 72 h. This monolith Pd-NP-β-CD had a good adsorption affinity with 4-NP, even un-degraded 4-NP would remain in the monolith rather than leaching out. By using this flow reaction system, the concentration of 4-NP can be reduced to a concentration that does not affect living organisms in the environment, and the five cycles reusability enables this monolith a promising multifunctional (adsorption, enrichment and degrade) adsorbents [212]. Wang et al. developed a β-CD based porous membrane for organic micropollutants removal. The soluble β-CD polymer (β-CDP) was first synthesized by polycondensation of β-CD with EPI in base, and the β-CDP was fixed onto a commercial nylon microfiltration membrane (MF) via interfacial crosslinking with trimesoyl chloride (TMC). The preparation process is presented in **Figure 2-*32***. In the optimized conditions, the β-CD loading capacity, permeation flux and treating capacity of the β-CDP porous membrane reached 6.2 g/m^2 and 1300 Lm^{-2}h^{-1} at 1bar and 440 mg/m^2 with 100% BPA removal efficiency. An ultrahigh permeation flux (2500L m^{-2}h^{-1}) with 100% removal efficiency can be obtained by this membrane in flow-adsorption test, which is two orders of magnitude higher than the commercial

nanofiltration membrane. Also, higher treating volume can be achieved by using a stacked membrane setup without losing the treating capacity of individual membrane [213].

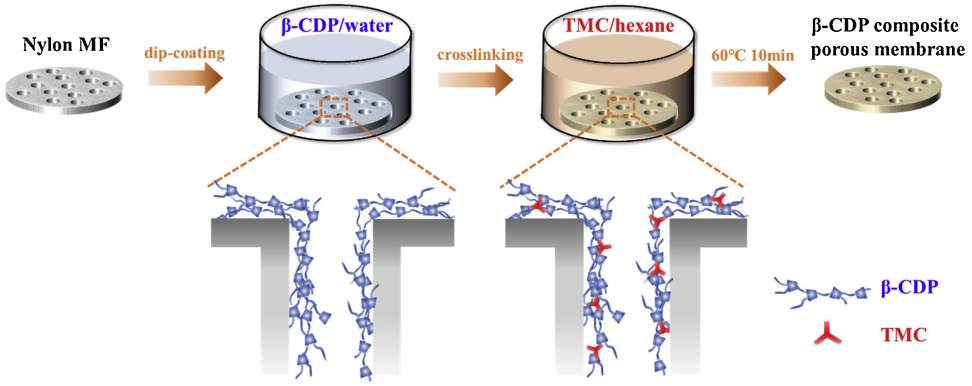


Figure 2-32 Schematic representation of β-CD composite porous membrane preparation. Adapted with permission from ref [213]. Copyright © 2019 Elsevier B.V. Z. Wang et al.

Chen et al. investigated an environmentally friendly adsorbent applied for different cationic dyes and heavy metal removal. Firstly, β-CD was crosslinked with citric acid to obtain CD-CA polymer, then dopamine was self-polymerized in the presence of a CD-CA adsorbent (CD-CA\PDA). The adsorption tests indicated that CD-CA\PDA possessed high adsorption capacity of 582.95, 1174.67, 473.01, 73.64 mg/g towards MB, malachite green (MG), crystal violet (CV) and copper ion (Cu^{2+}), respectively, at 25℃ with 12h contact time and 5-5.5 initial pH. To evaluate the adsorbent at practical condition, Tandem adsorption tests were conducted. The results showed that the adsorption capacity of MB was not affected by adding other cationic dyes, or Cu^{2+} to the system. However, both MG and CV presented a decreasing adsorption capacity when Cu^{2+} was added to the system, which might attribute to the different adsorption mechanisms. MB might be adsorbed by host-guest interaction, while MG and CV were mainly adsorbed by electrostatic interactions. In terms of the adsorption of Cu^{2+}, adding different cationic dyes gradually reduced its adsorption capacity, and this confirmed that the adsorption mechanism to Cu^{2+} was due to the negative charge on CD-CA\PDA. Because of the high adsorption capacity of CD-CA\PDA compared to other

biomass derivative adsorbents and good recyclability, it could be applied for simultaneous removal of dye and heavy metal ions [214]. In conclusion, β-CD could be functionalized on a wide range of synthetic polymers through different strategies for the target water treatment process. Compared with β-CD polymer-based adsorbent, using a supporting material could not only decrease the amount of β-CD used for synthesizing the material, but it also could combine the benefits of the base material and β-CD. On the other hand, employing a supporting material also solved the solubility issue of β-CD, resulting in an easier recovery β-CD based adsorbent.

In addition to synthetic polymers, natural organic material such as chitosan, CNC/CNF and agricultural products have also been used as a matrix for β-CD grafting. Because natural polymers have abundant sources, bio-compatible, cheap and eco-friendly. For example, an easy preparation of a chitosan adsorbent using citric acid modified β-CD (CA-CD/CS) was developed for reactive dye removal. The adsorption performance of CA-CD/CS was evaluated by a flow through experiment, the CA-CD/CS was packed in a glass column. And a simulated dye solution was allowed to pass through the column at a rate of 1.66 ml/min. The removal efficiency of Reactive Blue 49 (RB49) could reach 94% using 20% CA-CD loaded CS adsorbent, and the highest adsorption capacity approached 498 mg/g at pH 5. The regeneration of the used adsorbents could be conducted by passing 100 ml 0.1 M NaOH through the glass column, and 80% of removal efficiency could still be obtained after 6 adsorption-desorption cycles. The superior adsorption capacity and simple preparation allowed CA-CD/CS to be a promising adsorbent applied for dye effluent treatment [215]. Chitosan is a common material used for bead preparation, since it can form beads through ionic gelation. Karthikeyan and Meenakshi developed a cerium and β-CD incorporating chitosan microspheres (Ce-CS-β-CD) applied for anion removal. The fabrication process is presented in **Figure 2-*33***. The Ce-CS-β-CD beads showed good adsorption capacity

88.54 and 72.12 mg/g for phosphate and nitrate, respectively. Furthermore, this Ce-CS-β-CD beads were used to treat real contaminated water from eutrophic area of Dindigul District (India), and the results showed that both phosphate and nitrate concentration were reduced to below the critical limits [216]. Later, this team applied this Ce(III) network chitosan/ β-CD (Ce@CCD) beads for selective removal of dye molecules. The adsorption capacity of RB4, IC and AB158 dye were 29.56, 30.57 and 30.57 mg/g, respectively. The adsorption mechanism of Ce@CCD was a synergistic effect of electrostatic interaction, hydrogen bonding and host-guest inclusion, while the adsorption mechanism towards toxic anion were ion-exchange, electrostatic interaction and host-guest inclusion. The adsorption capacity and mechanical property was enhanced after the incorporation of β-CD into the system, and this Ce and β-CD included chitosan beads displayed great potential for the decontamination of different types of wastewater [217]. There are many different types of chitosan/ β-CD based beads applied as adsorbents. A chitosan/β-CD crosslinked beads presented 1000 mg/g adsorption capacity for indigo carmine, which was twice that compared with chitosan beads without β-CD [218]. Another nitrilotriacetic acid (NTA) crosslinked β-CD incorporated chitosan (NTA- β-CD-CS) adsorbent were synthesized for simultaneous removal of heavy metals and organic dyes. Surprisingly, the adsorption capacity of Hg (II), MB and MO were 178.3, 162.6 and 132.5 mg/g respectively in mono system, and the adsorption capacity was not reduced in Hg(II)/MB binary system [219].

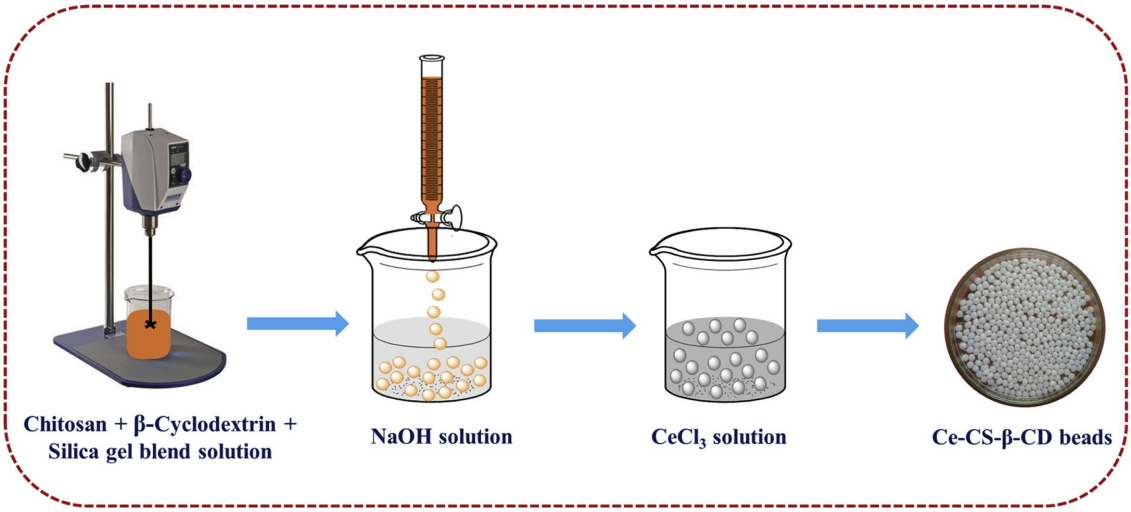


Figure 2-33 The synthesis procedure of Ce-CS-β-CD hybrid microsphere. Adapted with permission from ref [216]. Copyright © 2019 Elsevier B.V. P. Karthikeyan.

CNC and CNF are another abundant green natural polymer existed in the world, they have been used to develop superior adsorbents, such as aerogel, beads or membrane for pollutant treatments for many years. A highly efficient aerogel-based adsorbent prepared from β-CD functionalized CNF was developed for phenol pollutant removal. β-CD was crosslinked with EPI in the presence of CNF, then different amounts of crosslinking agent (polyamide-epichlorohydrin resin) was added to the β-CD grafted CNF suspension to form a gel under sonication, and the aerogel was obtained by freeze dry. The grafting efficiency of β-CD onto CNF was 19.03%, which was much higher than the grafting efficiency on regular wood fiber (8.07%) under the same condition. The maximum adsorption capacity of p-chlorophenol (PCP) using CNF-CD aerogel obtained by extrapolating the Langmuir adsorption isothermal curve was 148 μmol/g, while the adsorption capacity using CNF-CD membrane and CD modified CNF fibers were 39 and 63 μmol/g, respectively. This higher adsorption was due to the high porosity, high aspect ratio and high availability of β-CD cavities on CD-CNF aerogel [220]. Kono and coworkers prepared a hydrogel bead by crosslinking carboxymethylcellulose sodium salt (CMC) and β-CD with ethylene glycol diglycidyl ether (EGDE). The β-CD incorporated hydrogel beads presented much

higher adsorption capacity towards BPA and the adsorption capacity was proportional to the β-CD loading. However, the hydrogel beads produced from pure CMC showed almost no adsorption, and the highest adsorption of BPA was 167 μmol/g [221]. Another cellulose based β-CD were prepared by a two-stage reaction. Firstly, the cellulose beads were obtained from the casting method, where cellulose powder was mixed in precooled NaOH/urea/water (7:12:81 w/w) at -23℃, and quickly dropping into a mixture of 4wt% $CaCl_2$ with 5 wt% HCl. The prepared cellulose beads (CB) were neutralized by rinsing with DI water. Secondly, β-CD was grafted onto the surface of CB by crosslinking with EPI, and washed with DI water. The preparation procedure is presented in **Figure 2-*34*.** Similar to other research work for BPA removal, the pH was also the first factors needed to be investigated before the other adsorption isothermal study. The adsorption capacity of BPA increased from pH 2 to 7, which was due to the protonation of CD grafted CB and deprotonation of BPA at higher pH. No obvious adsorption was obtained from pure CB, which indicated the significance of β-CD cavities during the adsorption process. The Q_m of BPA was 30.77mg/g at 298K, pH 7, and it still presented an adsorption capacity of 20.96 mg/g after four regeneration cycles [222]. In summary, β-CD functionalized CNC/ CNF based green material could be used as a promising adsorbent, since their easy preparation process, mild reaction condition, biodegradable property and high adsorption capacity.

Thus far, a large proportion of cheap and environmentally friendly adsorbents have been produced from agricultural waste (AWM). However, the original form of AWMs usually has low adsorption capacity, thus appropriate modification such as grafting of functional material will increase the adsorption sites and optimize the microstructure necessary for the development of AWMs based adsorbent. Lately, a sugarcane bagasse (SB) modified with β-CD by crosslinking

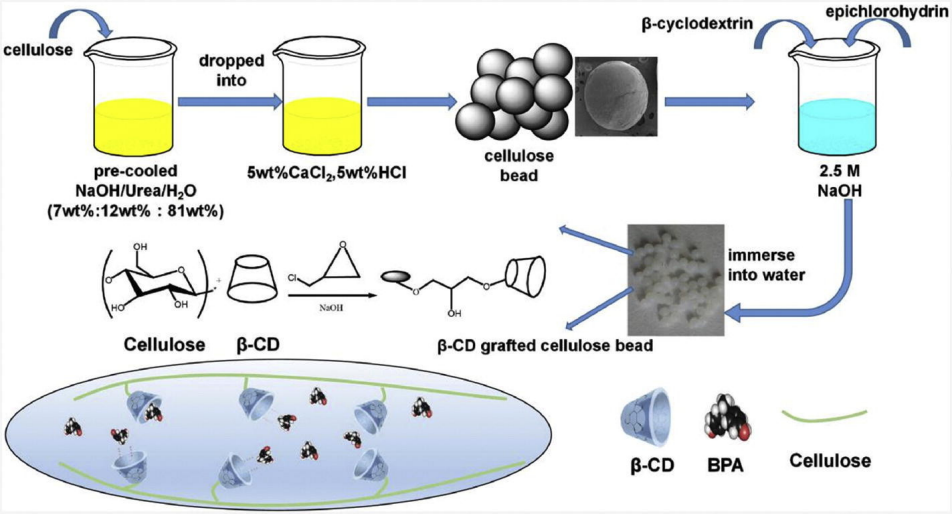


Figure 2-34 The preparation process of β-CD grafted cellulose beads. Adapted with permission from ref [222]. Copyright © 2019 Elsevier B.V, Q. Lin et al.

reaction with citric acid was employed to prepare the bagasse-β-CD (SB-β-CD) adsorbent for simultaneous removal of BPA, MB and neutral red (NR). The Q_m of BPA, MB and NR were determined at 298K, and found to be 51.6, 292.8 and 193.1 mg/g at pH 7, 9 and 6, respectively. The adsorption of BPA was mainly attributed to the host guest interaction and hydrogen bonding, while the adsorption of MB/ NR was mainly attributed to electrostatic interaction with the carboxyl groups of citric acid. The excellent adsorption capacity could be attributed to the improved surface area, pore size and adsorption sites after crosslinking β-CD onto SB [223]. Cotton fiber, another common natural cellulose fiber is attracting increasing attention due to their low cost and degradability. Yue et al. developed a high performance cotton fiber adsorbent used for dye removal. The cotton fiber was first activated by alkaline hydrolysis to produce activated cotton fiber (ACF), and then oxidized with sodium periodate to obtain dialdehyde-cotton fiber (DA-cotton). β-CD was grafted onto the DA-cotton via aldol condensation reaction, and a hyperbranched amino terminated polymer (HBP-NH_2) was also grafted onto the DA cotton (NC-cotton). Similar to other adsorption studies on dye removal, pH played an important role. The adsorption capacity of CR and MB using

raw cotton, CD-cotton and NC-cotton were compared at their optimized pH (7.3 and 8.0). The results indicated that after β-CD and HBP-NH_2 modification, the adsorption capacity of CR and MB were both improved. This illuminated that the electrostatic interaction between NH_2 groups and dyes were the main driving force for dye removal. Over 80% of removing efficiency could still be maintained after five cycles of adsorption-desorption [224].

After reviewing many β-CD functionalized natural polymers used as adsorbent for different types of wastewater treatment process, many benefits could be concluded, such as low cost, easy processing step, mild reaction condition, large resources, and degradability. Nowadays, the research focus of solving practical problems shifts to finding solutions from green chemistry, which aims to achieve a sustainable development process. More papers can be found in this field using CNC, CNF, chitosan and alginate-based adsorbents development, however only a few studies are available that use agriculture-based material. By considering their excellent adsorption performance and green property, more agriculture-based materials can be used as a building block for adsorbents.

- **Other types of β-CD based adsorbents**

β-CD polymer and β-CD functionalized on organic or inorganic matrix are the two most common way to construct a β-CD based adsorbent. Some other types of β-CD based adsorbent such as self-assembled, molecular imprinted polymers (MIPs) and stimuli-responsive β-CD based adsorbents will be introduced in the following section.

Self-assembling is a spontaneous process based on the association of disordered pre-exist components into a 3D well-defined structure as a consequence of various physical forces, such as amphiphilic property, host-guest interaction, electronic interaction, hydrogen bonding and π- π stacking interaction without external intervention [225] [226]. Nowadays, self-assembled hydrogel

driven by host-guest interaction between β-CD cavities and guest molecules have received increasing attention for removing contaminants from the aqueous system. The host-guest inclusion complex formed between hydrophobic cavity and aromatic organic pollutants could be achieved by hydrophobic interaction, polarity, electrostatic interaction, van der Waals forces, hydrogen bonding and dipole-dipole interactions [227]. Therefore, this non-permanent and reversible interaction between β-CDs and pollutants could be applied as adsorbents to remove contaminants from water without intrusive interactions. Moreover, the enrichment of trace contaminants could be achieved by eluting the inclusion complex with a small volume of solvent. The ability to form host-guest inclusion complex is a promising character of β-CD in terms of self-assembling system. However, the soluble property of β-CD in water limits its application in aqueous systems, since it is difficult to recover the material after its use. Also, the hydrogen bond formed between β-CD molecules restricted their inclusion with hydrophilic molecules or macromolecules [225]. As a consequence, three dimensional flexible polymeric network, hydrogel, which could be easily functionalized with β-CD and serve as an adsorbent [228]. Gao et al. prepared a CD polymer (poly-CD)/azobenzene-modified polyacrylic acid (PAA-Azo) composite hydrogel via simply mixing pre-synthesized PAA-Azo solution with different concentrations of poly-CD solutions under sonication for 30 min. The self-assembled hydrogel formed via host-guest interaction with trans azobenzene and β-CD without external stimulation. The binary composite hydrogel could remove various pollutants via different mechanisms. The maximum adsorption capacity of MB and BPA were 85.32 mg/g and 20.73 mg/g via electrostatic interaction, hydrogen bonding and host-guest interaction respectively. The hydrogel could also be disassembled into a sol status by UV irradiation, which due to the transition of azobenzene from trans to cis conformation [227]. Based on the similar concept, Hou et al. synthesized a self-assembling hydrogel by host-guest

interaction between β-CD polymers and ferrocene modified poly acrylic acid (P-CD/PAA-Fc). Compared with Gao's work, it has a comparable adsorption capacity of BPA (23.61 mg/g), whereas the adsorption capacity of MB (24.64 mg/g) was much lower. It might attributed to the lower specific area (1.63-2.13 m^2/g) of P-CD/PAA-Fc, that could affect the formation of hydrogen bonding between MB and hydrogel network in aqueous systems, which is the main driven forces of MB adsorption [229]. Later, their team developed another self-assembling hydrogel based on the hydrophobic interaction between β-CD polymers and adamantane modified poly acrylic acid (P-CD/PAA-Ad). The maximum adsorption capacity of MB (20.48 mg/g) is lower than previous work, which is also due to the reduced specific area [225].

Another main strategy to develop self-assembling β-CD adsorbents is realized in the forms of molecular imprinted polymers (MIPs). Molecular imprinting technology is a well-defined method by incorporating target molecule as a printing template during the polymerization process, which aims to develop a material that can selectively recognize and bind target molecules among a series of analogous compounds. MIPs first prepared by crosslinking target molecules, functional monomers and initiators into a 3D polymer network, then thoroughly washed out the imprinting molecules until no template molecules can be detected in the filtrate. These tailored polymeric micro-cavities have specific functional groups, size, geometry and chemistry that are exactly complementary to the printing models [230]. MIPs are widely applied in diverse fields like drug delivery [231], water purification [232], solid phase chromatography [233], biosensing [234] and other applications, since the ease of preparation, low cost, high stability and precise reorganization property.

However, there are some drawbacks of traditional MIPs, such as low binding site accessibility, low mass transfer rate and low adsorption capacity. Therefore, many different

materials have been used as a substrate for molecule imprinting technology that can improve the accessibility by surface functionalization. β-CD based MIPs are becoming attractive for removing contaminates in aqueous systems, since it's improved adsorption capacity, accessibility and reduced production cost. Also, aromatic target molecules can easily interact with β-CD cavities during the surface imprinting process that benefit from its unique truncated cone structure. Recently, a magnetic molecular imprinting polymer β-CD (MMIP-CD) was developed for detection and removal of zearalenone from the aqueous system. The MMIP-CD presented improved adsorption capacity compared with the non MIP-CD adsorbents, which can be attributed to the dual adsorption sites of β-CD cavities and MIP binding sites. It overcame the low effectiveness of MIPs structural identification and the low selectivity of hydrophobic compounds in CD cavities at the same time. Furthermore, by incorporating magnetic particles into the MIP system, contaminants captured MIP-CD adsorbents can be easily separated from water by external magnetic field [235]. Wei et al. developed two different magnetic MIPs by molecular printing chitosan (CTs) and β-CD with 2-aminopyridine respectively, named Fe_3O_4-CTs@MIP and Fe_3O_4-MAH-β-CD @MIP [236]. The preparation schematics are presented in **Figure 2-*35***. Similar strategy was used to develop the surface-imprinted magnetic beads incorporated with β-CD for extracting BPA from milk. The MIP presented much higher adsorption capacity compared with NIPs and lower the detection limit to 3.7μg/L [237].

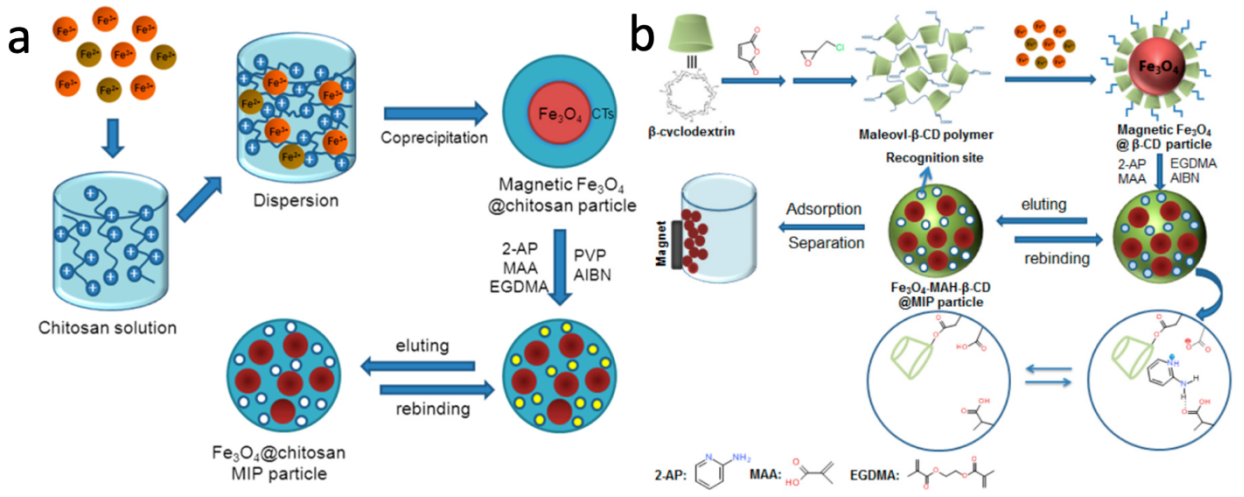


Figure 2-35 (a)Preparation procedure of Fe_3O_4-CTs@MIP (b)Preparation schematic of Fe_3O_4-MAH-β-CD @MIP and application of 2-aminoyridine removal. Adapted from ref [236]. Copyright © W. Zhang et al.

Although the adsorption performance of self-assembled β-CD based adsorbent exhibited a high adsorption capacity, the complex synthesis procedure and low productivity limit their applications. The adsorption site of β-CD cavities can improve the selectivity of the adsorbent, while it also stops them from multi-pollutant removal.

After a comprehensive review of all kinds of possibility for developing β-CD based material applied for water treatment, several critical points can be summarized here. Important factors that can affect the adsorption capacities include the amount of accessible CD cavities, the specific surface area of the supporting material, the porosity of the final adsorbent, and other functional groups existed in the adsorption system. The selection of the starting material to build up the CD based adsorbent should consider both the cost and environmental impact of the synthesis process, and also considers the target pollutants and the real condition of the applying system. So, more effort should be devoted to the development of high efficiency CD adsorbents for conventional pollutants and new emerging compounds such as PFAS.

Chapter 3: Synthesis and Characterization of pH-responsive Methacrylic acid/ Ethyl Acrylate Crosslinked Nanogel by Semi-continuous Emulsion Polymerization

Amphiphilic nanogel containing ionizable functional groups responsive to pH changes have attracted growing interests. This chapter presents a facile experimental process to synthesize methacrylic acid-ethyl acrylate (MAA-EA) nanogel crosslinked with diallyl phthalates (DAP) via a semi-batch seeded emulsion polymerization process. The effect of amounts of ionizable carboxyl groups, and degree of crosslinking on the photochemical properties of nanogels was investigated. Monodispersed spherical nanogel particles were successfully produced by crosslinking with more than 2 wt% DAP, which was observed under TEM after staining process. The particle size of the nanogel displayed an "S" shaped profile associated with the swelling from the ionization of carboxyl groups and de-swelling at high pH due to charge shielding. On the other hand, the surface charge of the nanogel displayed a "U" profile between pH of 3 to 11. The 50: 50 MAA-EA nanogel synthesized with various amount DAP possess a pKa value between 6.13 and 6.54, indicated the synthesis protocol is highly reproducible. Also, the swelling behavior of the nanogel at different pH condition is closely related to the quantity of carboxyl group existed in the nanogel network, which was calculated based on both forward and reverse titration. This robust nanogel provided many possibilities in synthesizing metal nanoclusters within the scaffold for addressing environmental and biomedical applications.

3.1 Introduction

Nanogels are hydrophilic, 3-dimensional (3D), cross-linked polymeric particles that can absorb large amounts of water or physiological fluids while retaining their internal network. As a distinctive class of material with properties of a hydrogel and nanoparticle, these nanogels possess long-term colloid stability and biocompatibility [238]. A variety of materials, such as natural and

synthetic polymers with abundant functional groups can be used to fabricate the nanogel. By harnessing physical or chemical interactions between various compounds and the functional groups, these nanogels can be used to encapsulate active ingredients [35]. For example, nanogels are extensively applied in delivery systems of specific drugs [239], controlled release [240], sensing [61], diagnostics [63], water treatment [3] and coating systems [241]. In addition, the embedded nanogel system with organic or inorganic matter can be extended to other applications, including bioimaging [242], antimicrobial applications [2], and catalytic applications [243].

The researchers manufactured nanogels in different structures or conformations to achieve certain functions, which can be used to classify them. There are three prevalent ways of categorizing nanogels: based on different nanogel structures, the way they are crosslinked and whether the nanogel system can respond to external simuli. Firstly, nanogel can be manufactured into different morphologies according to the target applications by varying the monomers or synthesis methods. Different spatial arrangements of nanogel have been classified based on the structure as presented in **Figure 3-1** [25]. These potential conformations include artificial chaperones, hairy, core-shell, hollow, functionalized nanogels and multilayer nanogels. Artificial chaperones can capture proteins and pharmaceuticals via hydrophobic interactions. This enables nanogel to be a promising vector for active agents that can be used in vaccines, medical imaging and disease therapies. They can also function as molecular chaperones by preventing the aggregation of denatured proteins [26][27]. Hairy nanogels are typically comprised of a core of inorganic or polymeric material and a shell with pendant polymer chains [24]. Functionalized nanogels have functional groups attached to the nanogel, either before or after synthesis, in order to be selective towards an external stimulus, encapsulation of active agents, or impart stability [34]. The core-shell conformation consists of two distinct regions with a dense core section and a porous

outer shell. This can be achieved by different polymerization techniques, reaction conditions and the monomers selected, which allows for different functionalities in a single nanogel particle. Hollow structural nanogels have a cavity inside them, resulting in a larger surface area with improved drug load capacity [33]. This nanogel is generally manufactured through molecular imprinting strategies, whereby the central polymer can be removed after the completion of its mission. Layer-by-layer conformation involves multiple layers of polymers stacked on top of each other by hydrogen bonding, ionic pairing or hydrophobic interactions. Their outer layer is responsive to external stimuli and the physical-chemical properties of nanogels vary according to the surrounding environment [28][29][30].

Different types of crosslinking strategies are another common way of categorizing nanogels, it can be divided into physical crosslinking, chemical crosslinking or a combination of both techniques. Physical crosslinking is typically achieved by the interactions of the monomers through hydrogen bonding, electrostatic interaction, hydrophobic association or host-guest interaction. Amphiphilic nanogel is a common type of nanogel formed through hydrophobic interactions, they have surfactant-like features that can disperse in both polar and non-polar solvents with reversible micellar structures. However, the nanogel formed by the self-assembly driven by physical forces have limited lifetime and can be damaged by simply varying the external environment. On the contrary, chemically crosslinked nanogels constructed by covalent bonds are highly stable and they can maintain structural integrity for an extended time. Vinyl monomers copolymerized with multifunctional crosslinkers can produce amphiphilic nanogels. The thickness of the latex can be manipulated using cross-linking agents with a different number of double bonds or by varying the amounts of cross-linking agent used [244]. Moreover, nanogel properties such as particle size, functional groups, swelling ratio and stimuli-responsive features can be controlled

by varying the experimental conditions during the emulsion polymerization process. Nanogels crosslinked by physical and chemical forces can be dissociated by changing the surrounding conditions. The switching properties serve as attractive characteristics of the nanogel when applied to various industries. For example, the variation in viscosity and thickness of the paint material may facilitate the application process. There is a special type of nanogel that can respond to external stimulation, such as temperature, pH, light, pressure, magnetic field, redox, enzyme, and ionic strength. Correspondingly, nanogel can present a switchable transition behavior, such as reversible swelling, hydrophilic to hydrophobic, change in refractive index, network permeability, latex viscosity or magnetic property [16]. The unique stimuli-responsive nanogel characters have been extensively researched in various fields, particularly in the biomedical science.

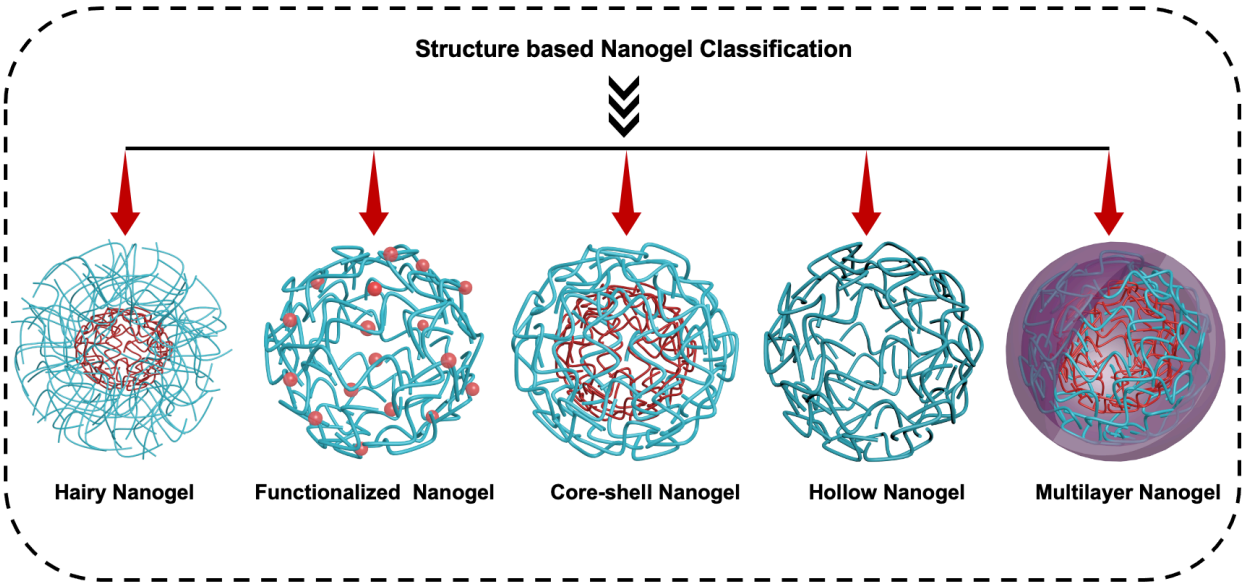


Figure 3-1 Nanogel classified based on different structures

Due to the distinctive features of nanogels, many research studies have focused on the synthesis of nanogel via a simple and reproducible method that is crucial for industrial applications. Generally, the nanogel synthetic method can be categorized as top-down and bottom-up

approaches [5]. The top-down approach means that nanogel particles are prepared from larger clusters or bulk materials by a physical, chemical or mechanical procedure. This may result in uneven size distribution, non-homogeneous nanogel system and inconsistent morphology. A bottom-up approach starts with monomers and forms nanogel via physical or chemical cross-linking [5]. For hydrophobic nanogel synthesis, conventional emulsion polymerization (Miro/Mini) is commonly used [245], whereas hydrophilic monomers comprise of nanogels are normally prepared by reverse emulsion polymerisation [246]. Amphiphilic copolymers can self-assemble into various nanogel structures without the use of surfactants. Therefore, simply interlocking the assembled polymer chains provides a common platform for making the nanogel. However, the low stability of self-assembled nanogel network may limit its application because of the low resistance to environmental changes. Currently, the most popular method for preparing nanogel is still emulsion polymerization due to its explicit mechanism and easier process compared to ATRP and other control polymerizations. Based on the different continuous phase, the emulsion polymerization may be divided into emulsion polymerization and inverse emulsion polymerization using the water or oil phase as the continuous phase respectively [247]. Although, the emulsion polymerisation procedure described in the literature usually required specific feeding rate [248], [249], [53] of monomer mixture and initiator, the feeding rate and feeding methods are mostly questionable in terms of reproducibility.

Till now, the preparation of reproducible, stable, monodispersed nanogel via a one pot synthesis method is still challenging. In order to apply the nanogel to different practical applications, this study provides a facile one-pot synthesis method to prepare methacrylic acid (MAA) and ethyl acrylate (EA) nanogel crosslinked with di-allyl phthalate (DAP) by emulsion polymerization. Simpler and less delicate setup is required when adding monomer mixtures and

initiators to the emulsion system, enabling large scale production in industries. This robust pH responsive nanogel incorporated with different amounts of carboxyl groups can be used as a "nano-reactor" for incorporating organic or inorganic ingredients. A series of monomer ratios with different amounts of crosslinkers (DAP) was used to prepare a series of nanogels, in order to study the properties of nanogels in different conditions. Characters of nanogels such as hydrodynamic radius (R_h), radius of gyration (R_g), chemical composition, quantity of functional groups (carboxyl groups), swelling ratio and morphology transition at different pH were explored. Multi-angle dynamic light scattering (MADLS), static light scattering (SLS), conductometric potentiometric titration, transmission electron microscopy (TEM) and zeta potential measurement were used to investigate the nanogel property. Moreover, the transition of nanogel conformation with different monomer ratios and different amounts of crosslinking agents was studied and related to the nanogel composition.

3.2 Experimental

3.2.1 Materials

Methacrylic acid (MAA), ethyl acrylate (EA), di-allyl phthalate (DAP), sodium persulfate and sodium hydroxide were purchased from Sigma-Aldrich. Aerosol OT (AOT, 75%) was supplied by Thermo Fisher Scientific.

3.2.2 Synthesis of Poly (MAA-EA-DAP) nanogels

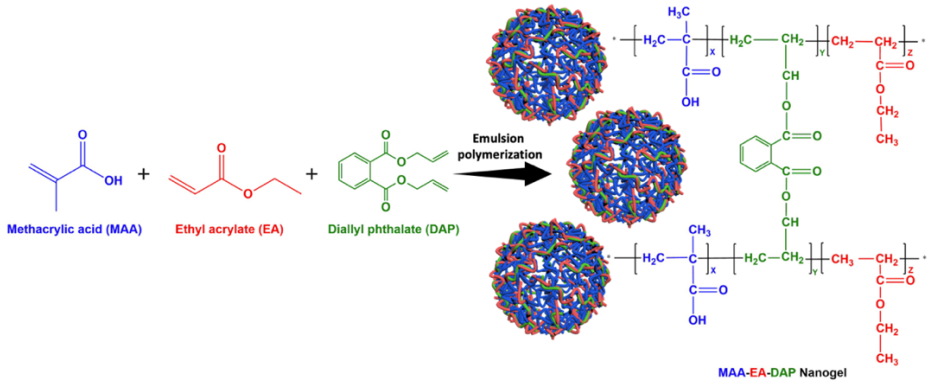
Polymeric nanogel was prepared by crosslinking methacrylic acid (MAA) and ethyl acrylate (EA) with di-allyl phthalate (DAP). The MAA-EA nanogel was synthesized using a conventional semi-continuous emulsion polymerization process. The recipe for synthesising the 50:50 (molar ratio) MAA-EA nanogel with 8 wt% DAP is described in the following section as an example. All other recipes for synthesizing nanogel with different monomer ratios and different weight

percentages of the crosslinking agent are summarized in **Table 3-1**. A pre-emulsion mixture was prepared in a 20 ml vial with the addition of 4.945 g MAA and 5.75 g EA (1:1 molar ratio) with 0.856 g DAP (8 wt% of the monomer mixture), 1 g of 75 wt% AOT solution and 1.4 g of Milli-Q water. The contents were thoroughly mixed with a sonication probe to generate a well-mixed pre-emulsion before adding to the reaction vessel. The reaction vessel (a 250 mL three-neck flask) contained 120 g Milli-Q water and 1g of 75 wt% AOT solution. The initiator solution was prepared by dissolving 0.25 g of sodium persulfate in 2 g of water.

The reaction vessel was seated on a magnetic hot plate and connected with a condenser. The reactor was heated up to 85 °C under continuous stirring while being purged with nitrogen for 30 minutes, whereupon the initiator solution was added using a syringe. When the contents were well dispersed, the agitation rate was reduced from 600 rpm to 300 rpm and 5 wt% of the pre-emulsion mixture was added dropwise into the reactor. One of the key factors influencing the successful synthesis of nanogel through emulsion polymerization was the agitation speed. The stirring speed could vary depending on the reactor sizes and stirring methods (mechanical stirring or magnetic stirring), however a one inch vortex must be formed in the center. After the reaction had proceeded for 30 minutes to form a seed solution, the remaining pre-emulsion mixture was added dropwise using a pressure equalizing-funnel. The remaining monomer mixture was re-mixed immediately prior to addition to the reactor to ensure that the monomer mixtures were in the emulsion state. The reaction was left to proceed for another 30 minutes. The final product was then cooled down to room temperature and filtered through a 200-mesh nylon cloth to remove the aggregates. The nanogel solution was charged into a dialysis bag with a molecular weight cut-off of 12 to 14 kDa and dialyzed against DI water until no excess surfactant could be observed (no visible bubble after

changing of dialysis water change) or the conductivity of the dialyzed water was equal to DI water.

The schematic illustration of the synthesis of MAA-EA nanogel is shown in **Scheme 3-1**.



Scheme 3-1 Schematic illustration of the emulsion polymerization synthesis procedure of MAA-EA nanogel

Table 3-1 Reagents for nanogel synthesis. Mass of components required for the synthesis a series of nanogels with different combinations of monomer ratios and quantity of crosslinking agents

Nanogel Model	**20/80 MAA-EA-8%DAP**	**30/70 MAA-EA-8%DAP**	**40/60 MAA-EA-8% DAP**	**50/50 MAA-EA-8%DAP**	**50/50 MAA-EA-4%DAP**	**50/50 MAA-EA-2%DAP**	**50/50 MAA-EA-1%DAP**	**50/50 MAA-EA-0.5%DAP**
Reactor								
Water (g)	120	120	120	120	120	120	120	120
5 wt% Monomer mixture (g)	0.7	0.7	0.7	0.7	0.68	0.67	0.66	0.66
AOT (g)	1	1	1	1	1	1	1	1
Initiator								
Water (g)	2	2	2	2	2	2	2	2
Sodium persulfate (g)	0.25	0.25	0.25	0.25	0.25	0.25	0.25	0.25
Monomer mixture								
MAA (g)	1.892	2.89	3.89	4.95	4.95	4.95	4.95	4.95
EA (g)	8.8	7.84	6.78	5.75	5.75	5.75	5.75	5.75
DAP (g)	0.856	0.856	0.856	0.856	0.428	0.214	0.107	0.054
AOT (g)	1	1	1	1	1	1	1	1
Water (g)	1.4	1.4	1.4	1.4	1.4	1.4	1.4	1.4
Sub-total (g)	13.947	13.986	13.926	13.956	13.528	13.314	13.207	13.154
MAA:EA molar ratio	20:80	30:70	40:60	50:50	50:50	50:50	50:50	50:50
DAP wt%	8	8	8	8	4	2	1	0.5

3.3 Characterization method

3.3.1 Fourier transform infrared spectroscopy (FTIR)

The FTIR spectrum of different monomer ratios and various amounts of DAP crosslinked nanogel were measured by a Bruker Tensor 27 spectrometer (Bruker, Billerica, MA, USA). The test specimens were prepared by compressing freeze-dried samples with the dried KBr powder into pellets. FTIR measurement was performed under room temperature and the spectrum was recorded over the wavenumber range of 400 to 4000 cm^{-1} with 32 scans at a resolution of 4 cm^{-1}.

3.3.2 Potentiometric and conductometric titration

A Metrohm 809 Titrando was used for the potentiometric and conductometric titration of the nanogel dispersions. Both forward and reverse titration was performed to investigate the nanogel composition and its conformation transition corresponding to the surrounding environmental conditions. A 25ml of 0.5 wt% nanogel emulsion was prepared and the pH was adjusted to 3 or 11 using 0.1M HCl or NaOH for the forward and reverse titration respectively prior to the start of the titration. The pH sensor and conductometer were placed in the nanogel solution to monitor the titration process. The 0.5 M NaOH or 0.5 M HCl was used as titrant for the nanogel solution at an addition rate of 0.1 ml/min for the forward titration and backward titration respectively. The entire titration process was conducted under mild stirring and the data was automatically recorded.

3.3.3 Multi-angle dynamic light scattering and static light scattering (MADLS and SLS)

The concentration of nanogel samples used in the measurement of DLS and SLS was 0.1 wt% and 0.002 wt%, respectively. The pH of each sample was adjusted by 0.1M NaOH and 0.1M HCl to the desired value (3 to 11) at least 24 hours prior to the measurements. All the samples were filtered through a Millipore membrane with a pore size of 0.8 μm to remove the dust, and the DLS and SLS measurements were conducted via a Brookhaven laser light scattering instrument together with a BI-200 SM goniometer (Brookhaven, NY, USA). The adjustable vertical polarized He-Ne

laser (5-30 mV) is the light scattering source with the wavelength of 636 nm. The pinhole size was 100-300 mm and 1-3 mm for DLS and SLS test respectively. The DLS test was performed at seven angles between 60° and 150° with an interval of 15° to obtain the hydrodynamic radius (R_h). The SLS test was measured at 10 angles from 30° to 155° with an interval of 15° to obtain the radius of gyration (R_g).

3.3.4 Zeta potential and average particle size measurement

Zeta-Sizer (Nanosizer ZS, Malvern Co., UK) was used to obtain the zeta potential of different nanogel dispersions by measuring the charge density on the surface of the nanogels. Different samples were prepared at 0.1 wt% and the pH of all the samples were adjusted to the desired value using 0.1 M NaOH or 0.1M HCl. All the measurements were performed at room temperature.

The average particle size of all the model nanogel was also measured by the Nanosizer, where the measurement was only performed when the angle of incident laser equals 90°, and the results were compared with the data obtained from MADLS.

3.3.5 Transmission electron microscopy (TEM)

TEM images were taken with a Philips CM10 electron microscope under an accelerating voltage of 60 kV. Model nanogels consisting of 20/80-MAA/EA-4 wt% DAP and 50/50-MAA/EA-4 wt% DAP were used to investigate the morphology at different pH (4, 7, 9) after drying on the TEM grid. The nanogel sample was stained with uranyl acetate and lead citrate (since the pristine nanogel was not visible in the TEM) and one drop of the nanogel sample was placed on the copper grid and left to dry.

3.3.6 Swelling factor

The swelling factor (SF) is a comparative assessed variable that defined as the increment of the mass or volume of the nanogel at different conditions [250]. In this work, the volume based swelling factor (SF_v) was calculated based on the following Eq (3.1), where V_{app} is the apparent volume of the nanogel at certain environmental pH; V_{min} is the minimum volume of the nanogel within the testing pH range. This equation accounts for the relationship between the swelling behaviour of nanogels associated with environmental pH and nanogel composition.

$$SF_v = \frac{V_{app} - V_{min}}{V_{min}} \quad (3.1)$$

3.4 Results and discussion

3.4.1 Fourier transform infrared spectroscopy (FTIR)

The FTIR spectra of nanogels fabricated with 50:50 of MAA and the EA nanogel crosslinked by 0.5, 1, 2, 4, or 8 wt% DAP is presented in **Figure 3-2 (a)**, and the FTIR spectra of nanogel with various MAA: EA ratios and 8 wt% DAP are shown in **Figure 3-2 (b)**. In both figures, the peak at 1700 to 1740 cm^{-1} was attributed to the carbonyl stretching of the MAA-EA nanogels. The peak of 1735 cm^{-1} originated from the vibration of C=O, particularly the peak of 1710 cm^{-1} represents the C=O of the carboxylic acid groups in the protonated state [251]. Since all the nanogel stock solutions possessed a pH value of between 3.5 and 4 (which was lower than the pKa of methacrylic acid (4.8)), the carboxylic acids were in the protonated state. The shoulder peak at 1650 cm^{-1}, represents the distortion vibration of C-OH [252]. The broad peak in the range of 3700-2600 cm^{-1} is assigned to the axis stretching of O-H originated from the COOH groups. The asymmetrical and symmetrical stretching of the CH_3 is associated with the two peaks at 2963 cm^{-1} and 2876 cm^{-1} [253]. The asymmetric and symmetric CH_2 stretching are indicated at 2940 and 2849 cm^{-1}, and the

peaks at 1254 and 1166 cm^{-1} are assigned to the C-O vibration [254]. Thus, the results confirmed that carboxylic acid and ester containing MAA-EA nanogels were successfully synthesized.

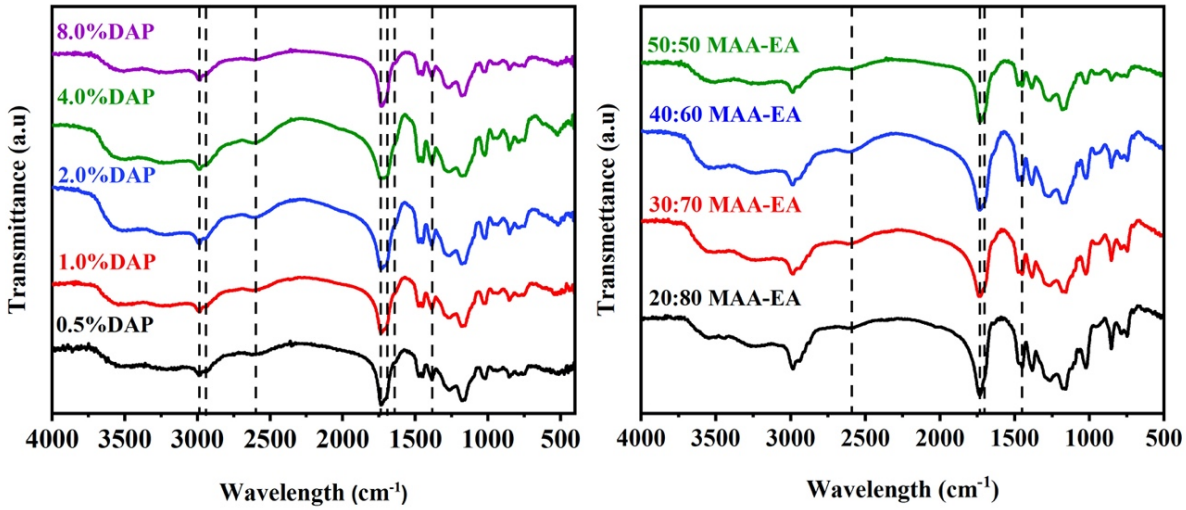


Figure 3-2 FTIR spectrum of different weight percentage of crosslinker (DAP) incorporated with 50:50 MAA-EA nanogels (a), and the FTIR spectrum of different combination of MAA:EA crosslinked with 8% DAP

3.4.2 Potentiometric and conductometric titration

Potentiometric and conductometric titrations were used to investigate the actual amounts of MAA present in each nanogel system. Changes in pH and conductivity during the titration process also indicated the availability of carboxyl groups and the transition of nanogel conformation under different conditions. The forward and reverse potentiometric and conductometric titration curve of 50:50 MAA-EA with 0.5 wt% DAP is shown in **Figure 3-3** (**a**) and (**b**), respectively. Before forward titration, the pH of the nanogel solution was adjusted to pH 3 using 0.1 M HCl, yielding a high conductivity value at the start of the titration process. In **Figure 3-3** (**a**) at Region 1 (R_1), with the addition of NaOH, the conductivity decreased until all the excess H^+ (added to adjust the pH) was neutralized by the NaOH. In the second stage (**R_2**), the COOH groups from the nanogel

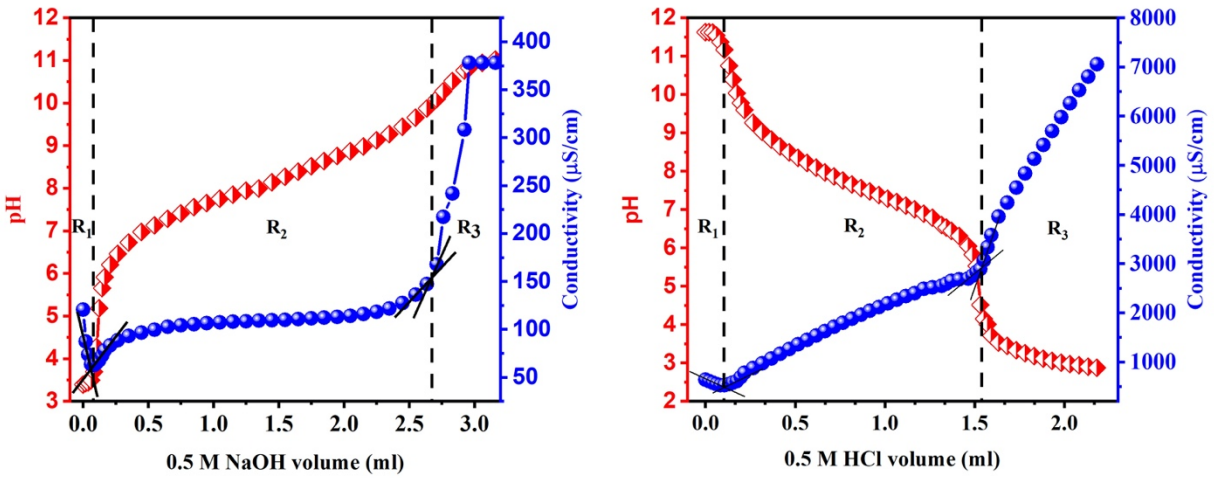


Figure 3-3 The potentiometric-conductometric curves of 0.5 wt% 50:50 MAA-EA crosslinked with 8 wt% DAP with 0.5M NaOH and 0.5M HCl as the titrant under forward (a) and reverse (b) titration

network were ionized and reacted with the NaOH added to the system. The slight increase in conductivity was due to the increase in Na^+ concentration during the titration. During this stage, the pH of the system was relatively stable, as all the NaOH added to the system was neutralized by the COOH groups from the nanogel. The actual amount of MAA incorporated into each nanogel was calculated based on the amounts of NaOH consumed. The rapid increase in conductivity after this stage is the result of excess NaOH added to the system after all COOH groups were neutralized. To obtain more precise MAA wt% involved in each nanogel, both forward and reverse titration were performed. The conductivity and pH of different amount of DAP wt% crosslinked 50:50 MAA-EA nanogels with the addition of titrant (0.5M NaOH) during the forward titration (**a**), (**b**), and the conductivity and pH of different amounts of DAP % crosslinked 50:50 MAA-EA nanogels with the addition of titrant (0.5M HCl) during the reverse titration (**c**), (**d**) are shown in **Figure 3-4**. The quantity of COOH groups calculated from forward titration and reverse titration, the weight percentage of MAA presents in the nanogel network and the proposed structure of MAA-EA (50:50) nanogel with different DAP wt% are summarized in

Table 3-2. The difference of the MAA wt% calculated from forward titration was only 3.4 % lower than those calculated from the reverse titration, which confirmed the accuracy of the titration measurements. The smooth titration curve also demonstrated a homogenous distribution of COOH groups on nanogel networks, since no dramatic changes of pH or conductivity change was observed from the titration curve. The titration curves (**Figure 3-4**) of all model nanogels displayed strong similarities, reflecting that this method used in the study offers a simple and repeatable protocol to synthesize MAA-EA nanogels.

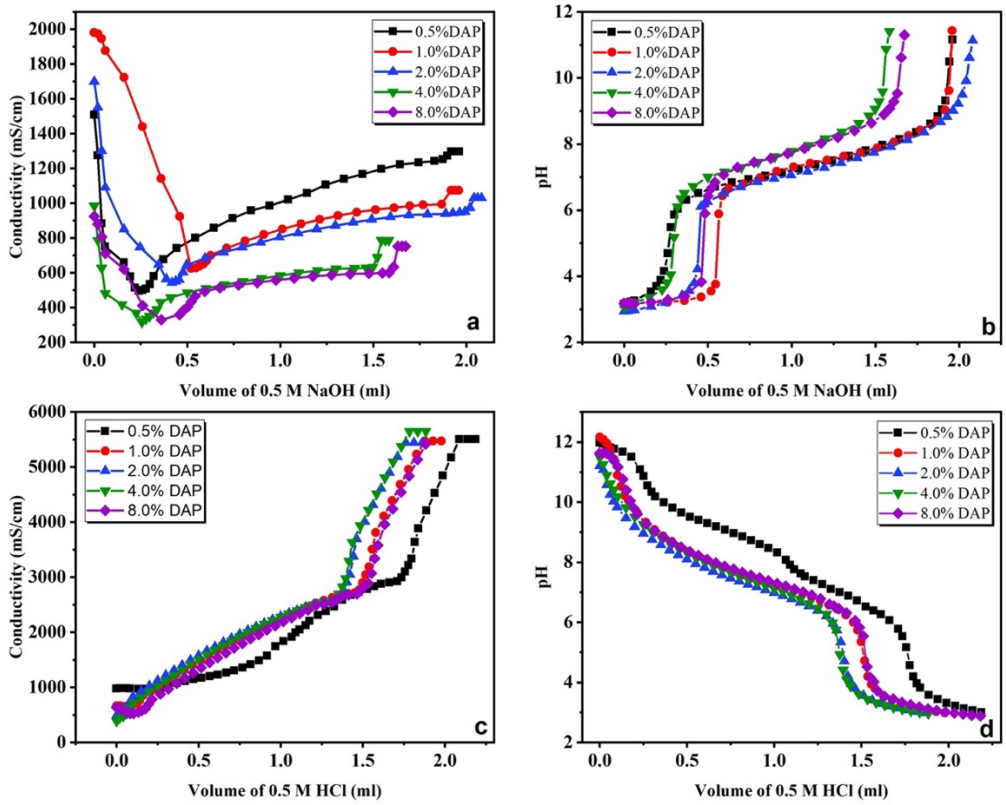


Figure 3-4 The conductivity and pH of different amounts of DAP wt% crosslinked nanogels versus volume of titrant (0.5M NaOH) under forward titration (a), (b), and the conductivity and pH of different amounts of DAP % crosslinked nanogels versus volume of titrant (0.5M HCl) under reverse titration (c), (d)

Table 3-2 Summary of quantities of COOH groups, MAA wt% and pKa value at half ionization degree(0.5 α) of 50:50 MAA-EA nanogel crosslinked with 0.5 to 8 wt% DAP calculated from both forward and reverse titrations

MAA:EA (Molar ratio in Monomer mixtures)	DAP wt%	Quantify of COOH (mmol/g) Forward	Quantify of COOH (mmol/g) Reverse	MAA wt% in nanogel (forward titration)	pKa	Structure
50:50	0.5	6.456	6.024	55.2	6.54	Polymer network
50:50	1	4.640	4.936	40	6.13	Polymer network & Nanogel sphere
50:50	2	6.496	5.112	56	6.51	Nanogel sphere
50:50	4	5.2	5.096	44.72	6.42	Nanogel sphere
50:50	8	5.0	5.176	43.04	6.24	Nanogel sphere

The acid dissociation constant (pKa) is an important physicochemical parameter used to elucidate the transition behavior of acid based polymeric nanogel at various pHs. The pKa value at half ionization degree (α=0.5) is commonly used to evaluate the acidic strength of the polyacids or polybases. The pKa value was obtained from the Henderson-Hasselbalch equation Eq (3.2), yielding a pKa value for acidic materials in aqueous systems [255]. In contrast to weak acid or weak base, polymer-based electrolytes contain large amounts of ionizable groups. Different arrangement of polyelectrolyte groups on the same polymer chain can cause a different behavior in the ionization process. Therefore, the smooth and non-stepwise titration curve is inappropriate to assign a pKa value to a specific ionized state [256]. In this study, the simultaneous conductometric curve and pH curve was used to obtain the pKa value and ionization degree. The calculated pKa values of 50:50 MAA-EA nanogel (0.5-8 wt% DAP) were between 6.13 to 6.54 (

Table 3-2), which is consistent with other reported studies, as the pKa value of microgels (MAA/EA/X) were between 6 to 7 [257], which is greater than the pKa value of linear PMAA (pKa= 6) [258] and MAA (pKa= 4.66) [259]. The elevated pKa value of nanogel compared to the pKa value of MAA and PMAA suggested a reduction in the accessible COOH groups, as the nanogel system also contained the hydrophobic segments associated with the EA and DAP moieties.

$$pKa = pH + log\frac{1-\alpha}{\alpha} \quad (3.2)$$

where pKa is the acid dissociation constant, pH is the pH value of the system, α represents ionization degree. **Figure 3-5** shows the conductivity and pH of various MAA-EA model nanogels crosslinked with 8 wt% DAP with the addition of the titrant (0.5 M NaOH) in the forward titration (**a**), (**b**), and the conductivity and pH of various MAA-EA model nanogels crosslinked with 8 wt% DAP with the addition of titrant (0.5 M HCl) in the reverse titration (**c**), (**d**). From **Figure 3-5** and **Table 3-3**, we concluded that as the MAA: EA ratio increased during the emulsion polymerization, more MAA was incorporated into the nanogel networks. However, the percentage of MAA in the composition of nanogel was lower than the percentage of MAA in the monomer mixtures prior to nanogel synthesis. This can be attributed to the high solubility of MAA in water, hence not all MAA could participate in nanogel formation. More carboxylic groups have been titrated from nanogel as the ratio of MAA:EA increased, confirming the effectiveness and successful fabrication of nanogel of different monomer ratios.

Changes in nanogel conformation in the surrounding conditions, such as solvent quality (good or bad), ionic strength, pH value may provide important information on the polyelectrolyte nanogel system. For the MAA-EA nanogel system, two main factors contributed to the conformation transition behavior at different pHs; Hydrophobic domains formed by the

crosslinking process and the ionization status of the COOH groups on the nanogel. When the solution pH was lower than the pKa value of the nanogel, the COOH groups on the nanogel were protonated. The hydrophobic crosslinking point further contributed to the compact structure of the nanogel at low pH. As pH approached the pKa of the nanogel system, the COOH groups began to ionize into COO^- groups. The tightly entangled chain structure of the nanogel led to a strong repulsive force among neighbouring ionized carboxylic groups that induced the swelling of the nanogels. On the other hand, the reduced free energy caused by the swelling and the permanent chemical crosslinking junctions contributed to the limited swelling property. Contrary to the physical crosslinked nanogel, the chemical crosslinked MAA-EA nanogel could provide a stable encapsulation function across a wide range of pH. As a result, the pH-dependent swelling behaviour and its good dispersity in water enabled the nanogel to be used in various applications, such as drug delivery, control release, tissue engineering, and bio-imaging.

3.4.3 Multi-angle dynamic light scattering and static light scattering (MADLS and SLS)

There are many fundamental properties commonly used to characterize the colloidal system, including particle size, morphology, surface charge, viscosity and stability under various conditions. Among these, particle size is one of the most basic physicochemical properties, which is the major factor in determining the target application [260]. The hydrodynamic radius (R_h) of particle is the radius of a hypothetical hard sphere having the same diffusion rate as the particles measured with the DLS [261]. To obtain more accurate and comprehensive information on the particle size, multi-angle dynamic light scattering (MADLS) was used to investigate both hydrodynamic radius (R_h) and radius of gyration (R_g) of the nanogels at different pHs. Seven angles (60°, 75°, 90°, 105°, 120° and 135°) were selected to perform the MADLS measurements. The R_h obtained from MADLS was based on the diffusion coefficient of nanogel particles in

aqueous solution. The relationship between the translational diffusion coefficient (D_t) and R_h can be described by the Stokes-Einstein equation:

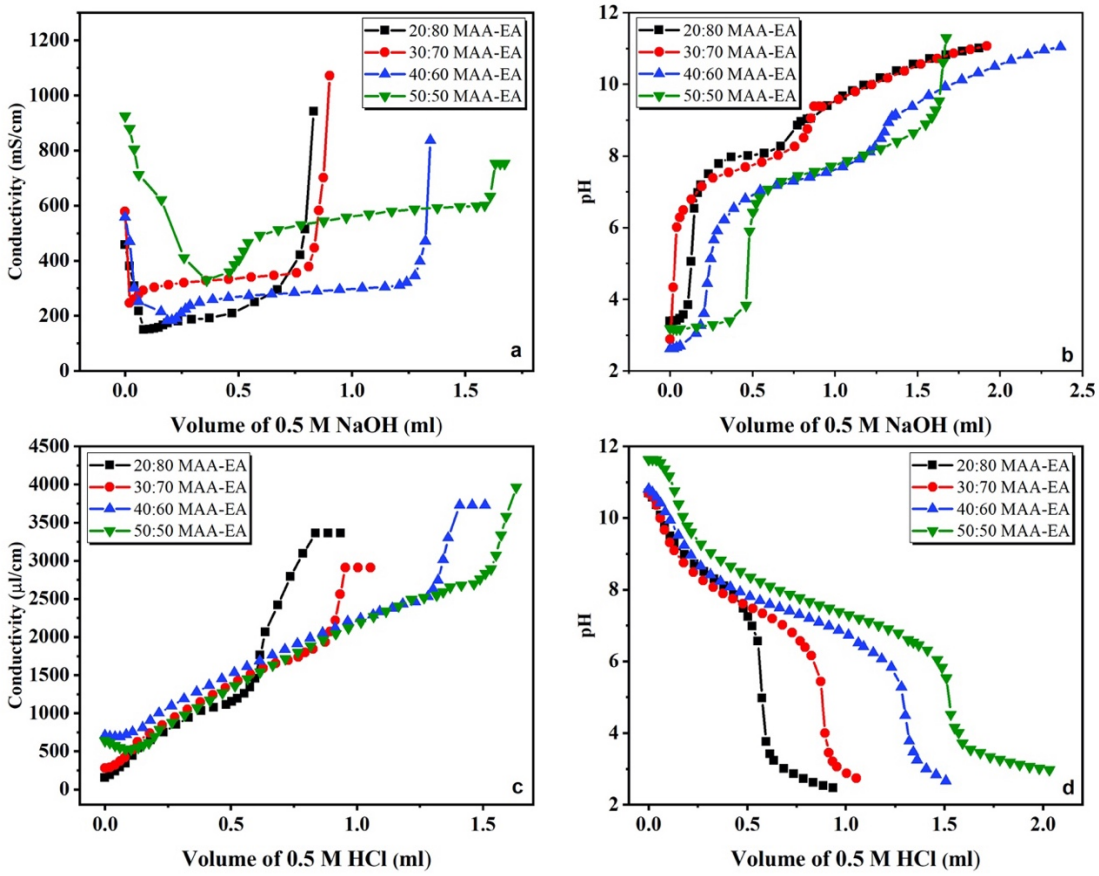


Figure 3-5 The conductivity and pH of different monomer ratios MAA-EA nanogels crosslinked with 8 wt% DAP as the addition of titrant (0.5 M NaOH) under forward titration (a), (b), and the conductivity and pH of different monomer ratios MAA-EA nanogels crosslinked with 8 wt% DAP nanogels as the addition of titrant (0.5M HCl) under reverse titration (c), (d)

Table 3-3 Summary table of the amount of COOH groups and MAA wt%, pKa value at half ionization degree (α= 0.5) of 20:80, 30:70, 40:60 and 50:50 MAA-EA nanogel crosslinked with 8 wt% DAP calculated from both forward and reverse titration

MAA:EA (Molar mass in monomer mixtures)	DAP wt%	Quantify of COOH (mmol/g) Forward	Quantify of COOH (mmol/g) Reverse	MAA wt% in nanogel (forward titration)	pKa	Structure
20:80	8	2.848	2.056	24.5	6.27	Nanogel sphere
30:70	8	3.16	3.176	27.19	6.42	Nanogel sphere

40:60	8	4.376	4.792	37.66	6.14	Nanogel sphere
50:50	8	5.177	5.176	44.6	6.80	Nanogel sphere

$$\boldsymbol{R_h = \frac{K_b T}{6\pi\eta D_t}} \quad (3.3)$$

where D_t represents the diffusion coefficient, R_h is the hydrodynamic radius of the particle, K_b is the Boltzmann constant (1.38×10^{-23} J/K), T (K) is the temperature and η is the bulk viscosity. For each scattering angle, there is a scattering vector (q) calculated from Eq (3.4) [262]. θ is the scattering angle, n is the refractive index, λ_0 is the incident laser wavelength. For a known scattering angle and solvent, q is a constant as determined from Eq (3.4).

$$q = \frac{\boldsymbol{4\pi n sin\left(\frac{\theta}{2}\right)}}{\boldsymbol{\lambda_0}} \quad (3.4)$$

An autocorrelation function (ACF) can be described by a function of decay time C (τ), that is related to the layout of the equipment. The decay rate (Γ) or linewidth can be obtained from the deconvolution of C (τ), where the ACF was analyzed by the inverse Laplace transformation technique based the GENDIST routine. This decay rate is correlated with scattering vector and transitional diffusion rate, and the D_t can be obtained as the slope of Eq (3.5). Finally, R_h can be calculated from Eq (3.3).

$$\Gamma = D_\tau q^2 \quad (3.5)$$

The radius of gyration (R_g) is defined as the mass weighted radius of the particle, which can be obtained from the partial Zimm equation (Eq (3.6)) [263], where, $I_{ex}(q)$ is the excess intensity of scattered light, q is the scattering wave vector, P is an experimental parameter. The R_g can be determined from the slope of $\frac{1}{I_{ex}(q)}$ versus q^2.

$$\frac{1}{I_{ex}(q)} = P\left(1 + \frac{R_g^2 q^2}{3}\right) \quad (3.6)$$

Figure 3-6 (a, b) shows the R_h and R_g values of 50:50 MAA-EA nanogel crosslinked with 0.5 to 8 wt% DAP at pH 3 to 11. At pH 3, all nanogels possessed a similar R_h value (40 nm), since they were in the most compact state due to the protonated carboxyl groups and chemical

crosslinking. As the pH was increased, the COOH groups gradually deprotonated to COO^-, and the electrostatic repulsion among the charged groups increased the osmotic pressure within the nanogels that induced the swelling of the nanogels. The variation in R_h was determined by the combined effect of the electrostatic repulsive forces (of the ionization process) and the hydrophobic interactions (of the chemical crosslinking junction). When the pH approached the pKa value of the nanogels, the complete deprotonation of the COOH groups led to a maximum R_h value. A further increase in pH resulted in a reduced particle size due to the charge shielding by the excess electrolyte. Reducing the charge density on the nanogel surface would cause the nanogel to de-swell. The R_h of (50:50) MAA-EA nanogel crosslinked with 0.5 and 8 wt% DAP was 450 and 110 nm respectively. Clearly, permanent hydrophobic interactions between polymer chains had a major effect on their swelling behavior, especially at pH above the pKa of the nanogel system. The R_h of the nanogel with different monomer ratios of MAA and EA displayed similar trends as the nanogel prepared with various wt% of DAP (**Figure 3-6 (c)**). Nanogels containing more MAA were more sensitive to changes in the pH where a higher maximum degree of swelling could be achieved. In the case of R_g at different pHs, it is primarily determined by the force balance between the elastic interaction of the crosslinking junctions and the electrostatic repulsion between the ionized COO^- groups. The R_g value of (50:50) MAA-EA nanogels for 0.5 to 8 wt% DAP gradually increased from pH 3 to 11, which was different from the R_h results. Although the distribution of the charge density has changed, the mass centre of the nanogel particles has not changed. The weighted average distance from this centre to each point on the nanogel was therefore slightly increased due to the swelling at higher pH. It should be noted that when a hydrophobic BA monomer was used as a physical cross-link in an AA-BA-EGDMA nano-gel system, there was a clear breakpoint for the R_g value at pH greater than the pKa value. Since the hydrophobic

interaction of BA has only limited effective distance, the nanogel would irreversibly break once the repulsive forces exceeds the hydrophobic interactions [264]. However, the integrity of nanomaterial is very important when considering their toxicity in biological related applications and secondary contamination in environmental remediation applications. The nanogels possessed different sizes depending on the synthesis conditions and their pH responsive property allowed the nanogel to be used in drug delivery without the burst release. For various MAA:EA ratios, nanogel crosslinked with 8 wt% DAP displayed no obvious change in the R_g value from pH 5 to 8 due to the uniform swelling or shrinkage of the nanogels. However, at higher pH, the nanogel was more extended due to the electrostatic repulsion of the polymer chains with the same charge, resulting in an uneven swelling or shrinkage of the nanogel system. The extremely high R_g obtained from 20/80 MAA-EA nanogel with 8 wt% DAP at pH 3 could be attributed to the dissociation of the nanogel network, where a white precipitated was observed for some model nanogel system at pH of 3.

3.4.4 Zeta average diameter and zeta potential

The stability of the colloidal system against agglomeration is a critical issue for both fundamental research and industrial applications. Colloidal stability is determined by several factors, such particle size, surface charge, temperature and pH, and solvent characteristics. An effective way to evaluate the stability of a nanogel system is the zeta potential. The average diameter and the zeta potential of nanogel was obtained using the Malvern Zeta-Sizer. Zeta average size and zeta potential of 50:50 MAA-EA nanogel crosslinked with 0.5 to 8 wt% DAP under pH 3-11 are presented in **Figure 3-7 (a, b)**; and the average diameter and zeta potential of MAA-EA

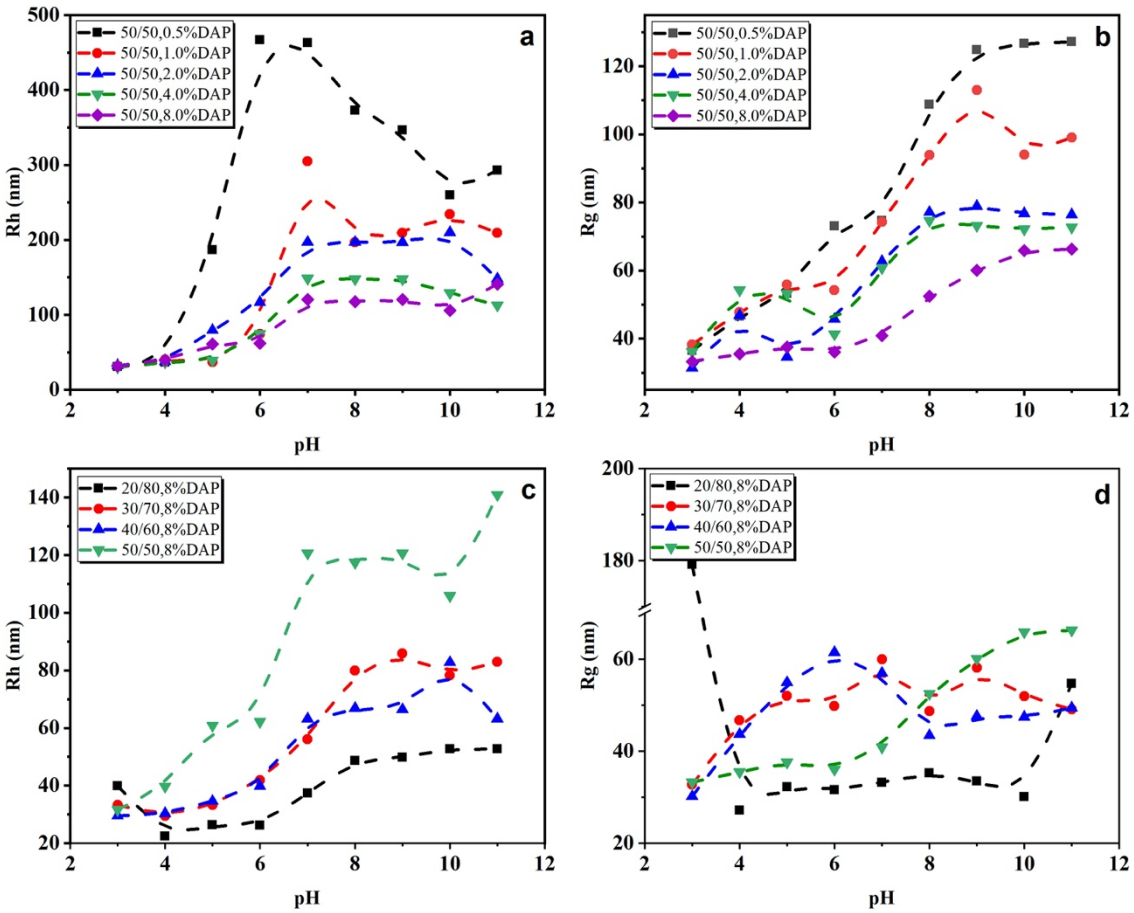


Figure 3-6 R_h and R_g value of 50:50 MAA-EA nanogels crosslinked with 0.5 to 8 wt% DAP under pH 3-11 (a,b); R_h and R_g value of MAA-EA nanogels consisted with different monomer ratios under pH 3-11(c,d). (All of the measurements were conducted with MADLS and SLS)

nanogels with different monomer ratios between pH 3 to 11 are shown in **Figure 3-7 (c, d)**. The error bar displayed in the figure was obtained by measuring the same sample for three times instead of sample-to-sample variations. The variation in the average diameter of nanogel at various pHs is consistent with the R_h value obtained from MADLS measurements. The diameter of the nanogel exhibited an "S" shape in the pH ranges of 3 to 11, indicating a three-stage transition pattern. In the first stage (pH 3-5), the nanogels remained in their maximum shrinkage state with a minimal particle size, since all the -COOH groups were protonated below their pKa value. In the second stage (pH 5-8), the particle size increased with increasing pH. Because the COOH groups have

been progressively deprotonated to COO^-, so the charge density of the neighbouring chains had increased leading to nanogel swelling. Particle size for nanogels at specific pH was determined by two factors: the amount of cross-linking agent and MAA involved in the nanogel system. As shown in **Figure 3-7 (a)**, the nanogel size was more sensitive to pH at lower DAP wt% in the nanogel system. For 0.5 wt% DAP 50:50 MAA-EA nanogel system, the amount of DAP was insufficient for the monomer mixture to form a robust nanogel, which is confirmed by the TEM images shown in **Figure 3-8 (b)**, where nonuniform polymeric clusters instead of spherical nanogels were evident after staining. Therefore, the nanogel system comprised of both crosslinked nanogel and conjugated polymer chains at a lower pH. When pH was increased, access to COOH groups in the free polymer chains was greater that in cross-linked nanogels. Thus, the particle size of 0.5 wt% DAP MAA-EA nanogel increased much faster with pH than other nanogels with higher amounts of crosslinker. In the third stage (pH 8-11), the particle size decreased due to the excess NaOH, which shielded effect, the repulsion of the COO^- groups, which restricted the expansion of the nanogel. In the case of different monomer ratios in the MAA-EA nanogel (**Figure 3-7, c**), the particle size displayed a "S" pattern that could be divided into three stages similarity compared to the MAA-EA nanogel with different DAP wt% as both presented an upon pH variation. However, nanogels with different monomer ratios and 8 wt% DAP did not maintain their minimal particle size when the pH was between 3 and 5 except 50:50 MAA-EA nanogel. Nanogel with lower MAA content (MAA: EA < 50: 50) would be less crosslinked with DAP and EA, most of the MAA segments would be aggregated within the center of the nanogel at low pH (3-4). As a result, a less compact structures were observed for 20:80 MAA-EA 8 wt% DAP nanogel compared to 50:50 MAA-EA 8 wt% DAP nanogel at low pH. In the second stage (pH 5-8, **Figure 3-7** (**c**)), the varying level of the particle size of nanogel with different monomer ratios at different pH displayed a

difference in the curve of particle size versus pH. Nanogel has more MAA presented a faster change in particle size when the pH increased from 5 to 8. The sensitivity of the nanogel responded to the environmental pH decreased as the MAA:EA ratio declined, which was labelled as 1 to 4 in **Figure 3-7** (**c**) representing a decreasing sensitivity. Furthermore, the maximal particle size was achieved earlier (~pH 7) for the MAA-EA 50:50 nanogel, as more COOH groups were available for deprotonation. The decrease in the MAA:EA ratio of the nanogel results in a delay in reaching the maximum particle size, as fewer carboxyl groups have led to a reduction in sensitivity to environmental pH. In the third stage (pH 8-11), 50:50 MAA-EA nanogel particle size reduces much more rapidly due to the more severe shielding effect.

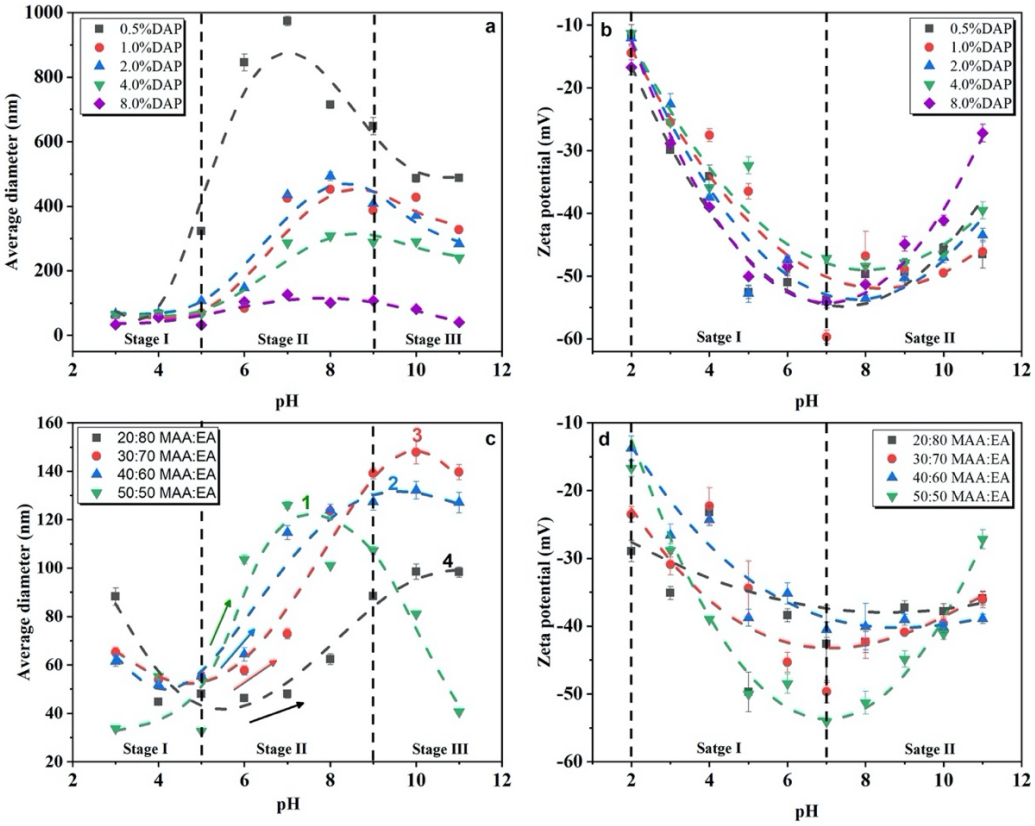


Figure 3-7 Zeta avergae diameter (nm) and zeta potential (mV) of 50:50 MAA-EA nanogels crosslinked with 0.5 to 8 wt% DAP under pH 3-11 (a, b); Zeta avergae diameter (nm) and zeta

potential (mV) of MAA-EA nanogels consisted with different monomer ratios under pH 3-11(c, d)

The zeta potential of nanogels exhibited a "U" shape trend with pH for all the nanogel systems (**Figure 3-7**: **b**, **d**), and it could be divided into two regions. When the pH was lower than the pKa (pH ≈ 6.5), the zeta potential of nanogel increased with pH due to the ionization of carboxyl groups up to their pKa value. When the pH was further increased from 7 to 11, the ionic strength of NaOH shielded the negative charges on the nanogels. Existing Na^+ ions screened the negatively charged nanogel, reducing the charge density on the nanogel and the swelling ratio. In All the nanogels were very stable between pH 3-11, since they possessed zeta potentials below -30 mV. However, at pH 2, some of the nanogel system aggregated and settled at the bottom of the vials (. The excellent stability of the MAA-EA nanogel over a wide range of pH allows it to be a promising scaffold for preparing stable metal clusters or applied to control drug release.

3.4.5 Morphology investigation (TEM)

TEM was used to exam the morphology and particle size of the nanogels at varying pHs. **Figure 3-8** shows the TEM images of 50:50 MAA-EA nanogel crosslinked with 0.5 wt% DAP **(a, b)**, 1 wt% DAP **(c, d)**, 2 wt% DAP **(e, f)**, 4 wt% DAP **(g, h)**, and 8 wt% DAP **(i, j)**. The TEM images of 20:80 MAA-EA with 8 wt% DAP at pH 4 **(k, l)**, pH 7 **(m, n)**, pH 10 **(o, p)**, and the TEM images of 50:50 MAA-EA with 8 wt% DAP at pH 4 **(q, r)**, pH 7 **(s, t)** and pH 10 **(u, v)** are shown in **Appendix 3-1**. All nanogels were stained with uranyl acetate and lead citrate prior to the TEM imaging to produce high contrast images. According to **Figure 3-8** (**a)** and (**b)**, non-uniform polymer clusters were observed, which is due to the MAA-EA chains cross-linked with DAP. **Figure 3-8** (**c**) and (**d**) illustrates two main types of morphologies: Irregularly dark grey spheres and clusters with radial light gray patterns corresponding to cross-linked MAA-EA nanogels and MAA-EA conjugated polymer chains respectively. Since the crosslinked nanogel possessed a

higher density of COOH groups, which provided a higher contrast after the staining process [265]. Similarly, the 1 wt% DAP was insufficient for all 50:50 MAA-EA monomer mixture to form a robust spherical nanogel (**Figure 3-8 c**, **d**), where the system contained irregular shape nanogels and polymer clusters. When the weight percentage of DAP was between 2 to 8 wt% (**Figure 3-8 e, f, g, h, i, j**), well-defined spherical nanogel was observed. Monodispersed nanogel possessed a uniform particle size, indicating the high quality of the MAA-EA nanogel synthesized by the emulsion polymerization. The morphology and particle size of 20:80 and 50:50 MAA-EA nanogel with 8 wt% DAP in acidic, neutral and basic pH were examined by TEM (**Appendix 3-1**). The average diameter of 20:80 MAA-EA nanogel with 8 wt% DAP at pH 4, 7, 10 measured by TEM was 30.6, 32.8 and 33.5 nm, while the particle size measured by DLS was 44, 76 and 104 nm, respectively. The diameter of 50:50 MAA-EA nanogel with 8 wt% DAP at pH 4, 7, 10 obtained by TEM were 51.6, 45.7 and 46.6 nm, while the particle diameter measured by DLS were 78, 240 and 226 nm, respectively. The diameter of the nanogel determined by TEM was significantly smaller than that measured by DLS due to dehydration and the shrinkage of nanogel when dried for the TEM analysis [266]. Thus, the hydrodynamic radius obtained using the DLS would more accurately describe the size of nanogels in aqueous systems, including the size dependent of the pH. The degree of swelling in the nanogel was mainly determined by the degree of crosslinking and quantity of hydrophilic functional groups in the nanogel system. With the same amount of crosslinking agent, more MAA integrated into the nanogel would absorb more water at a specific pH. As indicated by DLS measurement, the diameter of 20:80 MAA-EA (8 wt% DAP) nanogel increased by 60 nm when the pH was elevated from 4 to 10, while the 50:50 MAA-EA nanogel increased by 148 nm when the pH was increased from 4 to 10. However, the change in the actual

size of nanogel with the surrounding pH was not reflected in the TEM images since the drying process already induced the shrinkage of the nanogel.

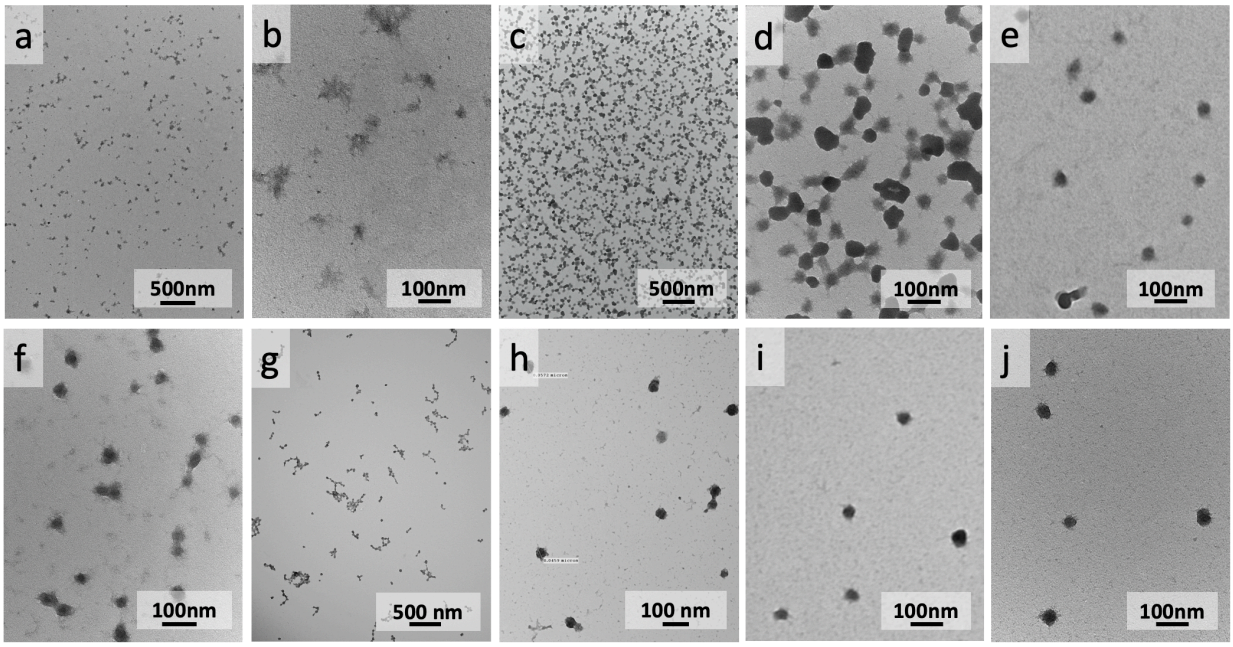


Figure 3-8 TEM images of 50:50 MAA-EA crosslinked with 0.5% DAP (a, b), 1% DAP (c, d), 2%DAP (e, f), 4% DAP (g, h), 8% DAP (i, j)

Table 3-4 Comparison of 20:80 and 50:50 MAA-EA nanogel (8 wt% DAP) particle size measured by MADLS, Zeta sizer and TEM

MAA:EA of nanogel (Preparation)	DAP wt%	pH	R_h by MADLS (nm)	R by zeta-sizer(nm)	R by TEM (nm)
20:80	8	4	22.43	22.35	30.6
	8	7	37.35	23.99	32.8
	8	10	52.72	49.26	30.6
50:50	8	4	39.72	33.62	51.6
	8	7	120.69	103.57	45.7
	8	10	105.91	101.07	46.6

3.4.6 Shape factor and pH dependent conformation transition

The shape factor (ρ), which is defined as the R_g/R_h ratio is an important parameter to evaluate the morphology of the nanogel. For this amphiphilic nanogel, there are two factors that impact the internal structure of the nanogel; (1) Synthesis parameters during the emulsion polymerization such as monomer ratios, quantity of crosslinkers and (2) the surrounding conditions, such as pH,

temperature or solvent type. The shape factor, ionization degree and internal structure of 50:50 MAA-EA nanogels crosslinked with 0.5 to 8 wt% DAP as a function of pH is shown in **Figure 3-9** (**a**). The shape factor varied between 0.17 and 1.52, which possessed a parabolic trend during the ionization process. When the environmental pH was 3, all the MAA-EA-X wt% DAP nanogels de-swelled due to the repulsive forces between the protonated -COOH groups of the nanogels and the H^+ ions in solution. At this stage, all the COOH groups partitioned to the inner core of the nanogel with ρ equaled to 1.2 suggesting a dense core and a low density shell structure. When the pH value was raised to 4 ($\rho\sim$ 0.77), a nanogel with a more homogeneous weight-distributed structure was obtained. In the second stage (pH 5-7), the shape factors of the nanogels were less than the theoretical value of a hard sphere (0.775) [267]. A lower shape factor value can be achieved with less DAP crosslinks within the nanogels, where the swelling of the nanogel was enhanced at low cross-linking densities [268]. Due to the slightly cross-linked nanogels composed of a dense inner core and a porous outer shell consisting of pendant polymer chains. When only 0.5 to 1 wt% of DAP was used in the nanogel, there was insufficient cross-linking agent for all monomers to form a stable spherical nanogel as confirmed by TEM (**Figure 3-8**). Fully crosslinked nanogels were obtained when 2-8 wt% of DAP was used, resulting in a reduction in the pendant polymer chains on the outer surface of the nanogel [269]. Consequently, the weight distribution of the nanogel shifted to the nucleus as the pH approached its pKa value. The ratio of the length of the polymer chain to the core radius determined the micro-conformation of the nanogels. This relationship is highly dependent on the type, quantity and distribution of the cross-linking agent in the nano-colloidal system [270]. Further increase the pH to 11, ρ of 50:50 MAA-EA-X wt% DAP nanogels increased as the ionization process until it reached the theoretical value of the hard sphere ($\rho\sim$0.77).

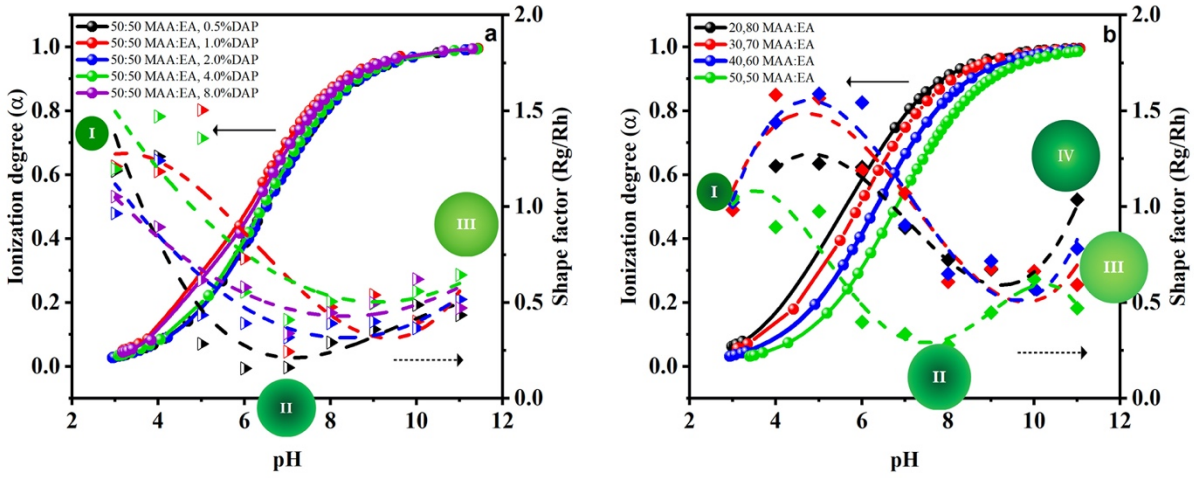


Figure 3-9 The shape factor, ionization degree and internal structure of 50:50 MAA-EA nanogels crosslinked with 0.5 to 8 wt% DAP upon pH variation (a); The shape factor and ionization degree of MAA-EA nanogels consisted with different monomer ratios as a function of pH

This value of the shape factor indicated that the MAA-EA 50:50 nanogel attained a hard sphere microstructure at its full ionization state (α=1).

For the nanogels with different monomer ratios (**Figure 3-9, b**), higher shape factor values (0.32-1.76) were observed. The value of shape factor as a function of pH displayed an 'S'-shape trend as ionization progressed. The different behavior of microstructure transition could be attributed to the composition difference. At pH 3, all nanogels were at their maximum compact state with a thin-walled structure (dense outer shell). When the pH was increased to 10, the shape factor decreased from the maximum value (ρ=1.0-1.5) to minimum value (ρ=0.32-0.62) for all the nanogels. This variation in the shape factor indicated that the morphology of the nanogels changed from a thin-walled structure (thicker shell) to a more homogeneous weight-distributed hard-sphere structure (at pH~8), and then to a dense core-loose shell structure at pH~10. Further increase in the solution pH beyond the full ionization state would result in a high concentration of Na^+. The screening effect of Na^+ ions on the surface of the nanogel inhibited the dissociation of the COOH groups, and caused the deswelling of the nanogels.

3.4.7 MAA-EA nanogel ionization process

Amphiphilic nanogels undergo a microstructural transition in response to surrounding conditions, and the microstructural variation is associated with the changes in the physiochemical properties of nanogels. These properties could be manipulated and controlled during the emulsion polymerization process, allowing for the multi-purpose nanogel to be applied in a variety of applications. The principle of microstructure transition in response to the external environment depends on the variation of the intermolecular or intramolecular force balance, including the forces between the neighbouring polymer networks or between solvents and the nanogels [271]. The degree of ionization is critical to the conformational structure of the nanogel with ionizable functional groups. Hydrogen bonding could be formed when the ionizable groups were at zero charge condition. The pKa value and conductivity versus and the ionization degree (α) of 50:50 MAA-EA nanogel (various DAP wt%) is shown in **Figure 3-10 (a, b)** and the pKa value and the conductivity versus the ionization degree (α) of MAA-EA nanogel with 8 wt% DAP (various monomer ratios) is shown in **Figure 3-10 (c, d)**. As the ionization progressed, the hydrogen bond was disrupted and the coulombic forces from the ionised COO^-, caused the nanogel to swell. However, at high pH environment, the swelling was limited to a certain level due to the shielding effect of the counter ion (Na^+) [272]. The ionized COO^- groups on MAA-EA nanogel increased the osmotic pressure of the nanogel due to the Donnan equilibrium partitioning of the counter ions that expanded the nanogels. As shown in **Figure 3-10 (a, b)**, the conductivity of the titration of the nanogel crosslinked with various DAP wt% was stable at the beginning of the titration when $\alpha <$ 0.5 . The degree of ionization began to increase after all HCl existed in the nanogel system were consumed, representing the ionizing process of the COOH groups. From **Figure 3-10 (a)**, there is

no evident difference of the pH as a function of ionization degree among different nanogels, since the quantity of MAA existed in each model nanogel is similar.

3.4.8 Swelling factor

The MAA-EA nanogel contained acidic segment that led to the swelling of the nanogel when these functional groups were deprotonated at high pH. The main mechanism for the swelling behaviour was caused by the increase in repulsive electrostatic forces and the increase in internal osmotic pressure. The pH dependent swelling factor (SF_v) of 50:50 MAA-EA nanogels crosslinked with 0.5 to 8 wt% DAP and the pH dependent SF_v of MAA-EA nanogels consisted with different monomer ratios is shown in **Figure 3-11 (a, b)**. The electrostatic repulsive forces and internal osmotic pressure became significant when the pH approached the pKa value of the nanogel.

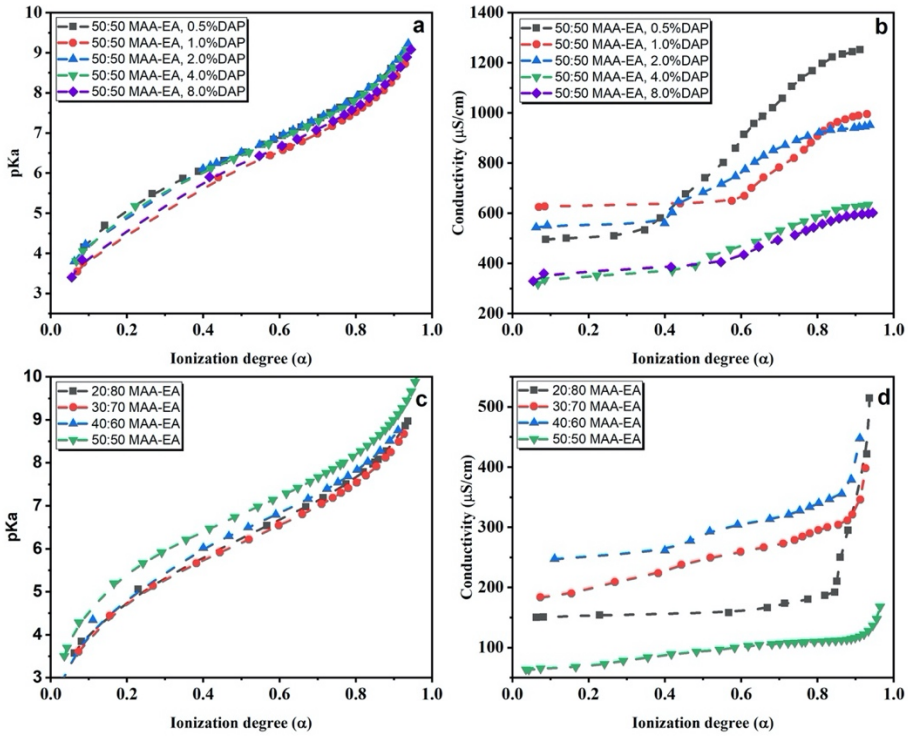


Figure 3-10 pKa (a) and conductivity (b) versus ionization degree of 50:50 MAA-EA nanogels crosslinked with 0.5 to 8 DAP%; pKa (c) and conductivity (d) versus ionization degree of MAA-EA nanogels consisted with different monomer ratios

However, further increase in the pH caused a reduction in the swelling behaviour due to the screening effect. With the increase of the MAA:EA ratio, the higher shielding effect was related to the pH, since more COO- groups could be shielded by these counterions. The degree of cross-linking is another critical factor that could affect the degree of swelling of the nanogel. Highly crosslinked nanogel has less space to swell as the ionization progressed, since chemical bonding limited the mobility of the nanogel network. **Figure 3-11 (b)** shows that the 0.5 wt% DAP nanogel possessed the highest swelling factor at the pH close to the pKa, which was caused by the incomplete formation of the nanogel. The nanogel system comprised of MAA-EA polymer chains cross-linked by DAP, where the more accessible MAA chains resulted in a more sensitive swelling behavior. The upper limit of nanogel size was determined by the amount of crosslinking agent incorporated into the nanogel system, where more compact structure was obtained when more DAP was added. The highest swelling factor decreased gradually as more DAP was involved in the polymerization, the swelling factor of 50:50 MAA-EA nanogel decreased from 3752.86 to 51.54 when the crosslinking agent increased from 0.5 wt% to 8 wt%.

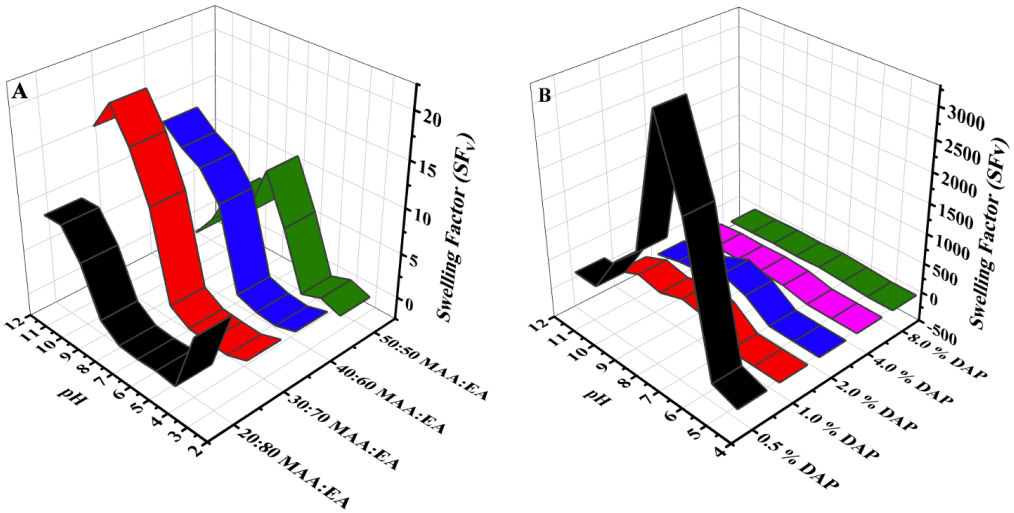


Figure 3-11 The pH dependent swelling ratio of 50:50 MAA-EA nanogels crosslinked with 0.5 to 8 wt% DAP (a); The pH dependent swelling ratio of MAA-EA nanogels consisted with different monomer ratios (b)

3.5 Conclusions

Nanogel as a conventional colloidal system that can be used as a nano-reactor or nano-carrier has attracted increasing interest. However, the complexity of the control polymerization techniques used to synthesize nanogel has limited the large-scale production of the nanogel, and the reproducibility of the production closely related to the physiochemical property of the nanogel. In this study, a facile seeded emulsion polymerization was successfully used to prepare MAA-EA nanogel in water without precise control of adding monomer mixtures and initiators during the polymerization, which was commonly required from other studies [53][43]. The model nanogels were composed of a hydrophilic MAA segment that could respond to the surrounding pH, and a hydrophobic portion (EA) that allows the encapsulation of active agents inside the nanogel. The MAA-EA crosslinked nanogel could maintain its particle integrity across a wide pH range (3 to 11), and the maximum particle size of 50: 50 MAA-EA nanogels were obtained at approximately pH 7 to 8 due to the complete ionization of the carboxyl groups. The conformation transition of the nanogel microstructure is related to the ionization state of the MAA. The nanogel represented a hard spherical structure distributed uniformly by weight at pH 3; swelling to a core-shell structure when the pH was around the pKa and a slightly de-swelling led to a thin-wall structure due to the screening effect at basic condition (pH 11). The maximum degree of swelling of the nanogel was determined by the monomer ratios of the monomer mixture and the degree of cross-linking, where more MAA and less DAP incorporated nanogel resulting the maximum swelling ratio. The physicochemical property and conformation transition of nanogel are the result of a combination of effects of swelling and chemical crosslinking which is strongly correlated to the degree of ionization of the carboxyl groups located within the nanogel network. The nanogel synthesized in this study possessed high colloidal stability and an adjustable pH-responsive property that

represents a promising platform for designing the systems for applications, such as encapsulation of active agents, control of drug release, nanoreactors, and environmental remediation [273]

Chapter 4: β-cyclodextrin functionalized magnetic nanoparticles for the removal of pharmaceutical residues in drinking water *

Trace amounts of pharmaceuticals and personal care products (PPCPs) are found in our water systems, and they are known to have adverse effects on wildlife and human at the ng/L to μg/L range, below the detection limit of most water analytical instruments. In this chapter, methacrylate acid (MAA)-ethyl acrylate (EA) colloidal scaffolds were prepared via emulsion polymerization and used as templates for the in-situ co-precipitation of Fe^{2+} to produce stable functional magnetic nanoparticles (MNPs) (<500 nm) decorated with β-cyclodextrin (β-CD) (FMNP). Emulsion polymerization with the controlled addition of monomer mixtures allowed for good size control, and silica coating was introduced to protect the oxidation of FMNP. The superparamagnetic FMNP with high saturation magnetization (33 emu/g) could be readily separated from water using a high gradient magnetic separator (HGMS). Procaine hydrochloride (PrHy) was used as a model pharmaceutical residue to evaluate the performance of the FMNP, and 53.65 mg PrHy/g FMNP was adsorbed using 600 ppm FMNP. A fast (30 mins) adsorption kinetic follows Pseudo-first-order kinetic model explained a physical adsorption through a 1 to 1 host-guest inclusion mechanism. And the adsorption behavior was followed Freundlich isotherm with a linear adsorption performance. The proposed system is scalable and adaptable to existing water treatment processes, which is promising to fill the gap of the detection of low concentration of pharmaceuticals by a pre-concentrating strategy.

---

*This chapter is adapted from a published paper "Xu, J., Tian, Y., Li, Z., Tan, B. H., Tang, K. Y., & Tam, K. C. (2022). β-Cyclodextrin functionalized magnetic nanoparticles for the removal of pharmaceutical residues in drinking water. *Journal of Industrial and Engineering Chemistry*, *109*, 461-474."

4.1 Introduction

The appearance of pharmaceuticals and personal care products (PPCPs) in water system has been reported over the last four decades [274] [275] [276]. PPCPs may directly or indirectly enter the aquatic environment via pharmaceutical waste, hospital effluent, livestock breeding, expired medicine, sewage discharge and waste from research activities. They may remain unmodified, undergo various forms of metabolisms, or present as a conjugated compound with glucuronic and sulfuric acid [277]. Many studies have identified various types of drugs discharged from the wastewater treatment plants (WWTPs) into the environment [278], and even after the conventional three-stage water treatment processes, ng/L (ppb) to μg/L (ppm) levels of pharmaceutical residues were found in tap water [279]. For instance, Stackelberg reported that 23 pharmaceutical residues are found in water discharge from water treatment plants, while the behavior of these chemicals during each processing step is not well understood [274]. PPCPs are persistent in WWTPs and the natural marine environment since most polar PPCPs cannot be degraded by microorganisms or be incorporated in the sewage sludge [278]. Even though the concentration of individual pharmaceuticals is relatively low, chronic exposure to a mixture of pharmaceuticals may have synergistic interactions that may have negative toxicological effects on humans. There are reported studies on the effects of various drug interactions, such as ibuprofen disrupting the cardioprotective properties of aspirin [280], updated cyclooxygenase-2 inhibitors affecting bone healing and re-growth after fracture [281], and caffeine enhancing the effectiveness of analgesics [282]. On the other hand, continuous exposure to pharmaceutical mixtures may result in potential adverse effects on other organisms. For example, tetracycline compounds can cause tissue changes in fish gills [283].

Due to the harmful effects of pharmaceuticals, the development of a cost-effective method to remove these compounds from drinking water has attracted increasing attention. Currently, three

processes (physical, biological and chemical) are used to remove these compounds from surface water and wastewater. However, many issues and limitations need to be resolved before they can be applied to large scale water treatment processes. In wastewater treatment, adsorption is the most widely used technology to remove contaminants. The adsorption capacities of activated carbon are often used as a benchmark to evaluate other treatment methods. However, the high cost of activated carbon regeneration (balanced by their high adsorption capacity and fast adsorption kinetics) limits their applications in many industries [11]. Photolysis and catalytic reduction of pharmaceuticals have also been highly studied. However, the resulting metabolites and transformation products from catalytic reaction can be more toxic and biologically more active than their parent compounds. This leads to research to examine the toxicology and chemistry using effect-directed analysis (EDA) [12]. Metal-based adsorbents are benefiting from their low cost and excellent mechanical properties; however, the slow adsorption capacity, high regeneration cost, and low stability limit their application [13]. The polymer-based adsorbents have been widely investigated due to their high adsorption capacity. But, an additional separation process, such as membrane filtration may be necessary, and this increase its operational cost, in addition to other challenges, such as membrane fouling [14]. Therefore, a cost-effective adsorbent with high adsorption capacity and simplicity in water treatment process, separation and regeneration is urgently needed.

There are only limited data on the persistence of pharmaceutical residues in drinking water due to their extremely low concentrations (ng/L), where cost-effective detection technology is not available. Hence, strict regulations on pharmaceutical residues in drinking water cannot be enforced. Analytical methods commonly used for water quality determination include solid-phase microextraction (SPME), fast gas chromatography/mass spectrometer (GC/MS), chiral separations (with chiral GC columns or capillary electrophoresis, CE), and enzyme-linked immunosorbent

assay (ELISA) methods. Other technologies that combine separation and detection, e.g. solid-phase extraction (SPE) and liquid chromatography/mass spectrometry (LC/MS) or GC/MS and ion chromatography coupled with plasma mass spectrometer (IC/ICPMS) are being used [284]. However, these advanced and costly detection technologies are not suitable for industrial applications due to issues like column plugging, low capacity, short contact time and pore diffusion limitation [285]. Therefore, there is a strong motivation to develop a cost-effective detection method for identifying pharmaceutical residues in the drinking water system.

There is an increasing interest in utilizing magnetic materials in water treatment, and they are widely used to remove various types of pollutants, such as heavy metals [16], dyes [17], [18] and drugs [19], [20]. Magnetic nanoparticles are ideal materials for use as separation medium as they possess high surface area to volume ratio, large adsorption capacity, high biocompatibility, low toxicity, and ease of modification [21]. Despite the attractive properties of magnetic materials, size control, aggregation and oxidation are major concerns when they are produced using conventional co-precipitation or hydrothermal method. Recently, an in-situ synthesis of MNPs surface modified with temperature and pH-responsive poly (N-isopropylacrylamide-co-2-aminoethyl methacrylate) P (NIPAAm-co-AEM) were developed for DNA capture [22]. The AEM introduced NH_2 groups to the system for electrostatic binding with DNA, and the amino groups could also chelate with the MNPs. The polymer coated MNPs were more stable, and they did not agglomerate when dried as shown by the SEM micrographs. However, an extremely large particle radius (1600 nm) was reported at a pH of 9.1 due to the deprotonation of amine groups that triggered the aggregation of the particles. Although the amino groups could stabilize the MNPs and bind to DNA (18.5 mg DNA/g MNP) at pH 5, the agglomeration at high pH reduced the operational pH, which limits its application. The one pot synthesis yielded impurities, such as

unreacted monomers that impacted the chemical composition and morphology of the MNPs [22]. Chariya and coworkers developed an amphiphilic poly (styrene-b-acrylic acid) magnetic clusters via a self-assembly for application in scale inhibition. The fabrication of magnetic particles was achieved via the synthesis of hydrophobic Fe_3O_4 particles in the presence of oleic acid (OA-MNPs) followed by the self-assembly of amphiphilic polyacrylic acid (PAA)-b-polystyrene (PS) copolymer. The formed magnetic latex particles were stabilized by the surfactant-like copolymer, and it was reported that 92% of Ca^{+} was removed using this system. However, only large magnetic clusters with 12 w/v% OA-MNP and large amounts of PAA-b-PS could form stable magnetic particles. The particle size was not uniform with a mixture of magnetic clusters of varying sizes that resulted in an inconsistent separation performance. This system could only be recycled 4 times due to the unstable structure that could not preserve the magnetic core after being subjected to strong magnetic field [23]. Other than the synthetic polymers, protein based natural polymers were used to prepare magnetic particles. A bovine serum albumin (BSA)-iron oxide colloidal particle was synthesized via the precipitation-crosslinking method. The magnetic particles were first prepared by co-precipitation, and BSA dissolved in phosphate buffer was added to the purified ferrofluid under agitation. The particle size of the formed magnetic colloidal particles was 140 nm, and non-homogeneous size distribution of magnetic clusters was reported. Although the magnetic colloidal clusters possessed high magnetization (40 emu/g), the size of the conjugated magnetic clusters were not monodispersed that may critically affect the biological application in lateral flow immunoassay [24]. Even though the preparation of high-quality magnetic particles has been improved using techniques, such as microwave assisted synthesis, they are however energy intensive, require skilled operators and need to optimize complicated experimental parameters [25]. Thus, using a facile method to synthesis polymer modified magnetic particles with sufficient

magnetization, controllable particle size and reproducible monodispersed colloidal magnetic particle is desirable and necessary.

This chapter describes a templated magnetic nanoparticle functionalized with β-cyclodextrin (FMNPs) for the removal and concentration of dilute pharmaceutical residues in drinking water. Monodispersed magnetic particles are necessary to achieve consistent response in a magnetic field, however, they cannot be produced via the co-precipitation process under mild reaction conditions. Thus, we proposed a novel colloidal scaffold method to prepare monodispersed MNPs with good control of size and shape. Also, the β-cyclodextrin (β-CD) consisting of a hydrophobic cavity and a hydrophilic outer shell was grafted to the FMNP to capture pharmaceutical compounds via the host-guest chemistry [286]. Procaine hydrochloride (PrHy) is a common local anesthetic drug commonly injected to the mucous membranes with harmful side effects like the cardiac and neurological toxicity [27]. Thus, the removal of PrHy is critical for human health. In this study, PrHy was selected as a model drug to investigate the adsorption capacity of the FMNP particles. And the magnetization of the system can be tuned by varying the strength of the magnetic field of the HGMS during the washing process.

4.2 Experimental

4.2.1 Materials

Methacrylic acid (MAA), ethyl acrylate (EA), di-allyl phthalate (DAP), sodium persulfate, sodium hydroxide, iron(II) sulfate heptahydrate ($FeSO_4 \cdot 7H_2O$), sodium nitrite ($NaNO_2$), ammonia solution (28-30%), tetraethyl orthosilicate (TEOS, 98%), sodium phosphate dibasic heptahydrate, sodium phosphate monobasic monohydrate, hydrochloric acid, β-Cyclodextrin, procaine hydrochloride, chloroacetic acid, ethanol, and acetone were purchased from Sigma-Aldrich.

Cyanamide (CH_2N_2, 95%), aerosol OT (AOT, 75%) and cyanamide (CH_2N_2, 95%) were supplied by Thermo Fisher Scientific.

4.3 Methods

4.3.1 Synthesis of MAA-EA nanogel scaffold

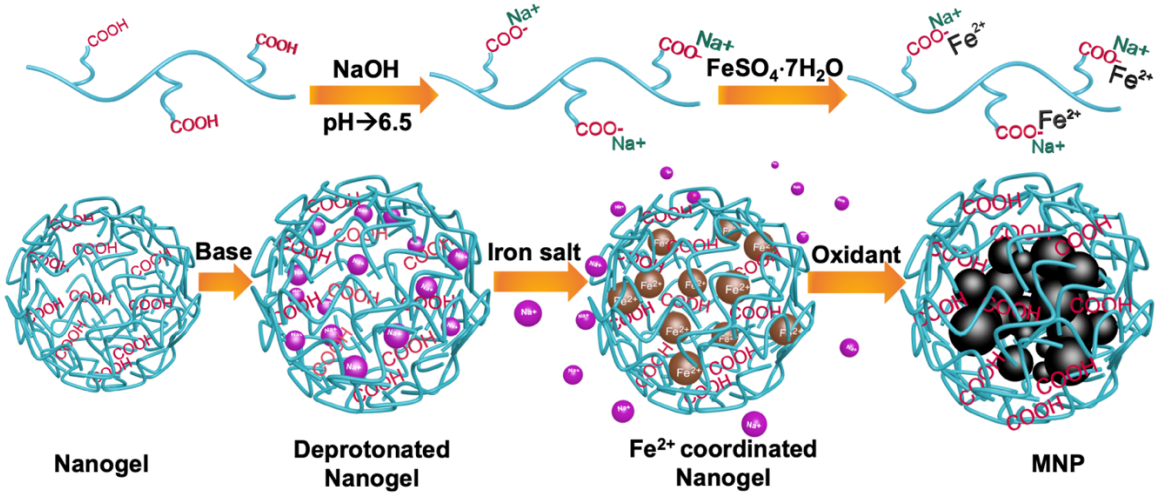
Nanogel scaffold was prepared from polymerized methacrylic acid (MAA) and ethyl acrylate (EA) crosslinked with di-allyl phthalate (DAP). The MAA-EA nanogel was synthesized using a conventional semi-continuous emulsion polymerization process. A 13.956 g pre-emulsion mixture consisting of 1:1 monomer ratio was prepared in a 20 mL vial by adding 35.47 wt% of MAA and 41.20 wt% of EA together with 8 wt% of DAP, 7.17 wt% of AOT solution and 10 wt% of water. The initiator solution was prepared with 2 g of 11.11 wt% of sodium persulfate solution.

The reactor comprising of 250 mL three-neck flask with 0.83 wt% of AOT in 120 g of water was purged with nitrogen for 30 minutes and heated to 85 °C, and the initiator solution was added. When the contents were well-mixed, the stirring speed was reduced from 800 rpm to 300 rpm and 5 wt% of the pre-emulsion mixture was then added dropwise. After the reaction had proceeded for 30 minutes to yield an in-situ seed solution, the remaining pre-emulsion mixture was added drop-wise and the reaction was left to proceed for another 30 minutes. The nanogel was cooled to room temperature and filtered through a 200-mesh nylon cloth. Then, the nanogel dispersion was transferred to a cellulose tubular membrane with a molecular weight cut-off of 12 to 14 kDa, and dialyzed against DI water. The dialysis was continued until no surfactant bubble was observed or the conductivity of the dialyzed water was close to DI water.

4.3.2 Synthesis of nanogel based magnetic nanoparticles (MNPs)

MNPs were synthesized via the in-situ coprecipitation of ferrous ions inside the nanogel template. 120 mL of 0.5 wt% MAA-EA nanogel solution was adjusted to pH 6.5, then transferred

to a 250 mL three-neck flask and purged with nitrogen for 30 minutes. Then, 2.5 g of $FeSO_4 \cdot 7H_2O$ was dissolved in 30 mL of de-oxygenated water and added dropwise to the reaction vessel with gentle mechanical stirring (250 rpm) for 2 hours. Subsequently, ultrafiltration under nitrogen was used to remove free Fe^{2+} outside the nanogel yielding a brown colour filtrate. The ultrafiltration was repeated several times until a clear filtrate was obtained confirming that all the un-coordinated Fe^{2+} was removed. The Fe^{2+} grafted nanogel was heated to 35°C under continuous stirring (400 rpm). Then 0.25 g $NaNO_2$ dissolved in 1 g of de-oxygen water and 15 mL of 28% NH_4OH was added to the reaction vessel forming a dark green suspension. Within 1 hour, the dark green suspension turned black indicating that the reaction was complete. After the reaction, the product was cooled and filtered through a 200-mesh nylon cloth. The synthesized MNPs were washed several times by passing it through the High Gradient Magnetic Separator (HGMS) until the washed liquid was clear. The MNP synthesis is illustrated in **Scheme 4-1**.

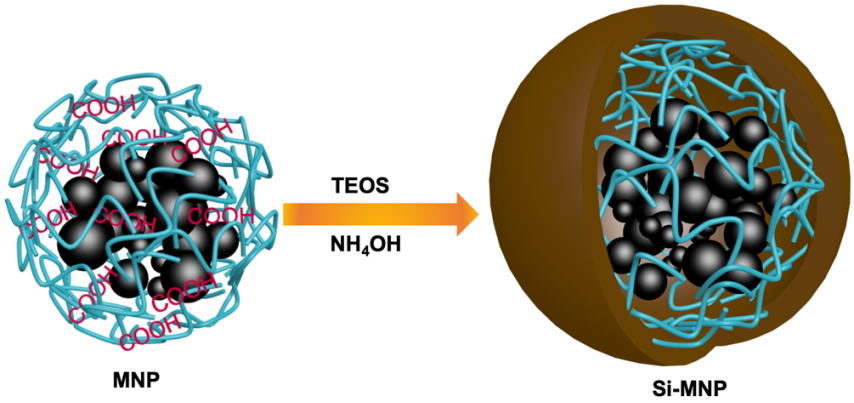


Scheme 4-1 Schematic describing the in-situ synthesis magnetic nanoparticles inside MAA-EA nanogel template

4.3.3 Synthesis of silica coated MNPs (Si-MNP)

To prevent the oxidation of the magnetic core, a thin layer of silica shell was coated on the iron-oxide loaded nanogel. 20 mL of the MNP solution (0.1 wt%) was dispersed in 80 mL of

ethanol solution, and then 5 mL ammonia solution and various amounts (**Table 4-1**) of TEOS were added dropwise to the MNP solution, and the reaction proceeded under mechanical stirring at room temperature for 24 hours. The product was then washed and recovered using the HGMS. The schematic illustration of TEOS coated on MNP is presented in **Scheme 4-2**.



Scheme 4-2 Schematic of silica coating on MNP **(**silica coating shown in brown**)**

Table 4-1 Summary of MNPs coated with varying amounts of TEOS

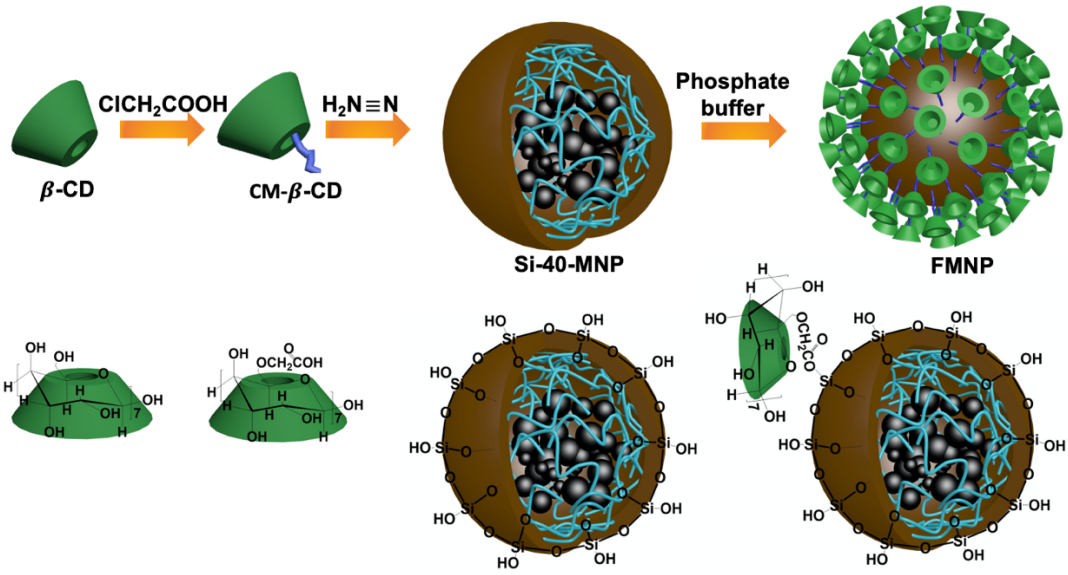
Sample name	Fe_3O_4 (g)	MNP solution (g)	TEOS (**μ**L)
Si-10-MNP	0.02	0.02/(0.1 wt%)=20	10
Si-20-MNP	0.02	20	20
Si-30-MNP	0.02	20	30
Si-40-MNP	0.02	20	40
Si-50-MNP	0.02	20	50
Si-100-MNP	0.02	20	100
Si-150-MNP	0.02	20	150
Si-200-MNP	0.02	20	200

4.3.4 Synthesis of CM-β-CD

The synthetic method of carboxymethyl-β-cyclodextrin (CM-β-CD) was modified according to the literature [287]. 5.675 g (5mmol) of β-CD was mixed with 5 g of NaOH (0.125mol in 20 ml water), and 0.4725 g (5 mmol) of chloroacetic acid was added. The reaction proceeded at 50 °C for 5 hours. After neutralization with HCl, the product was precipitated with excess acetone and subsequently separated by vacuum filtration. Finally, the CM-β-CD was obtained after vacuum drying overnight at 40 °C. The final product was ground into white powder for subsequent use.

4.3.5 Grafting of CM-β-CD onto Si-40-MNP

Typically, 250 mg of Si-40-MNP was mixed with 5 mL of phosphorous buffer (pH 6) and sonicated for 40 min. Then, 31.25 mg of cyanamide was dissolved in 1.25 ml of the same buffer and dropwise added to the reaction vessel. After 40 min of sonication, 187.5 mg of CM-β-CD was dissolved in 6.25 ml of buffer and added dropwise to the reaction vessel. The mixture was sonicated for another 90 min and then washed several times with buffer and collected by water to yield CM-β-CD functionalized Si-40-MNP (FMNP). The schematic illustration of grating β-CD onto Si-40-MNP is shown in **Scheme 4-3**.



Scheme 4-3 Schematic of FMNP preparation via grating carboxyl-β-CD (CM-β-CD) onto silica coated MNP (top), chemical structure (bottom)

4.4 Characterization methods

4.4.1 Transmission electron microscopy (TEM)

All the TEM images were taken using a Philips CM10 electron microscope under an accelerating voltage of 60 kV. The TEM samples were prepared by placing one drop of 0.02 wt% of the solution onto a 200-mesh carbon-coated copper grid. The dried nanogel sample was stained with uranyl acetate and lead citrate.

4.4.2 Fourier transform infrared spectroscopy (FTIR)

The FTIR of MAA-EA nanogel, Si-MNPs, β-CD, CM-β-CD, and FMNP were obtained using a Bruker Tensor 27 spectrometer (Bruker, Billerica, MA, USA). The samples prepared with KBr were scanned between 4000 to 400 cm^{-1} at room temperature.

4.4.3 Dynamic light scattering (DLS)

The DLS measurements were used to determine the diameter of nanogel, MNP, Si-MNP and FMNP. The measurements were conducted by measuring 0.1wt% dispersion of samples at pH 5 to 9 in a Zeta-Sizer (Nanosizer ZS, Malvern co., UK) at 25 °C.

4.4.4 Zeta potential measurement

Zeta-Sizer (Nanosizer ZS, Malvern co., UK) was used to obtain the zeta potential of different dispersions by measuring the charge density on the surface at 25 °C. Different samples at 0.1 wt% were prepared and adjusted to the desired pH by adding 0.1 M NaOH or 0.1 M HCl.

4.4.5 Adsorption kinetic study

The adsorption kinetic study was investigated with Si-40-MNP and FMNP to remove PrHy from water, respectively. The adsorption kinetic study was conducted in 20 ml vials, and in each vial, 3 ml of FMNP stock solution was added to the desired concentration of FMNP solution (500 ppm). The pH was adjusted to 8 with 0.01M NaOH prior to the addition of PrHy solution to achieve a concentration of 15 ppm. The solution mixtures were placed on a shaker for a fixed time (between 2 to 150 min), where it was then separated by a magnet and further filtered through a 0.22 μm PES syringe filter, and the filtrate was analyzed in a UV-Vis spectrometer. The adsorption data were fitted to a non-linear form of Pseudo-first order and Pseudo-second order kinetic models described in Eq. (4.1) and (4.2):

$$Q_t = Q_e(1 - e^{-k_1 t}) \tag{4.1}$$

$$Q_t = \frac{Q_e^2 k_2 t}{1+k_2 Q_e t} \quad (4.2)$$

where, Q_t (mg/g) is the adsorption capacity at time t (s); Q_e (mg/g) is the adsorption capacity at equilibrium; k_1 and k_2 are the rate constants of the non-linear Pseudo-first order and Pseudo-second order adsorption kinetic model, respectively.

4.4.6 FMNP concentration screening

A concentration screening test was conducted before the adsorption studies to determine the FMNP concentration for further adsorption experiments. The concentration screening adsorption tests were conducted in 20 ml vials, and 3 ml of FMNP stock solution was added to the desired concentration (100, 300, 500, 600, 700 and 1000 ppm). The pH was adjusted to 8 with 0.01M NaOH prior to the addition of PrHy stock solution to achieve a starting concentration of 15 ppm. The solution mixtures were placed on a shaker for 30 min, separated using a magnet, filtered through a 0.22 μm PES syringe filter, and the filtrate was tested using a UV-Vis spectrometer. The equilibrium adsorption capacity Q_e and removal efficiency R (%) were calculated using Eq. (4.3) and (4.4) respectively.

$$Q_e = \frac{(C_0 - C_t) * V}{m} \quad (4.3)$$

$$R\,\% = \frac{(C_0 - C_t)}{C_0} * 100 \quad (4.4)$$

where, C_0 (mg/L) is the initial concentration of PrHy; C_t the residue concentration of PrHy at time t (min or s); V (L) is the total volume of adsorption mixture; Q_e (mg/g) is the adsorption capacity at equilibrium and m represents the mass (g) of FMNP used for the adsorption test; R (%) is the removal percentage of the PrHy from the initial concentration.

4.4.7 Adsorption isotherm study

The adsorption tests were conducted in 20 ml vials, and 3 ml of FMNP stock solution was added to 600 ppm of FMNP concentration. The pH was adjusted to 8 with 0.01M NaOH prior to the addition of PrHy stock solution to achieve a starting concentration of between 5 to 100 ppm. The solution mixtures were placed on a shaker for 30 min, where it was then separated by a magnet and filtered through a 0.22 μm PES syringe filter, and the filtrate was tested using the UV-Vis spectrometer. The adsorption isotherm results were fitted to the non-linear Langmuir and Freundlich models described by Eq. (4.5) and (4.6) respectively [29]:

$$Q_e = \frac{Q_m K_L C_e}{1 + K_L C_e} \quad (4.5)$$

$$= K_F C_e^{\frac{1}{n}} \quad (4.6)$$

where Q_m (mg/g) is the maximum adsorption capacity of the adsorbent; K_L (g/L) is the Langmuir adsorption equilibrium constant that indicated the binding energy between the adsorbate and the adsorbent; K_F (mg/g) and n are Freundlich constant, which indicates the binding intensity and the spontaneity of the adsorption process.

4.4.8 X-Ray Diffraction (XRD)

The X-Ray Diffraction spectra of MNP and Si-MNP were obtained in an X-Ray Diffractometer (Bruker D8 Focus). The sample was scanned over a 2θ range from 10° to 90° with increment of 0.1° and a time step of 3 sec/step.

4.4.9 Vibrating sample magnetometer (VSM)

The magnetization of MNP, Si-MNP and FMNP prepared by freeze-dried powder were investigated by a vibrating sample magnetometer (VSM 880). The superconducting quantum interference device (SQUID) measurement was conducted from -1T to 1T at 300K.

4.4.10 Thermogravimetric analysis (TGA)

The chemical composition of MNP, Si-40-MNP, and FMNP was explored by TGA. The TGA was conducted under nitrogen with a heating rate of 10℃/min from 100 ℃ to 600℃ with TGA Q500 from TA instrument.

4.5 Results and discussion

4.5.1 Morphology of Nanogel, MNP and Si-MNP

The morphology of nanogel scaffold, MNP, and Si-MNP were examined by using TEM. The TEM images of stained MAA-EA nanogel (**Figure 4-1 (A)**) revealed a series of monodispersed and well-defined spherical particles with diameter of approximately 60 nm. The MNP consisted of well-defined clusters of magnetic nanoparticles incorporated within the nanogel **(Figure 4-1, B)**, no aggregation was observed due to the isolation of the nanogel scaffold. The TEM images of the filtrate correspond to the MNP solution not captured by the HGMS (power on) is shown in **Figure 4-1, C**. Smaller magnetic particles, and also non-magnetic material like nanogel were evident confirming the relevance of the cleaning step. Because of the contrast between the various components, the TEM images revealed a core-shell structure consisting of a magnetic core, a nanogel scaffold, and a silica coating layer. Different amounts of TEOS coated with MNP (0.02 g) are shown in **Figure 4-1**: **D, E, F, G, H** , displayed 40 μL, 50 μL, 100 μL, 150 μL and 200 μL TEOS coated MNP respectively, and the thickness of the silica coating layer was increased correspondingly. The coating layer thickness presented in each TEM image was obtained by the average value of measuring 40 to 50 particles by Image J, and the distribution of different amounts of TEOS coated MNP are shown in **Appendix 4-1** and the summary of silica shell thickness are summarized in **Table 4-3**. When the amount of TEOS was only 50 μL, very few silica shell contains multiple MNP clusters with a 12.05 nm shell thickness. When the TEOS content was

increased, more MNP clusters were encapsulated within one silica shell. The thickness of the silica shell was 14.83, 16.08, and 25.62 nm, corresponding to 100, 150 and 200 μL TEOS coating respectively. Further optimization of TEOS coating (10, 20, 30, 40, 50 μL) by decreasing the amount of TEOS was conducted to achieve individually coated MNP with a thinner layer of silica. On the other hand, no aggregation of MNP and Si-MNP were observed, confirming the stability of the material prepared by nanogel templating strategy. Also, TEOS would hydrolyze to form a silica cross-links as indicated by the grey network outside the silica shell as shown in **Figure 4-1: (D, E, F),** which was also observed from previous report [288]. **Figure 4-1**, **D** shows the Si-40-MNP where 40 μL of TEOS was used, most of the silica shell only contains one MNP clusters with a thinnest (11.45 nm) shell thickness. And further decreased the amount of TEOS lead to an invisible Si-O-Si vibration peak from the FTIR results (**Figure 4-2**, **b**). By considering the high surface area of the thinner silica shell and the higher magnetic content in each silica shell, Si-40-MNP was selected for further characterization and grafting with β-CD. The particle size of nanogel obtained from TEM images (46 nm) was smaller than the value determined from DLS (100 nm to 200 nm), which was 50% smaller due to removal of water when the nanogel was dried. Additionally, the drying step during the TEM sample preparation process resulted in the shrinkage of the nanogel. The size difference of silica shell obtained from TEM (150 nm) was slightly smaller than the size determined from DLS (250 nm to 300 nm). The hard silica shell limited the shrinkage of the nanogel, while the DLS measurement was based on the solvated status of the particle. It included all the attached part like silica hydrolysis cross-linked network that was not considered as the particle size from TEM images (the grey network in Figure 1: D, E, F). Similar size difference from TEM and DLS was observed by other works too [289].

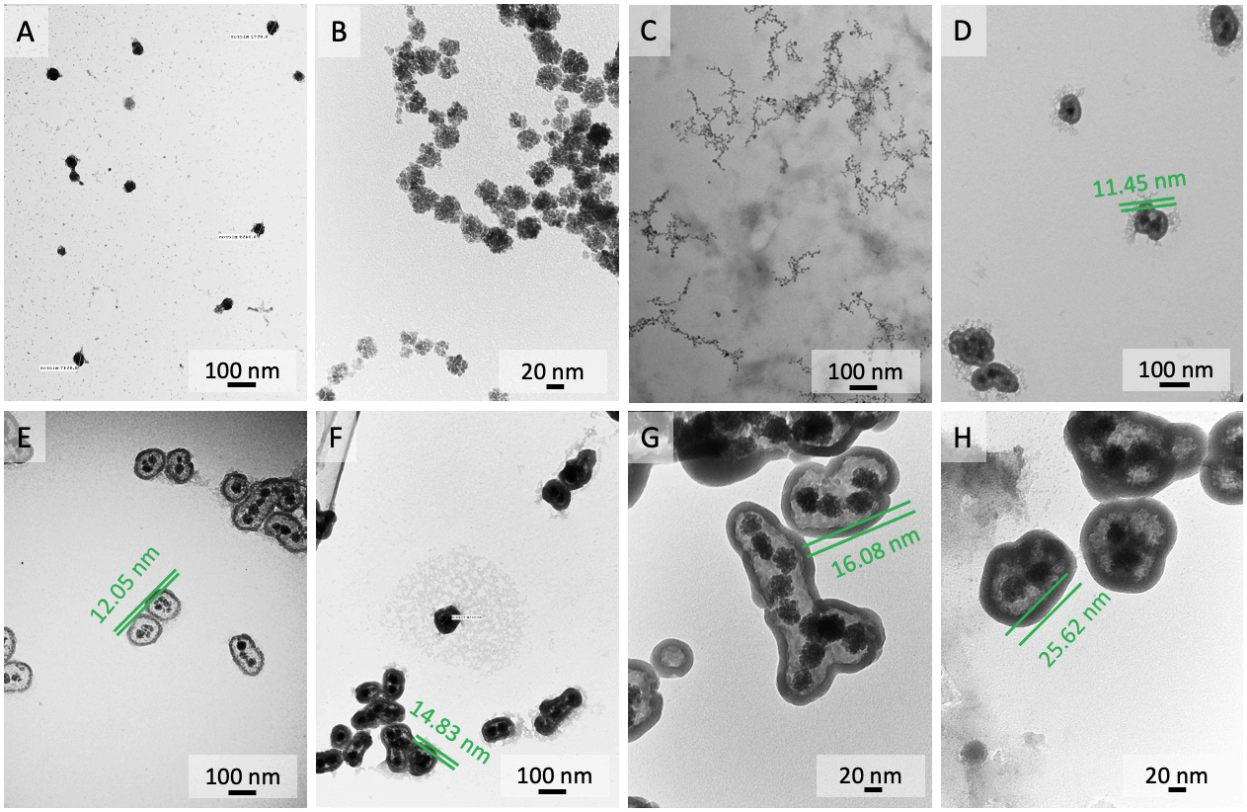


Figure 4-1 TEM images of MAA-EA nanogel (A); MNP (B); MNP-wash-out from the HGMS (C); Si-40-MNP (D); Si-50-MNP (E) ;Si-100-MNP (F); Si-150-MNP (G) and Si-200-MNP (H)

FTIR analysis of nanogel, CM-β-CD and silica coating

The successful synthesis of MAA-EA nanogel and silica coating on the surface of the MNP was confirmed by FTIR spectroscopy. **Figure 4-2 (a)** shows the FTIR spectra of pristine β-CD, carboxymethyl-β-cyclodextrin (CM-β-CD), and silica-coated magnetic nanoparticles functionalized with CM-β-CD (CM-CD-MNP). The broad peak between 3300 and 3500 cm^{-1} is attributed to the -OH stretching, and the C=O stretching of carbonyl groups is associated with the peak at 1748 cm^{-1} in the CM-β-CD spectra, which confirmed the modification of the carboxymethyl groups on β-CD. Several characteristic peaks at 940, 1020, 1155 and 1635 $cm^{-1}$are present in the CM-CD-MNP spectrum. The peak at 940 cm^{-1} is assigned to the R-1, 4-bond skeleton vibration of β-CD, and two small peaks at around 1100 cm^{-1} are the result of the

antisymmetric glycosidic υ_a (C-O-C) vibrations combined with υ (C-C/C-O) stretching [290]. The C=O stretching of carboxylate is correlated with the peak at 1635 cm^{-1} [291], while the peak at 2924 cm^{-1} is attributed to the asymmetric C-H stretching. In conclusion, the CM-β-CD was successfully grafted on the surface of the magnetic nanoparticles. **Figure 4-2 (b)** shows the FTIR spectra of MAA-EA nanogel and different amounts (10-50 μL) of TEOS coated magnetic nanoparticles. The absorption bands in the range of 1700 to 1740 cm^{-1} range are related to the carbonyl stretching of acid and ester bonds. Thus, the adsorption peak at 1700 cm^{-1} corresponded to carboxylic acid C=O stretching [251]. The wavenumber of peaks in all silica coated magnetic nanoparticles spectra were slightly different depending on the amounts of TEOS coated on the MNP. The adsorption peak at 561 cm^{-1} represents the characteristic Fe-O peak of the MNP. As the amounts of TEOS coated on the MNP increased, the wavenumber of Si-MNP increased from 415 to 478 cm^{-1}, which corresponds to Si-O-Si or O-Si-O peaks, while the peak at 790 cm^{-1} is from symmetric stretching of Si-O-Si [292]. Once the amount of TEOS was reduced to less than 40 μL, the symmetric Si-O-Si was not evident from the FTIR results. The bands between 1050 to 1100 cm^{-1} represents the Si-O symmetric stretch and the peaks between 1623 to 1630 cm^{-1} are related to the hydroxyl groups (O-H) on the MNPs in aqueous solution [293].

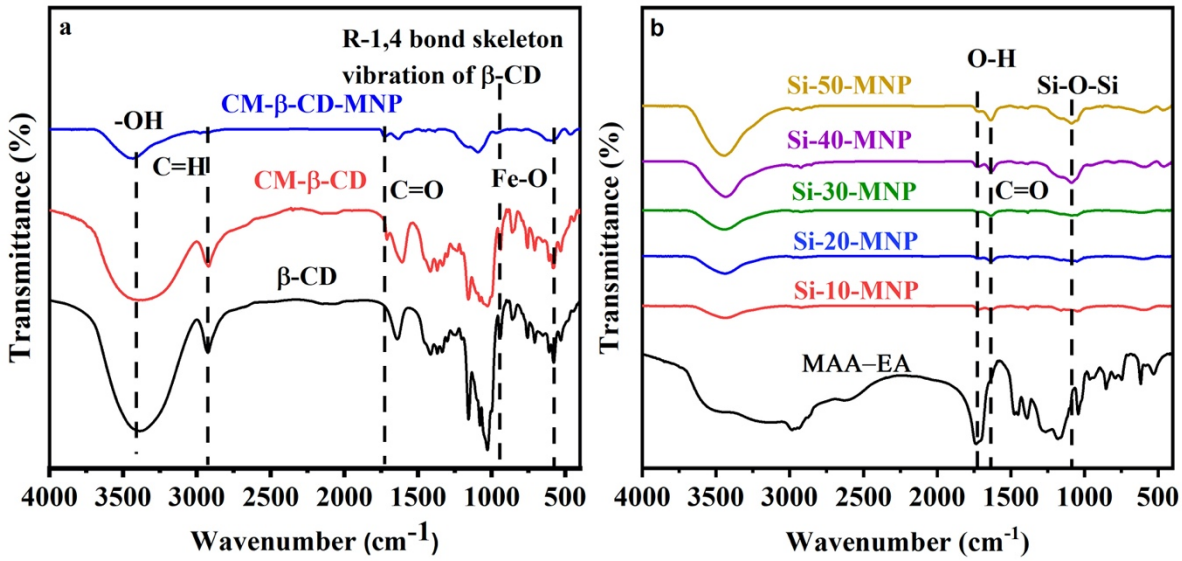


Figure 4-2 FTIR of CM-CD-MNP, CM-β-CD and β-CD (a), MAA-EA nanogel and 10 to 50 μL coated MNP

4.5.2 XRD analysis of the chemical structure of silica shell

To confirm if the silica shell on the MNP could prevent the oxidation of the magnetic core (Fe_3O_4) to Fe_2O_3 of lower magnetization, XRD was employed to examine the crystal structures of Si-MNP and MNP (**Figure 4-3**). The silica coated MNP displayed clear characteristic peaks 30.1°, 35.8°, 43.5°, 57.3°, 63.0° that corresponded to the (220), (311), (400), (422), (511) and (440) crystalline planes of Fe_3O_4 respectively [294]. The XRD pattern of MNP without silica coating exhibited peaks at 22.6°, 79.6° and 87.6° that corresponded to the rhombohedral structure of α-Fe_2O_3 [295]. The XRD patterns confirmed that the magnetic core inside the Si-40-MNP consisted of Fe_3O_4, where the silica shell prevented the oxidation of Fe_3O_4. On the other hand, in the absence of silica shell, the magnetic core inside the nanogel consisted mainly α-Fe_2O_3.

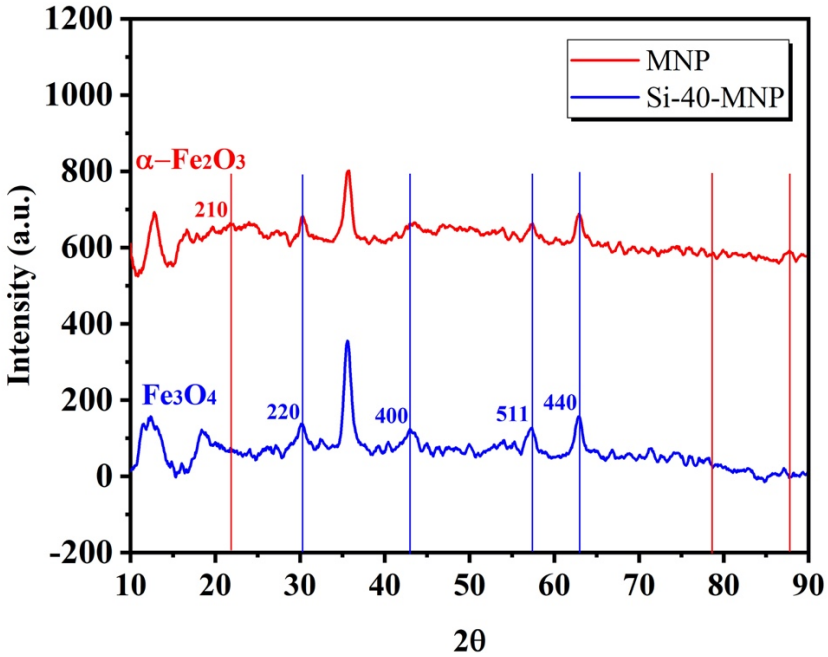


Figure 4-3 XRD pattern of the Si-MNP and MNP

4.5.3 Size control and stability of nanogel template, MNP, Si-MNP and FMNP

The particle size of nanogel prepared with different weight percentage of total monomer mixture during the seed formation stage was measured at pH 5 to 9. In **Figure 4-4 (a)**, the particle size of nanogel increased from pH 5 to 7 due to the increasing degree of ionization of carboxylic groups. When the pH was between 5 and 7, the carboxyl groups were protonated and repelled from the acidic environment led to a shrinking status of the nanogel. As the pH increase, the nanogels were gradually deprotonated to COO-, thus increasing the charge density on the nanogel surface as well. Hence, the increased counterion (Na^+) in the continuous phase increased the internal osmotic pressure of the nanogel, which caused the swelling of the nanogel until all the COOH groups were deprotonated. The maximum swelling of the nanogel remained constant at the maximum degree of ionization in the absence of electrolytes. Further increase the pH caused a reduction of the nanogel particle size, since the ionic strength of NaOH added for the pH

adjustment were not negligible. The shielding effect induced by the high NaOH concentration caused less COOH groups dissociated, and led to the reduction of the particle size [296].

The particle size of the nanogel during the emulsion polymerization process usually depends on the stirring speed, amount of surfactant, polymerization temperature, monomer adding speed, amount of initiator and many other factors. However, it is very challenging to achieve size control without an extensive experimental study of a specific emulsion polymerization system. Currently, the emulsion polymerization mechanism is being debated, and three major mechanisms are widely adopted: micellar nucleation, homogeneous nucleation and droplet nucleation [38]. To control the particle size of the final product (FMNP), an accurate control of the size of the nanogel template is critical. A simple seeded micelle control strategy was proposed based on the micelle nucleation mechanism. The final emulsion particle size was controlled by varying the amounts of micelles in the polymerization system, which was controlled by the weight percentage of the total monomer mixture added during the seed formation stage. The concentration of surfactant used in this emulsion polymerization system was much higher than its critical micelle concentration (CMC), which ensured the formation of a large amounts of micelles for the formation of primary particles. And the surfactant molecule would also be adsorbed on the monomer droplets and primary particles to provide colloidal stability. In this study, 5, 15 and 25 wt% of the monomer mixture were added during the seed formation stage. When increasing wt% of the monomer mixture used for seed formation, more monomer droplets (same size) were formed under same stirring speed. Consequently, more surfactant molecules were adsorbed on the monomer droplets when 25 wt% monomer mixture were added for seed formation. However, less surfactant molecules were adsorbed on 5 wt% monomer mixture seeded emulsion, and more surfactant molecules were functionalized to form more micelles. Thus, 25 wt% monomer mixture seeded nanogel had a

reduction in the number of micelles, larger nanogel particles would be produced. The average particle size of 5, 15 and 25 wt% monomer mixture seeded particles were increased sequentially (**Figure 4-4, (A)**), which confirmed the proposed size control mechanism. The 5 wt% MAA-EA nanogel also presented less pH responsive behavior, which was caused by less MAA was incorporated in each nanogel particle. The zeta potential profiles of MAA-EA nanogels fabricated with different wt% of the monomer mixtures for seed formation at various pH conditions are presented in **Figure 4-4 (B)**. The surface of all the nanogels were negatively charged at pH 5 to 9 due to the dissociation of the carboxylic acid (COOH) to carboxylate (COO^-) groups. 25 wt% monomer mixture seeded nanogel possess more MAA in each nanogel particle, a lower zeta potential was observed. All the nanogels have a zeta potential value lower than negative 35 mV in a wide pH range exhibited the outstanding stability of the nanogel.

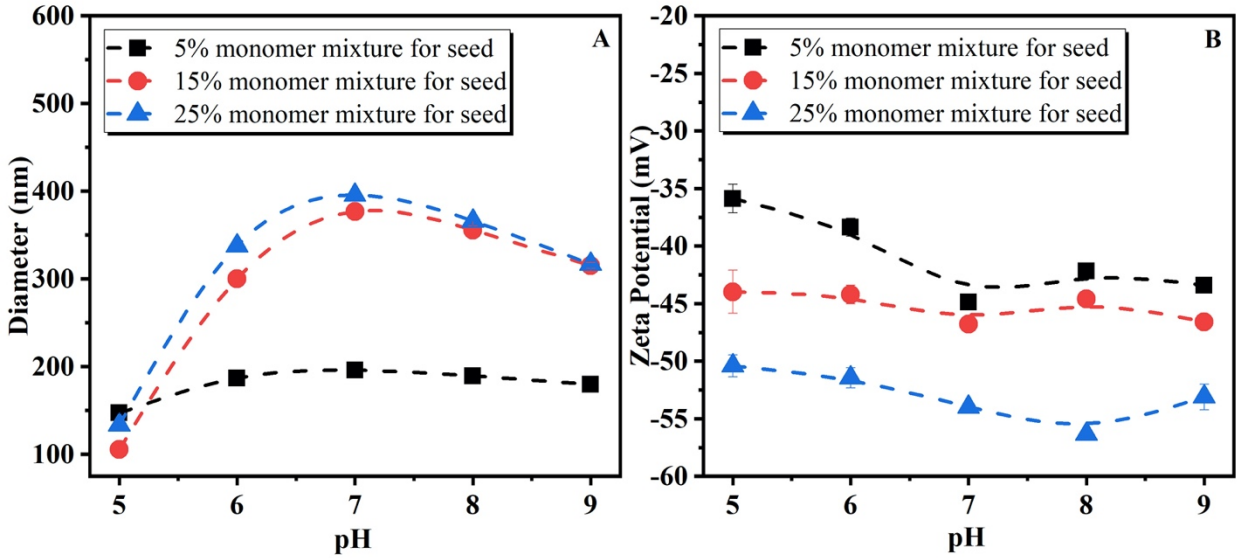


Figure 4-4 Particle size (a) and zeta potential of nanogel synthesized with 5 to 25 wt% of the monomer mixture used for seed formation

The average particle size of nanogel, MNP, Si-40-MNP, and FMNP are shown in **Figure 4-5**, **a**. Similarly, a pH-responsive trend was observed for the MNP, where the particle size increased with

increasing pH from 5 to 9. The particle size of MNP was larger than the nanogel due to the magnetic clusters inside the nanogel that expanded the nanogel scaffold. After the coating of 40 µL TEOS, the particles were no longer responsive to pH, which is due to the hard silica coating that prevented the neutralizing of carboxyl groups by NaOH, and restraining the swelling of the nanogel. The particle diameter of the nanogel, MNP, Si-40 MNP, and FMNPs were mostly below 500 nm at all pHs, meeting the requirement of magnetic particles for separation using the HGMS. The number based size distribution of nanogel, MNP, Si-MNP and FMNP at pH 6 are shown in **Appendix 4-2** and and the corresponding number based PDI value is summarized in **Table 4-2**. The size distribution peak of nanogel, MNP, Si-40-MNP and FMNP become wider in sequence, which is consistent with the PDI value. All the particles possessed a zeta potential of less than -30 mV, confirming the stability of the particles (**Figure 4-5**, **b**). The variation of zeta potential value of MNP at lower pH was reduced, since many COOH groups were chelated with the formed Fe_3O_4 particles inside the nanogel, indicated a less pH responsive property. Additionally, the FMNP exhibited better stability over Si-40-MNP, which might be due to the hydrophobic cavity and the hydrophilic interior of β-CD imparted the surfactant like behavior to the FMNPs.

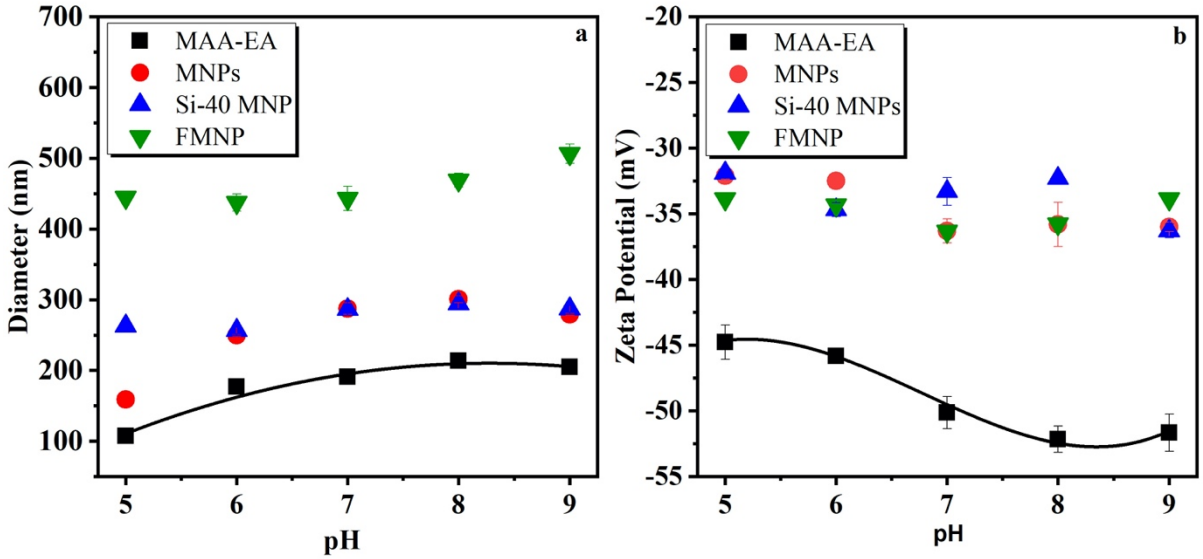


Figure 4-5 Average particle size (a) and zeta potential (b) of MAA-EA nanogel template, MNP, Si-40-MNP and FMNP

Table 4-2 The PDI value (number based) of nanogel , MNP, Si-40-MNP and FMNP at pH6

Sample name	Nanogel	MNP	Si-40-MNP	FMNP
PDI @ pH 6	0.120	0.383	0.422	0.351

Table 4-3 Summary of the thickness of silica shell (obtained from Images J)

Sample name	Si-40-MNP	Si-50-MNP	Si-100-MNP	Si-150-MNP	Si-200-MNP
Shell thickness (nm)	11.45 ± 2.6	12.05 ± 3.3	14.83 ± 3.6	16.08 ± 3.6	25.62 ± 4.7

4.5.4 Magnetization of Magnetic nanoparticles (VSM)

The magnetization of MNP, Si-40-MNP and FMNP were examined using the VSM 880 system. The magnetic hysteresis loop of MNP, Si-40-MNP and FMNP are shown in **Figure 4-6**. The saturation magnetization (Ms) of MNP, Si-40-MNP and FMNP were 53, 28 and 33 emu/g respectively. No hysteresis loops (zero coercivity) and high Ms values were observed indicating the excellent superparamagnetic property of the magnetic adsorbent associated with the novel in-situ templated synthetic method. The Fe_3O_4 clusters formed in the nanogel template possessed larger volume compared to individual Fe_3O_4 particles, imparted higher magnetization to the MNP system. The Ms value of MNP decreased after the silica coating, which confirmed the successful coating of TEOS. We observed that the Ms value of FMNP was higher than Si-40-MNP, which was probably due to the different washing process used. Both MNP and Si-MNP were washed with the HGMS connected to a peristaltic pump, and the HGMS column was filled with specific amount of steel wool. However, the washing process for FMNP was different, since the concentration of FMNP after synthesis was very high (determined by the reaction conditions) that may plug and aggregated inside the steel wool contained HGMS. As a result, a simplified washing process was adopted, which was conducted by directly placing the FMNP in the vial close to the

HGMS and the supernatant was removed after 3 mins. This process was repeated 3 times to ensure the complete removal of unreacted chemicals. The steel wool was employed as a matrix to generate high magnetic field gradient for capturing weak magnetic materials when conducting HGMS [297], while the absence of steel wool during washing FMNP led to a more limited magnetization. In other words, lower magnetic field applied for HGMS washing process would results in a higher magnetization product. Thus, when a lower magnetic field was used for washing FMNP would result in an increase in the magnetization of FMNP. Also, the control of the magnetization of the magnetic based material during the cleaning process via HGMS could be used as a strategy for magnetization selection for other magnetic based materials. Furthermore, the high Ms values and superparamagnetic properties of FMNPs would result in a rapid and complete separation after the adsorption process, which would reduce the energy consumption in water treatment plant.

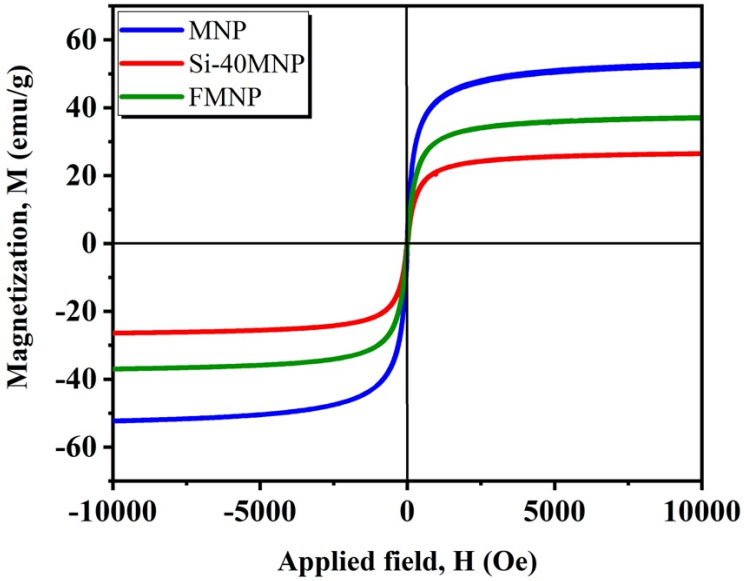


Figure 4-6 The magnetic hysteresis loops of MNP, Si-40-MNP and FMNP measured by SQUID at 300K between -1T and 1T

4.5.5 Thermogravimetric analysis (TGA)

The TGA was conducted under nitrogen with a heating rate of 10 ℃/min from 100 ℃ to 600℃. There are several distinct regions of weight loss observed from the TGA analyses of MNP, Si-40-MNP and FMNP (**Figure 4-7**). The first weight loss of between 100℃ and 200℃ was due to the loss of water adsorbed on the particles [42]. The second stage of weight loss occurred between 120℃ to 400℃ for all the samples due to the decomposition of the polymeric nanogel template [43]. The silica coating layered had a weight loss from 100℃ to 400℃ [44], so the differences in the weight loss (4.61%) between MNP and Si-40-MNP in the range of 100℃ to 400℃ was associated to the silica and silane on the surface of MNP. The weight loss (1.19 and 0.09 %) of FMNP compared with Si-40-MNP at 300℃ and 360-367℃ respectively was due to the decomposition of the glucose unit of the beta-cyclodextrin [45]. This confirmed the successful grafting of beta-CD on the surface of FMNP. The non-calcinated material after 400 ℃ was associated with the inorganic residues that were related to the iron oxide or silica on the nanogel. The magnetic contents in MNP, Si-40-MNP and FMNP determined at 400 ℃ were 85.1 wt%, 89.7 wt% and 89.0 wt% respectively. The increased magnetic content in Si-40-MNP and FMNP was due to multiple magnetic particles encapsulated within one silica shell. The magnetization of pure Fe_3O_4 was 75.3 emu/g [46], while the magnetization of FMNP was 33 emu/g. Thus, the magnetic content could be calculated and determined to be 43.8 wt%, which was smaller than the magnetic content determined by the TGA analysis (89 wt%). This is likely to be attributed to the existence of other non-magnetic inorganic content like $Fe(OH)_3$, $Fe(OH)_2$ or low magnification γ-Fe_2O_3 [24].

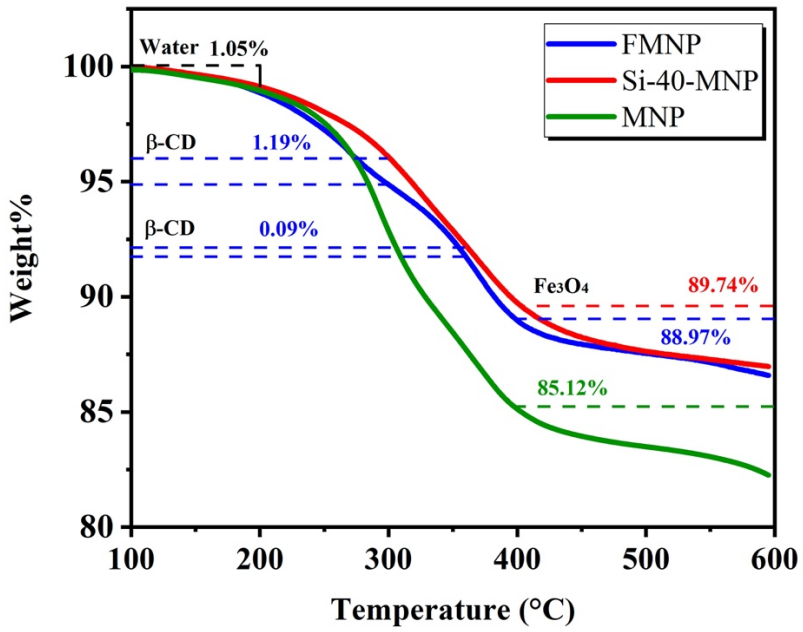


Figure 4-7 TGA curves of MNP, Si-40-MNP and FMNP

4.5.6 Adsorption kinetic study

The capability of the FMNP to remove low concentration of pharmaceutical compounds in drinking water was investigated using a model drug, procaine hydrochloride (PrHy). The residue concentration of 15 ppm PrHy after 2 to 150 mins adsorption tests with 500 ppm Si-40-MNP and 500 ppm FMNP are shown in **Figure 4-8**. Negligible reduction in the concentration of 15 ppm PrHy was evident for 500 ppm Si-40-MNP (**Black dash line**), while a significant reduction of PrHy concentration was observed after 2 mins with FMNP (**Red dash line**), where the concentration of PrHy decreased continuously and reached an asymptote after 30 mins. This fast adsorption kinetic is consistent with other β-CD based adsorbents [47], [48], [49], where the adsorption of bisphenol A (0.1 mM) reached an equilibrium within 1 min in the presence of 1000 ppm porous β-CD polymer [50]. Similar results were observed for pimavanserin (PMV) using both β and γ-CD nano-sponge, where the adsorption capacity was 12.8 and 2.9 mg/g, respectively [51].

In addition to the removal of pharmaceuticals, the absorption of As (V)/(III) using a Fe_3O_4 incorporated β-CD functionalized graphene oxide was completed within 10 min [29]. The removal of methylene blue (MB) using a carboxymethyl-β-CD modified magnetic particle (CMCD-MNP) revealed that thean equilibrium was achieved after 20 min [28]. We observed that the final concentration of PrHy after the adsorption test in 500 ppm FMNP was 10.84 ppm corresponding to an adsorption capacity of 8.12 mg/g. The adsorption data were fitted to non-linear pseudo-first order and pseudo-second order models (**Figure 4-9 A, B**) described by Eqs. (1) and (2) respectively, and all the model parameters are summarized in **Table 4-4**. As shown in **Figure 4-9** and the R^2 value of the models, both Pseudo-first order and Pseudo-second order fitted well to the experimental data (R^2> 0.97), which are in agreement with a reported study [52]. The Pseudo-first order model fitted better with an R^2 of 0.985, and the equilibrium adsorption capacity calculated from the first-order model agreed with the experimental data. This suggested that the adsorption kinetic of FMNP with PrHy was best described by the Pseudo-first order model driven by physical adsorption, where the binding of FMNP and PrHy was due to the formation of PrHy-CD inclusion complex. There was no covalent bond formed and this host-guest interaction is a reversible dynamic adsorption process.

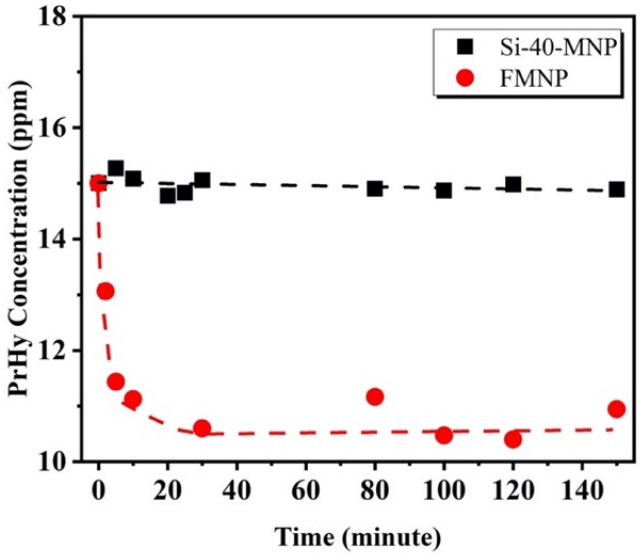


Figure 4-8 Final concentration of PrHy after adsorption test with 500 ppm Si-40-MNP (Black squares) and 500 ppm FMNP (Red circles)

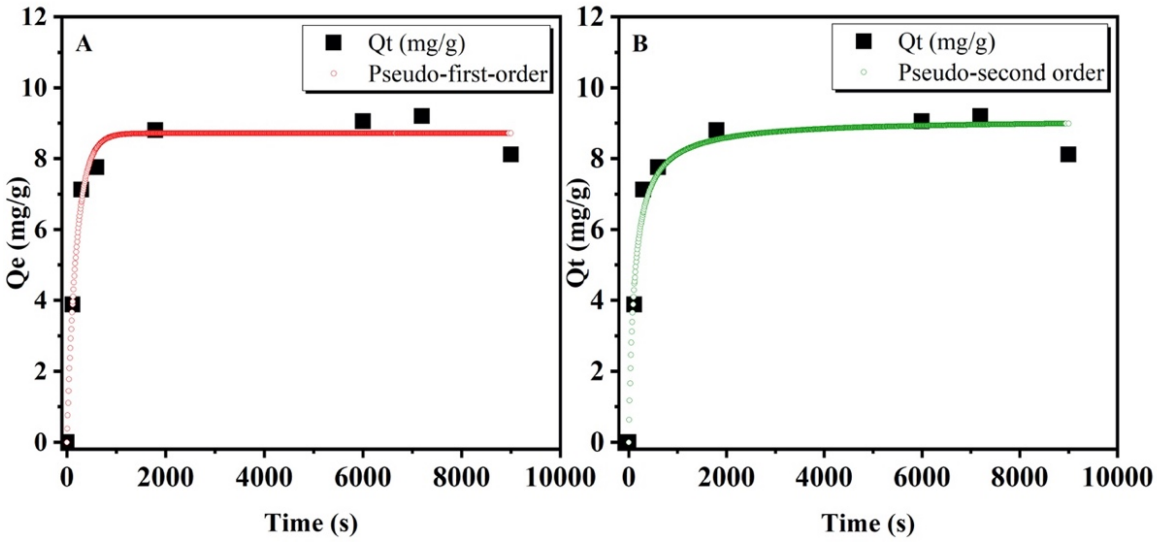


Figure 4-9 The adsorption kinetic of 500 ppm FMNP with 15 ppm PrHy in a 3ml batch solution fitted to the Pseudo-first order kinetic (A) and Pseudo-second order kinetic (B)

Table 4-4 Parameters of Pseudo-first order and Pseudo-second order model for FMNP adsorption kinetics

Sample	Pseudo-first- order			Pseudo-second- order		
	$k_1(s^{-1})$	R^2	Q_e	$k_2(g \cdot mg^{-1} \cdot s^{-1})$	R^2	Q_e
FMNP	0.0051	0.9845	8.718	0.0009	0.9756	9.114

4.5.7 FMNP concentration screening

Prior to the isotherm study, a concentration screening test was performed to identify the desirable concentration of the adsorbent (FMNP) for the removal of 15 ppm PrHy at pH 8. The UV absorbance curve of 15 ppm PrHy after 30 min adsorption test with 100 to 1000 ppm of FMNP is shown in **Figure 4-10 (A)**, and the final concentration of PrHy (ppm) and the removal efficiency (R %) are shown in **Figure 4-10 (B)**. The residual concentration of PrHy became nearly constant at 600 ppm FMNP and at 1000 ppm FMNP, the removal efficiency only increased from 38.8 % to 41 % with 66.67 wt% additional FMNP adsorbent. Thus, the adsorption isotherm was performed using 600 ppm of FMNP with 5 to 100 ppm of PrHy.

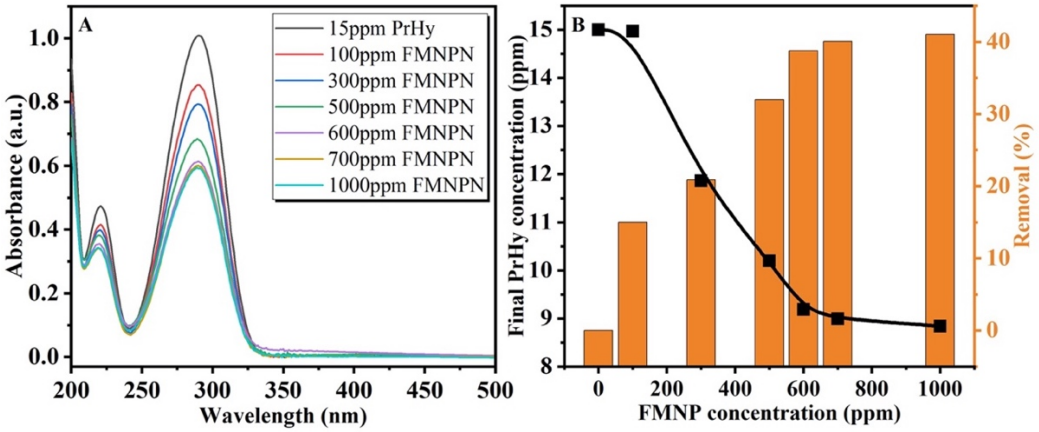


Figure 4-10 The UV-vis spectrum of 15 ppm PrHy after 30 mins adsorption test with 100 to 1000 ppm of FMNP (A), the final concentration of PrHy (ppm) and removal efficiency of 100 to 1000 ppm FMNP (B)

4.5.8 Equilibrium Adsorption study

There are various models used to describe the adsorption behavior, such as Langmuir (a theoretical equilibrium isotherm) and Freundlich (an empirical equilibrium isotherm). The adsorption isotherm of 600 ppm FMNP with 5 to 30 ppm PrHy with the Langmuir model fitting is presented in **Figure 4-11 (A**), while the adsorption data of 600 ppm FMNP and 5 to 100 ppm PrHy were fitted with Freundlich model (**Figure 4-11 (B)**). The Langmuir and Freundlich constant of FMNP are summarized in **Table 4-5**. The Langmuir model was only fitted to the experimental data for PrHy concentration below 30 ppm to satisfy the monolayer adsorption process. At higher PrHy concentration, the adsorption isotherm followed the Freundlich model with "n" close to 1 suggesting a linear adsorption behavior. Since the structure of beta-CD consisted of seven hydroxy groups on the secondary face, thus there might be more than one hydroxy group reacting with CM-β-CD leading to the formation of multiple overlapping CD cavities with steric hindrance effect. These CD cavities were not easily accessible at low PrHy concentration, but at higher concentration, the overlapping CD cavities became accessible for host-guest binding with PrHy with 47 % removal efficiency at 100 ppm PrHy.

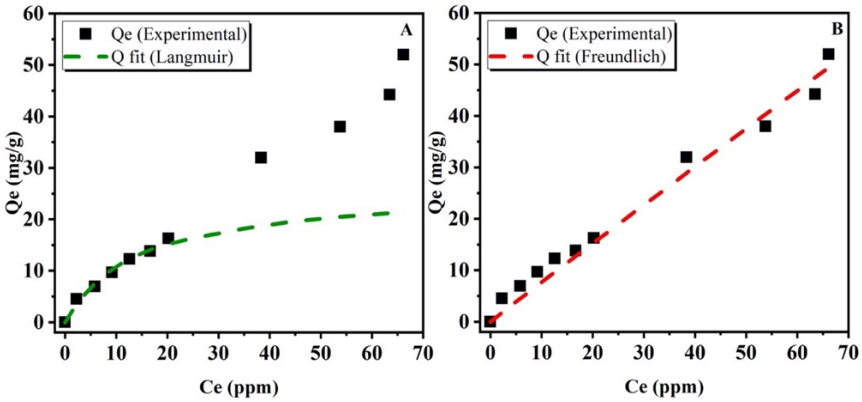


Figure 4-11 Adsorption isothermal of FMNP with 5 to 30 ppm PrHy fitted with Langmuir isothermal (A) and adsorption isothermal of FMNP with 5 to 100 ppm PrHy fitted with Freundlich model are presented in (B)

Table 4-5 Parameters of Langmuir and Freundlich isotherm fitting and the experimental Q_e of 600 ppm FMNP with 5 to 100 ppm PrHy

Samples	Experimental	Langmuir isotherm		Freundlich isotherm		
	Q_e (mg/g)	K_L	R^2 (5-30 ppm)	K_F	n	R^2 (5-100 ppm)
FMNP	53.65	0.073	0.916	0.8	1.02	0.930

Table 4-6 summarizes the adsorption capacity of various types of β-CD systems. β-CD based polymer shows a high adsorption capacity compared to other forms of adsorbent like hydrogel or MNP based adsorbent. However, the β-CD polymer based adsorbent usually requires organic solvent during the complex synthetic steps and large amount of β-CD involved in the polymerization process increased the preparation cost [298][191]. The β-CD modified hydrogel adsorbent possessed almost 10 times lower adsorption capacity compared to polymer-based adsorbent, while it can be easily separated after the water treatment process. The FMNP developed in this study possesses superior equilibrium adsorption capacity (53.65 mg/g) when the initial concentration of PrHy was 100 ppm. This result is much higher than other β-CD grafted magnetic based adsorbent listed in **Table 4-6**. Furthermore, the high magnetization property (33 emu/g) compared with other magnetic based adsorbents and the fast adsorption kinetic that approached an equilibrium within 30 mins enable this novel templated FMNP to be used as a promising adsorbent for removing low concentration contaminants from drinking systems.

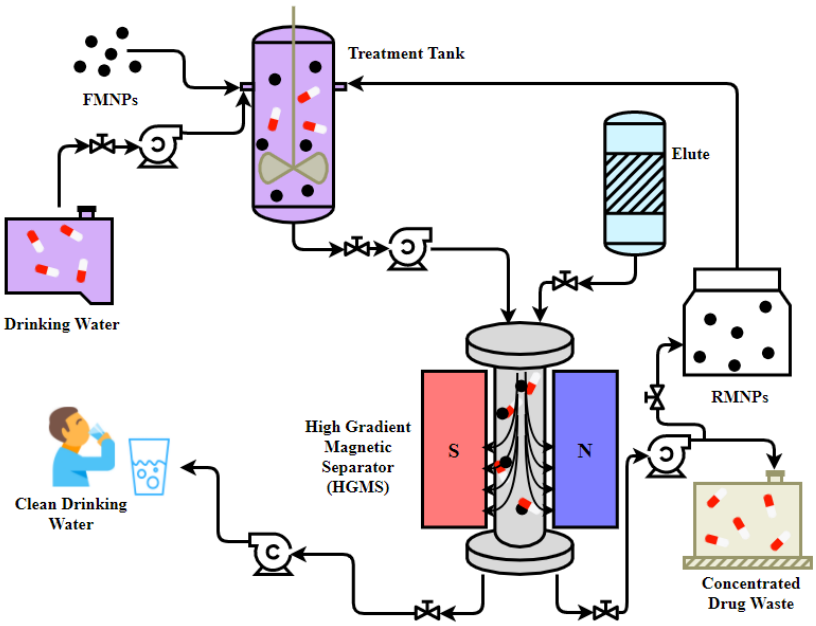
Table 4-6 Adsorption capacity of β-CD based materials

Adsorbent	Contaminates	Type/Structure	Capacity (mg/g)	Mechanism	References
PVA-SS-CD	MB	Polymer resin	187.97	Charge, host-guest	[298]
T-E-CDP	BPA	Polymer	128	Charge, host-guest	[191]
Water insoluble β-CD polymer	Phenol	Polymer	28.49	Host-guest	[299]
Poly-CD/PAA-Azo composite hydrogel	BPA	Hydrogel	19.01-20.73	Charge, H bond, host-guest	[227]
P-CD/PAA-Fc	MB, BPA	Hydrogel	16.96-24.64	Charge, H bond, host-guest	[229]
CDen-MNPs	Carbamazepine, naproxen, BPA	Magnetic particles (57.1 emu/g)	1.1-2.2	Host-guest	[300]
CNC@Fe_3O_4@SiO_2-100@ β-CD	Procaine. HCl	Magnetic particles (5.0 emu/g)	13	Host-guest	[301]
Fe_3O_4@CD MNPs	Co (II)	Magnetic particles (67.9 emu/g)	12.2	External surface site	[302]
POSS-PCL-β-CD/Fe_3O_4	BPA	Hybrid magnetic micelles (6.9 Am^2kg^{-1})	28.4	Host-guest	[303]
Fe_3O_4/AC/CD/Alg polymer beads	MB	Magnetic polymer nanocomposite (1.2 eum/g)	2.079	Host-guest	[304]
Fe_3O_4@ β -CD-CDI	BPA	Magnetic nanocomposite (40 eum/g)	38.4	Host-guest	[180]
FMNP	Procaine. HCl	Magnetic particles (33 emu/g)	53.65	Host-guest	This work

4.5.9 Enrichment process of trace pharmaceuticals from drinking water system

As described previously, the extremely low concentration (ppb to ppm level) of pharmaceuticals existed in drinking water system is very challenging and costly for existing detection technology. The FMNP developed in this study can be applied to an integrate water purification system, which can both concentrate trace pharmaceuticals by up to 100-1000 times and provide purified drinking water to households. The FMNP enhanced water purification system is presented in **Scheme 4-4**. Trace pharmaceuticals contained drinking water (10L) and FMNP can be added to a treatment tank for adsorption, then they can be pumped through the HGMS (switched on). The pharmaceutical included FMNP would be captured inside the HGMS, while the purified clean water passes through. Then, the enriched drug included FMNP can be collected with 10-100

ml eluent, such as ethanol, NaOH or methanol depending on the types of pollutants. After sufficient time for desorption, the FMNP can be recycled by the HGMS washing process. The washing process is described in the supporting information (**S5**). The recycled FMNP together with fresh FMNP would be injected into the treatment tank again for the next round of treatment. By using the isotherm results in **Figure 4-11**, 10 L drinking water contains 100 ppm of PrHy was removed by 47% after 30 mins adsorption with 600 ppm FMNP. After 5 rounds of adsorption test with the same concentration of desorbed FMNP, the 100 ppm PrHy can be reduced to 4.18 ppm. With 10 ml of elution volume for each round, this 10 L 100 ppm PrHy can be enriched to 50 ml of 19164 ppm PrHy solution, which is 191 times enrichment that can be easily detected. The proposed system can effectively remove trace pharmaceuticals from aqueous system and the pollutants can be enriched up to 100-1000 times depending on the elution efficiency and elution volume, thus enable the detection using a simple detection method, such as UV.



Scheme 4-4 Flow chart on the enrichment and purify of trace amounts of pharmaceuticals from drinking water system by employing recyclable FMNP

4.6 Conclusions

Highly stable MAA-EA nanogel scaffolds were synthesized using a one-pot emulsion polymerization process with good control of particle size by varying the amounts of monomer mixture in the seed formation phase. Fe_3O_4 clusters were nucleated within the nanogel scaffold via a in-situ coprecipitation method. A dual-functional silica coating reduced the oxidation of Fe_3O_4 and offers the possibility of surface functionalization of the FMNP. The successful grafting of β-CD onto the silica-coated MNP was confirmed by adsorption tests. A high equilibrium adsorption capacity (53.65 mg/g) was achieved with 600 ppm FMNP and 100 ppm PrHy at pH 8 with a 47% removal efficiency. The kinetic of adsorption was better described with the Pseudo-first order model with a high R^2 (0.98), due to the host-guest physical adsorption process. At higher PrHy concentration, the adsorption isotherm followed the Freundlich model with a n value close to 1 that corresponded to a 1:1 inclusion complexation. The FMNP is a promising adsorbent for removing and concentrating pharmaceuticals in drinking water due to its long-term stability, high dispersity, fast adsorption capacity and easy separation from the aqueous solution. The FMNP can be implemented in a treatment process with a HGMS to capture and enrich trace pharmaceuticals from drinking water system. Future studies will examine the binding isotherm of the FMNP at different pHs, quantification of active CD cavities and the effect of CD loading on the absorption performance. Additionally, a close loop of continuous adsorption, desorption and recycle process using HGMS will be investigated.

Chapter 5: Adsorption Mechanism of β-cyclodextrin Functionalized Magnetic Nanoparticles for the Removal of Procaine Hydrochloride

This chapter is a further study of the FMNP developed in Chapter 4. The nanogel templated magnetic particles functionalized with beta-cyclodextrin (β-CD) (FMNPs) containing low, moderate and high amounts of β-CD (designated as FMNP-L, FMNP-M and FMNP-H respectively) were evaluated for the removal of 5 to 100 ppm procaine hydrochloride (PrHy). The adsorption performance depended on the alignment of CD cavities on the surface of FMNPs, amounts of accessible CD cavities available for binding, and pH. The adsorption isotherm of FMNPs was fitted to the Langmuir and Freundlich models, where the Langmuir model fitting was observed for PrHy below 30 ppm confirming a monolayer surface adsorption. However, the adsorption isotherm fitted the Freundlich model for PrHy between 5 to 100 ppm suggesting the occurrence of multiple-stage adsorption process on CD cavities with different accessibility caused by overlapping or steric hindrance of CM-β-CD. The correlation of CD cavity alignment and adsorption behavior with the β-CD based adsorbent was demonstrated in this study. The adsorption capacity of the FMNP was depended on to the amount of β-CD on the adsorbents, and the steric hindrance of the CD cavities. This study provides a new perspective on the mechanism and the adsorption behavior of β-CD grafted nanomaterial.

5.1 Introduction

Although great effort has be devoted to restoring and reducing traditional pollutants in the environment, other emerging contaminants including pharmaceuticals, hormones, and endocrine disrupting chemicals (EDCs) have persisted due to their persistence in natural environment [305]. The presence of different kind of pharmaceuticals ,such as antibiotics (like procaine hydrochloride, erythromycin, trimethoprim and sulfamethoxazole), analgesics and anti-inflammatory drugs (like

ibuprofen, aspirin and diclofenac), painkillers (like acetaminophen, morphine and tramadol), steroids and hormones in sewage effluents, surface water and finished drinking water have been detected [306]. They may come from human activities like excretion with urine and feces and also inappropriate disposal of drugs [307]. Pharmaceuticals can also be introduced to the environment through agriculture, such as pharmaceuticals used in livestock, poultry and fish farming. Many drugs are frequently used to farm animals to reduce the illness and diseases and to promote the growth of the animals.

Despite their relatively low environmental concentrations (ng/L to mg/L), they are sufficient to cause inappropriate estrogen reaction and reproductive outcomes, such as malformation of sex organ and developmental effects on wildlife. For instance, 40 million condors in Pakistan (95% of the total population) are believed to have died from diclofenac in carcasses of cattle treated with this anti-inflammatory drug [308]. This tragic loss was considered "the worst wild animal poisoning incident in history", which significantly exceeds the dichlorodiphenyltrichloroethane (DDT) bird poisoning incident decades ago. Another case study revealed that very low concentration (e.g., 5-6ng/L) of 17α-ethinyl estradiol (EE2) caused the feminization and destruction of fish population after being introduced to the experimental Lake in Ontario, Canada [309]. There are many problems with emerging contaminants like bioaccumulation, toxicity, and persistence, and often these compounds are difficult to detect, due to the absence of high sensitivity and appropriate instruments. In addition, climate change can intensify their effects by enriching them in rivers during the drought period and resuspending nanomaterials during floods [101]. On the other hand, their effect on the aquatic ecosystem and human beings are not fully known [310].

Emerging contaminants found in the water system can be very different depending on factors such as reactivity, hydrophobicity and biodegradability. Usually, a multi-barrier process is used

simultaneously or sequentially to achieve the water quality standard, since a single step could not eliminate all the contaminants. Currently, the common techniques used to remove contaminants include oxidation (with ozone, chlorine, ferrate (IV) and potassium permanganate) and advanced oxidation processes (AOPs) by UV/H_2O_2 or O_3/H_2O_2 adsorption on powdered activated carbon (PAC), biological activated carbon (BAC) and granular activated carbon (GAC). The contaminants can also be rejected by membrane technologies include reverse osmosis (RO), nanofiltration (NF), microfiltration (MF) and ultrafiltration (UF) [101].

However, the above techniques shows disadvantages in practical applications, such as failure to meet target regulation due to technical limitation, cost, or side products that can be more harmful to the environment [204]. For instance, photolysis and catalytic reduction in pharmaceuticals have been well studied, and many studies have focused on developing advanced catalytic materials. However, metabolites and transformation products resulting from the reaction may be more toxic and biologically active than their parent compounds. This leads to increasing activities to examining the toxicology as well as chemistry, and study the active compounds in a contaminant mixture using effect-based analysis (DEA) [284]. Among all these current water purification technologies, adsorption is the most frequently studied and industrially relevant, since it is cost-effective, reliable, ease to operate and the adsorbents can be regenerated and reused for many cycles [311]. Currently, three types of adsorbents have been widely used in the water treatment plants: carbon based, metal-based adsorbent and polymer-based adsorbent. The adsorption capacity of activated carbon is regarded as the benchmark for a variety of contaminants, since it has fast adsorption kinetics, and high adsorption capacity. However, the high capital cost of regeneration and its contribution to carbon dioxide emission limits its broad adoption [312]. Affordable metal-based adsorbents with robust structure, such as aluminum oxides, manganese

oxides and iron oxides can effectively remove contaminants from water system. However, their slow adsorption kinetics and low adsorption capacity, difficulty in regeneration and low stability reduced their widespread adoption [313]. On the other hand, polymer-based adsorbents display high adsorption capacity, but they usually require complementary separation process, such as membrane thereby increasing their operation cost [102]. While using the polymer-based adsorbent in the form of a sponge may address the issue, but the loss of the high specific area reduces their adsorption capacity [314].

Recently, there is an increasing interest in applying nano-magnetic material for water treatment due to their beneficial characteristics, including high surface to volume ratio, good biocompatibility, low toxicity, ease of modification and excellent magnetic property for separation [315]. Despite the advantages of magnetic materials, size control, aggregation and oxidation are the major challenge as the magnetic material is produced by conventional co-precipitation or hydrothermal techniques.

As an effective adsorbent to remove pharmaceuticals from wastewater, β-cyclodextrin (β-CD) has attracted attention due to its amphiphilic property. β-CD is a cyclic oligosaccharide containing seven glucopyranose units produced from starch by enzyme digestion. The most unique character of β-CD is the truncated cone structure consisting of a hydrophobic cavity and hydrophilic outer shell capable of encapsulating pharmaceutical molecules via a host-guest chemistry [316]. Compared with α and γ cyclodextrin, β-cyclodextrin has the lowest solubility (18.5 mg/ml) [317], which enable an easier purification after usage via precipitation. However, modifying β-CD in a more soluble form is also important, since a more stable form could provide more accessible β-CD cavities in various applications. Also, grafting of β-CD onto a matrix will

promote the recovery of adsorbent and improve the accessibility of the hydrophobic cavities towards pharmaceutical molecules.

A β-CD functionalized on a magnetic particle fabricated from nanogel template was developed in our previous study [273]. The general concept is to synthesize magnetic nanoparticles (Fe_3O_4) within a methacrylate acid-ethyl acrylate (MAA-EA) nanogel scaffold. This strategy successfully addresses the challenge of size and shape control of producing magnetic particles using the traditional co-precipitation method. An optimized silica coating was introduced to minimize oxidation of the magnetic core, and also provided hydroxyl groups for the grafting of β-CD, which was modified with chloroacetic acid to produce carboxymethyl-β-cyclodextrin (CM-β-CD) and grafted onto the silica-coated magnetic nanoparticle to form the functionalized magnetic nanoparticles (FMNP).

In this study, an anaesthetic drug, procaine hydrochloride (PrHy) was used as a model drug to investigate the adsorption performance of FMNP due to its cardiac and neurological toxicity to humans [318]. The effect of different amounts of β-CD loading, and pH effect on the isotherm of FMNP were studied. Also, the quantification of active β-CD cavity at varying concentration of PrHy and pH were investigated, and a new insight on the steric hindrance effect caused by the overlapped structure of β-CD on the adsorption mechanism was reported for the first time.

5.2 Experimental section

5.2.1 Materials

All the materials used in this chapter is same as the chemical used in Chapter 4 (**4.2.1**)

5.3 Methods

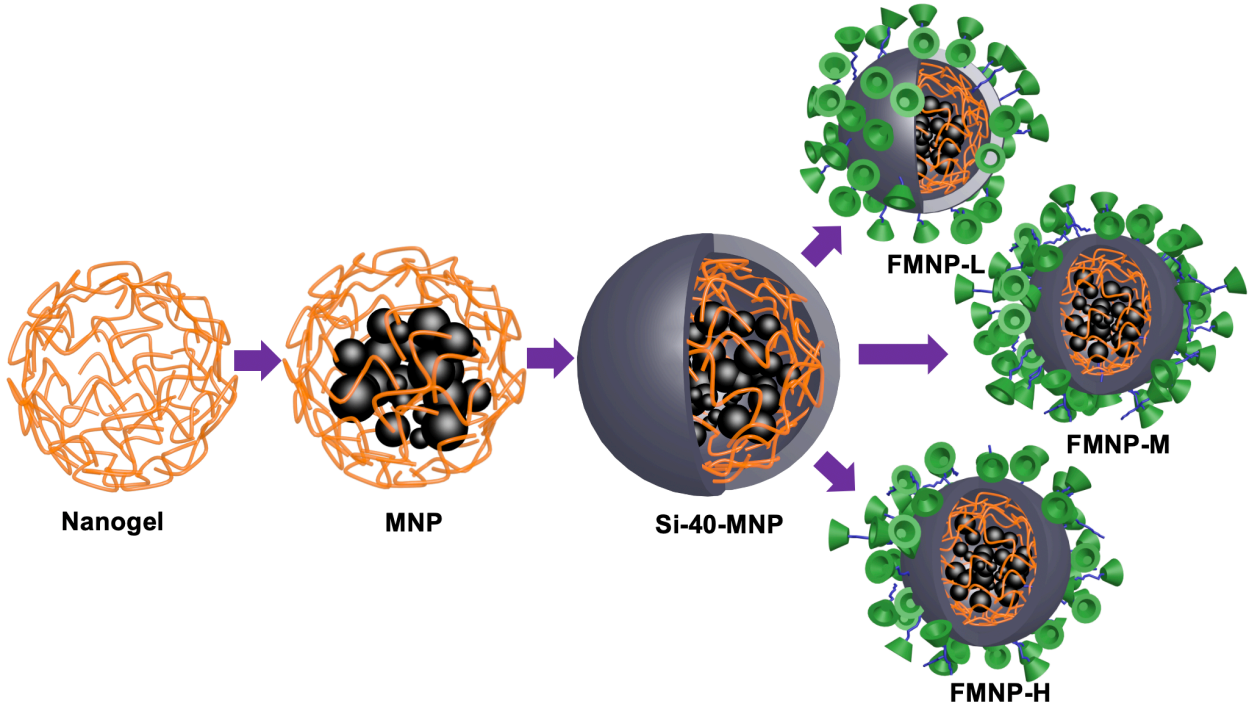
5.3.1 Nanogel preparation

All the material preparation steps were described previously, while the detailed optimization is reported here. In general, the fabrication of FMNP started from the MAA-EA nanogel scaffold that was synthesized by a semi-continuous emulsion polymerization process [319]. A pre-emulsion mixture (13.956 g) was prepared by mixing 4.945 g of MAA and 5.75 g of EA (1:1 molar ratio) together with 8 wt% of DAP, 1 g of AOT solution and water. The reaction vessel contained 120 g water and 1 g of AOT solution. The initiator solution was prepared by dissolving 0.25 g of sodium persulfate in 2 g of water. The initiator solution was added to the reaction vessel after 30 min of purging with nitrogen. After that, the reaction vessel was heated to 85 ℃ and 5 wt% of monomer mixture was added to produce the seed particles, which were formed within 30 min, as indicated by the color change from transparent to light milky color in the reaction vessel. Then, the remaining pre-emulsion mixture was added dropwise and left to proceed for another 30 min. The final product was then cooled to room temperature and filtered through a 200-mesh nylon cloth. The nanogel was then transferred to a 12 to 14 kDa cellulose tubular membrane and dialyzed against de-ionized water until the conductivity of the dialysis water remained constant.

5.3.2 Magnetic nanoparticles (MNPs) preparation

Magnetic nanoparticles were synthesized by in-situ coprecipitation of ferrous ions inside the nanogel template. 120 mL of 0.5 wt% MAA-EA nanogel suspension was prepared from the nanogel stock solution, and the pH was adjusted to 6.5 using 0.5M NaOH. After that, 2.5 g of $FeSO_4 \cdot 7H_2O$ was dissolved in 30 mL of de-oxygenated water and added dropwise to the reaction vessel that was purged nitrogen for 30 min. Fe^{2+} would chelate with the deprotonated COO^- groups of MAA under gentle mechanical stirring (250 rpm) for 2 hours. Afterwards, ultrafiltration under nitrogen was applied to remove the un-coordinated Fe^{2+} yielding a brownish colour in the filtrate

solution. The ultrafiltration was conducted several times until all the un-coordinated Fe^{2+} was removed as confirmed by the clear filtrate solution. The Fe^{2+} grafted nanogel (Fe^{2+}-nanogel) was heated to 35℃ under stirring, and 1 g of 25 wt% $NaNO_2$ solution and 15 mL of 28 wt% NH_4OH was added to the reaction vessel yielding a dark green dispersion. Within 1 hour, the reaction was completed by the color changed in the solution from green to black. The synthesized MNPs were washed several times using deoxygenated DI water through the High Gradient Magnetic Separator (HGMS) until the washed liquid was clear, and the solid content of the MNPs product was approximately 0.1 wt%.



Scheme 5-1 Schematic illustration of in-situ synthesis magnetic nanoparticles inside MAA-EA nanogel scaffold and the synthesize of FMNP-L, FMNP-M and FMNP-H

5.3.3 Silica coating of MNPs

A thin layer of silica shell was coated outside the nanogel to prevent the oxidation and provide functional groups for further modification. 20 mL of 0.1 wt% MNPs solution was

dispersed in 80 mL of ethanol solution, and then 5 mL ammonia solution and 40 μL of TEOS were added dropwise to the MNP solution. The reaction proceeded under mechanical stirring at room temperature for 24 hours and then purified by washing using the HGMS.

5.3.4 Grafting of CM-β-CD onto Si-40-MNP

The synthesis CM-β-CD is described in the supporting information (**S1**). Three different amounts CM-β-CD were grafted to the FMNP particles yielding FMNPs with different adsorption capacities. Three aliquots of 250 mg of Si-40-MNPs were mixed with 5 mL of phosphorous buffer (pH 6) in three vials and sonicated for 40 min. Then, 31.25 mg of cyanamide dissolved in 1.25 ml of phosphorous buffer solution was added dropwise to each reaction vessel. After 40 min of sonication, 187.5, 375 and 562.5 mg of CM-β-CD dissolved in 6.25 ml of phosphorous buffer solution respectively were added dropwise to each reaction vessel. The mixture was sonicated for another 90 min and then washed several times with buffer solution and collected by Milli-Q water to yield CM-β-CD functionalized MNPs-Si-40 (FMNPs). These three FMNPs loaded with 187.5, 375 and 562.5 mg of CM-β-CD was designated as FMNP-L, FMNP-M and FMNP-H. The mass ratio of CM-β-CD added in the synthesis FMNP-L, FMNP-M and FMNP-H were 0.5:1:1.5, and **Scheme 5-1** illustrate the synthesis of FMNP-L, FMNP-M and FMNP-H.

5.4 Characterization Methods

Morphologies of the MAA-EA nanogel template, MNP, Si-40-MNP and FMNPs were examined by the Philips CM10 transmission electron microscope (TEM) at an accelerating voltage of 60 kV. The TEM samples were prepared by placing one drop of 0.02 wt% solution onto a 200-mesh carbon-coated copper grid. The dried nanogel sample was stained with uranyl acetate and lead citrate, since pure nanogel is not visible under TEM. The FTIR of MAA-EA nanogel, Si-MNPs, β-CD, CM-β-CD, and FMNP-H were prepared in the KBr pellet and measured in a Bruker

Tensor 27 spectrometer (Bruker, Billerica, MA, USA) between 4000 to 400 cm^{-1} at room temperature. The test specimens were prepared by compressed freeze-dried samples with KBr powder into a pellet. Dynamic light scattering (DLS) measurements were used to determine the size of nanogel, MNP, Si-MNP FMN-L, FMNP-M and FMNP-H. by measuring 0.1 wt% dispersion at pH 7 in a Zeta-Sizer (Nanosizer ZS, Malvern Co., UK) at 25 °C. Zeta-Sizer (Nanosizer ZS, Malvern Co., UK) was also used to determine the zeta potential of the dispersions by measuring the charge density on the surface of the material at 25 °C. Different samples were prepared at 0.1 wt% and adjusted to pH 7 using 0.1 M NaOH or 0.1 M HCl. The chemical composition of MNP, Si-40-MNP, FMNP-L, FMNP-M and FMNP-H was studied in a TGA Q500 (TA instrument) from 100 ℃ to 600 ℃ under nitrogen at a heating rate of 10 ℃/min. The magnetization of MNP, Si-MNP, FMNP-L, FMNP-M and FMNP-H was quantified in a vibrating sample magnetometer (VSM 880) using a superconducting quantum interference device (SQUID) test operated from -1T to 1T at 300K.

5.5 Adsorption experiments

5.5.1 Concentration screening of FMNP-L, FMNP-M and FMNP-H

Prior to the adsorption isotherm analysis of FMNP-L, FMNP-M and FMNP-H, concentration screening tests were performed to identify the optimum concentration for the isotherm adsorption measurements. The concentration screening tests were conducted in 20 ml vials, where 3 ml of the FMNP-L, FMNP-M and FMNP-H stock solution was added to 100, 300, 500, 600, 700 and 1000 ppm FMNP solution respectively. The pH was adjusted to 8.0 using 0.01M NaOH prior to the addition of PrHy stock solution to achieve a concentration of 15 ppm. The adsorption kinetic was reported previously, and the results showed that equilibrium could be achieved within 30 minutes. Thus, all the concentration screening tests were performed by placing the adsorption mixture on

the shaker for 30 minutes. The mixture was then separated by a magnet, filtered with a 0.22 μm PES syringe filter and analyzed using the UV-Vis spectrophotometer. Equilibrium adsorption capacity Q_e and removal percentage R (%) were determined from Eq. (5.1) and (5.2) respectively:

$$Q_e = \frac{(C_0 - C_t) * V}{m} \quad (5.1)$$

$$R\ \% = \frac{(C_0 - C_t)}{C_0} * 100 \quad (5.2)$$

where, C_0 (mg/L) is the initial concentration of PrHy in the adsorption mixture; C_t is the remaining concentration of PrHy at time t (min or s); V (L) is the total volume of adsorption mixture; Q_e (mg/g) is the adsorption capacity at equilibrium and m represented the mass (g) of FMNP-L, FMNP-M and FMNP-H used for the adsorption test; R (%) is the removal percentage of the PrHy from the initial concentration.

5.5.2 pH effect on isotherm adsorption of PrHy with FMNP-L, FMNP-M and FMNP-H

The adsorption isotherm tests were conducted in 20 ml vials, and in each vial, 3 ml of FMNP-L, FMNP-M and FMNP-H stock solution was added to 600 ppm of FMNPs solution. The pH was adjusted to 6.5, 8.0 and 9.5 using 0.01 M HCl or 0.01 M NaOH prior to the addition of the PrHy stock solution to achieve an initial concentration ranging from 5 to 100 ppm. The solution mixtures were left on a shaker for 30 min of equilibration, and subsequently separated with a magnet, filtered through a 0.22 μm PES syringe filter, and analyzed with the UV-Vis spectrometer. The adsorption isotherm results were fitted to the nonlinear form of the Langmuir and Freundlich isotherm models, as described by Eq. (3) and (4) respectively [312]:

$$Q_e = \frac{Q_m K_L C_e}{1 + K_L C_e} \quad (5.3)$$

$$Q_e = K_F C_e^{\frac{1}{n}} \quad (5.4)$$

where Q_m (mg/g) is the maximum adsorption capacity of the adsorbent; K_L (g/L) is the Langmuir adsorption equilibrium constant that indicated the binding energy between the adsorbate and the adsorbent; K_F (mg/g) and n are Freundlich constant, which describes the binding intensity and the spontaneity of the adsorption process.

5.3 Results and discussion

5.3.1 Fourier-transform infrared spectroscopy (FTIR)

FTIR analysis was used to confirm the successful modification of CM-β-CD and the chemical composition of absorbents. The FTIR results of β-CD, CM-β-CD, nanogel, Si-40-MNP and FMNP-H is shown in **Figure 5-1**, where the broad peak between 3300 and 3500 cm^{-1} is associated with the -OH stretching. R-1, 4 bond skeleton vibration originated from β-CD reflected a characteristic peak at 940 cm^{-1}, which appeared on both β-CD and CM- β-CD FTIR spectrum. The C=O stretching at 1748 cm^{-1} was observed after β-CD was reacted with chloroacetic acid confirming the successful carboxymethylation of β-CD. The characteristic peak of Si-O-Si stretching between 418 to 478 cm^{-1} was observed in Si-40-MNP and FMNP-H due to the formation of silica shell via TEOS hydrolysis on the MNP. The formation of Fe_3O_4 within the nanogel was confirmed by the Fe-O vibration (561 cm^{-1}) in Si-40-MNP and FMNP-H. Therefore, we concluded that β-CD was converted to CM-β-CD and grafted onto silica coated nanogel MNP particles.

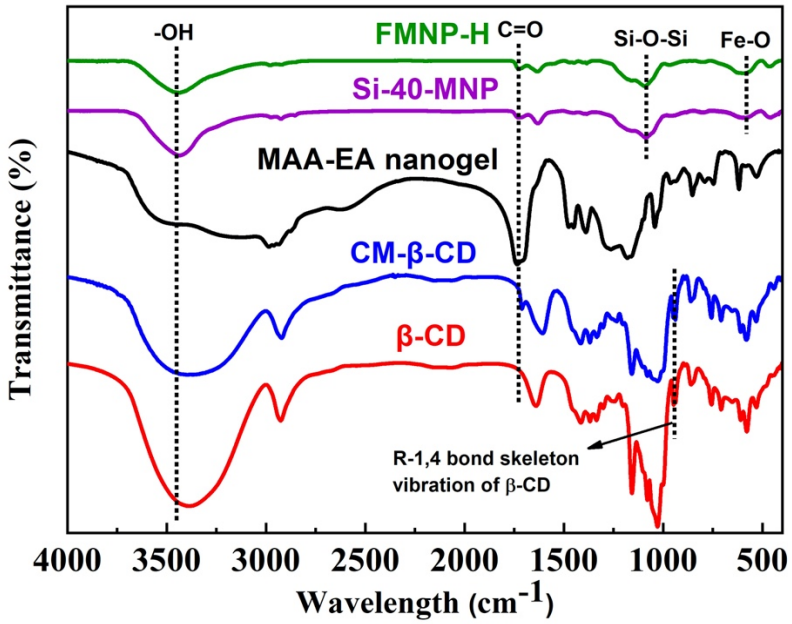


Figure 5-1 FTIR of β-CD, CM-β-CD, nanogel, Si-40-MNP and FMNP-H

5.3.2 Morphology investigation

The MAA-EA nanogel template was prepared by emulsion polymerization, and MNP was prepared by in-situ coprecipitation of ferrous ions chelated to COO^- groups on the nanogel. The FMNPs were produced by grafting CM-β-CD onto Si-40-MNP. Morphology of the synthesized material was examined using the TEM, and only the nanogels were stained with lead citrate, while all other TEM images were obtained from unstained samples. The TEM images of MAA-EA nanogel, MNP, Si-40-MNP and FMNP are shown in **Figure 5-2**, where well-defined and uniform spherical particles of diameter were observed from **Figure 5-2** (**A**). Magnetic particles (MNP) existed as clusters of Fe_3O_4 particles being encapsulated within the spherical nanogel scaffold is shown in **Figure 5-2** (**B**). The margins among neighbouring MNPs confirmed the presence of nanogel scaffold, which effectively prevented the aggregation of the MNPs. The coarse edge of the MNP was due to large amount of Fe_3O_4 generated inside the nanogel and expand the nanogel into a "litchi" structure.

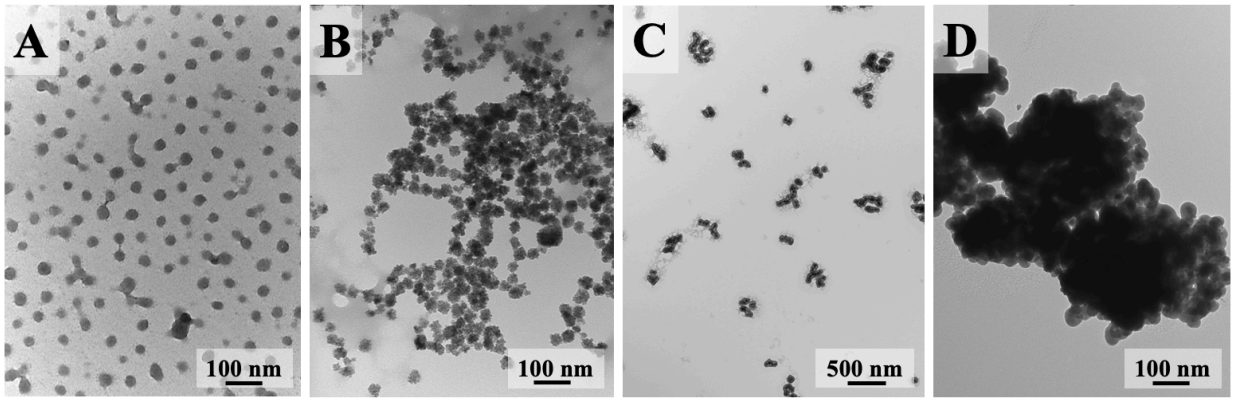


Figure 5-2 TEM images of (A) MAA-EA nanogel; (B) MNP; (C) Si-40-MNP; (D) FMNP-H

The optimization of different amounts of silica coated on MNP was conducted in our previous study, confirming that 40 μL TEOS was sufficient to coat the MNP. Most of the silica shell contained only one magnetic core and no aggregation was observed in the Si-40-MNPs (**Figure 5-2**, **C**). β-CD functionalized MNP (FMNP-H) is shown in **Figure 5-2** (**D**), revealing a dark magnetic core with light grey circles on the surface of the particles. The superimposed light gray circles were due to β-CD cavity grafting, similar structures were on the modified β-CD particles [320] [321]. However, the FMNP appeared to be larger due to the aggregation during the TEM preparation step. The rationale for this aggregation could be related to the carboxymethyl functionalization of β-CD due to the many active hydroxy groups on both the primary face and secondary face of β-CD that could react with chloroacetic acid. Even though the primary hydroxyl groups located at the 6-position have proved to be more reactive than the secondary hydroxyl groups due to the more nucleophilic nature, the seven primary hydroxyl groups still can be modified with equal chances [322][323]. Therefore, multiple primary hydroxyl groups can be modified to carboxymethyl groups and further grafted onto the Si-40-MNP, resulting in non-homogeneous distribution on the surface of FMNP. Moreover, the CM-β-CD modified by multiple

carboxymethyl groups could be grafted onto different Si-40-MNPs resulting in the agglomeration of the FMNP-H. Another possibility of the aggregation is the magnetic attraction between the FMNPs, especially when they are in proximity to each other. However, the large amounts of CD cavities were still grafted on the FMNP-H, illustrated by numerous grey circles located on the surface of FMNP-H and also confirmed by the Thermogravimetry Analysis (TGA) discussed in later section. Thus, the adsorption experiments were further performed to investigate the relationship between the amounts of β-CD conjugated to the FMNP and their effects on adsorption performance.

5.3.3 Particle size and stability

Size, morphology and surface charge of adsorbent particles are closely associated with their stability and adsorption performance. The nanogel template was prepared by a semi-continuous emulsion polymerization, and the control of the particle size was achieved by varying the size and number of seeded nanogel particles as described previously [273]. Particle size and zeta potential of the nanogel, MNP, Si-40-MNP and FMNPs (FMNP-L, FMNP-M and FMNP-H) are shown in **Figure 5-3**. The diameter of MNP was 287.57 ± 8.29 nm, which was much bigger than the size of the nanogel (190.73 ± 1.04 nm) due to the Fe_3O_4 nanoclusters that expanded the nanogel scaffold. A slight increase of the particle size of Si-40-MNP was evident due to the silica coating. However, the grafting of CM-β-CD resulted in a significant increase in the particle size since multiple β-CDs could be grafted onto several FMNPs as indicated in **Figure 5-2**, **D**. There was no obvious difference between the particle size of FMNP-L, FMNP-M and FMNP-H, since the size of β-CD was between 0.60-0.65 nm [324], which would not contribute to the final particle size. The abundant carboxyl groups on the surface of the nanogel generated a large and negative zeta potential of -50.13 ±1.21 mV, which ensured the high stability of the nanogel scaffold. The zeta

potential decreased after Fe_3O_4 was formed inside the scaffold caused by the coordination between the COOH groups and Fe_3O_4 particles. The silica coating further shielded the negative surface charge, where the zeta potential decreased slightly from -36.3 ± 0.92 mV to -33.3 ± 1.04 mV, as the hydroxyl groups from TEOS hydrolysis replaced the COOH groups on the surface of the nanogels. After the grafting of CM-β-CD on Si-40-MNP, it provided steric stabilization to the FMNP that enhanced its stability. An additional benefit of the scaffold method is that the size of the FMNPs is dependent on the nanogel dimension, which provided us a better control on the final morphology of the FMNPs.

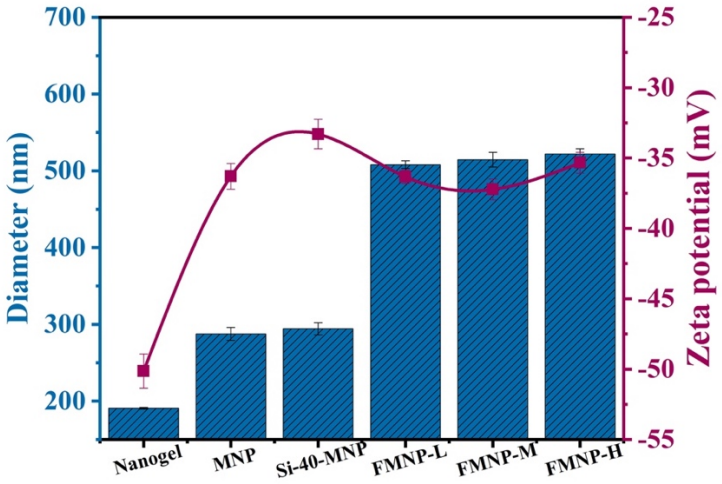


Figure 5-3 The particle size and zeta potential of nanogel, MNP, Si-40-MNP and FMNPs at neutral pH

5.3.4 Chemical composition

Thermogravimetric analysis (TGA) was conducted to investigate the chemical composition of present in the MNP, Si-40-MNP and FMNP. The TGA curves are shown in **Figure 5-4**, where the weight loss between 100 ℃ and 200 ℃ was attributed to the evaporation of water adsorbed on the particles [325]. The weight loss of MNP from 200 ℃ to 400 ℃ was due to the degradation of

the nanogel scaffold, and the non-calcinated inorganic residue left after 400 ℃ was associated with Fe_3O_4. The MNP composed of 1.05% water, 13.83% nanogel and 85.12% magnetic content. The degradation of β-CD was related to the distinct region of weight loss at 300 ℃ and 360 to 367 ℃, which was confirmed to be the degradation temperature of the sugar unit on β-CD [326]. The content of β-CD consisting in FMNP-L, FMNP-M and FMNP-H was determined to 0.55, 1.74 and 0.77 wt%. Surprisingly, the amounts of β-CD grafted onto the FMNPs did not follow the trend that corresponded to the amounts of CM-β-CD added during the synthesis. We believe this might be due to the amount of hydroxyl groups on the silica shell and the steric hindrance of β-CDs when excess CM-β-CD was used as in the case of FMNP-H. Moreover, excess added during the grafting reaction would cause a self-crosslinking of CM-β-CD [327], which was washed out during the HGMS purification due to non-magnetic property. The amount of water, nanogel, Fe_3O_4, silica and β-CD present in each of the FMNPs are summarised in

Table 5-1.

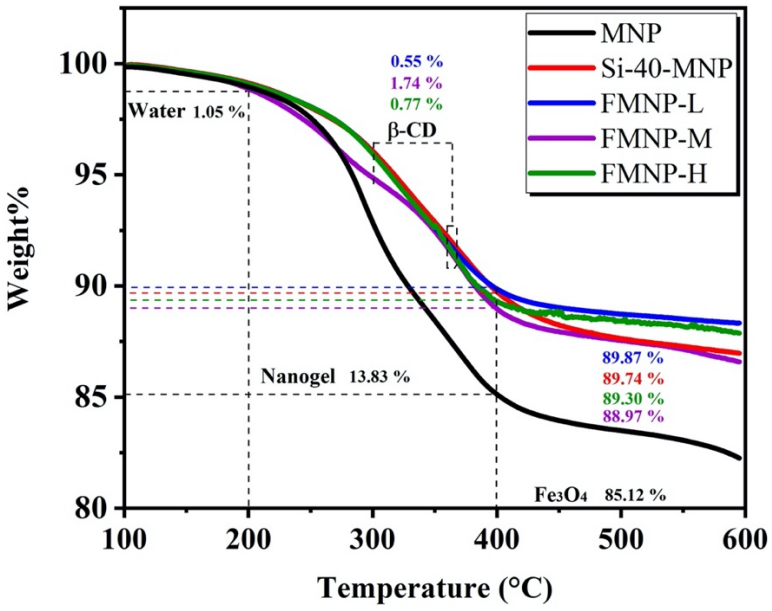


Figure 5-4 TGA curves of MNP, Si-40-MNP, FMNP-L, FMP-M and FMNP-H

Table 5-1 Chemical composition (in wt%) in MNP, Si-40-MNP, FMNP-L, FMNP-M and FMNP-H

Component	MNP	Si-40-MNP	FMNP-L	FMNP-M	FMNP-H
Water	1.05	0.87	0.91	1.14	0.91
Nanogel	13.83	9.37	8.57	8.04	8.88
Fe_3O_4	85.12	89.74	89.87	88.97	89.30
Silica	0	0.02	0.14	0.11	0.14
β-CD	0	0	0.55	1.74	0.77

5.3.5 Magnetization of magnetic nanoparticles

The magnetic property of MNP, Si-40-MNP, FMNP-L, FMNP-M and FMNP-H was studied using the VSM 880 equipment, and the magnetic hysteresis loop of MNP, Si-40-MNP FMNP-L, FMNP-M and FMNPH are shown in **Figure 5-5**. The saturation magnetization value (Ms) of MNP, Si-40-MNP, FMNP-L, FMNP-M and FMNP-H were 52.36, 26.44, 36.96, 30.98 and 31.82 emu/g, respectively. No hysteresis loop was evident, indicating a zero coercivity, and the high Ms value of FMNPs illustrated a good superparamagnetic property. The Fe_3O_4 clusters generated inside the nanogel occupied a large volume compared to individual Fe_3O_4 particles resulting in the high magnetization since this is proportional to the volume of the magnetic content. After the silica coating on the MNP, the magnetic property decreased slightly, which further confirmed the success of the TEOS coating process. The Ms value of FMNPs was higher than Si-40-MNP due to the different washing process used to remove un-coordinated iron oxide. MNP and Si-40-MNP were washed by pumping the solution through the steel wool placed inside the HGMS column. However, the purification process for FMNPs were accomplished by placing the vials with FMNPs on top of the HGMS, as the high concentration of synthesized FMNPs (due to the reaction conditions) might clog and bind in steel wool. The supernatant was removed following a 3-minute separation on HGMS, and the collected FMNPs were re-dispersed in water and separated again with the HGMS. This step was repeated 3 times to ensure that any the residue chemicals were eliminated.

Steel wool was widely used as a carrier matrix to produce a higher magnetic gradient to capture low magnetization magnetic nanomaterials during the running of the HGMS [297], whereas the lack of steel wool during the FMNP washing step caused a lower applied magnetic field. Thus, a lower magnetic field applied during the washing of FMNP led to a higher magnetizing product, where the Ms value of FMNP was greater than Si-40-MNP [273]. The Ms value of FMNP-M and FMN-H were 30.98 and 31.82 emu/g, which was lower than FMNP-L (36.96 emu/g). The increase in the amount of β-CD portion decreased the magnetic content in the composite, which is also consistent with the results determined from the TGA analysis. In conclusion, the high Ms value and superparamagnetic property of FMNPs provided a rapid separation after the adsorption, which could reduce the energy cost in the water treatment process.

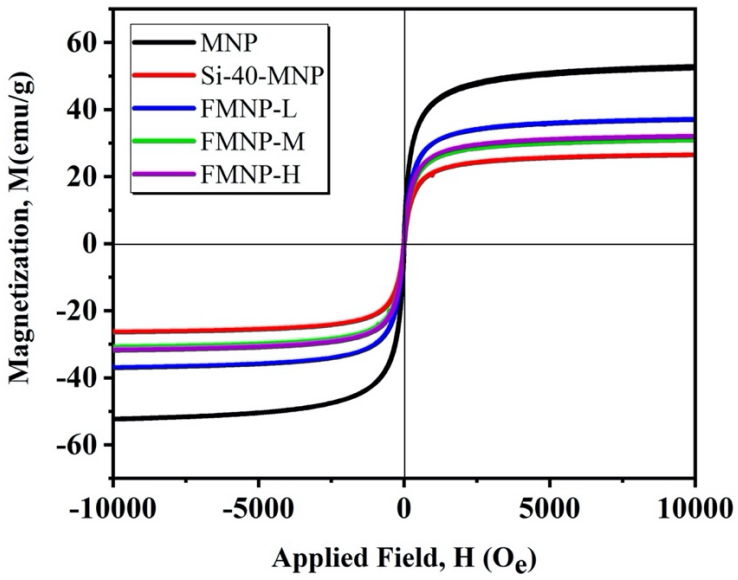


Figure 5-5 The magnetic hysteresis loops of MNP, Si-40-MNP, FMNP-L, FMNP-M and FMNP-H obtained by SQUID at 300K between -1T and 1T

5.3.6 Concentration screening of FMNP-L, FMNP-M and FMNP-H

An adsorption kinetic study was conducted to investigate the equilibrium time for the adsorption between FMNP-M and 15 ppm PrHy. The parameters for the adsorption data was fitted to the Pseudo-first order and Pseudo-second order models as described in chapter 4 (**4.5.6**). The results revealed a fast physical adsorption kinetic reaching an equilibrium within 30 min, which is consistent with previous reported studies [328][329][134][330][331]. Subsequently, the optimum concentration for the adsorbent (FMNP-L, FMNP-N or FMNP-H) was identified based on the binding experiments to remove 15 ppm of PrHy at pH 8. The final concentration of PrHy (ppm) after 30 min adsorption tests with 100 to 1000 ppm of adsorbents is presented in **Figure 5-6 (A**), and the removal (%) of PrHy is shown in **Figure 5-6 (B)**. The final concentration of PrHy decreased gradually to an asymptotic value when the concentration of FMNP-L, FMNP-M and FMNP-H was increased to 600 ppm. Low concentration of adsorbents provided a limited amount of adsorption sites, the PrHy concentration reduced dramatically as the increase of the adsorbent concentration. Further increase the concentration of FMNPs over 600 ppm, resulting in a slighted decline in PrHy residual concentration, since concentration of PrHy in the bulk solution was low and was not able to reach the CD cavities with huge steric hindrance. Thus, 600 ppm was selected as the proper concentration for later adsorption isotherm experiments. Surprisingly, FMNP-L was the most effective adsorbents, where the lowest amount of CM-β-CD was added during the synthesis of FMNPs. Also, the TGA results shown that FMNP-L has lowest weight percentage (0.55 %) of β-CD compared with FMNP-M (1.74 %) and FMNP-H (0.77 %). This result can be attributed to variations of the accessibility of the CM-β-CD cavities on FMNP-L, FMNP-M and FMNP-H. Even though the FMNP-L possess lowest quantity of β-CD, while they may arranged loosely on the FMNP-L without severe steric hindrance. However, FMNP-M and FMNP-H has

more β-CD grafted lead to severe steric hindrance caused low removal efficiency of PrHy compared with the same concentration of FMNP-L.

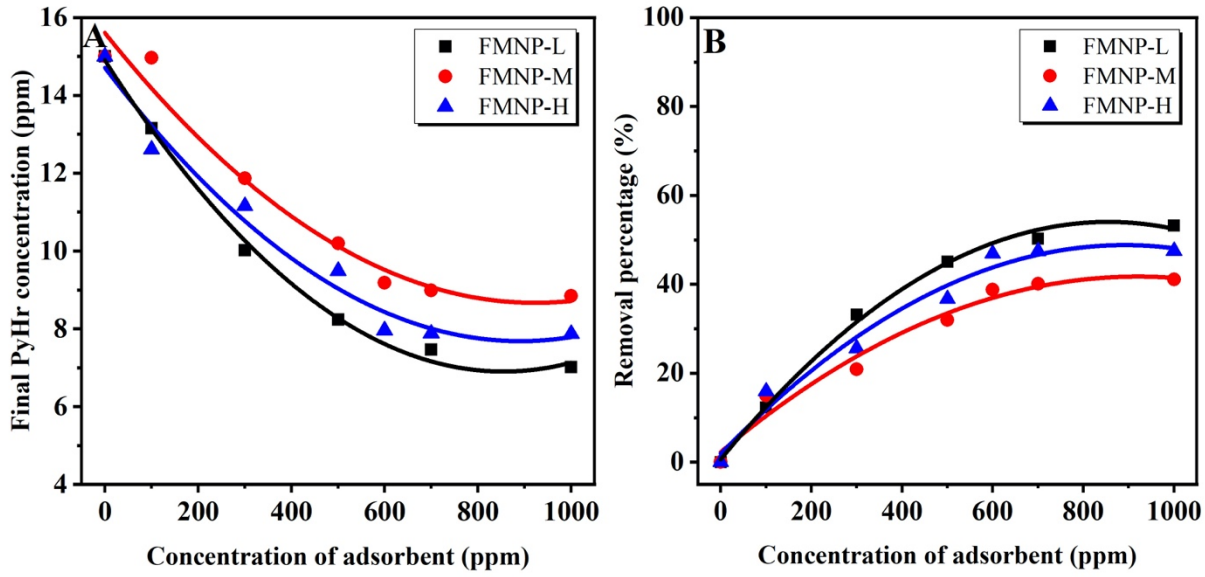


Figure 5-6 The final concentration of PrHy (ppm) (A), and the removal (%) of PrHy (B) after 30 mins adsorption with 100-100 ppm of FMNP-L, FMNP-M and FMNP-H

5.3.7 Equilibrium Adsorption study

Due to the increasing industrial and manufacturing activities, the treatment and discharge of pollutants from these industries are gathering increasing attention. The adsorption isotherm for PrHy on FMNP-L, FMNP-M and FMNP-H adsorbents were investigated, and the adsorption data were fitted to the Langmuir and Freundlich models to evaluate the adsorption mechanisms. The effect of pH on the adsorption isotherm were examined to understand how the binding interactions between the adsorbent and the adsorbate were affected by pHs. The absorbents were analyzed by fitting the data to the Langmuir and Freundlich models, which could provide useful information to elucidate the interactions between the adsorbate molecules and the surface of the adsorbent. The Langmuir isotherm describes a single layer adsorbent covering the adsorbent surface, where the interaction between adsorbent and adsorbate is driven by weak physical forces such as van der

Waal forces [332]. The Langmuir model is based on several hypotheses, such as all adsorption sites possess the same adsorption energy to bind molecules with finite adsorption sites. There are no interactions between the adsorbate molecules and only one layer adsorption occurs on the surface of the adsorbent. Another commonly used empirical adsorption model is the Freundlich isotherm model, which is used to describe a physical-chemical adsorption process between adsorbate and adsorption sites on heterogeneous surfaces [312]. Furthermore, the Freundlich model describes the adsorption process occurring on multiple layers, where the adsorbed molecules can also act as an adsorption site due to its affinity to other pollutant molecules [108]. It has been well documented that the adsorption between β-CD cavities and pollutant molecules is due to the formation of organic molecule-CD inclusion complex. However, there is limited studies that examine the relationship between the orientation of CD cavities grafted on the adsorbent surface and their effect on adsorption performance. Here, three absorbents, i.e. FMNP-L, FMNP-M and FMNP-H adsorbent was prepared with 0.5:1:1.5 mass ratio of CM-β-CD, and their adsorption performance were evaluated.

The fitting of the adsorption isotherms for 5 to 100 ppm of PrHy by FMNP-L at pH of 6.5, 8.0 and 9.5 were fitted to Langmuir and Freundlich isotherm as shown in **Figure 5-7** (**A**, **B**, **C**). At pH of 6.5, the adsorption could only fit to the Langmuir isotherm at PrHy concentration below 30 ppm, while the Freundlich model could describe all the concentration range. This is due to the different accessibility of CD cavities at lower or higher concentration of PrHy. At low concentration of PrHy, only steric unimpeded β-CD cavities are accessible that exhibit a monolayer adsorption behavior. A further increase in PrHy concentration results in a greater driving force (concentration difference) for including PrHy molecules into the cavities located with greater steric hindrance. β-CD possesses a hydrophobic inner cavity and a hydrophilic outer shell

and is capable of capturing pharmaceuticals via the host guest interaction. At elevated PrHy concentration, a smaller distance between the PrHy molecules and FMNP particles lead to the replacement of the water molecules with PrHy molecules in the CD cavities. Also, β-CD possess seven identical primary hydroxyl groups on the primary face, which has an equal probability of being modified. Thus, the FMNP-L could have a structure comprising of CD cavities with different accessibility due to the overlapping of multiple carboxymethyl group modified β-CD. When the PrHy concentration was low, only surface β-CD cavities were accessible as the driving force for the PrHy-CD inclusion complex was the physical forces (hydrophobic interaction). Hence, the adsorption at low PrHy concentration (5 to 30 ppm) could be described by the single-layer isotherm Langmuir model. When the concentration of PrHy was increased, the CD cavities located close to the inner surface of FMNP-L or within the channels of the silica shells became accessible due to the higher driving force for diffusion resulting from the higher concentration difference of PrHy between the bulk solution and the inner structure of FMNP-L. However, when the pH of the adsorption system was 8.0 and 9.5, the adsorption isotherm data could not fit the Langmuir model even at low PrHy concentration, where the fitting yielded a negative slope. This result is consistent with the adsorption isotherm study of Ibuprofen and β-CD grafted chitosan, where a negative slope was reported for the Langmuir isotherm model [333]. This non-monolayer adsorption behavior could be related to the alignment of CD cavities on the surface of FMNP-L, where the amounts of CM-β-CD grafted onto the surface of FMNP-L might be insufficient to fully cover the surface of adsorbent. The experimental data and the parameters from the Langmuir and Freundlich isotherm models of FMNP-L, FMNP-M and FMNP-H are summarized in **Table 5-2**.

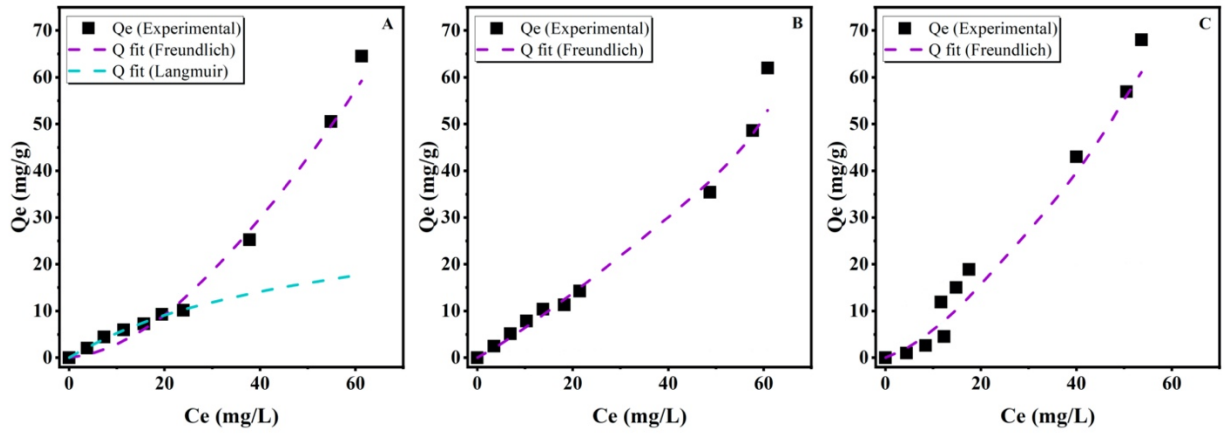


Figure 5-7 The adsorption isotherm of FMNP-L at pH 6.5 (A), 8.0 (B) and 9.5 (C) fitted with Langmuir and Freundlich isotherm model

The adsorption isotherm for 5 to 100 ppm of PrHy at pH 6.5, 8.0 and 9.5 and FMNP-M were fitted to Langmuir and Freundlich isotherm as shown in **Figure 5-8**. As in FMNP-L, the adsorption data could be fitted to both Langmuir and Freundlich isotherm model at a low PrHy concentration (5 to 30 ppm), while only Freundlich model could fit the whole concentration range of 5 to 100 ppm. The Qe value (C_0=100 ppm) increased gradually with pH (from 6.5 to 9.5), since PrHy is a positively charged molecule that could bind to negative charge surfaces. Hence, more PrHy could be adsorbed at higher pH due to the electrostatic interaction and the formation of CD-PrHy inclusion complex. When the PrHy concentration exceeded 30 ppm, more PrHy molecules were removed from the aqueous system with 600 ppm FMNP-M, rather than achieving the equilibrium as predicted by the Langmuir model. The higher PrHy concentration led to a higher driving force for the host-guest complexation between PrHy molecule and CD cavities located near the MNP core that was impeded by steric hindrance. Similar adsorption behavior was reported for FMNP-H (**Figure 5-9**), confirming a better fitting with Freundlich isotherm at higher PrHy concentration. However, the adsorption equilibrium (C_0=100 ppm) of FMNP-H was lower compared to FMNP-M, due to the lower β-CD content on to FMNP-H (0.77 wt%) compared to FMNP-M (1.74 wt%).

The adsorption capacity of FMNP-L (C_0=100 ppm) was also higher than FMNP-H, even though the β-CD content on FMNP-L (0.55 wt%) was lower than FMNP-H (0.77 wt%). Thus, we concluded that the adsorption performance was rather complex, and it is based on multiple factors such as the amount of available CD cavities, initial concentration of PrHy, coverage of CD cavities on the surface of the FMNP, steric hindrance between the CD cavities and the pH of the adsorption system. This also illustrates that there is an optimum condition between the amounts of CD grafted on the FMNPs and the adsorption capacity. Once more CD cavities were loaded to the FMNPs, steric hindrance might reduce the accessibility of the CD cavities and consequently reduced the adsorption capacity. A schematic illustration of the adsorption mechanism between FMNPs and PrHy molecules is shown in **Scheme 5-2**.

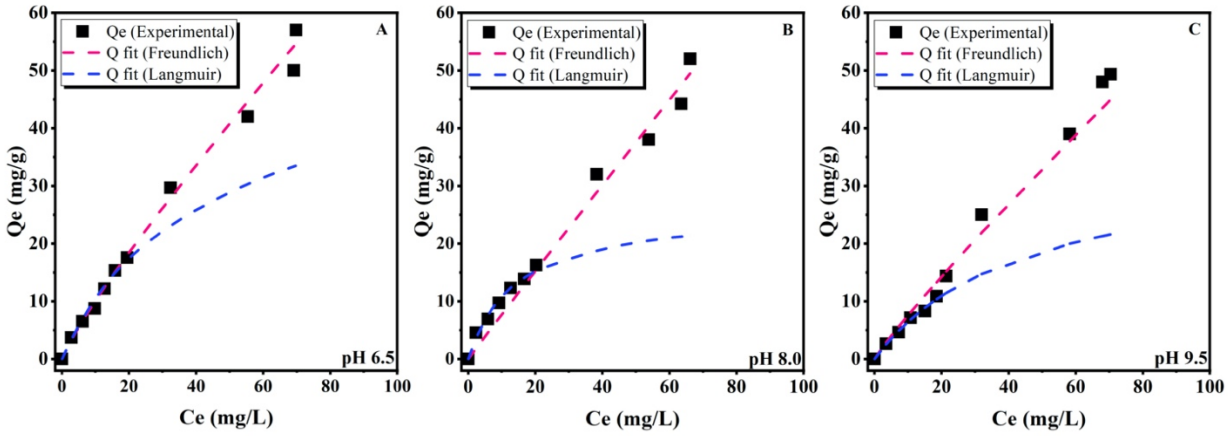


Figure 5-8 The adsorption isotherm of FMNP-M at pH 6.5, 8.0 and 9.5 fitted with Langmuir and Freundlich isotherm model is shown in A, B and C, respectively

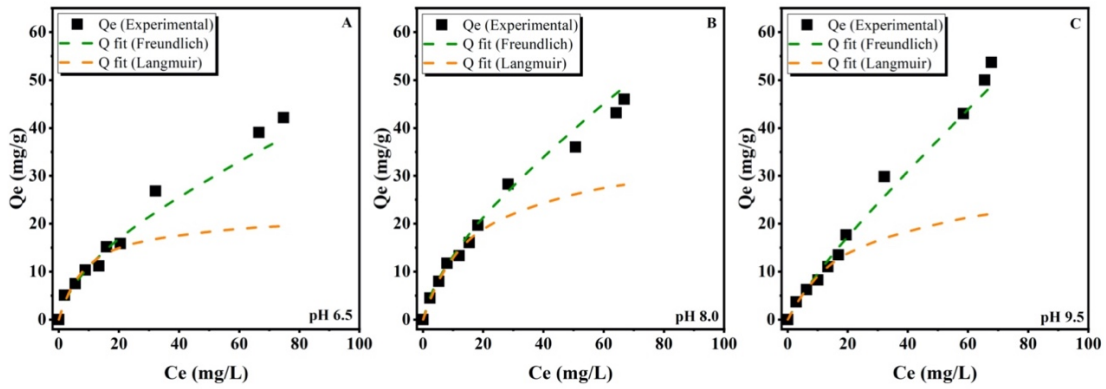
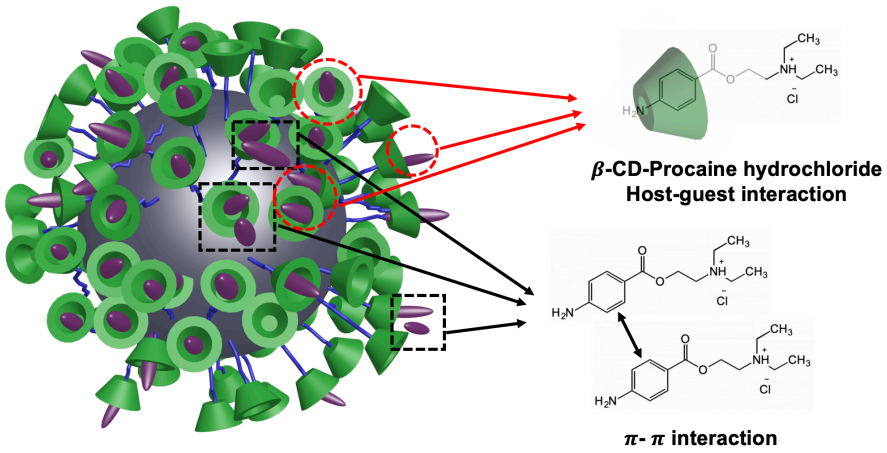


Figure 5-9 The adsorption isotherm of FMNP-H at pH 6.5, 8.0 and 9.5 fitted with Langmuir and Freundlich isotherm model is shown in A, B and C, respectively



Scheme 5-2 Schematic illustration of the adsorption mechanism between FMNPs and PrHy molecules

Table 5-2 The summary table of experimental data and the parameters of the fitted Langmuir and Freundlich isotherm models

Adsorbent	pH	Experimental		Langmuir		Freundlich		
		Q_e at 100 ppm	R% at 100 pm	K_L (L/mg)	R^2 (5-30 ppm)	K_F (mg/g)	n	R^2 (5-100 ppm)
FMNP-L	**6.5**	61.30	38.70	0.019	0.806	0.060	0.597	0.980
	8	62.00	42.32	-	-	0.503	0.904	0.995
	9.5	68.00	46.35	-	-	0.240	0.719	0.869
FMNP-M	**6.5**	57.00	30.21	0.025	0.869	1.373	1.152	0.930
	8	52.00	33.85	0.073	0.916	0.799	1.016	0.930
	9.5	49.35	29.61	0.023	0.748	0.932	1.098	0.932
FMNP-H	**6.5**	42.15	36.29	0.111	0.888	2.708	1.636	0.828
	8	46.00	33.19	0.059	0.908	2.799	1.473	0.915
	9.5	53.70	32.22	0.047	0.832	1.364	1.179	0.963

5.3.8 Removal percentage (R %)

Except for the adsorption capacity, the removal efficiency is another important parameter that should be evaluated in a large-scale water treatment process. The physical characteristics of the adsorbents and process variables could impact the adsorption performance. In this study, the effect of pH and amounts of CD cavities on FMNPs performance to bind and remove PrHy was studied. The adsorption process of a positively charged molecule is favorable when the surface charge of the adsorbent is negative, when the solution pH is higher than the isoelectric point of the adsorbents. The zeta potential of the FMNP-M from pH 5 to 9 was measured previously [273], where the surface charge was all negative and between -33 mV to -36 mV. Thus, PrHy adsorption on FMNPs is favorable within the pH range of 5 to 9. The targeted application of FMNPs is drinking water (or bottle water), where the pH is typically between 7 and 8.5 [334]. Thus, it is practical to examine the adsorption capacity of FMNPs at pH 6.5, 8 and 9.5, and the pharmaceutical residues in drinking water could be as low as hundreds of ng/L (ppb) [335] to hundreds of mg/L (ppm) [336]. The concentration of PrHy selected in this study was between 5 to 100 ppm, which was within the range of the reported pharmaceuticals in drinking water or after wastewater treatment that were detectable by the UV-Vis spectrometer. The removal percentage of PrHy using FMNP-L, FMNP-M and FMNP-H at pH 6.5, 8.0 and 9.5 are shown in **Figure 5-10** (**A**, **B**, **C**). When the PrHy concentration was below 50 ppm, the removal efficiency deceased with increasing PrHy concentration due to the reduced available CD adsorption site, except the adsorption performance of FMNP-L at pH 9.5. In general, the removal efficiency of the pollutants decreased with increasing initial PrHy concentration, which was due to the saturation of the adsorption sites on the adsorbent surface [337]. However, when the concentration of the PrHy increased beyond 50 ppm, the removal efficiency increased with increasing PrHy concentration due to the higher

driving force for adsorption enable the accessible of CD cavities was impeded by steric hindrance. This removal behavior was also reported in other studies, for the removal of tartrazine azo-dye onto the activated carbon [338]. In our study, the increase of PrHy removal could be due to the accessibility of the CD cavities, which increased when more PrHy molecules were present in the adsorption system. Also, the adsorbed PrHy might induce the stacking interactions between PrHy molecules due to the aromatic π-π interactions [321] [339]. As discussed previously, the adsorption performance was a multifaceted phenomenon comprising of several factors, such as the amounts of CD cavities, the PrHy initial concentration and pH. From the removal efficiency results shown in **Figure 5-10**, the adsorption performance was slightly enhanced when the system pH was 8.0 compared with the other two pH conditions. This was due to the FMNPs possessing the lowest zeta potential at pH 8.0 compared to the other two pHs, and nanogel, MNP and Si-40-MNP all presented a relatively low zeta potential at pH 8.0 compared to 6.5 and 9.5. At pH 6.5, the functional groups (COOH) were not fully ionized. However, the shielding effect introduced by NaOH used for the pH adjustment resulted a shielding effect that led to a higher zeta potential compared to pH 8.0. The COOH groups still needed to be considered since the silica coating layer was porous instead of a smooth solid shell [340].

A

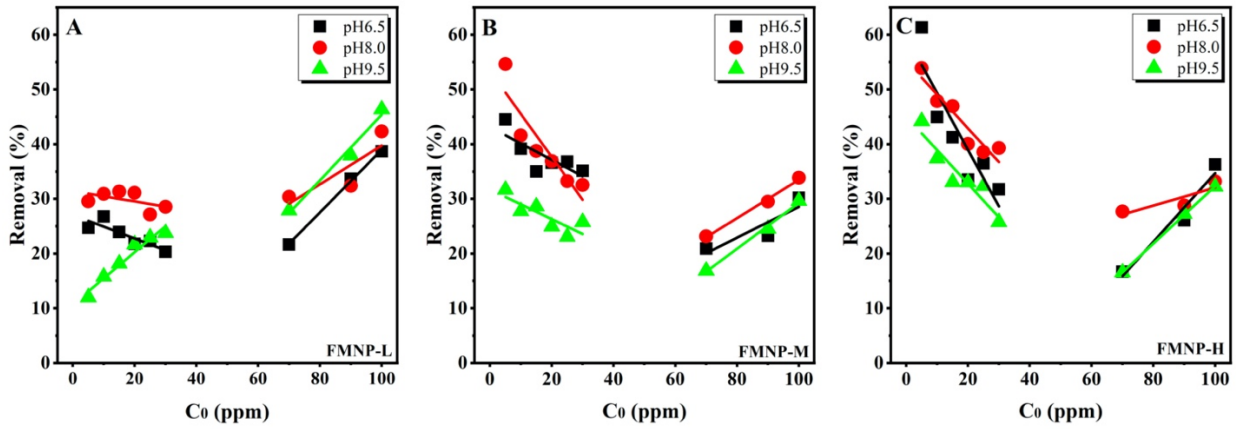


Figure 5-10 The removal percentage of 5 to 100 ppm PrHy by using 3ml of FMNP-L (A), FMNP-M (B) and FMNP-H (C) at pH 6.5, 8.0 and 9.5

5.3.9 Quantification of active β-CD cavities

Even though there are many factors affecting the adsorption capacity, the main adsorption process was due to the formation of CD-PrHy inclusion complex. Furthermore, the pH of the solution had a minor effect on the adsorption capacity, which was negligible. Thus, the active CD cavities of FMNP-L, FMNP-M and FMNP-H were estimated based on the Q_e value obtained from the adsorption isotherm study, and the results are presented in **Figure 5-11** (**A**, **B**, **C**). At pH 6.5 and 8, FMNP-H possessed the highest amounts of CD cavities (4.35×10^{20} and 4.06×10^{20}), while FMNP-M possessed the highest number of CD cavities (3.81×10^{20}) at pH 9.5. This method could a general estimation on the active CD cavities for capturing the PrHy molecules in addition to the adsorption capacity associated with the π–π stacking and pH. A more precise estimation of the β-CD content in FMNP-L, FMNP-M and FMNP-H were obtained from the TGA analysis. However, the adsorption capacity (Q_m) was not only depended on the quantity of β-CD grafted to the FMNPs. Electrostatic interactions, pH, π–π stacking among adsorbed PrHy and the accessibility of the CD cavities, since the active CD cavities calculated based on the Q_m was not proportional to the

quantity of β-CD quantity obtained from TGA analysis. This indirectly explained the accessibility of CD cavities dominated the adsorption performance, while the overlapping CD cavities induced a steric hindrance that impeded the adsorption performance.

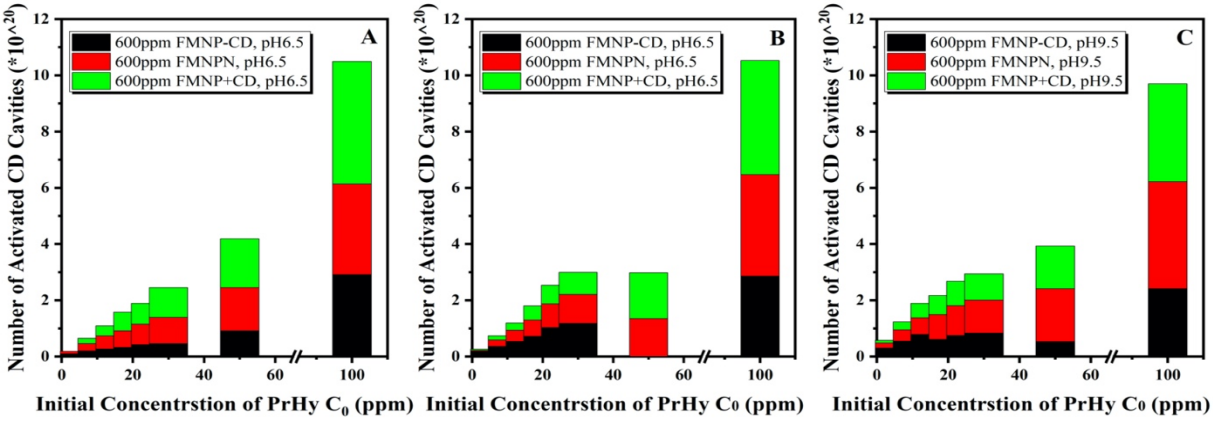


Figure 5-11 Estimation of active β-CD cavities at different PrHy initial concentration and pH by using FMNP-L (A), FMNP-M (B) and FMNP-H (C)

5.4 Conclusions

FMNPs prepared with different amounts of β-CD grafted magnetic nanoparticles were prepared, and the morphology displayed a "lichi"-like structure on the outer surface of the particle induced by the overlapping β-CDs. The particle size of nanogel deceased gradually after the formation of Fe_3O_4 particles, silica coating and β-CD grafting, where the size is constrained by the nanogel template. The adsorption isotherm of FMNP-L, FMNP-M and FMNP-H were examined using 5 to 100 ppm of PrHy, where the isotherm obeyed the Langmuir model at a low PrHy concentration (5 to 30 ppm) caused by the monolayer adsorption on the surface of the adsorbent. However, the adsorption isotherm obeyed to the Freundlich isotherm model when the concentration of PrHy exceeded 30 ppm. This linear adsorption behavior is associated with the orientation of the β-CD on the FMNP surface and the steric hindrance due to the overlapping or

cross-grafting of CD cavities on multiple FMNPs adsorbents. The highest equilibrium adsorption capacity approached 68 mg/g when the initial concentration was 100 ppm, and with the high magnetization (36.96 emu/g), the FMNPs could be a promising adsorbent to remove trace amounts pollutant or pharmaceutical residues from drinking water.

Chapter 6: Synthesis of Silver Nanoclusters in Colloidal Scaffold for Biolabeling and Antimicrobial Applications*

A robust method to prepare silver nanoclusters (AgNCs) inside a methacrylic acid-ethyl acrylate (MAA-EA) nanogel is developed in this chapter, where AgNCs were produced inside the nanogel scaffold via UV-photoreduction. The impact of UV irradiation time on the formation of AgNCs and their application in biolabeling and antimicrobial properties were examined. The AgNCs formation is described by two stages; (1) Ag_n (n=2-8) nanoclusters formation between 0-25 min, and (2) larger silver nanoparticles (AgNPs) formed via aggregation inside the nanogel. The antimicrobial performance depended on the size and concentration of silver ions (Ag^+). A low highest maximum inhibitory concentration (HMIC) of 1.1 ppm was observed for antimicrobial test with yeast, and a MIC of 11 and 22 ppm was recorded for *Escherichia. coli* and *Staphylococcus aureus* respectively. Combining with the green illumination property of AgNCs (emitted at 525 nm) with dead yeast, it could be used for biolabeling. By tuning the size through photoirradiation, the nanogel templated AgNCs is a promising candidate for antimicrobial and biolabeling applications.

*This chapter is adapted from a published paper " Xu, J., Ramasamy, M., Tang, T., Wang, Y., Zhao, W., & Tam, K. C. (2022). Synthesis of Silver Nanoclusters in Colloidal Scaffold for Biolabeling and Antimicrobial Applications. *Journal of Colloid and Interface Science*."

6.1 Introduction

Currently, there is a growing need for new antimicrobial agents due to the increase of antimicrobial resistance (AMR) and the emergence of new diseases including Covid-19. The World Health Organization has declared that AMR is one of the top public health threats and prioritizing the treatment and prevention of illnesses caused by bacteria, viruses, parasites, and fungi [341]. Antimicrobial compounds are being added to materials, such as ceramics [342], textiles [343]-[345], and polymers [346] for practical usage. Traditionally, metals and metal derivatives such as silver, titanium, gold, and copper have been preferred antimicrobial compounds since ancient times, with the most prominent being silver [347]. Furthermore, metal particles combined with nanotechnology have propagated the evolution of antimicrobial materials across different fields.

It is well-recognized that silver nanoparticles (AgNPs) possess many attractive properties include high electrical and thermal conductivity [348], chemical stability [349][350], and catalytic activity [351][352], which enable AgNPs being widely used in clothing [353], cosmetics [354], renewable energies [355], environmental remediation [356] and biomedicine [357][358]. For AgNPs, size and morphological control are important parameters with a direct impact on the physical and biological properties. AgNPs are commonly used due to their unique chemical and physical properties associated with their nanosize. If the size of the particle is further reduced to below 2 nm, which is analogous to the Fermi wavelength of electrons (~0.5 nm), the particles are described as nanoclusters [359]. Generally, AgNCs possessed better fluorescence property in aqueous solution compared to gold nanoclusters, therefore, ultrasmall AgNCs containing less than 100 silver atoms [360] have been considered as promising candidates for biosensing and bioimaging applications. However, the aggregation of AgNCs will reduce the benefits of many features at the nanoscale of the material, therefore, stability is the major challenge in the

development of AgNCs and AgNPs. Some strategies used to stabilize metallic nanoparticles include; (a) adding silica coating to the AgNPs [361], and (b) loading AgNPs into organic or inorganic templates. Extensive knowledge and research on AgNCs and AgNPs have been reported over the past century and the antimicrobial characteristic of silver is still an important function of this nanoparticle.

The synthesis of silver nanoparticles is well-known, and they are produced via chemical, physical, photochemical and biological process [358]. The chemical approach is widely used since the synthesis can be performed in an aqueous environment. The three main components of the chemical synthesis process are: (i) metal precursors, (ii) reducing agents and (iii) stabilizing/capping agents [358]. However, some reducing agents, such as sodium borohydride, $NaBH_4$ is known to have negative impact on both the environment and the human body. For example, 1 mg of sodium borohydride has a cumulative energy demand of 4.63×10^{-4} MJ and freshwater eco-toxicity of 2.49×10^{-9} kg [362], hence further purification is needed to remove the excess reducing agent. Additionally, it is difficult to obtain stable AgNCs via the conventional chemical reduction process, since the formed AgNCs tend to agglomerate into larger clusters due to the reduced surface energy [359]. Thus, light activated reduction of silver ions as a non-intrusive reduction strategy may be more attractive from the perspective of toxicity and the environment. Metal ions are reduced by the incorporation of lone pair electrons generated by photoirradiation where chemical reducing compounds are not used. Sato-Berru and co-workers reported on the photoreduction of metal salts and they found that UV light is the most effective light source compared to other visible light sources [363]-[365]. Moreover, UV irradiation of metal ions can introduce fluorescence characteristic that is beneficial in biosensing application [366]. In previous study, silver clusters were prepared using poly (acrylates) (PAA) as a template, where both UV

irradiation and $NaBH_4$ were used as a 'reducing agent' to explore their effect on the morphology of AgNCs. The AgNCs prepared with UV irradiation possessed a slower reduction rate and generated large amounts of small AgNCs in the early stage compared to the $NaBH_4$ reduction method. The produced AgNCs were coated onto cotton fabric for antimicrobial application. However, the Ag-PAA complex does not have a robust structure, and the AgNCs are easily ejected from the fabric causing harmful effect to the environment. Moreover, the coating of the small AgNCs onto the fabric reduced their surface area and sacrificed the antimicrobial performance [367]. In addition to using the polymer chain as a template, nanogel was also used to prepare AgNCs. Jing *et al.* reported a self-assembled nanogel by blending glutathione templated AgNCs with chitosan solution. The prepared AgNCs-nanogel possessed a spherical structure with patched AgNCs presented on the surface of the nanogel. This AgNCs-Nanogel-Chitosan system achieved a multifunctional composite in a single system. However, the open structure and outer surface of the AgNCs lead to a toxicity concern due to the detachment of the AgNCs [360]. In our previous study, a magnetic cluster was successfully encapsulated within the MAA-EA nanogel system, where the Fe_3O_4 were coprecipitated in-situ within the chemically crosslinked scaffold. Ultrafiltration applied after the coordination of Fe^{2+} ion with the COO^- groups from the nanogel could effectively remove all the Fe^{2+} outside the nanogel. This strategy preserved the formation of magnetic clusters within the nanogel scaffold [273], which is a promising strategy to synthesize metal nanoclusters.

In this study, a one-pot process consisting of UV irradiation to prepare silver nanoclusters (AgNCs) within a colloidal scaffold is proposed. The polymeric colloid (nanogel) was prepared via the emulsion polymerization of methacrylic acid (MAA) and ethyl acrylate (EA) crosslinked with diallyl phthalate (DAP). The silver ions chelate with the carboxylate groups of the nanogel,

and AgNCs are produced inside the nanogel under UV irradiation. The nanogel templated AgNCs were evaluated in an antimicrobial test demonstrating its ability to inhibit yeast metabolism and kill bacteria. With the use of a nanogel template, AgNCs can be easily recovered from the system due their size (between 200-500 nm). To the best of our knowledge, this is the first reported study that focuses on reducing agent free process to prepare silver clusters for antimicrobial and biolabeling applications. And the yeast test with simple setup originated from fungi culture was firstly used as a pre-evaluation of antimicrobial agent. The reduction mechanism of silver clusters under UV irradiation was examined and the colloidal scaffold strategy preserved the surface area while minimizing the toxicity of the synthesis process.

6.2 Experimental

6.2.1 Materials

Methacrylic acid (MAA, 99%), ethyl acrylate (EA, ≥ 99.5%), di-allyl phthalate (DAP, 97%), sodium persulfate (≥ 99%), sodium hydroxide (≥ 98%), silver nitrate (≥ 99%), methylene blue (dye content ≥ 82%) and yeast (*Saccharomyces cerevisiae*) were purchased from Sigma-Aldrich and used as received. Aerosol OT (AOT, 75 w/w%) was supplied by Thermo Fisher Scientific.

6.3 Methods

6.3.1 Synthesis of MAA-EA nanogel template

The MAA-EA nanogel was synthesized via a semi-continuous emulsion polymerization process. A pre-emulsion mixture was prepared in a scintillation vial by adding 4.945 g MAA and 5.75 g EA (1:1 molar ratio) together with 0.856 g of DAP (8 wt% of the monomer), 1 g of 75 wt% AOT solution and 1.4 g of Milli-Q water. The reaction vessel (a 250 mL three-neck flask) contained 120 g Milli-Q water and 1g of 75wt% AOT solution. The initiator solution was prepared by dissolving 0.25 g of sodium persulfate in 2 g of Milli-Q water in a separate vial.

The reaction vessel assembled with a condenser and an equalizing pressure funnel and was heated to 85 °C under continuous stirring while being purged with N_2 for 30 minutes, after which the initiator solution was added via a syringe. When the contents were well-dispersed, 5 wt% of the monomer mixture was added dropwise using a syringe. The nanogel seed was formed after 30 mins reaction, the remaining monomer mixture was added dropwise through a pressure equalizing-funnel. The reaction was left to proceed for another 30 minutes after the addition of the remaining monomer mixtures. The final product was then cooled to room temperature and filtered through a 200-mesh nylon cloth. The filtered nanogel solution was dialyzed against DI water until no excess surfactant was observed. The solid content of the dialyzed final product was approximately 5% by weight.

6.3.2 Synthesis of nanogel templated Ag^+-nanogel system

The synthesis of AgNCs inside the nanogel template was conducted via a two-step process. The recipe was determined based on the solid content and carboxyl concentration of MAA-EA nanogel scaffold. Nanogel with a solid content of 4.8 wt% was utilized, and the corresponding COOH concentration was 5mmol/g as determined by potentiometric titration. The molar ratio of Ag^+ and COOH group for the reaction was set at 1:1. First, 3.3 g of nanogel dispersion was diluted with 36.7 g of Milli Q water and the pH was adjusted to 8.2 using 0.5 M NaOH solution. Secondly, the deprotonated carboxyl groups on the nanogel co-ordinated with Ag^+ in basic condition by the dropwise addition of 0.136 g (in 40 ml water) silver nitrate under gentle magnetic stirring for 2h. The reaction vessel was covered with aluminum foil to shield visible light from the reaction mixture. After the reaction, the Ag^+ coordinated nanogel (Ag^+-nanogel) dispersion was purified by dialysis under dark environment to remove unbound Ag^+.

6.3.3 In-situ photoreduction of Ag^+ to AgNCs inside the nanogel template

A high intensity UV lamp (B-100AP/R) from Blak-Ray (100 Watt, 365nm) was used for the reduction of Ag^+ to AgNCs within the nanogel template. The Ag^+-nanogel dispersion was transferred to a 250 mL beaker placed on a magnetic stir plate set at 300 rpm and kept in the dark. The UV lamp was pre-illuminated for 15 min before initiating the photoreduction, and 4 mL of Ag^+-nanogel suspension was removed at different time interval (0-360 min). All the AgNCs prepared with different UV irradiation time was purified by dialysis to remove excess Ag^+ under dark environment for 2 days and stored under cover using an aluminum foil. AgNCs obtained from different time of UV irradiation were labeled as AgNCs@time. The schematic of synthesis of AgNCs subjected to UV irradiation is shown in **Figure 6-1**.

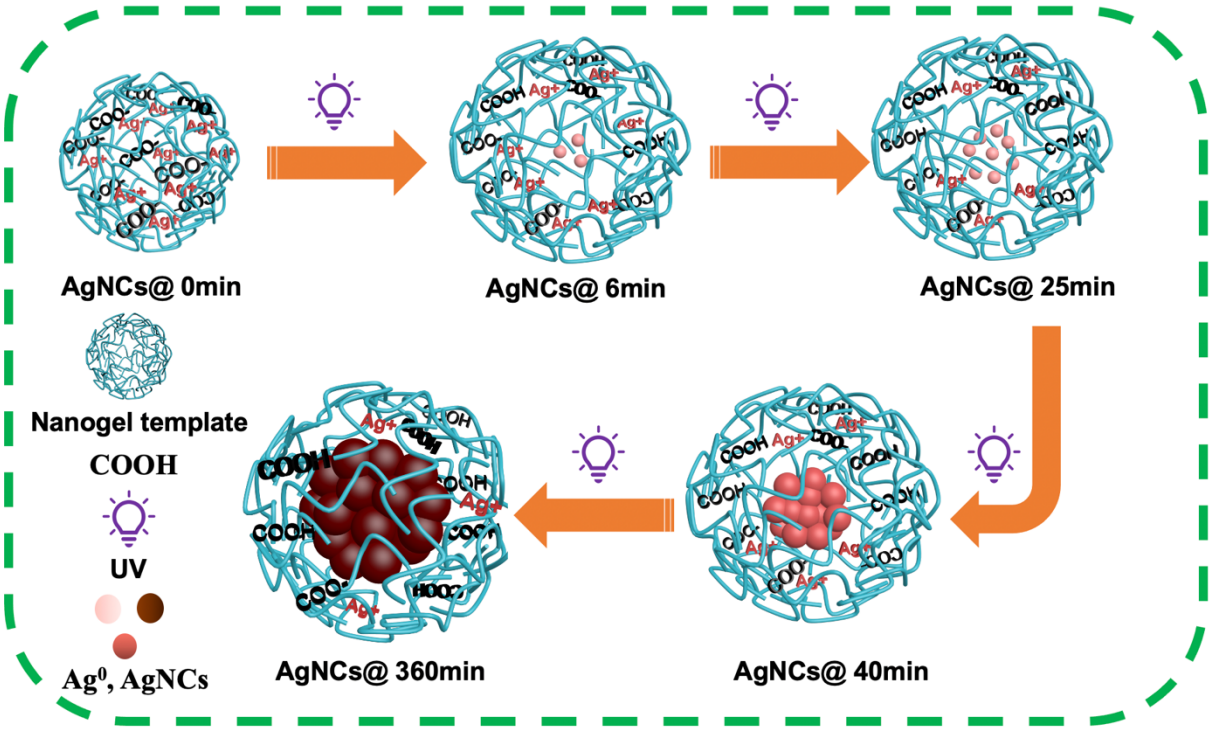


Figure 6-1 Schematic illustrating the preparation of AgNCs under UV irradiation

6.4 Characterization methods

6.4.1 Fourier transform infrared spectroscopy (FTIR)

The FTIR of MAA-EA nanogel, $AgNO_3$, AgNCs without UV irradiation, AgNC@25min, AgNC@1h, and AgNC@6h were determined using the Bruker Tensor 27 spectrometer (Bruker, Billerica, MA, USA). The freeze dried samples prepared with KBr were scanned between 4000 to 400 cm^{-1} at room temperature.

6.4.2 Transmission electron microscopy (TEM)

TEM images were taken with a Philips CM10 electron microscope under an accelerating voltage of 60 kV. The nanogel sample was stained with uranyl acetate and lead citrate (since the pristine nanogel was not visible under TEM) and the nanogel sample on the copper grid was left to dry. The morphological changes of AgNCs treated bacteria were examined using the TEM. AgNCs@0, 25, 360 min (100 μg/mL) were incubated with the bacteria, along with a negative control comprising of only the nanogel template. The bacteria solution was washed with PBS and fixed with 2.5% glutaraldehyde solution at 4 °C for 3 h. It was then purified 3 times via centrifugation in PBS solution and then dehydrated using a series of ethanol (10 to 99.9 % v/v). The dispersed samples were placed on a copper grid and imaged using TEM.

6.4.3 Dynamic light scattering (DLS)

DLS measurements were used to determine the size of nanogel and nanogel templated AgNCs@ different UV irradiation times (Nanogel-AgNCs). This measurement was conducted by measuring 0.1 wt% dispersion in a Zeta-Sizer (Nanosizer ZS, Malvern co., UK) at 25 °C. Three measurements with 10 scans were conducted for each sample.

6.4.4 Zeta potential measurement

Zeta-Sizer (Nanosizer ZS, Malvern co., UK) was used to measure the zeta potential of Nanogel-AgNCs by determining the surface charge at 25 °C. Different samples were prepared at 0.1 wt%. Three measurements with 10-100 times scanning were conducted for each measurement.

6.4.5 UV-Vis Spectroscopy

The UV vis spectrum of Nanogel-AgNCs @ different UV irradiation times were obtained using a Varian Cary 300 spectrophotometer. 3 mL of Nanogel-AgNCs solution was added to the quartz cell, and it was scanned from a wavelength of 200 nm to 800 nm.

6.4.6 Fluorescence Spectroscopy

The fluorescence emission spectrum was determined using a Varian Cary Eclipse Fluorescence Spectrophotometer. 100 μL of AgNCs solution diluted with 900 μL of water was excited at 275 nm and the emission spectra were recorded.

6.4.7 Silver ions concentration determination using a silver electrode

The Ag^+ concentration of the nanogel and Ag^+-nanogel solution as a function of UV irradiation time were measured using a Cole-Parmer Silver/Sulfide electrode. The Cole Parmer Ionic Strength Adjuster (ISA), 5 M $NaNO_3$ (10 mL), were freshly prepared. Five standard solutions were prepared by mixing 10 mL of 10, 30, 50, 70, 100 ppm $AgNO_3$ solution with 2 mL of ISA solution. The obtained calibration curve was used to determine the Ag^+ concentration existed in the reaction mixture.

The analysis of silver ions in 5 different conditions were performed.

1. nanogel template under UV irradiation,
2. Ag^+-nanogel system (silver ion coordinated with nanogel and dialyzed under dark environment) under UV irradiation,

3. Ag^{+}-nanogel system (silver ion coordinated with nanogel and dialyzed under dark environment) without UV irradiation,
4. addition of $AgNO_3$ to the nanogel template without UV irradiation
5. addition of $AgNO_3$ to the nanogel template under UV irradiation

6.4.8 Highest Maximum Inhibitory Concentration (HMIC) of antifungal test (yeast test)

The antimicrobial activity of AgNCs was evaluated using the yeast metabolic activity test. Approximately, 50 mg of sugar and 50 mg of yeast were mixed with appropriate amount of Milli Q water (adjusted to pH 5.1) and placed in a 10 mL volumetric flask, a certain concentration of Nanogel-AgNCs@0, 6,25, 40, 80, 200, 360 min was diluted from their stock solution and added to the volumetric flask. The volumetric flask was assembled with a bubble flow meter and placed in a water bath at 40℃ at stirring speed of 300 rpm. The yeast activity was evaluated by recording the carbon dioxide release every 2 minutes over a 30 min period. The concentrations of Nanogel-AgNCs were varied based on CO_2 production rate and dichotomy was used for concentration selection until zero CO_2 production rate was obtained. Nanogel template was used as a control test. To investigate the growth inhibition of AgNCs, the HMIC was determined from the yeast test results.

6.4.9 Antimicrobial Tests

The antibacterial activity of AgNCs towards Gram-negative *Escherichia coli (E. coli)* and Gram-positive *Staphylococcus aureus* (*S. aureus)* was evaluated. Both bacteria were inoculated and dispersed in Luria-Bertani (LB) broth at 37 °C with continuous shaking at 150 rpm to achieve the mid-log phase. The incubated bacteria were diluted in a fresh LB broth to obtain an initial turbidity of 0.05 at the optical density of 600 nm (equivalent to 10^8 CFU mL^{-1}). A standard broth dilution method was established to evaluate the antibacterial property of the samples. AgNCs@

different UV irradiation times (0, 6, 25, 80, 120 and 200 min) were treated with bacteria at 0-44 μg/mL and incubated at 37 °C for 24 h in a shaking incubator with a sample-free bacteria as the control and media as blank. Incubated bacteria-AgNCs dispersion was serially diluted in a sterile PBS, and 100 μL of the suspension was spread on the agar plate and incubated for 24 h at 37 °C. The minimum inhibitory concentration (MIC) was determined as the lowest concentration that inhibited visible bacteria population.

6.4.10 Microscope and fluorescent microscope

The optical and fluorescence micrographs were obtained using a Leica inverted Fluorescence microscope with a 40X objective. The MB dyed yeast test samples, and AgNCs samples (2μL) were placed on a microscope glass slide and sealed with a cover glass.

6.5 Results and discussion

6.5.1 Fourier-transform infrared spectroscopy (FTIR)

The successful synthesis of MAA-EA nanogel and AgNCs inside the nanogel template were confirmed by FTIR spectroscopy. **Figure 6-2** shows the FTIR spectra of the MAA-EA nanogel template, $AgNO_3$, and AgNCs with 0 min, 25 min, 1 h and 6 h of UV irradiation. The small peak from 1700 to 1740 cm^{-1} was attributed to the carbonyl stretching of the acid and ester components of the nanogel consisting of MMA and EA [248]. The characteristic peaks at 1377 and 1753 cm^{-1}corresponded to $AgNO_3$ [368]. After Ag^+ coordinated with deprotonated carboxyl groups on the nanogel template, the peak at 1377 cm^{-1} was reduced, which is the typical symmetry stretching of N=O of nitro-compounds [369]. This indicated that all the NO_3^- was removed and demonstrated the successful coordination of Ag^+ with COO^-. By comparing the FTIR spectra of $AgNO_3$ and the nanogel, the spectrum for AgNCs possessed a new band at 1541 cm^{-1} [370], which was due to the formation of Ag^0 after different UV irradiation times. Also, this characteristic band was present in

all the photo-treated samples confirming the formation, nucleation and growth of AgNCs. Moreover, the small shoulder peak at 1641 cm^{-1} could be attributed to the -CO-Ag linkage, which was also observed from the FTIR spectrum of an alginate-coordinated Ag nanoclusters, which was assigned to the characteristic peak of Ag^0 capped with COOH groups [371].

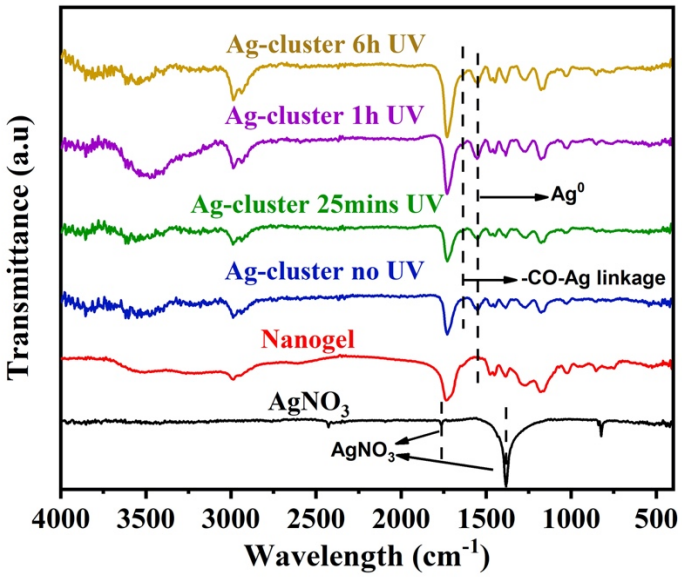


Figure 6-2 FTIR of MAA-EA nanogel, $AgNO_3$ and AgNCs with different time of UV irradiation

6.5.2 Transmission electron microscopy (TEM)

The morphology of MAA-EA nanogel and AgNCs were investigated by TEM. The TEM images of stained nanogel are shown in **Figure 6-3** (**a**, **b**). A well-defined monodispersed spherical nanogel was observed with a diameter of 46 $\pm$ 3.1 nm. Prior to UV irradiation, the AgNCs displayed a light grey shadow, which might be due to the coordinated Ag^+ exposed to the visible light during the preparation of the TEM grid, that resulted in the formation of Ag_2O **Figure 6-3** (**c**, **d**). After 6 min of UV irradiation **Figure 6-3** (**e**, **f**), scattered dark points were observed, indicating the nucleation of AgNCs. Interestingly, further increase in the UV irradiation time to 25 min **Figure 6-3** (**g**, **h**), darker and larger Ag^0 cores were formed within the nanogel template. However,

the size of dark silver cores was not homogenous, which could be attributed to the uneven reduction rate of Ag^{+} inside the entire nanogel. The smaller AgNCs ($t \leq 25$ mins) represented the nucleation phase, while when UV irradiation time > 25mins, the dark centre represented the growth phase of the Ag cores to form larger AgNCs. Increasing number of dark cores was recorded for AgNCs@60min samples due to the faster growth rate of AgNCs upon the continuous UV irradiation, **Figure 6-3** (**i**, **j**). At the end of UV irradiation at 360 min, a homogenous, and monodispersed AgNCs were observed in **Figure 6-3** (**k**, **l**)**,** confirming that more AgNCs were formed within the nanogels. The uniform silver cores within the nanogel scaffold without any darker background suggested the complete utilization of Ag ions to produce AgNCs.

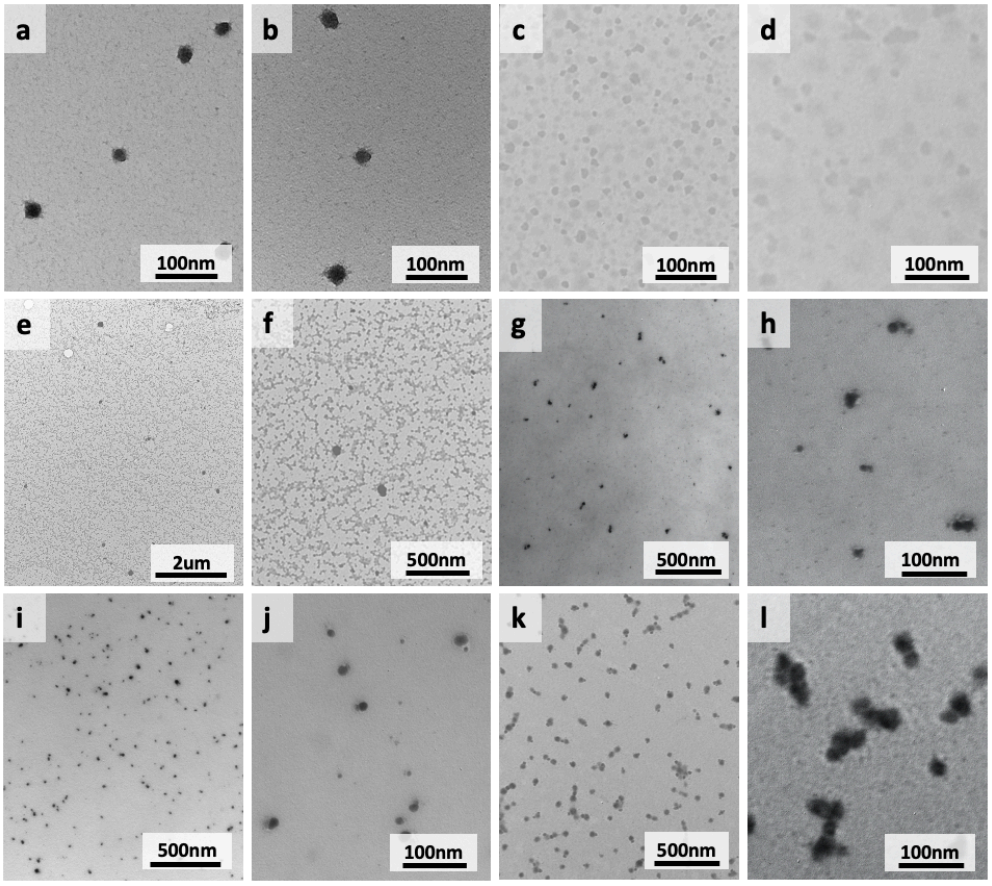


Figure 6-3 TEM images of normal and magnified views of stained MAA-EA nanogel (a, b), formation of AgNCs @ (c, d) 0, (e, f) 6, (g, h) 25, (i, j) 60, and (k, l) 360 min of UV irradiation

6.5.3 Particle size and zeta potential

The particle size and stability of synthesized AgNCs were evaluated from the average size and zeta potential of the Nanogel-AgNCs. The hydrodynamic radius of nanogel was 95.4 ± 0.3 nm at pH 7, and the radius of the AgNCs radius at different UV irradiation times are presented in supporting information (**Appendix 6-1**). The size of Nanogel-AgNCs@0min (85 ± 3.1 nm) was smaller compared to the pristine nanogel, due to the co-ordination of Ag^+ with COO^- groups that resulted in a slightly compact nanogel structure. When the UV irradiation time was increased to 40 min, the Nanogel-AgNCs radius decreased due to the formation of AgNCs, as more COOH groups were released from the strong ion chelating status and conjugated with AgNCs resulting in a more relaxed structure. After 40 minutes of UV radiation, there was no significant difference in the particle size, since the size of nanogel-AgNCs particles was constrained by the size of the nanogel scaffold. Small changes could be observed when larger AgNCs were formed, which expanded the nanogel template. In term of zeta potential, the surface charge of AgNCs increased from -41± 2.9 to -37.5 ± 4.7 mV when the UV irradiation was increased from 0 to 40 min, which was consistent with the particle size. The incomplete Ag^+ reduction contributed to the positive charges from the Ag^+ on the nanogel surface. With increasing UV irradiation time, the zeta potential decreased further, indicating the coordination of the COO^- groups with the Ag^+/AgNC during the growth and aggregation of AgNCs. All the zeta potential values were below -30 mV, resulting in a good stability of the AgNCs produced using the nanogel templating strategy.

6.5.4 UV-Vis analysis of formation of Ag^0

The UV-Vis spectra were used to confirm the formation of AgNCs inside the nanogel scaffold. The absorption spectra (200 to 800 nm) of AgNCs at different UV irradiation times are shown in **Figure 6-4** (**A**). From **Figure 6-4** (**A**), there is no obvious characteristic absorbance

observed for the AgNCs@0-6min. After 25 min, a local maximum absorption at 275 nm and a broad characteristic peak at 500 nm emerged and the intensity was increased significantly as the irradiation time was increased. Different sizes and morphologies of AgNCs could be differentiated from the frequencies of surface plasma resonance (SPR) bands, which were well-documented in many studies [372]. Silver clusters Ag_n containing 2 to 12 atoms possessed an absorption peak between

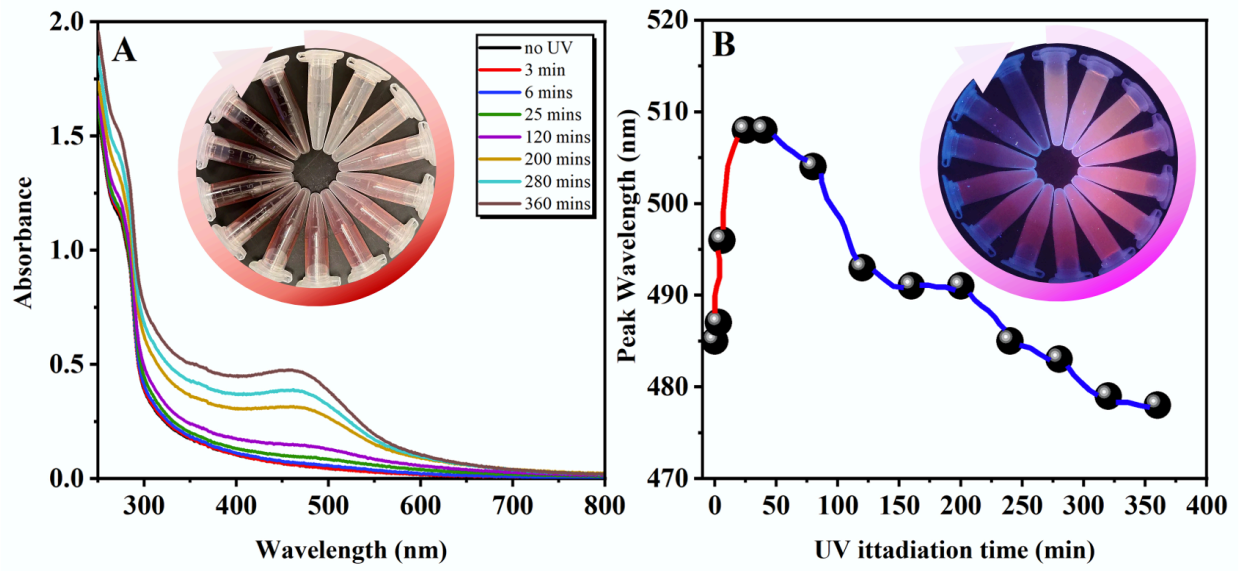


Figure 6-4 The UV curve of AgNCs under 0, 3, 6, 25, 120, 200, 280 and 360 min of UV irradiation (A), and the peak wavelength of different AgNCs (B). The picture of AgNCs under 0, 3, 6, 15, 40, 80, 120, 160, 200, 240, 280, 320, 360 and 400 min under visible light (from 12 o'clock point) is shown in (A) intersection image. The picture of AgNCs under 0, 3, 6, 15, 40, 80, 120, 160, 200, 240, 280, 320, 360 and 400 min under UV light (from 12 o'clock point) is shown in (B) intersection image

275 to 360 nm [371], and another absorption peak at 490-520 nm were assigned to the charged Ag_n^+ clusters (n=4-9) [373]. It was reported that the absorption peak at 560 nm was assigned to the complexation between Ag_n^+ clusters and the polymer chains in a poly(styrene sulfonate) (PSS) encapsulated electrolyte nano reactor for in-situ AgNPs (silver nanoparticles) synthesis [371]. Compared with the current templated Nanogel-AgNCs system, the absorbance at the wavelength

of 275 nm could be assigned to Ag_n (n= 2-12) and the intense absorption peak at 500 nm corresponded to the charged Ag_n^+ clusters (n=4-9) [374]. The UV absorption curves (400-800 nm) of AgNCs@0-360min are shown in **Appendix 6-2**, where a clear gradual increase of the characteristic peak at 500 nm was observed that represents the gradual reduction of Ag^+ to Ag_n. **Figure 6-4** (**B**), represents the maximum peak wavelength (475 to 525 nm) of AgNCs as a function of UV irradiation times. From 0 min to 25 min, the appearance of Ag^0 lead to a red plasmonic shift in the absorption band at 500 nm representing the slow formation of AgNCs, that corresponded to the increase of the particle size [371]. Neus et al synthesized spherical silver nanoparticles of between 10 to 200 nm via a controlled seed growth strategy. Their study revealed that as the size of the single silver nanoparticle increased, the surface plasmon absorption band displayed a red shift from 397 nm to 402.5 nm. Also, as more Ag_n (n=4-9) clusters were formed, the surface area and surface energy of AgNCs increased dramatically. At 25 min, the total surface area of AgNCs approached a maximum where the COO^- groups inside the nanogel could well coordinated and stabilized with the AgNCs . After that, the AgNCs tended to agglomerate into larger AgNCs aggregates to reduce the surface energy. In addition, the charged COO^- functional groups served as a growing modifier (capping agent) for Ag^0 during the UV reduction process, and it bound the AgNCs separately in the initial stage that prevented the aggregation of the AgNCs. Before 25 min, the invisible characteristic peak (**Appendix 6-2**) could be related to the incomplete reduction of Ag^+ ion to Ag^0, and sufficient amounts of AgNCs were formed after 25 min of UV irradiation [375]. After 25 min (**Figure 6-4** (**B**),), the absorption band of AgNCs displayed a small blue shift indicating that individual AgNCs dimerized or aggregated into bigger Ag cores inside the nanogels. The localized surface plasmon among AgNCs interacted with each other due to dimerization or agglomeration, resulting in the blue shift of UV absorbance peak [371] [376]. As a result, the core

of the templated AgNCs was made up of aggregates consisting of several small AgNCs, instead of the growth and formation of one large silver nanoparticle (AgNP). Furthermore, with increasing UV irradiation time, the absorbance intensity increased due to the reduction of more Ag^{+} ions to Ag^{0} [375]. The inset image in **Figure 6-4** (**A**) is the AgNCs suspensions obtained from 0 to 360 min UV irradiation time under visible light (from 12 o' clock), where AgNCs possessed a light pink color at 25 min UV irradiation time. The color of AgNCs suspension transformed from transparent to pink to deep reddish brown as the UV irradiation time extended. After 240 min UV irradiation, no obvious color change was observed, which is in corroboration with previous reported fluorescent silver nanocluster synthesized inside the poly(NIPAM-AA-HEA) microgel [373]. Another inset image in **Figure 6-4** (**B**) displayed the AgNCs suspensions obtained from 0 to 360 min UV irradiation time under UV light (from 12 o' clock). The color transferred from light fluorescent pink to brighter fluorescent pink and become less fluorescent at an extended UV irradiation time, indicated a size dependent illumination property.

6.5.5 Fluorescence characteristics of AgNCs

The nanogel templated AgNCs displayed a characteristic UV absorption peak at around 500 nm. The fluorescence spectra were obtained from the excitation at 275 nm, and the corresponding emission peak was recorded at 553 nm. In **Appendix 6-3** (**A**), the fluorescence intensity of AgNCs increased as the UV irradiation time was increased from 0 to 25 min, while further increase in the UV irradiation time led to a reduction in the fluorescence intensity. From **Appendix 6-3** (**B**), the AgNCs@0min possess an intermediate photoluminescence (PL), and the PL intensity increased from AgNCs@0min to AgNCs@25min. Continuously increase the UV irradiation time lead to a decline of the PL intensity, AgNCs@25min displayed the brightest emission intensity among all AgNCs. The results were consistent with the findings of Dickson et al., where only small Ag_n

(n=2-8) clusters displayed strong photoluminescence [377], which was achieved within 25 minutes of UV irradiation. Further increase in the UV irradiation time resulted in more Ag^+ being reduced on the surface of fluorescent AgNCs. Simultaneously, single AgNCs aggregated into large AgNCs aggregates to reduce the surface energy. Both these factors led to the reduction in the fluorescence intensity of AgNCs after 25 min UV irradiation. In comparison to the AgNCs produced using chemical reducing agent, the proposed photoreduction strategy could precisely control the fluorescence properties of the AgNCs by varying the UV irradiation time. However, the strong reducing agent, such as $NaBH_4$ and ascorbic acid rapidly reduced the Ag^+ into AgNPs that did not display fluorescence characteristics [374].

The relative Quantum Yield (QY) of the AgNCs@3, 6, 25, 120, 240, 360 min was calculated by comparing the photoluminescence to quinine sulphate (dissolved in 0.05 M H_2SO_4). The emission curve of quinine sulphate and corresponding integration peak is shown in **Appendix 6-4 (A)** and **(B)**, the emission curves of AgNCs and its corresponding integration peaks is shown in **Appendix 6-4 (C)** and **(D)**. The absorbance of AgNCs@3, 6, 25, 120, 240, 360 min and quinine sulphate were measured under UV-vis and the absorbance value was kept to below 0.05. The QY of quinine was reported to be 54 % with a reflex index (RI) of 1.33 when the excitation wavelength was 350 nm [378]. The same excitation wavelength was used to excite the AgNCs@3, 6, 25, 120, 240, 360 min and the PL spectrum was recorded. Thus, the relative QY of AgNCs were calculated based on the equation (6.1) reported in [379], where I_F and I_R are the integrated fluorescence intensities of AgNCs and quinine sulphate, respectively; A_F and A_R are the absorbance of AgNCs and quinine sulphate, respectively; n_F and n_R are the reflex index of sulfuric acid (0.05 M, n_F=1.33) and DI water (n_F=1.33), respectively; And QY_F and QY_R are the quantum yield of AgNCs and quinine sulphate, respectively [379].

$$QY_F = QY_R \frac{I_F A_R n_F^2}{I_R A_F n_R^2} \quad (6.1)$$

QY_F of AgNCs at different times are summarized in **Table 6-1**, where the highest QY_F (16.76%) was obtained from AgNCs@3min, which was attributed the smaller size of clusters formed. With the increase of the UV irradiation time, the QY of AgNCs decreased due to the increasing particle size, which was also confirmed by the TEM images. AgNCs@360min displayed a low QY (2.86 %) that could be attributed to the quench caused by the aggregation of AgNCs, and the shifted PL peak also confirmed this hypothesis [380].

Table 6-1 The summary of QY results of quinine sulphate and AgNCs

Sample	A_F	A_R	I_F	I_R	QY_F (%)
AgNCs@3mins	0.0074	0.0315	345.679	4274.99	16.76
AgNCs@6mins	0.0168		406.062		8.69
AgNCs@25mins	0.0523		426.166		2.93
AgNCs@120mins	0.0151		262.047		6.25
AgNCs@240mins	0.0182		215.995		4.25
AgNCs@360mins	0.0280		223.183		2.86

6.5.6 Electrochemical monitoring Ag^+ concentration under UV irradiation

The Ag^+ electrode was used to monitor the silver ion concentration ($[Ag^+]$) in the bulk solution (outside the nanogel template) during the UV irradiation process. It could provide information on the role of Ag^+ diffusion across the nanogel template and Ag^+ released from the dissolution of AgNCs inside the nanogel. The $[Ag^+]$ of Ag^+-nanogel (Ag^+ coordinated with COOH groups on the nanogel) and pure nanogel solution was monitored using a Cole-Parmer Silver/Sulfide electrode for 12 hours under UV irradiation. The $[Ag^+]$ variation of Ag^+-nanogel (after dialysis) system and nanogel solution as a function of UV irradiation time is shown in **Figure 6-5** (**A**), where a plot of log $[Ag^+]$ versus time is presented in **Figure 6-5** (**B**). As indicated from **Figure 6-5** (**A**), the concentration of Ag^+ in the nanogel system did not change during the UV

irradiation process, it was around 0 ppm after the initial stabilization of the electrode. Interestingly, the Ag^+ concentration in the Ag^+-nanogel dispersion displayed three distinct regimes as indicated in **Figure 6-5** (**A**) and (**B**). In Region 1 (0-20 min),"free" Ag^+ in the bulk solution increased right after the UV irradiation started, which was due to the Ag^+ diffusing out from the nanogel template. Before UV irradiation, the carboxyl groups of the nanogel chelated strongly with the silver ions. When the Ag^+ was reduced to Ag^0 as UV irradiation was applied, the interaction between COO^- and Ag^+ reduced, and the nanogel structure relaxed that led to the Ag^+ diffusing to the bulk solution, and an equilibrium was reached at 20 min. At Region 2, (20 min-5 h), free Ag^+ in the bulk solution diffused into the nanogel and reduced to AgNCs inside the nanogel assisted by -COOH groups within the nanogel. It was demonstrated by other studies that Ag^+ could be reduced to Ag^0 cluster in the presence of organic polyanions [381]. Several studies reported that the photoinduced reduction of silver ions to atomic silver requires the presence of organic compounds [371],[381]. In Region 3 (5h-12h), single AgNCs aggregated into larger AgNCs, and Ag^+ were continuously being reduced to Ag^0 on the surface of AgNCs, which results in a continuous reduction of silver ions, but at a slower rate compared to Region 2. As clearly indicated from **Figure 6-5** (**A**) and (**B**), there was an obvious difference of Ag^+ reduction rate between Region 2 and 3. In Region 3, the aggregation of small atomic Ag^0 into larger AgNCs decreased the surface area available for oxidative dissolution of silver ions, and the reduction rate of Ag^+ to Ag^0 was slower than in Region 2 as indicated by a diminished slope. The concentration of Ag^+ in the bulk solution of Ag^+-nanogel system (**Figure 6-5** (**C**)) and $AgNO_3$ mixed with nanogel system (**Figure 6-5** (**D**)) with or without UV irradiation were monitored by the silver electrode. **Figure 6-5** (**C**) shows that the Ag^+ concentration of Ag^+-nanogel system increased slightly over time in the absence UV irradiation (blue line), which was caused by Ag^+ concentration across the nanogel when Ag^+-nanogel solution

was mixed with water. The continuous increase in the Ag^+ concentration confirmed the diffusion of the Ag^+ from the nanogel template. However, the concentration of silver ion of Ag^+-nanogel system under UV irradiation displayed three stages, which confirmed the necessity of UV irradiation for the photoinduced reduction of silver ion to AgNCs. The silver electrode test was also conducted with AgNCs@25min (no UV irradiation during the test) by using a manual setup (**Figure S13**), and the results are shown in **Figure S14**. A high Ag^+ release rate was observed in the first 30 mins followed by a continuous gradual release of Ag^+ in the following 11 hours due to the lack of UV irradiation. **Figure 6-5** (**D**) shows two additional experiments on the Ag^+ concentration when 1 mL of 0.0005 M $AgNO_3$ was added to 19 mL of 1.74 wt% nanogel with or without UV irradiation. Without UV irradiation (D, black line), the concentration of silver ion spiked after the addition of $AgNO_3$, and it decreased exponentially as Ag^+ diffused into the nanogel and reached a steady state at around 2500s. When UV irradiation was applied once the Ag^+ ion concentration approached a steady state (D, red line), it then decreased again due to the photoinduced reduction of Ag^+ to Ag^0, where it then achieved the second equilibrium at around 6200 s. One thing need to be noticed is that the [Ag^+] of these two systems ranged between 1800-2500 ppm after the addition of $AgNO_3$ respectively, which was much higher than the Ag^+-nanogel system. This result is consistence with other studies, where only small amounts of -COOH inside a nanogel could be occupied by metal ions. For instance, only 12.5% of -COOH groups were occupied by Cd^{2+} in a thermal responsive nanogel system, due to the strong chelation of nanogel with Cd^{2+} ions, where multiple COO^- groups coordinated with one Cd^{2+} [382]. For the same reason, Su and coworkers conducted multiple Fe^{2+} coordination steps to improve the iron loading efficiency when synthesizing magnetic particles [383].

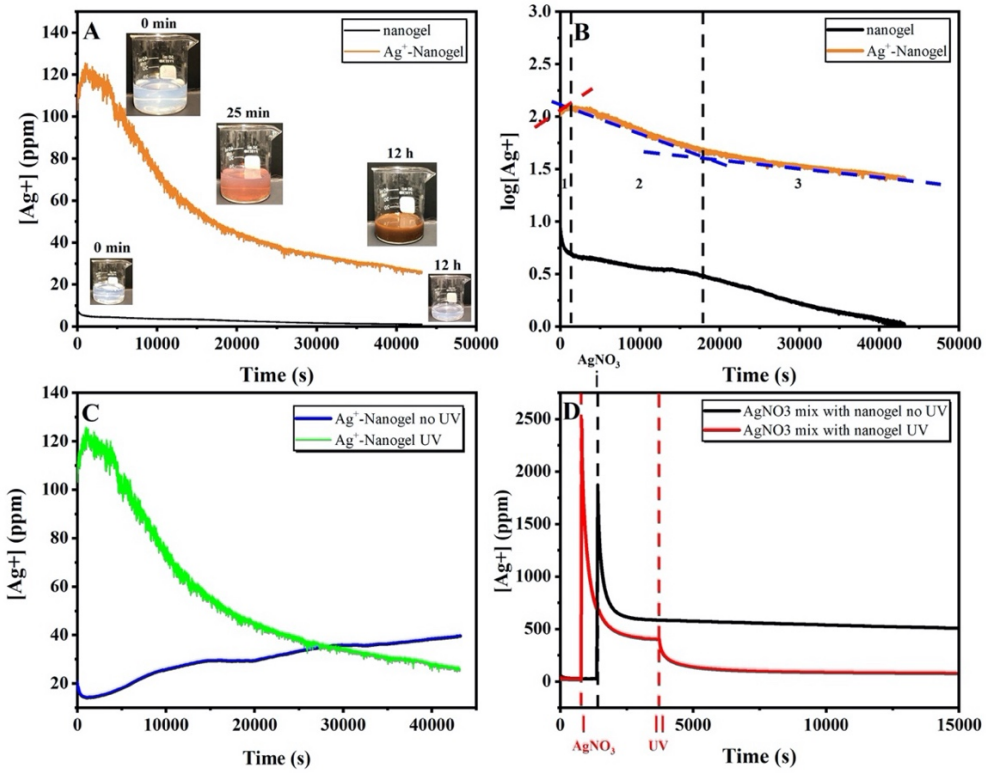


Figure 6-5 Ag^+ concentration as a function of UV irradiation time (A), and concentration in log scale (B), Ag^+ concentration of silver ion chelated nanogel (after dialysis) with or without UV irradiation during the silver titration process (C), Ag^+ concentration of $AgNO_3$ mixed with nanogel with or without UV irradiation during the silver titration process (D)

Additional silver electrode test with pure nanogel, $AgNO_3$ solution and Ag^+ incorporated nanogel (after dark dialysis) under UV irradiation is shown in **Appendix 6-5**, **Appendix 6-6** and **Appendix 6-7** respectively. The silver ion measurement experiments were conducted under the UV irradiation to investigate the change of [Ag^+] in the bulk solution. It can also provide the information about the diffusion of Ag^+ across the nanogel barrier, the dissolution of Ag^+ from the reduced AgNCs inside the nanogel. **Appendix 6-5 (d)** shows that the concentration of Ag^+ in the nanogel bulk solution presented a decreasing trend at the very beginning of the test (around 400s), this was due to the stabilization of the silver electrode at the starting point. Then, the [Ag^+] was stabilized at around 1 ppm, which roughly equals to 0 ppm. Also, there was no color change of the

nanogel solution before and after UV irradiation. **Appendix 6-6** presents the silver ion electrode test of pure $AgNO_3$ solution under UV irradiation. The Ag^+ ion release behavior of nanogel mixed with $AgNO_3$ under UV irradiation was conducted and monitored by silver electrode. The silver ion calibration curve, log [Ag^+] versus UV irradiation time (s), electrode measured value versus time (s) and silver concentration [Ag^+] versus UV irradiation time is shown in **Appendix 6-6 a**, **b**, **c**, **d** respectively. At beginning, the silver electrode was assembled in the silver nitrate solution. UV irradiation was applied when the concentration of silver ion became stable (at around 2500s). After a slightly increase of [Ag^+], there are some fluctuations in the electrode outputs. It was found that black silver oxide particles formed in the aqueous system, and they might bind to electrode surface resulting in the fluctuations in the [Ag^+] signals (**Appendix 6-6** (**b**)). Large black silver oxide particles were evident from the micrographs shown in **Appendix 6-6** (**d**) after 200 min UV irradiation. There is no color change after 12 hours UV irradiation of the nanogel solution mixed with $AgNO_3$ system, which indicated the necessity of the incorporation reaction of the Ag^+ with the nanogel scaffold before the UV irradiation process. The COOH groups from nanogel acted as a growing modifier for the formation of AgNCs. Also, there was no color change was observed from the nanogel solution mixed with $AgNO_3$ system that indicated no AgNCs was formed. **Appendix 6-7** (**d**) shows the variation of [Ag^+] in the Ag^+-nanogel system, the color of Ag^+-nanogel solution transformed from translucent to light pink to dark reddish brown during the UV irradiation, which confirmed the formation of AgNCs via photoinduced reduction process.

In the case of the Nanogel-AgNCs system, the continuous measurement of silver ion concentration of AgNCs@25min was conducted by assembling the silver electrode to a pH meter as shown in **Appendix 6-8**. The calibration curve, of log[Ag^+] versus time and [Ag^+] versus time are shown in **Appendix 6-9 (A, B, C, D)**, respectively. The concentration of Ag^+ increased

dramatically in the first 30 min after the AgNCs@25min was mixed with water to prepare a certain concentration of the test solution. This increase was due to the concentration difference of Ag^+ inside and outside the nanogel (**D**). Also, the dissolution of Ag^+ from AgNCs@25min also contributed to the increase in the Ag^+ concentration. As indicated from (**D**), the concentration increased gradually after 30 min till the end of the test (11h) due to the Ag^+ dissolution from the formed AgNCs@25min. However, without UV irradiation, no further reduction of Ag^+ occurred, which was similar to the Ag^+-Nanogel without UV irradiation as shown in **Figure 6-5, C** (Blue line), where it would approach a plateau at long time.

AgNCs possessed attractive antimicrobial property, due to the interaction between the oxidative dissociated silver ions and the living organisms. Thus, the release rate of Ag^+ from AgNCs determined the level of anti-bacterial performance, and the release of Ag^+ from AgNCs is controlled by three process that governs the silver ion concentration in the bulk solution: (1) the diffusion of Ag^+ coordinated with -COOH groups from the interior of the nanogel, (2) oxidative dissolution of Ag^+ from the AgNCs inside the nanogel, and (3) reduction of Ag^+ to Ag^0 or AgNCs inside the nanogel, which would indirectly determine the Ag^+ concentration in the bulk solution. The process (1) and (2) will elevate the Ag^+ concentration, while (3) reduces the $[Ag^+]$ inside the nanogel, leading to a reduction in the $[Ag^+]$ in the bulk solution. To investigate the correlation between the antimicrobial performance of AgNCs@ different UV irradiation times and the silver ion release rate, the variation of $[Ag^+]$ in the bulk solution were analyzed using different diffusion models. By fitting the concentration profile of silver ion in the bulk solution, the mechanism of reduction of Ag^+ to Ag^0 could be elucidated. There are various well documented diffusion and release models [384], in this work, zero and first order model was used to fit this photoinduced reduction process. The zero-order model explained a linear particle-forming mechanism, which

indicated a homogeneous growth mechanism without aggregation. However, the first order model described an exponential relationship of particle growth for the non-homogeneous particle formation process. The zero order (Eq. (6.2)) and first order (Eq. (6.3)) diffusion models were used to evaluate the diffusion rate of Ag^+-nanogel system and to elucidate the reduction mechanism of silver ions inside the nanogel.

$$\text{Zero order model: } C_0 - C_t = k_0 t \quad (6.2)$$

$$\text{First order model: } \log C_0 - \log C_t = k_1 t / 2.303 \quad (6.3)$$

where C_0 (ppm) is the initial concentration of Ag^+ in the bulk solution; C_t (ppm) is the concentration of Ag^+ at time t (S); k_0 (s^{-1}) and k_1 (s^{-1}) represents the zero-order diffusion constant and the first order diffusion constant, respectively.

The value of [Ag^+] at different regions and the diffusion constants determined from the zero and first order model are summarized in **Table 6-2**. Zero order model (R^2=0.95) fitted best in Region 1, describing the linear dependence of [Ag^+] with time. This is consistent with the results of increased particle size and zeta potential, where the Ag^+ were released from the relaxed nanogel structure. In Region 2 (R^2=0.99) and Region 3 (R^2=0.98), the first order model was a better fit, which is consistent with the growth of AgNCs and the aggregation of small AgNCs into large AgNCs. However, the slope in Region 2 was greater than Region 3, since in Region 2, the reduced Ag^0 clusters were smaller and possessed a higher surface area, which promoted the reduction of Ag^+ and accelerated the depletion of Ag^+ in the bulk solution. In Region 3, the AgNCs were larger and had a low surface area than Region 2 and the rate of reduction of the Ag^+ to Ag^0 was lower, which was consistent to a smaller slope.

Table 6-2 The concentration of remaining silver ions in the nanogel solution and the fitted 0 order and 1st order reaction rates

Region	t (s)	$[Ag^+]$ (ppm)	k_0 (s^{-1})	R^2	t (s)	$[Ag^+]$ (ppm)	k_1 (s^{-1})	R^2
-	0	103.11	-	-	0	2.01	-	-
1	0-668.7	122.41	-0.0219	0.95	0-1130.1	2.10	-4.48E-05	0.92
2	668.7-16149.9	48.91	0.0095	0.89	1130.1-15164.1	1.71	2.74E-05	0.99
3	16149.9-43187.4	25.95	0.0042	0.96	15164.1-43187.4	1.41	1.05E-05	0.98

6.5.7 Yeast test and CO_2 release studies

Metabolic processes of yeast produce carbon dioxide, which could be used to evaluate the antimicrobial or antifungal activity of the AgNCs. The yeast, *S. cerevisiae* produces CO_2 when incubated with sugar solution at 35 to 40 ºC under the aerobic fermentation condition [385]. Thus, the metabolic activity could be utilized to assess the antimicrobial performance of AgNCs by comparing the CO_2 release rates.

A simple, and reliable experimental set-up consisting of a magnetic stir plate, temperature-controlled water bath, and a volumetric flask connected to an inverted burette for capturing CO_2, is shown schematically in **Appendix 6-10.** Various concentrations of AgNCs were incubated with glucose and yeast at 40° C before the start of the experiment, and the volume of CO_2 generated was recorded.

Antimicrobial activity of AgNCs @ various UV irradiation times was assessed from the release of CO_2 from yeast (*Saccharomyces cerevisiae*). CO_2 release rate was recorded and analyzed over a 30 min period. Yeast tests were performed at pH 5 and 8, and there is no apparent difference in yeast activity at pH 5 and 8 (shown in **Appendix 6-11** (**a**) and **Appendix 6-12** (**a**)),

confirming that the pH had no impact on the CO_2 production [386]. To examine the antimicrobial performance of AgNCs@ different UV irradiation times and concentrations, CO_2 production rate from AgNCs (0, 6, 25, 40, 80, 200, 360) min UV were measured and shown in **Appendix 6-12** (**b**, **c**, **d**, **e**, **f**, **g**, **h**) respectively.

Figure 6-6 (A) shows the highest minimal inhibitory concentration (HMIC) of the AgNCs@ various UV irradiation time. AgNCs@0min possessed a relatively high HMIC (165 ppm), as illustrated by the relatively low antimicrobial activity of Ag^+-nanogel system. The release rate of Ag^+ across the nanogel was limited since the Ag^+ were strongly chelated to the carboxyl groups in the nanogel, this resulted in low antimicrobial activity. After 6 min of UV irradiation, the HMIC of Ag@6min decreased dramatically from 165 ppm to 11 ppm. When AgNCs were formed in the nanogel scaffold, upon UV irradiation the release of Ag^+ from Nanogel-AgNCs were not inhibited by the carboxylate groups that were coordinated with Ag^+. Moreover, the Ag^+ release rate was enhanced by the oxidative dissolution of Ag^0 to Ag^+, accelerating the diffusion of Ag^+ to the bulk solution [387].

As the UV irradiation proceeded, separate AgNCs were aggregated into large AgNCs with a reduced surface area and oxidative dissolution of Ag^+, resulting in a diminished antimicrobial activity. The lowest HMIC was observed for AgNCs@25min, where the AgNCs possess the highest Ag^+ release rate. Beyond the 25 min, further increase in the UV irradiation time to 360 min resulted in a much higher HMIC, which was associated with the reduction in the surface area of the aggregated AgNCs. These results are consistent with the blue shift of the UV absorbance bands of AgNCs produced between 25 to 360 min of UV irradiation. The proposed microstructure and antimicrobial mechanism of AgNCs @ different UV irradiation time against yeast is illustrated in

Figure 6-6 (**B**). The nucleation phase of the Ag formation should be completed between 6 to 40 min, followed by the growth and aggregation of small AgNCs into larger AgNCs.

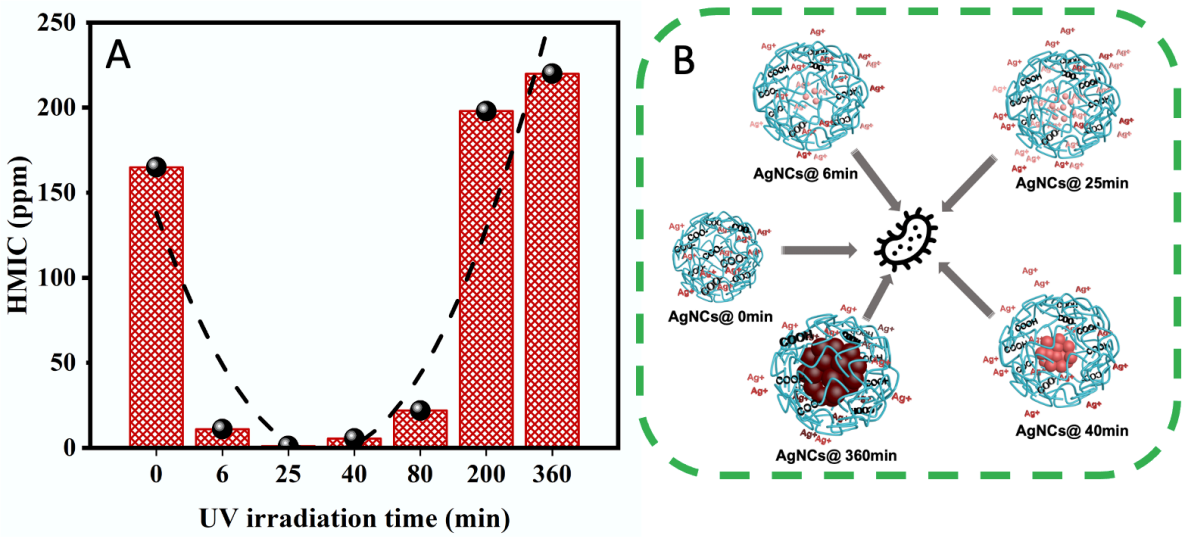


Figure 6-6 (A) Highest minimal inhibitory concentration (HMIC) of AgNCs under different UV irradiation time, (B) Proposed antimicrobial mechanism of AgNCs@ different UV irradiation times against yeast

The CO_2 production rate of yeast for AgNCs@ different UV irradiation times are summarized in **Figure 6-7**. When no UV irradiation was applied, (AgNCs@0min), the CO_2 production rate of yeast decreased rapidly and approached 0 at 170 ppm (black line). When the UV irradiation time was less than 25 min, the yeast CO_2 production rate dramatically decreased when the concentration of AgNCs was increased. However, there was a minor difference in the CO_2 production rate of AgNCs@>40min at low concentrations (<50ppm), and zero CO_2 production rate were achieved between 150 to 250 ppm. Because after 25min aggregation of AgNCs within the nanogel began to dominate the system and significantly weakened antimicrobial activities. The difference in antimicrobial susceptibility between AgNCs@<40 min and AgNCs@>40 min confirmed the importance of the surface area on the release of silver ions.

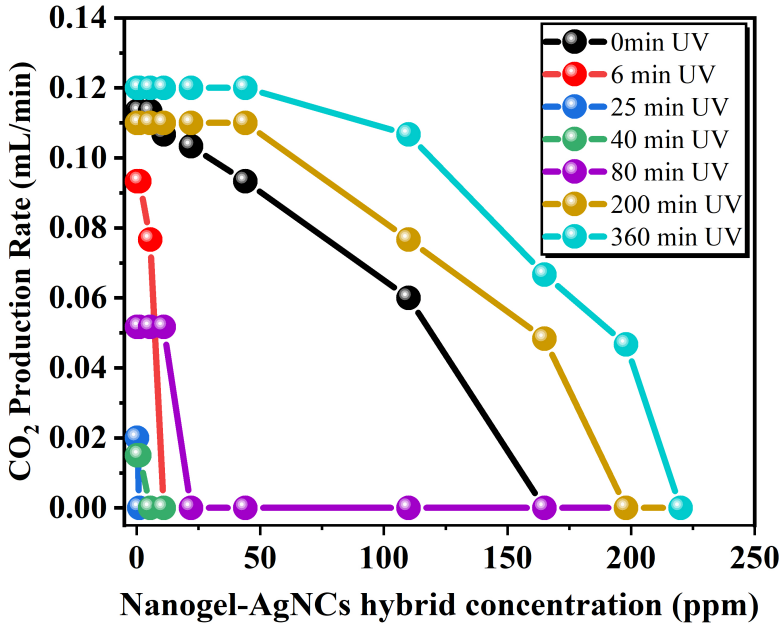


Figure 6-7 The CO_2 production rate versus concentrations of AgNCs

6.5.8 Microscopic and biolabeling applications

AgNCs synthesized via the photoinduced reduction possessed unique fluorescence emission, which could be harnessed for biolabeling application. **Figure 6-8** shows the microscopic and fluorescence images of yeast with and without AgNCs. Methylene blue (MB) dyed yeasts had an integrated "rice" shape structure when treated with the nanogel scaffold, confirming that the nanogel template had no antimicrobial activity (**Figure 6-8 (a)**). Under the FITC filter, the MB dyed yeast displayed red fluorescence illumination (**Figure 6-8 (b)**). Two different concentrations (1.1 ppm and 11 ppm) of 6 min-AgNCs treated yeast samples were selected for microscopic analysis, since the 11 ppm corresponded to the HMIC of AgNCs@6min. The microscopic images of 1.1 ppm and 11 ppm AgNCs@6min with MB-treated yeast test sample are presented in **Figure 6-8 (c, e)** and corresponding fluorescence images are shown in **Figure 6-8 (d, f),** respectively. Few disrupted yeasts were evident under the microscope, and they displayed red illumination when

imaged in a fluorescence microscope (**d**, **f**). As the concentration of AgNCs@6min was increased from 1.1 ppm (**c**, **d**) to 11 ppm **Figure 6-8** (**e**, **f**, **g**), some aggregation was observed,

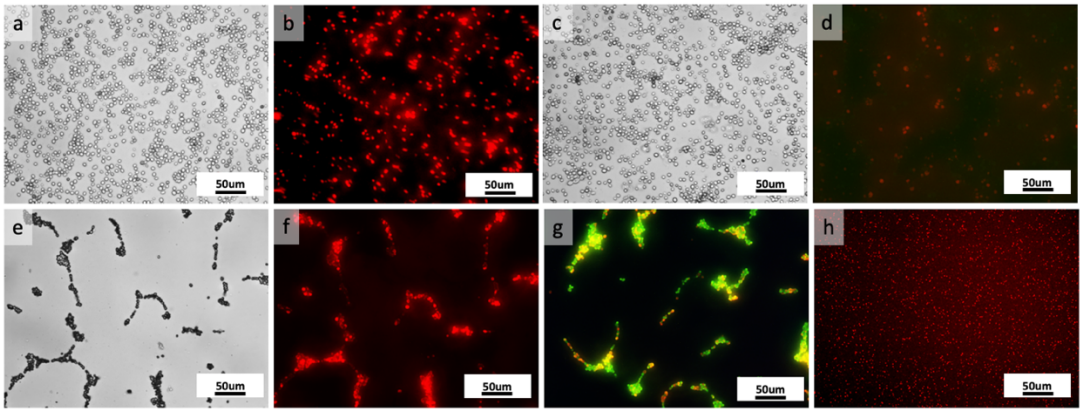


Figure 6-8 Microscopic image and fluorescence image (FITC filter) of nanogel treated yeast test sample dyed with MB (washed 2 times) a, b; Microscopic image and fluorescence image (FITC filter) of AgNCs@6min-1.1 ppm yeast test sample dyed with MB c, d; Microscopic image of AgNCs@6min-11 ppm yeast test sample dyed with MB e; Fluorescence microscopic image of AgNCs@6min-11 ppm yeast test sample dyed with MB under FITC, f and FITC merged with TRITC filter, g; Fluorescence microscopic image of AgNCs@6min-2.2 ppm under FITC filter, h

and this could be attributed to the lower repulsive forces caused by the ruptured yeast cell membrane. The AgNCs@6min treated yeast test, sample displayed red illumination under the FITC filter (**Figure 6-8** (**f**), **Appendix 6-13** (**f**)), while a bright green illumination with minor red illumination was observed under the merged filter (FITC-TRICT) mode (**Figure 6-8** (**g**), **Appendix 6-13** (**g**)).The fluorescence images of AgNCs@25min is presented in **Figure 6-8** (**h**). There's no illumination of AgNCs@0min yeast test samples (**Appendix 6-13** (**i**)), while strong illumination was observed in AgNCs@25min (**Figure 6-8** (**h**)) since there was no reduced Ag^0 in AgNCs@0min (**Appendix 6-13** (**i**)), which was responsible for the red fluorescence. For AgNCs@6h treated yeast test sample, weaker fluorescence was observed (**Appendix 6-13** (**l**)). As Ag ions were reduced to AgNCs, the aggregation of the small AgNCs to form larger AgNCs occurred, resulting in a reduction in the fluorescence emission [372]. AgNCs exhibited red

fluorescence under both FITC filter and (FITC-TRITC) merged filters (**Figure 6-8** (**h**), **Appendix 6-13** (**l**)). Live yeast dyed with MB also displayed red fluorescence (**Figure 6-8** (**b**)). On the other hand, when the filters were merged, dead yeast dyed with MB possessed green fluorescence (**Figure 6-8** (**g**)) [388], and the red fluorescence associated with the yeast aggregation were from the AgNCs bonded with dead yeast (**Figure 6-8** (**g**)). The fluorescence results agreed with the CO_2 release rate from the yeast studies, where a higher CO_2 release rate was observed for the 1.1 ppm AgNCs@6min and an almost zero CO_2 release rate was reported for the 11 ppm AgNCs@6min (**Appendix 6-13** (**c**)).

6.5.9 Antibacterial test

The mechanism describing the antimicrobial effect of silver is still unclear. Four major mechanisms have been proposed: (i) cell wall and membrane damage, (ii) cell permeation and intracellular disintegration, (iii) oxidative stress caused by reactive oxygen species (ROS), and (iv) modulation of signal transduction pathways [389]. Interestingly, studies suggested that smaller AgNPs are more efficient. Li et al. reported that the antimicrobial performance against *E. coli* and *S. aureus* colonies was better for small AgNPs than larger AgNPs [390].

The antibacterial activities of AgNCs@ different UV irradiation times against *E. coli* and *S. aureus* were evaluated by determining the MIC (**Figure 6-9**). Compared with the untreated control, *E. coli* treated with 2.2 ppm of AgNCs@0-200min showed considerable antibacterial activity. On the other hand, at the same concentration, Gram-positive *S. aureus* was more resistant. Furthermore, a superior antibacterial activity of AgNCs@0-200min was observed at 11 and 22 ppm for *E. coli* and *S. aureus*, and the respective MIC values were recorded. Interestingly, *E. coli* was more sensitive to the AgNCs than *S. aureus*. However, the AgNCs still showed excellent

inhibition of bacteria for *S. aureus* at higher concentrations, confirming that the synthesized materials possessed excellent antibacterial activity.

E. coli residing in the intestine are mostly harmless; some pathogenic strains cause diarrhea or other intestinal tract disorders. *S. aureus* grows on healthy human skin or nose, and they readily attach to the human proteins, such as fibrin, hence they would attach to bio-surfaces (e.g., catheters, valves). These organisms produce biofilm that protects the persister cells against antimicrobial agents responsible for the significant hospital-acquired infections [391]. Our AgNCs are highly potent towards Gram-negative bacteria, confirming the results reported in the literature [392] [393]. Gram-positive bacteria are resistant because of the thick, complex peptidoglycan layer compared to the weaker lipopolysaccharide layer of Gram-negative bacteria. All *E. coli samples* can be

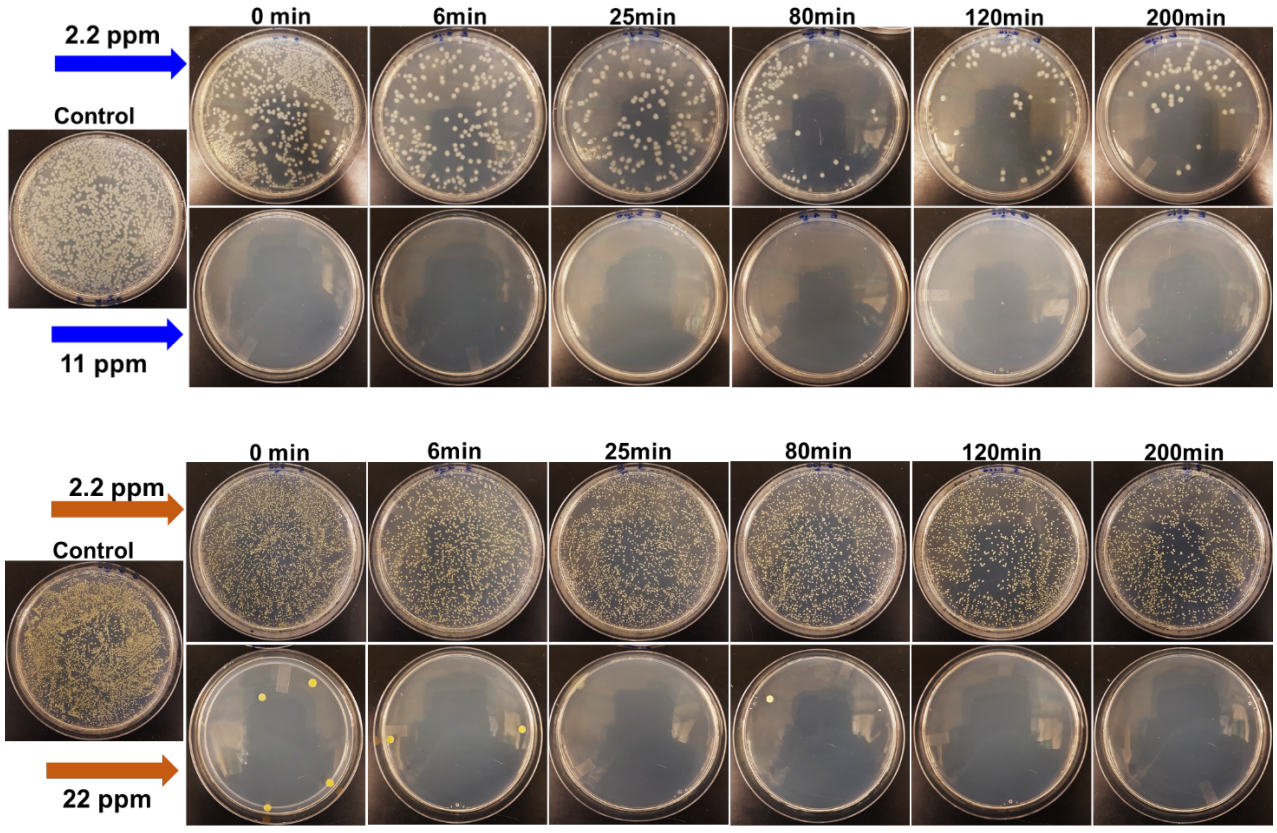


Figure 6-9 Antibacterial activity of AgNCs under 0, 6, 25, 80, 120 and 200 min UV irradiation time against E. coli (top) and S. aureus (bottom)

completely killed with 11 ppm AgNCs, while *S. aureus* samples required 22 ppm. According to UV-vis spectra, COO^- chelated Ag ions inside the nanogel scaffold would be immediately reduced to Ag^0 upon UV irradiation. The formation of AgNCs disrupted the strong coordination between Ag^+ and COO^- inside the nanogel, resulting in a more relaxed nanogel structure. Thus, the improved antibacterial activity was correlated to the elevated Ag^+ diffusion rate from the nanogel. At the same time, the formed AgNCs also promoted the Ag^+ release due to the oxidative dissolution mechanism. The smaller AgNCs displayed better antibacterial activity due to the larger surface area, resulting in a faster released of Ag^+ that interacted with the cell surfaces [394]. Additionally, the AgNCs prepared by in-situ photoreduction of Ag^+ inside the nanogel scaffold were highly stable over a long period due to the large repulsive forces between the negatively charged carboxylic groups.

Visible interaction of AgNCs with yeast, *E. coli* and *S. aureus* were examined by TEM, and to study the interactions between yeast and AgNCs, 11 ppm of AgNCs@40min was selected, as it had a 100% yeast killing in antifungal test (**Appendix 6-11**, **e**). Partial and fully dissociation of yeast cell membrane was clearly observed in the TEM images (**Appendix 6-*14*, (1-4)**). Also, the aggregation of "naked" yeast core was observed due to the breakage of the yeast membrane. AgNCs were observed in both the background and on the yeast cell membrane. This supported the traditional antibacterial mechanism of silver metals where the oxidative dissolution of Ag^+ ions penetrated the cell membrane [395]. The release and penetration of Ag^+ released from the AgNCs disrupted the cell wall structure and triggered the leakage of intra-cellular content of the yeast. In addition, the penetrated Ag^+ chelated with the thiol groups of the yeast protein, which interfered with the replication of DNA and disrupted the respiratory cycle [396] [397] [398].

TEM images of antimicrobial test against *E. coli* and the nanogel, AgNCs@0min, AgNCs@25min, AgNCs@360min are shown in **Appendix 6-*14*** (**5-8**). The TEM images of antimicrobial test against *S. aureus* in nanogel, AgNCs@0min, AgNCs@25min, AgNCs@360min are shown in **Appendix 6-*14*** (**9-12**). *E. coli* treated with nanogels only (**Appendix 6-*14*** (**5**)**)** possessed robust and complete cell membrane without aggregation. Many grey color AgNCs appeared in the background of AgNCs@0min (**Appendix 6-*14*** (**6**)), and only a few were attached to the surface of cell membrane causing the breakage of the cell membrane. *E. coli* treated with AgNCs@25min (**Appendix 6-*14*** (**7**)) resulted in the disintegration of the cell membrane and severe agglomeration confirming its effective antibacterial property, and darker AgNCs were observed to bind to the bacterial cells. In terms of AgNCs@360 min treated *E. coli* (**Appendix 6-*14*** (**8**)), larger and darker AgNCs were observed. However AgNCs@360 min was not as efficient as AgNCs@25min, as it had a lower surface area. Robust and well-preserved *S. aureus* bacterial structure was observed when treated with pure nanogel (**Appendix 6-*14*** (**9**)), confirming the bare nanogel did not possess antimicrobial activity. AgNCs@0min also showed no impact on *S. aureus* (**Appendix 6-*14*** (**10**)), indicating the it displayed weaker antibacterial activity compared to *E. coli.* However, AgNCs@25min treated *S. aureus* (**Appendix 6-*14*** (**11**)) showed a clear cell membrane dissociation caused by the released Ag^{+}. In comparison, AgNCs@360min treated *S. aureus* showed minimal antibacterial activity (**Appendix 6-*14*** (**12**)). Overall, at 25min UV irradiation yielded the optimum antibacterial property in the AgNCs-hybrid, and further increase in the UV irradiation time weakened the antibacterial property due to the reduced surface area of the AgNCs.

We observed that silver at specific concentrations was lethal to Gram-negative bacteria and to a much lesser extent on Gram-positive bacteria, due to the difference in the cell wall structure, composition and thickness of the cells, and the arrangement of the peptidoglycan layer [389].

Lipopolysaccharides (LPS) in the Gram-negative bacteria cell membrane contributed to the structural integrity and protection from chemical attacks. However, the negative charge of LPS renders the adhesion of silver making the bacteria more susceptible to antimicrobial treatment [389] [399]. On the other hand, the cell wall of Gram-positive bacteria comprised of negatively charged peptidoglycan layer, which was more stable than in Gram-negative bacteria. The lower susceptibility of Gram-positive bacteria towards antibiotics and silver ions can be explained by the thicker cell wall than Gram-negative bacteria [400]. Thus, the Gram-positive bacteria *S. aureus* prevents the immediate antibacterial action of silver ions, hence this bacterium is more resistant to silver [401].

6.6 Conclusions

The synthesis of AgNCs and AgNPs has been a challenging and many previous studies have focused on developing new approaches to fabricate stable AgNCs [360][372][402]. Due to the rapid reduction rate and the difficulty in controlling the particle size, photo-reduction [403] has been emerged as a good alternative. However, the stability and toxicity associated with pure AgNCs or AgNPs have limited their further application. In this study, MAA-EA nanogel was used as a "nano reactor" for the in-situ synthesis of AgNCs via the photoreduction process. The hypothesis is that the carboxyl groups from the nanogel could function as a growth modifier for AgNCs that could stabilize AgNCs of varying sizes within the nanogel under UV irradiation. The antimicrobial property is closely related to the rate of Ag^+ release, which was monitored by a silver electrode assembled with the UV irradiation system. A three-stage Ag^+ diffusion process from the Nanogel-Ag^+ system was observed, and they correlated with the antimicrobial performance, where the AgNCs@25min possessed the lowest HMIC (1.1 ppm or 1.1 μg/mL), which corresponded to the highest Ag^+ release rate. Aggregation of small AgNCs ($t > 25$ mins) occurred with increasing

UV irradiation time, resulting in a lower Ag^+ diffusion rate and a lower antimicrobial performance. Small AgNCs ($t \leq 25$mins) possessed unique fluorescent emission characteristics, enabling the possibility of distinguishing between live and dead yeast in a fluorescence microscope. The highly stable nanogel templated AgNCs are effective antimicrobial agents that could be recovered after use, thereby reducing the negative impact on the ecosystem compared with other AgNPs [404] and pristine AgNCs reported previously [372]. Herein, the nanogel scaffold functioned as both nanoreactor allowing for precise size and shape control and stabilizer of AgNCs in aqueous solution. The size dependent photoluminescence of AgNCs inside the nanogel template could be controlled by UV irradiation time and intensity. Based on these excellent chemical, physical and biocompatible properties of the fluorescent AgNCs, they could be utilized in drug delivery, antimicrobial and biolabeling applications. Furthermore, this nanogel template could be used for the synthesis and encapsulation of organic and inorganic materials with better morphology control.

Chapter 7: A Novel Magnetic Cluster modified Palladium-Cellulose Nanocrystal Hybrids as Recyclable Catalyst for 4-Nitrophenol Reduction

The development of noble metal catalysts with high catalytic performance and low metal loading has attracted a lot of interest. However, the separation of the used nanoscale catalyst from the applied system is challenging, most of the realization format like resin or membrane system lead to a sacrifice of the high surface area as well as catalytic efficiency. In this chapter, two series of recyclable catalysts were synthesized by loading palladium (Pd) particles onto melamine formaldehyde (MF) modified cellulose nanocrystals (CNC) and dopamine (DA) coated CNC. *In situ* co-precipitation of magnetic nanoparticle (MNP) clusters were used to impart magnetic characteristic to the catalysts. This magnetic cluster successfully achieved high magnetization without aggregation issue. The amount of palladium precursor added to the catalytic systems was optimized, where 10-Pd-PDC yielded 10.83 ± 2.43 nm discrete Pd loaded hybrids. The catalytic performance of the catalysts was assessed by the reduction of 4-nitrophenol (4-NP) in the presence of sodium borohydrides ($NaBH_4$). The 4-NP reduction mechanisms were analyzed using the Langmuir-Hinshelwood model and the apparent rate constant k (s^{-1}), turnover frequency (TOF, h^{-1}) and activity factors ($s^{-1}g^{-1}$) were determined to be 2.142×10^{-3}, 305.82 and 535.5 using MNP2-Pd-MC respectively. An induction time was observed for MNP-4 or 5-Pd-PDC, where was attributed to the unignitable diffusion time for reagents to across the thick PDA and MNP layer. The separation efficiency of the magnetic catalysts was evaluated by monitoring the absorbance at 400 nm as a function of separation time, and the MNP2-Pd-MC could be recycled 7 times without severe loss. Pd-MF-CNC displayed excellent catalytic performance for the reduction of 4-NP, while Pd-PDA-CNC possessed a lower catalytic reactivity due to the inferior catalytic surface

area. The developed templated MNP could be extended to other systems allowing for the recycling and reuse of the catalysts or adsorbents.

7.1 Introduction

Without adequate wastewater treatment, direct discharge of polluted water can adversely affect human health and the ecosystems. Many types of pollutants existed in wastewater including organic compounds, such as aromatic hydrocarbons, organic colourants, plasticizers, phenols, and endocrine disruptors [405]. Phenolic compounds (common organic pollutants in industrial and agricultural wastewater) can damage the central nervous system, liver, kidneys and blood of both humans and other animals [406]. 4-Nitrophenol (4-NP) is among the most abundant phenolic derivatives used in pesticides, dyeing and pharmaceuticals. It is an endocrine disrupting chemical (EDC) that interfere with the synthesis, secretion, transport, activity or elimination of natural hormones, inhibit or mimic hormonal action, and disrupt the human physiological system. The human body may respond with a series of inappropriate changes and this produces a wide range of adverse effects like obesity, cancer, malformation of sex organs etc [407]. Therefore, improving wastewater treatment for specific pollutants, such as 4-NP is urgently needed.

Currently, many strategies are being used to treat wastewater and reduce the concentration of pollutant to an acceptable level, including adsorption, membrane filtration, flocculation, ion exchange, and catalytic processes. Adsorption processes using activated carbon (AC) are considered to be one of the most effective methods to eliminate contaminants from wastewater, due to their fast kinetics, high adsorption capacity, low cost and easy operation [408]. However, the selectivity of AC-based adsorbent is generally low, and a secondary separation process is often required. In addition, the high temperature required to regenerate the used AC is energy-intensive with a significant carbon footprint [409]. Membrane processes offer advantages over traditional

wastewater treatment, such as compliance with the highest standards, reducing the environmental impacts of effluents, field requirements and potential of mobile processing units [115]. However, the primary challenge of membrane filtration is the reduction of permeate flux with time due to the build-up of contaminants within the pores and membrane surface [410]. These contaminants must be removed periodically since fouling will directly influence the separation efficiency and lifecycle costs. Coagulation or flocculation is an efficient process that is easy to use but suffers from high chemical costs [411]. Ion exchange systems are excellent for de-alkalization, deionization and water softening, and work by exchanging undesirable ions for more desirable ions of similar charge. However, non-ionic substances, such as 4-NP, cannot be eliminated by ion exchange. Catalytic processes can be a competitive alternative since they can break down the pollutant into non-toxic or less harmful compounds that can be directly released into the environment. Catalytic processes are less operationally sensitive and possess faster reaction kinetics. Contrary to ion exchange, membrane filtration, or adsorption, catalytic processes do not transfer contaminants into a separate, more concentrated waste streams [412]. The reduced product of 4-NP, 4-aminophenol (or 4-AP), is an effective component in various applications, such as production of analgesic and antipyretic, and as a corrosion inhibiting lubricant [152]. Therefore, the development of novel catalytic systems with the capability to effectively reduce 4-NP in an environmentally conscious manner has gained increasing attention in recent years.

Noble metals, such as Ag, Au, Pt and their alloys, have received attention for their application as high-performance catalysts in a wide range of reactions [413][414][415][416], due to their high surface area-to-volume ratio, inherent adsorptive properties, and easy access to a large number of active sites [413]. However, noble metal catalysts are scarce, costly, and sensitive to high temperatures, which has motivated the search for other replacement catalysts. Metal oxides

(semiconductors), such as TiO_2, ZnO and ZrO_2, are alternative catalysts for oxidative reactions, while being less active at low temperatures [417]. Moreover, nanoscale catalytic particles tend to aggregate, thus a support matrix is needed to prepare efficient catalysts. Recent studies using palladium (Pd) have demonstrated higher activity compared to other noble metals for a number of reactions, such as catalytic oxidation and hydrogenation, cross-coupling reactions, and most commonly, the reduction of 4-NP [418].

The catalytic activity of metal particles is highly dependent on the shape, size and distribution of metal particles. An effective way to achieve better use of these catalytic nanoparticles is to immobilize them on a suitable support consisting of three main characteristics: (i) large surface area, (ii) high affinity for catalytic metal and (iii) excellent chemical stability in the operating environment to maintain a stable catalytic structure [419]. A much lower amount of metal was required for nano-sized catalyst to yield the same surface area compared to its bulk equivalent. Currently, most of the agents used to stabilize Pd nanoparticles are non-biodegradable polymers or potentially toxic chemicals. A promising approach is by using sustainable nanomaterials as template, such as cellulose nanocrystals (CNCs) to load and stabilize Pd nanoparticles. CNCs are rod-shaped nanoparticles that possess high mechanical strength, and high surface area (~500 m^2/g). They are biodegradable, making them an ideal substrate for catalyst immobilization in aqueous media [420]. Using smaller nano-sized catalyst can achieve a higher catalytic reaction rate. By considering the separation issue after use, the concept of magnetic catalysts was implemented to allow the non-invasive separation in recovering the catalyst without sacrificing its reactivity. A major problem with magnetic catalyst is its tendency to form larger aggregates that affect the stability. Thus, a precise size control and sufficient magnetization is critical when preparing magnetic particles.

In this study, two types of magnetic catalysts for the degradation of 4-NP in the presence of sodium borohydride were developed. CNCs provide the mechanical strength necessary for magnetic separation, the surface area needed for high catalytic activity, and the biodegradability to maintain a sustainable and environmentally friendly process. The mussel-inspired polydopamine (PDA) or the semi-porous melamine-formaldehyde (MF) resin were coated onto the CNC surface as adhesives to bind the Pd nanoparticles. A nanogel scaffold templated magnetic clusters were prepared by the assembly of the Pt-CNC catalyst to impart the magnetic property to the catalytic system. Catalytic performance and recyclability of these catalytic systems were then evaluated using the 4-NP reduction process.

7.2 Experimental

7.2.1 Materials

Methacrylic acid (MAA, 99 %), ethyl acrylate (EA, 99.5 %), di-allyl phthalate (DAP), sodium persulfate ($Na_2S_2O_8$, 99 %), sodium hydroxide (≥ 98%), polyvinylpyrrolidone (PVP, Mw =10K), dopamine hydrochloride (≥ 98%), tris ((hydroxyethyl) aminomethane) (≥ 98%), hydrochloride acid (≥ 99%), melamine (99%), formaldehyde (37% in water), ethylene glycol (≥ 99.8%), potassium tetrachloropalladate (98%), ammonia solution (28-30 wt%), iron (II) sulfate heptahydrate ($Fe_3O_4 \cdot 7H_2O$, ≥ 99%), sodium borohydride ($NaBH_4$, ≥ 98%), 4-nitrophenol (4-NP, ≥ 99%) were purchased from Sigma-Aldrich. Aerosol OT (AOT, 75%) were supplied by Thermo Fisher Scientific. Cellulose nanocrystals (CNC) were provided by Celluforce Inc.

7.3 Methods

7.3.1 Preparation of MAA-EA nanogel template

The MAA-EA nanogel was synthesized via a conventional semi-continuous emulsion polymerization process. A pre-emulsion was prepared by mixing 4.945 g MAA and 5.75 g EA

(1:1 molar ratio) together with 0.856 g of DAP, 1 g of 75 wt% AOT solution and 1.4 g of water. The reaction vessel contained 120 g water and 1g of AOT solution, while the initiator solution was prepared by dissolving 0.25 g of sodium persulfate in 2 g of water. The reaction vessel assembled with a condenser and an equalizing pressure funnel was placed on a magnetic hot plate and heated to 85 °C under continuous stirring. After 30 min of nitrogen purging, the initiator solution was added via a syringe. When the contents were well-dispersed, 5 wt% of the pre-emulsion mixture was added dropwise, and the remaining pre-emulsion mixture was added dropwise using a pressure equalizing-funnel after 30 min stirring. The reaction was left to proceed for another 30 min after the addition of the remaining monomer mixtures. The final product was then cooled to room temperature and filtered through a 200-mesh nylon cloth. The filtered nanogel solution was dialyzed against DI water until no excess surfactant was observed. The solid content of the dialyzed final product was approximately 5% by weight [273].

7.3.2 Synthesis of nanogel templated magnetic particles (MNP)

The templated MNP were synthesized via the in-situ coprecipitation of ferrous ions inside the nanogel scaffold. 120 mL of 0.5 wt% MAA-EA nanogel solution was adjusted to pH 6.5, and purged nitrogen for 30 min. Then, 2.5 g of $FeSO_4 \cdot 7H_2O$ was dissolved in 30 ml of de-oxygenated water and added dropwise to the reaction vessel with gentle mechanical stirring (250 rpm) for 2 h. Afterwards, ultrafiltration under nitrogen was used to remove free Fe^{2+} outside the nanogel yielding a brown colour filtrate. The ultrafiltration was repeated several times until a clear filtrate was obtained confirming that all the un-coordinated Fe^{2+} was removed. The Fe^{2+} grafted nanogel was heated to 35℃ and then 0.25 g $NaNO_2$ dissolved in 1 g of de-oxygenated water and 15 ml of 28 wt% ammonia solution were added to the reaction vessel forming a dark green suspension. Within 1 h, the dark green suspension turned black indicating that the reaction was complete. After

the reaction, the product was cooled and filtered through a 200-mesh nylon cloth for removing aggregated particles.

7.3.3 Synthesis of PVP-PDA coated CNC (PDC)

The CNC solution was first prepared by dispersing 0.4 g CNC in 90 ml of water and a well dispersed suspension was obtained after probe sonication. Afterwards, 8 ml of 0.5 wt% PVP solution was added to the CNC suspension and stirred for 16 h. The buffer solution prepared by dissolving 12 mg of tris ((hydroxyethyl) aminomethane) in 1 ml of water was added to the reaction vessel, and 1 ml of 40 wt% dopamine hydrochloride was added to the reaction system. It should be noted that O_2 was needed for the polycondensation of dopamine hydrochloride. Thus, the reaction vessel was covered by a perforated parafilm containing 50 holes. This reaction was left agitated for another 24 h and purified by several days of dialysis.

7.3.4 Synthesis of melamine formaldehyde modified CNC (MF-CNC or MC)

The melamine formaldehyde coated CNC was prepared according to a published protocol [421]. Firstly, 2.2 g of melamine and 4 ml of formaldehyde solution (37% in H_2O) were mixed in 10 ml of water. After adjusting the pH to 8-9 using NaOH solution, the reaction mixture was agitated for 30 min at 80℃. Subsequently, 100 ml of 0.5 wt% CNC suspension was added to the melamine formaldehyde (MF) precursor, the pH of the mixture was adjusted to 4 with 0.1 M HCl solution and stirred overnight at 80℃. Finally, the MF-CNC was cooled to room temperature and purified by dialysis.

7.3.5 Deposition of Pd particles onto MF-CNC and PVP-PDA-CNC

(a) Synthesis of Pd-MF-CNC (Pd-MC)

MF-CNC (10 mg) was added to 20 ml of ethylene glycol solution to form a well-dispersed suspension, where ethylene glycol acts both as a dispersant and as reducing agent. Subsequently, 10 mg of the palladium precursor (potassium tetrachloropalladate) was added to the suspension.

The reaction mixture was adjusted to pH 8 using 0.1 M NaOH solution and kept stirred at 110℃ under reflux for 2 h. Repeated ultrafiltration was applied to the Pd-MF-CNC for final purification before further characterization.

(b) Synthesis of Pd-PVP-PDA-CNC (Pd-PDC)

PVP-PDA-CNC (35 mg) was added to 30 ml of water and a well-dispersed suspension was obtained after a 30-min of bath sonication. The palladium precursor solution was prepared by dissolving 3.26 mg potassium tetrachloropalladate into 0.5 ml of water, and dropwise added to the PVP-PDA-CNC suspension and kept stirring for 24 h. The obtained Pd-PDC was washed three times with water and ethanol respectively.

7.3.6 Optimization of Pd loading for Pd-PDC synthesis

Four glass vials were loaded with 6g of CNC-PVP-PDA solution (0.193 wt%) and 5 g of water sonicated for 10 min. Different amounts of potassium tetrachloropalladate (5, 10, 15 and 10 mg) were dispersed in 0.5 ml of water and added dropwise to each of the CNC-PVP-PDA solution under gentle magnetic stirring. Another 0.5 mg dopamine dissolved in 0.5 ml of water was introduced to the last vial to investigate the effect of additional dopamine on Pd particle formation. All the samples were agitated for 24 h and dialyzed against de-ionized water for several days. All four samples named as 5-Pd-PDC, 10-Pd-PDC, 15-Pd-PDC and 10-Pd-PDC+PDA.

7.3.7 Assembly of MNP and Fe_3O_4 particles onto Pd-MC and Pd-PDC

(1) Fe_3O_4 preparation

The Fe_3O_4 particles were prepared using a conventional coprecipitation method. Typically, 24 g $FeCl_3 \cdot 6H_2O$ and 9.8g $FeCl_2 \cdot 4H_2O$ were dissolved in 100 ml of H_2O under nitrogen purging. The temperature was elevated to 80℃ and 50 ml of ammonia solution (28 wt%) was introduced under vigorous stirring. After 30 min, the reaction mixture turned black and 3.76 g oleic acid was charged into the reaction vessel, and the reaction was left for another 1.5 h. The final product (Fe_3O_4) was washed with water and ethanol 3 times and recovered using a magnet.

(2) Fe-Pd-MC preparation

5 mg of pure Fe_3O_4 was dispersed in 4 ml of ethanol by probe sonication, then they were introduced into 10 ml, 30 ppm of Pd-MC solution. The Fe_3O_4 nanoparticles would deposit and trap inside the MF-CNC driven by and electrostatic interaction to form Fe-Pd-MC.

(3) MNP1 to 5-Pd-MC preparation

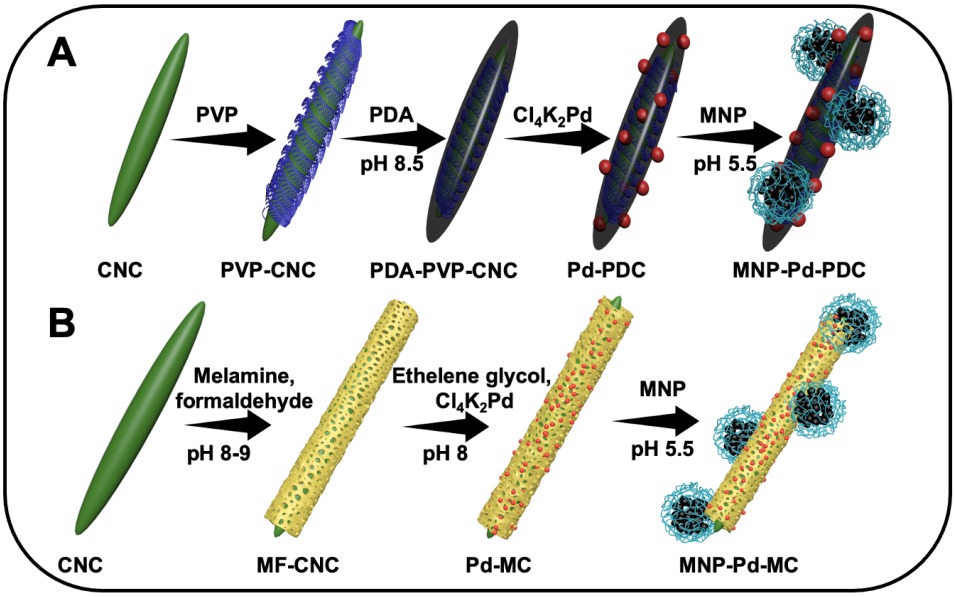
Five MNP-Pd-MC catalyst samples were prepared using 1 to 5 ml of MNP solution (solid content: 0.1 wt%). The magnetic particles were first separated from the MNP solution using a magnet and 1ml of water was charged into each vial to prepare MNP dispersions. Five other vials containing 1 ml of Pd-MC (0.03 wt%) were mixed with 14 ml of water. Subsequently, the five re-dispersed MNP solutions were introduced dropwise to each Pd-MC solution. The reaction was kept agitated for 24 h and then washed with water and ethanol three times. All the samples were designated as MNP1-Pd-MC to MNP5-Pd-MC.

(4) Fe-Pd-PDC preparation

5mg of pure Fe_3O_4 was dispersed into 4 ml ethanol by probe sonication, then it was introduced to 10 ml containing 30 ppm 10-Pd-PDC solution. The Fe_3O_4 nanoparticles loaded onto the PDA coating via electrostatic interactions to yield Fe-Pd-PDC. The reaction was maintained for 24 h and washed with water and ethanol three times.

(5) MNP1 to 5-Pd-PDC preparation

Five MNP-Pd-PDC catalyst samples were prepared using 1 to 5 ml of MNP solution (solid content: 0.1 wt%). The magnetic particles were first separated from the MNP solution using a magnet and 1ml of water was added to each vial. Five other vials containing 1ml of 10mg-Pd-PDA (0.193 wt%) and 14 ml of water were adjusted to 5.5 using 0.1 M HCl. Thereafter, these five 1ml of MNP dispersions were added to each Pd-PDA solution and mixed for 24 h. All the samples were washed with water an ethanol three times with the assistance of magnetic separation. All these five samples labeled as MNP1-Pd-PDC to MNP5-Pd-PDC. The schematic representation of MNP-Pd-PDC and MNP-Pd-MC are shown in **Scheme 7-1 A**, **B**.



Scheme 7-1 The schematics of synthesis pathway of MNP-Pd-PDC (A), and MNP-Pd-MC (B)

7.4 Characterization methods

7.4.1 Fourier transform infrared spectroscopy (FTIR)

The FTIR of MF modified CNC samples (CNC, MF-CNC, Pd-MC, Fe-Pd-MC, MNP-Pd-MC) and the PDA samples (PVP-CNC, PDA-PVP-CNC, Pd-PDC, Fe-Pd-PDC and MNP-Pd-PDC) were determined using the Bruker Tensor 27 spectrometer (Bruker, Billerica, MA, USA). The pellet consisted of freeze-dried samples with KBr were scanned between 4000 to 400 cm^{-1} with the signal averaging of 32 scans with a resolution of 4 cm^{-1} at room temperature.

7.4.2 Transmission electron microscopy (TEM)

TEM images were obtained with a Philips CM10 electron microscope under an accelerating voltage of 60 kV. All the samples were diluted to 0.01-0.05 wt% solution and one drop of the sample was placed on the copper grid and left to dry. Morphological changes of CNC after modification with various materials, including PVP, PDA, MF, Pd, Fe_3O_4 and MNP were examined using the TEM. Also, the optimization of the amount of Pd precursor added to the PDA-PVP-CNC system was evaluated by examining the palladium distribution and the particle size of nano palladium particles under TEM.

7.4.3 Dynamic light scattering (DLS)

The DLS measurements were used to determine the size of CNC and modified CNC prepared using different reaction conditions. This measurement was conducted on a 0.1 wt% dispersion in a Zeta-Sizer (Nanosizer ZS, Malvern Co., UK) at 25 °C.

7.4.4 Zeta potential measurement

Zeta-Sizer (Nanosizer ZS, Malvern Co., UK) was used to determine the zeta potential of different dispersions by measuring the charge density on the surface at 25 °C. Different samples were prepared at 0.1 wt%.

7.4.5 UV-Vis measurements

The solution of 4-NP, 4-AP and $NaBH_4$ mixed with 4-NP were scanned by a UV-Vis (Varian Cary 300 spectrophotometer). 3 ml of each solution was added to the quartz cell, and it was scanned from a wavelength of 250 nm to 800 nm.

7.4.6 Evaluation of catalytic performance

The catalytic reduction of 4-nitrophenol (4-NP) in the presence of $NaBH_4$ is commonly used to evaluate the catalytic performance of metallic catalyst. The catalytic performance of MNP1 to 5-MC, MNP1 to 5-PDC and 5, 10, 15-Pd-PDC and 10-Pd-PDC+PDAwere investigated by the reduction of 4-NP to 4-aminophenol (4-AP) using $NaBH_4$ as the reducing agent. In detail, 7.865 mg of $NaBH_4$ was added to 10 ml of 4-NP (0.104 mM) solution and mixed by gentle shaking on a mechanical shaker (the molar ratio of $NaBH_4$ to 4-NP was 200:1). The freshly prepared 4-NP, $NaBH_4$ mixture (1ml) was then transferred to a UV-vis cuvette. Then, 10 µL of each catalyst dispersion was added to the cuvette and mixed with a plastic pipette. The dispersion concentration of the MNP grafted catalysts was 400 ppm and 30 ppm for the dispersion of the non-magnetic catalysts. The color of the mixture changed from bright yellow to colorless with bubbled evolved as the catalytic reduction proceeded. The entire catalytic reaction was monitored by UV-vis spectrometer over a time interval of 1 min for the first 5 min and 5min time interval thereafter up to 30 min. Various parameters, such as apparent kinetic constants (k_{app}), turnover frequency (TOF) and activity factors (κ) were determined from the decay of 4-NP absorbance via the pseudo-first

order kinetic model. An excess amount of $NaBH_4$ was used to ensure that the catalytic reaction obeyed the pseudo-first order kinetics.

7.4.7 Magnetic separation efficiency

The separation test was performed with MNP1 to 5-Pd-MC and MNP1 to 5-Pd-PDC samples. The separation solution was diluted to 400 ppm and 1 ml of the solution was transferred to a glass vial. The glass vial was placed near a magnet and separated for 10 s, 30 s, 1 min, 3 min, 5 min, 10 min, and the supernatants were scanned by the UV-vis spectrometer from 250 to 600 nm. The absorbances at the characteristic peak of 4-NP (400 nm) after different separation time were recorded and plotted as a function of the separation time.

7.4.8 Reusability

The synthesized model catalysts: Fe-Pd-MC, MNP2-Pd-MC, Fe-Pd-PDC and MNP2-Pd-PDC were used to investigate the recyclability of the material. A freshly prepared 4-NP solution (200 μL) was mixed with 800 μL of 400 ppm model catalyst solution in a cuvette sealed with a cap. After 10 min of catalytic reaction, the cuvette was placed over the high gradient magnetic separator (HGMS) for 3 min of separation. The absorbance of the remaining 4-NP was obtained by scanning the supernatant in a UV-vis spectrometer. The collected catalyst was washed with water and ethanol 3 times, respectively, and 800 μL of water with 200 μL of fresh 4-NP solution were charged into the cuvette for the next round of catalytic tests. Each sample was subjected to 10 test cycles with 4NP solution and the absorbance of 4-NP at 10 min were compared with the value obtained from the first cycle to determine the conversion rate %.

7.5 Results and discussion

7.5.1 Fourier-transform infrared spectroscopy (FTIR)

The variation of the chemical bonds after each modification was investigated by FTIR analysis. Fe or MNP-Pd-MC samples and Fe or MNP-Pd-PDC series samples were characterized by FTIR (**Error! Reference source not found. A** and **B**) to examine the interactions between different coating materials and CNC. The spectra of MF-CNC (**Error! Reference source not found.**, **A**) show the absorbance of around 3300-3500 cm^{-1} representing the stretching vibration of secondary amine (N-H) that overlapped with the O-H stretching. The characteristic peak at 2960 cm^{-1} of C-H stretching vibration confirmed the formation of methylol group. The -C=N ring vibration and the C-N vibration were confirmed by the vibration at 1530 cm^{-1} and 1182 cm^{-1} respectively [422]. The triazine ring bending vibration occurred at 809 cm^{-1}, while the peak was significantly reduced after the loading of Pd [423]. The new peak appeared at 2338 cm^{-1}, which is associated with the vibration of bridging CH_2, which confirmed the crosslinking reaction of melamine formaldehyde [422]. The absorbance peak at 530 cm^{-1} of Fe-Pd-MC spectra was attributed to the Fe-O vibration from the loaded Fe_3O_4 particles [424]. The shift in the secondary amine (N-H) after the deposition of Pd particles was attributed to the coordination between nitrogen atom and Pd. All peak signals were reduced after the deposition of metallic particles, but no new peaks were observed, indicating the physical interaction between Pd and the modified CNC.

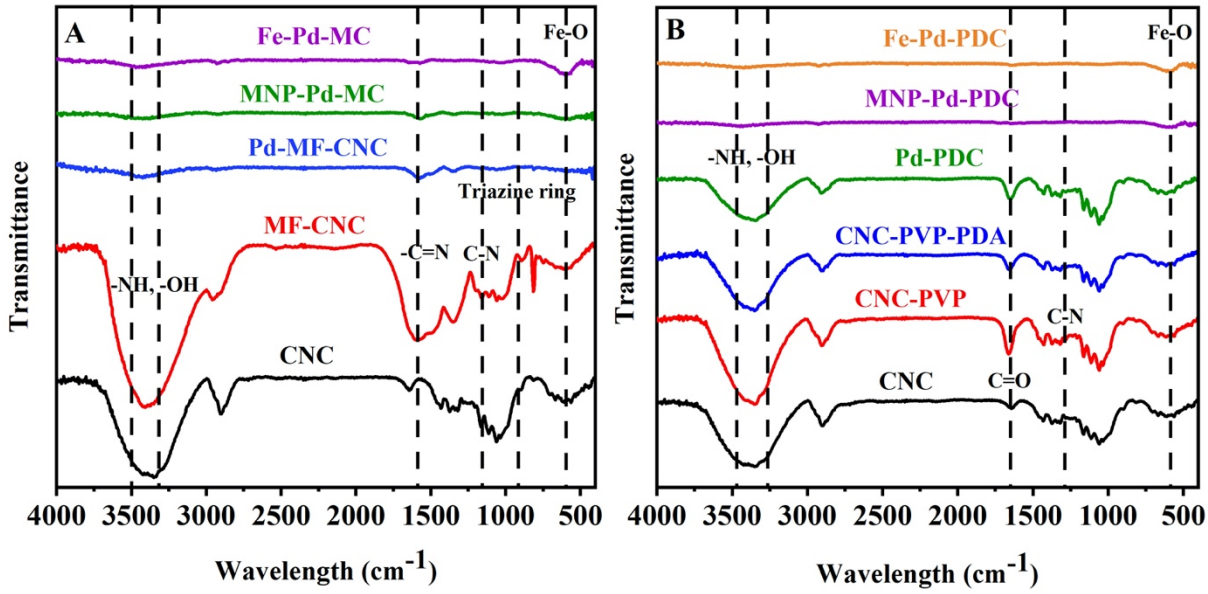


Figure 7-1 FTIR of (A) CNC, Melamine formaldehyde modified CNC, Pd loaded MF-CNC and Fe_3O_4 or MNP functionalized Pd-MC, (B) CNC, PVP-CNC, PDA-PVP-CNC, Pd loaded PDA-PVP-CNC and Fe_3O_4 or MNP functionalized Pd-PDC

7.5.2 Particle morphology

TEM was used to analysis the morphological variation of the material after each step of modification, since the catalytic performance is closely related to both morphology and quantity of the catalytic particles. Thus, the optimization of the Pd amount loaded into the Pd-PDC system was also evaluated by TEM investigation. It was also used to explore the optimum amount of MNP clusters added to the Pd-MC and Pd-PDC system. **Figure 7-2** shows the TEM images of (a) pristine CNC, (b) MF-CNC, (c) Pd loaded MF-CNC (Pd-MC), (d) MNP2-Pd-MC, (e) Fe-Pd-MC, (f) PVP-CNC, (g) PDA-PVP-CNC, (h) 5-Pd-PDC, (i) 10-Pd-PDC, and (j) 15-Pd-PDC. Pristine CNCs are shown as a high aspect ratio nanorod with a length of around 200 nm and a diameter of 10 nm that showed good dispersity in water (**Figure 7-2**, **a**). After the modification with melamine formaldehyde (MF), a stronger contrast was observed from MF-CNC (**Figure 7-2**, **b**) that confirmed the successful condensation of MF on the surface of CNC. In addition, all CNC

nanorods have been homogeneously covered by a thin layer of MF, which provided uniformly distributed amines sites for Pd deposition. After potassium tetrachloropalladate was reduced, 2-15 nm nano-Pd were uniformly decorated on the MF resin covering the CNC (**Figure 7-2**, **c**). In the case of CNC coated with PVP and dopamine in sequence, polydopamine (PDA) acted as an *in-situ* reducer to directly reduce Pd on PDA-PVP-CNC (PDC). A coating layer was observed on the CNC surface after the coating of PVP (**Figure 7-2**, **f**) and PDA (**Figure 7-2**, **g**), they possessed much thicker coating layer compared to MF-CNC. To optimize the method and the amounts of palladium precursor used to deposit Pd particles onto the PDC system were investigated, where 5, 10, and 15 mg of potassium tetrachloropalladate were added during the in-situ reduction process. In addition, 10 mg of potassium tetrachloropalladate together with the addition of dopamine during the reduction phase were also examined. A small amount of nanometric (3.37 ± 1.30 nm) Pd nanoparticles were deposited on 5-Pd-PDC catalytic particles, while more Pd particles were observed in the

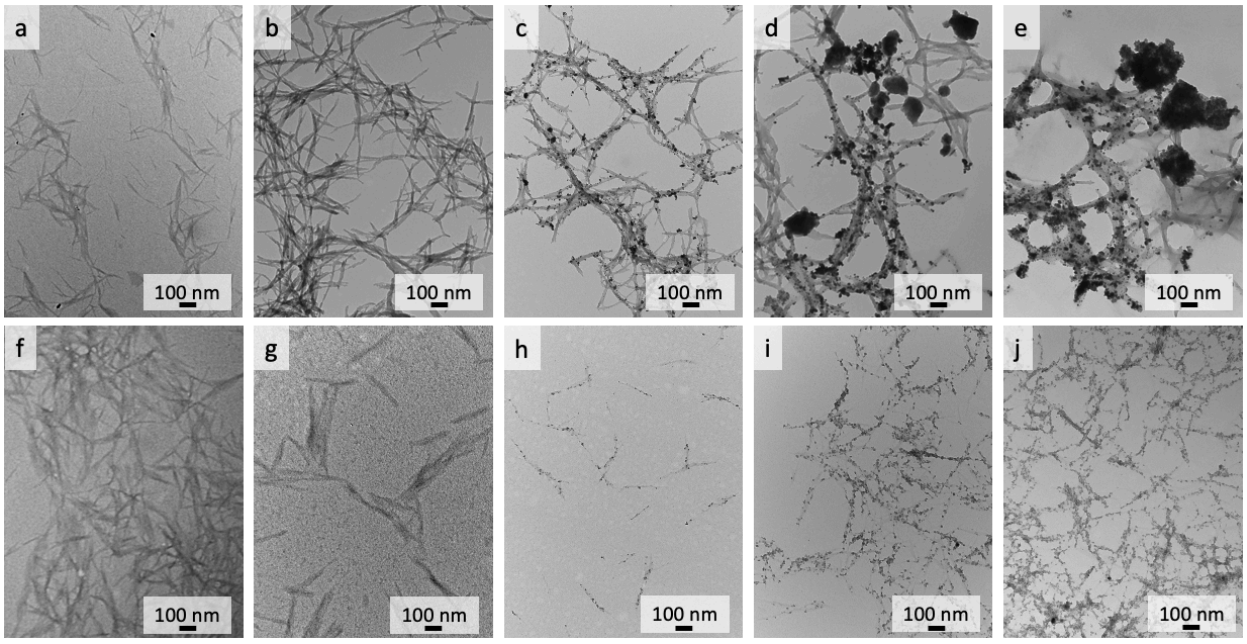
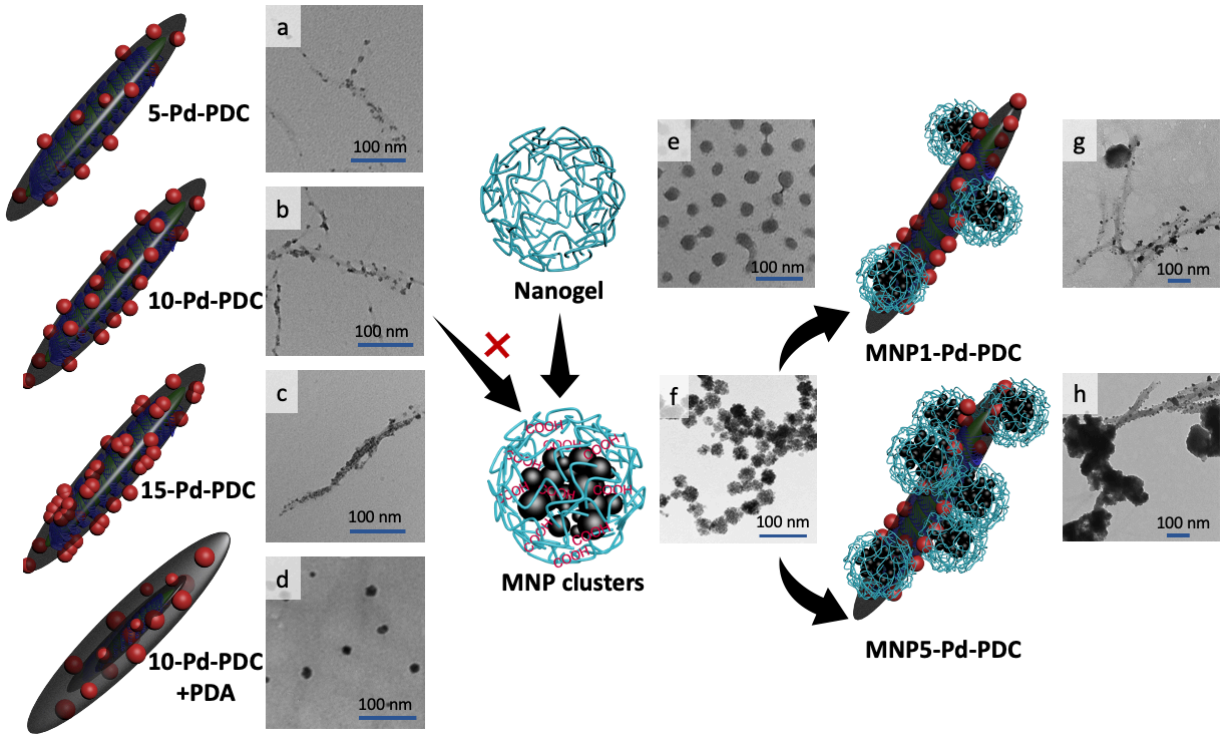


Figure 7-2 TEM images of pristine CNC (a), MF-CNC (b), Pd loaded MF-CNC (Pd-MC) (c), MNP2-Pd-MC (d), Fe-Pd-MC (e), PVP-CNC (f), PDA-PVP-CNC (g), 5-Pd-PDC (h), 10-Pd-PDC (i), 15-Pd-PDC (j)

10-Pd-PDC system with no aggregation. However, further increase in the amount of potassium tetrachloropalladate led to formation of networks between individual Pd particles that reduced the total surface area of Pd particles. Because PDA has been used as a reducing agent in other studies to prepare metal particles, we have also added dopamine to the system prior to the addition of metal precursor. The 10-Pd-PDC with extra PDA added to the system displayed a thick PDA layer on CNC and large Pd particles formed on the surface of PDC. This could be due to the faster reduction kinetics of potassium tetrachloropalladate in the presence of dopamine during the reduction reaction (**Appendix 7-1, c**). Thus, 10-Pd-PDC was selected for further modification and catalytic studies.

The MAA-EA nanogel templated magnetic clusters (MNP) and pure Fe_3O_4 were used to impart the magnetic property to the Pd-MC and Pd-PDC catalyst. Different amounts (1 to 5 ml) of MNP clusters grafted Pd-MC were investigated using the TEM. The MNP2-Pd-MC is shown in **Figure 7-2 d**, where appropriate amounts of well-defined spherical MNP clusters were observed. The MNP1-Pd-MC (**Appendix 7-1 d, e**), MNP3-Pd-MC (**Appendix 7-1 f, g**) and MNP5-Pd-MC (**Appendix 7-1, j**) were also examined by TEM. The MNP1-Pd-MC possessed several MNP clusters that might not provide sufficient magnetization to effectively separate the catalyst. Excess amount of MNP clusters were observed from MNP3 to 5-Pd-MC model catalyst, several MNP clusters were even entangled with each other resulting in a reduction of Pd particle surface area. The MNP2-Pd-MC has a high catalytic reaction rate that comparable to the MNP1-Pd-MC (the results are presented in the following sections **Figure 7-6**), but also has good separation

performance. Combined with the catalytic performance test and the separation efficiency test, 2ml MNP was selected as the optimal amount of MNPs. However, when pure Fe_3O_4 particles were loaded to Pd-MC, non-uniform Fe_3O_4 particles merged with Pd particles resulting in a reduction in catalytic performance. Also, the leaching of Fe-Pd-MC posed toxicity concern, where severe aggregation and free Fe_3O_4 were evident (**Figure 7-2 e** and **Appendix 7-1 a, b**). On the other hand, nanogel templated MNPs possessed well-controlled particle size and the nanogel served as a protection barrier between magnetic particles and Pd particles. The schematic illustration and TEM images for the Pd loaded Pd-PDC system, nanogel, MNP clusters and MNP1 or 5-Pd-PDC are shown in **Scheme 7-2**.



Scheme 7-2 Scheme illustration and high magnification TEM images of (a) 5-Pd-PDC, (b) 10-Pd-PDC, (c) 15-Pd-PDC, (d) 10-Pd-PDC+PDA, (e) stained MAA-EA nanogel, (f) MNP clusters, (g) MNP1-Pd-PDC and (h) MNP5-Pd-PDC

7.5.3 Particle size and stability

Particle size and stability are important factors that can affect the catalytic performance, hence the average particle size and zeta potential were used to evaluate the stability of CNC after each modification. **Figure 7-3** shows the particle size and zeta potential of (**A**) MF series samples and (**B**) PDA series samples. The average diameter of the CNC was 90.3 $\pm$ 9.1 nm, after melamine formaldehyde polycondensation, the particle size increased dramatically to 580 $\pm$ 38.2 nm. This large increase of the particle size was attributed to the entangled MF network as indicated by the TEM micrographs (**Figure 7-2**, **b**). The porous layer of MF provided many amino sites available for Pd deposition, as well as MNP conjugation. However, a reduced particle size was obtained after the incorporation of Fe_3O_4 into the MF-CNC system. Since Fe_3O_4 particles did not covalently bonded to MF-CNC, they could detached from the clusters resulting in the reduction of the average particle size of Pd-MC system. The surface charge of pristine CNC was -48 $\pm$ 6.7 mV brought about by the negative sulfate groups, imparting high stability to the CNC dispersions. The zeta potential of MF-CNC increased to +10 mV after the polycondensation of melamine formaldehyde, as large amounts of secondary amines were present on the CNC surface, which shielded the negative charges. MNP-Pd-MC possessed a zeta potential of -25 $\pm$ 1.1 mV, imparting good stability to the catalyst. The loading of MNP clusters did not eliminate the positive surface charge of MF-CNC, even though the Fe_3O_4 clusters shielded the positive surface charges.

For the PDA samples, the particle size of CNC increased after the modification of PVP and dopamine, which confirmed the successful deposition of PDA on the surface of CNCs. The particle size of PDC was much smaller compared to MF-CNC, while Pd-PDC possessed a size similar to Pd-MC. This is because the loading of Pd particles onto MF-CNC occurred within the porous MF layer, while the Pd particles deposited on the PDC surface aggregated resulting in a larger particle

size. The zeta potential was enhanced after the coating with dopamine due to the self-condensation of dopamine that yielded amine groups on the surface of PDC. After the loading of Pd particles, the NH_2 groups chelated with Pd particles that reduced the zeta potential. Overall, the zeta potential for all samples in the PDA series was below -27 mV, thus the colloidal particles were extremely stable.

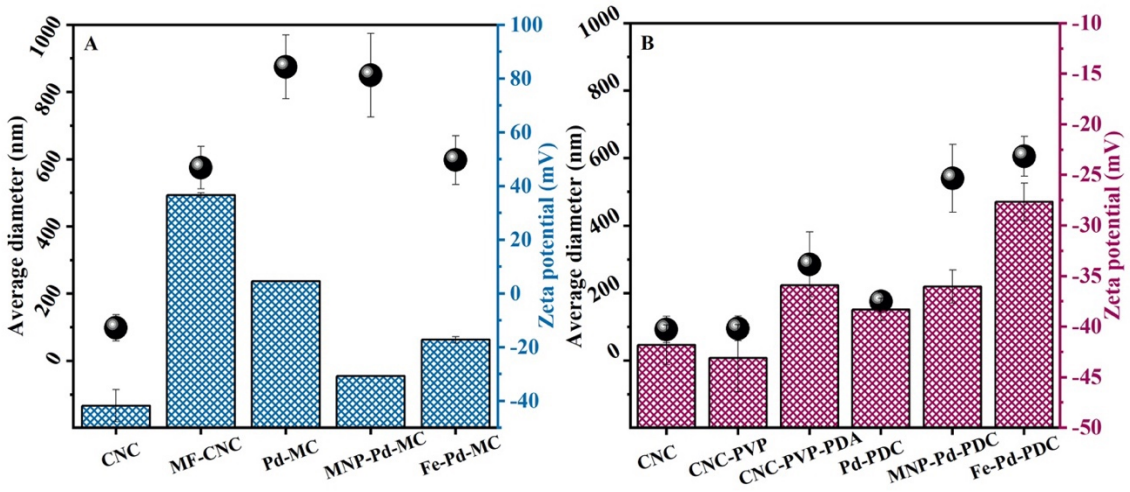


Figure 7-3 Average particle diameter (nm) and zeta potential (mV) of CNC, MF-CNC, Pd-MC, 2ml-MNP-Pd-MC and Fe-Pd-MC are shown in (A), average particle diameter (nm) and zeta potential (mV) of CNC, CNC-PVP, CNC-PVP-PDA, MNP2-PDC and Fe-PDC

7.5.4 Optimization of Pd loading for Pd-PDC

In the Pd-PDC system, dopamine functioned as both the surface modifier and reducing agent. Therefore, an appropriate quantity of palladium precursor was added, and the pathway of the reduction process is critical to the catalytic performance of the catalyst. Various amounts (5, 10, 15 mg) of potassium tetrachloropalladate were added to the PDC system for the synthesis of the catalyst. The 10-Pd-PDC was also used to investigate the effect of adding additional dopamine during the reduction of the palladium precursor. The catalytic performance of 5-Pd-PDC, 10-Pd-PDC, 15-Pd-PDC and 10-Pd-PDC+PDA are shown in **Figure 7-4 A, B, C, D**. The concentration of 4-NP as a function of the reaction time, and the correlation of $\ln(C_t/C_0)$ versus time of the four

catalysts are shown in **Scheme 7-2 A, B**. As shown in **Figure 7-4**, 10-Pd-PDC reduced the 4-NP to the lowest concentration after a 30-min reduction compared to the other three model catalysts. This result is consistent with the TEM images, where the 10-Pd-PDC catalyst possessed discrete Pd nanoparticles (**Scheme 7-2, b**, with no aggregation). However, the further increase of the palladium precursor (15-Pd-PDC) led to a decline in the catalytic performance due to the aggregation of the Pd particles (**Scheme 7-2, c**). Moreover, the addition of more dopamine during the reduction of palladium precursor resulted in a faster reduction rate yielding larger Pd particles that diminished the catalytic performance (**Scheme 7-2, d**). The Langmuir-Hinshelwood kinetics of heterogeneous catalyst could be used to model the catalytic reaction occurring at the surface of the particles. As the amount of $NaBH_4$ used was in excess compared to 4-NP, the reduction reaction was independent of $NaBH_4$ concentration. Thus, a pseudo-first order kinetic model was used to determine the reaction rates [425]. The equation of the degradation model is shown in Eq (7.1), where C_0 is the initial concentration of 4-NP, and C_t represents the concentration of 4-NP at time t. A_0 is the absorbance at 400 nm at time 0 and A_t represents the absorbance at 400 nm at time t of catalytic degradation of 4-NP. The apparent kinetic rates (k_{app}) were determined from the slope of $\ln(A_t/A_0)$ versus time. Another important parameter for evaluating the performance of the catalyst is the turnover frequency (TOF, h^{-1}), where the reaction rate constant was normalized by the mass of palladium present in the catalytic system. The equation used to calculate TOF is presented in Eq (7.2), where n (mol) is the molar amount of 4-NP used, MR is the mass ratio of palladium precursor to the total amount of all the components in the catalyst, m (g) is the mass of the catalyst used for the test, M_w is the molecular weight of palladium (106.42 g/mol) and k_{app} (h^{-1}) is the apparent kinetic rate constant.

$$\frac{dC_t}{dt} = -k_{app}t \text{ or } \ln\left(\frac{C_t}{C_0}\right) = \ln\left(\frac{A_t}{A_0}\right) = -k_{app}t \quad (7.1)$$

$$\text{TOF}=\frac{n(4-NP)}{MR\times\frac{m(Catalyst)}{M_W(Pd)}}\times k_{app} \quad (7.2)$$

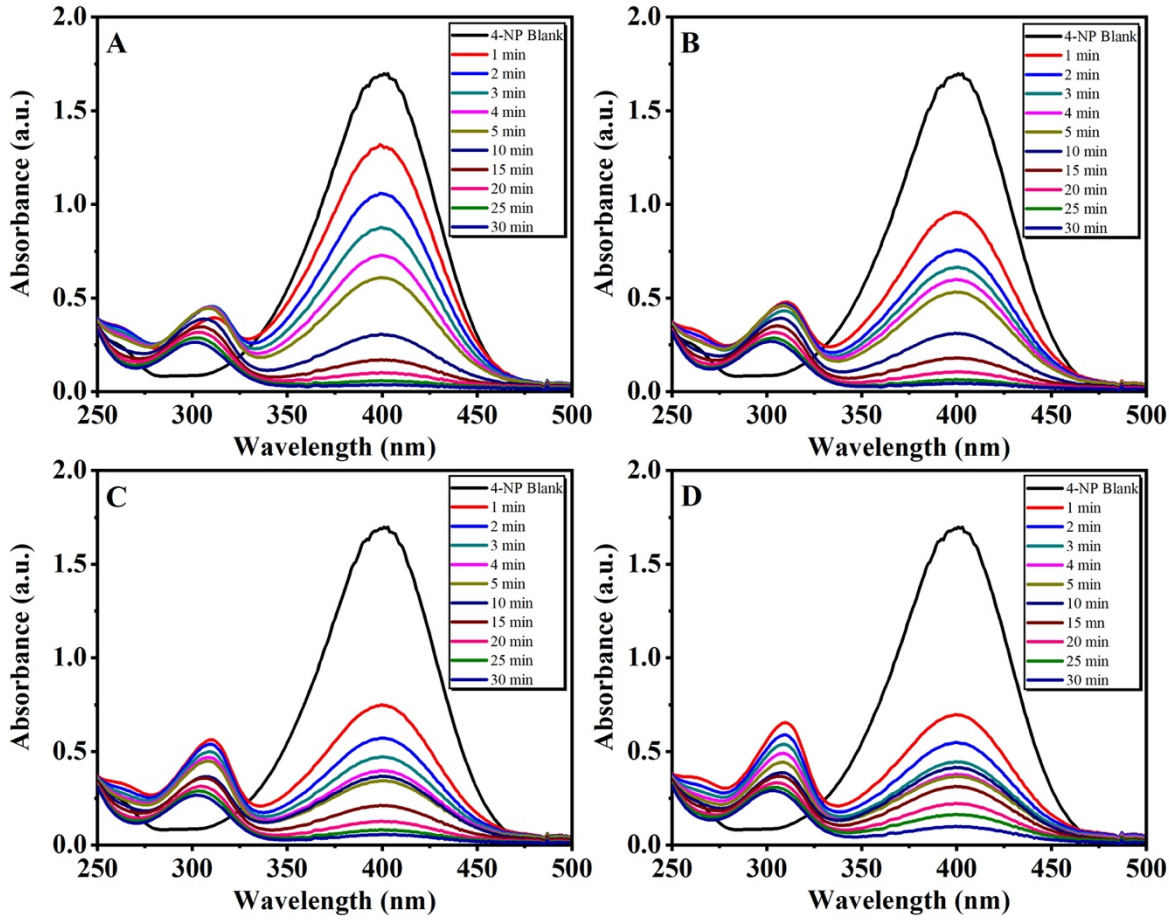


Figure 7-4 UV spectra of catalytic reduction of 4-NP using (A) 5-Pd-PDC, (B) 10-Pd-PDC, (C) 15-Pd-PDC and (D) 10-Pd-PDC+PDA for a 30 min reaction time

7.5.5 Evaluation of catalytic performance

Catalytic reduction of 4-NP to 4-AP was used to evaluate the performance of the catalysts by monitoring the absorbance of 4-NP using a UV-vis spectrometer over 30 min. As shown in **Figure 7-5 (A)**, 4-NP displays a characteristic absorbance at 317 nm (red line), while pure 4-AP possessed a characteristic absorbance peak at 300 nm (blue line) [426]. The characteristic absorbance peak possessed a red shift from 317 nm to 400 nm (black line) in the presence of freshly prepared $NaBH_4$ solution due to the formation of 4-nitrophenolate ions. The catalyst played an

important role in promoting the degradation of 4-NP, since the degradation of 4-NP by $NaBH_4$ took place over several days. When 10 µL of 30 ppm Pd-MC catalytic solution was introduced to the system, the absorption of 4-NP (0.104 mM) was progressively reduced. The solution in the cuvette transformed from bright yellow to transparent, and bubbles were generated due to H_2 production. Furthermore, the new peak at 290 nm was attributed to the formation of 4-AP. The logarithm of (A_t/A_0) versus time of blank 4-NP, MF-CNC and Pd-MC/4-NP mixture is shown in **Figure 7-5 (B)**. Compared with Pd-MC, MF-CNC displayed a zero catalytic reaction rate of 4-NP, which suggested that all the catalytic properties were attributed to the palladium nanoparticles on the MF coating. The pseudo first order reaction rate constant was obtained from the linear fitting, having a value of 2.11×10^{-3} $s^{-1}$for Pd-MC and 0 for MF-CNC and pure 4-NP solutions.

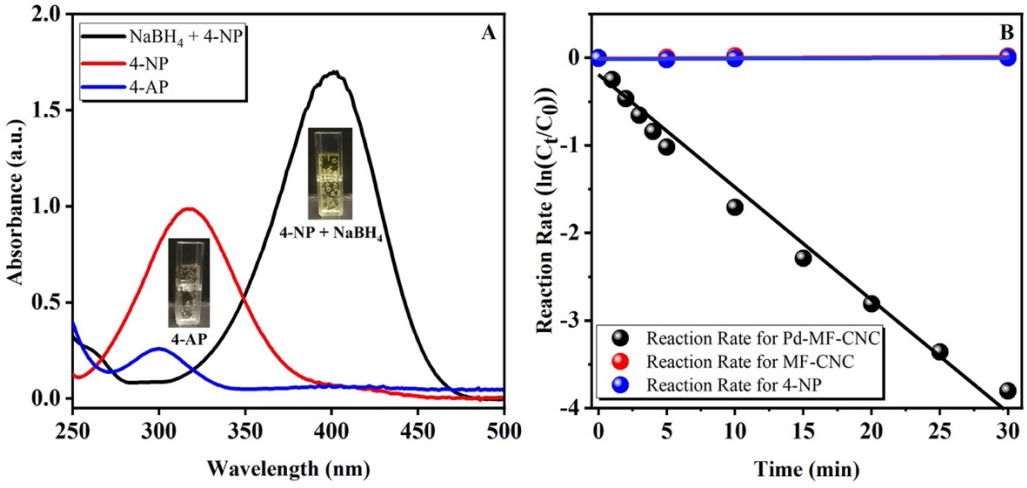


Figure 7-5 The UV spectra of 4-NP, 4-AP and 4-NP in the presence of $NaBH_4$ are presented in (A), the summary of logarithm of absorbance at 400 nm versus time of 30 ppm Pd-MC, 30 ppm MF-CNC and 4-NP solutions (B)

Fe_3O_4 particles and MNP clusters were used to introduce magnetic characteristic to the Pd-MC and Pd-PDC catalysts. Catalytic performance tests in all 4 catalytic systems (Fe-Pd-MC, MNP2-Pd-MC, Fe-Pd-PDC and MNP2-Pd-PDC) were conducted in 10 μL of 30 ppm 4-NP

solutions. The successive UV-vis absorption spectra on the reduction of 4-NP were recorded and the results are shown in **Appendix 7-3**, and the linear fitting of $\ln(A_t/A_0)$ versus time is presented in **Appendix 7-2**. The catalytic performance of Pd-MC catalysts was superior compared to the Pd-PDC catalysts, as demonstrated by a higher reduction rate constant and lower 4-NP absorbance. Because the MF coated CNC possessed a mesoporous structure with more palladium particles trapped within the pores, which provided more active sites for 4-NP reduction. By comparing the catalytic performance of both Fe_3O_4 based and MNP clusters functionalized catalyst, MNP2-Pd-MC and MNP2-Pd-PDC showed superior performance in reducing 4-NP compared to the corresponding Fe-Pd-MC and Fe-Pd-PDC catalysts. This could be associated to diminished surface area of Pd particles in MNP based catalyst, while the magnetic attraction between Fe_3O_4 particles generated aggregated clusters covering the surface of some Pd particles. Furthermore, the porous MF resin on the surface of CNC provided active amine groups for Pd deposition, while the grafting of MNP clusters did not significantly alter the total amount of NH_2 groups. Also, MNP clusters provided sufficient magnetization for separation without sacrificing the catalytic performance, which will be discussed later.

Various amounts of MNP clusters were introduced onto the Pd-MC and Pd-PDC systems and their catalytic performance and separation efficiency were examined to optimize the amount of MNP clusters for the catalyst system. The primary objective is to achieve an adequate separation without seriously impacting the catalytic performance. Successive 30-min UV-vis spectra of 4-NP catalytic reduction using MNP1 to 5-Pd-MC (10 μL of 400 ppm) are summarized in **Appendix 7-4, A to E**. After the introduction of MNP-Pd-MC catalysts, the characteristic peak of 4-NP at 400 nm decreased gradually and the characteristic peak of 4-AP at 300 nm increased progressively. The pseudo-first-order reaction constant k (s^{-1}), turnover frequency (TOF, h^{-1}) and the activity

factor κ ($s^{-1}g^{-1}$) of different catalysts were determined and summarized in **Table 7-1**. As indicated by the rate constant of MNP1 to 5-Pd-MC, MNP2-Pd-MC possessed the highest reaction rate constant (2.142×10^{-3} s^{-1}), which supported the conclusion from TEM analysis. The MNP2-Pd-MC possessed MNP clusters distributed over the Pd-MC surface with no aggregation of the Pd particles. The MNP5-Pd-MC possessed the lowest rate constant (0.570×10^{-3} s^{-1}), due to the agglomeration of MNP clusters within the MNP-Pd-MC systems that reduced the Pd sites, which significantly impacted the catalytic performance. However, the MNP4-Pd-MC possessed the highest TOF (540.42 h^{-1}) compared to the MNP2-Pd-MC since the TOF was normalized based on

Table 7-1 Comparison of catalytic performance of Pd-MC and Pd-PDC based catalyst

Sample name	Pseudo-first-order constant k (s^{-1})	Activity factor $\boldsymbol{\kappa}$ ($s^{-1}\cdot g^{-1}$)	Turnover frequency TOF (h^{-1})
MNP1-Pd-MC	1.467×10^{-3}	366.8	112.0
MNP2-Pd-MC	2.142×10^{-3}	535.5	305.8
MNP3-Pd-MC	0.884×10^{-3}	221.0	184.9
MNP4-Pd-MC	1.961×10^{-3}	490.3	540.4
MNP5-Pd-MC	0.570×10^{-3}	142.5	194.9
5-Pd-PDC	1.261×10^{-3}	4203.3	361.4
10-Pd-PDC	1.624×10^{-3}	5413.3	340.6
15-Pd-PDC	0.968×10^{-3}	3226.7	178.2
10-Pd-PDC+PDA	0.713×10^{-3}	2376.7	159.0

the amount of Pd present in each catalyst system. The concentration profile of 4-NP for 5, 10, 15-Pd-PDC and 10-Pd-PDC+PDA catalyst and the correlation between $\ln(A_t/A_0)$ and time are shown in **Appendix 7-5 A** and **Appendix 7-5 B** respectively. The catalytic reaction rate of 4-NP is directly proportional to the concentration of catalyst in the system. For homogeneous catalyst, the catalytic activity is depended on the total number of catalytic molecules, however, the catalytic activity of heterogeneous catalyst depends on the active sites on the surface of the catalysts [427]. The Langmuir-Hinshelwood kinetics of heterogeneous catalysis proposed by Wunder and coworkers could be used to model two prevalent mechanisms for the reduction of 4-NP, namely surface-mediated hydrogen transfer and surface mediated electron transfer. In most instances,

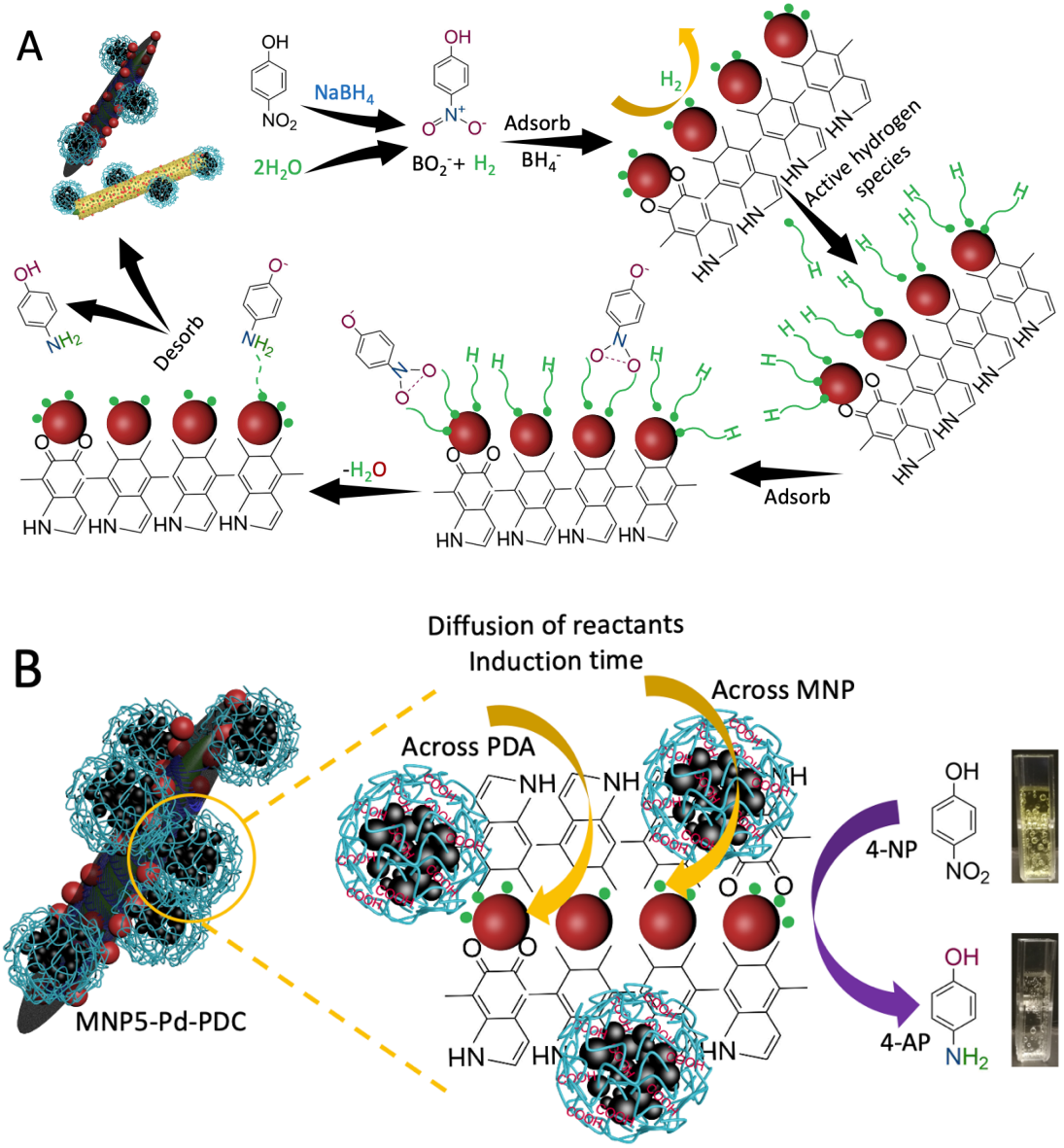
hydrogen and electron transfer could occur simultaneously during the 4-NP reduction. Both $NaBH_4$ and 4-NP molecules needed to be on the surface of metal catalyst prior to the reduction reaction, thus, the Langmuir isotherm could be used to describe the adsorption mechanism between reactants and the catalyst. The adsorption of BH_4^- is a fast and reversible process, and a hydrogen radical generated from electron transfer was transported to the catalytic particle surface via adsorption. The adsorption of 4-NP molecule onto the catalyst surface is also fast and reversable. Subsequently, the adsorbed 4-NP molecule would react with the hydrogen radicals to produce 4-AP via the 4-hydrocylaminophenol intermediate [428] [429], which is the rate-determining step for 4-NP reduction. Eventually, the 4-AP molecules detached from the catalyst surface releasing the adsorption site for subsequent 4-NP catalytic reduction.

The conversion of 4-NP to 4-AP using different Pd-PDC catalysts could described by a two-step process, which is different from the common 4-NP reduction with noble metals. Also, this non-linear relationship between ln (A_t/A_0) and time was not observed for the Pd-MC catalysts, indicating that the different mechanism could be associated with the PDA matrix. In this study, the reduction process could be divided into three steps: (1) both $NaBH_4$ and 4-NP molecules adsorb onto the surface of metallic catalyst, (2) 4-NP was reduced by the borohydride ions on the catalyst reduction sites, (3) generated 4-AP molecules desorb from the surface of the metal catalyst, where step two is the slowest process and the rate-determining step. The general 4-NP reduction mechanism in the presence of Pd-MC and Pd-PDC is shown in **Scheme 7-3 (A)**. Additionally, the phenomenon of "reconstruction" on the surface of the catalyst was previously reported, demonstrating that ligands could be replaced by the compounds adsorbed on the surface [430]. Normally, the induction time for ligand replacement could be ignored due to the fast kinetics, however, the strong interaction between the surface and ligands, gave rise to a longer induction

time [431][432]. As demonstrated in **Figure 7-6 A** and **Figure 7-6 B**, no induction time was observed with MNP-Pd-MC catalysts or when the MNP-Pd-PDC catalyst with less than 4ml MNP clusters. However, an induction time of around 5 min was observed when 4 or 5ml MNP clusters were involved the catalyst synthesis. The rate of adsorption of 4-NP molecules on the surface of the catalyst was determined by the concentration of 4-NP and the available surface area of the catalyst [433]. This delay of induction time was due to the lower accessible area of Pd in Pd-PDC catalyst compared to the Pd-MC catalyst. Apart from acting as a reducing agent during the reduction of Pd nanoparticles, DA acted as a stabilizer on the surface of the Pd particles. Other researchers have confirmed the presence of DA on the surface of gold nanorods synthesized using DA as an in situ reducing agent. DBA promotes the production of anisotropic nanostructure particles, and a reduction in the yield and purity were observed when the concentration of DBA exceeded a critical value [434]. As observed from the optimization of Pd precursor used in the preparation of Pd-PDC catalyst, 10-Pd-PDC+PDA displayed the worst reduction performance compared to 10-Pd-PDC. Thus, an excess amount of DA negatively impacted the Pd formation, and excess DA might cover and conjugate to the Pd particles that hindered the adsorption of 4-NP and $NaBH_4$ to the surface of Pd particles that consequently reduced their catalytic performance. Also, more catechol groups from the excess PDA loaded 10-Pd-PDC+PDA increased the pH of the catalytic system, which stabilized the $NaBH_4$ and prevented it from self-hydrolysis [435]. The Pd particles in the MNP incorporated system were covered by the MNP clusters, leading to a longer time for the reactant to diffuse through the MNP and bound to the Pd surface. Thus, the low $NaBH_4$ hydrolysis rate, excess PDA coverage and conjugation to the Pd particles impacted the binding between the reactants and catalysts. Thus, a longer induction time was required for the displacement of 4-NP molecules on the surface of 4ml/5ml MNP Pd-PDC catalysts. The schematic

illustration of the catalytic mechanism is presented in **Scheme 7-3 (B)**. A catalytic induction time of 11 min was reported by Yu and coworkers for gold nanoparticles prepared using 0.08 mM caffeic acid [432].

The reaction rate constant and other parameters were calculated from the linear regression of $\ln(A_t/A_0)$ versus time (10 to 30 min). The highest rate constant (1.624×10^{-3} s^{-1}) was observed for 10-Pd-PDC, which was associated with the large amounts of discrete Pd nanoparticles since the total surface area of Pd particles controlled the catalytic performance. The 15-Pd-PDC had more Pd, however interparticle entanglement led to a significant reduction in the total surface area of Pd. Furthermore, both 10-Pd-PDC and 10-Pd-PDC PDA possessed a similar mass ratio of palladium, however the later catalytic performance was reduced by more than 50% with excess PDA confirming the importance of Pd particle size on the catalytic performance. The average size of palladium particle of 10-Pd-PDC+PDA was 12.34 ± 2.06 nm (**Appendix 7-1 c, Appendix 7-6 (D)**), while the particle size of 10-Pd-PDC was 10.83 ± 2.43 nm (**Figure 7-2**, **i, Appendix 7-6 (B)**). Average particle sizes obtained from TEM (Image J measurement) are summarized in **Table 7-2**. The catalytic property of prepared MNP-Pd-MC and Pd-PDC catalyst were compared with other types of palladium-based catalyst supported on various matrices (such as mesoporous silica, chitosan hydrogel, carbon-based material and polymer modified fibrous material) are summarized in **Table 7-3**. The rate constant is directly proportional to the size of palladium particles, the Pd loaded PEI/PCL



Scheme 7-3 The schematic illustration of the possible mechanism of 4-NP degraded to 4-AP in the presence of Pd-MC and Pd-PDC (A), and the possible mechanism in the presence of extra PDA and MNP in the system (B)

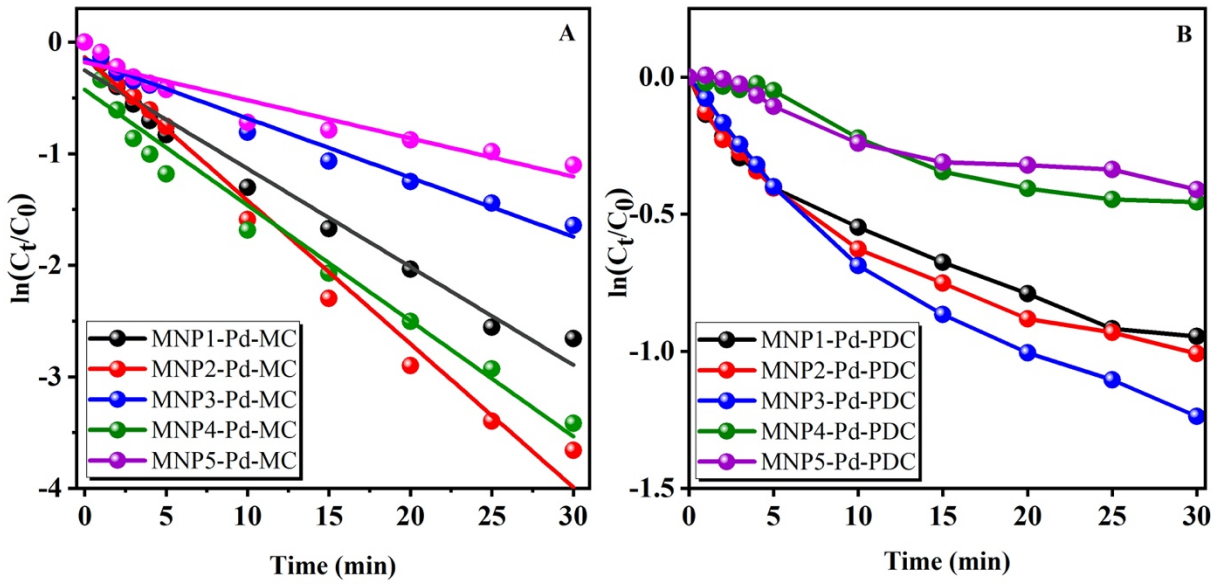


Figure 7-6 The logarithm of absorbance at 400 nm versus time of (A) MNP1 to 5-Pd-MC, and the logarithm of absorbance at 400 nm versus time of (B) MNP1 to 5-Pd-PDC

Table 7-2 Summary of average *Pd* particle size measure by Image J

Sample name	Average size
5-Pd-PDC	3.37 ± 1.30
10-Pd-PDC	10.83 ± 2.43
15-Pd-PDC	17.45 ± 3.17
extra PDA	12.34 ± 2.06
MNP	32.19 ± 3.44
Nanogel	32.30 ± 3.33
Pd-MF-CNC	15.48 ± 2.30

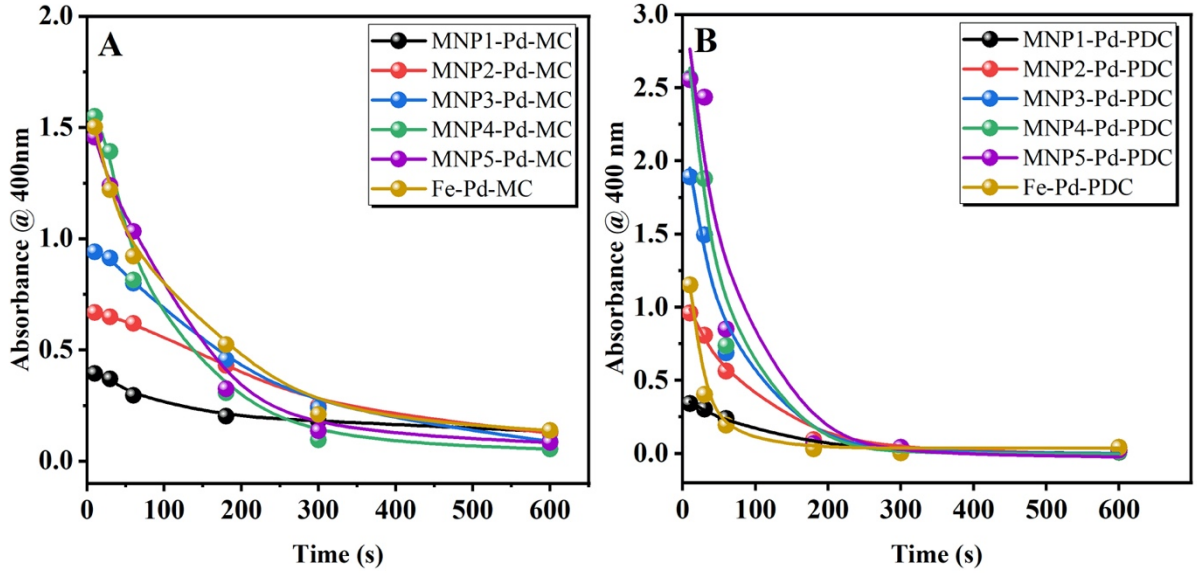
composite fiber possessed the highest reaction rate due to the 0.22 nm of Pd particle. Both MNP-Pd-MC and Pd-PDC possessed intermediate rate constant, high TOF and activity factor, especially 10-Pd-PDC with an activity factor κ of 4203.3 $s^{-1}g^{-1}$. As a result, the superior catalytic properties of Pd-MC and Pd-PDC catalysts make them attractive and effective catalysts for 4-NP degradation.

Table 7-3 Comparison of different palladium-based catalysts applied for 4-NP reduction

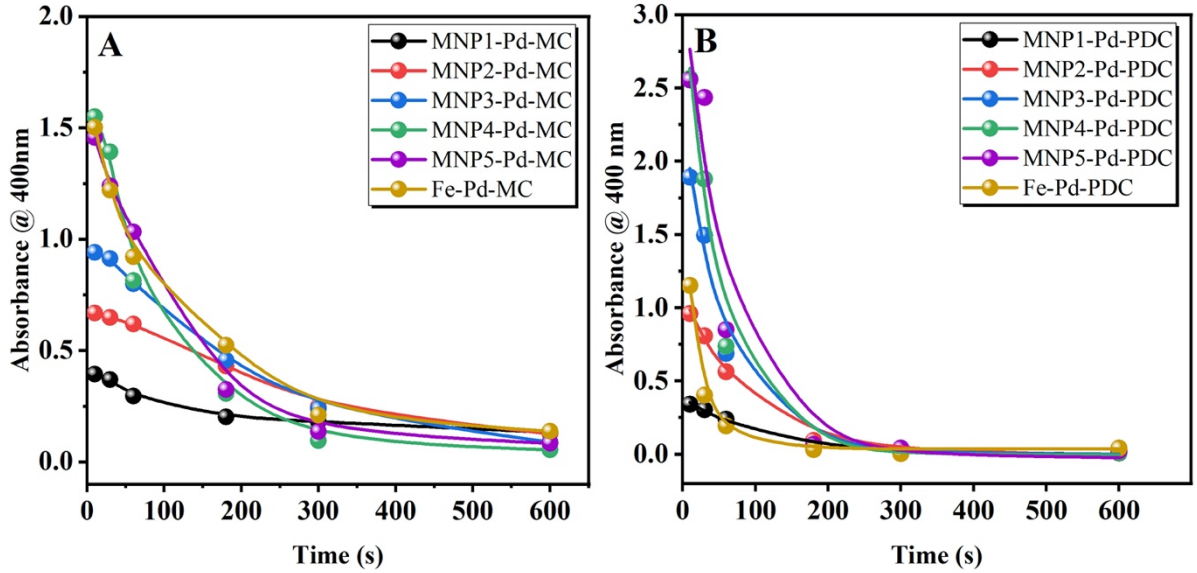
Supporting matrix	Size of Pd particles (nm)	Reaction rate constant k (s^{-1})	TOF (h^{-1})	Activity factor κ ($s^{-1}g^{-1}$)	Ref
Silica nanosphere	10.2	2.04×10^{-2}	-	510	[436]
CNC	1-40	5.7×10^{-3}	879.5	-	[437]
Chitosan hydrogel	28.33	1.47×10^{-3}	0.9	17.016	[68]
Fibrous silica nanosphere	4	19.6×10^{-3}	-		[438]
Polyethyleneimine (PEI)/Polycaprolactone (PCL) composite fiber	0.22	1.66×10^{-1}	-	-	[439]
Graphene@carbon hollow sphere	3-4	-	273.6		[440]
MF coated CNC	15.48	1.961×10^{-3}	540.42	490.25	This work
PDA coated CNC	3.37	1.261×10^{-3}	361.42	4203.33	This work

7.5.6 Separation efficiency

The magnetization is an important factor in the production of magnetic-based materials, which is directly related to their separation efficiency. A simple separation experiment was conducted to evaluate the separation efficiency of MNP1 to 5-Pd-MC and MNP1 to 5-Pd-PDC catalysts. The catalyst was introduced to a fresh 4-NP solution placed on a magnet for a fixed time, and the supernatant was withdrawn and scanned in a UV-Vis spectrometer. The absorbance at 400 nm was recorded and plotted against the separation times. Having more MNP clusters in the catalytic system would increase the separation efficiency, whereas more MNP clusters would contribute to more leaking of Fe_3O_4 particles after several rounds of separation and recovery with a strong magnet. Separation tests were conducted in the absence of 4-NP, therefore, the absorbance of 400 nm can be attributed to the MNP clusters that had not fully removed from the aqueous phase.



(A) presents the separation curve of MNP1 to 5-Pd-MC, where MNP1-Pd-MC presented a fast separation (the ratio of unseparated MNP versus the separated MNP). The separation was completed after 3 min, and no obvious change in the absorbance @ 400 nm was observed. The separation curve of MNP1 to 5-Pd-PDC and Fe-Pd-PDC are shown in



(B) revealed a similar absorbance after the magnetic separation of 300s, and the absorbance value was close to 0 at 400 nm. This could be attributed to the smaller particle size of MNP-Pd-PDC particles compared with MNP-Pd-MC particles. Both Fe-Pd-MC and Fe-Pd-PDC exhibited a higher UV absorbance than MNP based catalyst possibly caused by the aggregation of pristine Fe_3O_4 and the presence of small Fe_3O_4 particles that could not be separated due to their small size.

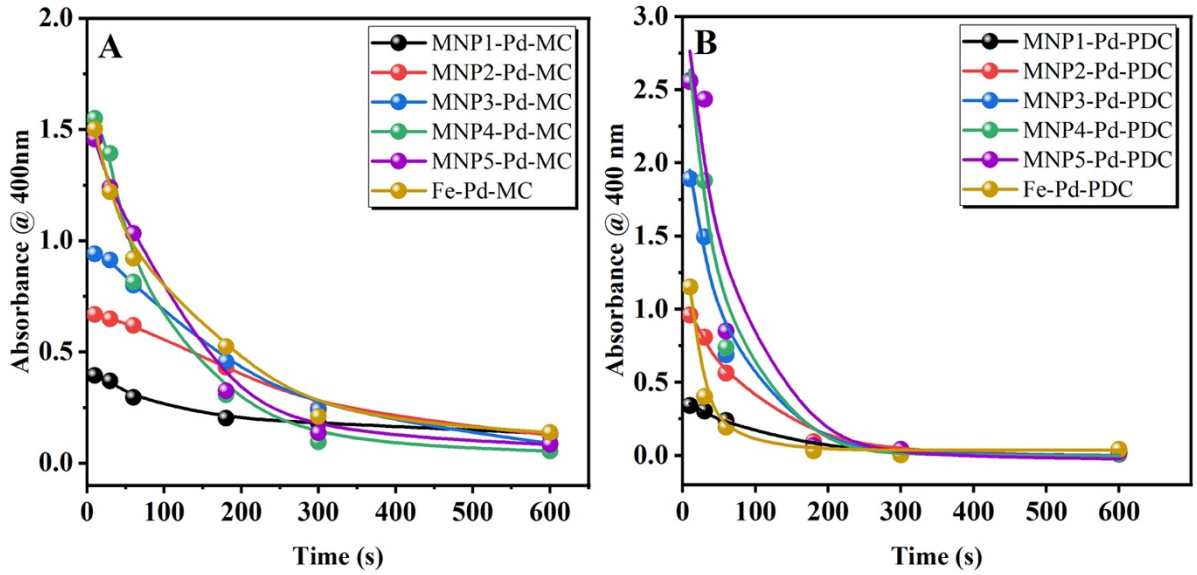


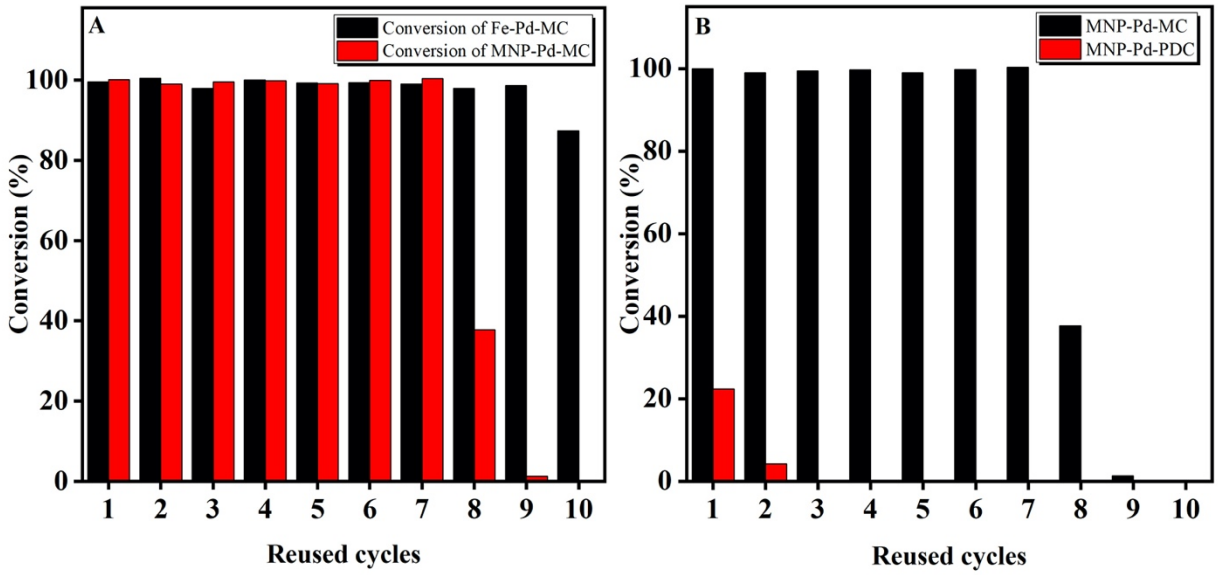
Figure 7-7 Separation performance of MNP1 to 5-Pd-MC (A), and MNP1 to 5-Pd-PDC samples evaluated by magnet separation (B)

The magnetic hysteresis loops of MNP clusters are shown in **Appendix 7-7**. MNP possessed a superparamagnetic character indicated by zero coercivity, and the high Ms (53.23 emu/g) s due to the high magnetic content in the nanogel template. The rapid separation performance of MNP grafted catalyst demonstrates the potential for a magnetic assisted catalytic process, where the nanogel barrier minimized the direct contact of Fe_3O_4 and reduced the toxicity of the system.

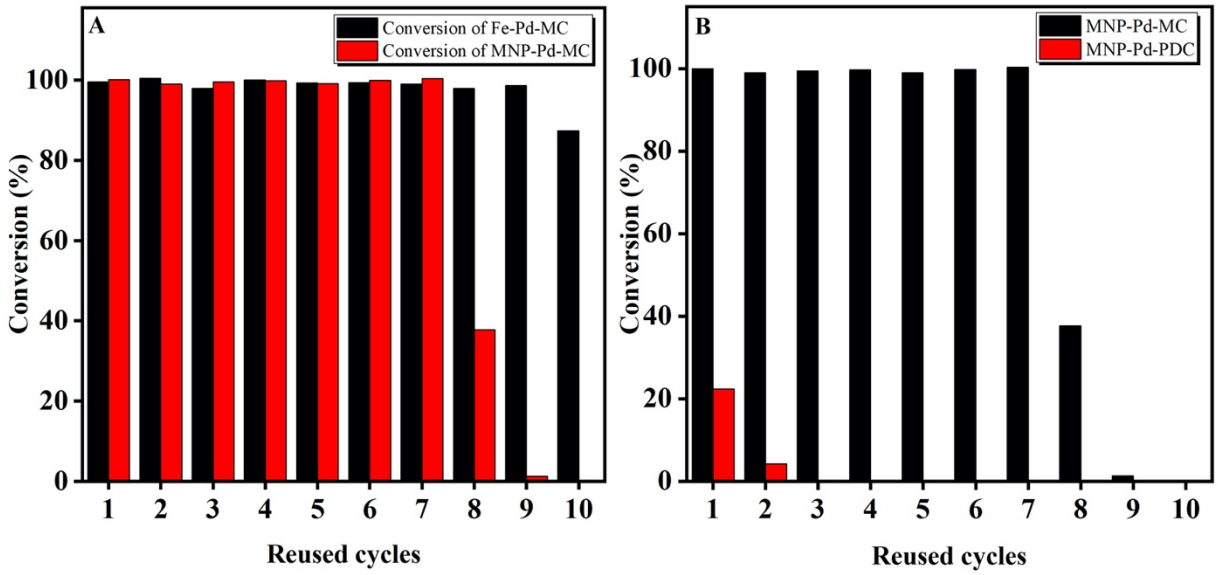
7.5.7 Reusability

Reusability of magnetic based catalyst is important as it is directly related to the processing and operation costs. Fe-Pd-MC, MNP2-Pd-MC and MNP2-Pd-PDC were examined in the

recyclability study.



(A) shows the result of 4-NP conversion after 10 cycles of catalytic-washing of Fe-Pd-MC and MNP2-Pd-MC. Almost 100% conversions were obtained from the Fe/MNP-Pd-MC catalyst until 7 cycles, while a severe drop was observed for MNP2-Pd-MC after cycle 8 due to the loss of catalyst caused by the reduced magnetization as the Fe_3O_4 particles/MNP clusters were lost after repeated recycling. Thus, the MNP2-Pd-MC particles lost more Fe_3O_4 from the MNPs clusters resulting in a lower amount of Pd particles that led to a lower conversion rate. The result indicated that MNP clusters could be recycled 7 times without severe loss when the cuvette was placed on top of the HGMS. In comparison, Fe-Pd-MC displayed better recyclability, due to the higher magnetization of the aggregated Fe_3O_4 particles. As shown in



(**B)**, the recyclability of MNP2-Pd-PDC deteriorated as the conversion rate of 4-NP decreased to 23%

after the first catalytic wash cycle. The MNP2-Pd-MC system possessed a better conversion rate for many cycles due to the highly porous structure of melamine formaldehyde shell for Pd deposition, and the strong coordination between NH_2 and Pd particles compared with OH-Pd in Pd-PDC systems. In conclusion, MNP2-Pd-MC displayed excellent reusability for the catalytic degradation of 4-NP.

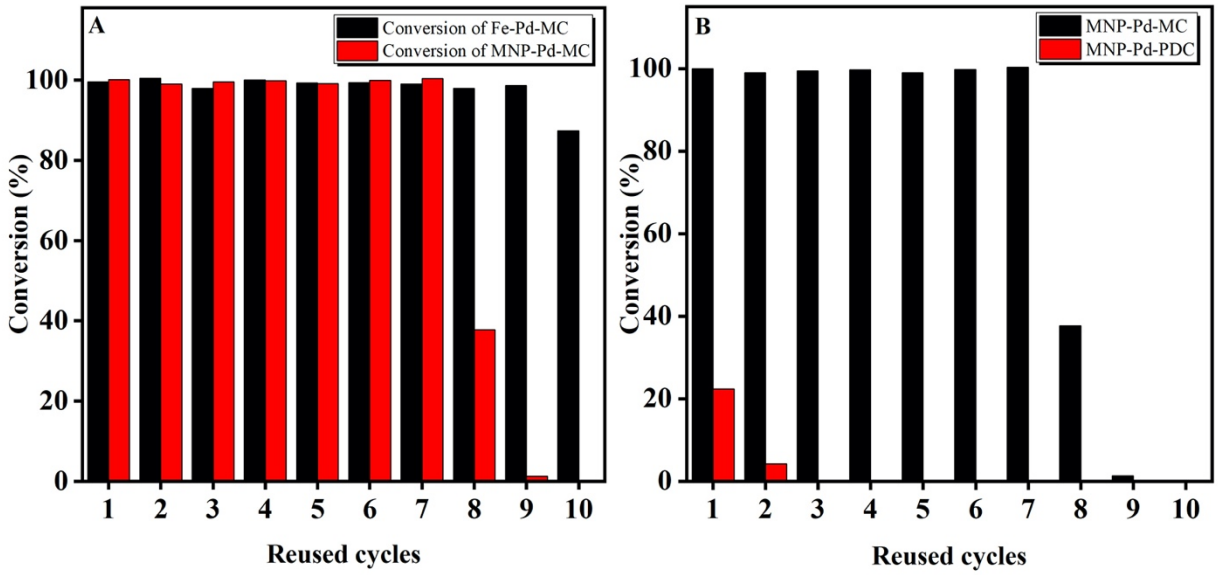


Figure 7-8 Recyclability test of Fe-Pd-MC and MNP-Pd-MC (A), recyclability test of MNP-Pd-PDC and MNP-Pd-MC

7.6 Conclusions

Synthesis catalyst with high catalytic activity has drawn a lot of attention, while it has been challenging due to the balance between the high surface area and difficulty of separation. Many works have devoted to the development of magnetic based catalyst, however, aggregation was frequently occurred on ununiform Fe_3O_4 attached magnetic catalyst system [441]. And the traditional polymer coated Fe_3O_4 caused severe leaking issue after three rounds of separation [442]. In this study, two different catalytic systems, namely Pd-MC and Pd-PDC were prepared. A MAA-EA nanogel with Fe_3O_4 clusters incorporated into the catalyst system imparted the magnetic separation characteristic to the catalysts prevented the aggregation issue. The melamine formaldehyde modified CNC possessed a highly porous structure for the loading of large amounts of Pd particles (15.48 ± 2.3 nm) resulting in a better catalytic performance. The MNP2-Pd-MC maintained an almost 100% 4-NP conversion rate up to 7 cycles of catalytic test and washing. However, the dopamine modified CNC displayed a lower rate constant determined from the first

order kinetic model. PDA interacted with the surface Pd, which hindered the adsorption of reactive species necessary for the catalytic reaction. A delay of induction time was observed at the very beginning of the catalytic reduction of 4-NP. Excess amount of PDA resulted in a faster reduction rate of Pd particles in the PDA-CNC system, that led to the formation of larger Pd particles. The highest TOF values were 540.42 and 340.57 h^{-1} from the MNP4-Pd-MC and 10-Pd-PDC catalytic system, respectively, matching the reported results of previous studies. The novel nanogel based MNP clusters effectively reduced the toxicity arising from the leaking of magnetic particles. The MNP clusters grafted to Pd-MC catalyst could be used at least 7 times without severe loss of magnetization and catalytic performance. This MNP based catalyst could be used in a magnetic assisted 4-NP reduction, and the MNP clusters could be combined with other system for the recycling and reuse of the catalysts.

Chapter 8: Sustainable high porosity adsorptive membrane for cationic/anionic dye, heavy metal ions, and PFAS removal

Persistence contaminants, such as perfluoroalkyl and polyfluoroalkyl substance (PFAS) are widely present in our water systems threatening human beings by negatively impacting the reproductive system. Additionally, heavy metal and organic dyes continues to contribute to challenges in wastewater treatment due to agriculture and industrial activities. In this chapter, a sustainable membrane was prepared from soft wood fiber (WF) crosslinked with (3-glycidyloxypropyl)trimethoxy silane (GPTMS) and poly(ethyleneimine) (PEI). Tanfloc (TF) (a natural tannin based commercial flocculant) was used to coat CNC for preparing Pickering emulsion in hexane. When the Pickering emulsion was added to the membrane formulations, the porosity of the membrane WGP-111-EM45 increased to 41.60 % compared to the membrane without emulsion (23.65 %). Gravity filtration with methyl orange (MO) was used to evaluate the performance of the membrane with various amounts of PEI or emulsion loadings. WGP-111-EM45 was selected and further evaluated in dynamic filtration system. A simple pressure controlled dynamic filtration system was designed and inlet flowrate, inlet concentration and number of membranes loaded to the filtration system were evaluated. The highest filtration capacity was obtained as 22679.1 mg/g with MO, inlet concentration of 50 ppm and inlet flowrate was 11.22 ml/min. An increased in the number of membranes (bed height) led to an increase in the removal efficiency with a lower slope in the breakthrough curve due to the enhanced diffusion mass transfer. Furthermore, the membrane filtration efficiency of the membrane towards copper ions (Cu^{2+}) and methylene blue (MB) was evaluated by gravity filtration and a 98% removal efficiency of 10 ml 1000 ppm Cu^{2+} was achieved with WGP-111-EM45 and an 89 % removal efficiency was achieved for 10 ml, 20 ppm MB. This sustainable porous membrane provided

adsorption sites towards cationic/anionic dye and heavy metal ions based on multiple mechanisms, such as ion exchange, electrostatic interactions, chelation and π-π interactions. This membrane displayed promising potential for removing pollutants via both gravity filtration and pressure driven dynamic filtration. Over 99% of removal efficiency was achieved by filtrate 10 ml 0.5 and 1 ppm PFOA through WGP-111-EM45 and PFOS (10 of of 0.5 or 1 ppm) was fully removed indicated by zero residues detected from LC-MS. This work provided a promising alternative for treating both traditional contaminates (organic dyes and heavy metal ions), and also emerging contaminates (PFAS) by low carbon footprint process.

8.1 Introduction

The rapid development of contemporary society has led to a wide range of innovation and uses of materials. Accordingly, the presence and potential impacts of emerging contaminants have raised many concerns and challenges. Among them, one class of synthetic compounds called per- and polyfluoroalkyl substances (PFASs), which are ecotoxic amphiphilic molecules comprising of alkyl-fluorinated chains and terminated with ether carboxylic or sulphonic acid functional groups has emerged as a major threat [157]. Both perfluorooctanoic acid (PFOA) and perfluorooctanesulfonic acid (PFOS) were widely used since the 1950's [443], and they have been detected in the environment and human bodies since 2000s [444] and it raises major concerns due to the possible health risk. These compounds have been widely used in the production of the fire-fighting foam, carpet, dental floss, non-sticky cookware, stain-resistant product, fast food packaging and pesticides due to their excellent water/oil resistance capability and long durability [445]. PFASs were proven to be extremely persistent, bio-accumulative and toxic due to the intrinsic stability of the C-F bonds. All these physicochemical properties of PFAS made them difficult to be degraded, and the accumulative effects in living organisms raised major toxicity

concerns. PFASs are also highly mobile, since they were found to display long-distance transportation via both ground water and surface water [446]. However, non-reduction of PFAS concentration after conventional water treatment process has contributed to the presence of high concentration of PFAS in our drinking water [443]. Long time exposure to PFAS is known to cause side effects on various living organisms, such as fish and birds. In terms of human beings, the progressive accumulation of PFAS in blood serum might lead to cancer, liver damage, malfunction of the physiological system, sex organs and it could impact the early childhood development [447]. In 2016 the United States Environmental Protection Agency (EPA) has issued a 70 ng/L limit for the total life time advisory (LTHA) concentration for PFOA and PFOS in drinking water based on their toxicity [448].

To meet the regulatory requirement, various water treatment techniques have been applied for PFAS removal. Granular activated carbon (GAC), ion exchange (IX), microfiltration (MF)/ nanofiltration (NF) and low-pressure reverse osmosis (RO) were considered to be relatively effective in PFAS removal. GAC can be easily fitted to the current water treatment process for PFAS removal, while it has limited effectiveness in removing short chain PFAS and the presence of other macromolecules like natural organic matters (NOM) can severely reduce its efficiency. Anion exchange (AIX) can capture long chain PFAS and some short chain PFAS, while the enriched high concentration waste stream needs an additional desalination step. Low pressure RO was considered as one of the most effective strategies in PFAS removal, however, the high operational cost limits its large-scale application. Nanofiltration is more effective in removing PFAS compared to GAC and AIX, whereas the high cost and large volume of waste stream lead to the necessity of a secondary treatment process. Improving the adsorption efficiency via the appropriate modification of adsorbents or reducing the cost of the filtration offers the most

promising pathway for PFAS remediation. Nicholas et al. developed a polysulfide polymer supported powdered activated carbon (PAC) for the removal of PFOA and PFOS from water. Sodium chloride porogen was used during the inverse vulcanization between sulfur and canola oil for polysulfide polymer preparation, which increased the surface area of the adsorbent. The polymer functioned not only as a support or lubricant, and also acts as a binding agent for PFAS. The removal efficiency of this polymer blended with carbon was examined by passing 10 L of field surface water containing 150 ± 20 ppt of PFOS through a 40g adsorbent packed column, where a 85% removal was achieved. Even though, blending the PAC with sulfur-based polymer effectively reduced the respiratory risk caused by the dust, a secondary separation was still required after the adsorption [449]. PFOS and PFOA possess low vapor pressure as 2.48×10^{-6} and 0.017 mmHg at 20℃, respectively, which enable the evaporative separation as an appropriate technique for PFAS removal and enrichment. Chen et al. used a commercial poly (tetrafluoroethylene) (PTFE) membrane to remove and concentrate PFAS from water via the direct contact membrane distillation (DCMD) strategy. The low molecular weight of the 5-carbon perfluoropentanoic acid (PFPeA) was used as a model PFAS to study the DCMD performance of the PTFE membrane. PFPeA has a boiling point of 140℃, which is much higher than water (100 ℃), thereby enabling the concentration of PFPeA through DCMC. Increasing the feed temperature led to an increase of the PFPeA drag-diffusion through the membrane, resulting in a higher PFPeA concentration in the permeate. The morphology of the membrane before and after the DCMD test were examined to investigate the fouling mechanism. Fouling occurred after the long time DCMD operation due to compaction and fouling of the membrane, which reduced the rejection rate, and also the permeate flux. A maximum rejection rate of 85% was obtained in DCMD below 6.2 kPa, which is superior than the rejection rate of 80% obtained with NF (600kPa). This work disclosed the possibility of

using DCMC strategy for PFAS removal, while further work is needed on the hydrophilic modification of the membrane to prevent severe fouling [157]. By considering the low concentration of PFAS and the energy consumption, a gravity driven membrane filtration was applied for PFAS remediation, where the membrane was fabricated by electrospinning of the quaternary ammonium (QA) grafted polyvinylidene fluoride (PVDF) onto a polyethylene terephthalate (PET) non-woven substrate. This PVFF-g-QA membrane provided a high affinity towards PFAS with both hydrophobic property and electrostatic interactions, achieving over 95% PFOX removal in synthetic ground water. The removal efficiency of PFOX could maintain over 90% with a 8 hour filtration test (258 L/m^2), and the concentration could be enriched by up to 39-fold with PFOS, which performed better than the decomposition process, such as advanced oxidation or thermal methods. It was found the PFOA removal was more favorable in basic pH and high conductivity, while the removal of PFOS was not affected due to its strong hydrophobic interaction with the components in the membrane. This work provides an insight into using electrospinning membrane via gravity filtration (less energy intensive process) for PFAS removal. However, the membrane produced from the more expensive and complex electrospinning process will increase the operational cost [450]. In a conclusion, a material with high affinity towards PFAS is highly desired, and the implementation of the material in a low energy-needed process is necessary.

This work proposes a sustainable membrane synthesized by crosslinking soft wood fiber with (3-glycidyloxypropyl)trimethoxy silane (GPTMS) and poly(ethyleneimine) (PEI). A positively charged biopolymer produced from natural condensed tannins [69], Tanfloc (TF), was coated onto cellulose nanocrystals (CNC) and used to stabilize a Pickering emulsion containing water and hexane. This emulsion was used to increase the porosity and surface area of the

membrane. Wood fiber is a cellulose based natural material that is abundant in nature, and PEI is a highly water-soluble amine-based polymer with a strong binding affinity towards acidic dye, which was also used to enhance the wet/dry strength of paper. This novel emulsion imprinting method for porosity enhancement is proposed in this study to increase the porosity of the membrane and improve PFAS removal efficiency by retaining the high surface area in the membrane. The TF-CNC not only functioned as a Pickering emulsier, it also provided abundant adsorption binding sites via electrostatic interaction for PFAS removal. Both gravity filtration (GF) and dynamic filtration setup was designed and used to evaluate the filtration performance of the membrane. Due to the restriction of the PFAS usage, methyl orange (MO), a negatively charged dye was used as a model compound to examine the filtration performance and optimize the membrane formulation at the initial stage. The removal efficiency of a cationic dye, methylene blue (MB), and a heavy metal copper (Cu^{2+}) were also studied to evaluate the filtration performance of the membrane for a wide range of pollutants. Finally, the removal of PFAS was investigated and the filtrate concentration will be quantified using a liquid chromatography-mass spectrometry (LC-MS).

8.2 Experimental

8.2.1 Materials

Soft wood fiber (WF)-BCTMP (bleached chemi-thermomechanical pulp) were provided by Brazil, hexane (98%), poly(ethyleneimine) solution (PEI, 50 wt% in water), (3-glycidyloxypropyl)trimethoxy silane (GPTMS > 98%), Hexane, methylene blue (MB, dye content > 82 %), methyl orange (MO dye content > 85 %) were purchased from Sigma Aldrich. Tanfloc (TF) was provided by TANAC, Brazil, cellulose nanocrystals (CNC) was supplied by Celluforce Inc.

perfluorooctanoic acid (PFOA, 95%), heptadecafluorooctanesulfonic acid solution (PFOS, 40% in water)

8.3 Methods

8.3.1 Preparation of Tanfloc coated CNC (TF-CNC)

The 2 wt% CNC suspension was first prepared by dispersing 6 g of CNC into 300 ml water with Glass-Ball-Mill Tube (IKA BMT-20 G), and further dispersed in a sonication bath for 30 mins. Another 4 wt% Tanfloc solution was prepared by dispersing 12 g of Tanfloc (TF) in 300 ml of water by homogenizing at 5000 rpm for 10 mins. The 2 to 1 mass ratio of Tanfloc coated CNC suspension was obtained by adding 300 ml of 4 wt% TF suspension into 300 ml of 2 wt% CNC suspension and homogenized (5000 rpm) for 3 mins, and the suspension was further stirred at 500 rpm for 24 hours. The TF coated CNC (TF-CNC) suspension was purified by centrifugation, and the TF-CNC template was obtained after removing the supernatant and it was then stored in the fridge prior to use.

8.3.2 Preparation of TF-CNC stabilized hexane emulsion

1.3 wt% of TF-CNC was prepared from the TF-CNC template in a 200 ml volume, and was then further dispersed for 5 minutes using a homogenizer running at 5000 rpm. To achieve a TF-CNC to hexane volumetric ratio of 2:1, 100 ml of hexane was added to the dispersed solution and homogenized at 7000 rpm for two minutes.

8.3.3 Fabrication of TF-CNC EM contained wood fiber membrane

The 0.6 wt% of wood fiber (WF) suspension was prepared by dispersing 12 g of WF into 2 L of water and transferred to the fiber beater vessel. All the components of the fiber beater were secured and the fiber beater was turned on and allowed to rotate for after 170 rotations to prepare finer WF suspension for membrane fabrication. 10 g of wood fiber membrane was prepared by

mixing 1666.67 g of 0.6 wt% WF suspension in a 2L beaker, followed by the addition of the same mass ratio of GPTMS (10 g) and left for 2 hrs to promote the crosslinking reaction. Then, 45ml of TF-CNC EM was added and mixed well for 5 mins, and 50 g of 20% PEI solution was added to the beaker to produce a 1:1:1 (WF: GPTMS: PEI) mass ratio WF membrane containing 45 ml of emulsion. The membrane suspension was left for another 30 mins stirring before the membrane was compressed (**Scheme 8-1, A**). The equipment and process images of the membrane fabrication process is shown in **Appendix 8-1**.

A polyvinyl chloride (PVC) mesh was used as a support when compressing and drying the membrane. The PVC mesh was placed on top of the hand sheet former (The HERMANN MANIFACTURING Co. Lancaster, OHIO, USA) and covered by a medical cloth (where the membrane will be formed). The forming cylinder was clamped onto the supporting mesh, and water was added to a preset level and the fiber suspension was poured into the forming cylinder (WF-GPTMS-EM-PEI suspension). The perforated shaker was placed in the forming cylinder and shake from top to bottom, 5 times for 6 seconds, and it was carefully removed. After 5 seconds, the water evacuation valve was opened to drain the pulp suspension over the mesh with medical cloth to form the membrane. The membrane was transferred to a vacuum oven and dried at 55 ℃, -5 to -10 bar. The membrane fabricated was designated based on the composition of the various components. For example, membrane prepared using the above recipe was designated as WGP-111-EM45, where 111 is the mass ratio (wood fiber: GPTMS: PEI) and EM45 corresponds to the membrane produced with 45 ml of the emulsion. The membrane was then overnight soaked in deionized water as a purification step before the desired membrane size was prepared using a puncher for conducing the adsorption experiments. The chemical reaction of the crosslinking

process and the chemical structure of the crosslinked membrane is shown in **Scheme 8-1 B** and **C**, respectively.

8.4 Characterization

8.4.1 FTIR

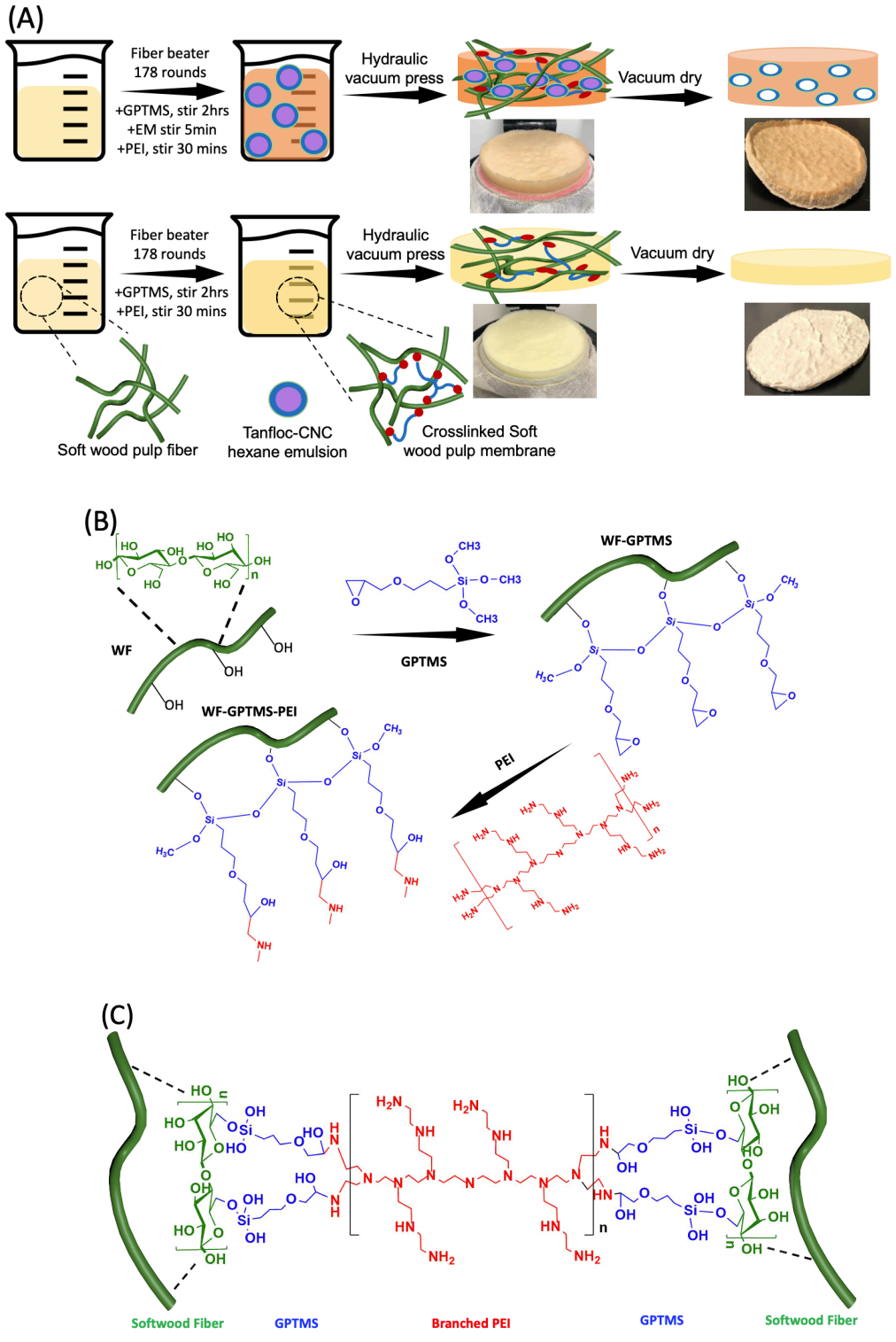
The FTIR spectra of CNC, Tanfloc, Tanfloc-CNC, wood fiber and membrane WGP-111-EM45 were obtained using a Bruker Tensor 27 spectrometer (Bruker, Billerica, MA, USA). The samples were mixed with KBr and compressed into transparent pellets, and scanned between 4000 and 400 cm^{-1} with a resolution of 4 cm^{-1} at room temperature.

8.4.2 Microscopic imaging

The optical images of different concentrations of CNC and TF-CNC stabilized hexane emulsion was investigated using a Leica inverted Fluorescence microscope with a 20X objective. Various concentrations of CNC (0.1 wt%, 0.2 wt%, 0.3 wt%, 0.5 wt% and 1.0 wt%) stabilized hexane was examined by microscopy in addition to the 0.3 wt%, 0.6 wt%, 1.0 wt%, 1.3 wt%, 1.5 wt% and 2.0 wt% TF-CNC stabilized hexane emulsion (with 1: 2 volume ratio of hexane: TF-CNC suspension). The microscopic samples were prepared by placing one drop on emulsion on the glass slide and covered with the coverslip.

8.4.3 Particle size and zeta potential

Zeta-sizer (Nanosizer ZS, Malvern Co., UK) was used to examine the particle size and zeta potential of 0.1 to 1.5 wt% TF-CNC and 2.0 wt% TF-CNC. The measurements were conducted by measuring 0.05 wt% dispersion in a zeta sizer at 25℃, and the particle size of TF-CNC stabilized emulsion was measured by the particle sizer.



Scheme 8-1 Fabrication process for sustainable softwood fiber, GPTMS, crosslinked membrane with or without emulsion (A); Chemical reaction of the crosslinking process (B); Chemical structure of the crosslinked membrane (C)

8.4.4 Emulsion particle size

Anton Paar (PSA 1190) was used to measure the size of 0.1 to 1.5 wt% and 2.0 wt% TF-CNC stabilized hexane emulsion (volume ratio of hexane: TF-CNC suspension equals to 1:2).

8.4.5 Porosity measurement

The porosity of the WF membranes produced with various formulations were calculated using Eq (8.1), where the porosity % corresponds to ratio of the pore volume versus the total volume of the membrane; V_{pore} is the pore volume (m^3); $V_{membrane}$ is the total volume of the membrane (m^3); V_{water} is the volume of the water that replaced the air in the membrane pores (m^3); m_{wet} (g) is the wet mass of the membrane after 24 hours soaking in the water and 1 hour of bath sonication (for removing air bubble trapped inside the membrane network). Excess surface water was removed by wiping it with a tissue paper, and the wet membrane was immediately transferred to a moisture analyzer (VWR). The drying process was performed from room temperature (25 ℃) and gradually heated to 90 ℃ at a heating rate of 5 ℃/min until a constant weight was obtained ; m_{WF} (g) is the mass of water absorbed by the wood fibers, m_{dry} (g) is the dry mass of the membrane, ρ_{water} is the density of water at 25 ℃ (0.997 g/ml).

$$Porosity\ \% = \frac{V_{pore}}{V_{membrane}} * 100 = \frac{V_{water}}{V_{membrane}} * 100 = \frac{(m_{wet} - m_{WF} - m_{dry})/\rho_{water}}{V_{membrane}} * 100 \qquad (8.1)$$

8.4.6 Gravity filtration

A simple gravity filtration test with 30 to 200 ppm MO was conducted with a series of membranes to investigate the removal efficiency and the flux of the membrane. The removal efficiency was calculated using Eq (8.2), where R describes the removal percentage of the pollutant; C_0 represents the initial concentration of the pollutants (ppm); C_f corresponds to the concentration of the pollutant after filtration (ppm). The flux of the filtration process was calculated according to Eq (8.3), where J is the flux of the pollutant solution passing through the membrane during the

filtration process (L/m^2·hr), Q is the volume of solution passed through the membrane; Δt is the time interval (hr) and A is the membrane area (m^2).

$$R\ \% = \frac{C_0 - C_f}{C_0} * 100 \quad (8.2)$$

$$J = \frac{Q}{\Delta t * A} \quad (8.3)$$

8.4.7 pH effect on gravity filtration

The effect of the pH of the membrane on the removal efficiency of negatively charge molecules was investigated. Methyl orange (MO) was employed as a model pollutant to elucidate the performance of the membrane. The experiment was conducted by filtering 10 ml of 50 ppm MO solution through a 10g of 1:1:1.5 (WF: GPTMS: PEI) membrane contained 45 ml of emulsion placed inside a syringe. The membrane was pre-conditioned by soaking it in a series of pre-adjusted pH (3.5, 5.5, 7.5, 9.5 and 11) solution. The filtration of each pH pre-conditioned membrane was repeated twice, and the MO concentration in the filtrate was measured by UV spectrometer and the filtration time was also recorded.

8.4.8 Multi-layer gravity filtration

Gravity filtration efficiency of MO in various number ofWGP-111-EM45 membranes (1, 3, 5, 10) was conducted. The membrane was soaked overnight in water and 7/8 inch diameter circular membrane was prepared using a puncher. For each test, 30 ml of 100 ppm MO was added to the membrane placed in a syringe, and the filtration time was recorded and the filtrate concentration was measured by UV spectrometer.

8.4.9 Mechanical test for membranes

The tensile strength of the membranes was measured by a CETR-UMT (Bruker) instrument. Both wet tensile tests (adding 5 ml of water) and dry tensile tests were conducted on five 60 × 15

mm membrane strips. The membrane strip was clamped between two clamps (assisted with a sand paper) at a distance of 40 mm. The elongation rate was set as 18 mm/min and the tensile index (TI) was calculated based on previous reported study [451] and also referred to the TAPPI method T494 om-01. The equation is given below Eq (8.4), where *F* (kg) represents the applied maximum force before the fracture of the membrane strip, *g* is the gravitational acceleration constant (9.81 m/s^2), *m* (g) is the weight of the membrane strip, *W* (m) and *L* (m) indicates the width and length of the membrane strip, respectively.

$$Tensile\ Index\ (TI) = \frac{tensile\ strength}{grammage} = \frac{F \cdot g/W}{m/L \cdot W} \tag{8.4}$$

8.4.10 Scanning Electron Microscope (SEM)

The morphology, structure and alignment of the WGP-11*Z*-EM*V* membranes were examined using the SEM. Samples for the SEM analyses were prepared by fracturing the liquid nitrogen frozen membrane followed by gold sputtered to minimize charging. The SEM images were obtained in a Carl Zeiss NTS GmbH instrument with an acceleration voltage of 20 kV.

8.4.11 Dynamic adsorption experiments

A dynamic filtration experiment was conducted using a "home-made" pressure driven filtration system. The schematic of the dynamic filtration setup is shown in **Scheme 8-2**, where (**A**), (**B**), (**D**) show the single membrane dynamic filtration set up, multiple membrane dynamic filtration setup and the flowchart of the dynamic filtration process, respectively. The membrane were assembled in series inside the membrane holder as shown in (**C**). Various factors were investigated for the dynamic filtration process using the WGP-111-EM45, such as MO initial concentration (2, 5, 15, 30, 50 ppm), flowrates (8.33, 45 and 100 ml/min) of 15 ppm MO, and the number of membranes (1, 3, 6, 10 membranes) or bed height. The apparent average diameter of the membrane was 23.9 mm, which was sealed by the O ring to prevent any leak, and the average

membrane height was 6.15 mm. The capacity of the membrane loaded column, q_c (mg) was obtained from area under the breakthrough curve (A) of the plot of adsorbed MO concentration C_{ads} (Eq (8.5)) versus elution time t (min) multiplied by the flowrate Q (ml/min) and inlet concentration C_0 (ppm) of MO (Eq (8.6)) [452][453].

$$C_{ads} = C_0 - C_t \tag{8.5}$$

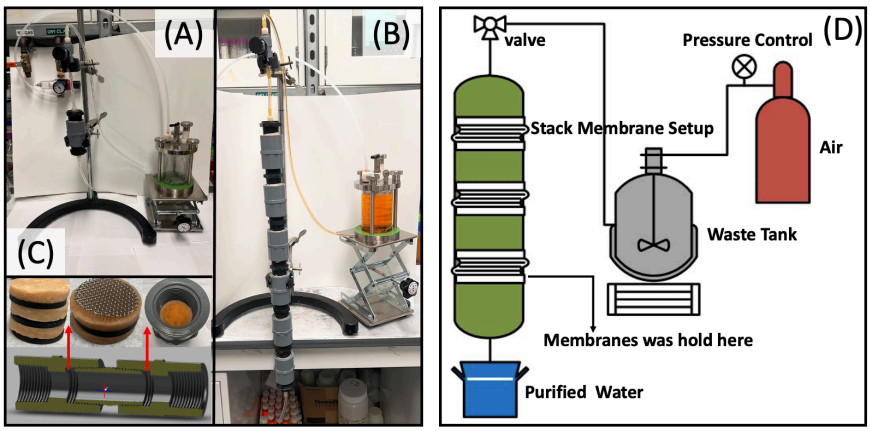
$$q_c = \frac{QA}{1000} = \frac{Q}{1000} \int_{t=0}^{t=t} C_{ads} dt \tag{8.6}$$

The amount of MO (m (mg)) used in the filtration system at different time was calculated from Eq (8.7), and the removal efficiency determined from Eq (8.8). Finally, the membrane sorption capacity q_c corresponding to the weight of MO (mg) adsorbed per one gram of dry membrane is described by Eq (8.9), where X (g) is the total mass of the dry membrane loaded to the filtration system [454].

$$m = \frac{C_0 * Q * t}{1000} \tag{8.7}$$

$$R\,\% = \frac{q_c}{m} * 100 \tag{8.8}$$

$$q = \frac{q_c}{X} \tag{8.9}$$



Scheme 8-2 Dynamic filtration setup with one membrane build into the system (A); Dynamic filtration setup with 10 membranes build into the system (B); Cross section of the designed membrane holder and the way membrane stacked in the membrane holder (C); Flow diagram of the designed dynamic filtration system (D)

8.5 Results and discussion

8.5.1 FTIR

FTIR spectra of CNC, TF, TF-CNC, WF and membrane WGP-111-EM45 are presented in **Figure 8-1**. The spectrum of cellulose-based material (CNC and WF) displayed an absorption band at 3200 and 3346 cm^{-1}, which was attributed to the stretching vibrations of O-H bond originated from the hydroxyl groups. Asymmetric and symmetric stretching vibration of C-H bonds is indicated by the absorption band at 2900 cm^{-1}, and the vibrational band of C-O-C from sugar unit is shown at 1053 cm^{-1}[455]. Tanfloc spectrum displayed a weak band centered at 1725 cm^{-1} that is associated with the C=O bonds, and the large absorption band located at 1608 cm^{-1} is due to the C=C stretching [69]. The hydroxyl groups (O-H) vibration band appeared at 1465 cm^{-1}[456]. The presence of the C=C stretching (1608 cm^{-1}) in the spectrum of TF-CNC confirmed the successful coating of TF onto CNC. Wood fiber still possesses lignin after the bleaching process, since the H_2O_2 treatment does not have the capability to remove all the aromatic lignin from the wood fiber. Thus, the vibrating band at 1500 cm^{-1} is evident in the FTIR spectra of wood fiber [457]. FTIR spectrum of membrane WGP-111-EM45 displayed an adsorption band of aromatic lignin at 1500 cm^{-1} and also a weak peak located at 1608 cm^{-1} (C=C), which indicated the successful loading of the TF-CNC hexane emulsion into the wood fiber membrane.

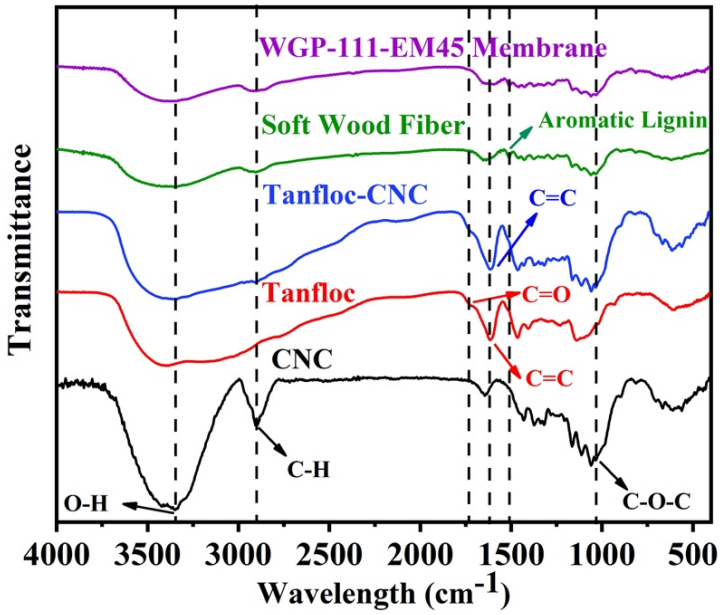


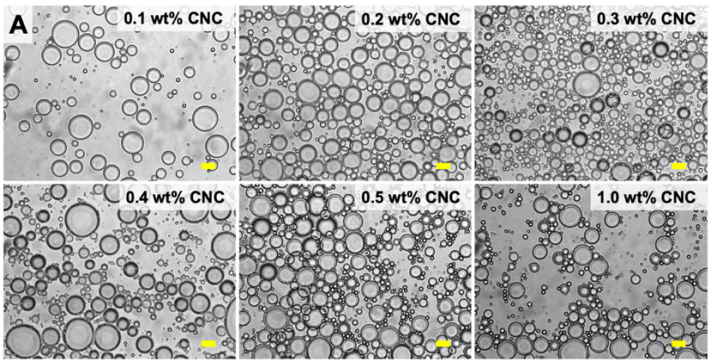
Figure 8-1 FTIR spectra of CNC, Tanfloc, TF-CNC, softwood fiber and WGP-111-EM45 membrane

8.5.2 Stability of the Pickering emulsions

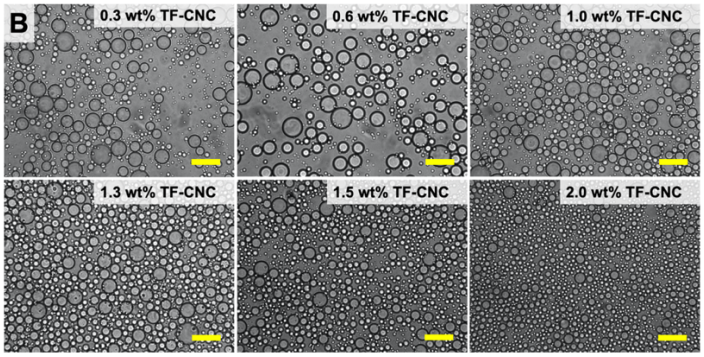
Stability is one of the most important standards to evaluate the performance of the surfactant when preparing the emulsion, and it was examined by the microscopic and digital images by observing the particle size and comparing the height of the creaming layer. Emulsions are prepared using spherical particles of two different categories of liquids that stabilized by amphiphilic molecules, such as surfactants or functioned polymers [458]. When using solid particles as stabilizing agent instead of conventional surfactant molecules, the produced system is defined as Pickering emulsion. It presents advantages, such as outstanding stability, controllable permeability and improved elastic responses over traditional emulsion system [459]. The increasing concern on the carbon footprints has fostered the use of sustainable material from abundant natural resources, such as CNC, a rod-shape cellulose particles with high aspect ratio and crystallinity. CNCs possess amphiphilic properties due to the presence of both hydrophilic face ($(010)\beta/(110)\alpha$), ((1-

10)β/(100)α) and also the ((200)β/(220)α) hydrophobic edge plane, which allow the CNC to become a promising renewable, economic nanoparticle to prepare Pickering emulsion [458]. However, the stability of CNC stabilized Pickering emulsion is closely determined by the characteristics of CNC, such as aspect ratio, charge density and wettability [460]. The CNC used in this study was obtained from sulfuric acid hydrolysis, which possessed large amounts of negative charge on its surface. Tanfloc, a natural tannin based commercial flocculant was used to impart a positive surface charge to CNC via surface coating. Abundant amino groups on TF coated CNC provided additional adsorption sites for negatively charged PFAS molecules. Both CNC and TF-CNC stabilized hexane emulsion was examined under the microscope. As shown in **Figure 8-2** (**A**), pristine CNC stabilized hexane possessed a similar morphology and particle size distribution when the concentration of CNC was increased from 0.1 to 1.0 %. Large emulsion droplet (> 50 μm) was observed in all microscopic images of the CNC stabilized emulsion system. In **Figure 8-2 (C)**, there was almost no differences in the height of creaming layer at varying concentration of CNC (0.1 to 1%), which indicated the negligible influence of CNC concentration on the stability of the hexane emulsion. This poor performance was due to the high negative surface charge of pristine CNC that induced large electrostatic repulsion between neighboring CNC particles. However, the particle size of the TF-CNC stabilized emulsion droplet (**Figure 8-3**) displayed a decreasing trend with increasing TF-CNC concentration. From **Figure 8-2** (**B**), there was negligible large droplets in all TF-CNC stabilized emulsion systems. Homogenous emulsion droplets were observed when the concentration of TF-CNC exceeded 1.3 % Since Tanfloc possessed a high density of positive surface charge, it was coated on the CNC via electrostatic interactions that counteracted the negative charge from CNC and the remaining positive charge stabilized the hexane-water emulsion (**Table 8-*1***). The particle size of the stabilized droplets

decreased with increasing TF-CNC concentration, which was due to the increased surface coverage of the TF-CNC on the surface of hexane droplets. The height of the creaming layer also displayed an increasing trend as more TF-CNC was added as shown in **Figure 8-2** (**D**).



* The scale bar in above image represents 50 μm



* The scale bar in above image represents 50 μm

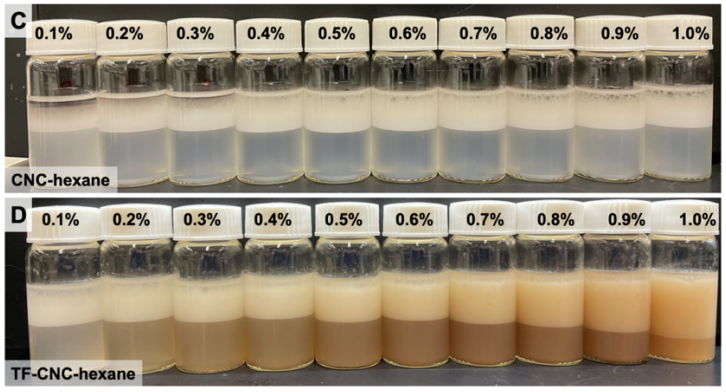


Figure 8-2 Microscopic images of 0.1, 0.2, 0.3, 0.4, 0.5, 1.0 wt% of CNC stabilized hexane Pickering emulsion (water: oil= 2:1) (A); the microscopic images of 0.3, 0.6, 1.0, 1.3, 1.5, 2.0 wt% of TF-CNC stabilized hexane Pickering emulsion (water: oil= 2:1) (B); the digital image of 0.1 to 1.0 wt% of CNC stabilized hexane Pickering emulsion (C); and the digital image of 0.1 to 1.0 wt% of TF-CNC stabilized hexane Pickering emulsion (D)

Table 8-1 Summary of zeta size and zetapotential

Sample	CNC	TF-CNC
Size (nm)	89.1 ± 3.2	485.3 ± 23.1
Zeta potential (mV)	-41 ± 2.6	28.2 ± 0.7

8.5.3 Emulsion particle size

The particle size of the TF-CNC hexane emulsion is closely related to the stability of the emulsion and the porosity of the membrane. The relationship between the concentration of TF-CNC and the emulsion particle size versus concentration is shown in **Figure 8-3**. The size of the emulsion droplet dramatically decreased from 44.3 μm to 17.5 μm when the TF-CNC concentration was increased from 0.1 to 0.5 wt%. A further reduction in the particle size was obtained up to 1.3 wt% TF-CNC, beyond which there was no obvious reduction. Together with the emulsion images shown in **Appendix 8-2**, no phase separation phase was observed. Thus, the 1.3 wt% TF-CNC was selected as the optimal concentration for further study.

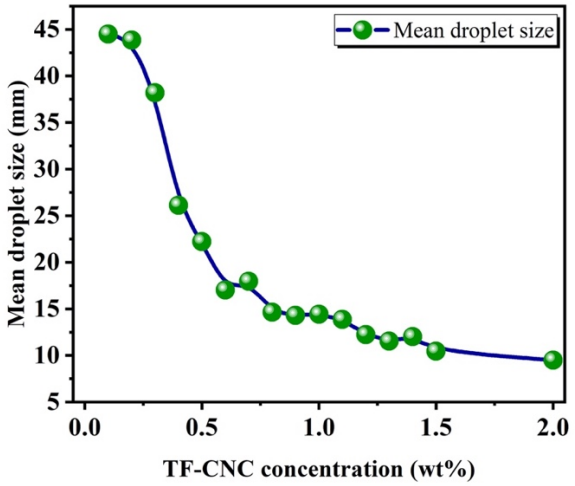


Figure 8-3 Emulsion particle size versus TF-CNC concentration (Volume ratio of TF-CNC suspension to hexane = 2: 1)

8.5.4 Porosity and permeation flux

TF-CNC stabilized hexane emulsion was used to enhance the porosity of the crosslinked membrane, since porosity is a critical factor that directly affect the adsorption or filtration efficiency. The porosity and removal efficiency of 10 ml MO via gravity filtration of the membrane for various amounts of EM incorporated membrane is shown in **Figure 8-4** (**A**), and the effect of the PEI mass ratio on the porosity and removal efficiency (%) of 10 ml 200 ppm MO is shown in **Figure 8-4** (**B**). The porosity variations versus volume of emulsion added to the membrane displayed a parabolic trend, where an optimum porosity (41.6) was obtained from membrane WGP-111-EM45 (45 ml emulsion). Surprisingly, the removal efficiency did not follow the same trend, where the membrane prepared with 120 ml emulsion displayed the best gravity filtration performance for the 200 ppm MO. The major adsorption mechanism in this membrane system consisted of electrostatic interactions between the negatively charged MO and positively charged PEI and TF-CNC in the membrane. High porosity provided a larger surface area for MO molecules binding to adsorption sites inside of the membrane. Too much emulsion led to a reduction in the porosity while the removal efficiency was enhanced due to more binding interactions with TF-CNC. The variation of PEI mass ratio also had a large effect on the removal efficiency, since the abundant ammonium groups are present on the branched PEI. The porosity of the WGP-11*Z*-EM45 membrane was enhanced by 39.27% when the PEI mass ratio was increased from 0 to 1.0, and the removal efficiency improved from 0 to 76 %. Nevertheless, further increase in the PEI mass ratio to 1.5 led to a reduction in both the porosity and removal efficiency. Even though increasing the amount of PEI provided more amine groups, while the highly crosslinking network reduced the porosity and the accessible surface area for binding with the MO molecules. Thus, the WGP-111-

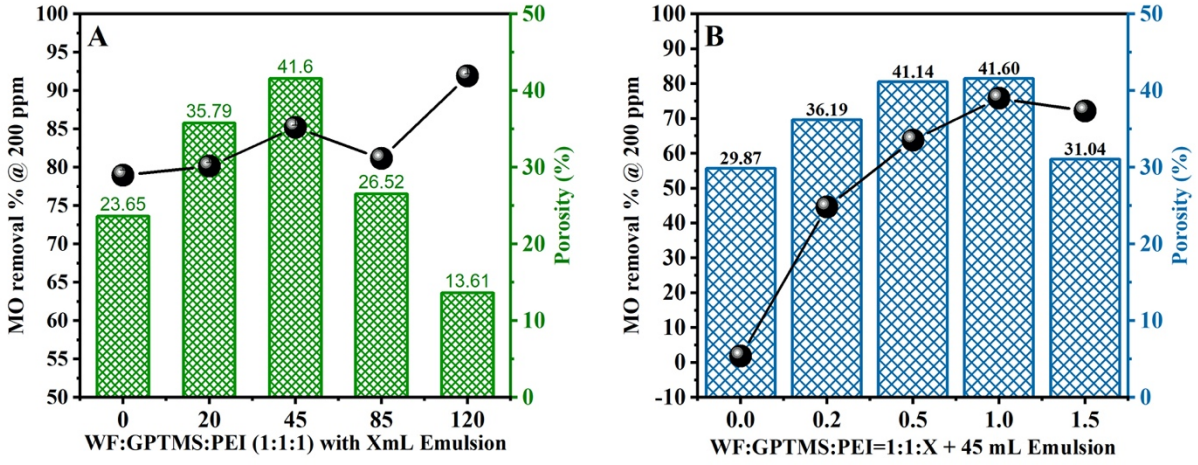


Figure 8-4 The effect of emulsion volume on the removal efficiency (%) of 10 ml 200 ppm MO and porosity (A); the effect of PEI mass ratio on the removal efficiency (%) of 10 ml 200 ppm MO and porosity (B)

EM45 was selected as the optimum membrane used for the gravity filtration test of MO, MB, Cu^{2+}, PFAS, and the dynamic filtration of MO.

8.5.5 Gravity Filtration Performance

Gravity-driven separation technique is commonly applied for oil/water separation due to its simple setup and ease of operation. By considering the energy consumption and the regulated purchase of the PFAS based chemicals, the performance of membranes fabricated with different compositions was firstly studied by treating MO with solely gravity-driven filtration experiments. The PFAS (PFOA and PFOS) removal test was also conducted and discusses in the last section. The removal efficiency and permeation flux for the gravity filtration experiments with 10 ml of MO using the WGP-11 (0.2/0.2/1.0/1.5)-EM45 and WGP-111.5-EM0 membranes are shown in **Figure 8-5** (**a, b, c, d, e**) and the summary of all removal efficiencies are shown in **Figure 8-5** (**f**) respectively. All WGP-11*Z*-EM45 membranes possessed similar trend, the removal efficiency of MO decreased with increasing MO initial concentration. This was commonly observed for other

adsorption system, where a higher initial concentration would lead to a lower removal efficiency due to the saturation of the adsorption sites [461]. WGP-110.2-EM45 removed 73 % of 20 ppm MO, while the other membranes achieved 100 % removal efficiency of 20 ppm MO. Surprisingly, the concentration had no effect on the permeation flux for all the membranes, which could be due the available of excess adsorption sites for low processing volumes. **Figure 8-5** (**f**) shows that the WGP-111-EM45 displayed a better filtration performance compared to the WGP-111.5-EM45 membrane, due to the lower porosity and high crosslinking to the membrane. This 21 % reduction confirmed the significance of the emulsion on the removal efficiency, since the optimum amount of emulsion successful improved the porosity of the degree

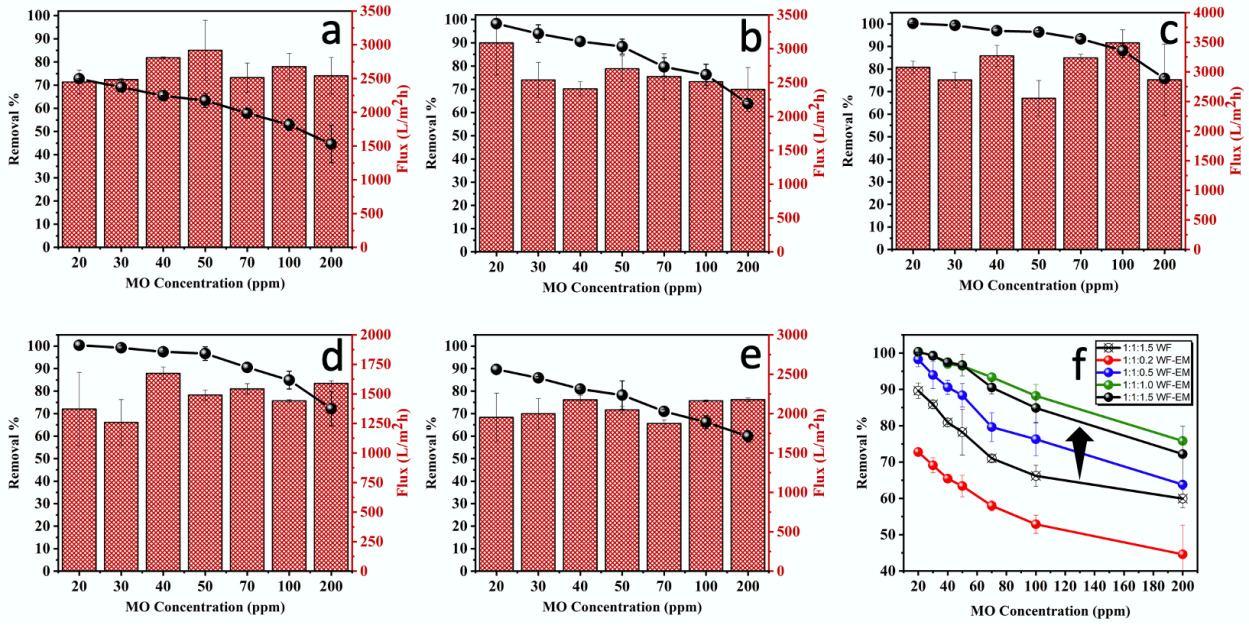


Figure 8-5 Removal efficiency and permeation flux for the gravity filtration of 10 ml MO (20, 30, 40, 50, 70, 100 and 200 ppm) by using WGP-11 (0.2/0.5/1.0/1.5) -EM45 membrane (a, b, c, d); Removal efficiency and permeation flux for the gravity filtration of 10 ml MO (20, 30, 40, 50, 70, 100 and 200 ppm) by using WGP-111.5-EM0 (e) membrane; Summary of removal efficiency of MO with WGP-11 (0.2/0.5/1.0/1.5) -EM45 membrane and WGP-111.5-EM0 (f)

caused by more PEI present in the membrane. The removal efficiency of 100 ppm MO reduced from 85 % (WGP-111.5-EM45) to 67 % (WGP-111.5-EM0) when no emulsion was added

membrane and the TF-CNC providing extra adsorption sites for MO. Briefly, the emulsion template increased the porosity of the membrane and displayed promising potential for the gravity driven removal of negatively charged pollutants. In addition to the testing of the filtration efficiency on negatively charged MO, another positive charged dye, methylene blue (MB) and heavy metal ions (Cu^{2+}) was used to investigate the filtration performance of the WGP membrane towards other types of pollutants. The permeation flux and the removal efficiency of 10 ml of 20 to 200 ppm MB by using WGP-111-EM0 and WGP-111-EM45 are shown in **Figure 8-6** (**A**) and (**B**). In contrast to the filtration performance for MO, the emulsion incorporated membranes displayed lower filtration performance on MB compared to the membrane without emulsion (WGP-111-EM0). This was due to the difference of the surface charge of MB and MO, since MO possessed negatively charge that could interact with the positively charged membrane network (PEI and TF-CNC). However, the positively charge MB would be repelled by the positive charge functional groups from PEI and Tanfloc. We observed that the WGP-111-EM0 membrane displayed a better removal efficiency for MB, due to the absence of TF-CNC. The removal mechanism of MB was mainly attributed to the components present in the wood fiber, including cellulose, hemicellulose and lignin, that contains aromatic ring can interact with the MB molecules via π- π interactions. The adsorption mechanism of MB on treated *Pinus elliottii* sawdust was associated with electrostatic interaction between the negatively charged adsorbent, π - π interaction with cellulose based components from the wood structure [462]. Also, the microporous structure of the *Pinus elliottii* sawdust adsorbent possessed a radius of 17 Å, which enhanced the binding to MB adsorption by diffusion due to its small molecule size (8-9 Å) [462]. The permeation flux and the removal efficiency of 10 ml of 20 to 1000 ppm Cu^{2+} using WGP-111-EM0 and WGP-111-EM45 membranes are shown in **Figure 8-6** (**C**) and (**D**). Superior filtration efficiency (nearly

100 %) was achieved, which was due to the strong chelation between the heavy metal ions (Cu^{2+}) and the N atoms from the PEI crosslinker and TF coated CNC. The ion-exchange process was the major mechanism for copper removal, since the electron-donor feature of the amine groups and the electron accepter nature of the copper ions [463]. Similarly, Wu reported that the removal of

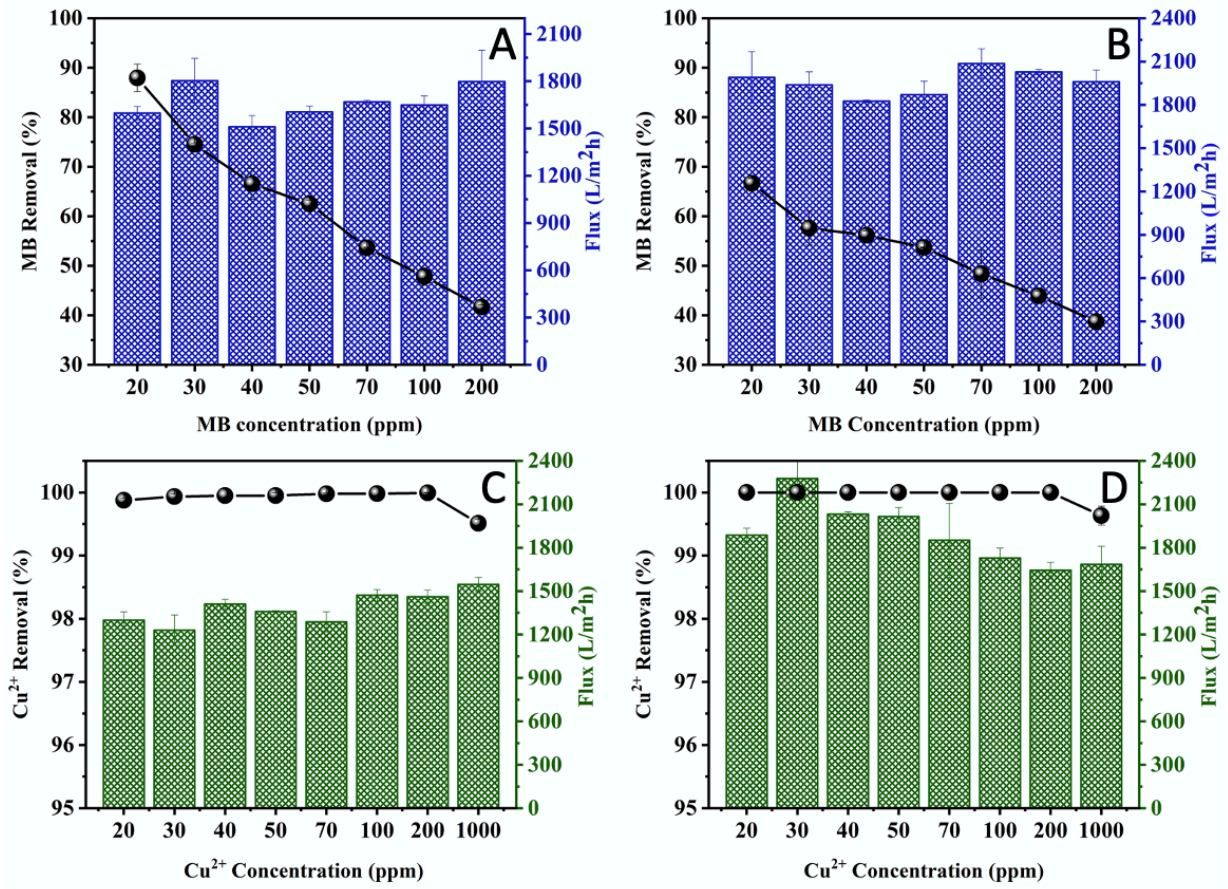


Figure 8-6 The permeation flux and removal efficiency of 20, 30, 40, 50, 70, 100 and 200 ppm of MB via gravity filtration by WGP-111-EM0 (A) and WGP-111-EM45 (B); the permeation flux and removal efficiency of 20, 30, 40, 50, 70, 100, 200 and 1000 ppm of Cu^{2+} via gravity filtration by WGP-111-EM0 (C) and WGP-111-EM45 (D)

Cu(II) using tetraethylenepentamine (TEPA) crosslinked cellulose adsorbent, and they attributed the chelation between the active adsorption sites (N, O, S) and cationic ions as confirmed by XPS results [464]. Another PEI modified cellulose/alginate crosslinked adsorbents was applied for

Cu(II) removal, where the main adsorption mechanism was due to the complexation between PEI and Cu(II) and also the ion exchanged between Na^+ and Cu(II) [465].

The permeation flux and the removal efficiency (%) of WGP-111-EM45 for 10 ml, 20 to 200 ppm MO, MB and Cu^{2+} is shown in **Figure 8-7**. As discussed previously, the highly porous wood fiber membrane displayed promising filtration efficiency for anionic dye, cationic dye and heavy metals via cooperative adsorption mechanisms, including electrostatic interaction, π- π interactions, ion exchange and chelation interactions.

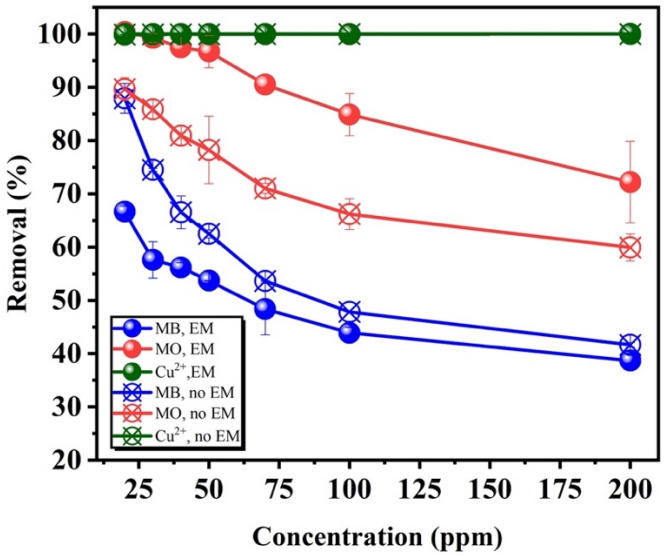


Figure 8-7 Summary graph of the removal efficiency (%) of MO, MB and Cu^{2+} by using WGP-111-EM45 and WGP-111-EM0

8.5.6 pH effect on MO gravity filtration

Electrostatic interaction between the positively charged membrane and negatively charged MO is the main mechanism for the excellent filtration performance, thus, the pH effect on the filtration efficiency is of great importance. WGP-111.5-EM45 was preconditioned at pH 3.5, 5.5, 7.5, 9.5 and 11.5, and gravity filtration with 10 ml of 50 ppm MO was performed, and the results is shown in **Figure 8-8**. The removal efficiency of MO was gradually decreased from 82 % to 71 %

as the pH of the membrane was increased from 5.5 to 11.5. A reduction of the permeation flux was also observed with increasing pH due to the reduced attractive forces between the less positively charged membrane and negatively charged MO molecules at elevated pH. At an extreme pH of 11.5, only 13.4 % reduction of filtration efficiency was observed, which confirmed that the main mechanism for MO removal was electrostatic interaction. Titration was also conducted to quantify the amount of amine groups existed in the membrane, the titration results is shown in **Appendix 8-3** and the results are summarized in **Table 8-2**.

Table 8-2 Summary of the titration results and calculated amine quantity (mmol/g)

Membrane	0.02 M NaOH (ml)	Membrane mass	Amine groups (mmol/g)
WGP-110.2-EM45	189	0.3	1.587
WGP-110.5-EM45	207.1	0.9	4.346
WGP-111-EM45	203.5	1.2	5.897
WGP-111-EM0	209.5	0.84	4.010
WGP-111.5-EM45	215.8	1.51	6.997
WGP-111.5-EM0	214.9	0.77	3.583

This WGP-111.5-EM45 membrane exhibited promising filtration performance over a wide range of pH (5.5 to 11.5), which could be used to remove pollutants from various sources with limited reduced filtration efficiency.

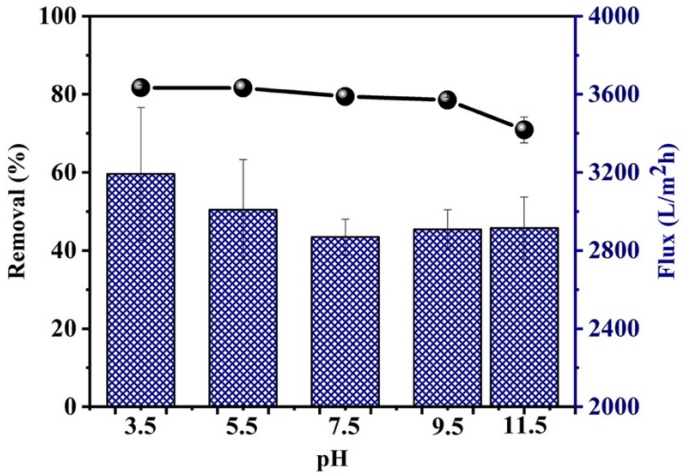


Figure 8-8 Removal efficiency and permeation flux of 10 ml, 50 ppm MO with different pH conditioned WGP-111.5-EM45

8.5.7 Gravity filtration of MO with different layers of membrane

The operation of the membrane system, including fouling removal and membrane replacement contributed to the high operational and capital costs. Therefore, the investigation of filtration efficiency of MO using multi-layer membranes assembled in series will be important. Various layers (1, 3, 5, 10) of WGP-111-EM45 membranes (d = 7/8 inches) were used to examine the removal efficiency of 30 ml, 100 ppm MO and the results are summarized in **Figure 8-9**. Single layer of membrane removed 31 % MO, an additional 52 % were removed using two membranes. Assembled gravity filtration with 6 membranes achieved almost 100 % removal efficiency. A reduction trend of the permeation flux was obtained, where a 78.7 % reduction was observed when the membrane layer was increased from 1 to 2. This explained that the permeation flux is closely related to the bed height (one membrane thickness = 5.45 $\pm$ 0.21 mm) of the filtration membrane when gravity is the only driving force in the filtration process.

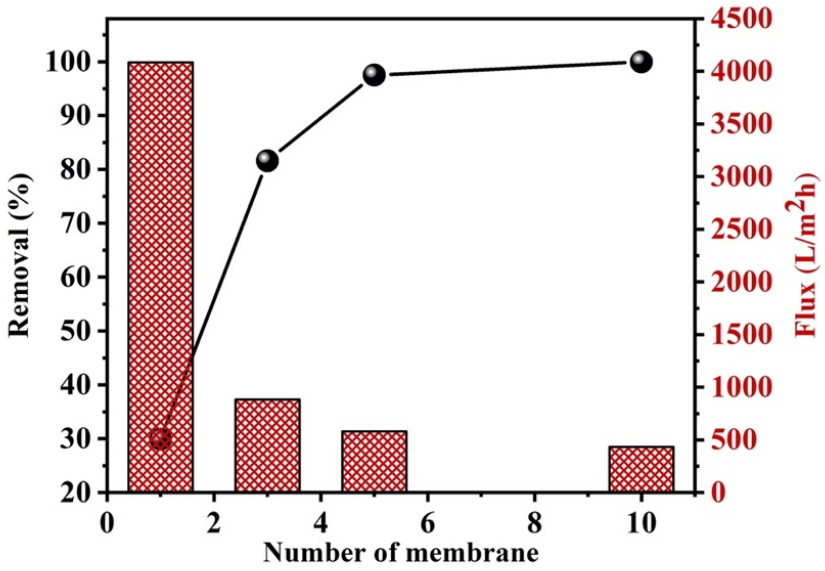


Figure 8-9 Removal efficiency (%) and permeation flux of WGP-111-EM45 when used for gravity filtration of 30 ml, 100 ppm MO by using1, 3, 5 and 10 membranes

8.5.8 Mechanical Strength (Tensile Index)

The mechanical strength of WGP membranes with various mass ratios of PEI and the 45 ml emulsion (WGP-11(0.2/0.5/1.0/1.5) were investigated. **Figure 8-10** shows both the dry (red point) and wet (black point) tensile index of these WGP membranes, where the dry tensile index increased from 2965 ± 198 Nm/g to 5002 ± 102 Nm/g at 1.5 (mass ratio) of PEI involved in the membrane system, which is a 68.7 % increase. This value is three orders of magnitude higher than the hard wood pulp membrane consisting of melamine formaldehyde modified CNC (MF-CNC) as the additive with a tensile index of 12.2 Nm/g when 14 wt% of MF-CNC was added [451]. The influence of branched PEI crosslinking degree on the tensile strength of the PVA/BPEI membrane increased from 13.2 to 42.5 MPa when the PEI content was increased from 3% to 18%. However, the elongation was reduced from 87.1 % to 18.2 % due to the prevention of the hydrogen bond formation [466]. The tensile index is related to the fiber strength and fiber length, and softwood pulp is longer (3 to 7 mm) compared to hard wood fiber (1 to 2 mm) resulting in a higher tensile index [75]. The mild beating process was also applied in our experiment, which straightened the curled fibers [467], and this contributed to the high tensile index of the membrane prepared from soft wood pulp. PEI worked as a dual functional additive that could both enhance the mechanical strength of the membrane by improving the crosslinking degree of neighboring fibers and also provided electrostatic adsorption sites for negatively charged pollutants. From the SEM images shown in **Figure 8-11** (**A**), more connecting junctions between fibers was observed as more PEI was added to the membrane. The network facilitated the transfer of forces among fibers, which enhanced the mechanical property of the membrane network. The mechanism of the enhanced mechanical property was well documented in a percolation model, where the stress transfer could be achieved when the concentration of the filler exceeded the percolation threshold [468]. Herein, PEI also acted as a bridging filler, and the significant improvement of tensile index for a mass ratio

of 1.5 indicated that the PEI content had reached the percolation threshold. However, the wet mechanical strength was only enhanced to a limited degree, and the tensile index was improved from 1387 ± 80 Nm/g to 1414 ± 125 Nm/g when the PEI content was increased from 0.2 to 1.5. After wetted with water, the tensile index decreased approximately 80 % when 1.5 times of PEI was added to the membrane. In the dry status, wood fibers were entangled, which enhanced the mechanical strength, while the wood fibers swelled after wetting with water molecules filled the voids in the membrane networks that reduced the physical frictions among between the fibers. Cellulose fibers have high affinity to water molecules due to the abundant hydroxyl groups, and the water filled in the network expanded the network due to the surface tension, and both these factors destroyed the inter-fiber interactions and reduced the tensile index. Compared with the membrane prepared with the emulsion, the tensile index of the membrane decreased by 11.4 % (1.5 PEI, dry status) when no emulsion was added to the system. This explained that the evaporated TF-CNC hexane emulsion acted as an adhesive within the membrane, and TF coated CNC also acted as a nano filler that enhanced the mechanical strength. Since CNC is a common material used as a reinforcing additive to improve the mechanical properties, which was closely related to the dispersity of the CNC in the hybrid system [469]. The addition of emulsion enhanced the porosity of the system, which improved the dispersion of the additives (PEI or TF-CNC) in the membrane. Therefore, the tensile index was enhanced with membrane prepared with emulsion compared to those prepared without emulsion.

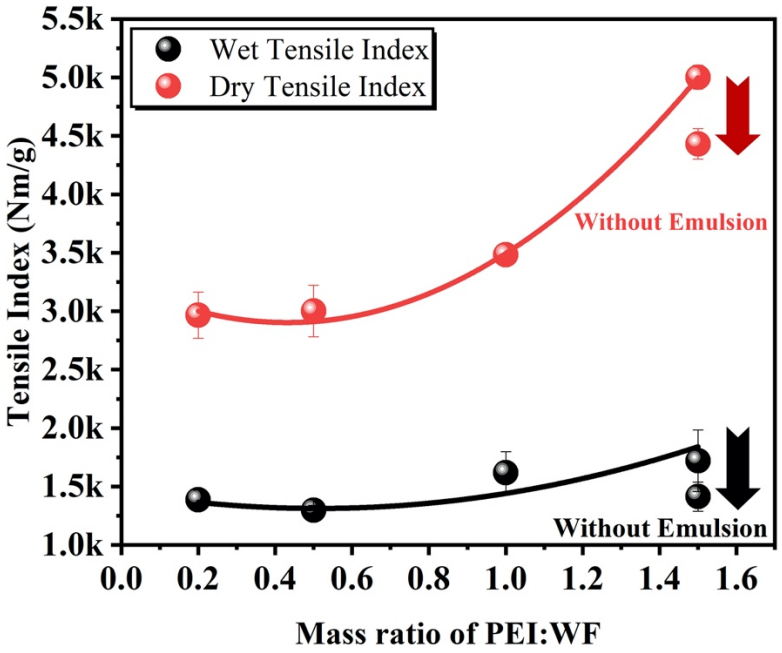


Figure 8-10 Wet and Dry tensile index of membranes with various mass ratios of PEI to WF, from 0.2 to 1.5

8.5.9 Morphology and macrostructure (SEM)

The wood fiber membranes fabricated with a fix mass ratio of wood fiber : GPTMS (1:1) together with 45ml EM were further crosslinked with a corresponding mass ratio as 0, 0.2, 0.5, 1.0 and 1.5 PEI. The effect of various amounts of the crosslinking agent (PEI) on the macrostructure of the prepared membrane was examined using the SEM. As shown in **Figure 8-11** (**A**), WGP-110-EM45 membrane displayed a smooth surface aligned along the direction of the cellulose fiber. The small amounts of the adhesive attached to the fiber surface was due to the reaction with GPTMS, and the fractures were due to the bleached chemi-thermomechanical processing during the pulp production, and also the fiber refining process with the fiber beater. The addition of PEI to the membrane system produced crosslinks between the cellulose fibers, resulting in a larger fiber width and adhesive networks. More PEI incorporated membrane possessed a denser structure (**Appendix 8-4**), which contributed to the reduced porosity at 1.5 PEI mass ratio (**Figure 8-4**, (**B**)).

However, the WGP-111-EM45 (PEI→EM) prepared by loading the EM after the PEI crosslinking process exhibited a smoother fiber surface compared to WGP-111-EM45. The results indicated that the addition of emulsion before the crosslinking reaction reduced the porosity of the final membrane. The influence of various amounts of emulsion added to the WGP-111-EM membranes were also compared in the SEM images (**Figure 8-11**, (**B**)). Fibers in WGP-111-EM0 possessed randomly orientated fibers with a relatively smooth surface. With the increase of the volume of the emulsion in the membrane system, a more compact network was observed. WGP-111-EM85 and WGP-111-EM120 displayed a dense and compact crosslinking network compared with other membranes (EM< 85ml), and the cellulose fibers were oriented in a parallel direction with fewer voids. The result is consistent with the reduction in the porosity from the increased in the volume of emulsion (>45ml) added. This arrangement of the crosslinked macro-fibers explained the increasing tensile strength when the emulsion was added to the system. The forces were well distributed among the oriented fibers that increased the forces necessary to fracture the fiber bundles. However, when the mechanical tests were performed on the membrane without emulsion, the forces were not transferred to the neighboring fibers as the emulsion as not present to form a connection. Instead, forces were applied to individual fibers, resulting in a low mechanical strength. Additionally, the SEM images provided a detailed analysis of the macrostructure of softwood cellulose fibers, where most of the fibers possessed a hollow rectangular prism-like structure with obvious edges. Surprisingly, the well-structured spherical pits (**Appendix 8-5**) were evident in the thin wall of most fibers, while the pits were commonly observed after deformation under uniaxial extension [470]. In conclusion, both PEI and emulsion enhanced the strength of the membrane via

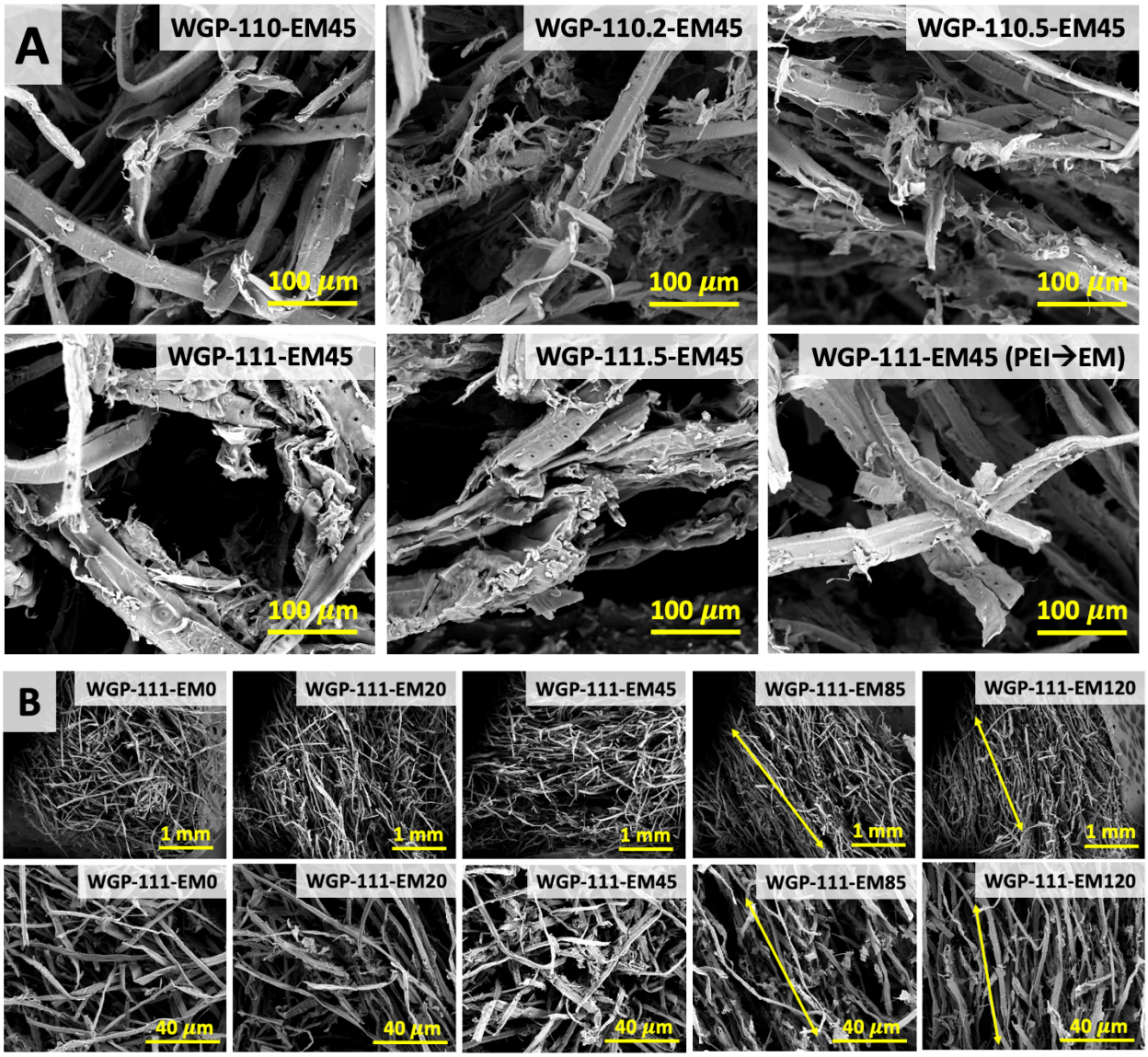


Figure 8-11 Cross-sectional SEM images of WGP-11 (0/0.2/0.5/1.0/1.5) -EM45 and WGP-111-EM45 (PEI→EM) (A); Cross-sectional SEM images of WGP-111-EM(0/20/45/85/120) (B)

bridging of the fiber networks, and our mild mechanical process and crosslinking reaction guaranteed the structural integrity of the fibers, which enhanced the mechanical property.

8.5.10 Dynamic filtration (Concentration effect)

Membrane replacement due to the fouling issue and operational cost is the major concern when a new membrane system was translated from lab to industry. Therefore, the performance of a dynamic filtration system that can accommodate multiple membranes are of great importance.

The influence of several factors, such as initial concentration of the pollutants, pressure drop of the system, inlet flow rate effect and the number of membranes loaded to the system on the filtration performance of MO were investigated using the WGP-111-EM45 membrane. **Figure 8-12** shows the effect of MO initial concentrations (2, 5, 15, 30, 50 ppm) on the breakthrough curve with one membrane assembled in the dynamic filtration system (0.075 MPa, 275-300 ml of MO solution). The filtrate was continuously sampled every 1 minute until a constant concentration was obtained. A 50 ppm initial concentration led to a rapid 50 % breakthrough in 2 mins, while a 30 ppm MO solution took 12 mins to achieve a 50 % breakthrough for one membrane. Surprisingly, the saturation of the membrane did not increase with increasing amounts of the treated solution, and only when the critical value of breakthrough of the membrane was observed, the outlet concentration was kept constant for a short time period. The breakthrough level was elevated when the initial concentration was increased, while a slow saturation behavior was observed for the 2 ppm MO solution. A high adsorption capacity was achieved when the same volume of higher initial MO concentration was used, since more MO was removed before the saturation stage. Also, the fluctuation of the outlet concentration in the 'plateau' period could be attributed to the accumulation effect of the MO on the wall of the pores in the membrane. When the amount of MO that could be bound to the membrane was exceeded, the outlet concentration would increase. At this point, the inlet flow may flush out the MO adsorbed on the surface, allowing extra adsorption sites to become available. This results in an increased outlet MO concentration, which causes the whole cycle to repeat. This can possibly explained the fluctuation in the data in the plateau region [471]. This explained the fluctuation behavior in the 'plateau' region during the dynamic filtration. The quantity of adsorbed MO before and after normalizing against the mass (g) of dry membrane was used to calculate the removal efficiency, which is summarized in **Table 8-3**. The amounts of

MO removed by one WGP-111-EM45 membrane increased from 0.279 mg to 4.876 mg when the MO inlet concentration was increased from 2 to 50 ppm. This was due to the increased driving force of the diffusion (concentration difference between the bulk solution and the membrane), and the dynamic filtration promoted the diffusion leading to the better adsorption-filtration efficiency, since more MO was adsorbed to the inner structure of the membrane. The highest capacity achieved was 22679.1 mg/g at 50 ppm MO inlet concentration of 15 ppm solution (275 ml), indicated its potential for large scale MO purification. The removal efficiency increased from 25.8 % to 64.2 % , that decreased to 39.6 % when the MO initial concentration was further increased. This was due to the increased flow rate (under the same pressure drop, 0.075 MPa) leading to a reduction in the contact time between MO molecules and adsorption sites on the membrane. The integration curve based on Eq (8.6) to obtain the value of the membrane sorption capacity (q_c) is shown in **Appendix 8-6**.

Table 8-3 Parameters of the dynamic filtration test with various initial concentrations of MO

Concentration (ppm)	Flowrate (ml/min)	Pressure Drop (MPa)	Volume (ml)	q_c (mg)	q (mg/g)	R %
2	5.00	0.075	300	0.279	1.29	46.50
5	6.88	0.075	275	0.883	4.07	64.17
15	8.09	0.075	275	1.733	7.99	42.00
30	7.43	0.075	275	4.049	18.66	49.10
50	11.22	0.075	275	4.876	22.47	35.49

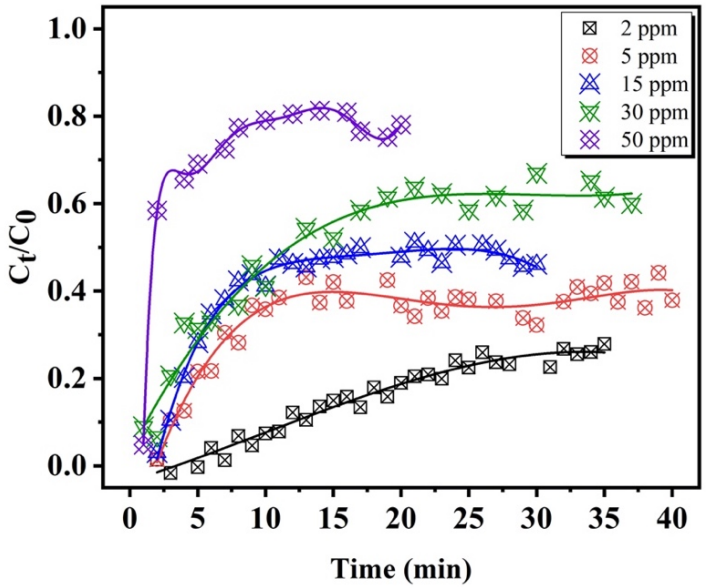


Figure 8-12 Dynamic filtration of various concentrations of MO solution with one layer of WGP-111-EM45 membrane (d = 23.9 mm), under 0.075 MPa

8.5.11 Dynamic filtration (Effect of flow rate)

The inlet flow rate and pressure applied to the dynamic filtration system is closely related to the operational cost. The effect of flow rates on the breakthrough curve was investigated at three pressure drops (0.050, 0.075 and 0.100 MPa) or 8.33, 45 or 100 ml/min, the bed height was equaled to one membrane height (6.15 mm) and the initial concentration was kept at 15 ppm. The breakthrough curve is shown in **Figure 8-13** with the parameters summarized in **Table 8-4**. A higher level of breakthrough could be achieved with an increased inlet flow rate (pressure drop), where a pressure drop of 0.1 MPa might drive the system to achieve an approximately 80 % breakthrough, while only 50% could be reached with 0.05 MPa. The increase in the inlet flow rate of MO led to a reduction in the process volume of the solution and time required to reach the breakthrough stage. This is displayed as the critical point as shown in **Figure 8-13**, and Qc, q and R % are summarized in **Table 8-4**. The removal efficiency of one membrane decreased from 56.9 to 24.4 % with increasing flowrates, since the lower flowrate resulted in a higher residence time

for the MO molecule transport through the porous membrane with accessible more adsorption sites for binding. Higher flowrate resulted in a sharper breakthrough curve, and a faster breakthrough point [454]. Elevated flowrate could partially overcome the resistance of the external film diffusion resulting in a faster saturation of the membrane. However, a lower inlet flowrate increased the interaction between the membrane and MO molecules resulting in a higher removal efficiency. This phenomenon has been well documented, where the removal efficiency of a fix bed column decreases with increasing flowrates and a reduced mass transfer zone [472]. Also, the shape of the breakthrough curve could be affected by various factors, such as the equilibrium isotherm, film diffusion, interparticle mass transfer and any other mass transfer processes [452]. The balance between the process time and removal efficiency should be considered in a real industrial application. The integration curve based on Eq (8.6) to obtain the value of the membrane sorption capacity (q_c) is shown in **Appendix 8-7**.

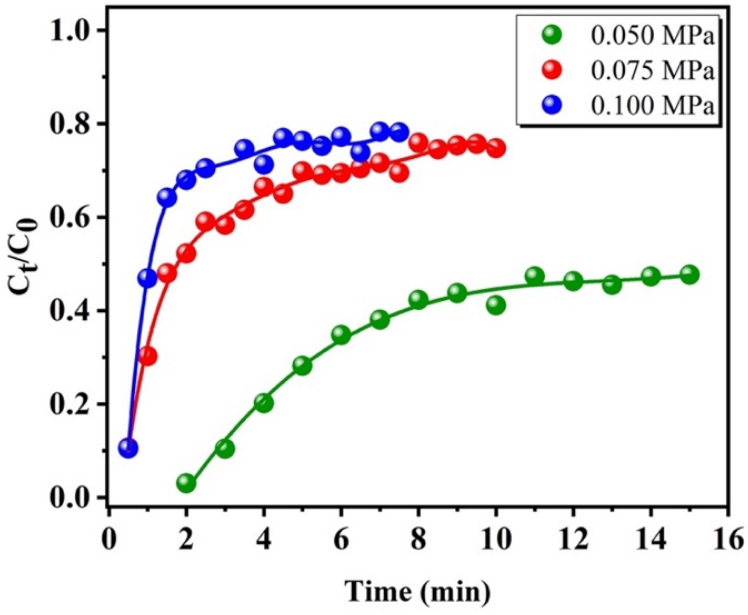


Figure 8-13 Dynamic filtration of 15 ppm MO solution with one layer of WGP-111-EM45 membrane (d = 23.9 mm), under various pressures (0.050, 0.075 and 0.100 MPa)

Table 8-4 Parameters of the dynamic filtration test with various inlet flow rates of MO solution

Concentration (ppm)	Flowrate (ml/min)	Pressure Drop (MPa)	Volume (ml)	q_e (mg)	q (mg/g)	R %
15	8.33	0.050	250	2.10	9.68	56.0
15	45	0.075	450	2.36	10.89	35.0
15	100	0.100	700	3.29	15.15	31.30

8.5.12 Dynamic filtration (Effect of number of membranes)

Figure 8-14 shows the breakthrough curve of 15 ppm MO filtrated for 1 to 10 layers of WGP-111-EM45 membranes, where the bed height was varied from 6.15 mm to 61.5 mm, corresponding $2.15x10^{-4}$ g to $2.15x10^{-3}$ g. All the dynamic filtration parameters are summarized in **Table 8-5**. As shown in **Figure 8-14**, the time prior to reaching the breakthrough point increased significantly with more membranes stacked inside the column. The breakthrough point appeared at 7, 12, 15 and 20 mins for 1, 3, 6 and 10 membranes respectively. This is due to more adsorption sites present when more membranes were loaded to the filtration system. Furthermore, more membrane loaded led to a lower slope in the breakthrough curve caused by a larger mass transfer zone [473]. The results of the lower slope in the breakthrough curve could be attributed to the competition between the axial dispersion and the diffusion mass transfer, where the later was the major mechanism with a larger bed height inside the column. Moreover, the removal efficiency increased from 38.1 % to 64.6 % when the bed height was increased from 6.15 to 61.5 mm. Thus, more membranes loaded to filtration system would be more desirable for real applications, while a balance between the energy consumption to overcome the higher pressure drop for the multiple membrane system and the elevated filtration efficiency should be considered. The integration curve based on Eq (8.6) to obtain the value of the membrane sorption capacity (q_c) is shown in **Appendix 8-8**.

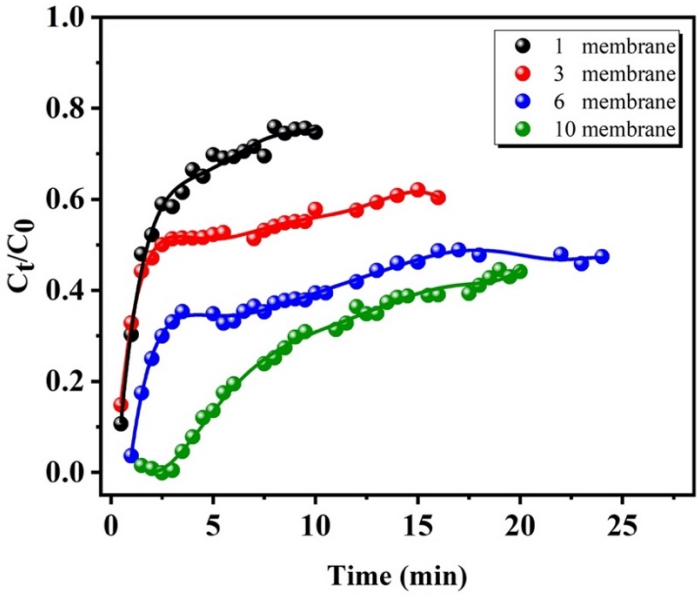


Figure 8-14 Dynamic filtration of 15 ppm MO solution with 1, 3, 6, 10 layers of WGP-111-EM45 membrane (d = 23.9 mm), under 0.075 MPa

Table 8-5 Parameters of the dynamic filtration test with various bed heights

Number of membrane	Concentration (ppm)	Flowrate (ml/min)	Pressure Drop (MPa)	Volume (ml)	q_c (mg)	q (mg/g)	R %
1	15	45.00	0.075	450	2.36	10.89	35.0
3	15	61.29	0.075	950	0.70	3.23	4.91
6	15	44.68	0.075	1050	1.80	8.15	11.4
10	15	71.62	0.075	1325	1.58	7.29	7.97

8.5.13 Gravity filtration of PFOA and PFOS

The gravity filtration results of WGP-111-EM45 for the removal 10 ml of 0.5 and 1ppm PFOA and PFOS is shown in **Figure 8-15**. A 99.4 % and 99.2 % removal efficiency were obtained by passing 10 ml of 500 µg/L and 1000 µg/L PFOA through the WGP-111-EM45 membrane (gravity filtration), where the concentration was reduced to 2.19 µg/L and 7.82 µg/L, respectively. Surprisingly, 10 ml of 0.5 ppm and 1 ppm of PFOS were completely removed and no residue PFOS were detected by LC-MS instrument. The results indicated that the membrane could effectively remove low concentration of PFOA and PFOS via a simple gravity filtration due to the electrostatic interactions. The removal efficiency of PFOA decreased with increasing initial concentration of

PFAS due to the reduction of accessible adsorption sites. The concentration of PFOA used in this test was much higher than the environmental relevant concentration of PFAS, thus an enhanced removal efficiency with lower initial PFAS concentration could be expected. Gravity filtration was more effective for PFOS compared to PFOA since the K_{ow} of PFOS (6.3) is higher than the K_{ow} of PFOA (5.3) [450]. This high porosity sustainable membrane showed promising potential in removing extremely low concentration PFAS that can be used as an alternative to other expansive strategies (AIX or RO) for PFAS removal.

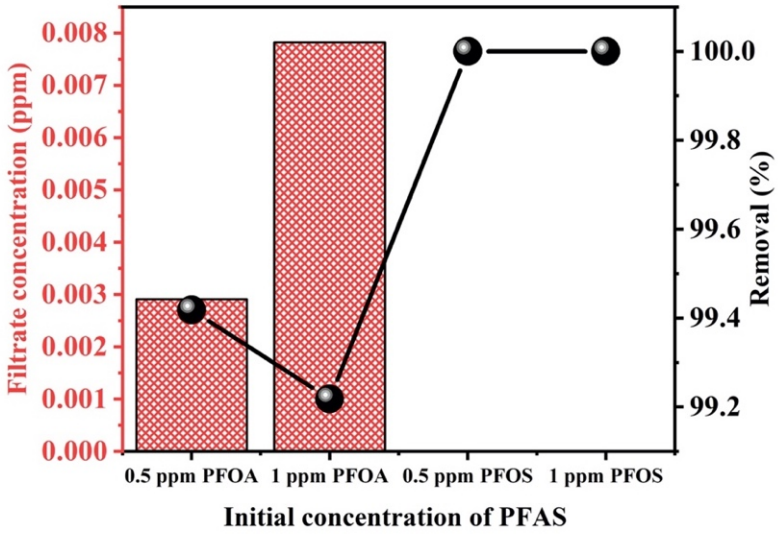


Figure 8-15 Filtrate concentration and removal efficiency of WGP-111-EM45 by removing 10 ml of 0.5 and 1 ppm PFOA and PFOS

Conclusions

Various pollutants with very distinctive physicochemical properties pose major difficulties in removing these multi-pollutants using a single material. This study successfully developed a sustainable membrane with enhanced porosity from wood fiber using a Pickering emulsion templating strategy. A 75 % increase in the porosity was observed for membrane prepared with 45 ml emulsion (WGP-111-EM45). This membrane possessed superior filtration efficiency towards

various pollutants, including cationic dye (MB)/anionic dye (MO) and heavy metal ions (Cu^{2+}) via gravity filtration. Increasing the emulsion volume led to an increase in the porosity up to 41.60 ml, and further increase the emulsion volume to 120 ml caused a reduction in the membrane porosity to 13.61 due to the Oswald opening of the emulsion droplets. With more crosslinking agent added to the membrane formulation, both the dry and wet tensile index were enhanced as the applied forces were transferred to the neighboring fibers. A dynamic filtration system was used for the continuous removal of MO, and the breakthrough curves were examined for various process factors, such as initial concentration, inlet flow rate, and membrane numbers (bed height). Increasing the initial MO concentration and bed height would enhance the removal efficiency of the dynamic filtration, while the increased flowrate led to a reduction in the filtration efficiency. The highest capacity of the membrane was achieved with a WGP-111-EM45 (d = 23.9 mm, h = 6.15 mm and $2.15x10^{-4}$ g), achieving a 22679.1 mg/g with MO when the inlet concentration of 50 ppm and inlet flowrate of 11.22 ml/min. The filtration performance of membrane WGP-111-EM45 on PFOA and PFOS was also evaluated via gravity filtration, over 99% of removal efficiency was achieved for PFOA (10 ml of 0.5 and 1 ppm) and there was no residue PFOS (10 ml of 0.5 and 1 ppm) detected after filtration. This sustainable membrane displayed promising potential for wastewater filtration, and further experiments should be conducted to evaluate the removal efficiency of the multi-pollutant system.

Chapter 9: Original Contributions and Recommendations

9.1 Original Contribution to Research

Water treatment strategies are enhanced by nanotechnology, and increasing attention has focused on nature materials with low carbon footprint due to their biodegradable characteristics. Cellulose based material, such as CNC, β-CD and wood fibers (WF) have been widely used to address environmental issues, while their small size presented a separation challenge when used in aqueous system. Various research activities have focused on integrating cellulose nanomaterials into a different configuration, such as hydrogel beads, aerogel and membrane that may lead to the sacrifice of high surface area of the cellulose nanomaterial. Therefore, the concept of magnetic separation is being considered as a good alternative, where the absorbents could be readily separated and recovered while preserving the high surface area. On the other hand, nanogel templating strategy was also employed throughout this doctoral research, since it could serve as a scaffold for the nucleating and forming metallic nanoparticles to achieve the desired size and shape control and minimized aggregation. This thesis focuses on the development of novel material using nanogel and CNC as templating strategies to address environmental related issues like wastewater treatment and antimicrobial applications. The main objectives of this thesis are:

1) development of a pH-responsive nanogel fabricated by crosslinking MAA and EA with DAP via semi-continuous emulsion polymerization,
2) development of β-CD functionalized magnetic nanoparticles (FMNPs) applied for PrHy removal from drinking water,
3) investigation the effect of β-CD loading and pH effect on the adsorption mechanism between PrHy and FMNPs,

4) development of fluorescence AgNCs by photo-induced colloidal scaffold method applied for antimicrobial and biolabeling applications,
5) development of magnetic cluster modified MF-CNC and PDA-CNC applied to the catalytic reduction of 4-nitrohenol (4-NP) to 4-aminophenol (4-AP),
6) development of sustainable membranes consisting of softwood fiber, GPTMS and PEI with enhanced porosity via Pickering emulsion templating strategy. Evaluation of removal efficiency of the membrane for MO, MB and Cu^{2+} via a simple gravity driven filtration process. Additionally, a column based dynamic filtration was applied for the removal of MO and the investigation of inlet flowrate, initial concentration, pressure drop, number of membrane (bed height) on filtration efficiency.

My research explores both the synthesis of advanced materials using the templating strategy, and also exploring their application in addressing environmental challenges. The major findings are summarized below.

9.1.1 Facile synthesis and characterization of pH-responsive methacrylic acid/ethyl acrylate crosslinked nanogel by semi-continuous emulsion polymerization

In this study, the pH-responsive nanogel was synthesized by crosslinking MAA and EA with DAP via the semi-continuous emulsion polymerization process. The effect of various MAA, EA monomer ratios and DAP percentage on the physicochemical properties of the nanogel was explored. pH-responsive property of the nanogel displayed a 'S' shape trend in the particle size from pH 3 to 11, where the particle size increased from pH 3 to 7 and decreased from 7 to 11. The zeta potential displayed a 'U' shape characteristic, which was due to the protonation of the carboxylic acids when the pH was increased from 3 to 7 and shielding effect caused by the excess NaOH at high pH condition. Well-defined monodispersed spherical nanogel was observed from the TEM images of stained nanogel (various compositions). Also, the pKa values of 50:50 MAA-

EA nanogels were between 6.13 to 6.54, and the quantity of carboxyl groups present in the nanogel was calculated from the titration measurements. At least 2 wt% of DAP was required to fabricated robust and stable spherical MAA-EA nanogel, while insufficient DAP led to a formation of a loosely crosslinked polymer network. All the characterization results provided a clear description of the MAA-EA nanogel, which could be easily reproduced. This robust pH-responsive nanogel provided a promising nano-reactor to fabricate other metallic nanoclusters.

9.1.2 β-cyclodextrin functionalized magnetic nanoparticles for the removal of pharmaceutical residues in drinking water

MAA)-EA colloidal scaffolds were prepared and was used as templates for the in-situ co-precipitation of Fe^{2+} to produce stable functional magnetic nanoparticles (MNPs) decorated with β-CD (FMNP < 500 nm). Emulsion polymerization with the controlled addition of monomer mixtures during the seed formation stage allowed for good size control, and silica coating was introduced to prevent the oxidation of FMNP. The superparamagnetic FMNP with high saturation magnetization (33 emu/g) could be readily separated from water using a high gradient magnetic separator (HGMS). Procaine hydrochloride (PrHy) was used as a model pharmaceutical residue to evaluate the performance of the FMNP, and 53.65 mg PrHy/g FMNP was adsorbed using 600 ppm FMNP. A fast (30 min) adsorption kinetic followed the pseudo-first-order kinetic model that described the physical adsorption through a 1 to 1 host–guest inclusion mechanism. The adsorption behavior obeyed the Freundlich isotherm with a linear adsorption performance. The proposed system was scalable and adaptable to existing water treatment processes, and it could be used to concentrate and detect low concentration pharmaceuticals via a pre-concentration strategy.

9.1.3 Adsorption mechanism of β-cyclodextrin functionalized magnetic nanoparticles for the removal of procaine hydrochloride

FMNPs functionalized with low, moderate and high amounts of β-CD (designated as FMNP-L, FMNP-M and FMNP-H respectively) were prepared and evaluated for the removal of 5 to 100 ppm PrHy. The adsorption performance depended on the alignment of CD cavities on the surface of FMNPs, where the amounts of accessible CD cavities available for binding, and pH were examined in detail. The adsorption isotherm of FMNPs was fitted to the Langmuir and Freundlich models, where the Langmuir model fitting was observed for PrHy below 30 ppm confirming a monolayer surface adsorption. However, the adsorption isotherm fitted the Freundlich model for PrHy between 5 to 100 ppm suggesting the occurrence of multiple-stage adsorption process for CD cavities with different accessibility caused by overlapping or steric hindrance of CM-β-CD. The correlation of CD alignment and adsorption behavior with the β-CD based adsorbent was demonstrated in this study. The adsorption capacity of the FMNP depended on to the amounts of β-CD on the adsorbents, and the steric hindrance of the CD cavities. This study provides a new perspective on the mechanism and the adsorption behavior of β-CD grafted nanomaterial.

9.1.4 Synthesis of silver nanoclusters in colloidal scaffold for biolabeling and antimicrobial applications

A robust method to prepare silver nanoclusters (AgNCs) inside a methacrylic acid-ethyl acrylate (MAA-EA) nanogel is proposed, where AgNCs were produced inside the nanogel scaffold via UV-photoreduction. The impact of UV irradiation time on the formation of AgNCs and their application in biolabeling and antimicrobial properties were examined. The AgNCs formation is described by two stages; (1) Ag_n (n=2-8) nanoclusters formation between 0-25 min, and (2) larger silver nanoparticles (AgNPs) formed via aggregation inside the nanogel. The antimicrobial

performance depended on the size and concentration of silver ions (Ag^{+}). A low maximum inhibitory concentration (MIC) of 1.1 ppm was observed for antimicrobial test with yeast, and a MIC of 11 and 22 ppm was recorded for *Escherichia. coli* and *Staphylococcus aureus* respectively. Combined with the green illumination property of AgNCs (emitted at 525 nm) with dead yeast, it could be used for biolabeling. By tuning the size through photoirradiation, the nanogel templated AgNCs is a promising candidate for antimicrobial and biolabeling applications.

9.1.5 A novel magnetic cluster modified palladium-cellulose nanocrystal hybrids as recyclable catalyst for 4-nitrophenol reduction

The development of noble metal catalysts with high catalytic performance and low metal loading has attracted increasing interest from the research communities. However, the separation of the spent nanoscale catalyst from the applied system is challenging, most of the recovery platform, such as resin or membrane system led to a sacrifice of high surface area as well as catalytic efficiency. Two series of recyclable catalysts were synthesized by loading palladium (Pd) particles onto melamine formaldehyde (MF) modified cellulose nanocrystals (CNC) and dopamine (DA) coated CNC. *In situ* co-precipitation of magnetic nanoparticle (MNP) clusters were used to impart magnetic characteristic to the catalysts. This magnetic cluster successfully achieved high magnetization without aggregation issue. The amount of palladium precursor added to the catalytic systems was optimized, where 10-Pd-PDC yielded 10.83 ± 2.43 nm discrete Pd loaded hybrids. The catalytic performance of the catalysts was assessed by the reduction of 4-nitrophenol (4-NP) in the presence of sodium borohydrides ($NaBH_4$). The 4-NP reduction mechanisms were analyzed using the Langmuir-Hinshelwood model and the apparent rate constant k (s^{-1}), turnover frequency (TOF, h^{-1}) and activity factors ($s^{-1}g^{-1}$) were determined to be 2.142×10^{-3}, 305.82 and 535.5 using MNP2-Pd-MC respectively. An induction time was observed for MNP-4 or 5-Pd-PDC, where was attributed to the diffusion of the reagents across the thick PDA and MNP layer. The separation

efficiency of the magnetic catalysts was evaluated by monitoring the absorbance at 400 nm as a function of separation time, and the MNP2-Pd-MC could be recycled 7 times without severe loss in activity. Pd-MF-CNC displayed excellent catalytic performance for the reduction of 4-NP, while Pd-PDA-CNC possessed a lower catalytic reactivity due to the inferior catalytic surface area. The developed templated MNP could be extended to other systems allowing for the recycling and reuse of the catalysts or adsorbents.

9.1.6 Sustainable high porosity adsorptive membrane applied for cationic/anionic dye, heavy metal and PFAS removal

Persistence contaminants, such as perfluoroalkyl and polyfluoroalkyl substance (PFAS) are widely founded in water systems threatening the health of human beings due to the negative impact of PFAS on the reproductive system. Also, heavy metal and organic dyes still contributed to a significant composition of the wastewater caused by agriculture and industrial activities. A sustainable membrane produced from soft wood fiber (WF) crosslinked with (3-glycidyloxypropyl)trimethoxy silane (GPTMS) and poly(ethyleneimine) (PEI). Tanfloc (TF) (a natural tannin based commercial flocculant) was used to coat CNC to prepare Pickering emulsion with hexane. When added to the membrane formulation, the porosity of the membrane WGP-111-EM45 increased to 41.60 % from the membrane without emulsion (23.65 %). Gravity filtration with methyl orange (MO) was used to evaluate the performance of the membrane with various amounts of PEI and emulsion loading. WGP-111-EM45 was selected and further studied in the dynamic filtration system. A simple pressure controlled dynamic filtration system was designed and inlet flowrate, inlet concentration and number of membranes loaded to the filtration system were evaluated. The highest filtration capacity was obtained as 22679.1 mg/g with MO, inlet concentration of 50 ppm and inlet flowrate was 11.22 ml/min. Increased membrane number (bed height) led to an increase in the removal efficiency with a lower slope in the breakthrough curve

due to the enhanced diffusion mass transfer. Furthermore, the membrane filtration efficiency of the membrane towards copper ions (Cu^{2+}) and methylene blue (MB) was also evaluated by gravity filtration and a 98% removal efficiency of 10 ml 1000 ppm Cu^{2+} was achieved with WGP-111-EM45 and an 89 % removal efficiency was achieved for 10 ml, 20 ppm MB. This sustainable porous membrane provided adsorption sites towards cationic/anionic dye and heavy metal ions based on various mechanisms, such as ion exchange, electrostatic interactions, chelation and π-π interactions. This membrane displayed promising potential to remove pollutants via both gravity filtration and pressure driven dynamic filtration. The filtration performance of membrane WGP-111-EM45 on PFOA and PFOS was also evaluated via gravity filtration, over 99% of removal efficiency was achieved for PFOA (10 ml of 0.5 and 1 ppm) and there was no residue PFOS (10 ml of 0.5 and 1 ppm) detected after filtration. This sustainable membrane displayed promising potential for wastewater filtration, and further experiments should be conducted to evaluate the removal efficiency of the multi-pollutant system.

9.2 Recommendations for Future Studies

Recommendations for the future study are proposed by considering the scope of the research in this thesis research, and the additional studies that can be conducted to address wastewater treatment or other new applications. In Chapter 3, a robust pH-responsive nanogel was developed and various characterization were conducted in the investigation of the physicochemical properties. The next step should focus on the emulsion polymerization mechanistic study during the synthesis. Together with the mechanistic study, a more universal polymerization recipe and experimental condition can be deduced and contributed to addressing the reproducibility issue for most nanogel preparation technique.

In Chapter 4 and 5, a β-CD functionalized magnetic nanoparticle (FMNP) was developed and applied for the PrHy removal. Further study related to the effect of various β-CD loaded FMNPs and pH and CD cavity alignment on the PrHy removal efficiency was explored. In the next step, fluorescence probe and molecular simulation can be performed to investigate the alignment of the CD cavities on the FMNP. A continuous magnetic assisted water purification system with the HGMS can be designed and enrichment of low concentration pollutants like PFAS can be performed.

In Chapter 6, silver nanoclusters synthesized within nanogel scaffold by photo-reduction was applied for antimicrobial and bio-labelling application. The reduction mechanism of the AgNCs with/without UV irradiation was investigated. The next step can extend the fundamental characterization of the AgNCs within the nanogel, such as the effect of AgNC size on the interaction between the nanogel scaffold and AgNCs. High resolution TEM can be used to monitor the growth of the AgNCs at different UV irradiation times.

In Chapter 7, magnetic nanoparticles assisted Pd-MF-CNC and Pd-PDA-CNC was developed and applied for 4-NP reduction. The quantity of Pd loaded to the system was optimized and the 2MNP-Pd-MC can be reused for seven times without severe loss of catalytic efficiency. Further study can be extended to the investigation of the mechanisms of induction time by monitoring the oxygen level in the system during the catalytic test.

In Chapter 8, wood fiber crosslinked membrane was developed and used to removal anionic dye (MO), cationic dye (MB), heavy metal (Cu^{2+}) and PFAS. Both gravity filtration and column based dynamic filtration was applied for the MO filtration, and various factors were investigated. Further study can be extended to investigate the dynamic filtration efficiency of PFAS in both

individual waste stream and simulated surface water that contains other contaminants like natural organic matters (NOM).

In summary, this thesis employed the templating strategy of nanomaterial, including cellulose based material and polymeric nanogel to address various environmental issues. Various water treatment processes enhanced by nanomaterials were conducted for the removal of pharmaceutical residues, organic dyes (MO, MB), heavy metals (Cu^{2+}) and emerging contaminants (PFAS). MAA-EA nanogel was first developed and studied exhaustively. Various metallic nanoclusters were further synthesized in the nanogel, where MNP were used to impart magnetic property to the attached material and AgNCs were used as antimicrobial and biolabeling agent. Finally, a sustainable membrane was developed, and the porosity was reinforced by a Pickering emulsion templating strategy. All the material and processes developed in this this dissertation, successfully addressed environmental issue from different perspectives.

References

[1] H. J. Kim, K. Zhang, L. Moore, and D. Ho, "Diamond nanogel-embedded contact lenses mediate lysozyme-dependent therapeutic release," *ACS Nano*, vol. 8, no. 3, pp. 2998–3005, 2014.

[2] D. Keskin *et al.*, "Highly Efficient Antimicrobial and Antifouling Surface Coatings with Triclosan-Loaded Nanogels," *ACS Appl. Mater. Interfaces*, vol. 12, no. 52, pp. 57721–57731, 2020.

[3] Y. Zhang *et al.*, "Amphiphilic Thiol Polymer Nanogel Removes Environmentally Relevant Mercury Species from Both Produced Water and Hydrocarbons," *Environ. Sci. Technol.*, vol. 55, no. 2, pp. 1231–1241, 2021.

[4] A. V. Kabanov and S. V. Vinogradov, "Nanogels as pharmaceutical carriers: Finite networks of infinite capabilities," *Angew. Chemie - Int. Ed.*, vol. 48, no. 30, pp. 5418–5429, 2009.

[5] I. Neamtu, A. G. Rusu, A. Diaconu, L. E. Nita, and A. P. Chiriac, "Basic concepts and recent advances in nanogels as carriers for medical applications," *Drug Deliv.*, vol. 24, no. 1, pp. 539–557, 2017.

[6] Y. Hashimoto, S. atsu Mukai, Y. Sasaki, and K. Akiyoshi, "Nanogel Tectonics for Tissue Engineering: Protein Delivery Systems with Nanogel Chaperones," *Adv. Healthc. Mater.*, vol. 7, no. 23, pp. 1–14, 2018.

[7] J. K. Oh, R. Drumright, D. J. Siegwart, and K. Matyjaszewski, "The development of microgels/nanogels for drug delivery applications," *Prog. Polym. Sci.*, vol. 33, no. 4, pp. 448–477, 2008.

[8] A. Vashist and A. K. K. Kaushik, *Nanogels for Biomedical Applications Smart Materials Series Editors : Titles in this Series :* 2017.

[9] S. Vinogradov, E. Batrakova, and A. Kabanov, "Poly(ethylene glycol)-polyethyleneimine NanoGel(TM) particles: Novel drug delivery systems for antisense oligonucleotides," *Colloids Surfaces B Biointerfaces*, vol. 16, no. 1–4, pp. 291–304, 1999.

[10] F. Sultana, Manirujjaman, Imran-Ul-Haque, M. Arafat, and S. Sharmin, "An overview of nanogel drug delivery system," *J. Appl. Pharm. Sci.*, vol. 3, no. 8 SUPPL, pp. 95–105, 2013.

[11] A. Pikabea, J. Ramos, and J. Forcada, "Production of cationic nanogels with potential use

in controlled drug delivery," *Part. Part. Syst. Charact.*, vol. 31, no. 1, pp. 101–109, 2014.

[12] S. Cuenot, S. Radji, H. Alem, S. Demoustier-Champagne, and A. M. Jonas, "Control of swelling of responsive nanogels by nanoconfinement," *Small*, vol. 8, no. 19, pp. 2978–2985, 2012.

[13] E. Kim *et al.*, "Solvent-responsive polymer nanocapsules with controlled permeability: Encapsulation and release of a fluorescent dye by swelling and deswelling," *Chem. Commun.*, no. 12, pp. 1472–1474, 2009.

[14] F. Ganji, S. Vasheghani-Farahani, and E. Vasheghani-Farahani, "Theoretical description of hydrogel swelling: A review," *Iran. Polym. J. (English Ed.*, vol. 19, no. 5, pp. 375–398, 2010.

[15] A. Roy, *Nanotechnology in Industrial Wastewater Treatment*, vol. 13. 2014.

[16] E. M. Ahmed, "Hydrogel: Preparation, characterization, and applications: A review," *J. Adv. Res.*, vol. 6, no. 2, pp. 105–121, 2015.

[17] H. Holback, Y. Yeo, and K. Park, *Hydrogel swelling behavior and its biomedical applications*. Woodhead Publishing Limited, 2011.

[18] H. Byun *et al.*, "Swelling behavior and drug release of poly(vinyl alcohol) hydrogel cross-linked with poly(acrylic acid)," *Macromol. Res.*, vol. 16, no. 3, pp. 189–193, 2008.

[19] L. Brannon-Peppast, "Equilibrium swelling behavior of pH-sensititive hydrogels," *Chem. Eng.*, vol. 46, no. 3, pp. 715–722, 1991.

[20] H. E. Yang and Y. C. Bae, "Group contribution method for the swelling behavior of thermo-responsive hydrogels," *J. Polym. Sci. Part B Polym. Phys.*, vol. 55, no. 5, pp. 455–463, 2017.

[21] K. Raemdonck, J. Demeester, and S. De Smedt, "Advanced nanogel engineering for drug delivery," *Soft Matter*, vol. 5, no. 4, pp. 707–715, 2009.

[22] D. M. Eckmann, R. J. Composto, A. Tsourkas, and V. R. Muzykantov, "Nanogel carrier design for targeted drug delivery," *J. Mater. Chem. B*, vol. 2, no. 46, pp. 8085–8097, 2014.

[23] K. S. Soni, S. S. Desale, and T. K. Bronich, "Nanogels: An overview of properties, biomedical applications and obstacles to clinical translation," *J. Control. Release*, vol. 240, pp. 109–126, 2016.

[24] F. Sabir *et al.*, "Polymeric nanogels as versatile nanoplatforms for biomedical

applications," *J. Nanomater.*, vol. 2019, 2019.

[25] M. D. Moya-Ortega, C. Alvarez-Lorenzo, A. Concheiro, and T. Loftsson, "Cyclodextrin-based nanogels for pharmaceutical and biomedical applications," *Int. J. Pharm.*, vol. 428, no. 1–2, pp. 152–163, 2012.

[26] Y. Sasaki, D. Iida, H. Takahashi, S. Sawada, and K. Akiyoshi, "Artificial Chaperone Polysaccharide Nanogels for Protein Delivery: A Thermodynamic Study of Protein-Nanogel Interactions Using Fluorescence Correlation Spectroscopy," *Curr. Drug Discov. Technol.*, vol. 8, no. 4, pp. 308–313, 2011.

[27] N. Singh, V. Gill, and P. Gill, "Nanogel Based Artificial Chaperone Technology : an Overview," *Am. J. Adv. Drug Deliv.*, vol. 1, pp. 271–276, 2013.

[28] K. C. Clarke, S. N. Dunham, and L. A. Lyon, "Core/shell microgels decouple the ph and temperature responsivities of microgel films," *Chem. Mater.*, vol. 27, no. 4, pp. 1391–1396, 2015.

[29] R. Acciaro, C. Aulin, L. Wågberg, T. Lindström, P. M. Claesson, and I. Varga, "Investigation of the formation, structure and release characteristics of self-assembled composite films of cellulose nanofibrils and temperature responsive microgels," *Soft Matter*, vol. 7, no. 4, pp. 1369–1377, 2011.

[30] O. Zavgorodnya, C. A. Carmona-Moran, V. Kozlovskaya, F. Liu, T. M. Wick, and E. Kharlampieva, "Temperature-responsive nanogel multilayers of poly(N-vinylcaprolactam) for topical drug delivery," *J. Colloid Interface Sci.*, vol. 506, pp. 589–602, 2017.

[31] W. Richtering and A. Pich, "The special behaviours of responsive core-shell nanogels," *Soft Matter*, vol. 8, no. 45, pp. 11423–11430, 2012.

[32] N. Zhang, L. Yu, Y. C. Li, H. Liu, and Z. Y. Lu, "Novel nano-patterned structures of mixed hairy nanoparticles in single layer," *Polymer (Guildf).*, vol. 192, no. December 2019, p. 122295, 2020.

[33] S. Shah, N. Rangaraj, K. Laxmikeshav, and S. Sampathi, "'Nanogels as drug carriers – Introduction, chemical aspects, release mechanisms and potential applications,'" *Int. J. Pharm.*, vol. 581, no. February, p. 119268, 2020.

[34] E. Mauri, G. Perale, and F. Rossi, "Nanogel Functionalization: A Versatile Approach to Meet the Challenges of Drug and Gene Delivery," *ACS Appl. Nano Mater.*, vol. 1, no. 12, pp. 6525–6541, 2018.

[35] A. J. Sivaram, P. Rajitha, S. Maya, R. Jayakumar, and M. Sabitha, “Nanogels for delivery, imaging and therapy,” *Wiley Interdiscip. Rev. Nanomedicine Nanobiotechnology*, vol. 7, no. 4, pp. 509–533, 2015.

[36] Y. Sasaki and K. Akiyoshi, “Nanogel engineering for new nanobiomaterials: From chaperoning engineering to biomedical applications,” *Chem. Rec.*, vol. 10, no. 6, pp. 366–376, 2010.

[37] S. Uthaman, S. Maya, R. Jayakumar, C. S. Cho, and I. K. Park, “Carbohydrate-based nanogels as drug and gene delivery systems,” *J. Nanosci. Nanotechnol.*, vol. 14, no. 1, pp. 694–704, 2014.

[38] D. C. Sherrington, *Emulsion polymerization and emulsion polymers*, vol. 36, no. 1. 1998.

[39] S. R. George, “Amphiphilic Diblock Copolymers As Stabilizers in Emulsion Polymerization,” Queen’s University, 2017.

[40] Qun Wang, Shoukuan Fu, and Tongyin Yu, “Emulsion polymerization,” *Prog. Polym. Sci.*, vol. 19, no. 4, pp. 703–753, Jan. 1994.

[41] R. G. Gilbert, *Emulsion polymerization: a mechanistic approach*, Acadamic p. Elsevier, 1995.

[42] J. Herrera-Ordonez, R. Olayo, and S. Carro, “The kinetics of emulsion polymerization: Some controversial aspects,” *J. Macromol. Sci. - Polym. Rev.*, vol. 44, no. 3, pp. 207–229, 2004.

[43] B. H. Tan, P. Ravi, and K. C. Tam, “Synthesis and characterization of novel pH-responsive polyampholyte microgels,” *Macromol. Rapid Commun.*, vol. 27, no. 7, pp. 522–528, 2006.

[44] P. J. Feeney, D. H. Napper, and R. G. Gilbert, “Coagulative Nucleation and Particle Size Distributions in Emulsion Polymerization,” *Macromolecules*, vol. 17, no. 12, pp. 2520–2529, 1984.

[45] H. Wang, Q. Pan, and G. L. Rempel, “Micellar nucleation differential microemulsion polymerization,” *Eur. Polym. J.*, vol. 47, no. 5, pp. 973–980, 2011.

[46] J. L. Reimers and F. J. Schork, “Predominant droplet nucleation in emulsion polymerization,” *J. Appl. Polym. Sci.*, vol. 60, no. 2, pp. 251–262, 1996.

[47] F. K. Hansen and J. Ugelstad, “Particle Nucleation in Emulsion Polymerizations - 4. Nucleation in Monomer Droplets.,” *J. Polym. Sci. A1.*, vol. 17, no. 10, pp. 3069–3082,

1979.

[48] G. L. Li, H. Möhwald, and D. G. Shchukin, “Precipitation polymerization for fabrication of complex core-shell hybrid particles and hollow structures,” *Chem. Soc. Rev.*, vol. 42, no. 8, pp. 3628–3646, 2013.

[49] A. Pich and W. Richtering, “Microgels by Precipitation Polymerization: Synthesis, Characterization, and Functionalization,” in *Springer Berlin Heidelberg*, 2010, pp. 1–37.

[50] A. K. Gupta and M. Gupta, “Synthesis and surface engineering of iron oxide nanoparticles for biomedical applications.,” *Biomaterials*, vol. 26, no. 18, pp. 3995–4021, 2005.

[51] M. K. Selatile, S. S. Ray, V. Ojijo, and R. Sadiku, “Recent developments in polymeric electrospun nanofibrous membranes for seawater desalination,” *RSC Adv.*, vol. 8, no. 66, pp. 37915–37938, 2018.

[52] H. Zhang, “Controlled/"living" radical precipitation polymerization: A versatile polymerization technique for advanced functional polymers,” *Eur. Polym. J.*, vol. 49, no. 3, pp. 579–600, 2013.

[53] M. Ashrafizadeh, K. C. Tam, A. Javadi, M. Abdollahi, S. Sadeghnejad, and A. Bahramian, “Synthesis and physicochemical properties of dual-responsive acrylic acid/butyl acrylate cross-linked nanogel systems,” *J. Colloid Interface Sci.*, vol. 556, pp. 313–323, 2019.

[54] R. Setiati, S. Siregar, T. Marhaendrajana, and D. Wahyuningrum, “Challenge sodium lignosulfonate surfactants synthesized from bagasse as an injection fluid based on hydrophil liphophilic balance,” *IOP Conf. Ser. Mater. Sci. Eng.*, vol. 434, no. 1, 2018.

[55] S. Anjum, A. Gupta, D. Sharma, P. Dalal, and B. Gupta, “Skin compatibility and antimicrobial studies on biofunctionalized polypropylene fabric,” *Mater. Sci. Eng. C*, vol. 69, pp. 1043–1050, 2016.

[56] S. Anjum and B. Gupta, “Bioengineering of Functional Nanosilver Nanogels for Smart Healthcare Systems,” *Glob. Challenges*, vol. 2, no. 10, p. 1800044, 2018.

[57] Y. Meng *et al.*, “Biomimic-Inspired and Recyclable Nanogel for Contamination Removal from Water and the Application in Treating Bleaching Effluents,” *Ind. Eng. Chem. Res.*, vol. 59, no. 18, pp. 8622–8631, 2020.

[58] L. Zang, S. Zheng, L. Wang, J. Ma, and L. Sun, “Zwitterionic nanogels modified nanofibrous membrane for efficient oil/water separation,” *J. Memb. Sci.*, vol. 612, no. February, p. 118379, 2020.

[59] W. Li *et al.*, “A nanogel sensor for colorimetric fluorescence measurement of ionizing radiation doses,” *Chem. Commun.*, vol. 55, no. 65, pp. 9614–9617, 2019.

[60] D. Gan and L. A. Lyon, “Interfacial nonradiative energy transfer in responsive core-shell hydrogel nanoparticles,” *J. Am. Chem. Soc.*, vol. 123, no. 34, pp. 8203–8209, 2001.

[61] M. Zhu *et al.*, “Responsive Nanogel Probe for Ratiometric Fluorescent Sensing of pH and Strain in Hydrogels,” *ACS Macro Lett.*, vol. 6, no. 11, pp. 1245–1250, 2017.

[62] W. Wu, J. Shen, Z. Gai, K. Hong, P. Banerjee, and S. Zhou, “Multi-functional core-shell hybrid nanogels for pH-dependent magnetic manipulation, fluorescent pH-sensing, and drug delivery,” *Biomaterials*, vol. 32, no. 36, pp. 9876–9887, 2011.

[63] M. Oishi and Y. Nagasaki, “Stimuli-responsive smart nanogels for cancer diagnostics and therapy,” *Nanomedicine*, vol. 5, no. 3, pp. 451–468, 2010.

[64] Y. Wu *et al.*, “Fluorescent Nanodiamond–Nanogels for Nanoscale Sensing and Photodynamic Applications,” *Adv. NanoBiomed Res.*, vol. 1, no. 7, p. 2000101, 2021.

[65] N. Mohammed, N. Grishkewich, and K. C. Tam, “Cellulose nanomaterials: Promising sustainable nanomaterials for application in water/wastewater treatment processes,” *Environ. Sci. Nano*, vol. 5, no. 3, pp. 623–658, 2018.

[66] J. Araki, M. Wada, S. Kuga, and T. Okano, “Flow properties of microcrystalline cellulose suspension prepared by acid treatment of native cellulose,” *Colloids Surfaces A Physicochem. Eng. Asp.*, vol. 142, no. 1, pp. 75–82, 1998.

[67] N. Mahfoudhi and S. Boufi, “Nanocellulose as a novel nanostructured adsorbent for environmental remediation: a review,” *Cellulose*, vol. 24, no. 3, pp. 1171–1197, 2017.

[68] J. Zhu *et al.*, “Preparation of PdNPs doped chitosan-based composite hydrogels as highly efficient catalysts for reduction of 4-nitrophenol,” *Colloids Surfaces A Physicochem. Eng. Asp.*, vol. 611, no. September 2020, p. 125889, 2021.

[69] D. P. Facchi *et al.*, “Polyelectrolyte complexes based on alginate/tanfloc: Optimization, characterization and medical application,” *Int. J. Biol. Macromol.*, vol. 103, pp. 129–138, 2017.

[70] O. Nechyporchuk, M. N. Belgacem, and J. Bras, “Production of cellulose nanofibrils: A review of recent advances,” *Ind. Crops Prod.*, vol. 93, pp. 2–25, 2016.

[71] N. Mohammed, N. Grishkewich, and K. C. Tam, “Cellulose nanomaterials: Promising sustainable nanomaterials for application in water/wastewater treatment processes,”

Environ. Sci. Nano, vol. 5, no. 3, pp. 623–658, 2018.

[72] F. Trotta, C. Dianzani, F. Caldera, B. Mognetti, and R. Cavalli, "The application of nanosponges to cancer drug delivery," *Expert Opin. Drug Deliv.*, vol. 11, no. 6, pp. 931–941, 2014.

[73] A. K. Bledzki, P. Franciszczak, Z. Osman, and M. Elbadawi, "Polypropylene biocomposites reinforced with softwood, abaca, jute, and kenaf fibers," *Ind. Crops Prod.*, vol. 70, pp. 91–99, 2015.

[74] W. Stelte and A. R. Sanadi, "Preparation and characterization of cellulose nanofibers from two commercial hardwood and softwood pulps," *Ind. Eng. Chem. Res.*, vol. 48, no. 24, pp. 11211–11219, 2009.

[75] M. Fišerová, J. Gigac, and J. Balberčák, "Relationship between fibre characteristics and tensile strength of hardwood and softwood kraft pulps," *Cellul. Chem. Technol.*, vol. 44, no. 7–8, pp. 249–253, 2010.

[76] A. H. Lu, E. L. Salabas, and F. Schüth, "Magnetic nanoparticles: Synthesis, protection, functionalization, and application," *Angew. Chemie - Int. Ed.*, vol. 46, no. 8, pp. 1222–1244, 2007.

[77] W. Wu, Z. Wu, T. Yu, C. Jiang, and W. S. Kim, "Recent progress on magnetic iron oxide nanoparticles: Synthesis, surface functional strategies and biomedical applications," *Sci. Technol. Adv. Mater.*, vol. 16, no. 2, 2015.

[78] A. G. et al. Pereira, Clara, André M. Pereira, Carlos Fernandes, Mariana Rocha, Ricardo Mendes, María Paz Fernández-García, "Superparamagnetic MFe_2O_4 (M = Fe, Co, Mn) Nanoparticles: Tuning the Particle Size and Magnetic Properties through a Novel One-Step Coprecipitation Route Clara," *Chem. Mater.*, vol. 24, pp. 1496–1504, 2012.

[79] H. D. Nguyen, T. D. Nguyen, D. H. Nguyen, and P. T. Nguyen, "Magnetic properties of Cr doped Fe 3 O 4 porous nanoparticles prepared through a co-precipitation method using surfactant," *Adv. Nat. Sci. Nanosci. Nanotechnol.*, vol. 5, no. 3, p. 035017, 2014.

[80] K. W. Bong, P. S. Doyle, D. K. Hwang, T. A. Hatton, S. K. Suh, and K. Yuet, " Synthesis of Nonspherical Superparamagnetic Particles: In Situ Coprecipitation of Magnetic Nanoparticles in Microgels Prepared by Stop-Flow Lithography ," *J. Am. Chem. Soc.*, vol. 134, no. 17, pp. 7337–7343, 2012.

[81] N. A. Frey, S. Peng, K. Cheng, and S. Sun, "Magnetic nanoparticles: Synthesis,

functionalization, and applications in bioimaging and magnetic energy storage," *Chem. Soc. Rev.*, vol. 38, no. 9, pp. 2532–2542, 2009.

[82] B. Geng, X. Liu, J. Ma, and Q. Du, "A new nonhydrolytic single-precursor approach to surfactant-capped nanocrystals of transition metal sulfides," *Mater. Sci. Eng. B*, vol. 145, no. 1–3, pp. 17–22, Dec. 2007.

[83] W. W. Yu, J. C. Falkner, C. T. Yavuz, and V. L. Colvin, "Synthesis of monodisperse iron oxide nanocrystals by thermal decomposition of iron carboxylate saltst," *Chem. Commun.*, vol. 0, pp. 2306–2307, 2004.

[84] A. P. et al Patsula, Vitalii, Lucie Kosinová, Marija Lovrić, Lejla Ferhatovic Hamzić, Mariia Rabyk, Rafal Konefal, "Superparamagnetic Fe_3O_4 Nanoparticles: Synthesis by Thermal Decomposition of Iron(III) Glucuronate and Application in Magnetic Resonance Imaging," *Appl. Mater. surfaces*, vol. 8, pp. 7238–7247, 2016.

[85] J. Park *et al.*, "Ultra-large-scale syntheses of monodisperse nanocrystals," *Nat. Mater.*, vol. 3, no. 12, pp. 891–895, 2004.

[86] D. Amara, J. Grinblat, and S. Margel, "Solventless thermal decomposition of ferrocene as a new approach for one-step synthesis of magnetite nanocubes and nanospheres," *J. Mater. Chem.*, vol. 22, no. 5, pp. 2188–2195, 2012.

[87] Y. Wang, B. Zhu, Y. Wang, and F. Wang, "Solvothermal synthesis of LiFePO4nanorods as high-performance cathode materials for lithium ion batteries," *Ceram. Int.*, vol. 42, no. 8, pp. 10297–10303, 2016.

[88] J. Zhang *et al.*, "Pb(II) removal of Fe_3O_4@SiO_2-NH_2 core-shell nanomaterials prepared via a controllable sol-gel process," *Chem. Eng. J.*, vol. 215–216, pp. 461–471, 2013.

[89] O. M. Lemine *et al.*, "Sol-gel synthesis of 8 nm magnetite (Fe_3O_4) nanoparticles and their magnetic properties," *Superlattices Microstruct.*, vol. 52, no. 4, pp. 793–799, 2012.

[90] J. Xu *et al.*, "Preparation and magnetic properties of magnetite nanoparticles by sol-gel method," *J. Magn. Magn. Mater.*, vol. 309, no. 2, pp. 307–311, 2007.

[91] S. Laurent *et al.*, "Magnetic Iron Oxide Nanoparticles: Synthesis, Stabilization, Vectorization, Physicochemical Characterizations, and Biological Applications," *Chem. Rev.*, vol. 108, no. 6, pp. 2064–2110, 2008.

[92] C. Cheng, F. Xu, and H. Gu, "Facile synthesis and morphology evolution of magnetic iron oxide nanoparticles in different polyol processes," *New J. Chem.*, vol. 35, no. 5, pp. 1072–

1079, 2011.

[93] C. Okoli, M. Boutonnet, L. Mariey, S. Järås, and G. Rajarao, “Application of magnetic iron oxide nanoparticles prepared from microemulsions for protein purification,” *J. Chem. Technol. Biotechnol.*, vol. 86, no. 11, pp. 1386–1393, 2011.

[94] P. Cintas and J. L. Luche, “Green chemistry: The sonochemical approach,” *Green Chem.*, vol. 1, no. 3, pp. 115–125, 1999.

[95] M. A. Teo, Boon M., Fei Chen, T. Alan Hatton, Franz Grieser, “Novel one-pot synthesis of magnetite latex nanoparticles by ultrasound irradiation,” *Langmuir*, vol. 25, no. 5, pp. 2593–2595, 2009.

[96] V. Sreeja and P. A. Joy, “Microwave-hydrothermal synthesis of γ-Fe2O3 nanoparticles and their magnetic properties,” *Mater. Res. Bull.*, vol. 42, no. 8, pp. 1570–1576, 2007.

[97] L. Hu, A. Percheron, D. Chaumont, and C. H. Brachais, “Microwave-assisted one-step hydrothermal synthesis of pure iron oxide nanoparticles: Magnetite, maghemite and hematite,” *J. Sol-Gel Sci. Technol.*, vol. 60, no. 2, pp. 198–205, 2011.

[98] S. Liu, F. Lu, X. Jia, F. Cheng, L. P. Jiang, and J. J. Zhu, “Microwave-assisted synthesis of a biocompatible polyacid-conjugated Fe 3O4 superparamagnetic hybrid,” *CrystEngComm*, vol. 13, no. 7, pp. 2425–2429, 2011.

[99] W. Wu, Z. Wu, T. Yu, C. Jiang, and W. S. Kim, “Recent progress on magnetic iron oxide nanoparticles: Synthesis, surface functional strategies and biomedical applications,” *Sci. Technol. Adv. Mater.*, vol. 16, no. 2, 2015.

[100] H. Zare Abyaneh, “Evaluation of multivariate linear regression and artificial neural networks in prediction of water quality parameters.,” *J. Environ. Heal. Sci. Eng.*, vol. 12, no. 1, p. 40, 2014.

[101] S. D. Richardson and S. Y. Kimura, “Emerging environmental contaminants: Challenges facing our next generation and potential engineering solutions,” *Environ. Technol. Innov.*, vol. 8, pp. 40–56, 2017.

[102] Z. Cai *et al.*, “Application of nanotechnologies for removing pharmaceutically active compounds from water: Development and future trends,” *Environ. Sci. Nano*, vol. 5, no. 1, pp. 27–47, 2018.

[103] M. Králik, “Adsorption, chemisorption, and catalysis,” *Chem. Pap.*, vol. 68, no. 12, pp. 1625–1638, 2014.

[104] K. Y. Foo and B. H. Hameed, “Insights into the modeling of adsorption isotherm systems,” *Chem. Eng. J.*, vol. 156, no. 1, pp. 2–10, 2010.

[105] I. Langmuir, “The adsorption of gases on plane surfaces of glass, mica and platinum,” *J. Am. Chem. Soc.*, vol. 40, no. 1914, pp. 1361–1403, 1919.

[106] R. Kecili and C. M. Hussain, “Mechanism of Adsorption on Nanomaterials,” in *Nanomaterials in Chromatography*, Elsevier, 2018, pp. 89–115.

[107] R. A. Latour, “The Langmuir isotherm: A commonly applied but misleading approach for the analysis of protein adsorption behavior,” *J. Biomed. Mater. Res. - Part A*, vol. 103, no. 3, pp. 949–958, 2015.

[108] M. Vigdorowitsch, A. Pchelintsev, L. Tsygankova, and E. Tanygina, “Freundlich isotherm: An adsorption model complete framework,” *Appl. Sci.*, vol. 11, no. 17, pp. 1–7, 2021.

[109] B. S. Zadeh, H. Esmaeili, and R. Foroutan, “Cadmium(II) removal from aqueous solution using microporous eggshell: Kinetic and equilibrium studies,” *Indones. J. Chem.*, vol. 18, no. 2, pp. 265–271, 2018.

[110] R. Foroutan *et al.*, “Zinc, nickel, and cobalt ions removal from aqueous solution and plating plant wastewater by modified Aspergillus flavus biomass: A dataset,” *Data Br.*, vol. 12, pp. 485–492, 2017.

[111] D. Nunes, A. Pimentel, R. Branquinho, E. Fortunato, and R. Martins, “Metal oxide-based photocatalytic paper: A green alternative for environmental remediation,” *Catalysts*, vol. 11, no. 4, 2021.

[112] C. Descorme, “Catalytic wastewater treatment: Oxidation and reduction processes. Recent studies on chlorophenols,” *Catal. Today*, vol. 297, no. February, pp. 324–334, 2017.

[113] K. Mondal and A. Sharma, “Recent advances in the synthesis and application of photocatalytic metal-metal oxide core-shell nanoparticles for environmental remediation and their recycling process,” *RSC Adv.*, vol. 6, no. 87, pp. 83589–83612, 2016.

[114] A. Ketola, “Determination of surfactants in industrial waters of paper- and board mills Master ’ s Thesis University of Jyväskylä Department of Chemistry,” 2016.

[115] E. O. Ezugbe and S. Rathilal, “Membrane technologies in wastewater treatment: A review,” *Membranes (Basel).*, vol. 10, no. 5, 2020.

[116] I. Kowalska, M. Kabsch-Korbutowicz, K. Majewska-Nowak, and T. Winnicki,

"Separation of anionic surfactants on ultrafiltration membranes," *Desalination*, vol. 162, no. 1–3, pp. 33–40, 2004.

[117] D. Barceló, A. G. Kostianoy, and (ed.), *The Handbook of Environmental Chemistry: Emerging Organic Contaminants and Human Health*, vol. 20. 2012.

[118] Y. Q. Huang *et al.*, "Bisphenol A (BPA) in China: A review of sources, environmental levels, and potential human health impacts," *Environ. Int.*, vol. 42, no. 1, pp. 91–99, Jul. 2012.

[119] M. Patel, R. Kumar, K. Kishor, T. Mlsna, C. U. Pittman, and D. Mohan, "Pharmaceuticals of Emerging Concern in Aquatic Systems: Chemistry, Occurrence, Effects, and Removal Methods," 2019.

[120] Z. Yuan *et al.*, "Cyclodextrin Hydrogels: Rapid Removal of Aromatic Micropollutants and Adsorption Mechanisms," *J. Chem. Eng. Data*, vol. 65, no. 2, pp. 678–689, 2020.

[121] H. Orelma *et al.*, "Cyclodextrin-Functionalized Fiber Yarns Spun from Deep Eutectic Cellulose Solutions for Nonspecific Hormone Capture in Aqueous Matrices," *Biomacromolecules*, vol. 19, no. 2, pp. 652–661, 2018.

[122] S. H. Choi, J. W. Chung, R. D. Priestley, and S. Y. Kwak, "Functionalization of polysulfone hollow fiber membranes with amphiphilic β-cyclodextrin and their applications for the removal of endocrine disrupting plasticizer," *J. Memb. Sci.*, vol. 409–410, pp. 75–81, 2012.

[123] Y. Liu *et al.*, "β-Cyclodextrin-based hollow nanoparticles with excellent adsorption performance towards organic and inorganic pollutants," *Nanoscale*, vol. 11, no. 40, pp. 18653–18661, 2019.

[124] R. Guo *et al.*, "β-Cyclodextrin Polymerized in Cross-Flowing Channels of Biomass Sawdust for Rapid and Highly Efficient Pharmaceutical Pollutants Removal from Water," *Cite This ACS Appl. Mater. Interfaces*, vol. 12, pp. 32817–32826, 2020.

[125] V. K. Gupta, S. Agarwal, H. Sadegh, G. A. M. Ali, A. K. Bharti, and A. S. Hamdy Makhlouf, "Facile route synthesis of novel graphene oxide-β-cyclodextrin nanocomposite and its application as adsorbent for removal of toxic bisphenol A from the aqueous phase," *J. Mol. Liq.*, vol. 237, pp. 466–472, 2017.

[126] L. Jiang *et al.*, "Fabrication of β-cyclodextrin/poly (L-glutamic acid) supported magnetic graphene oxide and its adsorption behavior for 17β-estradiol," *Chem. Eng. J.*, vol. 308, pp.

597–605, 2017.

[127] W. Huang *et al.*, “Citric acid-crosslinked β-cyclodextrin for simultaneous removal of bisphenol A, methylene blue and copper: The roles of cavity and surface functional groups,” *J. Taiwan Inst. Chem. Eng.*, vol. 82, pp. 189–197, 2018.

[128] Y. Zhou, Y. Hu, W. Huang, G. Cheng, C. Cui, and J. Lu, “A novel amphoteric B-cyclodextrin-based adsorbent for simultaneous removal of cationic/anionic dyes and bisphenol A,” *Chem. Eng. J.*, vol. 341, no. 130, pp. 47–57, 2018.

[129] L. Järup, “Hazards of heavy metal contamination,” *Br. Med. Bull.*, vol. 68, pp. 167–182, 2003.

[130] M. Jaishankar, T. Tseten, N. Anbalagan, B. B. Mathew, and K. N. Beeregowda, “Toxicity, mechanism and health effects of some heavy metals,” *Interdiscip. Toxicol.*, vol. 7, no. 2, pp. 60–72, 2014.

[131] E. Renard, A. Deratani, G. Volet, and B. Sebille, “Preparation and characterization of water soluble high molecular weight β-cyclodextrin-epichlorohydrin polymers,” *Eur. Polym. J.*, vol. 33, no. 1, pp. 49–57, Jan. 1997.

[132] E. Gholibegloo, T. Mortezazadeh, F. Salehian, A. Ramazani, M. Amanlou, and M. Khoobi, “Improved curcumin loading, release, solubility and toxicity by tuning the molar ratio of cross-linker to β-cyclodextrin,” *Carbohydr. Polym.*, vol. 213, pp. 70–78, Jun. 2019.

[133] X. Yang and J. C. Kim, “pH-Dependent release of blue dextran from carboxymethyl-β-cyclodextrin hydrogels,” *J. Ind. Eng. Chem.*, vol. 16, no. 5, pp. 763–766, Sep. 2010.

[134] X. Hu *et al.*, “Multifunctional β-Cyclodextrin Polymer for Simultaneous Removal of Natural Organic Matter and Organic Micropollutants and Detrimental Microorganisms from Water,” *ACS Appl. Mater. Interfaces*, vol. 12, no. 10, pp. 12165–12175, 2020.

[135] D. Zhao, L. Zhao, C. Zhu, Z. Tian, and X. Shen, “Synthesis and properties of water-insoluble β-cyclodextrin polymer crosslinked by citric acid with PEG-400 as modifier,” *Carbohydr. Polym.*, vol. 78, no. 1, pp. 125–130, Aug. 2009.

[136] V. S. Ghorpade, A. V. Yadav, and R. J. Dias, “Citric acid crosslinked cyclodextrin/hydroxypropylmethylcellulose hydrogel films for hydrophobic drug delivery,” *Int. J. Biol. Macromol.*, vol. 93, pp. 75–86, Dec. 2016.

[137] V. S. Ghorpade, A. V. Yadav, and R. J. Dias, “Citric acid crosslinked β-

cyclodextrin/carboxymethylcellulose hydrogel films for controlled delivery of poorly soluble drugs," *Carbohydr. Polym.*, vol. 164, pp. 339–348, May 2017.

[138] F. Zhao, E. Repo, Y. Meng, X. Wang, D. Yin, and M. Sillanpää, "An EDTA-β-cyclodextrin material for the adsorption of rare earth elements and its application in preconcentration of rare earth elements in seawater," *J. Colloid Interface Sci.*, vol. 465, pp. 215–224, Mar. 2016.

[139] N. Liu, Y. Wu, and H. Sha, "Characterization of EDTA-cross-linked β-cyclodextrin grafted onto Fe-Al hydroxides as an efficient adsorbent for methylene blue," *J. Colloid Interface Sci.*, vol. 516, pp. 98–109, Apr. 2018.

[140] M. Verma, I. Lee, Y. Hong, V. Kumar, and H. Kim, "Multifunctional β-Cyclodextrin-EDTA-Chitosan polymer adsorbent synthesis for simultaneous removal of heavy metals and organic dyes from wastewater," *Environ. Pollut.*, vol. 292, no. PB, p. 118447, 2022.

[141] F. Zhao, E. Repo, D. Yin, Y. Meng, S. Jafari, and M. Sillanpää, "EDTA-Cross-Linked β-Cyclodextrin: An Environmentally Friendly Bifunctional Adsorbent for Simultaneous Adsorption of Metals and Cationic Dyes," *Environ. Sci. Technol.*, vol. 49, no. 17, pp. 10570–10580, 2015.

[142] F. Zhao *et al.*, "One-pot synthesis of trifunctional chitosan-EDTA-β-cyclodextrin polymer for simultaneous removal of metals and organic micropollutants /," *Sci. Rep.*, vol. 7, no. 1, pp. 1–14, 2017.

[143] A. R. Pedrazzo *et al.*, "Eco-Friendly β-cyclodextrin and Linecaps Polymers for the Removal of Heavy Metals," *Polymers (Basel).*, vol. 11, no. 10, p. 1658, 2019.

[144] X. Qin, L. Bai, Y. Tan, L. Li, F. Song, and Y. Wang, "B-Cyclodextrin-crosslinked polymeric adsorbent for simultaneous removal and stepwise recovery of organic dyes and heavy metal ions: Fabrication, performance and mechanisms," *Chem. Eng. J.*, vol. 372, no. May, pp. 1007–1018, 2019.

[145] Z. Wang *et al.*, "Cyclodextrin functionalized 3D-graphene for the removal of Cr(VI) with the easy and rapid separation strategy," *Environ. Pollut.*, vol. 254, p. 112854, 2019.

[146] L. Fan, C. Luo, M. Sun, and H. Qiu, "Synthesis of graphene oxide decorated with magnetic cyclodextrin for fast chromium removal," *J. Mater. Chem.*, vol. 22, no. 47, pp. 24577–24583, 2012.

[147] J. Wang, W. Zhang, and J. Wei, "Fabrication of poly(β-cyclodextrin)-conjugated magnetic

graphene oxide by surface-initiated RAFT polymerization for synergetic adsorption of heavy metal ions and organic pollutants," *J. Mater. Chem. A*, vol. 7, no. 5, pp. 2055–2065, 2019.

[148] A. Abdolmaleki, S. Mallakpour, and S. Borandeh, "Efficient heavy metal ion removal by triazinyl-β-cyclodextrin functionalized iron nanoparticles," *RSC Adv.*, vol. 5, no. 110, pp. 90602–90608, 2015.

[149] A. Z. M. Badruddoza, B. Bhattarai, and R. P. S. Suri, "Environmentally Friendly β-Cyclodextrin-Ionic Liquid Polyurethane-Modified Magnetic Sorbent for the Removal of PFOA, PFOS, and Cr(VI) from Water," *ACS Sustain. Chem. Eng.*, vol. 5, no. 10, pp. 9223–9232, 2017.

[150] B. Chen, S. Chen, H. Zhao, Y. Liu, F. Long, and X. Pan, "A versatile B-cyclodextrin and polyethyleneimine bi-functionalized magnetic nanoadsorbent for simultaneous capture of methyl orange and Pb(II) from complex wastewater," *Chemosphere*, vol. 216, pp. 605–616, 2019.

[151] K. Thakur and B. Kandasubramanian, "Graphene and Graphene Oxide-Based Composites for Removal of Organic Pollutants: A Review," *J. Chem. Eng. Data*, vol. 64, no. 3, pp. 833–867, 2019.

[152] Y.-T. Woo and D. Y. Lai, "Aromatic Amino and Nitro-Amino Compounds and Their Halogenated Derivatives," *Patty's Toxicol.*, vol. 2, no. 104, pp. 1–96, 2012.

[153] H. L. Jiang *et al.*, "A novel crosslinked β-cyclodextrin-based polymer for removing methylene blue from water with high efficiency," *Colloids Surfaces A Physicochem. Eng. Asp.*, vol. 560, no. October 2018, pp. 59–68, 2019.

[154] X. Liu *et al.*, "A magnetic graphene hybrid functionalized with beta-cyclodextrins for fast and efficient removal of organic dyes," *J. Mater. Chem. A*, vol. 2, no. 31, pp. 12296–12303, 2014.

[155] R. Zhao, Y. Wang, X. Li, B. Sun, and C. Wang, "Synthesis of β-cyclodextrin-based electrospun nanofiber membranes for highly efficient adsorption and separation of methylene blue," *ACS Appl. Mater. Interfaces*, vol. 7, no. 48, pp. 26649–26657, 2015.

[156] L. A. Schaider *et al.*, "Fluorinated Compounds in U.S. Fast Food Packaging," *Environ. Sci. Technol. Lett.*, vol. 4, no. 3, pp. 105–111, Mar. 2017.

[157] X. Chen *et al.*, "Direct contact membrane distillation for effective concentration of

perfluoroalkyl substances – Impact of surface fouling and material stability," *Water Res.*, vol. 182, pp. 1–10, 2020.

[158] W. J. Backe, T. C. Day, and J. A. Field, "Zwitterionic, cationic, and anionic fluorinated chemicals in aqueous film forming foam formulations and groundwater from U.S. military bases by nonaqueous large-volume injection HPLC-MS/MS," *Environ. Sci. Technol.*, vol. 47, no. 10, pp. 5226–5234, May 2013.

[159] A. B. Lindstrom, M. J. Strynar, and E. L. Libelo, "Polyfluorinated compounds: Past, present, and future," *Environ. Sci. Technol.*, vol. 45, no. 19, pp. 7954–7961, Oct. 2011.

[160] United States Environmental Protection Agency (EPA), "Drinking Water Health Advisories for PFOA and PFOS." [Online]. Available: https://www.epa.gov/ground-water-and-drinking-water/drinking-water-health-advisories-pfoa-and-pfos. [Accessed: 24-Jul-2020].

[161] 11044−11049 Letter pubs.acs.org/journal/ascecg Cite This: ACS Sustainable Chem. Eng. 2019, 7, P. S. C. for S. and E. R. of P. P.-C. Water, and and J. M. C. Nicholas A. Lundquist,† Martin J. Sweetman, Kymberley R. Scroggie, Max J. H. Worthington, Louisa J. Esdaile, Salah F. K. Alboaiji, Sally E. Plush, John D. Hayball, "Polymer Supported Carbon for Safe and Effective Remediation of PFOA- and PFOS-Contaminated Water," *Sustain. Chem. Eng.*, vol. 7, no. 13, pp. 11044–11049, 2019.

[162] A. H. Karoyo and L. D. Wilson, "Nano-Sized cyclodextrin-based molecularly imprinted polymer adsorbents for perfluorinated compounds—a mini-review," *Nanomaterials*, vol. 5, no. 2, pp. 981–1003, 2015.

[163] L. Xiao *et al.*, "Cross-linker Chemistry Determines the Uptake Potential of Perfluorinated Alkyl Substances by β-Cyclodextrin Polymers," *Macromolecules*, vol. 52, no. 10, pp. 3747–3752, May 2019.

[164] L. Xiao, Y. Ling, A. Alsbaiee, C. Li, D. E. Helbling, and W. R. Dichtel, "β-Cyclodextrin Polymer Network Sequesters Perfluorooctanoic Acid at Environmentally Relevant Concentrations," *J. Am. Chem. Soc.*, vol. 139, no. 23, pp. 7689–7692, 2017.

[165] J. Yu, L. Lv, P. Lan, S. Zhang, B. Pan, and W. Zhang, "Effect of effluent organic matter on the adsorption of perfluorinated compounds onto activated carbon," *J. Hazard. Mater.*, vol. 225, pp. 99–106, 2012.

[166] C. Wu, M. J. Klemes, B. Trang, W. R. Dichtel, and D. E. Helbling, "Exploring the factors

that influence the adsorption of anionic PFAS on conventional and emerging adsorbents in aquatic matrices," *Water Res.*, vol. 182, p. 115950, 2020.

[167] N. R. Lien and J. R. Telford, "An investigation of the inclusion complex of cyclomaltoheptaose (β-cyclodextrin) with N-methylanthranilic acid in the solid state," *Carbohydr. Res.*, vol. 344, no. 18, pp. 2606–2608, 2009.

[168] A. P. Sherje, B. R. Dravyakar, D. Kadam, and M. Jadhav, "Cyclodextrin-based nanosponges: A critical review," *Carbohydr. Polym.*, vol. 173, no. 1, pp. 37–49, 2017.

[169] F. Caldera, M. Tannous, R. Cavalli, M. Zanetti, and F. Trotta, "Evolution of Cyclodextrin Nanosponges," *Int. J. Pharm.*, vol. 531, no. 2, pp. 470–479, 2017.

[170] S. Kawano *et al.*, "Adsorption capability of urethane-crosslinked heptakis(2,6-di-O-methyl)-β-cyclodextrin polymers toward polychlorobiphenyls in nonpolar organic media," *Polym. J.*, vol. 47, no. 6, pp. 443–448, 2015.

[171] T. J. Mhlanga, S. D., Mamba, B. B., Krause, R. W., & Malefetse, "Removal of organic contaminants from water using nanosponge cyclodextrin polyurethanes," *J. Chem. Technol. Biotechnol. Int. Res. Process. Environ. Clean Technol.*, vol. 84, no. 4, pp. 382–388, 2007.

[172] S. Tang, L. Kong, J. Ou, Y. Liu, X. Li, and H. Zou, "Application of cross-linked β-cyclodextrin polymer for adsorption of aromatic amino acids," *J. Mol. Recognit.*, vol. 19, no. 1, pp. 39–48, Jan. 2006.

[173] T. Mizobuchi, Y., Tanaka, M., & Shono, "Preparation and sorption behaviour of cyclodextrin polyurethane resins," *J. Chromatogr. A*, vol. 194, no. 2, pp. 153–161, 1980.

[174] B. B. Mamba, R. W. Krause, T. J. Malefetse, G. Gericke, and S. P. Sithole, "Cyclodextrin nanosponges in the removal of organic matter to produce water for power generation," *Water SA*, vol. 34, no. 5, pp. 657–660, 2008.

[175] D. Li and M. Ma, "Nanosponges for water purification," *Clean Prod. Process.*, vol. 2, no. 2, pp. 0112–0116, 2000.

[176] E. Y. Ozmen and M. Yilmaz, "Use of β-cyclodextrin and starch based polymers for sorption of Congo red from aqueous solutions," *J. Hazard. Mater.*, vol. 148, no. 1–2, pp. 303–310, 2007.

[177] K. Dong, F. Qiu, X. Guo, J. Xu, D. Yang, and K. He, "Adsorption Behavior of Azo Dye Eriochrome Black T from Aqueous Solution by β-Cyclodextrins/Polyurethane Foam

Material," *Polymer - Plastics Technology and Engineering*, vol. 52, no. 5. pp. 452–460, 2013.

[178] E. Yilmaz, S. Memon, and M. Yilmaz, "Removal of direct azo dyes and aromatic amines from aqueous solutions using two β-cyclodextrin-based polymers," *J. Hazard. Mater.*, vol. 174, no. 1–3, pp. 592–597, 2010.

[179] T. I. Nkambule, R. W. M. Krause, B. B. Mamba, and J. Haarhoff, "Characterisation of natural organic matter (NOM) and its removal using cyclodextrin polyurethanes," *Water SA*, vol. 35, no. 2, pp. 200–203, 2009.

[180] D. Liu, Z. Huang, M. Li, X. Li, P. Sun, and L. Zhou, "Construction of magnetic bifunctional β-cyclodextrin nanocomposites for adsorption and degradation of persistent organic pollutants," *Carbohydr. Polym.*, vol. 230, no. July 2019, p. 115564, 2020.

[181] L. Li *et al.*, "One-step synthesis of an environment-friendly cyclodextrin-based nanosponge and its applications for the removal of dyestuff from aqueous solutions," *Res. Chem. Intermed.*, vol. 46, no. 3, pp. 1715–1734, 2020.

[182] S. Bai *et al.*, "Reduction stimuli-responsive unimolecular polymeric prodrug based on amphiphilic dextran-framework for antitumor drug delivery," *Carbohydr. Polym.*, vol. 182, no. September 2017, pp. 235–244, 2018.

[183] S. Bai *et al.*, "Reduction-active polymeric prodrug micelles based on α-cyclodextrin polyrotaxanes for triggered drug release and enhanced cancer therapy," *Carbohydr. Polym.*, vol. 193, no. February, pp. 153–162, 2018.

[184] Y. Kang, X. Ju, L. S. Ding, S. Zhang, and B. J. Li, "Reactive Oxygen Species and Glutathione Dual Redox-Responsive Supramolecular Assemblies with Controllable Release Capability," *ACS Appl. Mater. Interfaces*, vol. 9, no. 5, pp. 4475–4484, 2017.

[185] F. Zhao, E. Repo, Y. Meng, X. Wang, D. Yin, and M. Sillanpää, "An EDTA-β-cyclodextrin material for the adsorption of rare earth elements and its application in preconcentration of rare earth elements in seawater," *J. Colloid Interface Sci.*, vol. 465, pp. 215–224, 2016.

[186] and R. H. E. Solms, J., "Harze mit Einschlusshohlräumen von Cyclodextrin-Struktur," *Helv. Chim. Acta*, vol. 48, no. 6, pp. 1225–1228, 1965.

[187] I. Krabicová *et al.*, "History of cyclodextrin nanosponges," *Polymers*, vol. 12, no. 5. p. 1122, 2020.

[188] M. Arslan, R. Sanyal, and A. Sanyal, “Cyclodextrin embedded covalently crosslinked networks: Synthesis and applications of hydrogels with nano-containers,” *Polym. Chem.*, vol. 11, no. 3, pp. 615–629, 2020.

[189] N. Morin-Crini, P. Winterton, S. Fourmentin, L. D. Wilson, É. Fenyvesi, and G. Crini, “Water-insoluble β-cyclodextrin–epichlorohydrin polymers for removal of pollutants from aqueous solutions by sorption processes using batch studies: A review of inclusion mechanisms,” *Prog. Polym. Sci.*, vol. 78, pp. 1–23, 2018.

[190] A. Celebioglu, F. Topuz, and T. Uyar, “Water-Insoluble Hydrophilic Electrospun Fibrous Mat of Cyclodextrin–Epichlorohydrin Polymer as Highly Effective Sorbent,” *ACS Appl. Polym. Mater.*, vol. 1, no. 1, pp. 54–62, 2019.

[191] G. Xu *et al.*, “Simple synthesis of a swellable porous β-cyclodextrin-based polymer in the aqueous phase for the rapid removal of organic micro-pollutants from water,” *Green Chem.*, vol. 21, no. 22, pp. 6062–6072, 2019.

[192] Sumio lijima, “Helical microtubules of graphitic carbon,” *Nature*, vol. 354, pp. 56–58, 1991.

[193] A. Leudjo Taka, E. Fosso-Kankeu, K. Pillay, and X. Yangkou Mbianda, “Metal nanoparticles decorated phosphorylated carbon nanotube/cyclodextrin nanosponge for trichloroethylene and Congo red dye adsorption from wastewater,” *J. Environ. Chem. Eng.*, vol. 8, no. 3, p. 103602, 2020.

[194] J. P. Raval, P. Joshi, and D. R. Chejara, “Carbon nanotube for targeted drug delivery,” in *Applications of Nanocomposite Materials in Drug Delivery*, Elsevier, 2018, pp. 203–216.

[195] I. Rafique, A. Kausar, Z. Anwar, and B. Muhammad, “Exploration of Epoxy Resins, Hardening Systems, and Epoxy/Carbon Nanotube Composite Designed for High Performance Materials: A Review,” *Polym. - Plast. Technol. Eng.*, vol. 55, no. 3, pp. 312–333, 2016.

[196] B. Bina, Y. Hajizadeh, H. Pourzamani, A. Mohammadi, A. Ebrahimi, and M. Amin, “Effectiveness of nanozeolite modified by cationic surfactant in the removal of disinfection by-product precursors from water solution,” *Int. J. Environ. Health Eng.*, vol. 1, no. 1, p. 3, 2012.

[197] W. Liu, X. Jiang, and X. Chen, “A novel method of synthesizing cyclodextrin grafted multiwall carbon nanotubes/iron oxides and its adsorption of organic pollutant,” *Appl.*

Surf. Sci., vol. 320, pp. 764–771, 2014.

[198] J. Cheng, P. R. Chang, P. Zheng, and X. Ma, "Characterization of magnetic carbon nanotube-cyclodextrin composite and its adsorption of dye," *Ind. Eng. Chem. Res.*, vol. 53, no. 4, pp. 1415–1421, 2014.

[199] A. Mohammadi and P. Veisi, "High adsorption performance of β-cyclodextrin-functionalized multi-walled carbon nanotubes for the removal of organic dyes from water and industrial wastewater," *J. Environ. Chem. Eng.*, vol. 6, no. 4, pp. 4634–4643, 2018.

[200] Z. J. Nie *et al.*, "Cyclodextrin self-assembled graphene oxide aerogel microspheres as broad-spectrum adsorbent for removing dyes and organic micropollutants from water," *J. Environ. Chem. Eng.*, vol. 9, no. 2, p. 104749, 2021.

[201] L. T. Gibson, "Mesosilica materials and organic pollutant adsorption: Part B removal from aqueous solution," *Chem. Soc. Rev.*, vol. 43, no. 15, pp. 5173–5182, 2014.

[202] B. Bhattarai, M. Muruganandham, and R. P. S. Suri, "Development of high efficiency silica coated β-cyclodextrin polymeric adsorbent for the removal of emerging contaminants of concern from water," *J. Hazard. Mater.*, vol. 273, pp. 146–154, 2014.

[203] H. M. Shen *et al.*, "Surface immobilization of β-cyclodextrin on hybrid silica and its fast adsorption performance of p-nitrophenol from the aqueous phase," *RSC Adv.*, vol. 5, no. 103, pp. 84410–84422, 2015.

[204] L. Lin and C. Zou, "Kinetic and Thermodynamic Study of Magnetic Separable β-Cyclodextrin Inclusion Complex with Organic Phosphoric Acid Applied to Removal of Hg2+," *J. Chem. Eng. Data*, vol. 62, no. 2, pp. 762–772, Feb. 2017.

[205] B. Chen, S. Chen, H. Zhao, Y. Liu, F. Long, and X. Pan, "A versatile B-cyclodextrin and polyethyleneimine bi-functionalized magnetic nanoadsorbent for simultaneous capture of methyl orange and Pb(II) from complex wastewater," *Chemosphere*, vol. 216, pp. 605–616, 2019.

[206] M. Tajuddin Sikder, S. Tanaka, T. Saito, and M. Kurasaki, "Application of zerovalent iron impregnated chitosan-caboxymethyl-β- cyclodextrin composite beads as arsenic sorbent," *J. Environ. Chem. Eng.*, vol. 2, no. 1, pp. 370–376, 2014.

[207] Y. Shi *et al.*, "Magnetite nanoparticles modified β-cyclodextrin PolymerCoupled with KMnO4 oxidation for adsorption and degradation of acetaminophen," *Carbohydr. Polym.*, vol. 222, no. June, p. 114972, 2019.

[208] J. H. Lee and S. Y. Kwak, “Rapid adsorption of bisphenol A from wastewater by β-cyclodextrin-functionalized mesoporous magnetic clusters,” *Appl. Surf. Sci.*, vol. 467–468, no. October 2018, pp. 178–184, 2019.

[209] J. H. Lee and S. Y. Kwak, “Branched polyethylenimine-polyethylene glycol-β-cyclodextrin polymers for efficient removal of bisphenol A and copper from wastewater,” *J. Appl. Polym. Sci.*, vol. 137, no. 12, pp. 1–9, 2020.

[210] Y. He *et al.*, “Improving the anti-fouling property and permeate flux of hollow fiber composite nanofiltration membrane using β-cyclodextrin,” *Sci. Rep.*, vol. 9, no. 1, pp. 1–10, 2019.

[211] Y. Liu, D. Wu, X. Wang, J. Yu, and F. Li, “Fabrication of eco-friendly nanofibrous membranes functionalized with carboxymethyl-β-cyclodextrin for efficient removal of methylene blue with good recyclability,” *RSC Adv.*, vol. 8, no. 66, pp. 37715–37723, 2018.

[212] S. Mizuno, T. A. Asoh, Y. Takashima, A. Harada, and H. Uyama, “Palladium nanoparticle loaded β-cyclodextrin monolith as a flow reactor for concentration enrichment and conversion of pollutants based on molecular recognition,” *Chem. Commun.*, vol. 56, no. 92, pp. 14408–14411, 2020.

[213] Z. Wang, S. Guo, B. Zhang, J. Fang, and L. Zhu, “Interfacially crosslinked β-cyclodextrin polymer composite porous membranes for fast removal of organic micropollutants from water by flow-through adsorption,” *J. Hazard. Mater.*, vol. 384, no. August 2019, p. 121187, 2020.

[214] H. Chen, Y. Zhou, J. Wang, J. Lu, and Y. Zhou, “Polydopamine modified cyclodextrin polymer as efficient adsorbent for removing cationic dyes and Cu^{2+},” *J. Hazard. Mater.*, vol. 389, no. 130, p. 121897, May 2020.

[215] J. Zhao *et al.*, “Chitosan adsorbent reinforced with citric acid modified β-cyclodextrin for highly efficient removal of dyes from reactive dyeing effluents,” *Eur. Polym. J.*, vol. 108, no. July, pp. 212–218, 2018.

[216] P. Karthikeyan and S. Meenakshi, “In-situ fabrication of cerium incorporated chitosan-β-cyclodextrin microspheres as an effective adsorbent for toxic anions removal,” *Environ. Nanotechnology, Monit. Manag.*, vol. 12, no. October, p. 100272, 2019.

[217] P. Sirajudheen, P. Karthikeyan, S. Vigneshwaran, M. Nikitha, C. A. A. Hassan, and S.

Meenakshi, “Ce(III) networked chitosan/β-cyclodextrin beads for the selective removal of toxic dye molecules: Adsorption performance and mechanism,” *Carbohydr. Polym. Technol. Appl.*, vol. 1, no. September, p. 100018, 2020.

[218] T. Kekes and C. Tzia, “Adsorption of indigo carmine on functional chitosan and β-cyclodextrin/chitosan beads: Equilibrium, kinetics and mechanism studies,” *J. Environ. Manage.*, vol. 262, no. February, p. 110372, 2020.

[219] M. Usman, A. Ahmed, B. Yu, S. Wang, Y. Shen, and H. Cong, “Simultaneous adsorption of heavy metals and organic dyes by β-Cyclodextrin-Chitosan based cross-linked adsorbent,” *Carbohydr. Polym.*, vol. 255, no. May 2020, p. 117486, 2021.

[220] F. Zhang, W. Wu, S. Sharma, G. Tong, and Y. Deng, “Synthesis of Cyclodextrin-functionalized Cellulose Nanofibril Aerogel as a Highly Effective Adsorbent for Phenol Pollutant Removal,” *BioResources*, vol. 10, no. 4, pp. 7555–7568, 2015.

[221] H. Kono, K. Onishi, and T. Nakamura, “Characterization and bisphenol A adsorption capacity of β-cyclodextrin-carboxymethylcellulose-based hydrogels,” *Carbohydr. Polym.*, vol. 98, no. 1, pp. 784–792, 2013.

[222] Q. Lin, Y. Wu, X. Jiang, F. Lin, X. Liu, and B. Lu, “Removal of bisphenol A from aqueous solution via host-guest interactions based on beta-cyclodextrin grafted cellulose bead,” *Int. J. Biol. Macromol.*, vol. 140, pp. 1–9, 2019.

[223] F. M. Mpatani *et al.*, “Uptake of micropollutant-bisphenol A, methylene blue and neutral red onto a novel bagasse-β-cyclodextrin polymer by adsorption process,” *Chemosphere*, vol. 259, p. 127439, 2020.

[224] X. Yue, F. Jiang, D. Zhang, H. Lin, and Y. Chen, “Preparation of adsorbent based on cotton fiber for removal of dyes,” *Fibers Polym.*, vol. 18, no. 11, pp. 2102–2110, 2017.

[225] N. Hou *et al.*, “Facile preparation of self-assembled hydrogels constructed from poly-cyclodextrin and poly-adamantane as highly selective adsorbents for wastewater treatment,” *Soft Matter*, vol. 15, no. 30, pp. 6097–6106, 2019.

[226] R. Palao-Suay, L. G. Gómez-Mascaraque, M. R. Aguilar, B. Vázquez-Lasa, and J. S. Román, “Self-assembling polymer systems for advanced treatment of cancer and inflammation,” *Prog. Polym. Sci.*, vol. 53, pp. 207–248, 2016.

[227] Y. Gao *et al.*, “Self-Assembled Hydrogels Based on Poly-Cyclodextrin and Poly-Azobenzene Compounds and Applications for Highly Efficient Removal of Bisphenol A

and Methylene Blue," *ACS Omega*, vol. 3, no. 9, pp. 11663–11672, 2018.

[228] Z. Yuan *et al.*, "Cyclodextrin Hydrogels: Rapid Removal of Aromatic Micropollutants and Adsorption Mechanisms," *J. Chem. Eng. Data*, vol. 65, no. 2, pp. 678–689, 2020.

[229] N. Hou *et al.*, "Self-assembled hydrogels constructed via host-guest polymers with highly efficient dye removal capability for wastewater treatment," *Colloids Surfaces A Physicochem. Eng. Asp.*, vol. 579, no. May, p. 123670, 2019.

[230] R. Sedghi, B. Heidari, and M. Yassari, "Novel molecularly imprinted polymer based on β-cyclodextrin@graphene oxide: Synthesis and application for selective diphenylamine determination," *J. Colloid Interface Sci.*, vol. 503, pp. 47–56, 2017.

[231] F. Trotta *et al.*, "Molecularly imprinted cyclodextrin nanosponges for the controlled delivery of L-DOPA: perspectives for the treatment of Parkinson's disease," *Expert Opin. Drug Deliv.*, vol. 13, no. 12, pp. 1671–1680, 2016.

[232] J. Dolai, H. Ali, and N. R. Jana, "Molecular Imprinted Poly-Cyclodextrin for Selective Removal of Dibutyl Phthalate," *ACS Appl. Polym. Mater.*, vol. 2, no. 2, pp. 691–698, 2020.

[233] S. Nestora, F. Merlier, E. Prost, K. Haupt, C. Rossi, and B. Tse Sum Bui, "Solid-phase extraction of betanin and isobetanin from beetroot extracts using a dipicolinic acid molecularly imprinted polymer," *J. Chromatogr. A*, vol. 1465, pp. 47–54, 2016.

[234] H. Duan, X. Wang, Y. Wang, Y. Sun, J. Li, and C. Luo, "An ultrasensitive lysozyme chemiluminescence biosensor based on surface molecular imprinting using ionic liquid modified magnetic graphene oxide/β-cyclodextrin as supporting material," *Anal. Chim. Acta*, vol. 918, pp. 89–96, 2016.

[235] H. Fu, J. Liu, W. Xu, H. Wang, S. Liao, and G. Chen, "A new type of magnetic molecular imprinted material combined with β-cyclodextrin for the selective adsorption of zearalenone," *J. Mater. Chem. B*, vol. 8, no. 48, pp. 10966–10976, 2020.

[236] W. Zhang, Z. Zhu, H. Zhang, and Y. Qiu, "Selective removal of the genotoxic compound 2-aminopyridine in water using molecularly imprinted polymers based on magnetic chitosan and β-cyclodextrin," *Int. J. Environ. Res. Public Health*, vol. 14, no. 9, pp. 1–22, 2017.

[237] Y. Yuan, Y. Liu, W. Teng, J. Tan, Y. Liang, and Y. Tang, "Preparation of core-shell magnetic molecular imprinted polymer with binary monomer for the fast and selective

extraction of bisphenol A from milk," *J. Chromatogr. A*, vol. 1462, pp. 2–7, 2016.

[238] M. Molina, M. Asadian-Birjand, J. Balach, J. Bergueiro, E. Miceli, and M. Calderón, "Stimuli-responsive nanogel composites and their application in nanomedicine," *Chem. Soc. Rev.*, vol. 44, no. 17, pp. 6161–6186, 2015.

[239] S. S. Suner, M. Sahiner, S. B. Sengel, D. J. Rees, W. F. Reed, and N. Sahiner, *Responsive biopolymer-based microgels/nanogels for drug delivery applications*. Elsevier Ltd., 2018.

[240] X. Yu *et al.*, "Temperature and salt responsive zwitterionic polysulfamide-based nanogels with surface regeneration ability and controlled drug release," *Polym. Chem.*, vol. 10, no. 47, pp. 6423–6431, 2019.

[241] A. S. Sonzogni *et al.*, "Thermoresponsive nanogels with film-forming ability," *Polym. Chem.*, vol. 9, no. 8, pp. 1004–1011, 2018.

[242] T. K. Mandal, N. Parvin, and S. W. Joo, "pH-Responsive Biocompatible Fluorescent Core-Shell Nanogel for Intracellular Imaging and Control Drug Release," *Part. Part. Syst. Charact.*, vol. 2100110, pp. 1–7, 2021.

[243] B. L. Moore, D. Moatsou, A. Lu, and R. K. O'Reilly, "Studying the activity of the MacMillan catalyst embedded within hydrophobic cross-linked polymeric nanostructures," *Polym. Chem.*, vol. 5, no. 10, pp. 3487–3494, 2014.

[244] A. Setia and P. Ahuja, "Nanohydrogels," in *Organic Materials as Smart Nanocarriers for Drug Delivery*, Elsevier, 2018, pp. 293–368.

[245] W. S. J. Li *et al.*, "Cardanol-based polymer latex by radical aqueous miniemulsion polymerization," *Polym. Chem.*, vol. 9, no. 18, pp. 2468–2477, 2018.

[246] K. McAllister *et al.*, "Polymeric nanogels produced via inverse microemulsion polymerization as potential gene and antisense delivery agents," *J. Am. Chem. Soc.*, vol. 124, no. 51, pp. 15198–15207, 2002.

[247] R. T. Chacko, J. Ventura, J. Zhuang, and S. Thayumanavan, "Polymer nanogels: A versatile nanoscopic drug delivery platform," *Adv. Drug Deliv. Rev.*, vol. 64, no. 9, pp. 836–851, 2012.

[248] M. Jassal, B. N. Acharya, and P. Bajaj, "Synthesis, characterization, and rheological studies of methacrylic acid-ethyl acrylate-diallyl phthalate copolymers," *J. Appl. Polym. Sci.*, vol. 89, no. 5, pp. 1430–1441, 2003.

[249] M. Bandiera, R. Balk, and M. J. Barandiaran, "One-pot synthesis of waterborne polymeric

dispersions stabilized with alkali-soluble resins," *Polymers (Basel).*, vol. 10, no. 1, pp. 1–14, 2018.

[250] J. Sievers *et al.*, "Determination of hydrogel swelling factors by two established and a novel non-contact continuous method," *J. Appl. Polym. Sci.*, vol. 138, no. 18, pp. 1–9, 2021.

[251] M. Jassal, B. N. Acharya, and P. Bajaj, "Synthesis, characterization, and rheological studies of methacrylic acid-ethyl acrylate-diallyl phthalate copolymers," *J. Appl. Polym. Sci.*, vol. 89, no. 5, pp. 1430–1441, 2003.

[252] N. Vishal Gupta and H. G. Shivakumar, "Investigation of Swelling Behavior and Mechanical Properties of a pH-Sensitive Superporous Hydrogel Composite," *Iran. J. Pharm. Res.*, vol. 11, no. 2, pp. 481–493, 2012.

[253] S. Asman, S. Mohamad, and N. M. Sarih, "Exploiting F-Cyclodextrin in molecular imprinting for achieving recognition of benzylparaben in aqueous media," *Int. J. Mol. Sci.*, vol. 16, no. 2, pp. 3656–3676, 2015.

[254] L. Feng, H. Yang, X. Dong, H. Lei, and D. Chen, "pH-sensitive polymeric particles as smart carriers for rebar inhibitors delivery in alkaline condition," *J. Appl. Polym. Sci.*, vol. 135, no. 8, p. 45886, Feb. 2018.

[255] C. Wang, K. C. Tam, R. D. Jenkins, and D. R. Bassett, "Potentiometric titration and dynamic light scattering of hydrophobically modified alkali soluble emulsion (HASE) polymer solutions," *Phys. Chem. Chem. Phys.*, vol. 2, no. 9, pp. 1967–1972, 2000.

[256] J. Landsgesell *et al.*, "Simulations of ionization equilibria in weak polyelectrolyte solutions and gels," *Soft Matter*, vol. 15, no. 6, pp. 1155–1185, 2019.

[257] S. Lally, T. J. Freemont, F. Cellesi, and B. R. Saunders, "pH-responsive microgels containing hydrophilic crosslinking co-monomers: Shell-exploding microgels through design," *Colloid Polym. Sci.*, vol. 289, no. 5–6, pp. 647–658, 2011.

[258] O. Pinprayoon, R. Groves, and B. R. Saunders, "A study of poly(butadiene/methacrylic acid) dispersions: From pH-responsive behaviour to the effects of added Ca^{2+}," *J. Colloid Interface Sci.*, vol. 321, no. 2, pp. 315–322, 2008.

[259] H. L. Abd El-Mohdy, E. A. Hegazy, E. M. El-Nesr, and M. A. El-Wahab, "Synthesis, characterization and properties of radiation-induced Starch/(EG-co-MAA) hydrogels," *Arab. J. Chem.*, vol. 9, pp. S1627–S1635, 2016.

[260] M. M. Modena, B. Rühle, T. P. Burg, and S. Wuttke, “Nanoparticle Characterization: What to Measure?,” *Adv. Mater.*, vol. 31, no. 32, pp. 1–26, 2019.

[261] A. Hawe, W. L. Hulse, W. Jiskoot, and R. T. Forbes, “Taylor dispersion analysis compared to dynamic light scattering for the size analysis of therapeutic peptides and proteins and their aggregates,” *Pharm. Res.*, vol. 28, no. 9, pp. 2302–2310, 2011.

[262] P. M. Carvalho, M. R. Felício, N. C. Santos, S. Gonçalves, and M. M. Domingues, “Application of light scattering techniques to nanoparticle characterization and development,” *Front. Chem.*, vol. 6, no. June, pp. 1–17, 2018.

[263] H. Yin, H. C. Kang, K. M. Huh, and Y. H. Bae, “Biocompatible, pH-sensitive AB2 miktoarm polymer-based polymersomes: Preparation, characterization, and acidic pH-activated nanostructural transformation,” *J. Mater. Chem.*, vol. 22, no. 36, pp. 19168–19178, 2012.

[264] M. Ashrafizadeh, K. C. Tam, A. Javadi, M. Abdollahi, S. Sadeghnejad, and A. Bahramian, “Dual physically and chemically cross-linked polyelectrolyte nanohydrogels: Compositional and pH-dependent behavior studies,” *Eur. Polym. J.*, vol. 122, no. November 2019, p. 109398, 2020.

[265] Z. Liu *et al.*, “Amphiphilic core–shell nanoparticles containing dense polyethyleneimine shells for efficient delivery of microRNA to Kupffer cells,” *Int. J. Nanomedicine*, vol. 11, pp. 2785–2797, 2016.

[266] Y. Zhang, C. Fang, S. Zhang, R. E. Campbell, and M. J. Serpe, “Controlled Osteogenic Differentiation of Human Mesenchymal Stem Cells Using Dexamethasone-Loaded Light-Responsive Microgels,” *ACS Appl. Mater. Interfaces*, 2021.

[267] E. Niezabitowska *et al.*, “Insights into the internal structures of nanogels using a versatile asymmetric-flow field-flow fractionation method,” *Nanoscale Adv.*, vol. 2, no. 10, pp. 4713–4721, 2020.

[268] I. Varga, T. Gilányi, R. Mészáros, G. Filipcsei, and M. Zrínyi, “Effect of cross-link density on the internal structure of poly(N-isopropylacrylamide) microgels,” *J. Phys. Chem. B*, vol. 105, no. 38, pp. 9071–9076, 2001.

[269] G. R. Deen and J. S. Pedersen, “Investigation on the structure of temperature-responsive N -isopropylacrylamide microgels containing a new hydrophobic crosslinker,” *Cogent Chem.*, vol. 1, no. 1, p. 1012658, Dec. 2015.

[270] C. L. Lin, W. Y. Chiu, and C. F. Lee, “Thermal/pH-sensitive core-shell copolymer latex and its potential for targeting drug carrier application,” *Polymer (Guildf).*, vol. 46, no. 23, pp. 10092–10101, 2005.

[271] M. W. Toepke and W. L. Murphy, “1.31 Dynamic Hydrogels,” in *Comprehensive Biomaterials II*, vol. 1, Elsevier, 2017, pp. 705–724.

[272] W. KUHN, B. HARGITAY, A. KATCHALSKY, and H. EISENBERG, “Reversible Dilation and Contraction by Changing the State of Ionization of High-Polymer Acid Networks,” *Nature*, vol. 165, no. 4196, pp. 514–516, Apr. 1950.

[273] J. Xu, Y. Tian, Z. Li, B. H. Tan, K. Y. Tang, and K. C. Tam, “β-Cyclodextrin functionalized magnetic nanoparticles for the removal of pharmaceutical residues in drinking water,” *J. Ind. Eng. Chem.*, vol. 109, pp. 461–474, May 2022.

[274] M. Huerta-Fontela, M. T. Galceran, and F. Ventura, “Occurrence and removal of pharmaceuticals and hormones through drinking water treatment,” *Water Res.*, vol. 45, no. 3, pp. 1432–1442, 2011.

[275] O. A. Jones, J. N. Lester, and N. Voulvoulis, “Pharmaceuticals: A threat to drinking water?,” *Trends Biotechnol.*, vol. 23, no. 4, pp. 163–167, 2005.

[276] V. G. Samaras, A. S. Stasinakis, D. Mamais, N. S. Thomaidis, and T. D. Lekkas, “Fate of selected pharmaceuticals and synthetic endocrine disrupting compounds during wastewater treatment and sludge anaerobic digestion,” *J. Hazard. Mater.*, vol. 244–245, pp. 259–267, 2013.

[277] B. Tiwari, B. Sellamuthu, Y. Ouarda, P. Drogui, R. D. Tyagi, and G. Buelna, “Review on fate and mechanism of removal of pharmaceutical pollutants from wastewater using biological approach,” *Bioresour. Technol.*, vol. 224, pp. 1–12, 2017.

[278] T. Heberer, “Tracking persistent pharmaceutical residues from municipal sewage to drinking water,” *J. Hydrol.*, vol. 266, no. 3–4, pp. 175–189, 2002.

[279] J. M. Choubert, L. Ribeiro, M. Euse, M. Coquery, and C. Mie, “Fate of pharmaceuticals and personal care products in wastewater treatment plants – Conception of a database and first results,” vol. 157, pp. 1721–1726, 2009.

[280] T. M. MacDonald and L. Wei, “Effect of ibuprofen on cardioprotective effect of aspirin,” *Lancet*, vol. 361, no. 9357, pp. 573–574, 2003.

[281] A. M. Simon, M. B. Manigrasso, and J. Patrick O ’connor, “Cyclo-Oxygenase 2 Function

Is Essential for Bone Fracture Healing," *J. Bone Miner. Res.*, vol. 17, no. 6, pp. 963–976, 2002.

[282] I. J. Buerge, T. Poiger, M. D. Müller, and H. R. Buser, "Caffeine, an anthropogenic marker for wastewater contamination of surface waters," *Environ. Sci. Technol.*, vol. 37, no. 4, pp. 691–700, 2003.

[283] S. R. Taheran M, Naghdi M, Brar SK, Knystautas EJ, Verma M, "Covalent Immobilization of Laccase onto Nanofibrous Membrane for Degradation of Pharmaceutical Residues in Water," *ACS Sustain. Chem. Eng.*, vol. 5, no. 11, pp. 10430–10438, 2017.

[284] S. D. Richardson and T. A. Ternes, "Water Analysis: Emerging Contaminants and Current Issues," *Anal. Chem.*, vol. 90, no. 1, pp. 398–428, 2018.

[285] S. Bucak, D. A. Jones, P. E. Laibinis, and T. A. Hatton, "Protein separations using colloidal magnetic nanoparticles," *Biotechnol. Prog.*, vol. 19, no. 2, pp. 477–484, 2003.

[286] M. Wang *et al.*, "Fe_3O_4@β-CD nanocomposite as heterogeneous Fenton-like catalyst for enhanced degradation of 4-chlorophenol (4-CP)," *Appl. Catal. B Environ.*, vol. 188, pp. 113–122, Jul. 2016.

[287] A. Z. M. Badruddoza, G. S. S. Hazel, K. Hidajat, and M. S. Uddin, "Synthesis of carboxymethyl-β-cyclodextrin conjugated magnetic nano-adsorbent for removal of methylene blue," *Colloids Surfaces A Physicochem. Eng. Asp.*, vol. 367, no. 1–3, pp. 85–95, 2010.

[288] Y. H. Deng, C. C. Wang, J. H. Hu, W. L. Yang, and S. K. Fu, "Investigation of formation of silica-coated magnetite nanoparticles via sol-gel approach," *Colloids Surfaces A Physicochem. Eng. Asp.*, vol. 262, no. 1–3, pp. 87–93, 2005.

[289] Z. Cao, X. Zhou, and G. Wang, "Selective Release of Hydrophobic and Hydrophilic Cargos from Multi-Stimuli-Responsive Nanogels," *ACS Appl. Mater. Interfaces*, vol. 8, no. 42, pp. 28888–28896, 2016.

[290] A. Z. M. Badruddoza, G. S. S. Hazel, K. Hidajat, and M. S. Uddin, "Synthesis of carboxymethyl-β-cyclodextrin conjugated magnetic nano-adsorbent for removal of methylene blue," *Colloids Surfaces A Physicochem. Eng. Asp.*, vol. 367, no. 1–3, pp. 85–95, Sep. 2010.

[291] A. Z. M. Badruddoza, A. S. H. Tay, P. Y. Tan, K. Hidajat, and M. S. Uddin,

"Carboxymethyl-β-cyclodextrin conjugated magnetic nanoparticles as nano-adsorbents for removal of copper ions: Synthesis and adsorption studies," *J. Hazard. Mater.*, vol. 185, no. 2–3, pp. 1177–1186, 2011.

[292] X. C. Shen, X. Z. Fang, Y. H. Zhou, and H. Liang, "Synthesis and characterization of 3-aminopropyltriethoxysilane-modified superparamagnetic magnetite nanoparticles," *Chem. Lett.*, vol. 33, no. 11, pp. 1468–1469, 2004.

[293] B. Thangaraj, Z. Jia, L. Dai, D. Liu, and W. Du, "Effect of silica coating on Fe_3O_4 magnetic nanoparticles for lipase immobilization and their application for biodiesel production," *Arab. J. Chem.*, vol. 12, no. 8, pp. 4694–4706, Dec. 2019.

[294] S. Shin and J. Jang, "Thiol containing polymer encapsulated magnetic nanoparticles as reusable and efficiently separable adsorbent for heavy metal ions," *Chem. Commun.*, no. 41, pp. 4230–4232, 2007.

[295] K. Gandha *et al.*, "Mesoporous iron oxide nanowires: Synthesis, magnetic and photocatalytic properties," *RSC Adv.*, vol. 6, no. 93, pp. 90537–90546, 2016.

[296] S. Zhou and B. Chu, "Synthesis and Volume Phase Transition of Poly(methacrylic acid-co - N -isopropylacrylamide) Microgel Particles in Water," *J. Phys. Chem. B*, vol. 102, no. 8, pp. 1364–1371, 1998.

[297] W. Ge, A. Encinas, E. Araujo, and S. Song, "Magnetic matrices used in high gradient magnetic separation (HGMS): A review," *Results Phys.*, vol. 7, pp. 4278–4286, 2017.

[298] R. Zhao, Y. Wang, X. Li, B. Sun, Z. Jiang, and C. Wang, "Colloids and Surfaces B : Biointerfaces Water-insoluble sericin / B-cyclodextrin / PVA composite electrospun nanofibers as effective adsorbents towards methylene blue," *Colloids Surfaces B Biointerfaces*, vol. 136, pp. 375–382, 2015.

[299] H. Huang, Y. Fan, J. Wang, H. Gao, and S. Tao, "Adsorption kinetics and thermodynamics of water-insoluble crosslinked β-cyclodextrin polymer for phenol in aqueous solution," *Macromol. Res.*, vol. 21, no. 7, pp. 726–731, Jul. 2013.

[300] S. Ghosh, A. Z. M. Badruddoza, K. Hidajat, and M. S. Uddin, "Adsorptive removal of emerging contaminants from water using superparamagnetic Fe_3O_4 nanoparticles bearing aminated β-cyclodextrin," *J. Environ. Chem. Eng.*, vol. 1, no. 3, pp. 122–130, 2013.

[301] L. Chen, R. M. Berry, and K. C. Tam, "Synthesis of β-Cyclodextrin-modified cellulose nanocrystals (CNCs)@Fe_3O_4@SiO2 superparamagnetic nanorods," *ACS Sustain. Chem.*

Eng., vol. 2, no. 4, pp. 951–958, 2014.

[302] X. Zhang, Y. Wang, and S. Yang, "Simultaneous removal of Co(II) and 1-naphthol by core-shell structured Fe_3O_4@cyclodextrin magnetic nanoparticles," *Carbohydr. Polym.*, vol. 114, pp. 521–529, 2014.

[303] W. Yuan, J. Shen, L. Li, X. Liu, and H. Zou, "Preparation of POSS-poly(ε-caprolactone)-β-cyclodextrin/Fe_3O_4 hybrid magnetic micelles for removal of bisphenol A from water," *Carbohydr. Polym.*, vol. 113, pp. 353–361, 2014.

[304] S. Yadav *et al.*, "Cationic Dye Removal Using Novel Magnetic/Activated Charcoal/β-Cyclodextrin/Alginate Polymer Nanocomposite," *Nanomaterials*, vol. 10, no. 1, p. 170, Jan. 2020.

[305] S. D. Richardson, "Water Analysis: Emerging Contaminants and Current Issues," *Anal. Chem*, vol. 75, no. 12, pp. 4295–4324, 2003.

[306] R. Loos, J. Wollgast, T. Huber, and G. Hanke, "Polar herbicides, pharmaceutical products, perfluorooctanesulfonate (PFOS), perfluorooctanoate (PFOA), and nonylphenol and its carboxylates and ethoxylates in surface and tap waters around Lake Maggiore in Northern Italy," *Anal. Bioanal. Chem.*, vol. 387, no. 4, pp. 1469–1478, 2007.

[307] J. Fick, H. Söderström, R. H. Lindberg, C. Phan, M. Tysklind, and D. G. J. Larsson, "Contamination of surface, ground, and drinking water from pharmaceutical production," *Environ. Toxicol. Chem.*, vol. 28, no. 12, pp. 2522–2527, 2009.

[308] J. L. Oaks *et al.*, "Diclofenac residues as the cause of vulture population decline in Pakistan," *Nature*, vol. 427, no. 6975, pp. 630–633, 2004.

[309] K. A. Kidd *et al.*, "Collapse of a fish population after exposure to a synthetic estrogen," *Proc. Natl. Acad. Sci. U. S. A.*, vol. 104, no. 21, pp. 8897–8901, 2007.

[310] F. Zhao *et al.*, "One-pot synthesis of trifunctional chitosan-EDTA-β-cyclodextrin polymer for simultaneous removal of metals and organic micropollutants /," *Sci. Rep.*, vol. 7, no. 1, pp. 1–14, 2017.

[311] V. K. Gupta, P. J. M. Carrott, M. M. L. Ribeiro Carrott, and Suhas, "Low-Cost adsorbents: Growing approach to wastewater treatmenta review," *Crit. Rev. Environ. Sci. Technol.*, vol. 39, no. 10, pp. 783–842, 2009.

[312] L. Jin, Q. Sun, Q. Xu, and Y. Xu, "Adsorptive removal of anionic dyes from aqueous solutions using microgel based on nanocellulose and polyvinylamine," *Bioresour.*

Technol., vol. 197, pp. 348–355, 2015.

[313] J. S. Hu, L. S. Zhong, W. G. Song, and L. J. Wan, "Synthesis of hierarchically structured metal oxides and their application in heavy metal ion removal," *Adv. Mater.*, vol. 20, no. 15, pp. 2977–2982, 2008.

[314] C. Zhang *et al.*, "Triptycene-Based Hyper-Cross-Linked Polymer Sponge for Gas Storage and Water Treatment," *Macromolecules*, vol. 48, no. 23, pp. 8509–8514, 2015.

[315] S. Villa, P. Riani, F. Locardi, and F. Canepa, "Functionalization of Fe_3O_4 NPs by silanization: Use of amine (APTES) and thiol (MPTMS) silanes and their physical characterization," *Materials (Basel).*, vol. 9, no. 10, 2016.

[316] S. Fourmentin and G. Crini, *Cyclodextrin Applications in Medicine, Food, Environment and Liquid Crystals*, vol. 17. 2018.

[317] T. F. Cova, D. Murtinho, A. A. C. C. Pais, and A. J. M. Valente, "Combining Cellulose and Cyclodextrins: Fascinating Designs for Materials and Pharmaceutics," *Front. Chem.*, vol. 6, no. July, pp. 1–19, 2018.

[318] N. B. Li, S. P. Liu, and H. Q. Luo, "Frequency doubling scattering and second-order scattering technology as novel methods for the determination of the inclusion constant of procaine hydrochloride to β-cyclodextrin," *Anal. Chim. Acta*, vol. 472, no. 1–2, pp. 89–98, 2002.

[319] B. H. Tan, K. C. Tam, Y. C. Lam, and C. B. Tan, "Dynamics and microstructure of charged soft nano-colloidal particles," *Polymer (Guildf).*, vol. 45, no. 16, pp. 5515–5523, 2004.

[320] R. A. Praphakar *et al.*, "A pH-sensitive guar gum-: Grafted -lysine-β-cyclodextrin drug carrier for the controlled release of 5-flourouracil into cancer cells," *J. Mater. Chem. B*, vol. 6, no. 10, pp. 1519–1530, 2018.

[321] J. Li, C. Chen, Y. Zhao, J. Hu, D. Shao, and X. Wang, "Synthesis of water-dispersible Fe_3O_4β-cyclodextrin by plasma-induced grafting technique for pollutant treatment," *Chem. Eng. J.*, vol. 229, pp. 296–303, 2013.

[322] I. Antoniuk and C. Amiel, "Cyclodextrin-Mediated Hierarchical Self-Assembly and Its Potential in Drug Delivery Applications," *J. Pharm. Sci.*, vol. 105, no. 9, pp. 2570–2588, 2016.

[323] F. Topuz and T. Uyar, "Cyclodextrin-functionalized mesostructured silica nanoparticles

for removal of polycyclic aromatic hydrocarbons," *J. Colloid Interface Sci.*, vol. 497, pp. 233–241, 2017.

[324] L. Szente, A. Singhal, A. Domokos, and B. Song, "Cyclodextrins: Assessing the impact of cavity size, occupancy, and substitutions on cytotoxicity and cholesterol homeostasis," *Molecules*, vol. 23, no. 5, pp. 1–15, 2018.

[325] M. Tarhini *et al.*, "Structured Magnetic Core/Silica Internal Shell Layer and Protein Out Layer Shell (BSA@SiO2@SME): Preparation and Characterization," *Chem. Africa*, vol. 3, no. 1, pp. 127–134, 2020.

[326] S. Indrajit, S. Banerjee, A. V. Ramchandran, K. E. Geckeler, and C. N. Murthy, "Synthesis of cyclodextrin and sugar-based oligomers for the efavirenz drug delivery," *Macromol. Symp.*, vol. 287, no. 1, pp. 51–59, 2010.

[327] X. Li, L. Xie, X. Yang, and X. Nie, "Adsorption behavior and mechanism of β-cyclodextrin-styrene-based polymer for cationic dyes," *RSC Adv.*, vol. 8, no. 70, pp. 40321–40329, 2018.

[328] R. Zhao, Y. Wang, X. Li, B. Sun, Z. Jiang, and C. Wang, "Water-insoluble sericin/β-cyclodextrin/PVA composite electrospun nanofibers as effective adsorbents towards methylene blue," *Colloids Surfaces B Biointerfaces*, vol. 136, pp. 375–382, 2015.

[329] D. M. Alzate-Sánchez *et al.*, "β-Cyclodextrin Polymers on Microcrystalline Cellulose as a Granular Media for Organic Micropollutant Removal from Water," *ACS Appl. Mater. Interfaces*, vol. 11, no. 8, pp. 8089–8096, 2019.

[330] A. Alsbaiee, B. J. Smith, L. Xiao, Y. Ling, D. E. Helbling, and W. R. Dichtel, "Rapid removal of organic micropollutants from water by a porous β-cyclodextrin polymer," *Nature*, vol. 529, no. 7585, pp. 190–194, 2016.

[331] K. Hemine, A. Skwierawska, A. Kernstein, and K. Kozłowska-Tylingo, "Cyclodextrin polymers as efficient adsorbents for removing toxic non-biodegradable pimavanserin from pharmaceutical wastewaters," *Chemosphere*, vol. 250, 2020.

[332] N. Ayawei, A. N. Ebelegi, and D. Wankasi, "Modelling and Interpretation of Adsorption Isotherms," *J. Chem.*, vol. 2017, pp. 1–11, 2017.

[333] K. A.-S. Bany-Aiesh, Hashem, Raid Banat, "Kinetics and Adsorption Isotherm of Ibuprofen onto Grafted [Beta]-CD/Chitosan Polymer," *Am. J. Appl. Sci.*, vol. 12, no. 12, 2015.

[334] T. H. Hansen *et al.*, "The effect of drinking water pH on the human gut microbiota and glucose regulation: results of a randomized controlled cross-over intervention," *Sci. Rep.*, vol. 8, no. 1, pp. 1–12, 2018.

[335] C. W. Pai, D. Leong, C. Y. Chen, and G. S. Wang, "Occurrences of pharmaceuticals and personal care products in the drinking water of Taiwan and their removal in conventional water treatment processes," *Chemosphere*, vol. 256, p. 127002, 2020.

[336] I. Ferrer and E. M. Thurman, "Analysis of Pharmaceuticals in Drinking Water, Groundwater, Surface Water, and Wastewater," in *Comprehensive Analytical Chemistry*, 2nd ed., vol. 62, Elsevier B.V., 2013, pp. 91–128.

[337] M. A. Al-Ghouti and R. S. Al-Absi, "Mechanistic understanding of the adsorption and thermodynamic aspects of cationic methylene blue dye onto cellulosic olive stones biomass from wastewater," *Sci. Rep.*, vol. 10, no. 1, pp. 1–18, 2020.

[338] H. I. Albroomi, M. A. Elsayed, A. Baraka, and M. A. Abdelmaged, "Batch and fixed-bed adsorption of tartrazine azo-dye onto activated carbon prepared from apricot stones," *Appl. Water Sci.*, vol. 7, no. 4, pp. 2063–2074, 2017.

[339] A. S. K. Kumar and S. J. Jiang, "Synthesis of magnetically separable and recyclable magnetic nanoparticles decorated with β-cyclodextrin functionalized graphene oxide an excellent adsorption of As(V)/(III)," *J. Mol. Liq.*, vol. 237, pp. 387–401, 2017.

[340] A. Glaria *et al.*, "Silica coated iron nanoparticles: Synthesis, interface control, magnetic and hyperthermia properties," *RSC Adv.*, vol. 8, no. 56, pp. 32146–32156, 2018.

[341] D. Sun, M. Babar Shahzad, M. Li, G. Wang, and D. Xu, "Antimicrobial materials with medical applications," *Mater. Technol.*, vol. 30, no. B2, pp. B90–B95, 2015.

[342] J. J. Reinosa, M. M. Rojo, A. Del Campo, M. Martín-González, and J. F. Fernández, "Highly Efficient Antimicrobial Ceramics Based on Electrically Charged Interfaces," *ACS Appl. Mater. Interfaces*, vol. 11, no. 42, pp. 39254–39262, 2019.

[343] W. Chen *et al.*, "Wool/Acrylic Blended Fabrics as Next-Generation Photodynamic Antimicrobial Materials," *ACS Appl. Mater. Interfaces*, vol. 11, no. 33, pp. 29557–29568, 2019.

[344] L. K. Ista *et al.*, "Conjugated-polyelectrolyte-grafted cotton fibers act as 'micro Flypaper' for the removal and destruction of bacteria," *ACS Appl. Mater. Interfaces*, vol. 3, no. 8, pp. 2932–2937, 2011.

[345] Shahid-Ul-Islam, M. Shahid, and F. Mohammad, “Green chemistry approaches to develop antimicrobial textiles based on sustainable biopolymers - A review,” *Ind. Eng. Chem. Res.*, vol. 52, no. 15, pp. 5245–5260, 2013.

[346] N. F. Kamaruzzaman *et al.*, “Antimicrobial Polymers: The Potential Replacement of Existing Antibiotics?,” *Int. J. Mol. Sci.*, vol. 20, no. 11, p. 2747, Jun. 2019.

[347] R. J. Turner, “Metal-based antimicrobial strategies,” *Microb. Biotechnol.*, vol. 10, no. 5, pp. 1062–1065, 2017.

[348] P. Peng, A. Hu, A. P. Gerlich, G. Zou, L. Liu, and Y. N. Zhou, “Joining of Silver Nanomaterials at Low Temperatures: Processes, Properties, and Applications,” *ACS Appl. Mater. Interfaces*, vol. 7, no. 23, pp. 12597–12618, 2015.

[349] D. Li, W. Fang, Y. Zhang, X. Wang, M. Guo, and X. Qin, “Stability and Thermal Conductivity Enhancement of Silver Nanofluids with Gemini Surfactants,” *Ind. Eng. Chem. Res.*, vol. 56, no. 43, pp. 12369–12375, 2017.

[350] M. M. Shahjamali, M. Salvador, M. Bosman, D. S. Ginger, and C. Xue, “Edge-gold-coated silver nanoprisms: Enhanced stability and applications in organic photovoltaics and chemical sensing,” *J. Phys. Chem. C*, vol. 118, no. 23, pp. 12459–12468, 2014.

[351] S. I. Mogal *et al.*, “Single-step synthesis of silver-doped titanium dioxide: Influence of silver on structural, textural, and photocatalytic properties,” *Ind. Eng. Chem. Res.*, vol. 53, no. 14, pp. 5749–5758, 2014.

[352] H. Homma, S. Harada, T. Ito, A. Kanda, and T. Nemoto, “Atypical Dearomative Spirocyclization of β-Naphthols with Diazoacetamides Using a Silver Catalyst,” *Org. Lett.*, vol. 22, no. 20, pp. 8132–8138, Oct. 2020.

[353] B. Tang, M. Zhang, X. Hou, J. Li, L. Sun, and X. Wang, “Coloration of cotton fibers with anisotropic silver nanoparticles,” *Ind. Eng. Chem. Res.*, vol. 51, no. 39, pp. 12807–12813, 2012.

[354] K. Miura, “Aquatic Risk Assessment of 2-Sulfonato Fatty Acid Methyl Ester Sodium Salt (MES),” *J. Oleo Sci.*, vol. 56, no. 3, pp. 123–128, 2007.

[355] J. Mo *et al.*, “Superior Performance of Ag over Pt for Hydrogen Evolution Reaction in Water Electrolysis under High Overpotentials,” *ACS Appl. Energy Mater.*, vol. 2, no. 2, pp. 1221–1228, 2019.

[356] H. S. H. M. Ali and S. A. Khan, “Stabilization of Various Zero-Valent Metal

Nanoparticles on a Superabsorbent Polymer for the Removal of Dyes, Nitrophenol, and Pathogenic Bacteria," *ACS Omega*, vol. 5, no. 13, pp. 7379–7391, 2020.

[357] S. Mukherjee *et al.*, "Silver Prussian Blue Analogue Nanoparticles: Rationally Designed Advanced Nanomedicine for Multifunctional Biomedical Applications," *ACS Biomater. Sci. Eng.*, vol. 6, no. 1, pp. 690–704, 2020.

[358] Q. H. Tran, V. Q. Nguyen, and A.-T. Le, "Corrigendum: Silver nanoparticles: synthesis, properties, toxicology, applications and perspectives," *Adv. Nat. Sci. Nanosci. Nanotechnol.*, vol. 9, no. 4, p. 049501, Dec. 2018.

[359] H. Xu and K. S. Suslick, "Water-Soluble Fluorescent Silver Nanoclusters," *Adv. Mater.*, vol. 22, no. 10, pp. 1078–1082, Jan. 2010.

[360] J. Liu, L. Liu, S. Li, Q. Kang, R. Zhang, and Z. Zhu, "Self-assembled nanogels of luminescent thiolated silver nanoclusters and chitosan as bactericidal agent and bacterial sensor," *Mater. Sci. Eng. C*, vol. 118, no. September 2020, p. 111520, 2021.

[361] B. J. Jankiewicz, D. Jamiola, J. Choma, and M. Jaroniec, "Silica-metal core-shell nanostructures," *Adv. Colloid Interface Sci.*, vol. 170, no. 1–2, pp. 28–47, 2012.

[362] P. Pati, S. McGinnis, and P. J. Vikesland, "Life Cycle Assessment of 'green' Nanoparticle Synthesis Methods," *Environ. Eng. Sci.*, vol. 31, no. 7, pp. 410–420, 2014.

[363] R. Sato-Berŕu, R. Redón, A. Vázquez-Olmos, and J. M. Saniger, "Silver nanoparticles synthesized by direct photoreduction of metal salts. Application in surface-enhanced Raman spectroscopy," *J. Raman Spectrosc.*, vol. 40, no. 4, pp. 376–380, 2009.

[364] S. Rathnakumar *et al.*, "Plasmon-Coupled Silver Nanoparticles for Mobile Phone-Based Attomolar Sensing of Mercury Ions," *ACS Appl. Nano Mater.*, vol. 4, no. 8, pp. 8066–8080, 2021.

[365] D. R. Mota, G. A. S. Lima, G. B. Helene, and D. S. Pellosi, "Tailoring Nanoparticle Morphology to Match Application: Growth under Low-Intensity Polychromatic Light Irradiation Governs the Morphology and Optical Properties of Silver Nanoparticles," *ACS Appl. Nano Mater.*, vol. 3, no. 5, pp. 4893–4903, 2020.

[366] C. Li, G. Chen, Y. Zhang, F. Wu, and Q. Wang, "Advanced fluorescence imaging technology in the near-infrared-II window for biomedical applications," *J. Am. Chem. Soc.*, vol. 142, no. 35, pp. 14789–14804, 2020.

[367] E. Falletta *et al.*, "Clusters of poly(acrylates) and silver nanoparticles: Structure and

applications for antimicrobial fabrics," *J. Phys. Chem. C*, vol. 112, no. 31, pp. 11758–11766, 2008.

[368] D. Wang *et al.*, "Coalescence of functional gold and monodisperse silver nanoparticles mediated by black Panax ginseng Meyer root extract," *Int. J. Nanomedicine*, vol. 11, no. December, pp. 6621–6634, 2016.

[369] K. Jyoti, M. Baunthiyal, and A. Singh, " Characterization of silver nanoparticles synthesized using Urtica dioica Linn. leaves and their synergistic effects with antibiotics ," *J. Radiat. Res. Appl. Sci.*, vol. 9, no. 3, pp. 217–227, 2016.

[370] S. Bhagyaraj and I. Krupa, "Alginate-Mediated Synthesis of Hetero-Shaped Silver Nanoparticles and Their Hydrogen Peroxide Sensing Ability," *Molecules*, vol. 25, no. 3, p. 435, Jan. 2020.

[371] D. G. Shchukin, I. L. Radtchenko, and G. B. Sukhorukov, "Photoinduced Reduction of Silver inside Microscale Polyelectrolyte Capsules," *ChemPhysChem*, vol. 4, no. 10, pp. 1101–1103, 2003.

[372] Y. Ding, J. Gao, X. Yang, J. He, Z. Zhou, and Y. Hu, "Preparation of water dispersible, fluorescent Ag-PAA-PVP hybrid nanogels and their optical properties," *Adv. Powder Technol.*, vol. 25, no. 1, pp. 244–249, 2014.

[373] K. E. Zhang JI, Xu SH, "Photogeneration of fluorescent silver nanoclusters in polymer microgels," *Adv. Mater.*, vol. 17, no. 19, pp. 2336–2340, 2005.

[374] H. Xu and K. S. Suslick, "Sonochemical synthesis of highly fluorescent Ag nanoclusters," *ACS Nano*, vol. 4, no. 6, pp. 3209–3214, 2010.

[375] N. G. Bastús, F. Merkoçi, J. Piella, and V. Puntes, "Synthesis of highly monodisperse citrate-stabilized silver nanoparticles of up to 200 nm: Kinetic control and catalytic properties," *Chem. Mater.*, vol. 26, no. 9, pp. 2836–2846, 2014.

[376] J. S. Kim *et al.*, "Antimicrobial effects of silver nanoparticles," *Nanomedicine Nanotechnology, Biol. Med.*, vol. 3, no. 1, pp. 95–101, 2007.

[377] J. Zheng and R. M. Dickson, "Individual water-soluble dendrimer-encapsulated silver nanodot fluorescence," *J. Am. Chem. Soc.*, vol. 124, no. 47, pp. 13982–13983, 2002.

[378] Q. Xu *et al.*, "Preparation of highly photoluminescent sulfur-doped carbon dots for Fe(iii) detection," *J. Mater. Chem. A*, vol. 3, no. 2, pp. 542–546, Nov. 2015.

[379] M. Das, H. Thakkar, D. Patel, and S. Thakore, "Repurposing the domestic organic waste

into green emissive carbon dots and carbonized adsorbent: A sustainable zero waste process for metal sensing and dye sequestration," *J. Environ. Chem. Eng.*, vol. 9, no. 5, p. 106312, 2021.

[380] N. Yan, S. Xie, B. Z. Tang, and W. X. Wang, "Real-time monitoring of the dissolution kinetics of silver nanoparticles and nanowires in aquatic environments using an aggregation-induced emission fluorogen," *Chem. Commun.*, vol. 54, no. 36, pp. 4585–4588, 2018.

[381] A. Henglein, T. Linnert, and P. Mulvaney, "Reduction of Ag + in Aqueous Polyanion Solution: Some Properties and Reactions of Long-Lived Oligomeric Silver Clusters and Metallic Silver Particles," *Berichte der Bunsengesellschaft für Phys. Chemie*, vol. 94, no. 12, pp. 1449–1457, Dec. 1990.

[382] J. Zhang, S. Xu, and E. Kumacheva, "Polymer Microgels: Reactors for Semiconductor, Metal, and Magnetic Nanoparticles," *J. Am. Chem. Soc.*, vol. 126, no. 25, pp. 7908–7914, Jun. 2004.

[383] S. K. Suh, K. Yuet, D. K. Hwang, K. W. Bong, P. S. Doyle, and T. A. Hatton, "Synthesis of nonspherical superparamagnetic particles: In situ coprecipitation of magnetic nanoparticles in microgels prepared by stop-flow lithography," *J. Am. Chem. Soc.*, vol. 134, no. 17, pp. 7337–7343, May 2012.

[384] S. M. Sreedharan and R. Singh, "Ciprofloxacin functionalized biogenic gold nanoflowers as nanoantibiotics aic bacterial strains against pathogen," *Int. J. Nanomedicine*, vol. 14, pp. 9905–9916, 2019.

[385] H. Janssens, L. Kim, I. Lee, and M. Salehzadeh, "Effect of varying temperature on the rate of CO2 production in baker's yeast (Saccharomyces cerevisiae)," *Expedition*, no. 5, 2015.

[386] F. N. Arroyo-López, S. Orlić, A. Querol, and E. Barrio, "Effects of temperature, pH and sugar concentration on the growth parameters of Saccharomyces cerevisiae, S. kudriavzevii and their interspecific hybrid," *Int. J. Food Microbiol.*, vol. 131, no. 2–3, pp. 120–127, 2009.

[387] N. Alissawi *et al.*, "Tuning of the ion release properties of silver nanoparticles buried under a hydrophobic polymer barrier," *J. Nanoparticle Res.*, vol. 14, no. 7, p. 928, Jul. 2012.

[388] L. Maretti, P. S. Billone, Y. Liu, and J. C. Scaiano, "Facile photochemical synthesis and

characterization of highly fluorescent silver nanoparticles," *J. Am. Chem. Soc.*, vol. 131, no. 39, pp. 13972–13980, 2009.

[389] T. C. Dakal, A. Kumar, R. S. Majumdar, and V. Yadav, "Mechanistic basis of antimicrobial actions of silver nanoparticles," *Front. Microbiol.*, vol. 7, no. NOV, pp. 1–17, 2016.

[390] Y. Li *et al.*, "Rational Design of Silver Gradient for Studying Size Effect of Silver Nanoparticles on Contact Killing," *ACS Biomater. Sci. Eng.*, vol. 5, no. 2, pp. 425–431, 2019.

[391] M. Ramasamy and J. Lee, "Recent Nanotechnology Approaches for Prevention and Treatment of Biofilm-Associated Infections on Medical Devices," *Biomed Res. Int.*, vol. 2016, pp. 1–17, 2016.

[392] E. I. Alarcon *et al.*, "The biocompatibility and antibacterial properties of collagen-stabilized, photochemically prepared silver nanoparticles," *Biomaterials*, vol. 33, no. 19, pp. 4947–4956, 2012.

[393] A. Taglietti *et al.*, "Antibacterial activity of glutathione-coated silver nanoparticles against gram positive and gram negative bacteria," *Langmuir*, vol. 28, no. 21, pp. 8140–8148, 2012.

[394] J. R. Morones *et al.*, "The bactericidal effect of silver nanoparticles," *Nanotechnology*, vol. 16, no. 10, pp. 2346–2353, 2005.

[395] E. Amato *et al.*, "Synthesis, characterization and antibacterial activity against gram positive and gram negative bacteria of biomimetically coated silver nanoparticles," *Langmuir*, vol. 27, no. 15, pp. 9165–9173, 2011.

[396] C. Liao, Y. Li, and S. Tjong, "Bactericidal and Cytotoxic Properties of Silver Nanoparticles," *Int. J. Mol. Sci.*, vol. 20, no. 2, p. 449, Jan. 2019.

[397] A. Roy, O. Bulut, S. Some, A. K. Mandal, and M. D. Yilmaz, "Green synthesis of silver nanoparticles: Biomolecule-nanoparticle organizations targeting antimicrobial activity," *RSC Adv.*, vol. 9, no. 5, pp. 2673–2702, 2019.

[398] H. Fu, J. Yuan, and H. Gao, "Microbial oxidative stress response: Novel insights from environmental facultative anaerobic bacteria," *Arch. Biochem. Biophys.*, vol. 584, pp. 28–35, 2015.

[399] S. Pal, Y. K. Tak, and J. M. Song, "Does the antibacterial activity of silver nanoparticles

depend on the shape of the nanoparticle? A study of the gram-negative bacterium Escherichia coli," *Appl. Environ. Microbiol.*, vol. 73, no. 6, pp. 1712–1720, 2007.

[400] M. K. Rai, S. D. Deshmukh, A. P. Ingle, and A. K. Gade, "Silver nanoparticles: The powerful nanoweapon against multidrug-resistant bacteria," *J. Appl. Microbiol.*, vol. 112, no. 5, pp. 841–852, 2012.

[401] Q. L. Feng, J. Wu, G. Q. Chen, F. Z. Cui, T. N. Kim, and J. O. Kim, "A mechanistic study of the antibacterial effect of silver ions on Escherichia coli and Staphylococcus aureus," *J. Biomed. Mater. Res.*, vol. 52, no. 4, pp. 662–668, 2000.

[402] M. R. Romero, N. A. Coser, M. A. Pérez, and C. G. Gomez, "Poly(N-isopropylacrylamide)-interpenetrated chitosan coils working as nanoreactors for controlled silver nanoparticle growth," *Carbohydr. Polym.*, vol. 288, no. March, p. 119374, 2022.

[403] Y. Ma, L. Shi, F. Liu, Y. Zhang, Y. Pang, and X. Shen, "Self-assembled thixotropic silver cluster hydrogel for anticancer drug release," *Chem. Eng. J.*, vol. 362, no. December 2018, pp. 650–657, 2019.

[404] Y. Xia, C. Cheng, R. Wang, C. Nie, J. Deng, and C. Zhao, "Ag-nanogel blended polymeric membranes with antifouling, hemocompatible and bactericidal capabilities," *J. Mater. Chem. B*, vol. 3, no. 48, pp. 9295–9304, 2015.

[405] I. Ali and V. K. Gupta, "Advances in water treatment by adsorption technology," *Nat. Protoc.*, vol. 1, no. 6, pp. 2661–2667, 2007.

[406] E. Farzad and H. Veisi, "Fe_3O_4/SiO2 nanoparticles coated with polydopamine as a novel magnetite reductant and stabilizer sorbent for palladium ions: Synthetic application of Fe_3O_4/SiO_2@PDA/Pd for reduction of 4-nitrophenol and Suzuki reactions," *J. Ind. Eng. Chem.*, vol. 60, pp. 114–124, 2018.

[407] T. T. Schug, A. Janesick, B. Blumberg, and J. J. Heindel, "Endocrine disrupting chemicals and disease susceptibility," *J. Steroid Biochem. Mol. Biol.*, vol. 127, no. 3–5, pp. 204–215, 2011.

[408] O. M. A. Faust, Samuel D., *Adsorption Processes for Water Treatment*. Elsevier, 2013.

[409] G. Crini and E. Lichtfouse, "Advantages and disadvantages of techniques used for wastewater treatment," *Environ. Chem. Lett.*, vol. 17, no. 1, pp. 145–155, 2019.

[410] S. Jiang, Y. Li, and B. P. Ladewig, "A review of reverse osmosis membrane fouling and

control strategies," *Sci. Total Environ.*, vol. 595, pp. 567–583, 2017.

[411] S. Sadri Moghaddam, M. R. Alavi Moghaddam, and M. Arami, "Coagulation/flocculation process for dye removal using sludge from water treatment plant: Optimization through response surface methodology," *J. Hazard. Mater.*, vol. 175, no. 1–3, pp. 651–657, 2010.

[412] K. N. Heck, S. Garcia-Segura, P. Westerhoff, and M. S. Wong, "Catalytic Converters for Water Treatment," *Acc. Chem. Res.*, vol. 52, no. 4, pp. 906–915, 2019.

[413] K. Zhang, C. Wang, Z. Rong, R. Xiao, Z. Zhou, and S. Wang, "Silver coated magnetic microflowers as efficient and recyclable catalysts for catalytic reduction," *New J. Chem.*, vol. 41, no. 23, pp. 14199–14208, 2017.

[414] P. Rodriguez, Y. Kwon, and M. T. M. Koper, "The promoting effect of adsorbed carbon monoxide on the oxidation of alcohols on a gold catalyst," *Nat. Chem.*, vol. 4, no. 3, pp. 177–182, 2012.

[415] N. Cheng *et al.*, "Platinum single-atom and cluster catalysis of the hydrogen evolution reaction," *Nat. Commun.*, vol. 7, pp. 1–9, 2016.

[416] B. Zugic *et al.*, "Dynamic restructuring drives catalytic activity on nanoporous gold-silver alloy catalysts," *Nat. Mater.*, vol. 16, no. 5, pp. 558–564, 2017.

[417] M. Ferrandon, "Mixed metal oxides-Noble metal catalysts for total oxidation of volatile organic compounds and carbon monoxide," Kemiteknik, 2001.

[418] J. X. Ma *et al.*, "Well-dispersed graphene-polydopamine-Pd hybrid with enhanced catalytic performance," *RSC Adv.*, vol. 5, no. 118, pp. 97520–97527, 2015.

[419] M. R. Feaviour and E. R. Schofield, "Scientific bases for the preparation of heterogeneous catalysts," *Platin. Met. Rev.*, vol. 51, no. 1, pp. 42–44, 2007.

[420] F. Paquin, J. Rivnay, A. Salleo, N. Stingelin, and C. Silva, "Multi-phase semicrystalline microstructures drive exciton dissociation in neat plastic semiconductors," *J. Mater. Chem. C*, vol. 3, pp. 10715–10722, 2015.

[421] X. Wu, Z. Shi, S. Fu, J. Chen, R. M. Berry, and K. C. Tam, "Strategy for synthesizing porous cellulose nanocrystal supported metal nanocatalysts," *ACS Sustain. Chem. Eng.*, vol. 4, no. 11, pp. 5929–5935, 2016.

[422] D. J. Merline, S. Vukusic, and A. A. Abdala, "Melamine formaldehyde: Curing studies and reaction mechanism," *Polym. J.*, vol. 45, no. 4, pp. 413–419, 2013.

[423] X. Wu, Z. Shi, S. Fu, J. Chen, R. M. Berry, and K. C. Tam, "Strategy for synthesizing

porous cellulose nanocrystal supported metal nanocatalysts," *ACS Sustain. Chem. Eng.*, vol. 4, no. 11, pp. 5929–5935, 2016.

[424] M. Mahdavi *et al.*, "Synthesis, surface modification and characterisation of biocompatible magnetic iron oxide nanoparticles for biomedical applications," *Molecules*, vol. 18, no. 7, pp. 7533–7548, 2013.

[425] T. B. Nguyen, C. P. Huang, and R. an Doong, "Enhanced catalytic reduction of nitrophenols by sodium borohydride over highly recyclable Au@graphitic carbon nitride nanocomposites," *Appl. Catal. B Environ.*, vol. 240, no. August 2018, pp. 337–347, 2019.

[426] Y. Y. Liu *et al.*, "High-efficient catalytic reduction of 4-nitrophenol based on reusable Ag nanoparticles/graphene-loading loofah sponge hybrid," *Nanotechnology*, vol. 29, no. 31, 2018.

[427] N. C. Antonels and R. Meijboom, "Preparation of well-defined dendrimer encapsulated ruthenium nanoparticles and their evaluation in the reduction of 4-nitrophenol according to the langmuir-hinshelwood approach," *Langmuir*, vol. 29, no. 44, pp. 13433–13442, 2013.

[428] S. Gu *et al.*, "Kinetic analysis of the catalytic reduction of 4-nitrophenol by metallic nanoparticles," *J. Phys. Chem. C*, vol. 118, no. 32, pp. 18618–18625, 2014.

[429] X. Kong, H. Zhu, C. Le Chen, G. Huang, and Q. Chen, "Insights into the reduction of 4-nitrophenol to 4-aminophenol on catalysts," *Chem. Phys. Lett.*, vol. 684, pp. 148–152, 2017.

[430] S. Wunder, Y. Lu, M. Albrecht, and M. Ballauff, "Catalytic activity of faceted gold nanoparticles studied by a model reaction: Evidence for substrate-induced surface restructuring," *ACS Catal.*, vol. 1, no. 8, pp. 908–916, 2011.

[431] R. Ciganda *et al.*, "Gold nanoparticles as electron reservoir redox catalysts for 4-nitrophenol reduction: A strong stereoelectronic ligand influence," *Chem. Commun.*, vol. 50, no. 70, pp. 10126–10129, 2014.

[432] Y. S. Seo *et al.*, "Catalytic reduction of 4-nitrophenol with gold nanoparticles synthesized by caffeic acid," *Nanoscale Res. Lett.*, vol. 12, no. 1, p. 7, Dec. 2017.

[433] R. D. Neal, Y. Inoue, R. A. Hughes, and S. Neretina, "Catalytic Reduction of 4-Nitrophenol by Gold Catalysts: The Influence of Borohydride Concentration on the Induction Time," *J. Phys. Chem. C*, vol. 123, no. 20, pp. 12894–12901, 2019.

[434] A. Liopo, S. Wang, P. J. Derry, A. A. Oraevsky, and E. R. Zubarev, “Seedless synthesis of gold nanorods using dopamine as a reducing agent,” *RSC Adv.*, vol. 5, no. 111, pp. 91587–91593, 2015.

[435] H. N. Abdelhamid, “A review on hydrogen generation from the hydrolysis of sodium borohydride,” *Int. J. Hydrogen Energy*, vol. 46, no. 1, pp. 726–765, 2021.

[436] Z. Dong, X. Le, C. Dong, W. Zhang, X. Li, and J. Ma, “Ni@Pd core-shell nanoparticles modified fibrous silica nanospheres as highly efficient and recoverable catalyst for reduction of 4-nitrophenol and hydrodechlorination of 4-chlorophenol,” *Appl. Catal. B Environ.*, vol. 162, pp. 372–380, 2015.

[437] X. Wu, C. Lu, W. Zhang, G. Yuan, R. Xiong, and X. Zhang, “A novel reagentless approach for synthesizing cellulose nanocrystal-supported palladium nanoparticles with enhanced catalytic performance,” *J. Mater. Chem. A*, vol. 1, no. 30, pp. 8645–8652, 2013.

[438] X. Le *et al.*, “Palladium nanoparticles immobilized on core-shell magnetic fibers as a highly efficient and recyclable heterogeneous catalyst for the reduction of 4-nitrophenol and Suzuki coupling reactions,” *J. Mater. Chem. A*, vol. 2, no. 46, pp. 19696–19706, 2014.

[439] C. Wang *et al.*, “Preparation of Palladium Nanoparticles Decorated Polyethyleneimine/Polycaprolactone Composite Fibers Constructed by Electrospinning with Highly Efficient and Recyclable Catalytic Performances,” *Catalysts*, vol. 9, no. 6, p. 559, Jun. 2019.

[440] Z. Zhang *et al.*, “Encapsulating Pd nanoparticles in double-shelled graphene@carbon hollow Spheres for excellent chemical catalytic property,” *Sci. Rep.*, vol. 4, pp. 1–5, 2014.

[441] A. K. Sharma, H. Joshi, and A. K. Singh, “Catalysis with magnetically retrievable and recyclable nanoparticles layered with Pd(0) for C-C/C-O coupling in water,” *RSC Adv.*, vol. 10, no. 11, pp. 6452–6459, 2020.

[442] J. Shen, Y. Zhou, S. Li, P. Gu, and G. Xue, “Hydrogel-coated Fe_3O_4 nanoparticles as an efficient heterogeneous Fenton catalyst for degradation of phenol,” *J. Mater. Sci.*, vol. 54, no. 15, pp. 10684–10694, 2019.

[443] M. F. Rahman, S. Peldszus, and W. B. Anderson, “Behaviour and fate of perfluoroalkyl and polyfluoroalkyl substances (PFASs) in drinking water treatment: A review,” *Water Res.*, vol. 50, pp. 318–340, 2014.

[444] K. Steenland, T. Fletcher, and D. A. Savitz, “Epidemiologic evidence on the health effects of perfluorooctanoic acid (PFOA),” *Environ. Health Perspect.*, vol. 118, no. 8, pp. 1100–1108, 2010.

[445] V. Franke, P. McCleaf, K. Lindegren, and L. Ahrens, “Efficient removal of per- And polyfluoroalkyl substances (PFASs) in drinking water treatment: Nanofiltration combined with active carbon or anion exchange,” *Environ. Sci. Water Res. Technol.*, vol. 5, no. 11, pp. 1836–1843, 2019.

[446] L. Ahrens and M. Bundschuh, “Fate and effects of poly- and perfluoroalkyl substances in the aquatic environment: A review,” *Environ. Toxicol. Chem.*, vol. 33, no. 9, pp. 1921–1929, 2014.

[447] A. Östlund, “Removal Efficiency of Perfluoroalkyl Substances (PFASs) in Drinking Water dissolved organic carbon,” 2015.

[448] M. Sun *et al.*, “Legacy and Emerging Perfluoroalkyl Substances Are Important Drinking Water Contaminants in the Cape Fear River Watershed of North Carolina,” *Environ. Sci. Technol. Lett.*, vol. 3, no. 12, pp. 415–419, 2016.

[449] N. A. Lundquist *et al.*, “Polymer Supported Carbon for Safe and Effective Remediation of PFOA- and PFOS-Contaminated Water,” *ACS Sustain. Chem. Eng.*, vol. 7, no. 13, pp. 11044–11049, Jul. 2019.

[450] H. Wan *et al.*, “Gravity-driven electrospun membranes for effective removal of perfluoro-organics from synthetic groundwater,” *J. Memb. Sci.*, vol. 644, no. November 2021, p. 120180, Feb. 2022.

[451] N. Grishkewich *et al.*, “Dye Removal Using Sustainable Membrane Adsorbents Produced from Melamine Formaldehyde-Cellulose Nanocrystals and Hard Wood Pulp,” *Ind. Eng. Chem. Res.*, vol. 59, no. 47, pp. 20854–20865, 2020.

[452] K. H. Chu, “Improved fixed bed models for metal biosorption,” *Chem. Eng. J.*, vol. 97, no. 2–3, pp. 233–239, 2004.

[453] J. Cruz-Olivares, C. Pérez-Alonso, C. Barrera-Díaz, F. Ureña-Nuñez, M. C. Chaparro-Mercado, and B. Bilyeu, “Modeling of lead (II) biosorption by residue of allspice in a fixed-bed column,” *Chem. Eng. J.*, vol. 228, pp. 21–27, 2013.

[454] A. Abdolali *et al.*, “Application of a breakthrough biosorbent for removing heavy metals from synthetic and real wastewaters in a lab-scale continuous fixed-bed column,”

Bioresour. Technol., vol. 229, pp. 78–87, 2017.

[455] L. T. Teixeira, W. F. Braz, R. N. Correia de Siqueira, O. G. Pandoli, and M. C. Geraldes, "Sulfated and carboxylated nanocellulose for Co+2 adsorption," *J. Mater. Res. Technol.*, vol. 15, pp. 434–447, 2021.

[456] Y. T. Hameed, A. Idris, S. A. Hussain, and N. Abdullah, "A tannin-based agent for coagulation and flocculation of municipal wastewater: Chemical composition, performance assessment compared to Polyaluminum chloride, and application in a pilot plant," *J. Environ. Manage.*, vol. 184, pp. 494–503, 2016.

[457] Y. Wu, J. Wu, F. Yang, C. Tang, and Q. Huang, "Effect of H2O2 bleaching treatment on the properties of finished transparent wood," *Polymers (Basel).*, vol. 11, no. 5, pp. 1–13, 2019.

[458] I. Kalashnikova, H. Bizot, B. Cathala, and I. Capron, "Modulation of cellulose nanocrystals amphiphilic properties to stabilize oil/water interface," *Biomacromolecules*, vol. 13, no. 1, pp. 267–275, 2012.

[459] W. Wang, G. Du, C. Li, H. Zhang, Y. Long, and Y. Ni, "Preparation of cellulose nanocrystals from asparagus (Asparagus officinalis L.) and their applications to palm oil/water Pickering emulsion," *Carbohydr. Polym.*, vol. 151, pp. 1–8, 2016.

[460] H. Dai *et al.*, "Recent advances on cellulose nanocrystals for Pickering emulsions: Development and challenge," *Trends Food Sci. Technol.*, vol. 102, no. 2, pp. 16–29, 2020.

[461] S. Noreen, H. N. Bhatti, S. Nausheen, S. Sadaf, and M. Ashfaq, "Batch and fixed bed adsorption study for the removal of Drimarine Black CL-B dye from aqueous solution using a lignocellulosic waste: A cost affective adsorbent," *Ind. Crops Prod.*, vol. 50, pp. 568–579, 2013.

[462] J. Bortoluz, F. Ferrarini, L. R. Bonetto, J. da Silva Crespo, and M. Giovanela, "Use of low-cost natural waste from the furniture industry for the removal of methylene blue by adsorption: isotherms, kinetics and thermodynamics," *Cellulose*, vol. 27, no. 11, pp. 6445–6466, 2020.

[463] M. G. Bisheh, M. Ghorbani, M. Peyravi, and M. Jahanshahi, "Static and dynamic filtration of nickel and lead ions by adsorptive membrane induced by POP via layer by layer technique," *Chem. Eng. Res. Des.*, vol. 153, pp. 829–838, 2020.

[464] Q. Wu *et al.*, "Multiple active sites cellulose-based adsorbent for the removal of low-level

Cu(II), Pb(II) and Cr(VI) via multiple cooperative mechanisms," *Carbohydr. Polym.*, vol. 233, no. November 2019, p. 115860, Apr. 2020.

[465] W. Zhan, C. Xu, G. Qian, G. Huang, X. Tang, and B. Lin, "Adsorption of Cu(ii), Zn(ii), and Pb(ii) from aqueous single and binary metal solutions by regenerated cellulose and sodium alginate chemically modified with polyethyleneimine," *RSC Adv.*, vol. 8, no. 33, pp. 18723–18733, 2018.

[466] Y. Xiao, W. Huang, K. Xu, M. Li, M. Fan, and K. Wang, "Preparation of anion exchange membrane with branch polyethyleneimine as main skeleton component," *Mater. Des.*, vol. 160, pp. 698–707, 2018.

[467] X. Yang and L. A. Berglund, "Structural and Ecofriendly Holocellulose Materials from Wood: Microscale Fibers and Nanoscale Fibrils," *Adv. Mater.*, vol. 33, no. 28, p. 2001118, Jul. 2021.

[468] W. Meesorn, A. Shirole, D. Vanhecke, L. M. De Espinosa, and C. Weder, "A Simple and Versatile Strategy to Improve the Mechanical Properties of Polymer Nanocomposites with Cellulose Nanocrystals," *Macromolecules*, vol. 50, no. 6, pp. 2364–2374, 2017.

[469] E. Limousin, I. Rafaniello, T. Schäfer, N. Ballard, and J. M. Asua, "Linking Film Structure and Mechanical Properties in Nanocomposite Films Formed from Dispersions of Cellulose Nanocrystals and Acrylic Latexes," *Langmuir*, vol. 36, no. 8, pp. 2052–2062, 2020.

[470] X. Yang, F. Berthold, and L. A. Berglund, "Preserving Cellulose Structure: Delignified Wood Fibers for Paper Structures of High Strength and Transparency," *Biomacromolecules*, vol. 19, no. 7, pp. 3020–3029, 2018.

[471] J. Wang, A. Cahyadi, B. Wu, W. Pee, A. G. Fane, and J. W. Chew, "The roles of particles in enhancing membrane filtration: A review," *J. Memb. Sci.*, vol. 595, no. September 2019, p. 117570, Feb. 2020.

[472] M. Riazi, A. R. Keshtkar, and M. A. Moosavian, "Biosorption of Th(IV) in a fixed-bed column by Ca-pretreated Cystoseira indica," *J. Environ. Chem. Eng.*, vol. 4, no. 2, pp. 1890–1898, 2016.

[473] M. A. Acheampong, K. Pakshirajan, A. P. Annachhatre, and P. N. L. Lens, "Removal of Cu(II) by biosorption onto coconut shell in fixed-bed column systems," *J. Ind. Eng. Chem.*, vol. 19, no. 3, pp. 841–848, 2013.

List of Appendices

Appendix 3-1 The TEM images of 20:80 MAA-EA (8 wt% DAP check) at pH 4 (k, l), pH 7 (m, n), pH 10 (o, p), the TEM images of 50:50 MAA-EA at pH 4 (q, r), pH 7 (s, t) and pH 10 (u, v) 373

Appendix 4-1 Silica shell thickness distribution of Si-40-MNP (A); Si-50-MNP (B); Si-100-MNP (C); Si-150-MNP (D); Si-200-MNP (E); summary of average thickness of Si-MNPs (F) 374

Appendix 4-2 The summary size distribution (by number) of nanogel, MNP, Si-40-MNP and FMNP at pH 6 374

Appendix 6-1 Zeta average radius and zeta potential of AgNCs with different UV irradiation time 374

Appendix 6-2 The UV curve (focused on the wavelength between 400 and 700 nm) of AgNCs under 0, 3, 6, 15, 40, 80, 120, 160, 200, 240, 280, 320 and 360 min of UV irradiation 375

Appendix 6-3 The fluorescence UV spectrum of Ag clusters (excitation at 275 nm, and emission at 520 nm), (B) the florescence intensity of Ag cluster and the photoluminescence 375

Appendix 6-4 The emission curve of quinine sulphate (A) and its corresponding integration peak (B); The emission curves of AgNCs (C) and its corresponding integration peaks (D) 376

Appendix 6-5 Silver ion titration results of pure nanogel solution 377

Appendix 6-6 Silver ion titration results of $AgNO_3$ solution 377

Appendix 6-7 Silver ion titration results of Ag^+ incorporated nanogel (after dialysis in the dark) 378

Appendix 6-8 Manual setup of silver electrode analysis 378

Appendix 6-9 Calibration curve (A), measured value of AgNCs@25min system versus time (B), log[Ag^+] versus time (C) and [Ag^+] versus time (D) 379

Appendix 6-10 Experimental set-up of yeast test 379

Appendix 6-11 Yeast test with different concentration of Ag-clusters obtained with different UV irradiation time, a: Ag-clusters 360min UV @pH5 and pH 8, b: AgNCs@0min, c: AgNCs@6min, d: AgNCs@25min, e: AgNCs@40min, f: AgNCs@80min, g: AgNCs@200min, h: AgNCs@360min UV irradiation 380

Appendix 6-12 The CO_2 production rate (ml/min) of yeast with AgNCs obtained with different UV irradiation time, a: AgNCs@360min UV @pH5 and pH 8, b: AgNCs@0min UV, c:

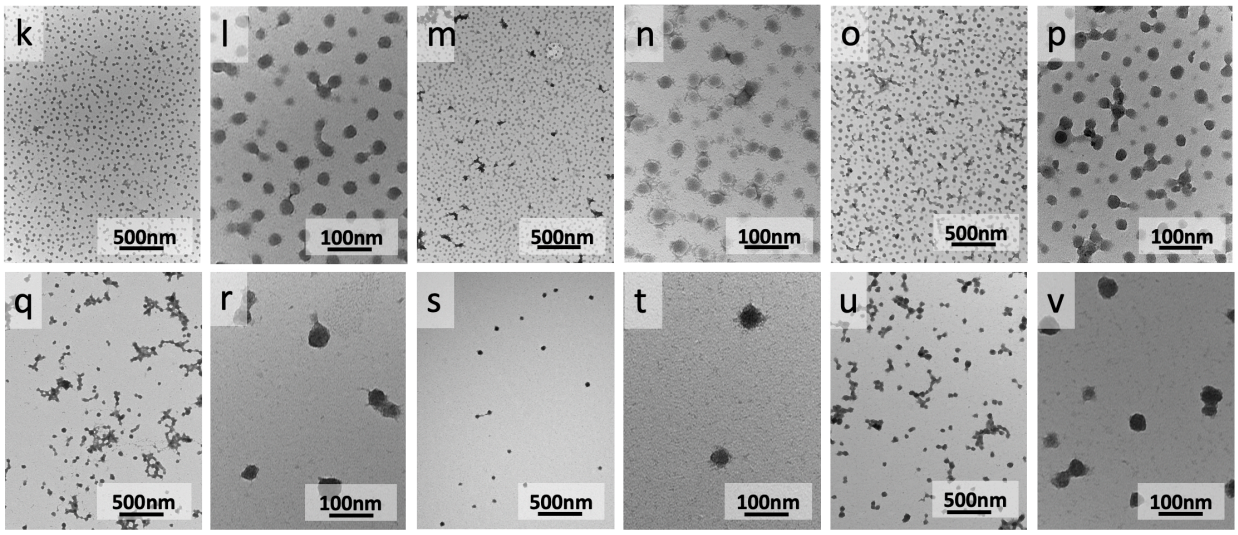
AgNCs@6min UV, d: AgNCs@25min UV, e: AgNCs@40min UV, f: AgNCs@80min UV, g: AgNCs@200min UV, h: AgNCs@360min UV 381
Appendix 6-13 Microscopic image of 8%DAP nanogel treated yeast test sample dyed with MB (washed 2 times) a, b. AgNCs@6min-1.1 ppm yeast test sample dyed with MB c, d. AgNCs@6min-11 ppm yeast test sample dyed with MB e, f, g. AgNCs@0min h, i. AgNCs@ 25min UV j. AgNCs@ 6h UV k, l 382
Appendix 6-14 TEM image of yeast test and antimicrobial test sample, yest test with AgNCs@40min (1-4), E·coli with nanogel (5), AgNCs@0min (6), AgNCs@25min (7), AgNCs@360min(8), S·aureus with nanogel (9), AgNCs@0min (10), AgNCs@25min (11), AgNCs@360min(12) 383
Appendix 7-1 TEM image of Fe-Pd-MC (a, b), 10mg Pd-PDC with extra dopamine (c), 1ml MNP-Pd-MC (d, e), 3ml MNP-Pd-MC (f, g), 4ml MNP-Pd-MC (h, i), 5ml MNP-Pd-MC (j) 384
Appendix 7-2 Summary of catalytic reaction rate of four different catalyst: Fe-Pd-MC, 2ml MNP Pd-MC, Fe-Pd-PDC and 2ml MNP Pd-PDC catalyst 384
Appendix 7-3 Catalytic test with 4-NP by using Fe-Pd-MC (A), 2ml MNP Pd-MC (B), Fe-Pd-PDC (C) and 2ml MNP Pd-PDC catalyst (D) 385
Appendix 7-4 Catalytic performance of 1ml MNP Pd-PDC, 2ml MNP Pd-PDC, 3ml MNP Pd-PDC, 4ml MNP-Pd-PDC, 5ml MNP Pd-MNP 386
Appendix 7-5 The remaining concentration of 4-NP versus catalytic reaction time by using 5, 10, 15 mg Pd-PDC and 10mg Pd-PDC with extra dopamine (A), 4-NP degradation rate by using 5, 10, 15 mg Pd-PDC and 10mg Pd-PDC with extra dopamine (B) 386
Appendix 7-6 The size distribution of 5-Pd-PDC (A), 10-Pd-PDC (B), 15-Pd-PDC (C), 10-Pd-PDC+PDA (D) and Pd-MF-CNC (E) obtained by TEM analysis with Image J 386
Appendix 7-7 The magnetic hysteresis loops of MNP measured by SQUID at 300 K between -1T and 1T 387
Appendix 8-1 Equipment and process images of the membrane fabrication process 387
Appendix 8-2 TF-CNC hexane emulsion (0.1-1.5,2wt%) Hexane : TF-CNC = 1:2 387
Appendix 8-3 Titration results of WGP-110.2-EM45, WGP-110.5-EM45, WGP-111-EM45, WGP-111-EM0, WGP-111.5-EM45, WGP-111.5-EM0 388
Appendix 8-4 Low magnification SEM images of PEI mass ratio effect on membrane structure (PEI:WF= 0, 0.1, 0.5, 1.0, 1.5) 388

Appendix 8-5 SEM images of WGP-111-EM0, WGP-110.5-EM45, WGP-111-EM45, WGP-111-EM85, and WGP-111-EM120 389
Appendix 8-6 q_c integration with various MO initial concentration 389
Appendix 8-7 q_c integration with various pressure drop (flowrate) 390
Appendix 8-8 q_c integration with various number loaded to the column filtration system 390

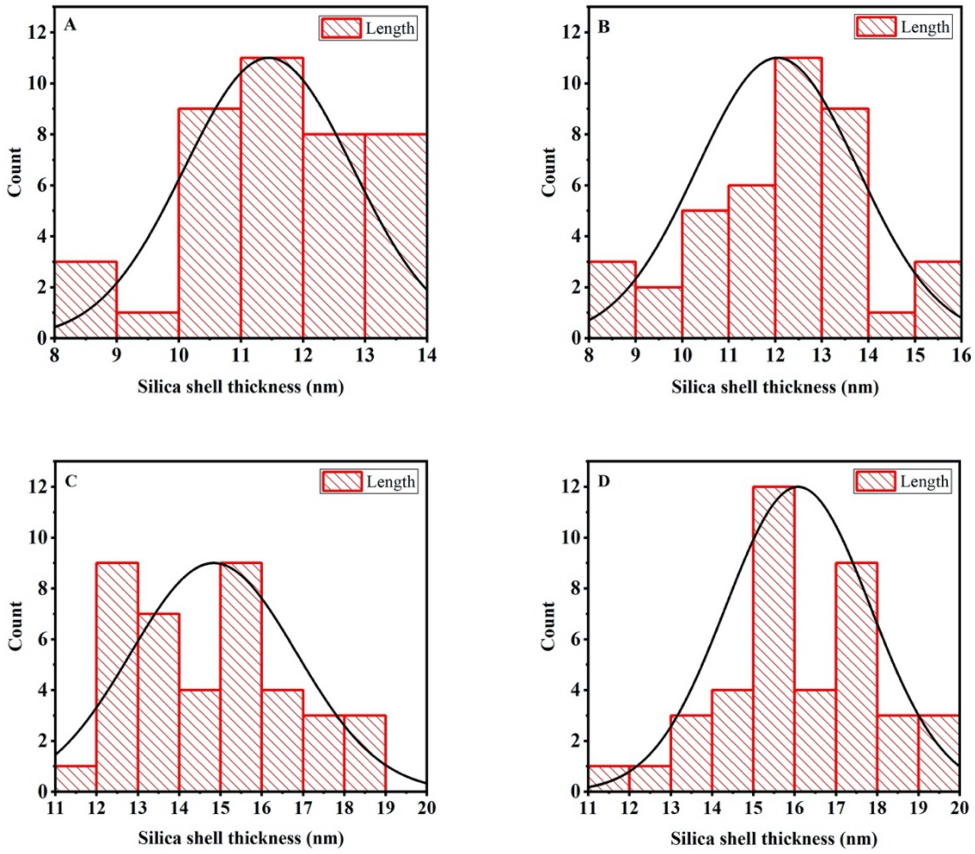
Appendix

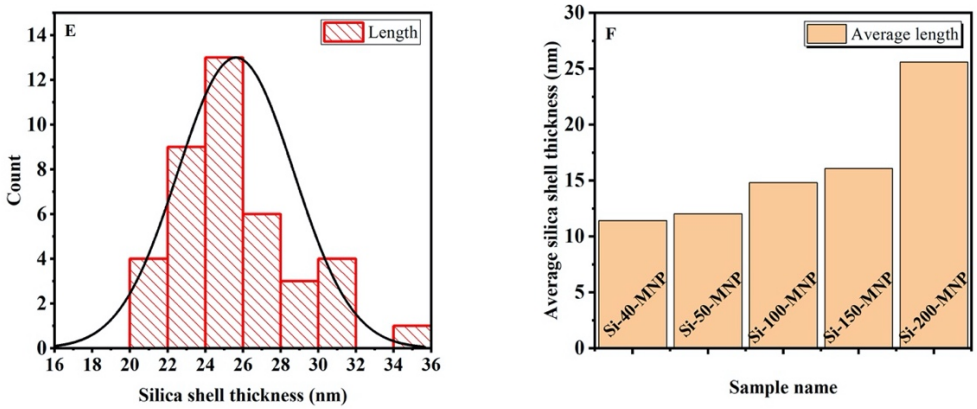
Figure 2-1	Open access (OA)
Figure 2-2	5343970166601
Figure 2-3	OA
Figure 2-4	OA
Figure 2-5	OA
Figure 2-6	Ref [3] ACS permission
Figure 2-7	1245667-1
Figure 2-8	5344280155546
Figure 2-9	5344280155546
Figure 2-10	Ref [78] ACS permission
Figure 2-11	Ref [80] ACS permission
Figure 2-12	Ref [84] ACS permission
Figure 2-13	5344300100119
Figure 2-14	Ref [95]
Figure 2-15	https://www.lacsd.org/home/showpublisheddocument/3578/637644521003970000
Figure 2-16	Self-drawn
Figure 2-17	OA
Figure 2-18	OA
Figure 2-19	1245667-1
Figure 2-20	OA
Figure 2-21	Self-drawn
Figure 2-22	5344420539481
Figure 2-23	Ref [161] ACS permission
Figure 2-24	Ref [163] ACS permission
Figure 2-25	5344460060725
Figure 2-26	5344470342988
Figure 2-27	5344470756552
Figure 2-28	OA
Figure 2-29	5344480067673
Figure 2-30	5344480067673
Figure 2-31	5344480610733
Figure 2-32	5344481105527
Figure 2-33	5344481311151
Figure 2-34	5344490288956
Figure 2-35	Ref [236] ACS permission

Appendix 2-1 Summary of rights and permission licence for the reprinted figures

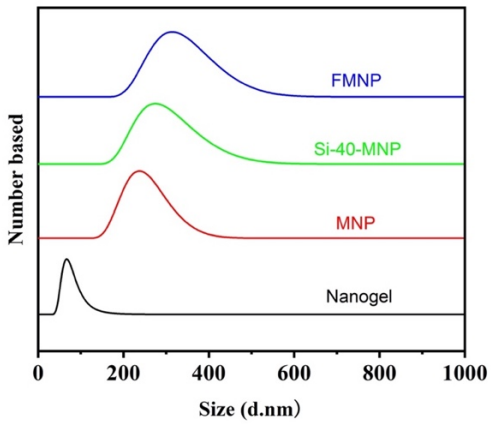


Appendix 3-1 The TEM images of 20:80 MAA-EA (8 wt% DAP check) at pH 4 (k, l), pH 7 (m, n), pH 10 (o, p), the TEM images of 50:50 MAA-EA at pH 4 (q, r), pH 7 (s, t) and pH 10 (u, v)

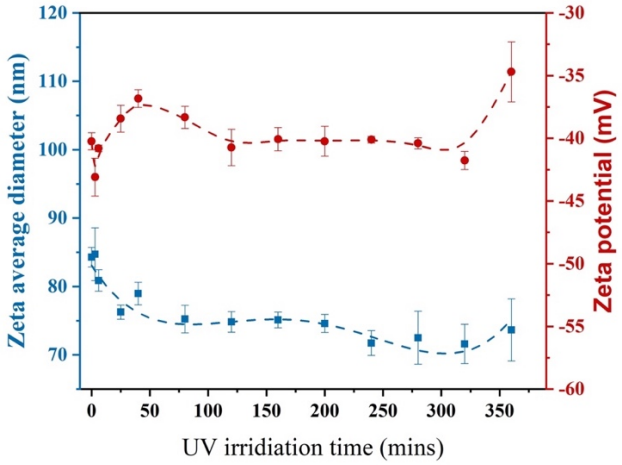




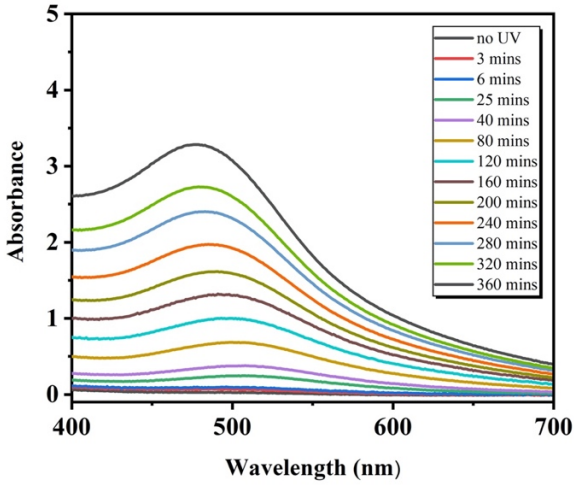
Appendix 4-1 Silica shell thickness distribution of Si-40-MNP (A); Si-50-MNP (B); Si-100-MNP (C); Si-150-MNP (D); Si-200-MNP (E); summary of average thickness of Si-MNPs (F)



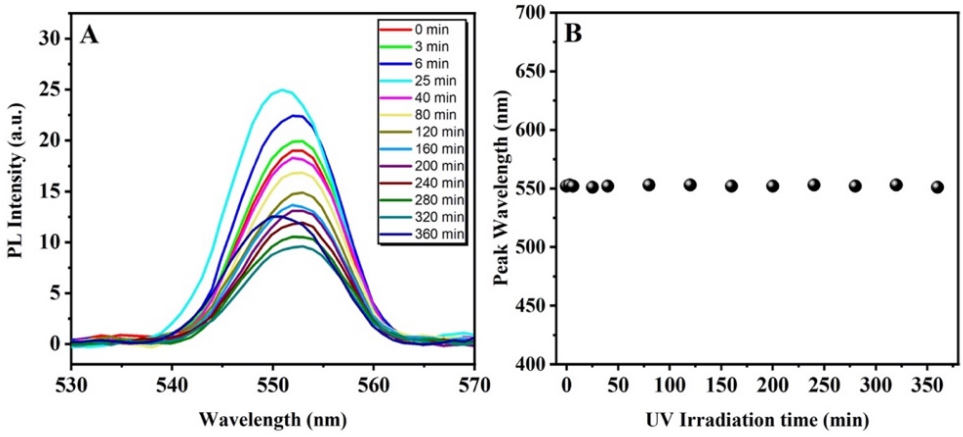
Appendix 4-2 The summary size distribution (by number) of nanogel, MNP, Si-40-MNP and FMNP at pH 6



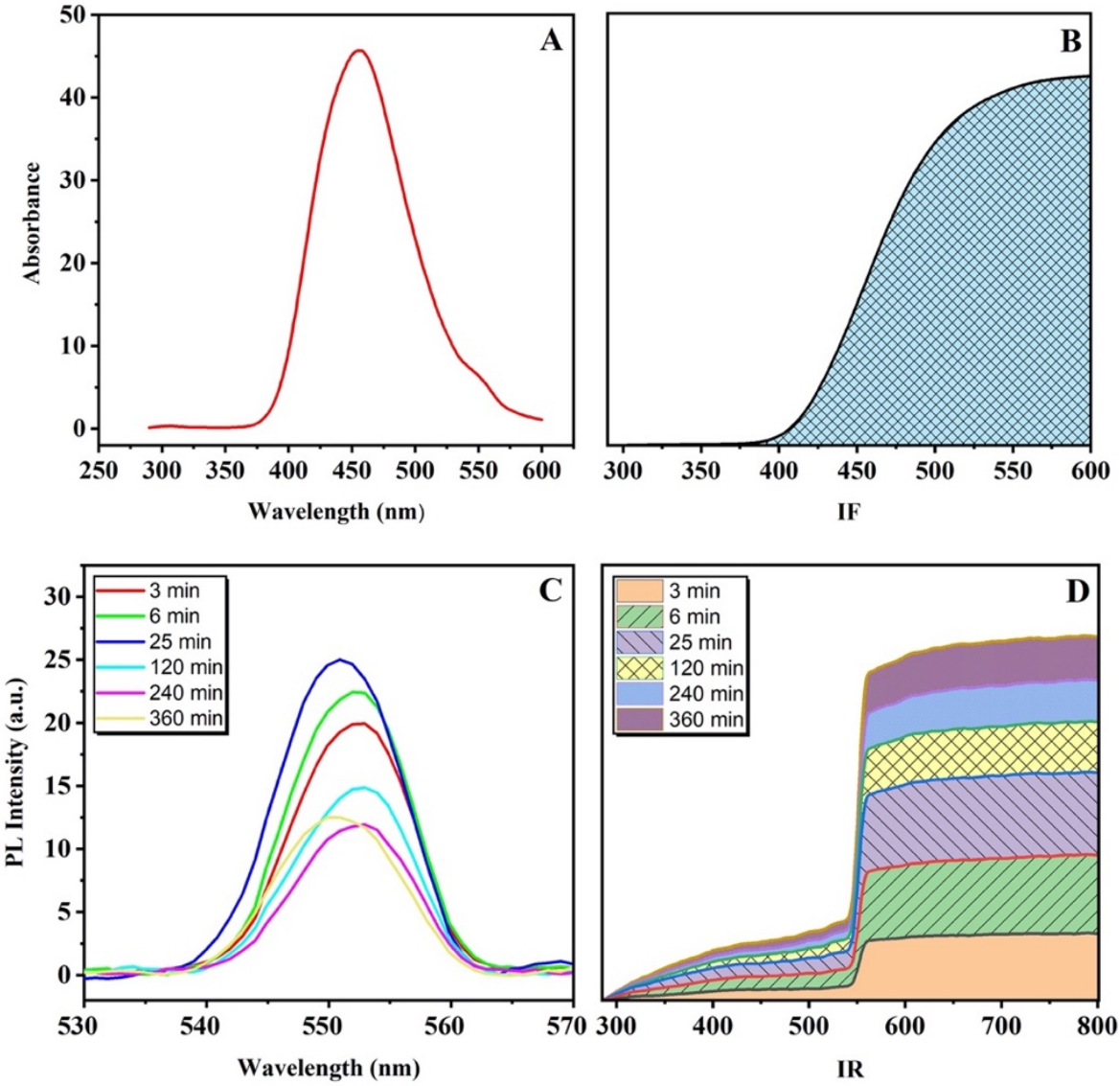
Appendix 6-1 Zeta average radius and zeta potential of AgNCs with different UV irradiation time



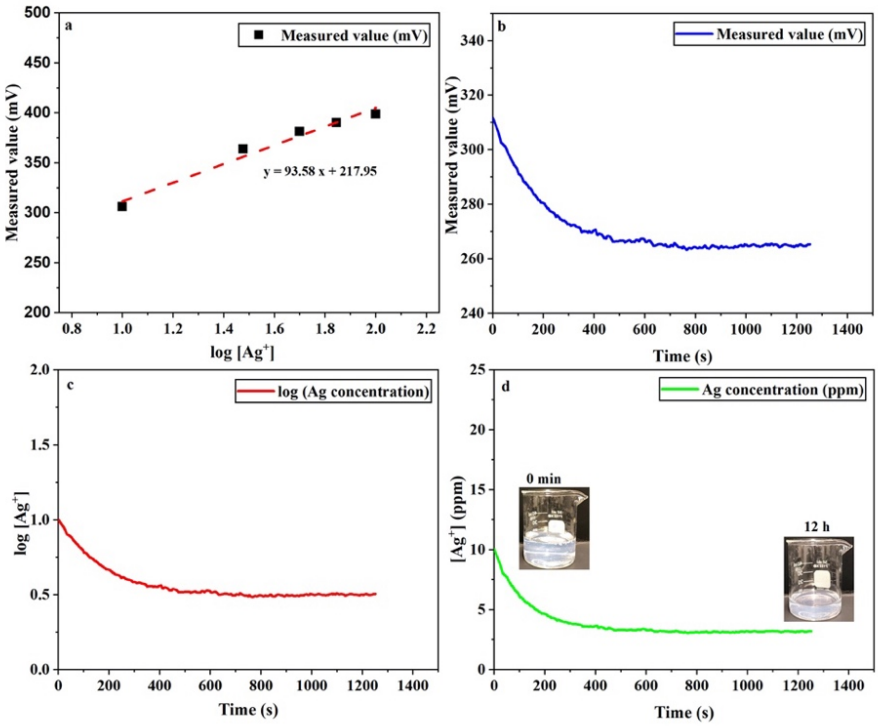
Appendix 6-2 The UV curve (focused on the wavelength between 400 and 700 nm) of AgNCs under 0, 3, 6, 15, 40, 80, 120, 160, 200, 240, 280, 320 and 360 min of UV irradiation



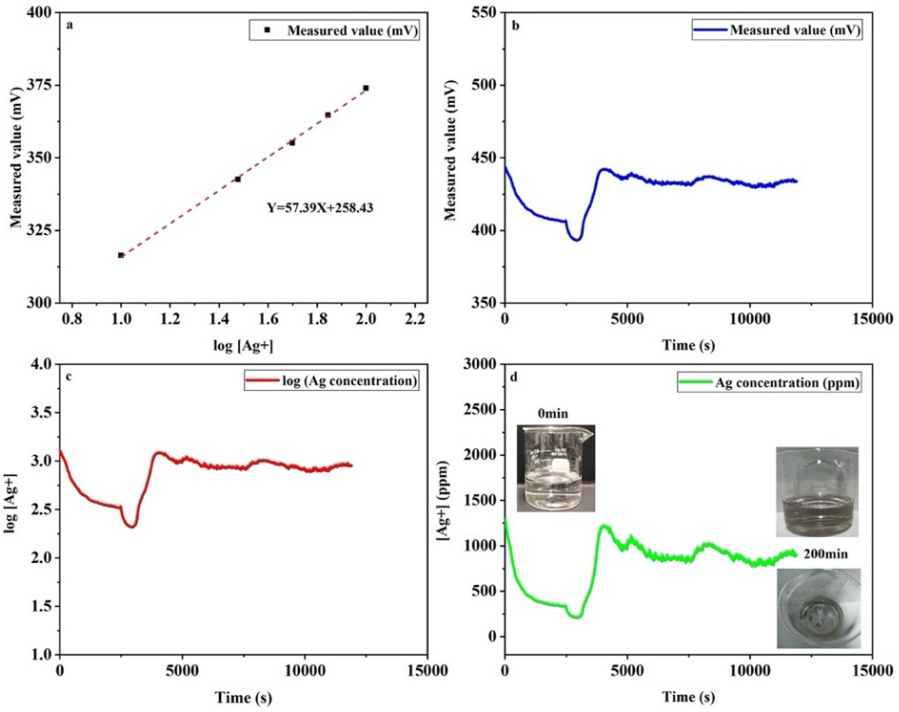
Appendix 6-3 The fluorescence UV spectrum of Ag clusters (excitation at 275 nm, and emission at 520 nm), (B) the florescence intensity of Ag cluster and the photoluminescence



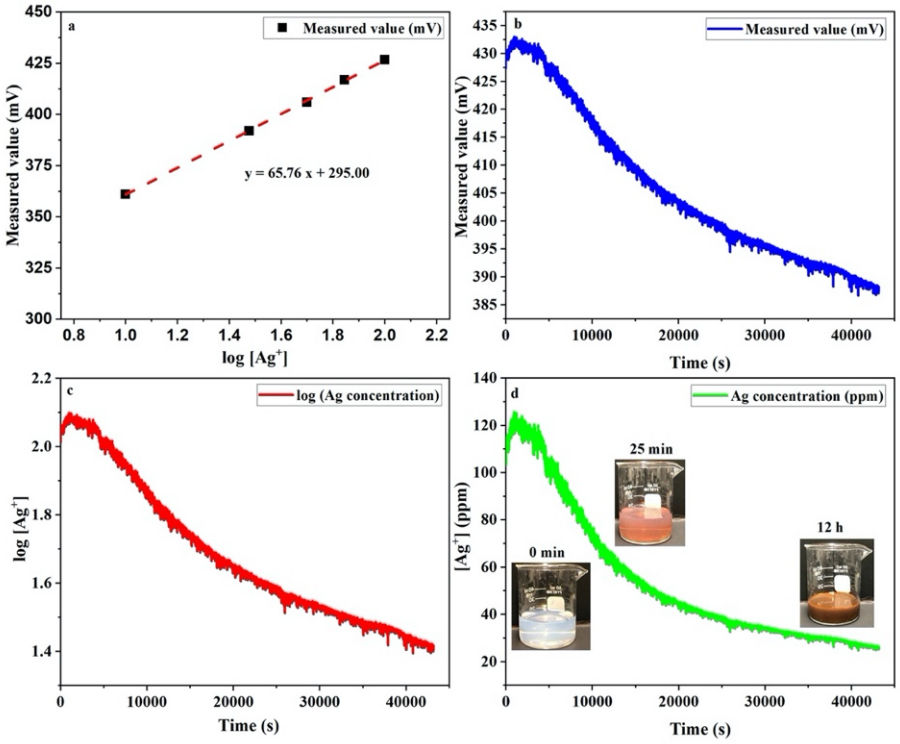
Appendix 6-4 The emission curve of quinine sulphate (A) and its corresponding integration peak (B); The emission curves of AgNCs (C) and its corresponding integration peaks (D)



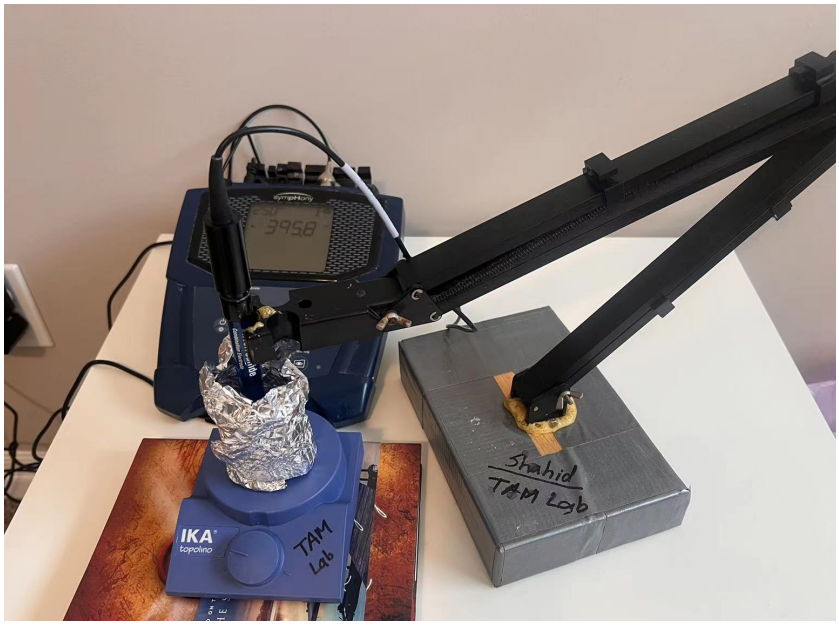
Appendix 6-5 Silver ion titration results of pure nanogel solution



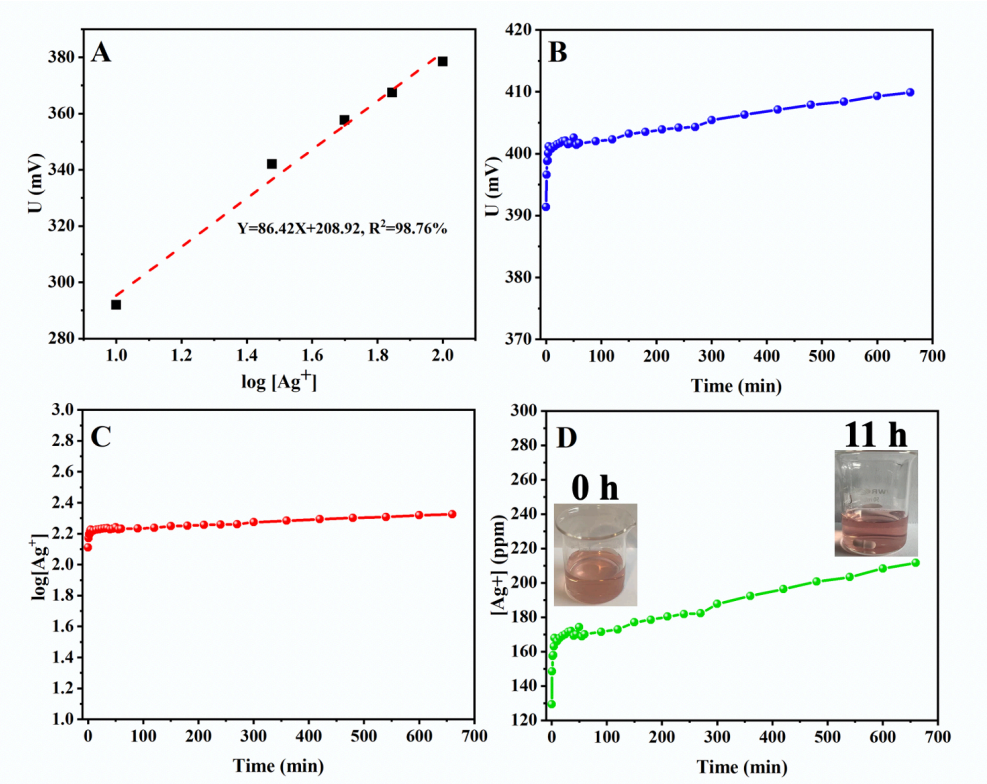
Appendix 6-6 Silver ion titration results of $AgNO_3$ solution



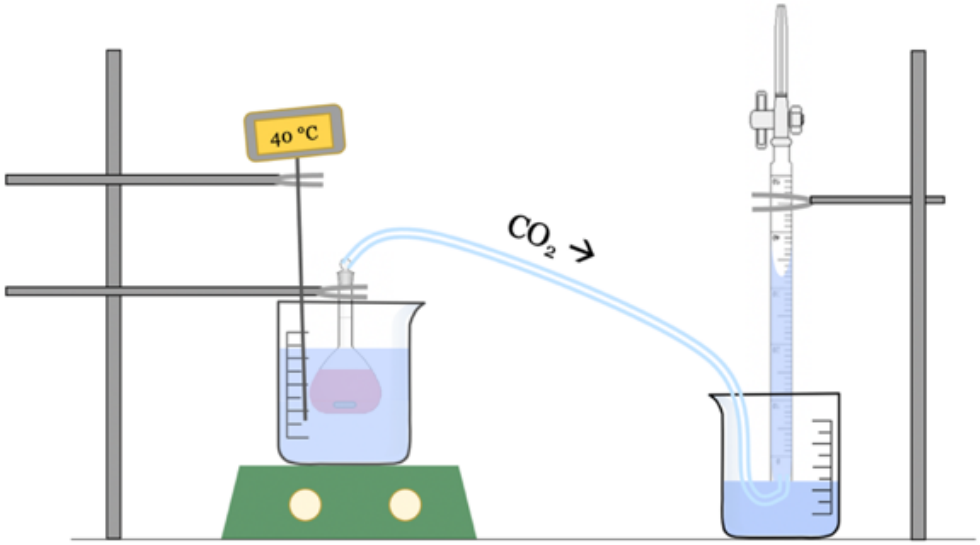
Appendix 6-7 Silver ion titration results of Ag^+ incorporated nanogel (after dialysis in the dark)



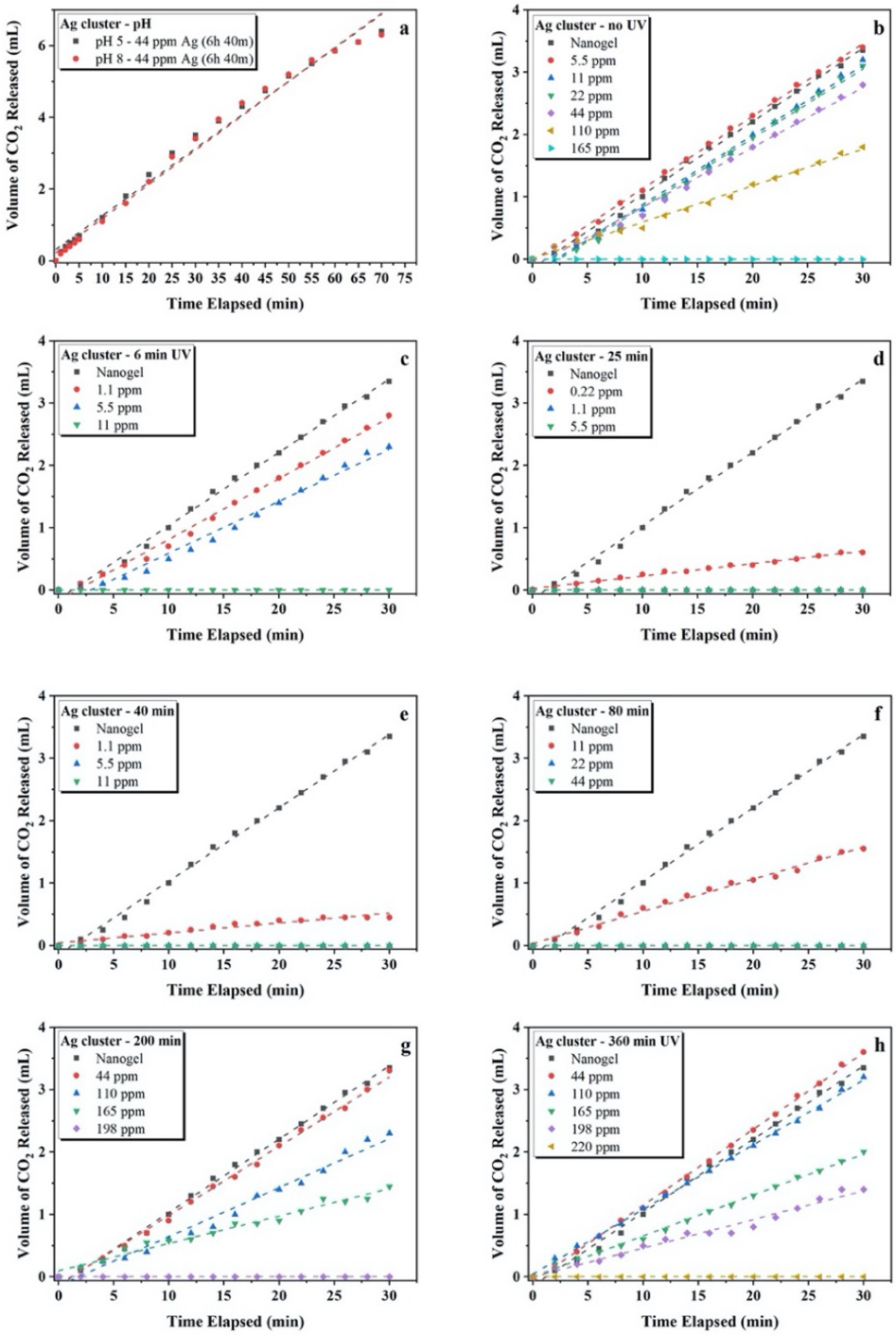
Appendix 6-8 Manual setup of silver electrode analysis



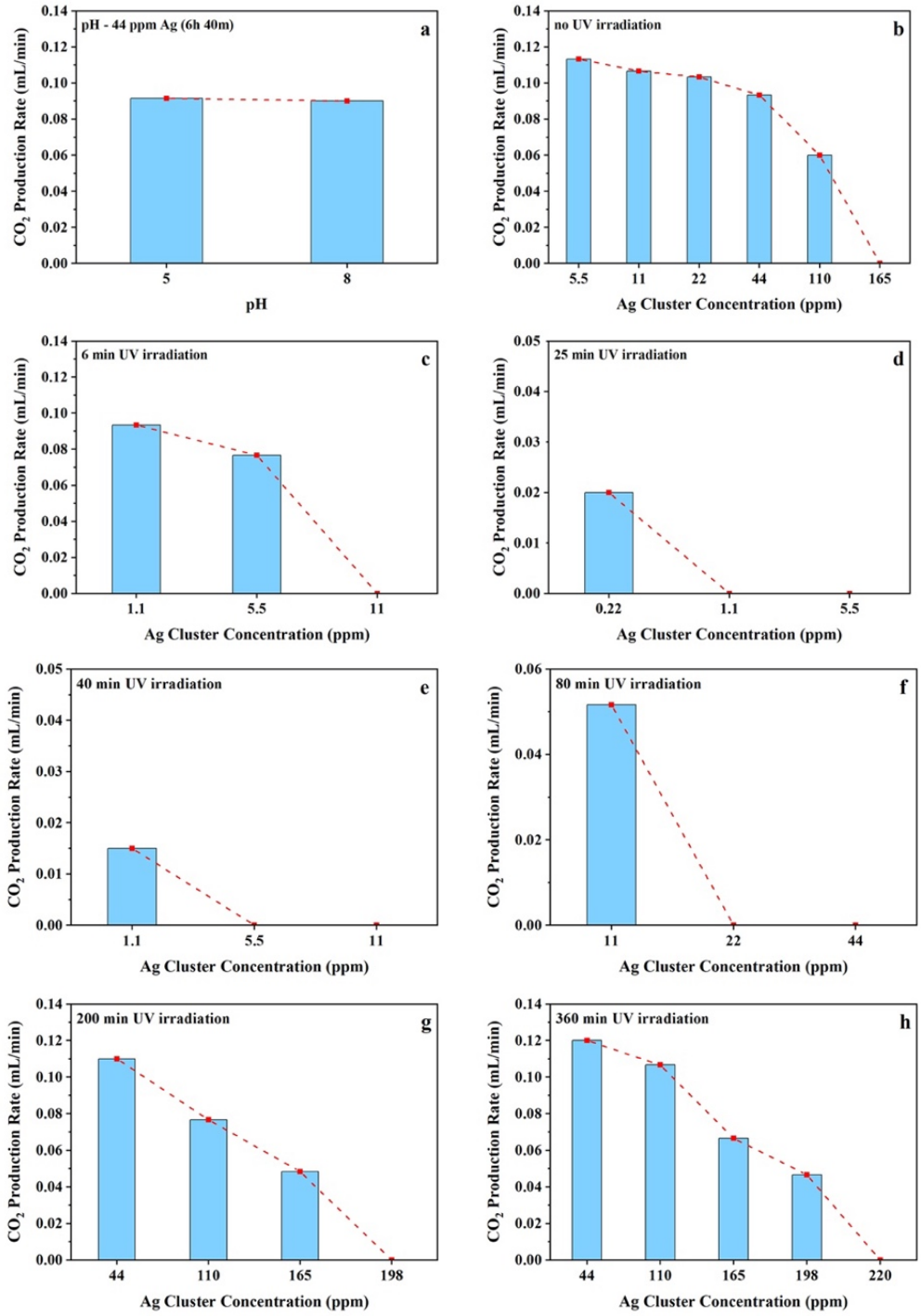
Appendix 6-9 Calibration curve (A), measured value of AgNCs@25min system versus time (B), log[Ag^+] versus time (C) and [Ag^+] versus time (D)



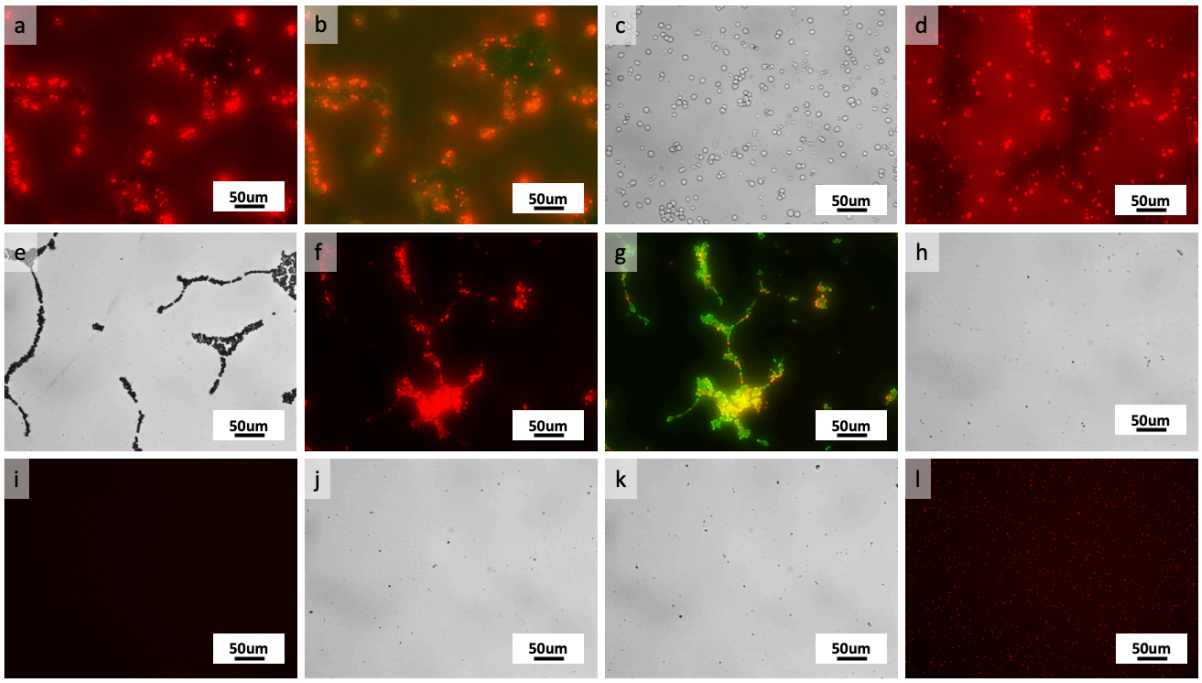
Appendix 6-10 Experimental set-up of yeast test



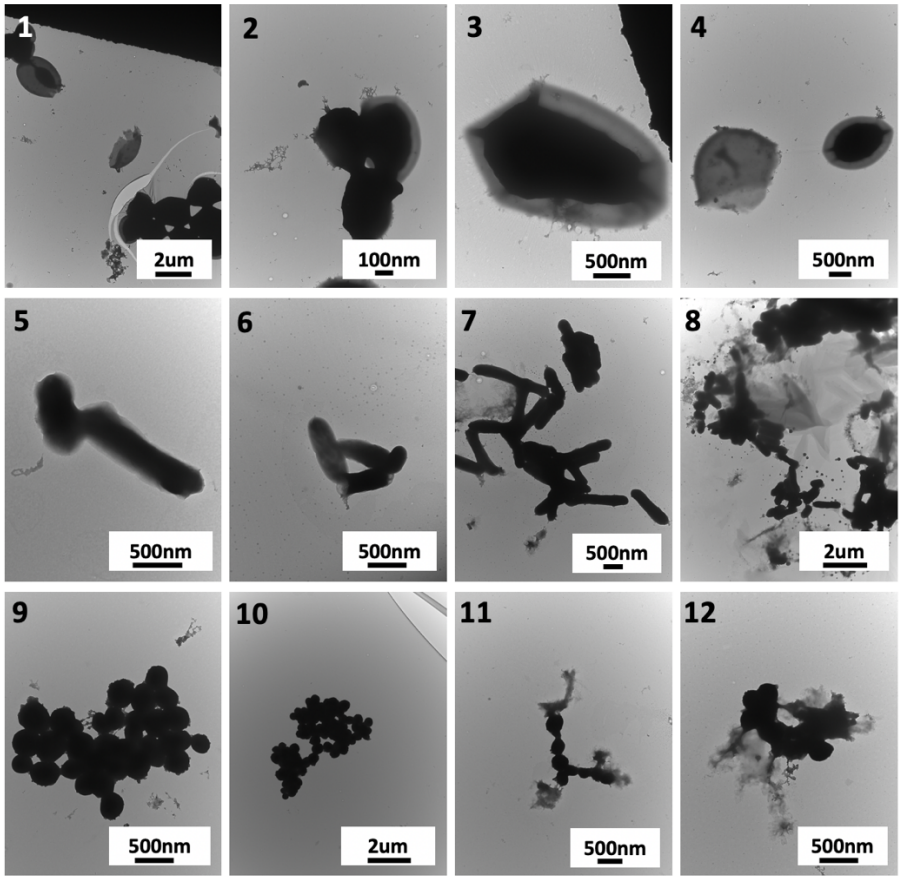
Appendix 6-11 Yeast test with different concentration of Ag-clusters obtained with different UV irradiation time, a: Ag-clusters 360min UV @pH5 and pH 8, b: AgNCs@0min, c: AgNCs@6min, d: AgNCs@25min, e: AgNCs@40min, f: AgNCs@80min, g: AgNCs@200min, h: AgNCs@360min UV irradiation



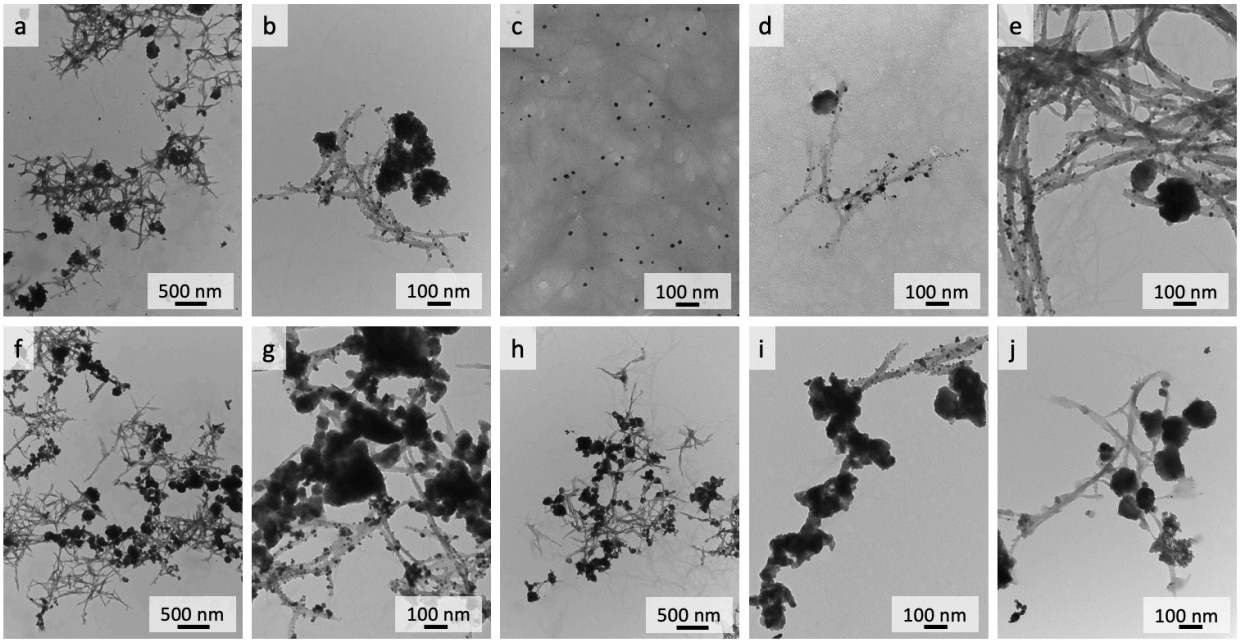
Appendix 6-12 The CO_2 production rate (ml/min) of yeast with AgNCs obtained with different UV irradiation time, a: AgNCs@360min UV @pH5 and pH 8, b: AgNCs@0min UV, c: AgNCs@6min UV, d: AgNCs@25min UV, e: AgNCs@40min UV, f: AgNCs@80min UV, g: AgNCs@200min UV, h: AgNCs@360min UV



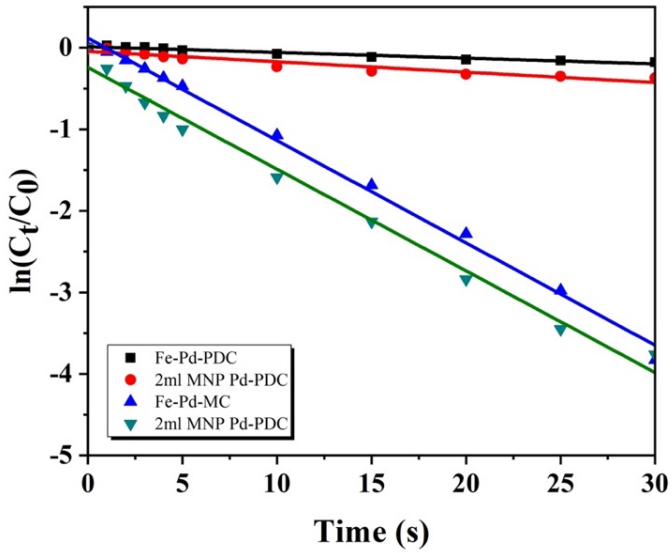
Appendix 6-13 Microscopic image of 8%DAP nanogel treated yeast test sample dyed with MB (washed 2 times) a, b. AgNCs@6min-1.1 ppm yeast test sample dyed with MB c, d. AgNCs@6min-11 ppm yeast test sample dyed with MB e, f, g. AgNCs@0min h, i. AgNCs@ 25min UV j. AgNCs@ 6h UV k, l



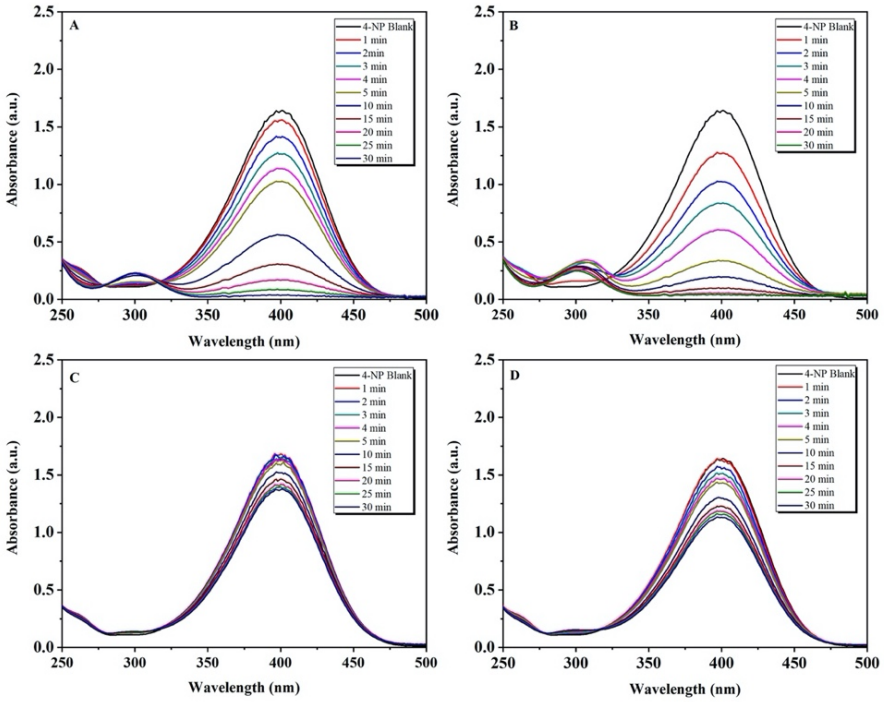
Appendix 6-14 TEM image of yeast test and antimicrobial test sample, yest test with AgNCs@40min (1-4), E · coli with nanogel (5), AgNCs@0min (6), AgNCs@25min (7), AgNCs@360min(8), S · aureus with nanogel (9), AgNCs@0min (10), AgNCs@25min (11), AgNCs@360min(12)



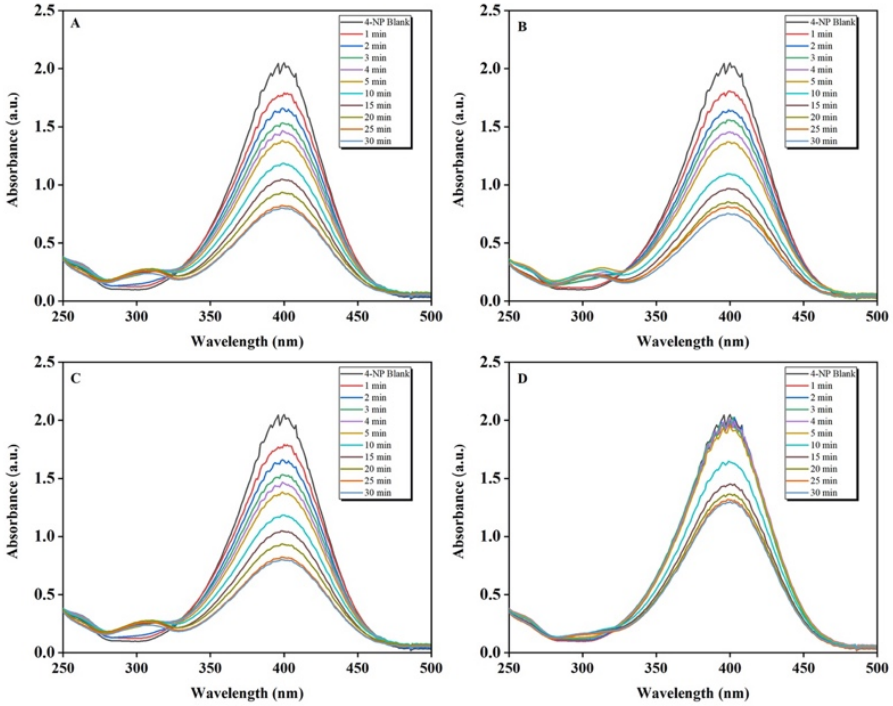
Appendix 7-1 TEM image of Fe-Pd-MC (a, b), 10mg Pd-PDC with extra dopamine (c), 1ml MNP-Pd-MC (d, e), 3ml MNP-Pd-MC (f, g), 4ml MNP-Pd-MC (h, i), 5ml MNP-Pd-MC (j)

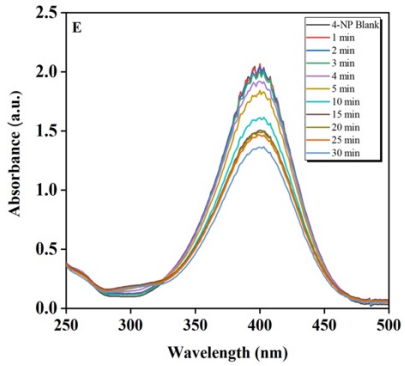


Appendix 7-2 Summary of catalytic reaction rate of four different catalyst: Fe-Pd-MC, 2ml MNP Pd-MC, Fe-Pd-PDC and 2ml MNP Pd-PDC catalyst

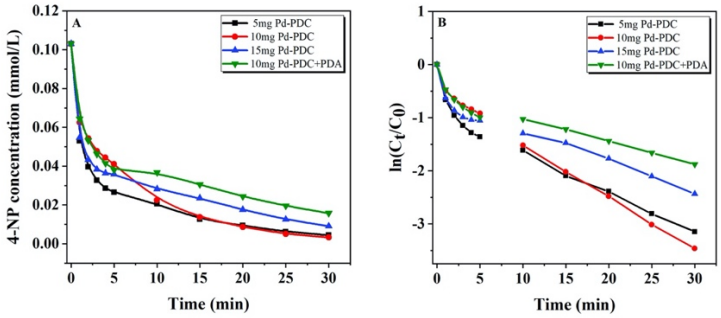


Appendix 7-3 Catalytic test with 4-NP by using Fe-Pd-MC (A), 2ml MNP Pd-MC (B), Fe-Pd-PDC (C) and 2ml MNP Pd-PDC catalyst (D)

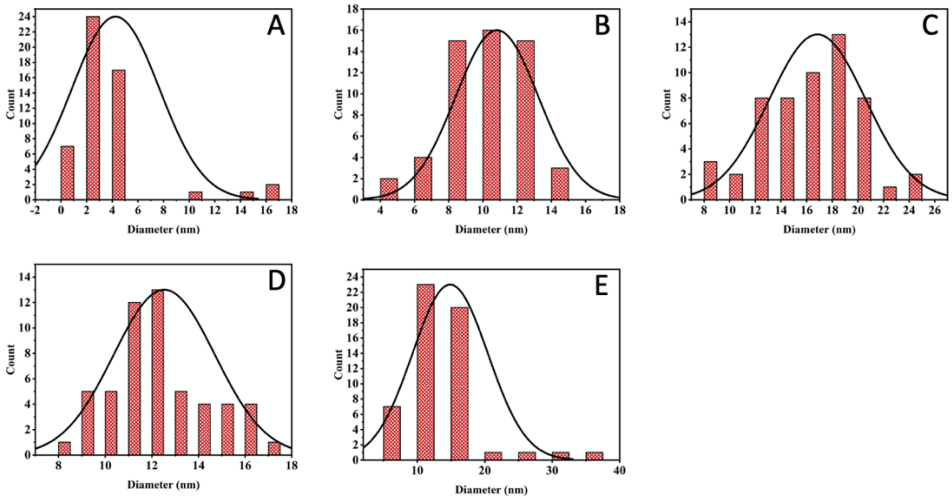




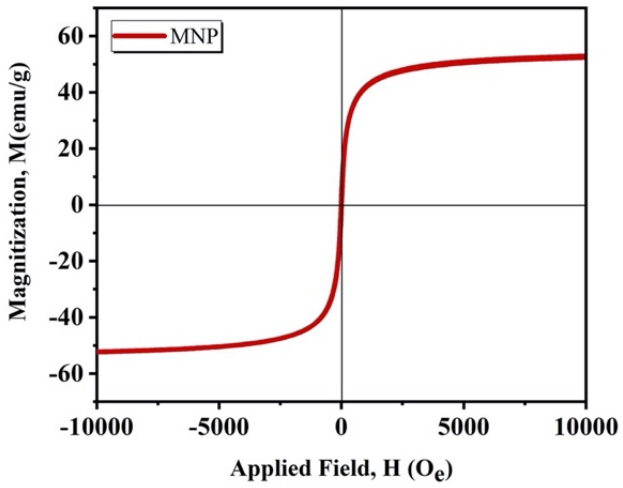
Appendix 7-4 Catalytic performance of 1ml MNP Pd-PDC, 2ml MNP Pd-PDC, 3ml MNP Pd-PDC, 4ml MNP-Pd-PDC, 5ml MNP Pd-MNP



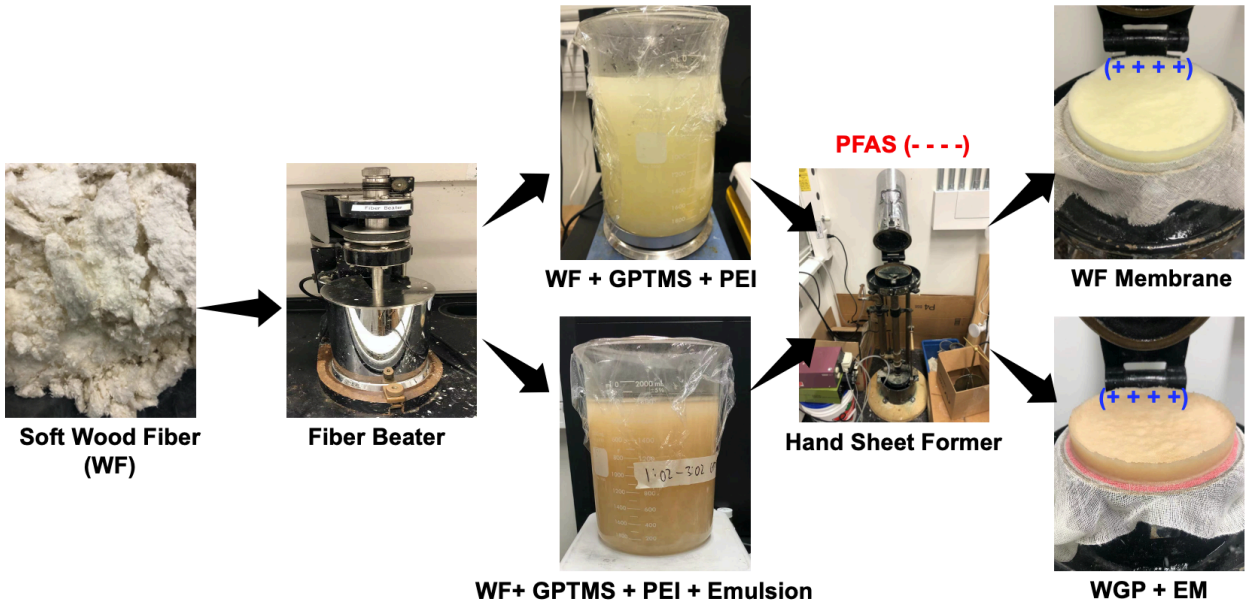
Appendix 7-5 The remaining concentration of 4-NP versus catalytic reaction time by using 5, 10, 15 mg Pd-PDC and 10mg Pd-PDC with extra dopamine (A), 4-NP degradation rate by using 5, 10, 15 mg Pd-PDC and 10mg Pd-PDC with extra dopamine (B)



Appendix 7-6 The size distribution of 5-Pd-PDC (A), 10-Pd-PDC (B), 15-Pd-PDC (C), 10-Pd-PDC+PDA (D) and Pd-MF-CNC (E) obtained by TEM analysis with Image J



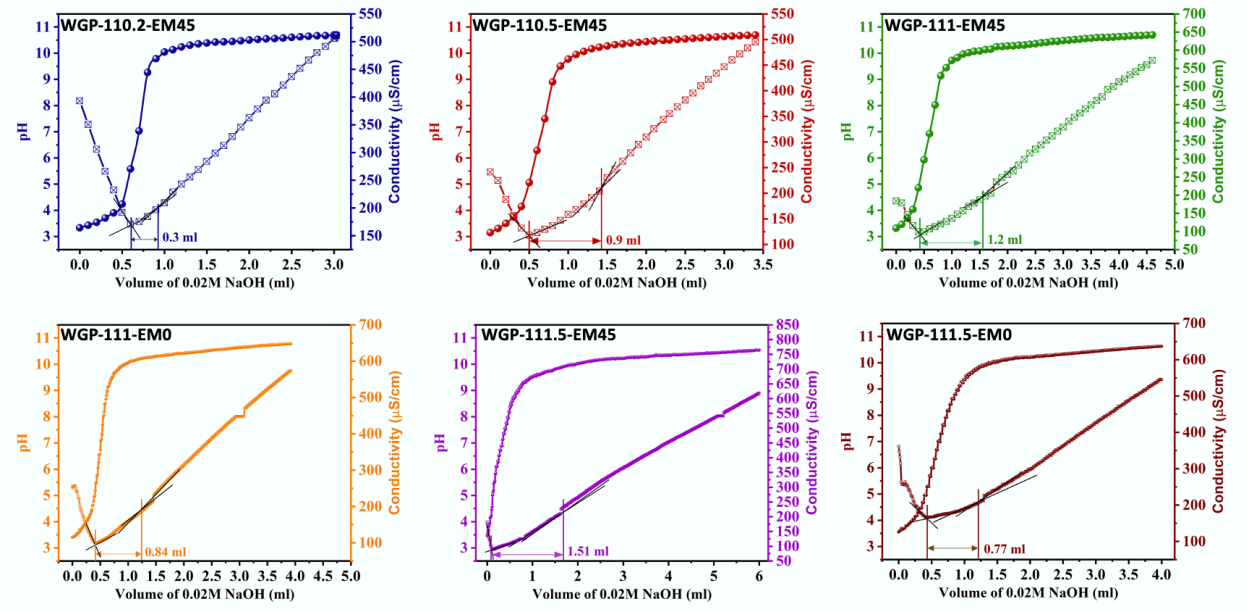
Appendix 7-7 The magnetic hysteresis loops of MNP measured by SQUID at 300 K between -1T and 1T



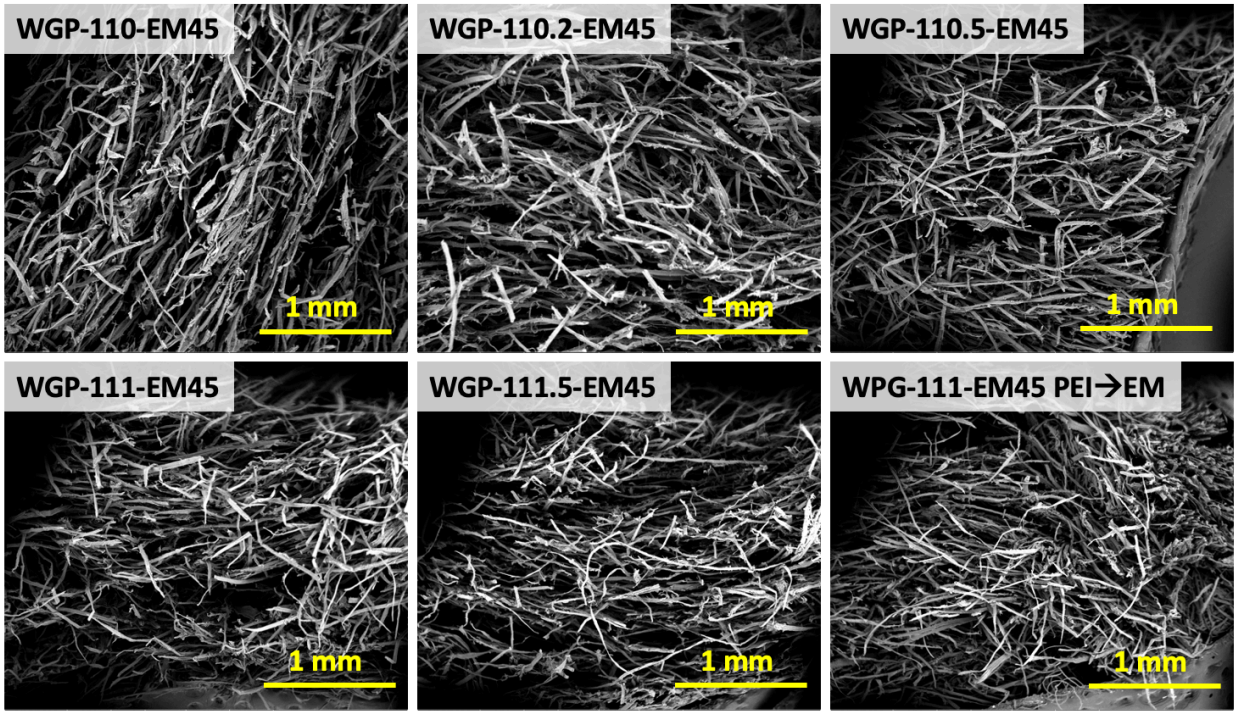
Appendix 8-1 Equipment and process images of the membrane fabrication process



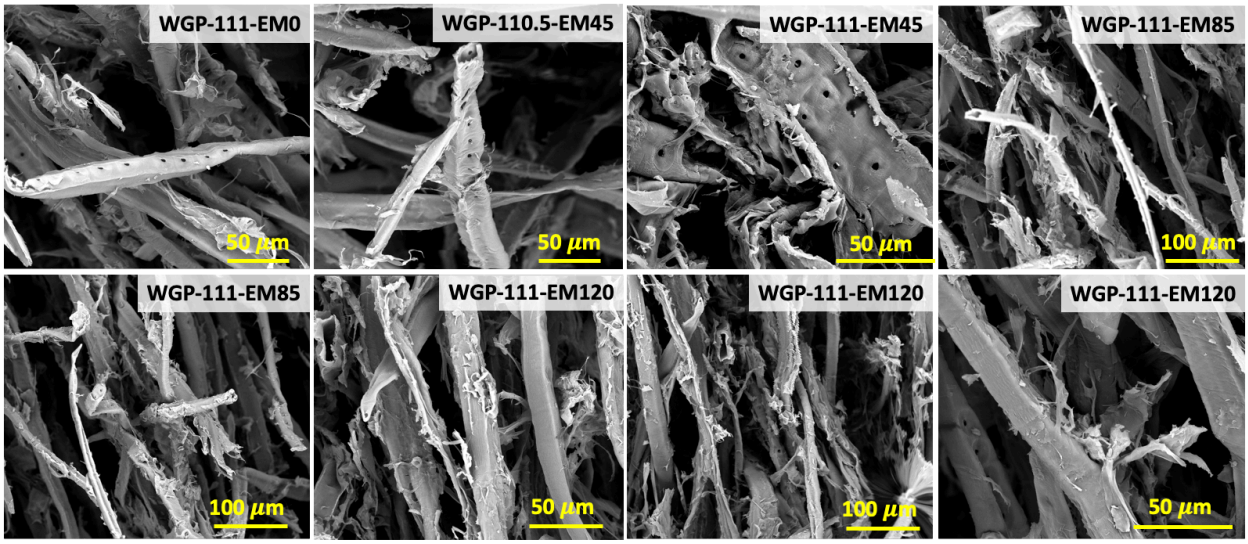
Appendix 8-2 TF-CNC hexane emulsion (0.1-1.5,2wt%) Hexane : TF-CNC = 1:2



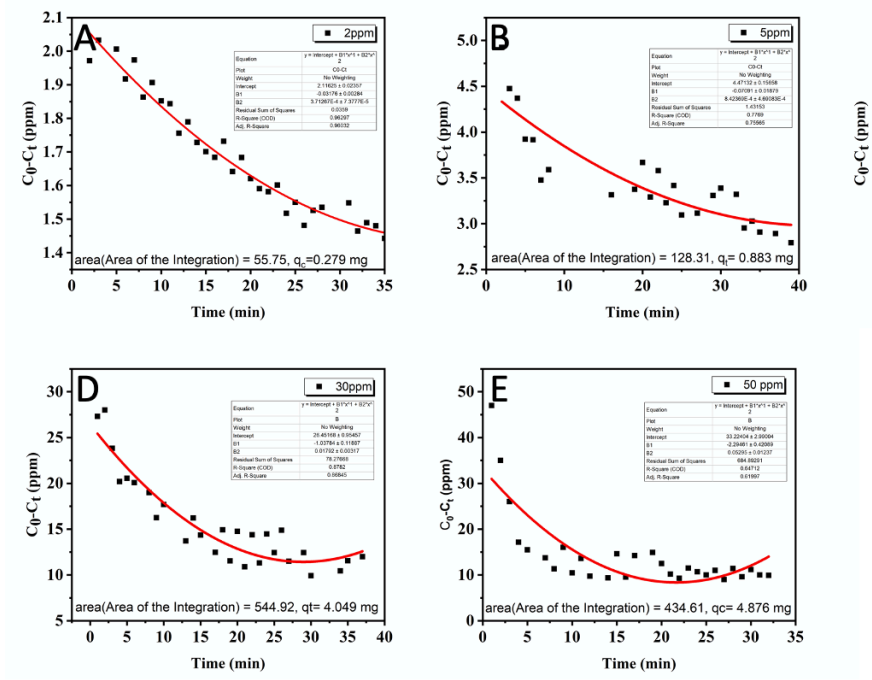
Appendix 8-3 Titration results of WGP-110.2-EM45, WGP-110.5-EM45, WGP-111-EM45, WGP-111-EM0, WGP-111.5-EM45, WGP-111.5-EM0



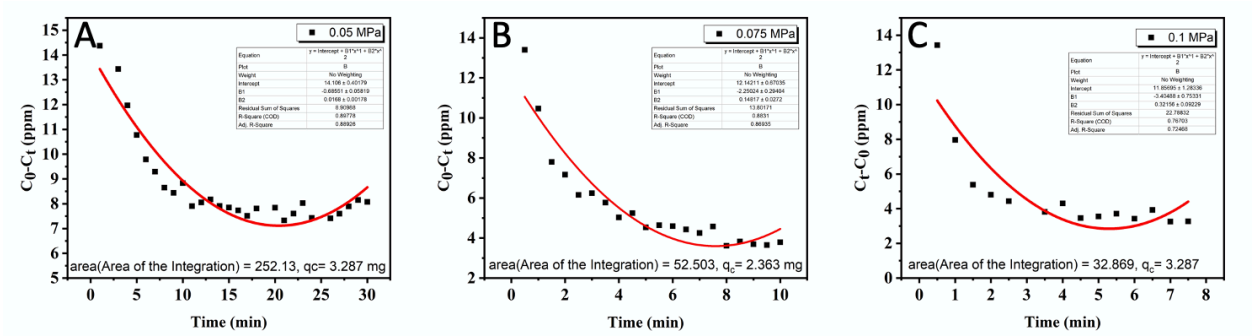
Appendix 8-4 Low magnification SEM images of PEI mass ratio effect on membrane structure (PEI:WF= 0, 0.1, 0.5, 1.0, 1.5)



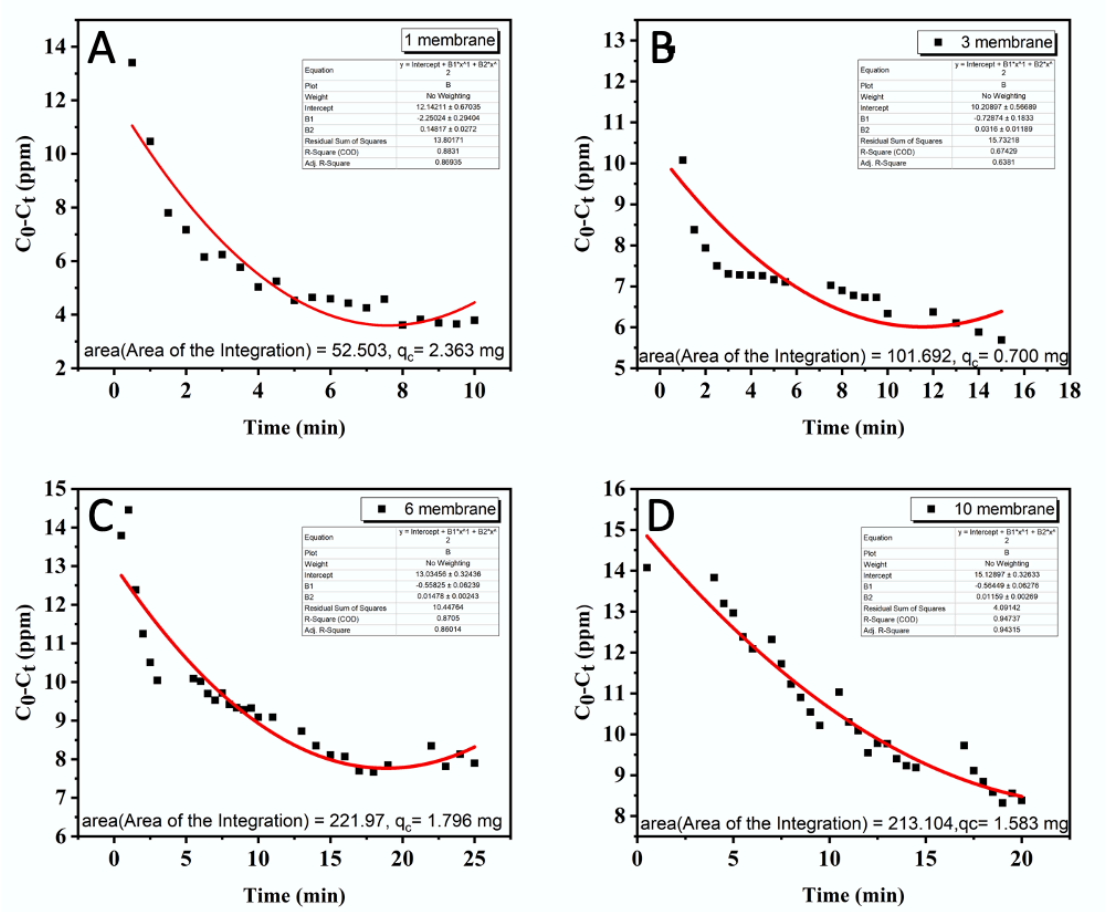
Appendix 8-5 SEM images of WGP-111-EM0, WGP-110.5-EM45, WGP-111-EM45, WGP-111-EM85, and WGP-111-EM120



Appendix 8-6 q_c integration with various MO initial concentration



Appendix 8-7 q_c integration with various pressure drop (flowrate)



Appendix 8-8 q_c integration with various number loaded to the column filtration system